Developing magnetite chemistry as an exploration tool for porphyry copper deposits

Robert Hume Sievwright

Department of Earth Science and Engineering
Imperial College London

submitted in fulfilment of the requirements for the degree of Doctor of Philosophy

Declaration

The work presented in this thesis is my own, except where otherwise acknowledged.

The copyright of this thesis rests with the author and is made available under a Creative Commons Attribution Non-Commercial No Derivatives licence. Researchers are free to copy, distribute or transmit the thesis on the condition that they attribute it, that they do not use it for commercial purposes and that they do not alter, transform or build upon it. For any reuse or redistribution, researchers must make clear to others the licence terms of this work

Abstract

There is increasing interest in the use of magnetite as a geochemical proxy to interpret ore forming processes. Using laser ablation inductively-coupled plasma mass spectrometry (LA-ICP-MS), a large range of trace elements in magnetite are detectable. However, in order to utilise magnetite as a petrogenetic indicator, a comprehensive understanding of the controls of its chemistry is required. Experiments were conducted, both at 1-atm and at high-pressure, investigating magnetite-melt partitioning as a function of oxygen fugacity (fO_2), temperature, bulk composition, pressure and water content.

Magnetite-melt partitioning can be explained in terms of thermodynamic equilibria between magnetite and melt. The presence of magnetite-rich spinel in equilibrium with melt over a range of fO_2 implies a reciprocal relationship between $a(Fe^{2+}O)$ and $a(Fe^{3+}O_{1.5})$ in the melt. This relationship can be used to derive expressions which explain magnetite-melt partitioning as a function of aFe_3O_3(spinel), $XFe^{2+}O$(melt), $XFe^{3+}O_{1.5}$(melt) and fO_2. As a result of this, there is an increase in magnetite-melt partitioning of divalent cations and Cu with increasing fO_2 in silicic, but less so in mafic bulk compositions. There are also strong decreases in magnetite-melt partitioning of 4+ and higher valence cations with increasing fO_2.

A study was conducted to develop a method which optimises the use of LA-ICP-MS to analyse natural magnetite. Using this method, over 2000 magnetite grains, both hydrothermal and igneous, were analysed in rocks associated with porphyry copper systems. Discriminant projection analysis using elements frequently detected using LA-ICP-MS can be used to effectively discriminate various populations of hydrothermal magnetite. Using these discrimination methods, it is possible to distinguish well-mineralised from less-mineralised porphyry ore-forming environments. Igneous magnetite is susceptible to having its chemistry modified by hydrothermal fluids and commonly undergoes oxy-exsolution, which alters its chemistry. Consequently, it is difficult to petrogenetically study the magmatic environment using magnetite associated with porphyry copper systems.

Contents

1 Introduction 14
1.1 Definition of research problem 14
1.2 Porphyry copper deposits 15
1.2.1 Relationship of porphyry copper deposits to arc magmatism 16
1.2.2 The importance of fO_2 in controlling the metal content of arc magmas 23
1.2.3 Indicator minerals for porphyry copper systems 29
1.3 Magnetite chemistry as an indicator mineral for porphyry copper deposits 29
1.3.1 Magnetite chemistry and crystallography 30
1.3.2 Controlling factors and processes on the composition of magnetite 32
1.3.3 Distinguishing hydrothermal magnetite from igneous magnetite 43
1.4 PhD project 44
1.4.1 Experimentally investigating controls on magnetite chemistry 44
1.4.2 Studying the chemistry of natural magnetite from porphyry copper systems 45
2 Titanomagnetite-melt partitioning in an andesitic-dacitic bulk system at 1-atm 47
2.1 Introduction 47
2.1.1 Theoretical background 47
2.2 Experimental procedures 50
2.2.1 Starting compositions 50
2.2.2 Choice of trace elements and doping 50
2.2.3 Magnetite synthesis method 51
2.2.4 Analytical methods 52
2.3 Results 53
2.3.1 Attainment of equilibrium 56
2.3.2 Titanomagnetite-melt partitioning 65
2.4 Discussion 69
2.4.1 Prevailing valence states of elements in the melt 69
2.4.2 Thermodynamic explanation of element partitioning 69
2.4.3 Melt polymerisation 82

2.4.4 Implications for studying natural systems 84

3 Diffusion and partition coefficients in magnetite as a function of fO_2 87

3.1 Introduction 87

3.1.1 Cation diffusion in magnetite 88

3.1.2 Experimental techniques for studying diffusion in minerals 91

3.2 Experimental procedures 91

3.2.1 Experimental technique 93

3.2.2 Analytical technique 94

3.2.3 Experimental conditions 95

3.2.4 Calculation of diffusion and partition coefficients 96

3.3 Results 99

3.3.1 Mt-1 composition 99

3.3.2 Glass composition 100

3.3.3 Partition coefficients 102

3.3.4 Diffusion coefficients 116

3.4 Discussion 124

3.4.1 Controls on magnetite-melt partitioning 124

3.4.2 Diffusion in magnetite as a function of fO_2 136

4 Titanomagnetite-melt partitioning at high-pressure and temperature in an andesitic hydrous bulk system 142

4.1 Introduction 142

4.2 Experimental methods 142

4.2.1 Starting compositions 142

4.2.2 Addition of magnetite seeds 143

4.2.3 Experimental technique 145

4.2.4 Analytical techniques 148

4.2.5 SEM 148

4.2.6 LA-ICP-MS 149

4.3 Experimental Results 150

4.3.1 Determining interface concentrations using LA-ICP-MS 150

4.3.2 Demonstrating that magnetite seed rim concentration is at equilibrium 152
4.3.3 Time series 153
4.3.4 Loss of elements to capsule 154
4.3.5 Pressure series 155
4.3.6 fO_2 series 159
4.3.7 Temperature series 166
4.4 Discussion 173
4.4.1 Titanomagnetite-melt partitioning as a function of fO_2 at elevated pressure 173
4.4.2 Titanomagnetite-melt partitioning at elevated pressure 181
4.4.3 Effect of adding sulphur on magnetite-melt partitioning 182
5 Developing a method for LA-ICP-MS analysis of natural magnetite 183
5.1 Introduction 183
5.2 Analysing grains with exsolution features 184
5.2.1 Determining the internal standard for LA-ICP-MS 184
5.2.2 Incorporating exsolution into LA-ICP-MS analysis 188
5.2.3 Effect of laser spot size and use of different external standards 190
5.2.4 Filtering contamination from other phases 195
5.3 Summary of recommended analytical method 199
6 Geochemistry of magnetite from porphyry Cu systems 201
6.1 Introduction 201
6.2 Analytical method 202
6.2.1 Sample selection and preparation 202
6.2.2 SEM-EDS analysis 207
6.2.3 LA-ICP-MS analysis 207
6.3 Results 208
6.3.1 Petrography 208
6.3.2 Chemistry of magnetite 212
6.4 Discussion 225
6.4.1 Hydrothermal vs. Igneous magnetite 225

6.4.2 Comparing the chemistry of igneous and hydrothermal magnetite 229
6.4.3 Comparison with literature data 232
6.4.4 Discriminant projection analysis 236
6.4.5 Analysing igneous magnetite with exsolution 266
6.4.6 Effect of Hydrothermal Alteration on Chemistry of Igneous Magnetite 266
6.4.7 Using Igneous Magnetite as a Petrogenetic Indicator 267
7 Discussion 274
7.1 Using magnetite as a petrogenetic indicator 274
7.1.1 Discriminating igneous and hydrothermal magnetite 274
7.1.2 Igneous magnetite 275
7.1.3 Hydrothermal magnetite 289
7.2 Advice on how to use magnetite chemistry as an exploration tool 295
7.2.1 Hydrothermal vs. Igneous magnetite 295
7.2.2 Analytical method 297
7.2.3 Vectoring with composition variations 299
7.2.4 Multielement discrimination diagrams 300
7.2.5 Flow chart on how to use magnetite chemistry as an exploration tool 303
7.2.6 Comparing magnetite with other mineral indicators 304
8 Conclusions and future work 307
8.1 Conclusions 307
8.2 Future work 309
Acknowledgements 312
References 314
Appendices 331

List of Figures

Figure 1-1: Cartoon of a subduction zone 18
Figure 1-2: Illustration of the MASH zone 18
Figure 1-3: Alteration zones in a porphyry copper system 21
Figure 1-4: Sulphur speciation curve vs. fO_2 24
Figure 1-5: The variation of FeOtot and Cu as a function of fO_2 for arc-related volcanics 24
Figure 1-6: Igneous magnetite and hydrothermal magnetite in porphyry copper systems. 30
Figure 1-7: Spinel group minerals and stability of Fe-bearing phases in log fO_2 space 32
Figure 1-8: D(Sc) as a function of fO_2 and D(Co) as a function of temperature 34
Figure 1-9: D(V) as a function of fO_2 35
Figure 1-10: D(Co) and D(Mn) as a function of fO_2 36
Figure 1-11: D(Cu) as a function of spinel composition and fO_2 38
Figure 1-12: Discriminant diagrams for Fe-oxides from a variety of deposit types 41
Figure 2-1: LA-ICP-MS spectra for a titanomagnetite analysis 53
Figure 2-2: BSE image of experimental run products 54
Figure 2-3: Comparison of D(Mn), D(Ti) and D(Mg) determined by EPMA and LA-ICP-MS 55
Figure 2-4: Comparions of D values from experiments with different durations 56
Figure 2-5: lnD(Mn), lnD(Co), lnD(Zn), lnD(Ni) and lnD(Cu) vs. lnD(Mg) 65
Figure 2-6: D(Mg), D(Al), D(Ti) and D(V) as a function of logfO_2 67
Figure 2-7: lnD(V), lnD(Zr), lnD(Hf), lnD(Nb) and lnD(Ta) as a function of lnD(Ti) terms 69
Figure 2-8: lnD(Ga) and lnD(Sc) vs. lnD(Al) 75
Figure 2-9: D(Mg), D(Mn) and D(Co) vs. aFe_3O_4(mgt)/$XFe^{2+}O$(melt) 78
Figure 2-10: D(Al), D(Sc) and D(Ga) as a function of $aFe_3O_4(mgt)^{0.5}/XFe^{3+}O_{1.5}$(melt). 80
Figure 2-11: D(Ti) and D(Nb) vs. terms including aFe_3O_4(mgt), $XFe^{3+}O_{1.5}$(melt) and fO_2 81
Figure 2-12: D(Mn) vs. NBO/T and optical basicity 83
Figure 2-13: Melt $Fe^{2+}O$ (wt. %) and SiO_2 (wt. %) as a function of NBO/T 84
Figure 2-14: Titanomagnetite MnO vs. V from GEOROC 85
Figure 3-1: Fe diffusion coefficient in magnetite with fO_2 and T 90
Figure 3-2: Diffusion coefficient for Fe, Co, Cr, Al and Ni with fO_2 in magnetite 91
Figure 3-3: Geometry of experimental products and analytical procedure 96
Figure 3-4: Representative diffusion profiles for Mn, Zn, Ni, Sc, U and Lu 98
Figure 3-5: Comparison of partition coefficients with Wijbrans et al. (2015) 102
Figure 3-6: K(Li), K(Co) and K(Sc) as a function of fO_2 113
Figure 3-7: K(Mo), K(V) and K(U) as a function of fO_2 115
Figure 3-8: Example of analytical traverse for Si 117

Figure 3-9: Examples of analytical traverses for In with fO_2 118
Figure 3-10: Comparison of log D values from experiments over different durations 118
Figure 3-11: Predicted cation diffusion coefficients with fO_2 at 1150°C 120
Figure 3-12: Cation diffusion coefficients with fO_2 121
Figure 3-13: lnK(Cu) vs lnK(Li) 124
Figure 3-13: lnK(Mn), lnK(Co), lnK(Zn), lnK(Ni) and lnK(Ca) vs. lnK(Mg) 124
Figure 3-15: lnK(Cu) vs. lnK(Mg) 126
Figure 3-16: lnK(Al), lnK(Ga), lnK(Cr), lnK(Y) and lnK(Lu) vs. lnK(Sc) 127
Figure 3-17: lnK(Sc) and lnK(Ga) vs. lnK(Al) 128
Figure 3-18: lnK(Zr), lnK(Hf), lnK(Nb), lnK(Ta) and lnK(V) vs. lnK(Ti) terms 129
Figure 3-19: lnK(U), lnK(W) and lnK(Mo) vs. lnK(Ti) 130
Figure 3-20: K(Mg), K(Mn) and K(Co) vs. aFe_3O_4(mgt)/$XFe^{2+}O$(melt) 132
Figure 3-21: K(Ti), K(Zr) and K(Nb) vs. terms with aFe_3O_4(mgt), $XFe^{3+}O_{1.5}$(melt) and fO_2 133
Figure 3-22: K(Al) and K(Sc) vs aFe_3O_4(mgt)^0.5/$XFe^{3+}O_{1.5}$(melt) 133
Figure 3-23: Magnetite-melt partition coefficients vs. ionic radius 136
Figure 3-24: The logarithm of D_V^0 vs. various parameters 136
Figure 3-25: The logarithm of D_i^0 vs. various parameters 136
Figure 3-26: log D_i^0 vs. log D_V^0 141
Figure 4-1: Assemblies used in piston cylinder experiments 148
Figure 4-2: BSE image of experimental run products showing analytical traverse 150
Figure 4-3: Si concentration with distance from the magnetite-melt interface 151
Figure 4-4: Ti concentration with distance from the magnetite-melt interface 152
Figure 4-5: Lu concentration with distance from the magnetite-melt interface 152
Figure 4-6: Comparing magnetite concentrations determined with EPMA and LA-ICP-MS 153
Figure 4-7: Comparison of D values from experiments with different durations 154
Figure 4-8: Analytical total determined with EPMA for glass phase as a function of P 155
Figure 4-9: BSE image showing the presence of Re and ReO_2 in buffer phases 156
Figure 4-10: BSE images of experiments in the pressure series 158
Figure 4-11: BSE images showing the presence of buffer phases in NNO and MH experiments 159
Figure 4-12: Titanomagnetite cpfu for Al, Mg, Mn, Fe^{3+}, Fe^{2+} and Ti as a function of fO_2 160
Figure 4-13: Effect of fO_2 on D(Mg), D(Mn), D(Zn), E(Co), D(Ni) and D(Cu) at pressure 162
Figure 4-14: Partition coefficients for 3+ and higher valence cations vs. fO_2 at pressure 163
Figure 4-15: BSE images of experimental products in the fO_2 series at 960°C 164
Figure 4-16: BSE images of experimental products in the fO_2 series at 920°C 165
Figure 4-17: BSE image of experimental products using starting material with added FeS 166
Figure 4-17: D(Mg), D(Mn), D(Co) and D(Ni) plotted against aFe_3O_4(mgt)/$XFe^{2+}O$(melt). 166

Figure 4-19: D(Cu) plotted against $a Fe_3O_4$(mgt)*fO_2^0.25/$XFe^{2+}O$ (melt) 175
Figure 4-20: D(Ti), D(Zr) and D(Nb) vs. terms with aFe3O4(mgt), $XFe^{3+}O_{1.5}$(melt) and fO_2 176
Figure 4-21: lnD(Zr), lnD(Hf), lnD(Nb) and lnD(Ta) vs. lnD(Ti) 177
Figure 4-22: D(Al) and D(Sc) plotted against $a Fe_3O_4$(mgt)^0.5/$XFe^{3+}O_{1.5}$(melt) 178
Figure 4-23: D(V) as a function of fO_2 179
Figure 4-23: Comparison of measured and predicted values of D(V) 180
Figure 4-24: Diagram illustrating the effect of increasing pressure on D(mgt-melt) 180
Figure 5-1: BSE and 'ImageJ' processed image of natural magnetite with exsolution 186
Figure 5-2: Spot size vs. Mg, Al, Ti, Mn, Ni, Mo and In in magnetite with exsolution 189
Figure 5-3: Element concentrations in BC28 vs. spot size 193
Figure 5-4: Bias for concentrations in BC28 determined using different external standards 194
Figure 5-5: LA-ICP-MS spectra illustrating the effect of a zircon inclusion in magnetite. 195
Figure 5-6: Scatter plots showing evidence for contamination in LA-ICP-MS analyses. 196
Figure 5-7: Flow chart describing how to filter analyses with contamination 198
Figure 6-1: World map showing location of samples used in this study. 206
Figure 6-2: BSE images showing textures in igneous magnetite. 210
Figure 6-3: BSE and RL images showing textures in hydrothermal magnetite 211
Figure 6-4: BSE images showing textures observed in replacement hydrothermal magnetite 212
Figure 6-5: Comparison of Ti in magnetite determined using LA-ICP-MS and SEM-EDS. 213
Figure 6-6: Scatterplots showing trends in hydrothermal magnetite compositions 216
Figure 6-7: Scatterplots showing trends in igneous magnetite compositions 219
Figure 6-8: Scatterplots showing trends in igneous magnetite compositions 220
Figure 6-9: Box and whisker plot comparing element contents in ilmenite and magnetite 220
Figure 6-10: Geological map and samples from Rosia Poieni 221
Figure 6-11: Sc, Sn, Cr and Sr vs. Ti content in igneous magnetite from Rosia Poieni 222
Figure 6-12: Zr, Nb, Hf and Ta vs. Ti content in igneous magnetite from Rosia Poieni 223
Figure 6-13: Mg, Al and Co vs. Ti content in igneous magnetite from Rosia Poieni 223
Figure 6-14: Zn, Mn, Cu and Ni vs. Ti content in igneous magnetite from Rosia Poieni 224
Figure 6-15: Ga, Ge, V and Mo vs. Ti content in igneous magnetite from Rosia Poieni 225
Figure 6-16: Normal probability plot for Ti in magnetite using all LA-ICP-MS data 226
Figure 6-17: Normal probability plot for Ti for a subset of samples from separate systems 228
Figure 6-18: Box and whisker plot of element contents in different forms of magnetite 230
Figure 6-19: Box and whisker plot of element contents in different forms of magnetite 230
Figure 6-20: Box and whisker plot of element contents in different forms of magnetite 231
Figure 6-21: Box and whisker plot comparing Bi content in different forms of magnetite 231
Figure 6-22: Diagram for the discrimination of magnetite from different deposit types 233

Figure 6-23: Plot of Sn vs. Ga for magnetite discrimination....234
Figure 6-24: Ti vs. Ni/Cr plot to discriminate igneous and hydrothermal magnetite....235
Figure 6-25: Failure of Ti vs. Ni/Cr plot to separate igneous from hydrothermal magnetite 235
Figure 6-26: Discriminant diagram to identify alteration type 239
Figure 6-27: Discriminant diagram to identify metal association (potassic altered only)....243
Figure 6-28: Box and whisker plot comparing magnetite from different metal assocations. 244
Figure 6-29: Li content vs. DP-B-1 and Sb content vs. DP-B-2 245
Figure 6-30: Discriminant diagram to identify metal association (all alteration) 247
Figure 6-31: Location of the central Wasatch Mountains and Bingham Canyon 247
Figure 6-32: East-West cross section across the Central Wasatch mountains. 250
Figure 6-33: Geological map of the central Wasatch Mountains 250
Figure 6-34: Estimate of depth and geochronology of intrusions in C. Wasatch mountains 251
Figure 6-35: DP-C-2 vs. DP-C-1 for samples from c. Wasatch Mountains and Bingham 252
Figure 6-36: DP-D-2 vs. DP-D-1 to categorise metal endowment. 255
Figure 6-37: Test of DP-D-1 vs. DP-D-2 to categorise endowment for all data....256
Figure 6-38: Alteration discriminant diagram (DP-A-2 vs. DP-A-1) with potassic cut-off....257
Figure 6-39: Metal association discriminant diagram for PoCu-prospects and background 258
Figure 6-40: Discrimination diagram to classify size of PoCuMo system....260
Figure 6-41: Discrimination diagram to classify size of PoCuAu system....263
Figure 6-42: Box and whisker plot comparing magnetite compositions in PoCuAu deposits 264
Figure 6-43: Titanomagnetite data plotted on DP-A-2 vs. DP-A-1 and DP-C-2 vs. DP-C-1....265
Figure 6-44: BSE-SEM images of coexisting igneous magnetite and ilmenite pairs....265
Figure 6-45: Box and whisker plots of relative redox ratios in igneous magnetite....271
Figure 6-46: Box and whisker plot for Al, Ga, Sn, Ni and Cr contents in igneous magnetite 272
Figure 7-1: Compilation of magnetite-melt partition coefficients from experiments 287
Figure 7-2: Relative redox ratios in magnetite vs. whole rock MgO....287
Figure 7-3: Magnetite and coeval melt inclusion within a quartz phenocryst....287
Figure 7-4: Robust linear regressions of D values vs. thermodynamic expressions....287
Figure 7-5: Comparing different techniques for estimating % of hydrothermal magnetite 287
Figure 7-6: % of hydrothermal magnetite vs. Ti content of igneous magnetite....287
Figure 7-7: Use of magnetite associated with porphyry copper systems in exploration....300
Figure 7-8: Discriminant diagram to classify alteration in Pisiak et al. (2017) 302
Figure 7-9: Flow chart describing how to use magnetite chemistry as an exploration tool 287
Figure 7-10: Igneous magnetite inclusion in amphibole 305

List of Tables

Table 2-1: Major element composition of experimental starting materials 50
Table 2-2: Experimental conditions 51
Table 2-3: Glass and titanomagnetite major element composition and partition coefficients 57
Table 2-4: Glass and titanomagnetite trace element composition and partition coefficients 62
Table 2-5: Values of a_M^0 and a_M^1 for non-linear least-squares models 77
Table 3-1: Experimental conditions 95
Table 3-2: Composition of magnetite crystal (Mt-1) prior to annealing 100
Table 3-3: Starting composition and final glass composition for some experiments 100
Table 3-4: Diffusion coefficients, c_i, c_0, glass concentration and partition coefficients 103
Table 3-5: D_v^0, D_i^0, minimum log fO_2 and D for cations in magnetite 123
Table 3-6: Values of a_M^0 and a_M^1 for non-linear least-squares models 131
Table 3-7: Values of E and K_0 as a function of fO_2 for trivalent cations 135
Table 4-1: Composition of experimental starting materials 144
Table 4-2: Experimental conditions 146
Table 4-3: Phases present in experiments 157
Table 4-4: Glass and titanomagnetite major element composition and partition coefficients 167
Table 4-5: Glass and titanomagnetite trace element composition and partition coefficients 170
Table 5-1: Composition of exsolved magnetite, exsolution and bulk Fe-Ti oxide 187
Table 5-2: Recommended analytical conditions for LA-ICP-MS of natural magnetite 200
Table 6-1: List of deposits and samples studied 200
Table 6-2: Analyses above limit of detection in hydrothermal magnetite 215
Table 6-3: Analyses above limit of detection in igneous magnetite 217
Table 6-4: Results of DPA to categorise magnetite according to alteration style 238
Table 6-5: Results of DPA to classify metal association in potassically altered rocks 242
Table 6-6: Results of DPA to classify metal association in all alteration types 246
Table 6-7: Results of DPA to classify porphyry endowment using magnetite from Utah, USA 254
Table 6-8: Results of DPA to classify size of PoCuMo system in potassically altered rocks 259
Table 6-9: Results of DPA to classify size of PoCuAu system in potassically altered rocks 262
Table 6-10: T and fO_2 estimates using 'two-oxide' oxybarometry 269
Table 6-11: Estimate of Cu contents in melt in a selection of unaltered volcanic samples 273
Table 7-1: Summary of controls of magnetite-melt partitioning 277
Table 7-2: Diffusion rates of Mg in silicate phases compared with magnetite 293

1 Introduction

1.1 Definition of research problem

Porphyry copper deposits represent the world's main source of copper. These deposits are large anomalies of sulphide-hosted copper mineralisation and owe their origin to magmatic-hydrothermal phenomena associated with the emplacement of hydrous intermediate to felsic complexes in the upper crust (Sillitoe, 2010). The magmatic stage represents a critical step in the evolution of porphyry copper systems, however, the exact conditions conducive to form significant mineralisation are still a matter of debate. Some have emphasised the importance of high magmatic water contents in order to release sufficient hydrothermal fluids (Williamson et al., 2016), whereas others have suggested interaction with a more mafic sulphur rich magma is the key trigger, enabling an abundance of sulphide ore minerals to form (Blundy et al., 2015). Notwithstanding, large economic porphyry copper deposits are particularly rare and barren intrusions are the norm, which suggests that the magmatic environment permitting the formation of a significant porphyry ore body to also be anomalous. Comparison of the geochemical characteristics associated with mineralised and barren terranes could be used to identify specific geochemical signals, which could in turn be used to filter out areas with low potential to form an economic deposit, so that exploration can be focussed on more prospective fertile regions.

Magnetite and other Fe-Ti oxides have been recognized as potential indicator minerals in mineral deposits. Magnetite is relatively resistant to mechanical breakdown and chemical alteration and forms in a wide variety of geologic environments. Moreover, a very large range of trace elements can be incorporated into magnetite at levels detectable using modern analytical techniques (e.g. Dare et al., 2012). A number of studies have shown that trace elements in Fe-Ti oxides can be used as a means to determine the provenance of the Fe-Ti oxides (e.g. Dupuis and Beaudoin, 2011; Dare et al., 2014). Magnetite is an ubiquitous accessory mineral in porphyry Cu systems. Importantly, both magmatic magnetite, crystallising at high temperature from silicate melts, and hydrothermal magnetite precipitating at low temperature from hydrothermal fluids can form. Thus, the two types of magnetite can serve as geochemical proxies to interpret both magmatic and hydrothermal processes involved in the formation of porphyry copper deposits.

Consequently, I have investigated the potential application of magnetite as a tool in mineral exploration. The chemistry of magnetite, both igneous and hydrothermal, associated with a large variety of porphyry copper systems world-wide has been studied, in search geochemical signals in magnetite that reflect conditions conducive for forming porphyry copper deposits. Such proxies could thereby provide an effective tool to aid discovery of new porphyry copper deposits

and enhance our ability to distinguish mineralised from barren porphyry intrusions at an early stage in exploration. The study of natural magnetite chemistry is corroborated by experimental work, investigating controls on the chemistry of a large range of trace elements in magnetite as a function of oxygen fugacity (fO_2), temperature, bulk composition, pressure and water content.

1.2 Porphyry copper deposits

Porphyry copper deposits constitute our main source of copper, molybdenum and rhenium and also contribute significant resources of gold and other rare metals (Sillitoe, 2010). These form at depths of 1-6 km below the palaeosurface, and owe their origin to magmatic-hydrothermal phenomena associated with the emplacement of hydrous intermediate to felsic intrusive complexes (Richards, 2003; Seedorff et al., 2005; Hedenquist and Lowenstern, 1994). Most porphyry-style deposits are constructed at convergent plate margins in supra-subduction settings, where hydrous melts are generated in the subarc mantle (Richards, 2003). From here, oxidised melts transport metals and volatiles to magma chambers located in the upper crust, where fractional crystallisation and decompression drive the exsolution of magmatic-hydrothermal fluids composed largely of water and chloride salts. Such fluids are typically enriched in ore metals and sulphur, and may form an ore deposit if the fluid becomes supersaturated and precipitates ore minerals in a relatively small volume of rock (Sillitoe, 2010).

All porphyry deposits share that they are related spatially, temporally and chemically to intermediate to felsic silicate magma intrusions in the Earth's upper crust. In order to maximise metal contents of the parental magma, and ultimately the exsolved fluid phase, it is important that the primary magmas are water rich (>4 wt % H_2O), have a high sulphur and chlorine content, and are highly oxidised (Sillitoe, 2010). Water-rich magmas reach water saturation at an earlier stage, which minimises loss of metals to crystallising phases whilst facilitating transport of chloride and copper to the exsolving aqueous phase (Cline, 1995). High sulphur and chlorine contents offer complexing agents for ore metal transport, increasing metal solubility in exsolved aqueous phases (Cline, 1995). Notably, a high oxidation state of the magma is advantageous as this increases sulphur solubility as SO_4^{2-}. This inhibits early precipitation of magmatic sulphides which would scavenge chalcophile elements, such as Cu and Au, prior to arrival at the trap site; consequently, an oxidised magma maximises metal availability at the hydrothermal stage.

Once a shallow-crustal magma chamber is established, porphyry copper mineralisation depends on a series of concentration processes during the ensuing hydrothermal stage. Mineralisation is associated with magmatic aqueous fluids exsolved from the crystallising batholith during the transition from a magmatic to a high-temperature hydrothermal system (Sillitoe, 2010). The physical state of the exsolved ore fluid is dictated by the Cl/H_2O in the melt, and the prevailing

pressure and temperature at the time of volatile saturation (Shinohara, 1994; Candela and Piccoli, 2005). The multiple generations aqueous fluids generate large volumes of hydrothermally altered rock and may result in mineralisation, typically associated with hydrothermal veins, but also commonly disseminated throughout the altered rock mass.

1.2.1 Relationship of porphyry copper deposits to arc magmatism

Intermediate arc magmas originate in the mantle wedge overlying subduction zones, located at the junction of two converging tectonic plates. During subduction, the denser plate sinks deep into the mantle and dehydrates under increasing pressure. Upon dehydration, aqueous fluids carrying 'fluid-mobile' elements are released to the overlying mantle wedge, enriching it in volatiles, sulphur, silica and fluid-mobile large ion lithophile elements (LILE). Metasomatism, in particular hydration, of the mantle wedge lowers the mantle solidus temperature, thereby triggering fluid fluxed melting (Figure 1-1). The resultant flux of basaltic magma, chemically seasoned by fluid addition from the subducting slab, ultimately solidifies and is the main mechanism for the creation of continental crust (Tatsumi and Eggins, 1995; Kay, 1980).

Intermediate andesitic magmas represent the largest volume of magma which reaches the upper crust in arc environments (Hildreth and Moorbath, 1988). Traditionally, arc andesites were modelled as direct differentiates from primary mantle melts (e.g. Ringwood, 1977). More recent studies have revealed disequilibrium petrographic characteristics in andesites, suggesting andesitic magmas could instead be generated via the physical mixing of felsic and mafic components in upper crustal magma chambers (e.g. Reubi and Blundy, 2009). However, there is now overwhelming evidence that andesitic magmas originate at greater depths, and are generated as a result of multiple processes. Such processes include crustal melting and assimilation of primary basaltic magmas, magma ponding at the base of the crust, and magma homogenisation. Collectively, this model has been termed the melting-assimilation-storage-homogenisation (MASH) model, first developed by Hildreth and Moorbath (1988).

Density contrasts are fundamental in explaining the MASH model. In summary, mafic magmas ascend buoyantly from the mantle wedge until they reach the base of the crust, where they pool as a consequence of their elevated density relative to crustal rocks. As the accumulating mafic magma begins to crystallise and fractionate to more evolved compositions, a significant amount of heat is released which causes partial melting of crustal rocks. Consequential mixing between crustal- and mantle-derived magmas results in the development of crystal-mush zones which yield more evolved intermediate (andesitic-dacitic) magmas (Bergantz and Dawes, 1994). These evolved hybrid melts are enriched in volatiles, sulphur, metals and other incompatible elements,

and have densities sufficiently low to buoyantly rise up to the upper crust (Hildreth and Moorbath, 1988). Basaltic magmas are unable to rise through the MASH zone, which acts as a density filter, and basaltic melts are left behind to form mafic cumulates (Figure 1-2). Evidence for 20% partial melting beneath the Andes volcanic arc (e.g. Schilling and Partzsch, 2001) and the presence of mafic and ultramafic cumulates at the crust-mantle boundary (e.g. Greene et al., 2006) provide strong support for the MASH hypothesis. Several workers have since refined the MASH model, and it is envisaged that the chemical diversity in arc magmas is largely acquired through modifications of the MASH process, whereas textural diversity is related to shallow-level crystallisation (Annen et al., 2006).

Compressive tectonism leads to a slowdown in magma ascent, aiding the development of MASH zones in the lower crust over time frames of 3-10 Myr. This allows a cyclic ramp up of incompatible elements and volatiles through multiple events of chamber recharge and fractional crystallisation, generating particularly fertile magmas which may be periodically tapped to shallow crustal magma chambers (Rohrlach and Loucks, 2005). These highly evolved andesitic-dacitic magma have high water contents (> 4 wt. %) which induces fluid exsolution and crystallisation at greater depths permitting magmas to stall in the upper crust and form large parental magma chambers (Richards, 2003). More primitive types of magma, such as arc basalts, may penetrate to the shallow regime, but at times when the MASH zone is less established, for example during a change in dip of the subducting slab. The resultant, relatively dry magmas tend not to stall in the upper crust, but erupt effusively and do not generate large magmatic-hydrothermal systems (Richards et al., 2012).

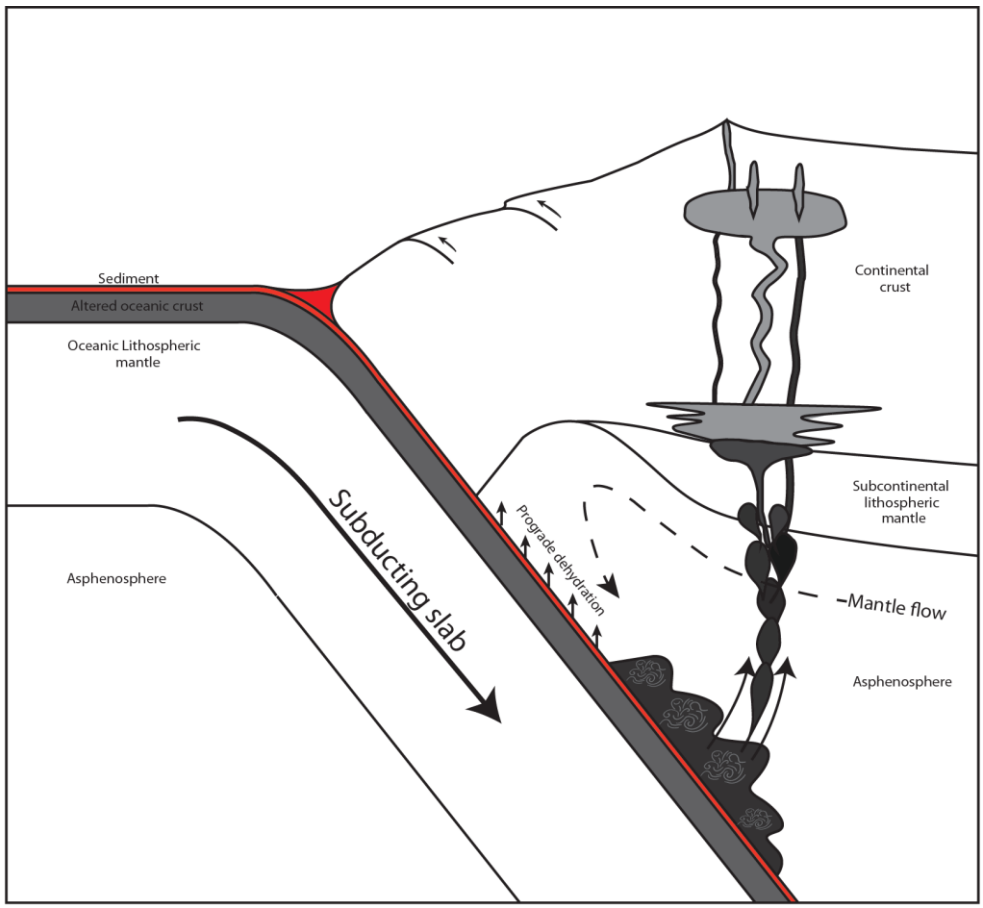


Figure 1-1: Cartoon of a subduction zone illustrating the relationship of porphyry copper deposits to arc magmatism.

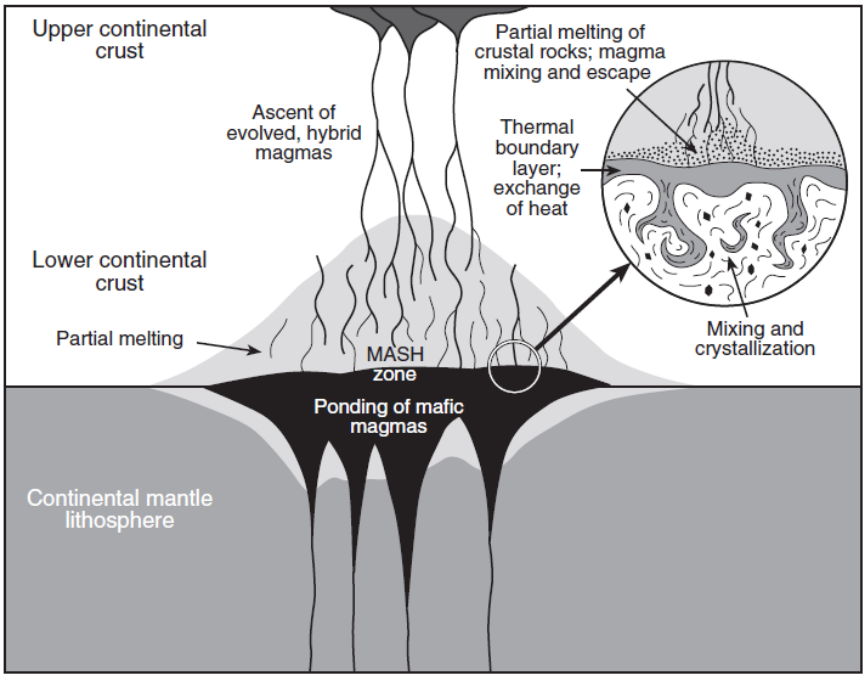


Figure 1-2: Illustration of the MASH zone. Hot, dense primitive magmas pool at the base of the crust and interact with crustal rocks generating less dense, hybrid intermediate magmas (from Richards, 2003).

1.2.1.1 The formation of porphyry copper deposits from intermediate melts

Porphyry copper systems typically span the upper 6 km of the crust, with their centrally located stocks stratigraphically above, and connected to larger parental magma chambers at depths of approximately 5 to 15 km. The parental chambers are believed to be the sources of both the magmas and metal-charged aqueous phase responsible for ore deposition (Sillitoe, 2010). Thus, the formation of such magma chambers appears to be an essential step in the generation of porphyry copper deposits. The formation of large, long-lived parental magma bodies in the upper crust necessitates specific magma influx rates. In order to maintain a large magma body, the magma influx rate needs be sufficiently high to prevent previous magma batches from complete solidification before the next batch arrives, yet not too high that the majority of the magma erupts (Audetat and Simon, 2013).

Richards et al. (2012) have emphasized the importance of high magmatic water contents as a prerequisite for the shallow crustal emplacement of intermediate melts and the generation of ore-forming magmatic-hydrothermal systems. Through a study of several temporally distinct arc systems, they observed that porphyry-related magmas form during the later stages of the arc's history, and are consistently more geochemically evolved and more hydrous, as demonstrated by the presence of hydrous mineral assemblages and high Sr/Y ratios in porphyry-related rocks (Richards et al., 2012). If water contents are too low (< 2 wt. % H_2O), fluid exsolution will not be sufficient to provide the energy to cause extensive fracturing. Nevertheless, it has been suggested that if water contents are greater than 5 wt. % fluid exsolution and melt crystallisation would occur at greater depths than those typically inferred for porphyry deposits (Cline and Bodnar, 1991).

Once the parental magma chambers have been established in the mid-upper crust, they can act as a source of dyke- or pipe-like intrusions that are episodically emplaced to shallower crustal levels; these intrusion events could be triggered by hot mafic intrusions into the main chamber, which induce volatile saturation and the rise of buoyant, bubble-rich magma (Hattori and Keith, 2001). In arc settings, transpressional strain can aid the formation of porphyry intrusions by producing vertical, extensional conduits which are ideal for focusing magma, whilst still maintaining the compression necessary for MASH processes in the lower crust (Brown, 1994; Richards, 2003). In most arcs, volcanism appears to cease prior to formation of a porphyry copper system. Volcanic activity probably inhibits the ability of the magmatic system to produce a porphyry deposit due to loss of water and metals to a volcanic gas phase, which is vented to the atmosphere (Pasteris, 1996).

Convection within the magma provides an efficient mechanism for delivering the aqueous phase from the parental chamber to the porphyry stock, which acts as a conduit for the upward transmission of the fluid (Sillitoe, 2010). Brittle failure will occur when fluid pressures exceed the combined effects of lithostatic load and the tensile strength of the surrounding rock. The transition from lithostatic to hydraulic pressure that may occur on catastrophic rock failure reduces the overall pressure, inducing additional fluid exsolution and crystallisation. Rapid pressure quenching causes groundmass crystallisation, producing the characteristic porphyritic texture from which porphyry deposits derive their name. Cycles of volatile accumulation, brittle failure and fluid release produces the classic vein crosscutting relationship observed in porphyry deposits (Cooke et al., 2013).

1.2.1.2 Hydrothermal alteration and mineralisation

The physical state of the exsolved ore fluid is determined by the Cl/H_2O ratio of the melt and the depth of magma crystallisation, with the latter itself being a function of volatile content, magma temperature and tectonic setting (Shinohara, 1994; Candela and Piccoli, 2005). At higher pressure, the fluid phase exsolved is a single phase, low-salinity (2-10 wt. % NaCl eq.) aqueous fluid, whereas at shallower depths (< 4 km), the fluid phase exists as a two-phase fluid, consisting of a hypersaline brine and a low-density vapour. The two-phase fluid can be produced either by direct exsolution from the melt (Shinohara, 1994), or more typically as a single-phase fluid decompresses, cools and intersects its solvus (Cline and Bodnar, 1991). The brine phase is enriched in Na, K and Fe chlorides which gives rise to high salinities (35-70 wt. % NaCl eq.), whereas the vapour phase is enriched in acidic volatile species, including SO_2, H_2S, CO_2, HCl and HF (Sillitoe, 2010). During phase separation, specific element suites are fractionated between the brine and vapour. Although the brine phase was originally considered to be the dominant phase responsible for metal transport, more recently it has been shown that metals could preferentially partition into the vapour phase in two phase systems (Ulrich et al., 1999). The relative importance of brine and the vapour in metal transport is a topic of ongoing research.

i Alteration

As the exsolved aqueous fluids extend into the adjacent rock, they generate a range of distinctive styles of hydrothermal alteration with characteristic mineral assemblages, both within the ore zones and extending into a larger volume (>10 km^3) (Meyer and Hemley, 1967). The style of alteration depends on the chemistry and temperature of the fluids, and the chemistry of the wall rock. Hydrothermal alteration may include replacement of pre-existing minerals, but also the precipitation of new phases. These alteration assemblages typically form in distinct zones, radially and vertically around the causative intrusion (Figure 1-3; Sillitoe, 2010). Alteration

assemblages are significant because they can be used to approximate the physico-chemical conditions of the formation environment. Furthermore, mapping the spatial distribution of these alteration styles can be particularly useful when guiding towards ore (Seedorff, et al., 2005).

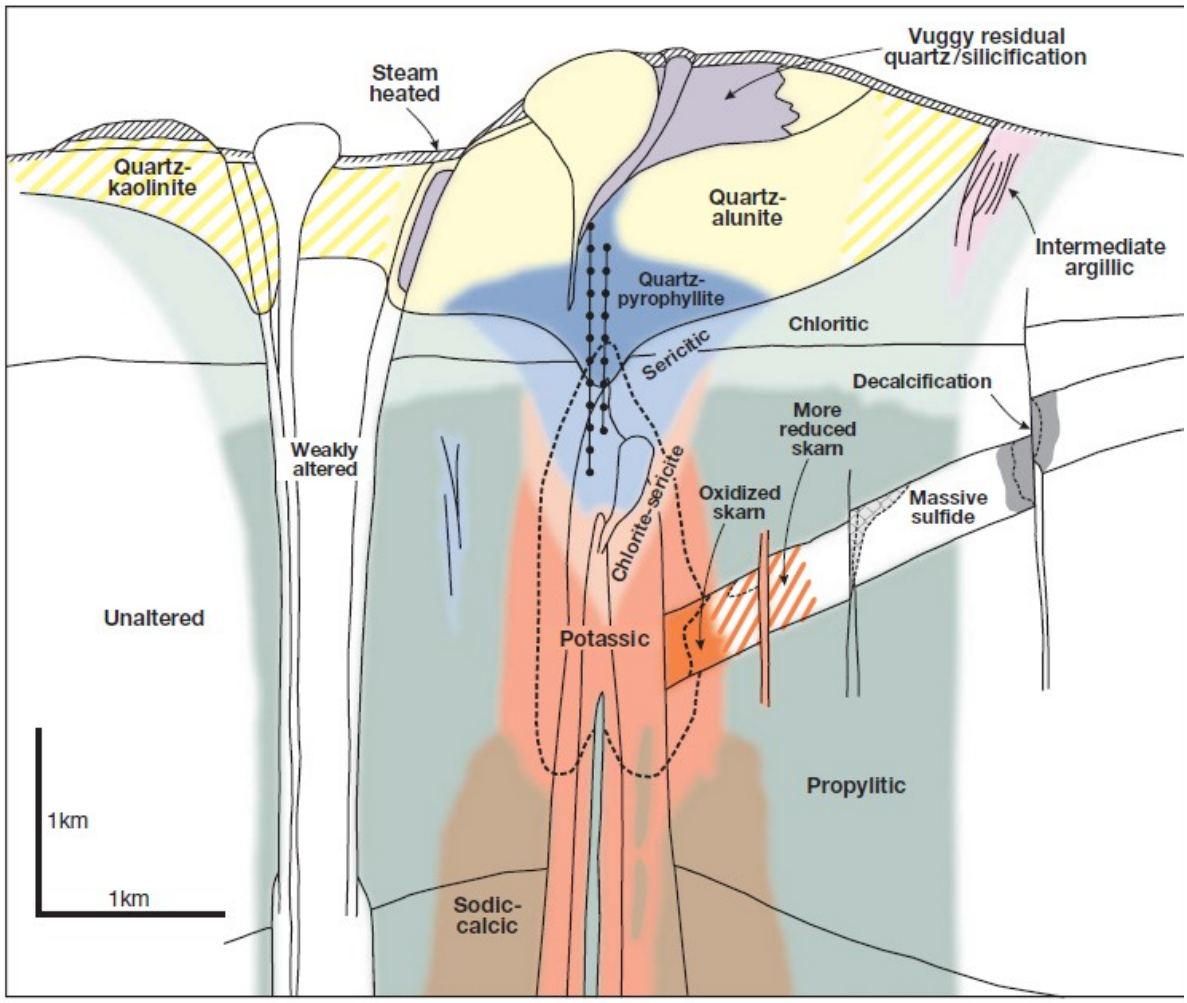


Figure 1-3: Alteration zones in a porphyry copper system. Potassic is located deeply in the core of the system and grades laterally to propylitic alteration. Phyllic (sericitic) and argillic alteration are located more shallowly and overprint early potassic alteration. From Sillitoe (2010).

Potassic alteration is "the main hypogene-contributor" (Cooke et al., 2013), where the greatest volume of Cu-sulphides form. This alteration forms as high temperature hydrothermal fluids cool through 700-550°C and is usually located centrally and deeply seated around the central stock. Generally, potassium is introduced into alumina-silicates and there is commonly abundant stockwork-rich veins as a result of hydraulic fracturing. K-feldspar and biotite are introduced by the replacement of plagioclase and hornblende. A lesser amount of magnetite, anhydrite, apatite and occasionally albite is also typically added (Lowell and Guilbert, 1970; Sillitoe, 2010). In felsic rocks, K-feldspar usually dominates, whereas in mafic wall rocks, biotite is the dominant K-silicate phase formed.

Phyllic (sericitic) alteration forms via replacement of all rock minerals by fine grained white mica (sericite), some Cu-Fe sulphides and specular hematite (Seedorff et al., 2005). Phyllic alteration is located centrally and more shallowly and is largely structurally controlled on fractures and faults. This form of alteration is likely produced by interaction with more acidic hydrothermal fluids in the 350-250°C, either through late-stage exsolution directly from the magma chamber, or via contraction of a vapour as it cools at elevated pressure (Sillitoe, 2010).

Propylitic alteration is characterised by an inner actinolite zone (actinolite, chlorite, pyrite, magnetite, hematite and chalcopyrite), a middle epidote zone (epidote, chlorite, pyrite, hematite and chalcopyrite zone) and distal chlorite zone (chlorite, calcite, pyrite, prehnite and zeolites). It is located in shallow-moderate depths in the peripheral zone of potassic and phyllic alteration. This form of alteration is generated by heated external water (mostly meteoric) during the protracted potassic alteration events which influence the early and inter-mineral porphyries and their immediate wall rocks (Cooke et al., 2013). The propylitic zone is generally barren except for sub-epithermal veins. Notwithstanding this, mapping the alteration assemblages in this zone can provide a useful tool to understand the location relative to mineralisation.

Intermediate-argillic alteration is a clay bearing assemblage formed by hydrolytic alteration at lower temperature than phyllic alteration and relatively low pH. It forms as phyllic alteration wanes (Arancibia and Clark, 1996). This type of alteration is characteristically pervasive, but textures are usually preserved. Typically, the mineral assemblage includes smectite, kaolinite, K-feldspar and some Fe-Mg minerals (e.g. chlorite and pyrite) (Seedoorf et al., 2005). As the vapour phase ascends buoyantly to shallower levels, SO_2 disproportionates to H_2S and H_2SO_4 during cooling. This generates an extremely acidic fluid capable of intense hydrolytic alteration and base cation leaching which generates advanced argillic alteration. Advanced argillic alteration is typically pervasive and texturally destructive, leaving residual quartz and introducing clay minerals, such as kaolinite, smectite and illite. The vapour has a low metal transporting capability at low pressure, so this style of alteration is usually barren.

As the intrusion cools and the hydrothermal systems decays, shallowly formed alteration types become superimposed over the more deeply formed ones (Heinrich et al., 2004). This process is known as telescoping and causes a succession of remobilisation and reprecipitation as the temperature front retreats downward. Consequently, areas may be subjected to a sequence of overprinting alteration events, starting with potassic and ending with advanced argillic. Telescoping is promoted in areas of rapid, synhydrothermal erosion which could arise during high uplift or gravity induced sector collapse (Sillitoe, 2010).

ii Mineralisation

Finally, in order to form an economic deposit, a large volume of exsolved metal-rich fluid must be focused into a confined fracture network. Ore deposition may occur as a result of a combination of physical and chemical processes that may include: fluid decompression (e.g. Henley and Berger, 2013); fluid cooling (e.g. Klemm et al., 2007; Redmond et al., 2004); mixing of magmatic and surface-derived fluids; and chemical reaction of the fluids with the wall-rocks (e.g. Ulrich et al., 2001). Notwithstanding this, such depositional processes are not uncommon; thus, precipitation efficiency is unlikely to represent the key step in the formation of particularly large deposits. Furthermore, pre-mineralisation fluids from economic porphyry deposits have been shown to have 1-3 orders of magnitude higher copper concentrations than comparable fluids from barren intrusions (Audetat et al., 2008). This suggests that processes governing the ore metal budget of fluids exsolved from the melt are more critical for porphyry mineralisation than ore depositional processes.

iii Metal Association

As well as hosting economic grades of Cu, porphyry copper systems commonly contain resources of Au and Mo. There is typically a distinction between those porphyry copper deposits that are enriched in Cu-Au and those that are predominantly mineralised in Cu-Mo. Less frequently, porphyry copper systems may be enriched in all three metals at economic levels. Most porphyry copper deposits are associated with sub-alkaline rocks. Within this subclass, porphyry Cu-(Au-Mo) deposits typically occur in island arc settings and are usually associated with tonalitic-granodioritic rocks. Porphyry Cu-Mo deposits associated with sub-alkaline magmas, however, occur predominantly in continental arcs and are associated with more silicic, quartz-monzodioritic-granitic rocks. Although less common, porphyry copper deposits may also occur with more alkaline rocks. These include the monzonite porphryry Cu-(Mo-Au) deposits and silica-undersaturated porphyry Cu-(Au) sub-types (Seedorff et al., 2005).

1.2.2 The importance of oxygen fugacity in controlling the metal content of arc magmas

Oxygen fugacity (fO_2) is an important parameter controlling the evolution of magmatic systems. The fO_2 of a magma controls the oxidation state of elements with multiple valence states, such as sulphur and iron. fO_2 is a particularly important variable in geological systems, influencing aspects such as mineral phase equilibria (Lindsley and Frost, 1992), trace element partitioning (particularly for elements with variable valency), diffusivity and mechanical behaviour (Arculus, 1985). Moreover, fO_2 varies over nine orders of magnitude in terrestrial rocks, a greater relative

variation than any other parameter, including temperature, pressure or composition (Parkinson and Arculus, 1999). Thus, the fO_2 exerts a strong control on the mineralisation potential during the formation of porphyry copper deposits (e.g. Ishihara, 1981; Blevin, 2004). The fO_2 is commonly expressed in log units relative to that of a buffer assemblage, such as the fayalite-magnetite-quartz (FMQ) buffer.

1.2.2.1 Controls on sulphur speciation and solubility

The stability of sulphur-bearing phases and the solubility of sulphur during the magmatic evolution of silicate melts is primarily dependent on the magmatic fO_2. At fO_2 conditions below the sulphide-sulphur oxide redox buffer (SSO - $fO_2 \sim$ FMQ + 1), the dominant oxidation state of sulphur is S^{2-} and if the melt is saturated with sulphur the saturating phase will be sulphide, which will sequester chalcophile elements from the melt. Above SSO, however, S^{6+} will dominate, and sulphur will be transported primarily as SO_4^{2-} which is highly soluble in the melt; if sulphur is in excess, anhydrite will be the saturating phase (Carroll and Rutherford, 1988; Wallace and Carmichael, 1994). The change from sulphide-dominated to sulphate dominated speciation in the melt occurs over a relatively narrow range of fO_2 between FMQ and FMQ + 2 (Figure 1-4, Carroll and Rutherford, 1988; Jugo et al., 2010). This fO_2 range is relevant because it overlaps with the expected fO_2 conditions prevalent during arc magma genesis (Parkinson and Arculus, 1999).

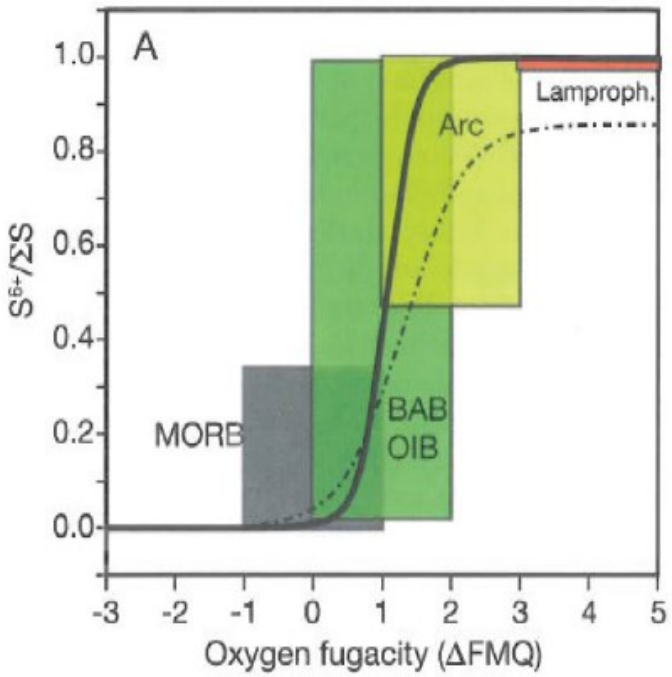


Figure 1-4: Sulphur speciation curve vs. fO_2 in mafic silicate melts derived from $S^{6+}/\Sigma S$ estimates of XANES data (black line), compared to the ranges of fO_2 and $S^{6+}/\Sigma S$ measured in magmas and melt inclusions from different tectonic settings. The dashed-dotted line provides a comparison of the empirical $S^{6+}/\Sigma S$ vs. fO_2 curve derived from data obtained from EPMA (Jugo et al., 2010).

As well as fO_2, the solubility of sulphur in silicate melts also depends strongly on sulphur fugacity (fS_2), melt composition, temperature and pressure (Audetat and Simon, 2013). The dissolution of sulphur as sulphide in silicate melts is considered to follow the reaction:

$$FeO + ½\ S_2 = FeS + ½\ O_2$$

Correspondingly, the sulphur content at sulphide saturation (SCSS) is proportional to the square root of fO_2/fS_2. The FeO content of the melt will exert a strong control on the sulphur solubility in magmas. Divalent Fe is the most electronegative among all the major network modifier cations (Mg, Ca, Fe, Na and K) in silicate melts and therefore empty d orbitals of divalent Fe will be bond to S^{2-} in preference to other ions lacking d orbitals, or with filled d orbitals. Notwithstanding this, the activity of divalent Fe is affected by other components in the silicate melt and consequently the concentrations of other cations in the melt will also influence the sulphur solubility (Liu et al., 2007). A number of studies have also demonstrated a positive influence of temperature on the SCSS, i.e. the sulphur concentration at which a magma will become saturated in a sulphide phase will be lower at lower temperatures (e.g. O'Neill and Mavrogenes, 2002). Furthermore, the SCSS has been noted to decrease with increasing pressure at constant temperature (e.g. Mavrogenes and O'Neill, 1999).

1.2.2.2 The importance of sulphur-bearing phases in controlling the metal contents of arc magmas

Porphyry deposits are first and foremost sulphide anomalies. In order to deposit such large volumes of sulphide ore minerals, abundant sulphur must be carried by the magma to the porphyry system. Notwithstanding, the role of sulphur in magmatic processes prior to or during the formation of porphyry copper deposits is controversial.

If the magma reaches sulphide-saturation, sulphide phases will sequester ore metals from the silicate melt, potentially rendering it incapable of forming an economic ore deposit. Conversely, the formation of a sulphide phase could act to pre-concentrate ore metals. Subsequent destruction of these highly enriched regions could relinquish a high concentration of ore metals which could then be redeposited to form an ore deposit; the formation of sulphides could thereby promote mineralisation potential (Wilkinson, 2013). It is becoming increasingly apparent that sulphides are important in controlling the enrichment or depletion of ore metals at various stages, covering a range of spatial and temporal scales, during the evolution of porphyry Cu-forming magmas.

There is compounding evidence that the sulphur content of primary arc magmas is buffered by a sulphide phase in the mantle wedge (Rowe et al., 2009; Metrich and Clocchiati, 1996). Several

workers have suggested that relatively high degrees of partial melting of the sub-arc mantle could lead to complete exhaustion of sulphides in the source region of arc magmas (e.g. Mungall, 2002). In order to extract all the sulphides present, around 25% partial melting of 'typical' upper mantle would be required (Mungall, 2002), although just ~6% may be required if an oxidised arc magma source region is assumed (Jugo, 2009). Most evidence points to oxidising conditions in the source region of arc magmas (e.g. Parkinson & Arculus, 1999; Brandon & Draper, 1996; Wood et al., 1990), however, there are increasing lines of evidence inconsistent with the presumption of an oxidised sub-arc mantle (Lee et al., 2005; 2010; and 2012; Mallmann and O'Neill, 2009). On the regional scale, whether sulphides are exhausted from the arc magma source region might explain why well established arcs, with high degrees of melting are favourable for generating large ore deposits.

Magmatic sulphides have also been documented in mafic cumulates, developed at the base of the lowermost crust, potentially in MASH zones (Dromgoole and Pasteris, 1987). Here, sulphide precipitation may take place in response to magma cooling and magma mixing, thereby depleting the silicate melt in metals strongly partitioned into sulphide. Subsequent partial melting of the crystal-mush zone could result in redissolution of lower crustal sulphides, relinquishing metals to the evolving silicate melt. Regardless of the mechanism of remelting, the partial melting of sulphide cumulates offers an attractive mechanism for generating particularly Cu-rich magmas.

The differing trends of Au, Cu, Ag and Se during the differentiation of arc-related and MORB magmas provide further evidence for the importance of fO_2 and its control on the stability of magmatic sulphide phases (Jenner et al., 2010). Results from arc-related volcanic rocks from an island arc setting indicate that during the evolution of arc magmas, the contents of Au, Cu, and Ag are built up to levels substantially in excess of those in MORB probably because they are not saturated in a sulphide phase (Figure 1-5). This phenomenon is not observed in MORB magmas which are saturated with an immiscible sulphide as a consequence of their lower fO_2. It might be that the sulphide under-saturated nature of arc magmatism allows a prolonged history of sulphide-free fractionation, explaining the predominance of porphyry copper deposits in arc settings.

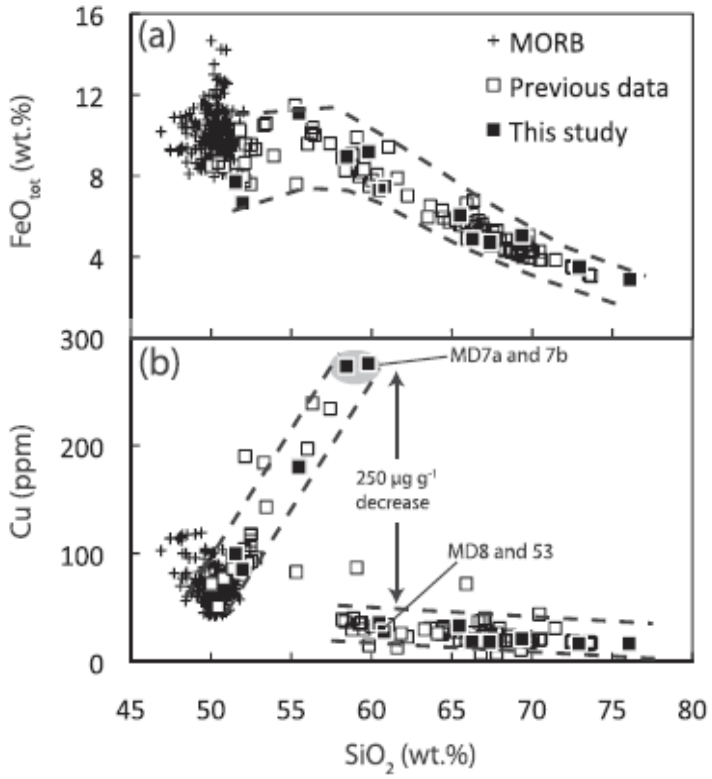


Figure 1-5: The variation of a) FeO_{tot} and b) Cu as a function of SiO_2 for arc-related volcanic rocks from the Pual Ridge, Eastern Manus Basin. At approximately 60 wt % SiO_2, there is a sudden drop in the Cu contents. This coincides with a change in the FeO_{tot} partitioning, implying that this abrupt decrease could be induced by the appearance of magnetite (from Jenner et al., 2010).

Later in the arc magmatic evolution an abrupt decrease in the contents of Cu, Au, Ag and notably Se is commonly observed at ~60 wt % SiO_2. This sharp drop has been interpreted to be a result of saturation in a Cu-rich sulphide phase, which abruptly scavenges Au, Cu, Ag and Se (Figure 1-5 - Jenner et al., 2010). Interestingly, sulphide saturation appears to coincide with the appearance of magnetite on the liquidus, implying that magnetite fractionation triggers sulphide saturation. Petrological modelling suggests that limited magnetite crystallisation is sufficient to convert most of the S, originally dissolved as sulphate to sulphide, triggering saturation in a Cu-rich sulphide phase. Alternatively, the abrupt depletion of gold and copper at 60 wt % SiO_2 could also be explained by magnetite fractionation triggering sulphur reduction, which subsequently results in enhanced formation of copper-gold hydrosulphide complexes, which scavenge chalcophiles from the crystallising melts into the cogenetic magmatic-hydrothermal fluids (Sun et al., 2004). Despite the well-defined trend observed in the evolving island-arc magmas, the chalcophile element behaviour is likely to be more complex in continental arc settings, where the protracted interaction of the magma with the thick continental crust would ensue a more complicated multi-stage magmatic evolution.

Sulphide saturation could also occur in the shallow crustal magma chambers parental to the porphyritic intrusions. Often within fertile terranes, there are pockets of barren and low-grade intrusions, which suggest that melt fertilization, if it takes place, operates in the mid- to shallow-crustal magma chambers. On this scale, the local saturation of sulphides could convert a system

with a dispersed, low concentration of metals into one with pockets of highly enriched sulphide, on the scale of tens to hundreds of kilometres, which could later be made accessible to magmatic-hydrothermal fluids exsolved from the magma. Such cannabilization of sulphide-rich domains might be traceable using geochemical proxies. Such proxies may include sulphur zonation (e.g. Streck and Dilles, 1998), or variable trace element chemistry in coexisting minerals. If identified, such proxies could enable distinction of fertile from barren porphyry systems (Wilkinson, 2013).

Studies on intermediate arc magmas have shown that they commonly contain sulphides in abundance, whereas mafic arc magmas are generally sulphide undersaturated (Keith et al., 1997). Active sulphur-rich volcanoes, however, have shown that magmatic sulphides are not locked up in the phenocryst phases, but decompose during magma crystallisation and degassing and are replaced by fine-grained iron oxides (Hattori, 1997; Audetat and Simon, 2013). In a number of studies, it has been observed that the metal ratios in magmatic sulphides match those of the associated porphyry mineralisation (e.g. Bajo de la Alumbrera: Halter et al., 2005). Bornite- and chalcopyrite-rich enclaves associated with the Last Chance Stock, an intrusion parental to the giant Bingham porphyry deposit (Utah, USA) have also been suggested to represent relics of precursor sulphides which were later partially destroyed, relinquishing ore metals to a mineralising magmatic-hydrothermal phase (Core et al., 2006)

To conclude, magmatic sulphides appear to be critical in influencing the metal budget at several stages during the evolution of porphyry Cu-forming magmas, from their source region in the sub-arc mantle, to their final solidification at shallow depth. The fO_2 exerts a strong control on the stability of sulphur-phases, therefore an understanding of the redox processes during the evolution of arc magmas is imperative in order to evaluate the ore-forming potential of a magma. Recent work has highlighted that the formation of sulphide-phases may act to pre-concentrate ore metals. Subsequent destruction of these highly-enriched sulphide regions could relinquish high concentrations of ore metals and could thereby promote mineralisation potential (Wilkinson, 2013). Cannibalization of enriched sulphide regions might be traceable using geochemical proxies in specific mineral phases crystallizing during the process. If so, then such proxies could be used to assess the role of sulphide saturation in ore formation, and potentially to distinguish fertile from barren porphyry systems providing a valuable tool for mineral exploration. Alternatively, the study of co-crystallising mineral chemistry from barren and mineralised porphyry intrusions could highlight proxies indicative of other processes conducive for ore formation.

1.2.3 Indicator minerals for porphyry copper systems

Porphyry copper systems are becoming increasingly difficult to discover. Most porphyry copper systems which formed closer to the surface, with more obvious signs of alteration and mineralisation, have been discovered. Consequently, exploration is increasingly focussing on deeper systems, often under cover of sedimentary rocks.

Drilling is one of the largest costs in exploration. If geochemical signals can be used to determine the presence of a mineralised porphyry copper system at an early stage of exploration, or even locate an ore body, they have potential to significantly reduce the cost of exploration for deeply buried systems. The chemistry of individual minerals could be used to fingerprint specific processes governing the formation of a mineral deposit. Furthermore, specific minerals carrying such information may survive weathering and erosion and become concentrated in sediments. Mineral chemistry therefore offers strong potential as an exploration tool for porphyry copper systems.

Characteristics of a good mineral indicator are:

1) Abundant and widespread in rocks related to or within the deposit
2) Robust and resistant to physical abrasion and chemical alteration
3) Chemical composition sensitive to the environment in which it formed
4) Easy to identify and separate from host rock
5) Easy to analyse using relatively cheap analytical techniques (e.g. SEM, EPMA, LA-ICP-MS)

1.3 Magnetite chemistry as an indicator mineral for porphyry copper deposits

Magnetite and other Fe-Ti oxides have been recognized as potential indicator minerals for mineral deposits. (e.g. Nadoll et al., 2014) Magnetite is relatively resistant to mechanical breakdown and chemical alteration in comparison to other coexisting mineral phases. Moreover, magnetite incorporates a large number of minor and trace elements into its structure, including a number of chalcophile elements (e.g. Dare et al., 2012). Magnetite also has physical properties, such as its strong magnetism, which make it convenient for mineral separation. Consequently, there is increasing interest in the study of trace elements in magnetite as a means to determine its provenance (e.g. Dupuis and Beaudoin, 2011).

Magnetite forms over a wide variety of geologic conditions and is an easily identifiable accessory mineral in its host rock. Only recently, however, have studies highlighted differences in the compositional signatures of magnetite from specific geologic settings (e.g. Dare et al., 2014).

Minor and trace element chemistry offers the most important overall discriminators between magnetite populations. In fact, variations in trace element composition of magnetite could record specific physio-chemical processes, such as redox conditions, melt/fluid origin or temperature. Thus, investigating the partitioning of elements between magnetite and coexisting phases could be used to reveal processes imperative for generating ore deposits.

Magnetite is near ubiquitously associated with porphyry copper systems. Igneous magnetite can form as liquidus phase in intermediate to silicic arc magmas and hydrothermal magnetite can also form as disseminated grains, massive aggregates, veins, or replacements of other minerals (Nadoll et al., 2014). The volume of magnetite associated in mineralised zones in porphyry copper systems can locally exceed 10% (Canil et al., 2016).

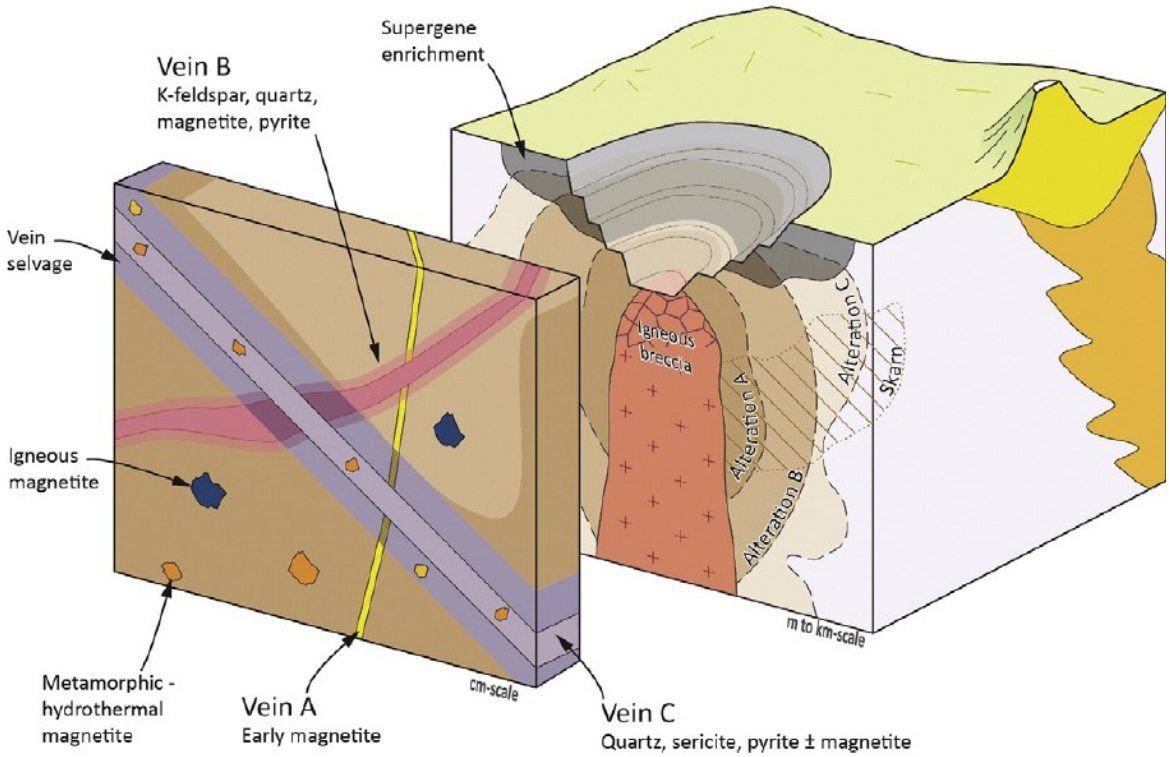


Figure 1-6: Both igneous magnetite and hydrothermal magnetite are associated with the formation of porphyry copper systems. Igneous magnetite occurs as phenocrysts, whereas hydrothermal magnetite can form in veins, massive aggregates, disseminated grains, or replacing other minerals. (From Nadoll et al., 2014).

1.3.1 Magnetite chemistry and crystallography

Magnetite has an inverse cubic spinel-type structure with the general formula AB_2O_4, where A is a 4-fold coordinated site and B is 6-fold coordinated. In normal spinels, divalent cations occupy A and twice as many trivalent cations occupy B, whereas in inverse spinels, trivalent cations occupy A, and B is filled with equal amounts of 2+ and 3+ cations (Lindsley, 1976). Examples of divalent cations include Mg, Fe^{2+}, Ni, Mn, Co or Zn and trivalent cations include Al, Fe^{3+}, Cr, V, Mn or Ga, all

of which are known to substitute widely into the magnetite structure (O'Neill and Navrotsky, 1984). Ulvospinel incorporates 4+ cations, such as Ti, into the B site, provided that there is coupled substitution to maintain charge balance. The location of cations in the spinel structure is determined predominantly by crystal-field stabalization energy, ionic radius and valence (Papike et al., 2005).

The spinel group can be divided into three series depending on the trivalent cation: the spinel series (Al^{3+}), the magnetite series (Fe^{3+}) and the chromite series (Cr^{3+}). Magnetite ($Fe^{2+}Fe_2^{3+}O_4$) forms complete solid solution with magnesioferrite ($MgFe_2O_4$) and ulvospinel (Fe_2TiO_4). Chromite exhibits complete solid solution between the Fe-end member chromite ($FeCr_2O_4$) and Mg-end member magnesiochromite ($MgCr_2O_4$). The spinel series end-members include spinel ($MgAl_2O_4$), hercynite ($FeAl_2O_4$), gahnite ($ZnAl_2O_4$) and galaxite ($MnAl_2O_4$), of which magnetite only displays solid-solution with hercynite. Magnetite may also show partial solid solution with franklinite ($ZnFe_2O_4$), jacobsite ($MnFe_2O_4$) and trevorite ($NiFe_2O_4$) (Dupuis and Beaudoin, 2011). Figure 1-7A provides a schematic representation of the relations between the spinel group minerals.

The minimum fO_2 for any given temperature at which magnetite is stable is the iron-magnetite (IM) or magnetite-wustite (MW) buffer (Frost, 1991). The FMQ buffer marks the lower limit of fO_2 space where Fe is predominantly incorporated into magnetite. Below the FMQ buffer, Fe is mostly present in silicates (Nadoll et al., 2014). The upper limit of magnetite stability is defined by the magnetite-hematite (MH) buffer, above which hematite is the dominant iron oxide phase (Nadoll et al., 2014). Figure 1-7B illustrates the regions where different Fe-bearing species predominate in log fO_2-T space.

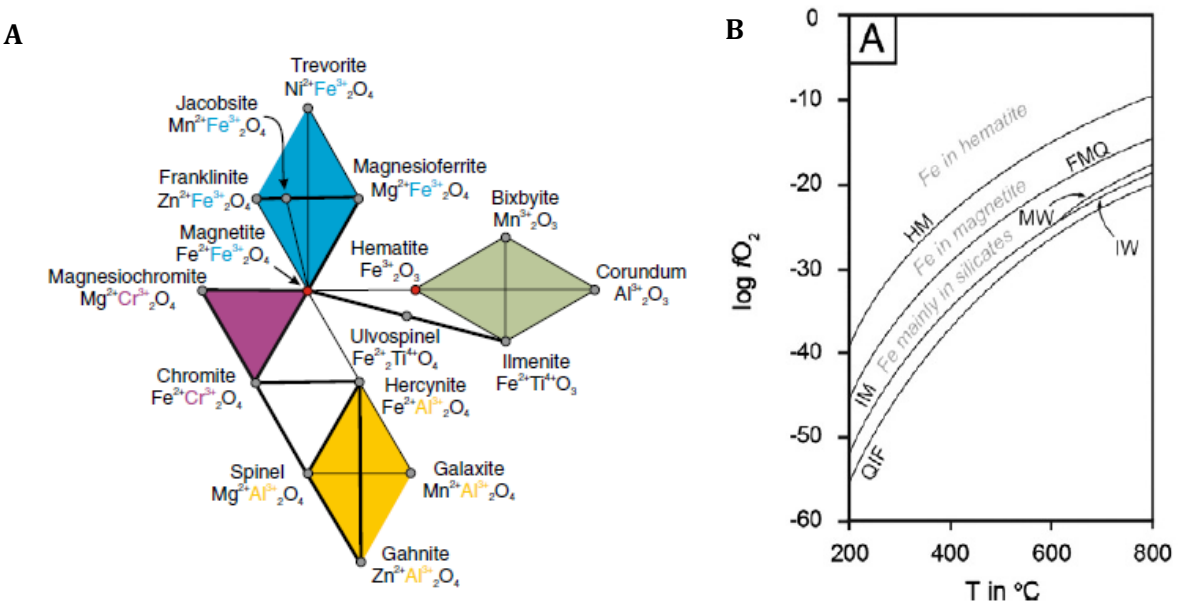


Figure 1-7: A) Schematic representation of the relations between the spinel group minerals. Complete solid solution is shown by solid lines and partial solid solution represented as thin lines (From Dupuis and Beaudoin, 2011). B) Log fO_2-T diagram showing relevant buffers for the Fe-Si-O system and the regions where different Fe-bearing phases are dominant. HM: hematite-magnetite, FMQ: fayalite-magnetite-quartz, MW: magnetite-wustite, IW: iron-wustite, IM: iron-magnetite, and QIF: quartz-iron-fayalite (From Nadoll et al., 2014).

1.3.2 Controlling factors and processes on the composition of magnetite

Magnetite can incorporate a large range of foreign cations, ranging from alkali and alkaline earth metals to transition metals, metalloids, REE and non-metals (Dare et al., 2012; Dupuis and Beaudoin, 2011; Nadoll et al., 2012; Righter et al., 2006). Recent developments in analytical techniques, such as LA-ICP-MS, have made it possible to determine a much wider range of trace elements than previously. Notably, the most commonly substituted elements into magnetite are: Mg, Al, Ti, V, Co, Ni, Zn, Cr, Mn, Ga and Sn, which are often present at levels detectable by electron probe micro-analysis (EPMA) (10 to >1000 ppm) (Nadoll et al., 2014). The chemical diversity between trace and minor elements in minerals ensures that different elements behave in different ways in certain situations. As a result, trace element geochemistry can be particularly useful in identifying specific processes occurring during the evolution of magmas.

Major controls for the geochemistry of magnetite are: lithology/fluid composition; temperature; pressure; cooling rate; fO_2; fS_2; and silicate and sulphide activity (Frost and Lindsley, 1991; Buddington and Lindsley, 1964; Nadoll et al., 2014). Notwithstanding, crystallographic factors, such as ionic radius and charge of the trace ion relative to the size and charge of the lattice site, will also control the partitioning of cations (Goldschmidt, 1954). Generally, siderophile and lithophile elements that have similar ionic radii and bonding environments to Fe^{2+} and Fe^{3+} are most readily incorporated into magnetite, whereas chalcophile elements or other elements with more dissimilar ionic radii are lesser incorporated (Nadoll et al., 2014). Oxide-silicate, oxide-

oxide and intra-oxide re-equilibration reactions can additionally influence magnetite stability and geochemistry during cooling of plutonic and metamorphic rocks (Nadoll et al., 2014). Thus, in order to track processes during the magmatic stages the latter effects of sub-solidus alteration to be removed.

Several of the factors which control magnetite composition are inter-related. For example, changes in the fO_2 can influence the melt composition, thereby effecting magnetite partitioning. Consequently, isolating the individual effects of different parameters on Fe-Ti oxide partitioning can often prove taxing. In order to develop a quantitative model of igneous differentiation, a comprehensive understanding of the factors which control spinel composition is required. Experiments offer the easiest means to identify and quantify the parameters controlling the mineral chemistry and element partitioning.

1.3.2.1 Experimental studies

Several studies have investigated the compositional variations in magnetite experimentally over a range of conditions and magma compositions.

The effect of bulk composition and temperature on the magnetite-melt partitioning of a number of elements, including the V, Sc, Ni and the high field strength elements (HFSE - Zr, Nb, Ta and Hf) was investigated at atmospheric pressure by Nielsen et al. (1994). A range of natural silicate melts were studied, ranging from mafic to intermediate in composition, at atmospheric pressure. The bulk composition of the system was found to exert the strongest control on partitioning behaviour. The partition coefficients (D(X) – calculated as (wt. % in mineral)/(wt. % in melt)) for the HFSE positively correlate with D(Ti), and vary considerably between the different spinel end-members, increasing as the composition changes from Al- and Cr-rich to Ti-rich spinel compositions (Nielsen et al., 1994). Contrarily, Ni is more compatible in Al- and Cr-rich magnetite than in ulvospinel (Nielsen et al., 1994).

Similar to Nielsen et al. (1994), Horn et al. (1994) investigated the partition coefficients for the HFSE, V and Sc, and also Ga, Zn and Co, between spinel and melt in a basaltic bulk composition at 1-atm. Both studies report the relative partition coefficients for the HFSEs to be uniform; thereby magnetite fractionation could influence the absolute abundances of the HFSEs, but not their ratios. Like the HFSEs, the partitioning of Sc also correlates with D(Ti), although the absolute values for D are significantly higher for Sc than for the HFSEs (Nielsen et al., 1994). Scandium partitioning also correlates with fO_2 (Horn et al., 1994) (Figure 1-8A). Since Sc occurs in just one valence state within the experimental range of fO_2 studied, its partitioning is likely to be

compositionally dependent, and may be related to a similarity in behaviour with Fe^{3+} (Horn et al., 1994). Gallium was found to be relatively compatible in magnetite ($D(Ga)_{spinel\text{-}melt} \sim 3.2$), but showed no dependency on either fO_2 or spinel composition (Horn et al., 1994). Previous work on natural spinel had noted a strong correlation of increasing Zn content with decreasing temperature (Griffin et al., 1991), although no such trend was apparent in experiments by Horn et al. (1994). Co partitioning, however, exhibits a strong temperature dependence and a lesser dependence on fO_2, with $D(Co)_{spinel\text{-}melt}$ increasing with decreasing temperature (Figure 1-8B) and increasing with fO_2 (Horn et al., 1994).

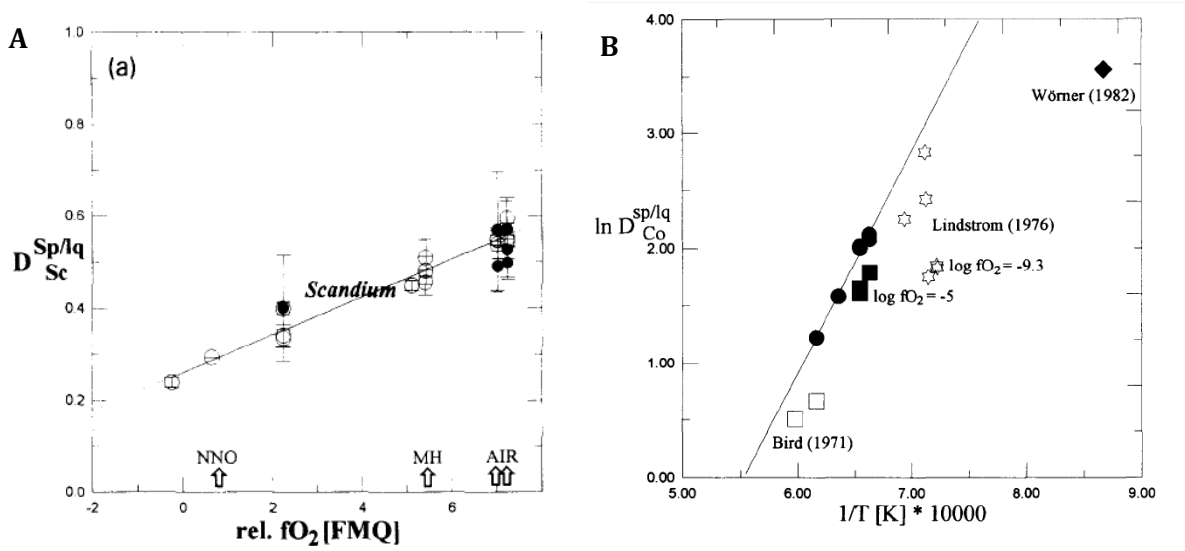


Figure 1-8: A) Spinel-melt D(Sc) as a function of fO_2. Since Sc only occurs in one valence state within the experimental range of fO_2 studied, Sc partitioning in spinel is likely compositionally dependent, probably related to a similarity in behaviour to Fe^{3+} (from Horn et al., 1994). B) D(Co) for spinel as a function of the reciprocal of temperature. Filled circles are fO_2 = air (Horn et al., 1994); filled squares are logfO_2 = - 5 (Horn et al., 1994); stars are from Lindstrom (1976); open squares are from Bird (1971).

Both studies by Horn et al. (1994) and Nielsen et al. (1994) noted V to be compatible in spinel. Vanadium is negatively correlated with D_{Ti} and positively correlates with Al, demonstrating V is most likely partitioned in its 3+ state, with a similar charge and ionic radius to that of Cr^{3+} (Nielsen et al., 1994). Vanadium partitioning also shows a strong dependence on fO_2, with $D(V)_{spinel\text{-}melt}$ decreasing with increasing fO_2. This further suggests that V is compatible in spinel in its 3+ state, and with increasing fO_2, V is increasingly incompatible as V^{5+} becomes increasingly predominant. Nevertheless, because of the number of valence states of V, a more thorough experimental study is required to more adequately define D(V) as a function of fO_2.

Toplis and Corgne (2002) investigated the mineral-melt partitioning of V and a series of divalent trace elements (Ni, Co, Mn and Sr) between magnetite, clinopyroxene and a ferrobasaltic melt at 1-atm as a function of fO_2 (between NNO – 0.7 to NNO + 2.6). Once more, magnetite-melt partitioning of V exhibits a strong dependence on fO_2 (Figure 1-9). The effect of fO_2 on the

partitioning of V is difficult to quantify given the number of valence states of V. In view of this, Toplis and Corgne (2002) developed a thermodynamic model for V speciation in the melt as a function of fO_2. Through combining this model with experimentally derived partition coefficients, a model was developed to predict the expected V partitioning in magnetite as function of differentiation and fO_2. Results imply strong enrichments of V in magnetite only over a narrow fO_2 range between NNO and NNO – 1.5, a premise which is corroborated by the observations made on vanadium-rich seams of the Bushveld intrusion (Toplis and Corgne, 2002). Nonetheless, the inter-relation between temperature, fO_2 and spinel chemistry means unravelling the controlling parameters individually still remains a challenge.

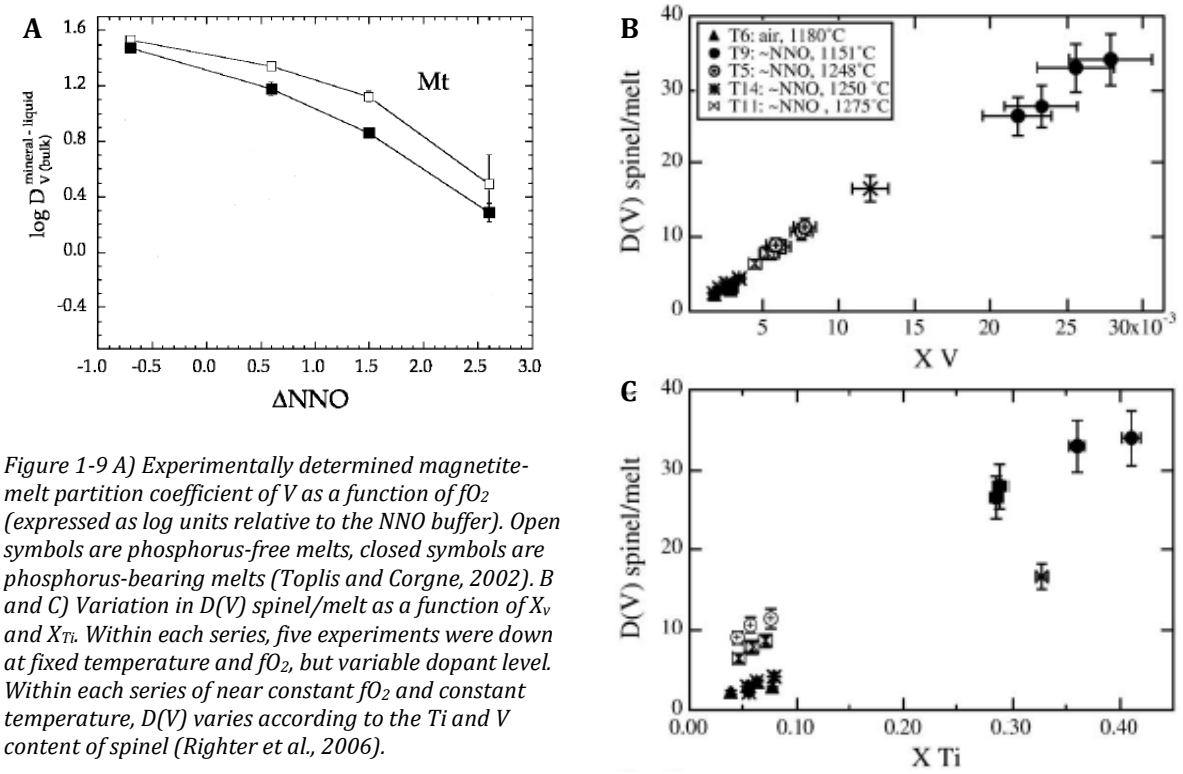


Figure 1-9 A) Experimentally determined magnetite-melt partition coefficient of V as a function of fO_2 (expressed as log units relative to the NNO buffer). Open symbols are phosphorus-free melts, closed symbols are phosphorus-bearing melts (Toplis and Corgne, 2002). B and C) Variation in D(V) spinel/melt as a function of X_V and X_{Ti}. Within each series, five experiments were down at fixed temperature and fO_2, but variable dopant level. Within each series of near constant fO_2 and constant temperature, D(V) varies according to the Ti and V content of spinel (Righter et al., 2006).

Variations in the fO_2 can induce significant changes in the mineral composition and melt structure. As a result, partitioning of single valence divalent cations (M^{2+}) might be expected to exhibit some variation as a function of fO_2. In spite of this, Toplis and Corgne (2002) observed no systematic dependence of magnetite-melt M^{2+} partitioning on fO_2 (Figure 1-10), suggesting mineral composition does not play a significant role in affecting divalent element partitioning. The partitioning of Ca, Co, Ni and Mn does correlate positively with D(Mg). Magnesium partitioning inversely correlates with the degree of melt polymerization, exhibiting a clear trend of decreasing D(Mg) with increasing NBO/T (non-bridging oxygens per tetrahedrally coordinated cations - a measure of melt polymerization) (Figure 1-10). It could be that melts rich in network-

modifying cations contain more potential sites for divalent cations to partition, explaining their lower mineral-melt partition coefficients (Toplis and Corgne, 2002).

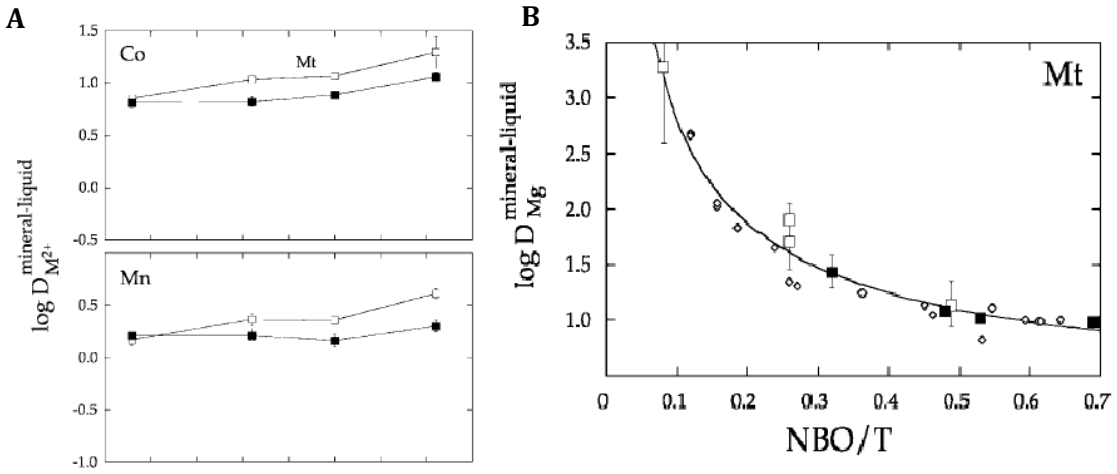


Figure 1-10: A) Experimentally determined magnetite-melt partition coefficient of Co and Mn as a function of fO_2 (expressed as log units relative to the NNO buffer). B) Variation in D(Mg) as a function of NBO/T. Open symbols are phosphorus-free melts, closed symbols are phosphorus-bearing melts. Diamond symbols are data from Toplis et al. (1994) and Toplis and Carroll (1995).

In order to better understand the compositional dependence of Ni, Co and V partitioning during magma differentiation, Righter et al. (2006) conducted a series of experiments at atmospheric pressure to generate spinels over a wide compositional range, whilst also assessing the effect of temperature and fO_2 on partitioning. Partitioning of Ni and Co reveal no clear dependence upon temperature or fO_2 alone (Righter et al., 2006), an observation corroborated by Toplis and Corgne (2002). For these elements, Righter et al. (2006) interpret that spinel composition is the dominant factor effecting Ni and Co partitioning, a premise supported by earlier work by Nielsen et al. (1994). The partitioning trends of Co observed by Righter et al. (2006) however, are contradicted by results from Horn et al. (1994) who observed that D(Co) decreases with increasing temperature (Figure 1-8B) and decreasing fO_2. Again, vanadium partitioning in magnetite exhibits a strong dependence on fO_2 (Righter et al., 2006). Nevertheless, some variation in V partitioning could also be attributed to spinel composition, notably the V and TiO_2 content (Figure 1-9B and C). Since spinels crystallised at lower fO_2 generally have higher TiO_2 contents, it is difficult to identify whether the variation in D(V) is attribute to TiO_2 content, fO_2 or both (Righter et al., 2006).

Spinel-melt partition coefficients for a large range of elements were determined in experiments by Wijbrans et al. (2015) as a function of fO_2 and spinel composition. This study focussed on partitioning between Al- and Cr-rich spinels and a synthetic Ca-Mg-Al-Si±Fe silicate melt,

although magnetite-rich spinel was also crystallised in some experiments. Partition coefficients for V and Mo are strongly dependent on redox conditions, with a decrease in D(V) and D(Mo) with increasing fO_2. Spinel composition is interpreted as the major controlling factor for partitioning of Ti, HFSEs, Sc and Lu, with these elements more strongly incorporated into Fe^{3+}- and Cr-rich spinels. The partitioning of Ni, Ga and Co was also investigated although there is little effect of either fO_2 or composition on the spinel-melt partitioning of these elements.

Although several experimental studies have investigated the partitioning of major, minor and trace elements as a function of temperature, spinel/melt composition and fO_2 at atmospheric pressure, few studies have extended these experiments to higher pressures. Nielsen and Beard (2000) conducted a series of experiments to investigate magnetite-melt partitioning of HFSEs over a range of natural silicate melt compositions, but at 2 and 5 kbar pressure. As observed at atmospheric pressure, at elevated pressure D(HFSE)s correlate with D(Ti), and Al content of the magnetite. At higher pressures, however, the partitioning of HFSEs is also observed to vary as a function of pressure and temperature, with the HFSE becoming more incompatible relative to Ti at lower temperatures and/or higher pressures (Nielsen and Beard, 2000). Consequently, magnetite-melt partition coefficients derived at one atmosphere are not applicable to hydrous, aluminous systems.

The behaviour of Cu during mantle melting is poorly understood, largely as a result of uncertainties in the Cu partition coefficients between minerals and melts. In order to better constrain D(Cu) values, Liu et al. (2014) experimentally investigated D(Cu) for olivine, orthopyroxene, spinel and garnet at upper mantle conditions. Notably, $D(Cu)_{spinel\text{-}melt}$ increases with increasing fO_2 and spinel Fe_2O_3 (Figure 1-11). A set of partitioning experiments conducted by Simon et al. (2008) corroborate that spinel composition exerts a strong control Cu partitioning. With increasing Ti content of magnetite, the Cu- and Au- scavenging potential markedly increases. Cu generally shows preference for octahedral coordinated sites with oxygen, which suggests that Cu^{2+} might substitute preferentially into trivalent sites in spinel. There is, however, no clear correlation between Cu partitioning and Cr- and Al-content as would be expected on the basis of their systematic substitution (Stanton, 1994). Instead, it is possible that the significant increase in Cu partitioning is a consequence of lattice distortion by the presence of Ti in magnetite, which acts to alter the size of the different tetrahedral and octahedral sites in spinel allowing incorporation of the Cu^{2+} ion (Simon et al., 2008). It is interesting to note that earlier studies also show that Al and Ti partitioning in magnetite are directly linked with temperature (e.g. Nielsen et al., 1994; Toplis and Corgne, 2002), with greater concentrations indicating hotter temperatures. Thereby, the affiliation of Ti with higher-temperature formation conditions could

have subsequent implications for the incorporation of elements such as Au and Cu (Nadoll et al., 2014).

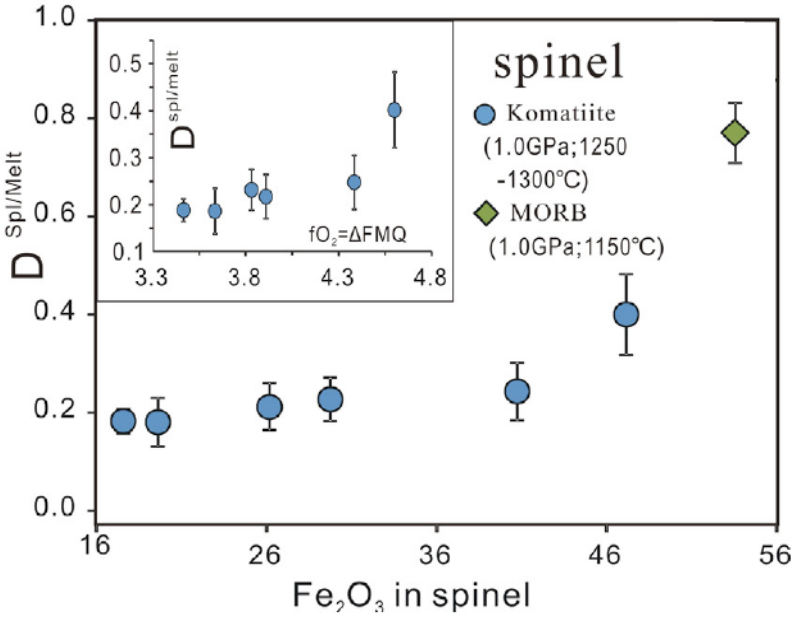


Figure 1-11: Cu partition coefficients as a function of spinel composition and fO_2. Error bars are 1σ standard deviation (Liu et al., 2014).

1.3.2.2 Natural rock studies

Spinel-group minerals occur in magmatic, sedimentary and metamorphic rocks, and are common and widespread phases in a range of mineral deposit types. As mentioned previously, variations in the whole rock chemical environment in which magnetite grows control its chemical composition. Thus, the study of magnetite chemistry could be used to fingerprint the physio-chemical conditions associated with the formation of contrasting types of mineral deposits. A number of studies have been devoted to evaluating the chemistry of natural magnetite to build up a petrogenesis.

Laser ablation inductively coupled plasma mass spectroscopy (LA-ICP-MS) was employed to measure a wide range of trace elements in magnetite from the Cloncurry district in Australia, including iron oxide-copper-gold (IOCG) deposits, barren ironstones and hydrothermally altered rock (Carew et al., 2006). In general, magnetite associated with IOCG deposits is characterised by higher Sn and Mn, and lower V, Ti, Mg, Si, Cr and Zn compared to barren ironstones. A similar study was later conducted by Rusk et al. (2009), measuring trace element chemistry of hydrothermal magnetite from a suite of mineralised and barren magnetite breccias, also from the Cloncurry region. Magnetite from barren breccias is enriched in V and depleted in Mn relative to ore-related magnetite from the Ernest Henry IOCG deposit. Fluid inclusion analysis reveals that the compositions of hydrothermal fluids in the barren breccias are similar to those from mineralised systems. This suggests that the difference in magnetite chemistry is likely a

consequence of differing mineral equilibrium at the site of magnetite deposition, rather than differing fluid sources or fluid-rock interaction processes (Rusk et al., 2009).

Igneous magnetite composition from carbonatites has been shown to be sensitive to controlling factors such as fO_2 and interdependencies among substituting cations (Reguir et al., 2008). As the carbonatite magma evolves, there is a well-defined trend of decreasing Mg and Ti, and increasing Al content. Vanadium also inversely correlates with Al content, decreasing as the magma evolves. Vanadium partitioning has been demonstrated experimentally to be a sensitive function of fO_2 (e.g. Horn et al., 1994; Toplis and Corgne, 2002; Righter et al., 2006), thus it is likely that the decrease in V partitioning reflects an increase in fO_2 during the precipitiation of magnetite (Reguir et al., 2008). This study also shows that Zn and Mn exhibit covariation, indicating that these elements are likely to be linked by a coupled substitution (Reguir et al., 2008).

The composition of magnetite crystallised in large layered intrusions can be used to provide valuable information regarding its provenance and paragenetic sequence (e.g. Dare et al., 2012). Magnetite coexisting with massive sulphides which form the Ni-Cu-PGE deposits at the base of the Sudbury Igneous Complex in Canada were crystallised from an immiscible sulphide liquid. During fractional crystallisation, the composition of the sulphide liquid changes from an earlier formed Fe-rich monosulphide solution (MSS) to a residual Cu-Pt-Pd rich intermediate solid solution (ISS). Interestingly, magnetite shows strong variations according to the type of sulphide from which it crystallised. Lithophile elements, such as Ti, V and Cr, are concentrated in early crystallised titanomagnetite, but decrease with continued crystallisation of Fe-oxide, so that the later forming magnetite in the Cu-Pt-Pd rich ore is depleted in lithophile elements. Accordingly, the Cr-Ti-V content of magnetite could be used to identify whether the ore is Cu-Pt-Pd rich or Fe-rich and Pt-Pd poor. The behaviour of chalcophile elements are also largely controlled by the coexisting sulphide phase. Ni, Mo and Co are compatible in Fe-rich MSS, so the co-crystallising Fe-oxide is depleted in these elements. In contrast, Sn and Pb are incompatible in Fe-rich MSS, such that their concentrations are greatest in later-formed magnetite, which formed from the residual Cu-rich ISS (Dare et al., 2012).

Other work has investigated the minor and trace element content of Fe-Ti oxides with a more statistical approach, focusing on differentiating different types of ore deposit based on compositional trends. Through a study of magnetite from selected volcanogenic massive sulphide (VMS), skarn, IOCG, and Broken Hill-type Pb-Zn deposit, Singoyi et al. (2006) indicated certain trace element ratios, such as Al/Co vs. Sn/Ga can be used to distinguish skarn from VMS deposits and potentially provide a fingerprinting technique for mineral exploration. Likewise, a plot of Sn vs. Ga compiled by Nadoll et al. (2014) shows distinct grouping of the various hydrothermal

magnetite populations (Figure 1-12D). Moreover, this plot suggests that Ga and Sn partitioning could be related to temperature with lower Sn and Ga concentrations found in cooler temperature magnetite.

Dupuis and Beaudoin (2011) analysed the minor and trace element contents of magnetite and hematite from a range of mineral deposit types using electron microprobe, in order to identify compositional differences which can be related to deposit type. Deposit types include IOCG, Kiruna apatite-magnetite, banded-iron formation, porphyry, Fe-Cu skarn, Fe-Ti, V, Cr, Ni-Cu-PGE and Cu-Pb-Zn VMS. A number of discriminant diagrams are constructed which empirically plot and distinguish different mineral deposit types according to their mineral chemistry. Whereas some of the diagrams serve to separate one deposit type from all other types, other diagrams allow distinction of several different deposit types. The Ni/(Cr + Mn) vs. Ti + V and Al + Mn (+ Ca) vs. Ti + V diagram efficiently distinguishes between a wide variety of mineral deposits, including porphyry Cu, Fe-Ti, Fe-Cu skarn, VMS, IOCG, Kiruna-type and V deposits. To further refine the field boundaries first suggested by Dupuis and Beaudoin (2011), Nadoll et al. (2014) supplemented additional data to the discriminant diagrams. It is interesting to note that the Ti + V vs. Al + Mn plot reflects a semi-quantitative temperature trend in the data, from lower temperature BIF, medium temperature Ag-Pb-Zn veins, medium-high temperature hydrothermal skarn and porphyry magnetite, to high temperature igneous magnetite from porphyry and Climax-Mo deposits (Figure 1-12B) (Nadoll et al., 2014). Although additional data from Nadoll et al. (2014) generally confirms the fields earlier proposed by Dupuis and Beaudoin (2011), some of the added porphyry and BIF data points plot outside the formerly suggested boundaries (Figure 1-12A and C). This indicates that such element discriminant diagrams still require further verification (Nadoll et al., 2014). Dare et al. (2014) identified trace element variations in magnetite from a variety of ore deposit types. Furthermore, Dare et al. (2014) developed a discrimination diagram, based on covariation of Ti, Ni and Cr, to distinguish hydrothermal and igneous magnetite.

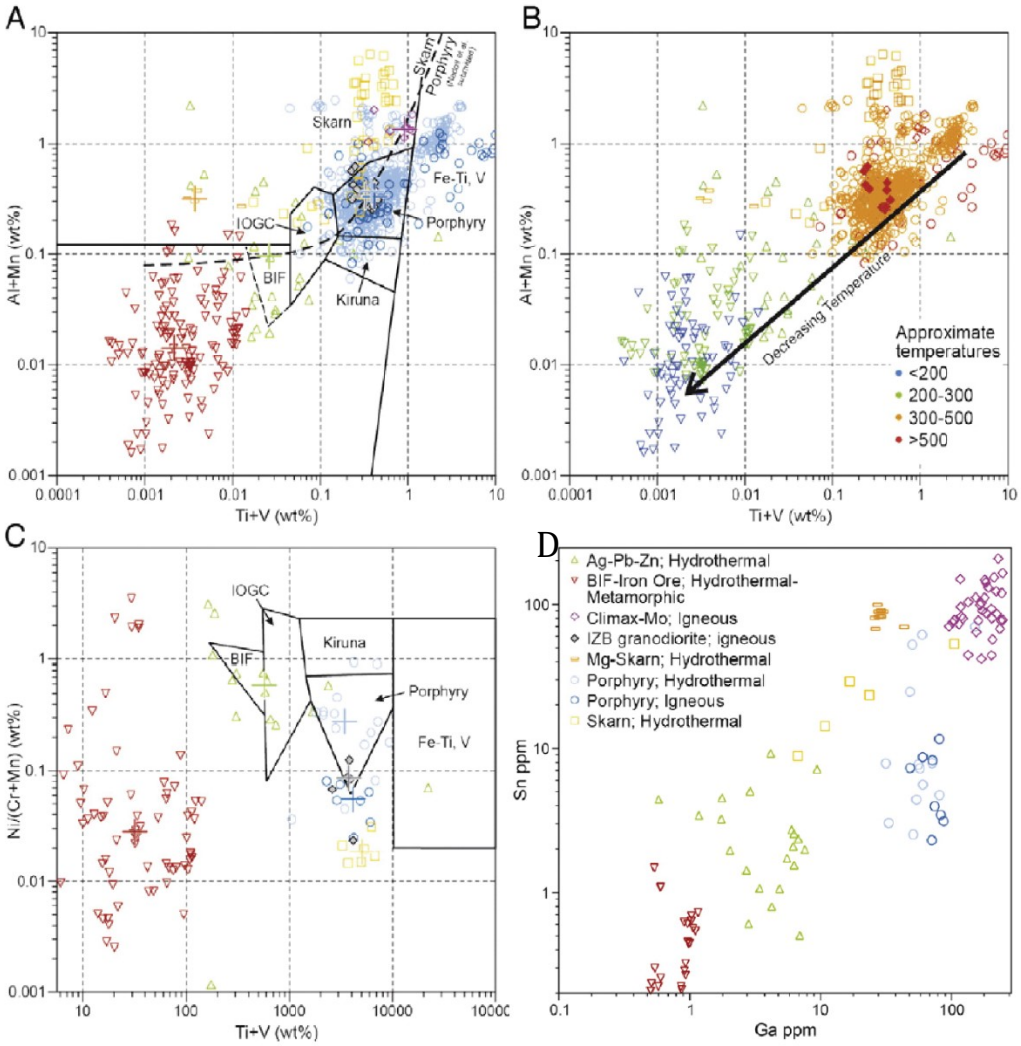


Figure 1-12: A -C) Al + Mn vs. Ti + V and Ni/(Cr + Mn) vs. Ti + V discriminant diagram for average Fe-oxide compositions from a variety of deposit types compiled by Nadoll et al. (2014). Deposits field boundaries shown by solid lines represent fields proposed by Dupuis and Beaudoin (2011). Although these diagrams effectively distinguish Kiruna, IOCG, porphyry Cu, Fe-Ti-V and BIF deposits, several of the porphyry and BIF data points plot outside the suggested fields. The Ti + V vs. Al + Mn plot highlights a clear decreasing temperature trend when data is plotted according to their respective formation temperatures (Nadoll et al., 2014). D) Gallium vs. Sn diagram for the different types of magnetite; this plot suggests that concentrations of Ga and Sn positively correlate with temperature (Nadoll et al., 2014).

Previous work has shown that the chemistry of detrital magnetite can be used for sediment provenance studies (Razjigaeva and Naumova, 1992) or to discriminate between felsic, intermediate and mafic intrusive and extrusive host rocks (Grigsby, 1990). Makvandi et al. (2015) have also highlighted that the surface textures, grain size, shape and mineral associations could offer use as sediment provenance indicators.

More recently, there have been a number of studies studying magnetite specifically associated with porphyry copper systems. Nadoll et al. (2015) identified discriminant features of hydrothermal and igneous magnetite from porphyry Cu and skarn deposits in southwestern USA, and igneous magnetite from an unmineralised, granodioritic batholith, Japan. Canil et al. (2016)

studied the chemistry of hydrothermal magnetite from porphyry Cu and skarn deposits and used principal component analysis to identify positive correlations of Al, Ti and V, which were attributed to variations in temperature and fO_2, and negative correlations of Sn and Mo with Mn and Co, which were ascribed to changes in fluid chemistry. A study by Berzina (2012) investigated the concentration of platinum group elements (PGE) in igneous magnetite from porphyry Cu-Mo deposits in Siberia, Russia. Magnetite with higher levels of Rh and lower contents of Pt and Pd were shown to discriminate magnetite associated with mineralisation from those in host rocks. Pisiak et al. (2017) investigated the use of magnetite as an indicator mineral in till surrounding the Mount Polley porphyry Cu-Au deposit, British Columbia, Canada. Linear discriminant analysis was applied to distinguish the chemistry of hydrothermal magnetite associated with mineralised porphyry systems from igneous magnetite, both related to ore and from barren rocks. This suggests their LDA model could be used to identify hydrothermal magnetite from mineralised porphyry systems in glacial till providing a potential tool in mineral exploration for buried porphyry systems.

1.3.2.3 Alteration of magnetite

Magnetite may undergo several forms of modification post-crystallisation including: oxidation "exsolution"; sphenitization; maghematization; martitization; and mushketovization (Haggerty, 1976; Nadoll et al., 2014). If we are to use magnetite as a petrogenetic indicator, it is important to understand the different alteration mechanisms, and their potential effects on the chemical composition, so that the best approximation of the original magnetite composition is studied.

i Oxidation

Oxidation "exsolution" in titanomagnetite commonly results in the formation of ilmenite solid solution lamellae. In most cases, this process of oxidation takes place at moderate pressure and above 600°C. Ilmenite solid solution intergrowths usually occurs in a trellis style along {111} spinel planes, and is often localised along cracks, around silicate inclusions, or along grain boundaries. Sphenitization can also occur through metasomatic alteration, whereby Ca and Si are added and Fe is depleted from titanomagnetite. Metasomatism can be related to late-stage fluids, synkinematic intrusions or post-supergene or low temperature deuteric oxidation (Haggerty, 1976).

Exsolution in igneous magnetite may result in the host magnetite becoming Ti-poor. Minor and trace cations may also be continuously expelled by the process (Nadoll et al., 2014). Careful petrography prior to EPMA and LA-ICP-MS analysis is therefore crucial in order to identify the

occurrence and abundance of oxidation-exsolution features so that the original composition of the titanomagnetite is best approximated.

ii Maghemitization, martitization and mushketovization

Alteration of spinel can occur via maghemitization or martitization. Maghemite (γFe_2O_3) is a cationic deficient spinel, which is cubic and optically isotropic, whereas martite (αFe_2O_3) is common hematite. Alteration to maghemite is usually associated with more titaniferous magnetite, while martitization is more commonly observed in more Ti-deficient magnetite (Haggerty, 1976). Formation of maghemite or martite from magnetite can be induced by oxidising or acidic fluids during hydrothermal alteration. The reversed alteration, magnetite after hematite under reducing fluid-rock interaction, is known as mushketovization (Nadoll et al., 2014).

With the exception of Mg, most minor cations in spinel are suggested to be retained during moderate-temperature hydrothermal oxidation. Nevertheless, it is possible that the martitization process could expel divalent cations due to their incompatible valency and ionic radii in martite (Cornell and Schwertmann, 2003), which could result in concomitant enrichment of Si, Al, Ti and Cr in martite.

iii Inclusions

Magnetite commonly contains mineral inclusions. In some cases, inclusion phases can provide useful information regarding the formation conditions and evolution of the corresponding host rock. Mineral inclusions can also be particularly valuable in cases where the host rock is lost or significantly altered, by providing geological context (Nadoll et al., 2014). Mineral inclusions in magnetite include sulphide, phosphate, quartz, silicate, and carbonate. Such inclusions may contain high concentrations of elements which are generally considered incompatible in magnetite, such as Ca, REE, and P in apatite. Elevated concentrations of such 'non-typical' magnetite elements could therefore not represent true solid solution in magnetite, and could be contributed by small-scale inclusions. Careful petrographic analysis is therefore essential in order to identify mineral inclusions prior to compositional analysis.

1.3.3 Distinguishing hydrothermal magnetite from igneous magnetite

Magnetite forms under a wide range of conditions. As well as crystallising at high temperature from silicate, sulphide or carbonatite magmas, it can also precipitate at lower temperatures from hydrothermal fluids. Importantly, both igneous and hydrothermal magnetite may be associated with porphyry copper systems. The onset of crystallisation of igneous magnetite typically occurs in arc magmas on reaching 60 wt. % SiO_2, although this can vary as a function of fO_2 (Jenner et al.,

2010). Hydrothermal magnetite can form during various alteration stages, including prior to and during early potassic alteration (Arancibia and Clark, 1996), but also later alteration phases and in more distal parts of the alteration halo (Sillitoe, 2010). The reaction of Fe^{2+}-chloride complexes with H_2O or aqueous SO_2 drives precipitation of magnetite from the fluid in shallow porphyry systems (Canil et al., 2016). Furthermore, it is possible that this mechanism could offer a means to reduce oxidised S species, thereby ensuing sulphide mineralisation (Simon et al., 2004).

It is important the two forms of magnetite are accurately discriminated and separated in order to study the contrasting igneous and hydrothermal processes in isolation. Thus, attention must be paid to distinguishing igneous and hydrothermal magnetite using detailed petrography, as well as chemistry. Hydrothermal magnetite is most easily distinguished from magmatic magnetite based on Ti content, with lower contents of Ti typically observed in hydrothermal magnetite (< 0.5 wt. % TiO_2), in comparison to magmatic magnetite (>1.5 wt. % TiO_2) (Arancibia and Clark, 1996).

1.4 PhD project

1.4.1 Experimentally investigating controls on magnetite chemistry

A goal of this project is to identify chemical disparities in magnetite, both igneous and hydrothermal, which indicate areas prospective for porphyry copper deposits. However, if we are to utilise magnetite chemistry to understand the processes advantageous for generating mineralised porphyry copper systems, a comprehensive understanding of how different factors (e.g. temperature, pressure, fO_2, mineral/melt composition) affect magnetite chemistry is required. This is merrost easily gleaned through conducting experiments since it is possible to have effective control of the different parameters of the system in which it formed. Thus, a series of experiments were designed to better constrain controls on the chemistry of a large range of elements in magnetite as a function of different parameters including fO_2, temperature, pressure and bulk composition.

1.4.1.1 Titanomagnetite-melt partitioning in an andesitic-dacitic bulk system at 1-atm

Previous experimental work has focused on investigating the partitioning of only relatively few trace elements in magnetite in a mafic bulk system, which is not appropriate for the compositional space of natural porphyry copper forming environments. An initial set of water-free experiments were devised at atmospheric pressure (0.1 MPa) using a gas-mixing furnace. Experiments at 1-atm allow the fO_2 to be varied continuously over 14 orders of magnitude. The melt, however,

cannot contain water because of volatile loss, which generally augments the liquidus to higher temperatures, in excess of 1100°C. Because of their geological relevance to porphyry systems, a natural calc-alkaline dacite and andesite were chosen as starting compositions. The use of LA-ICP-MS for analysing experiments allowed the partitioning of a large number of elements to be studied.

1.4.1.2 Diffusion and partition coefficients in magnetite in a synthetic Ca-Fe-Si bulk system

An additional consideration when using magnetite as a petrogenetic tool is diffusional re-equilibration. This is important in order to understand the likelihood and timescales necessary for the trace element chemistry to be influenced by disequilibrium element partitioning. Consequently, an additional suite of experiments were conducted to investigate diffusion in magnetite at magmatic conditions (1150°C) as a function of fO_2, within the stability range of magnetite. A novel experimental approach was used equilibrating single crystals of natural magnetite with a synthetic silicate melt reservoir. Scanning LA-ICP-MS was used to measure diffusion profiles. In addition to measuring diffusion coefficients for 27 elements in magnetite, equilibrium magnetite/melt partition coefficients can also be extracted using the interface and liquid element concentrations.

1.4.1.3 Titanomagnetite-melt partitioning in a hydrous andesitic bulk composition

Experiments conducted at atmospheric pressure enable careful control of the oxidation state and results should be applicable to magmatic processes at low pressures. However, in order to better simulate geological conditions in magma chambers linked to porphyry ore systems, experiments should be conducted at elevated pressure. In experiments conducted at 1-atm, volatile loss means it is not possible to study systems including water. Piston-cylinder apparatus, however, provide the capability to crystallise magnetite in a hydrous system at pressures representative of those at which porphyry systems form.

1.4.2 Studying the chemistry of natural magnetite from porphyry copper systems

Experimental work provides a comprehensive understanding of how different factors, notably fO_2, temperature, pressure and bulk composition, influence the chemistry of magnetite. In chapters 6 and 7 of this PhD, the chemistry of natural magnetite is studied. The ultimate goal from an exploration perspective is to use magnetite chemistry to discriminate economically-mineralised from less mineralised systems. Consequently, the chemistry of magnetite associated

with 35 porphyry copper systems covering a range of metal associations and varying degrees of mineralisation was studied using LA-ICP-MS.

Prior to embarking on collection of a large dataset of magnetite compositions by LA-ICP-MS, it is important to develop a consistent and reliable method of analysis. There is a paucity of reliable data on the trace element composition of magnetite, and few datasets lack consistency and commonly contain suspiciously high levels of elements usually deemed incompatible in magnetite (e.g. Berzina et al., 2012). Various factors, such as exsolution, alteration and impurities, create complications and uncertainties in the analysis of Fe-Ti oxides. For example, ilmenite exsolution in igneous magnetite can result in the host magnetite becoming Ti-poor and other cations may be continuously expelled by the process. Thus, a study was conducted to research and develop a method which optimises the use of LA-ICP-MS to accurately and reliably measure the concentration of natural Fe-Ti oxides.

Using the optimised analytical method, over 2000 magnetite grains were analysed from the sample set using LA-ICP-MS. The sample set consists of rocks mostly from porphyry intrusions, but also includes other intrusive phases associated with porphyry copper systems and coeval volcanics. The style of alteration in the samples was documented so the effect of alteration on the magnetite chemistry could be evaluated. Importantly, all magnetite grains analysed were subject to detailed petrographic study prior to LA-ICP-MS analysis to assess the formation process of magnetite and document textures which could be related to compositional variations.

The natural magnetite analysed includes both igneous and hydrothermal magnetite. Given the contrasting formation environments of the two forms of magnetite, first, particular attention was paid to distinguishing igneous and hydrothermal magnetite based on chemistry and textural observations. Once hydrothermal and igneous magnetite were identified, the potential effects of porphyry system type, host lithology, alteration type and degree of mineralisation on magnetite composition was investigated. Discriminant plots were developed that separate populations of hydrothermal magnetite between strongly mineralised, less mineralised and barren porphyry intrusions based on their chemistry.

2 Titanomagnetite-melt partitioning in an andesitic-dacitic bulk system at 1-atm

2.1 Introduction

Although previous experimental work has studied partitioning of various elements into magnetite as a function of different bulk composition, temperature, fO_2 and pressure, few studies have covered the range of trace elements detectable using LA-ICP-MS. To develop a better understanding of the partitioning behaviour of a wide range of elements into magnetite, a set of experiments were conducted at atmospheric pressure (0.1 MPa) as a function of fO_2 (FMQ + 0.2 to FMQ + 3.7) and temperature (1070 to 1120°C).

The growth of crystals large enough to measure low trace element abundances has previously posed a challenge in experimental petrology because of the inverse relationship between analysis volume and detection limits. LA-ICP-MS analysis of trace elements requires the crystal size to be large (generally > 20 μm). Previous studies have overcome issues regarding crystal size by doping starting materials to high concentrations e.g. 10,000 ppm (Nielsen et al., 1994) and analysing magnetite composition by EPMA. However, recent work has highlighted that such highly doped systems could in fact overestimate partition coefficients (Righter et al., 2006; Prowatke and Klemme, 2006a). Moreover, only a few elements can be added at such levels without compromising the systems bulk chemistry. Fortunately, the development of LA-ICP-MS has significantly enhanced the ease with which the trace element chemistry of magnetite can be determined. Magnetite associated with magmatic-hydrothermal mineral deposits has been recognized as a potential indicator mineral for fertility (Dare et al., 2014). Such deposits are commonly associated with calc-alkaline, intermediate to felsic magmas. Consequently, a natural calc-alkaline andesite and dacite were chosen as starting compositions for this study. Previous work has not investigated in detail the influence of fO_2 on the trace element partitioning of magnetite in an andesitic-dacitic bulk compositional range.

2.1.1 Theoretical background

Magnetite-melt partitioning relations are not only useful for petrogenetic modelling, they also hold theoretical interest for understanding some of the fundamental principles of trace-element geochemistry. In particular, the very large variation in magnetite-melt partition coefficients observed for many elements over a restricted range of melt compositions at a given temperature and pressure highlights the importance of the "stoichiometric control" in trace-element partitioning. In magnetite, the major-element components providing the stoichiometric control are $Fe^{2+}O$ and $Fe^{3+}O_{1.5}$, whose activities in the melt, unlike those of silicate minerals, can be varied

greatly while still maintaining magnetite on the liquidus. However, this variation in the activities can only occur subject to two constraints, namely the homogeneous equilibrium involving fO_2:

$$Fe^{2+}O_{(silicate\ melt)} + ¼\ O_2 = Fe^{3+}O_{1.5(silicate\ melt)} \quad (2\text{-}1)$$

And the condition of magnetite saturation:

$$Fe^{2+}O_{(silicate\ melt)} + 2\ Fe^{3+}O_{1.5(silicate\ melt)} = Fe_3O_{4(spinel)} \quad (2\text{-}2)$$

These constraints impose a correlation between the variables in magnetite-melt partitioning experiments, which must be deconvoluted by recourse to the underlying thermodynamic principles.

Magnetite has the spinel structure, with the ideal stoichiometry of 3 cations to 4 oxygens per formula unit (i.e., Fe_3O_4). The deviations from this ideal stoichiometry are very small over the temperature-fO_2 range relevant to this study, with $\delta < 0.002$ in the formula $Fe_{3-\delta}O_4$, according to the thermogravimetric measurements of Dieckmann (1982). The spinel structure has two distinct crystallographic sites for cations, one having perfectly regular tetrahedral coordination, the other with almost regular octahedral coordination (e.g., O'Neill and Navrotsky, 1984), providing suitable environments for cations with a preference for highly symmetrical coordination environments. For example, Ni^{2+} and Cr^{3+} would be expected to partition readily into magnetite because of their large crystal-field stabilization energies in regular octahedral coordination, but cations with potentially strong Jahn-Teller distortions like Cr^{2+} are less favoured. The cation distribution in magnetite at room temperature is that of an inverse spinel $(Fe^{3+})_{tet}[Fe^{2+}Fe^{3+}]_{oct}O_4$, but at magmatic temperatures it is disordered towards the random distribution, $(Fe^{2+}_{1/3}Fe^{3+}_{2/3})_{tet}[Fe^{2+}_{2/3}Fe^{3+}_{4/3}]_{oct}O_4$ (Wu and Mason, 1981). Its structure therefore provides crystallographic sites suitable for both 2+ and 3+ cations in both tetrahedral and octahedral coordination. The presence of Fe in two valence states (2+ and 3+) also facilitates charge-balancing of cations with other valence states. Tetravalent cations such as Ti^{4+} or Ge^{4+} can substitute easily onto octahedral or tetrahedral sites, as appropriate, charge-balanced by additional Fe^{2+}, e.g., $Ti^{4+} + Fe^{2+}$ for $2\ Fe^{3+}$. In addition to the large range of 2+, 3+ and 4+ cations forming ferrite spinels with extensive binary solid solutions with Fe_3O_4 (e.g. O'Neill and Navrotsky 1984), there may be extensive incorporation of 1+ and 5+ cations. Examples are Li^{1+}, as in the end-member spinel $Li^{1+}_{0.5}Fe^{3+}_{2.5}O_4$ ($Li^+ + Fe^{3+}$ for $2\ Fe^{2+}$); and Nb^{5+}, for which the phase relations in the system Fe-Nb-O at 1180-1200°C show that niobian magnetites may be synthesized with up to ~80% solid solution towards the hypothetical end-member $Fe^{2+}_{2.33}Nb^{5+}_{0.67}O_4$ (Turnock, 1966; Kitayama, 1987).

A distinctive feature of magnetite-melt trace-element partitioning is that while the oxidation states of redox-variable elements, including Fe, change with fO_2 in the melt, they do not change with fO_2 in magnetite. The reason is obvious for Fe, because stoichiometry obviously fixes Fe^{3+}/Fe^{2+} at 2 for pure magnetite. But this same constraint also applies to some redox-variable trace elements, because its redox speciation will be controlled by an electron-exchange reaction with Fe^{2+} and Fe^{3+}. A well-known example is V, whose substitution into Fe_3O_4 has been studied by thermodynamic measurements on the spinel solid solution FeV_2O_4-Fe_3O_4 (O'Neill and Navrotsky, 1984). Here, the two oxidation states of V are 3+ and 4+, hence the electron-exchange reaction is:

$$Fe^{3+} + V^{3+} = Fe^{2+} + V^{4+}$$

Thus the ratio of V^{3+} to V^{4+} in FeV_2O_4-Fe_3O_4 spinels is independent of fO_2 at a given temperature and pressure; this includes the ratio at infinite dilution. When the free energy of such an electron exchange reaction is small, the phenomenon contributes a considerable configurational entropy, as seen for example, by the large negative deviations from ideality in Fe_3O_4-FeV_2O_4 (O'Neill and Navrotsky, 1984). This effect makes V, usually moderately incompatible in common silicate minerals, compatible in magnetite. By contrast, V^{3+}/V^{4+} in a spinel without Fe or other redox-variable major elements, such as $MgAl_2O_4$, can only vary in a way that depends on fO_2. For example, in the system MgO-Al_2O_3-V-O, the relevant V components in spinel would be $MgV^{3+}{}_2O_4$ and $Mg_2V^{4+}O_4$, hence the redox speciation of V in the spinel phase is given by the equilibrium:

$$0.5\ MgV^{3+}{}_2O_4 + 1.5\ MgO + 0.25\ O_2 = Mg_2V^{4+}O_4$$

For a detailed consideration of the thermodynamics of the mineral/melt partitioning of V as a function of fO_2, see Mallmann and O'Neill (2009). Insofar as the spinels of this study are rich in the Fe_3O_4 component, the redox speciation of redox-variable elements may be expected to be dominated by electron-exchange reactions and stoichiometry, rather than directly reflecting fO_2. Hence the effect of fO_2 on the partitioning of redox-variable elements, such as V, Cu and Mo, between Fe_3O_4–rich spinel and melt requires a particularly careful formulation of the underlying thermodynamic relations.

2.2 Experimental procedures

2.2.1 Starting compositions

Two natural lavas were chosen as experimental starting materials: a natural dacite, 'Japanese Andesite-1' (JA-1); and an andesite 'Andesite 190' (Henderson et al., 1985). Two additional compositions were prepared from these starting materials by adding an extra 5 wt. % Fe_2O_3 to promote magnetite saturation. In order to check the bulk chemistry of the starting materials, superliquidus experiments were conducted in a 1-atm furnace at 1400°C. The glasses produced were subsequently characterised by EPMA (Table 2-1).

Table 2-1 Major element composition of experimental starting materials as determined by EPMA of glasses

	JA-1 (n = 12)	JA-1 + Fe_2O_3 (n = 11)	And-190 (n = 14)	And-190 + Fe_2O_3 (n = 8)
Major elements (wt. %)				
Na_2O	3.50(5)	3.37(7)	4.15(6)	3.6(1)
SiO_2	65.9(5)	62.7(9)	57.5(3)	55.4(7)
MgO	1.57(5)	1.48(5)	3.41(3)	3.3(1)
Al_2O_3	15.1(1)	14.4(4)	17.8(1)	16.74(4)
P_2O_5	0.13(1)	0.12(2)	0.16(2)	0.14(2)
K_2O	0.78(1)	0.76(3)	1.88(5)	1.65(9)
CaO	5.8(2)	5.5(2)	6.6(1)	6.6(2)
TiO_2	0.86(3)	0.84(2)	0.90(2)	0.86(2)
FeO*	6.4(4)	10.3(6)	6.2(1)	10.2(4)
MnO	0.15(1)	0.12(2)	0.12(2)	0.12(2)

n = number of replicate analysis. Errors = 1 σ standard deviation. FeO = total FeO assuming all Fe is FeO*

2.2.2 Choice of trace elements and doping

The initial starting materials used in this study were not doped with additional trace elements. However, some elements were not detectable with LA-ICP-MS analysis using this approach. Therefore, an additional starting material was prepared by doping the And-190 + Fe_2O_3 starting material with trace elements, but only in sufficient quantity to raise the expected concentration above the limit of detection for LA-ICP-MS. Expected detection limits based on a 15 micron spot size, were sourced from Nadoll et al. (2014), and expected partition coefficients were derived from existing literature values (Ewart and Griffin, 1994; Luhr and Carmichael, 1980; Nielsen and Beard, 2000). Consequently, Co, Ni, V, Zn, Ga, Nb, Cu and Sn were doped at 10 ppm; and Sc, Zr, Hf, Ta, Mo, Pb, Th, U and In were doped at 100 ppm. Trace elements were added to the starting composition as inductively-coupled-plasma standard nitrate solutions; the mixture was then dried under a heat lamp and finally re-homogenized in an agate mortar.

2.2.3 Magnetite synthesis method

Approximately 100 mg of each starting material was mixed with polyethylene oxide and water to form a paste, which was pressed onto 0.3 mm diameter Pt wire loops. Thin loops were used to avoid Fe loss. The Pt wire loops were then suspended from a Pt chandelier at the end of an alumina rod in the hot zone of a GERO 1-atm vertical furnace at a temperature of 600°C and the gas mixing ratios set to produce the desired fO_2. Gas mixing ratios were regulated using Celerity FC2900 mass flow controllers (see Burnham et al., (2015) for further experimental details).

Samples were heated to 1250°C and held for 9h, in order to promote homogeneity and equilibration with the imposed fO_2. The temperature was then cooled at 20°C/h to 1190°C, and subsequently cooled at 3°C/h to the desired temperature where samples were held for 36 hours. The temperature was then cycled up at 5°C/h to reduce the number of magnetite nucleation sites, then cooled at 3°C/h again to the desired temperature where samples were held for at least three days before drop-quenching into water. The incorporation of a temperature cycle significantly increased magnetite crystal size in experiments with composition And-190 + Fe_2O_3 (some >100 micron) generating crystals sufficiently large for LA-ICP-MS analysis. It is worth noting that although the absolute fO_2 in the furnace varies with temperature, gas mixing ratios used to define the fO_2 do not substantially vary the fO_2 relative to common fO_2 buffers. As a result, only a negligible change in oxidation state (< 0.05 $Fe^{3+}/\Sigma Fe$) of the melt would have occurred during temperature fluctuations in experimental runs. Details of all experimental runs are provided in Table 2-2.

Table 2-2: Experimental conditions

Run[a]	Final T (°C)	log *f*O2	ΔFMQ[b]	Time (h)[c]
RSM-20	1070	-9.82	0.2	112
RSM-6	1070	-9.02	1	78
RSM-11	1070	-8.02	2	102
RSM-21	1070	-7.02	3	109
RSM-9	1070	-6.31	3.7	97
RSM-19	1095	-8.38	1.2	136
RSM-15	1095	-7.68	2	121
RSM-12	1095	-6.68	3	112
RSM-18	1095	-5.98	3.7	101
RSM-16	1120	-7.16	2.2	115
RSM-4	1120	-6.36	3	114
RSM-17	1120	-5.66	3.7	103
RSM-10	1070	-9.02	1	344

[a] *For each experimental run, all starting compositions were equilibrated*
[b] *ΔFMQ = logfO_2 (experiment) – logfO_2 (FMQ buffer); values of FMQ calculated using Hemmingway (1990)*
[c] *Time represents dwell time in hours at the final temperature after temperature cycle was completed*

Temperature inside the furnace was calibrated using a type B thermocouple and the fO_2 calibrated using a SIRO2 solid state electrode. Temperature is considered accurate to ±1°C, and log fO_2 is accurate to ± 0.1.

2.2.4 Analytical methods

Run products were examined using a Zeiss EVO 15LS scanning electron microscope in the Imaging and Analysis Centre at the Natural History Museum, London. Energy-dispersive spectroscopy (EDS) was used in conjunction with back-scattered electron (BSE) imaging to identify the composition of the phases. Analytical conditions were 20 kV accelerating voltage, 3 nA sample current and a 1 μm spot size.

A Cameca SX-100 electron microprobe, also at the Natural History Museum, London, was used to measure major and some trace element contents. Silicon, Al, Mg, Fe, Ca, P, Ti, Mn, Na, Cr, K and V were analysed for in both titanomagnetite and silicate glass analyses. Alkali elements, such as Na and K, were included in the analysis of titanomagnetite to be sure no contamination by glass occurred. A 20 kV accelerating voltage, 10 nA sample current and focused electron beam with 1 μm spot size was used for titanomagnetite analyses. For glass analyses, analytical conditions were 20 kV, 2 nA and a defocused (10-20 μm) beam in order to minimise migration of alkalis.

Trace elements below the limit of detection of EPMA, were obtained by LA-ICP-MS. This was carried out in the LODE laboratory at the Natural History Museum, London using a New Wave Research 193 nm excimer laser coupled with an Agilent 7700x quadrupole ICP-MS. For titanomagnetite analyses, the laser was operated with a pulse rate of 5 Hz, a fluence of 3.5 J cm^{-2}, and a spot size of 11-35 μm depending on the crystal size. With decreasing spot size, the limits of detection increase and there is more variability in the data, and thus larger spot sizes were utilised wherever possible. Occasionally, the laser drilled through a target magnetite crystal into the underlying glass; in such cases, only the portion of the signal within titanomagnetite was integrated (Figure 2-1). Each batch of analyses was bracketed by three analyses of a primary calibration standard (GSD-1g) and a secondary standard (GSE-1g). Each batch of magnetite analyses also included one analysis of a Ti-rich magnetite (BC28) studied by Dare et al. (2012). The Fe concentration, determined by EPMA, was used as the internal standard. For glass analyses, a pulse rate of 10 Hz, fluence of 3.5 J cm^{-2}, and a spot size of 20-50 μm were used. GSD-1g was used as the primary calibration standard, and NIST 612 as a secondary standard. Ca determined by EPMA was used as the internal standard. In all cases the analysis duration was 90 s, with the first 30 s monitoring a gas blank prior to ablation. The isotopes analysed were ^{23}Na, ^{24}Mg, ^{27}Al, ^{29}Si, ^{31}P, ^{39}K, ^{43}Ca, ^{45}Sc, ^{49}Ti, ^{51}V, ^{52}Cr, ^{55}Mn, ^{57}Fe, ^{59}Co, ^{60}Ni, ^{63}Cu, ^{65}Cu, ^{66}Zn, ^{69}Ga, ^{72}Ge, ^{89}Y, ^{90}Zr, ^{93}Nb,

^{95}Mo, ^{115}In, ^{118}Sn, ^{177}Hf, ^{181}Ta, ^{182}W, ^{208}Pb, ^{232}Th and ^{238}U, for both titanomagnetite and glass. Data were reduced using ExLAM 2000 (Zacharias and Wilkinson 2007).

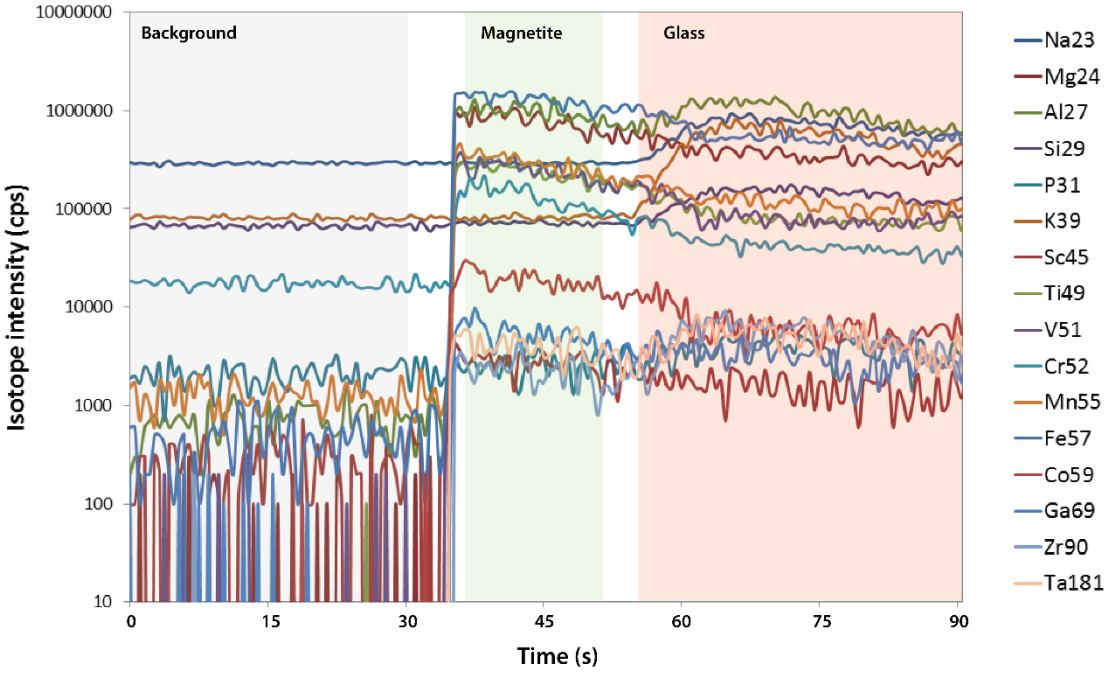


Figure 2-1: Time-resolved analytical signal for an analysis of a titanomagnetite grain from experiment RSM-19 (T = 1095°C, fO_2 = FMQ+1.3) using And-190+Fe_2O_3 starting material using an 18 µm laser spot size. Mid-way through the ablation signal, the laser has drilled through the titanomagnetite grain into the underlying glass; in this case only the start of the ablation signal was used for data processing. Note only a selection of isotopes analysed is shown for clarity.

2.3 Results

Experimental charges consist of quenched melt + plagioclase ± titanomagnetite ± orthopyroxene ± clinopyroxene (Figure 2-2). Titanomagnetite was present in all experiments conducted with And-190 with added Fe_2O_3 (And-190 + Fe_2O_3), and in all experiments using And-190 without added Fe_2O_3, excluding one experiment at T = 1070°C and fO_2 = FMQ + 0.2. At constant T, with increasing fO_2, the proportion of quenched melt decreases and the proportion of titanomagnetite and plagioclase increases. With increasing fO_2 there is also a decrease in the crystal size of the silicate mineral phases. Addition of Fe_2O_3 to both starting compositions significantly increased the modal proportions and average crystal size of titanomagnetite, generating some crystals > 100 µm across. Consequently, results in the dacitic bulk system focus on experiments using JA-1 with added Fe_2O_3, where titanomagnetite was also present over a greater range of fO_2 and temperature. Titanomagnetite crystals exhibit variable morphology and crystal size. Some display euhedral to subhedral equant forms whereas others are more skeletal.

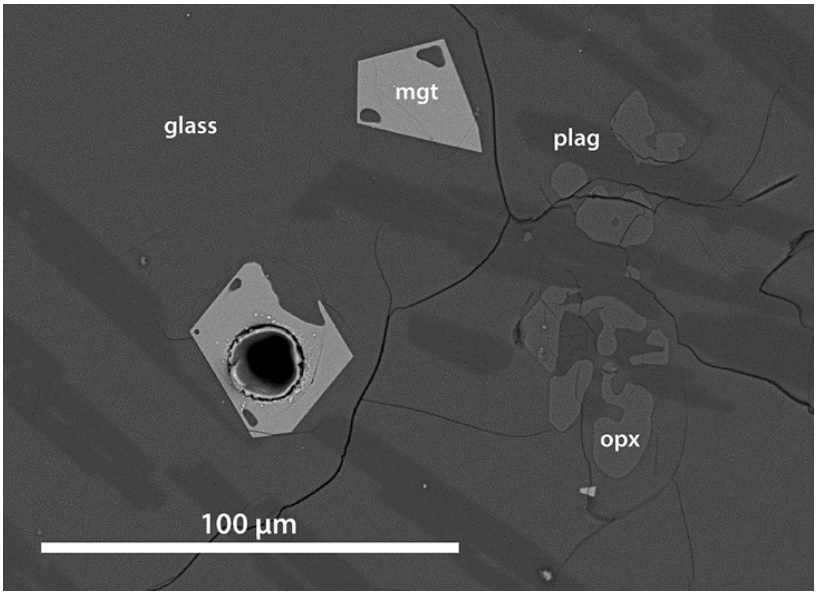


Figure 2-2: Back-scattered electron image of titanomagnetite (mgt), plagioclase (plag) and orthopyroxene (opx) in silicate glass synthesised from Andesite-190 + 5 wt. % Fe_2O_3 at 1095°C and fO_2 = FMQ + 1.2. The hole is a laser-ablation pit in titanomagnetite.

Melts in all experiments quenched to a homogeneous glass without any evidence of quench crystallisation, apart from one experiment using And-190 + Fe_2O_3 at 1070°C and fO_2 = FMQ + 3.7 (RSM-9), in which fine grained plagioclase throughout the glass made it impossible to analyse.

The major-element compositions of titanomagnetite and glass, as well as D(X) values for some elements analysed with EPMA are listed in Table 2-3. Trace element concentrations of titanomagnetite and glass, as well as D(X) values, are given in Table 2-4.

Addition of Fe_2O_3 to Andesite-190 does not significantly affect partition coefficients for elements detectable using EPMA (Table 2-3), namely: Al, Ti, Mn and Mg. Using LA-ICP-MS it was also possible to determine Sc, V, Co, Ni, Zn, Ga, Zr, and sometimes Cu, Mo, Nb, Hf and Ta concentrations in titanomagnetite in experiments with larger titanomagnetite grains (generally higher fO_2). The concentrations of Y, W, Pb, Th and U were not above their limits of detection by LA-ICP-MS in titanomagnetite in any experiments, including those doped with trace elements, and are therefore not reported. Furthermore, Ge, Sn, In and Pb suffered significant volatile loss, as evinced by lower concentrations than would be expected after doping, so that reliable titanomagnetite-melt partitioning data could not be determined for these elements. Using EPMA, it was possible to detect Si, Al, Mg, Fe, Ca, P, Ti, Mn, Na and K in glass. All other elements reported for glass composition were analysed by LA-ICP-MS. Using GSD-1g as a calibration standard for titanomagnetite and glass produces strong correlation between EPMA and LA-ICP-MS for those elements detectable by both techniques, offering a means to cross-check the accuracy of the LA-ICP-MS data (Figure 2-3).

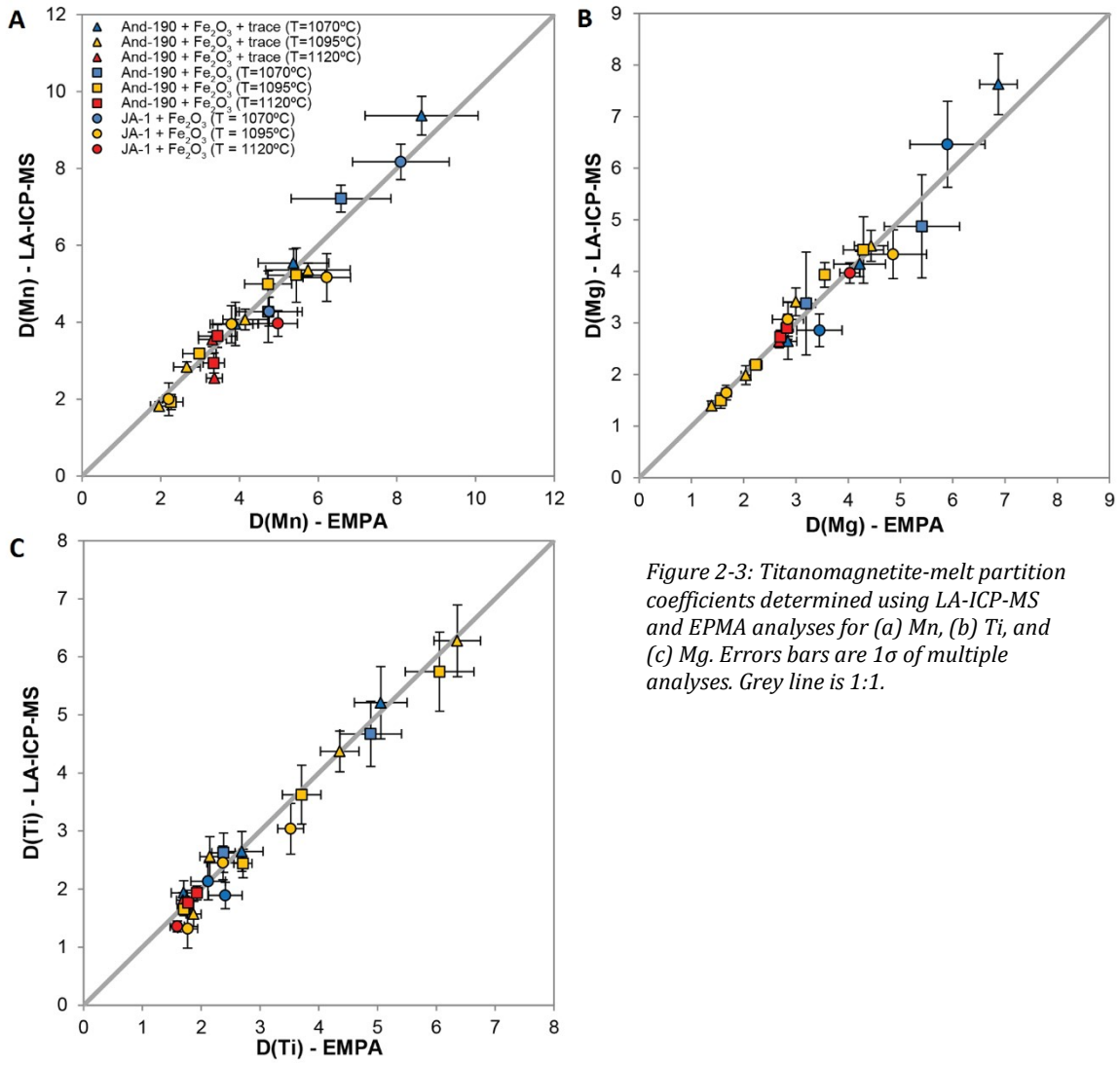


Figure 2-3: Titanomagnetite-melt partition coefficients determined using LA-ICP-MS and EPMA analyses for (a) Mn, (b) Ti, and (c) Mg. Errors bars are 1σ of multiple analyses. Grey line is 1:1.

Titanomagnetites are dominated by a magnetite (Fe_3O_4) component, but also have significant ulvospinel (Fe_2TiO_4), spinel ($MgAl_2O_4$) and magnesioferrite ($MgFe_2O_4$) components. Although the same bulk starting compositions were used in all experiments, there are consistent variations in the composition of the titanomagnetite and quenched melt compositions as a function of fO_2. Notably, with increasing fO_2 there is a decrease in Ti cations per formula unit (cpfu) and increase in Mg and Mn cpfu, whilst the total FeO* and Al cpfu remain relatively constant. In the melt, there is a marked decrease in FeO* and CaO, and increase in SiO_2 contents with increasing fO_2, as a consequence of the increased modal abundance of titanomagnetite and plagioclase.

2.3.1 Attainment of equilibrium

Experiments conducted for longer durations (> 14 days) indicate that the dwell time at the final temperature (3 days) was sufficient to provide a close approach to equilibrium (Figure 2-4). Incorporation of a temperature cycle was also shown to have no significant impact on the experimentally determined partition coefficients for elements detected using EPMA (Figure 2-4). BSE images of the experimental charges do not reveal any compositional zoning in titanomagnetite or glass (Figure 2-2), which is supported by homogeneous compositions determined in line traverses across grains, and low standard deviations for replicate analyses of both titanomagnetite and glass. Collectively, these data suggest that equilibrium was attained in all experiments.

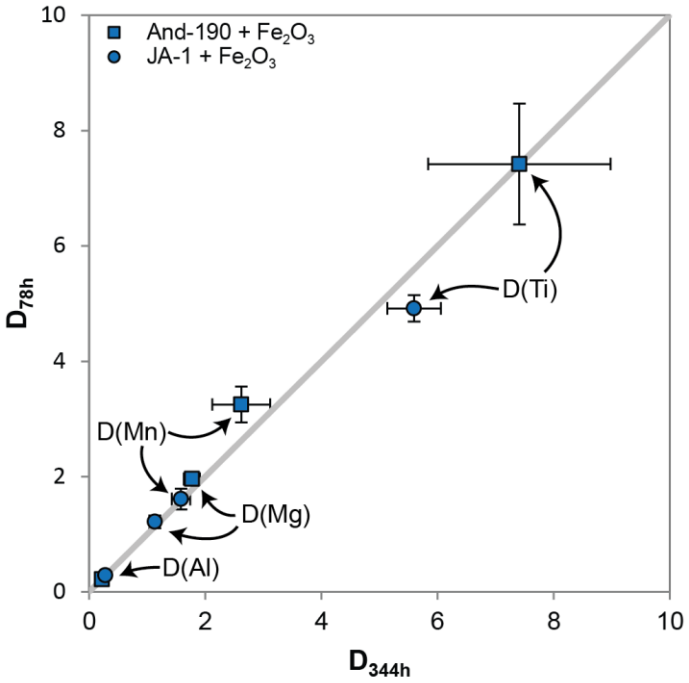


Figure 2-4: Experimentally determined partition coefficients (D) from an experiment with a dwell time of 78h vs. D values determined from an experiment with a dwell time of 344h. Both experiments were conducted at 1070°C and fO_2 = FMQ + 1 and included both JA-1 + Fe2O3 and And-190 + Fe_2O_3. No temperature cycle was used in the longer 344h experiment. Grey line is 1:1 and error bars = 1σ .

Loss of certain elements during an experiment could present issues when determining equilibrium partition coefficients. For example, Ni, Co and Cu could be susceptible to alloying with the Pt wire, and Zn could be lost through volatility. For Co and Ni, concentrations in the glass do not decrease with decreasing fO_2, which indicates that there was not significant loss of these elements during the experiments. There is a slight decrease in Cu concentration with decreasing fO_2 suggesting that there was minor loss during the experiments. Zinc concentrations are also lowest at low fO_2, which suggests there was some volatile loss at low fO_2. Thus values of D(Cu) and D(Zn) should be viewed with caution.

Table 2-3: Glass and titanomagnetite major element composition determined using EPMA and partition coefficients for major elements

Experiment	RSM-6	RSM-11	RSM-21	RSM-9	RSM-19	RSM-15	RSM-12	RSM-18	RSM-16	RSM-4	RSM-17
log fO_2	-9.02	-8.02	-7.02	-6.31	-8.38	-7.68	-6.68	-5.98	-7.16	-6.36	-5.66
ΔFMQ	1	2	3	3.7	1.3	2	3	3.7	2.2	3	3.7
T (°C)	1070	1070	1070	1070	1095	1095	1095	1095	1120	1120	1120
Starting material	A-190	A-190	A-190	A-190	A-190	A-190	A-190	A-190	A-190	A-190	A-190
Coexisting phases	mgt, plag, opx, liq	mgt, plag, opx, cpx, liq	mgt, plag, opx, cpx, liq	mgt, plag, opx, cpx, liq	mgt, plag, opx, liq	mgt, plag, opx, liq	mgt, plag, opx, liq	mgt, plag, opx, cpx, liq	mgt, plag, opx, liq	mgt, plag, opx, liq	mgt, plag, opx, liq
Glass (wt. %)											
n	13	14	17	7	14	10	15	14	9	5	11
Na_2O	3.4(5)	3.6(2)	4.1(3)	3.5(2)	3.4(4)	3.65(6)	3.9(2)	3.7(3)	3.77(6)	3.79(6)	3.8(1)
Al_2O_3	13.3(1)	13.4(1)	13.8(4)	13.5(3)	14.0(3)	14.0(1)	13.9(1)	14.2(5)	14.70(7)	14.10(2)	14.3(2)
K_2O	3.3(3)	3.7(3)	3.72(9)	4.2(1)	2.9(2)	3.14(9)	3.3(2)	3.1(1)	2.29(5)	2.79(3)	2.53(8)
CaO	3.7(2)	2.9(1)	2.6(2)	2.61(8)	4.3(3)	4.1(2)	3.8(1)	3.8(3)	5.0(1)	4.80(6)	4.5(2)
P_2O_5	0.37(3)	0.35(5)	0.32(5)	0.38(6)	0.29(5)	0.35(3)	0.31(5)	0.30(3)	0.25(2)	0.26(1)	0.25(4)
TiO_2	1.6(1)	1.4(1)	1.37(9)	1.42(6)	1.42(6)	1.38(5)	1.37(4)	1.32(3)	1.11(2)	1.16(4)	1.08(5)
FeO*	6.2(3)	4.4(2)	3.3(2)	3.2(2)	6.2(9)	5.4(2)	4.7(1)	4.0(2)	6.6(2)	5.4(2)	4.8(1)
MnO	0.12(1)	0.106(5)	0.09(1)	0.08(1)	0.14(1)	0.13(2)	0.12(1)	0.11(1)	0.15(2)	0.14(1)	0.136(7)
MgO	1.7(1)	1.40(4)	1.4(1)	1.40(3)	2.3(2)	2.2(1)	2.09(5)	2.1(1)	4.4(2)	3.9(3)	4.0(2)
SiO_2	66.4(9)	68.7(9)	69.5(8)	71.2(2)	64(1)	66.0(8)	67.4(7)	67(1)	61.9(3)	63.8(7)	64(1)
Fe^{3+}/Total Fe[a]	0.229(6)	0.325(2)	0.437(4)	0.514(3)	0.249(5)	0.320(1)	0.429(2)	0.502(1)	0.366(1)	0.4240(6)	0.500(2)
NBO/T[b]	0.17(2)	0.109(5)	0.084(9)	0.072(2)	0.19(2)	0.16(1)	0.130(4)	0.102(7)	0.25(1)	0.217(1)	0.19(1)
Optical Basicity[c]	0.552	0.548	0.546	0.544	0.558	0.555	0.553	0.551	0.566	0.561	0.559
XFeO1.5[d]	0.0112	0.0111	0.0114	0.0128	0.0123	0.0134	0.0155	0.0157	0.0188	0.0175	0.0188
XFeO[d]	0.0376	0.0232	0.0147	0.0121	0.0371	0.0285	0.0207	0.0155	0.0325	0.0239	0.0189
Mgt (wt. %)											
n	7	13	5	5	6	10	12	9	8	11	5
Al_2O_3	2.93(5)	2.73(4)	3.3(3)	3.2(2)	3.63(7)	3.39(6)	3.36(8)	3.5(2)	5.5(3)	5.3(2)	6.0(3)
CaO	0.18(7)	0.17(2)	0.12(3)	0.15(3)	0.17(5)	0.16(4)	0.14(3)	0.13(2)	0.14(2)	0.14(3)	0.13(2)
TiO_2	11.3(1)	6.2(5)	3.5(6)	3.3(2)	6.7(2)	4.7(2)	3.9(4)	2.4(1)	3.4(2)	2.1(1)	2.1(1)
FeO*	74.3(8)	78.0(5)	77.3(3)	77.6(1)	77(2)	78.6(7)	78.4(4)	76.4(5)	75.4(5)	73.9(5)	72.7(4)
MnO	0.36(1)	0.49(3)	0.64(6)	0.65(5)	0.37(2)	0.43(2)	0.48(2)	0.63(2)	0.32(2)	0.47(2)	0.46(2)
V_2O_3	0.7(1)	0.26(4)	0.08(3)	< dl	0.37(2)	0.17(2)	0.09(2)	< dl	0.10(1)	< dl	< dl
Cr_2O_3	0.20(6)	0.2(2)	0.16(6)	0.11(2)	1(1)	0.4(1)	0.15(6)	0.08(4)	1.7(5)	0.15(4)	0.12(6)
MgO	3.56(8)	4.7(2)	7.8(8)	8.5(3)	4.51(4)	5.5(1)	6.7(2)	9.2(2)	6.9(4)	10.2(3)	11.6(4)
SiO_2	0.4(1)	0.31(9)	0.14(2)	0.21(1)	0.3(1)	0.2(1)	0.25(7)	0.21(1)	0.18(3)	0.4(3)	0.3(3)
Mg#	0.151(7)	0.22(1)	0.39(4)	0.42(2)	0.213(4)	0.267(6)	0.33(2)	0.464(8)	0.34(2)	0.51(2)	0.57(1)
$a Fe_3O_4$[e]	0.488	0.551	0.495	0.481	0.516	0.542	0.521	0.541	0.476	0.409	0.359
D(mgt/melt)											
D(Al)	0.220(4)	0.204(4)	0.24(2)	0.23(2)	0.259(7)	0.243(5)	0.242(6)	0.25(2)	0.37(2)	0.37(1)	0.42(2)
D(Ti)	7.0(8)	4.4(5)	2.5(5)	2.4(2)	4.7(3)	3.4(2)	2.9(3)	1.84(1)	3.1(2)	1.8(1)	2.0(1)
D(Mn)	3.0(4)	4.7(4)	7(1)	8(1)	2.7(3)	3.2(5)	4.2(5)	5.7(8)	2.1(3)	3.3(3)	3.3(2)
D(Mg)	2.1(2)	3.3(2)	5.5(7)	6.0(3)	1.9(2)	2.5(1)	3.2(1)	4.4(3)	1.6(1)	2.6(2)	2.9(2)

[a] Fe^{3+}/Total Fe in melt calculated using Kress and Carmichael (1991)
[b] NBO/T calculated as described in Toplis and Corgne (2002)
[c] Optical basicity calculated using optical basicity values of component oxides provided in Duffy (1993)
[d] Number of moles of $Fe^{3+}O_{1.5}$ and $Fe^{2+}O$ on a single cation basis as described in O'Neill and Eggins (2002)
[e] Mg# is Mg/(Mg + Fe^{2+}). Fe^{2+} calculated from stoichiometry.
[f] Activity of Fe_3O_4 in titanomagnetite calculated using model from O'Neill and Wall (1987)
Precision (± 1σ) is standard deviation of multiple (n) analyses.
< dl = less than limit of detection

Table 2-3 continued

Experiment	RSM-20	RSM-6	RSM-11	RSM-21	RSM-19	RSM-15	RSM-12	RSM-18	RSM-16	RSM-4	RSM-17
log f_{O_2}	-9.82	-9.02	-8.02	-7.02	-8.38	-7.68	-6.68	-5.98	-7.16	-6.36	-5.66
ΔFMQ	0.2	1	2	3	1.3	2	3	3.7	2.2	3	3.7
T (°C)	1070	1070	1070	1070	1095	1095	1095	1095	1120	1120	1120
Starting material	A-190 + Fe	A-190 + Fe	A-190 + Fe	A-190 + Fe	A-190 + Fe	A-190 + Fe	A-190 + Fe	A-190 + Fe	A-190 + Fe	A-190 + Fe	A-190 + Fe
Coexisting phases	mgt, plag, opx, liq	mgt, plag, opx, cpx, liq	mgt, plag, opx, liq	mgt, plag, opx, cpx, liq	mgt, plag, opx, cpx, liq	mgt, plag, opx, cpx, liq	mgt, plag, opx, cpx, liq	mgt, plag, opx, cpx, liq	mgt, plag, opx, liq	mgt, plag, opx, liq	mgt, plag, opx, liq
Glass (wt. %)											
n	10	15	8	13	14	9	16	12	10	5	12
Na_2O	3.1(5)	3.6(3)	3.17(9)	4.0(7)	3.5(3)	3.7(1)	3.8(3)	3.7(3)	3.74(4)	3.71(7)	3.85(6)
Al_2O_3	13.5(1)	13.5(1)	13.3(2)	14.1(7)	14.0(2)	14.2(3)	13.7(2)	13.5(4)	14.6(2)	13.9(1)	14.1(2)
K_2O	3.2(1)	3.5(2)	4.10(8)	3.6(1)	2.87(7)	3.00(5)	3.3(2)	2.9(1)	2.23(5)	2.67(7)	2.55(6)
CaO	4.1(3)	3.7(2)	2.86(7)	2.8(4)	4.4(1)	4.29(1)	3.56(8)	3.9(2)	5.1(1)	4.84(9)	4.6(2)
P_2O_5	0.39(3)	0.35(4)	0.37(3)	0.32(4)	0.28(2)	0.31(4)	0.32(3)	0.27(4)	0.24(2)	0.29(2)	0.27(3)
TiO_2	1.1(2)	1.1(1)	1.01(9)	1.10(6)	1.08(8)	1.02(4)	1.10(5)	1.16(7)	0.92(2)	1.02(3)	1.00(4)
FeO*	8.6(7)	6.7(4)	4.4(1)	3.4(4)	7.6(2)	5.6(2)	4.5(1)	4.3(3)	7.1(1)	5.2(1)	4.9(1)
MnO	0.11(1)	0.105(1)	0.08(1)	0.08(1)	0.13(2)	0.12(2)	0.09(1)	0.10(1)	0.14(2)	0.118(8)	0.11(2)
MgO	1.68(7)	1.56(5)	1.34(3)	1.5(2)	2.31(6)	2.25(9)	1.96(3)	2.2(2)	3.95(8)	3.76(9)	3.5(1)
SiO_2	62.3(6)	66.1(9)	70.0(7)	69(1)	63.1(5)	66.0(6)	68.8(4)	67.2(6)	62.0(4)	64.6(3)	64.9(5)
Fe^{3+}/Total Fe[a]	0.166(1)	0.231(4)	0.3220(9)	0.44(1)	0.246(4)	0.319(2)	0.428(3)	0.505(5)	0.3650(6)	0.423(2)	0.501(1)
NBO/T[b]	0.224(1)	0.17(1)	0.101(6)	0.08(2)	0.208(8)	0.165(5)	0.119(3)	0.12(2)	0.235(6)	0.211(6)	0.176(1)
Optical Basicity[c]	0.562	0.556	0.545	0.546	0.562	0.556	0.55	0.55	0.565	0.559	0.557
$XFeO_{1.5}$[d]	0.0116	0.0121	0.011	0.0115	0.0148	0.0139	0.0148	0.0171	0.02	0.0169	0.019
XFeO[d]	0.0581	0.0401	0.0231	0.0149	0.0454	0.0296	0.0199	0.0167	0.0349	0.0231	0.0189
Mgt (wt. %)											
n	8	16	7	10	19	17	11	15	14	20	16
Al_2O_3	3.14(7)	3.04(8)	2.85(3)	3.3(3)	3.77(4)	3.5(1)	3.28(3)	3.7(2)	5.4(2)	4.99(9)	4.98(6)
CaO	0.18(3)	0.15(5)	0.11(3)	0.11(3)	0.11(2)	0.09(2)	0.07(4)	0.09(3)	0.12(3)	0.06(2)	0.09(2)
TiO2	11.9(7)	8.0(4)	5.0(3)	2.6(2)	6.5(4)	3.8(3)	3.00(1)	1.98(6)	2.83(9)	1.82(6)	1.92(5)
FeO*	75.2(8)	78.8(3)	81.2(5)	77.8(6)	78.9(9)	80.6(3)	79.7(5)	76.5(4)	77.9(3)	75.3(3)	75.8(2)
MnO	0.26(2)	0.28(2)	0.36(3)	0.50(2)	0.30(2)	0.35(2)	0.44(1)	0.52(2)	0.27(2)	0.40(2)	0.38(2)
V_2O_3	0.61(8)	0.37(3)	0.17(2)	< dl	0.34(4)	0.14(1)	0.063(8)	< dl	0.09(1)	< dl	< dl
Cr_2O_3	0.20(3)	0.11(7)	0.17(8)	0.05(6)	0.3(1)	0.09(5)	0.12(5)	0.05(2)	0.11(2)	0.04(3)	0.07(2)
MgO	2.5(2)	2.75(8)	4.3(2)	8.2(3)	3.6(2)	5.0(2)	6.95(7)	9.6(2)	6.63(9)	10.2(1)	9.9(2)
SiO_2	0.35(9)	0.28(3)	0.3(1)	0.2(1)	0.19(2)	0.16(4)	0.14(4)	0.18(8)	0.2(1)	0.14(2)	0.14(2)
Mg#	0.106(7)	0.125(5)	0.21(1)	0.41(1)	0.168(9)	0.25(1)	0.348(4)	0.486(8)	0.329(5)	0.510(6)	0.493(7)
$a Fe_3O_4$[e]	0.502	0.572	0.595	0.489	0.559	0.579	0.529	0.596	0.52	0.415	0.426
D(mgt/melt)											
D(Al)	0.232(6)	0.225(6)	0.215(4)	0.23(3)	0.269(5)	0.25(1)	0.239(4)	0.27(2)	0.37(1)	0.359(7)	0.354(6)
D(Ti)	11(2)	7(1)	4.9(5)	2.4(2)	6.1(6)	3.7(3)	2.7(2)	1.7(1)	3.1(1)	1.78(9)	1.93(9)
D(Mn)	2.4(3)	2.6(3)	4.7(7)	7(1)	2.3(3)	3.0(4)	4.7(6)	5.4(7)	2.0(3)	3.3(3)	3.4(5)
D(Mg)	1.5(1)	1.77(8)	3.2(2)	5.4(7)	1.6(1)	2.2(1)	3.55(7)	4.3(4)	1.68(4)	2.70(7)	2.8(1)

Table 2-3 continued

Experiment	RSM-20	RSM-6	RSM-11	RSM-21	RSM-9	RSM-19	RSM-15	RSM-12	RSM-18	RSM-16	RSM-4	RSM-17
log fO_2	-9.82	-9.02	-8.02	-7.02	-6.31	-8.38	-7.68	-6.68	-5.98	-7.16	-6.36	-5.66
ΔFMQ	0.2	1	2	3	3.7	1.3	2	3	3.7	2.2	3	3.7
T (°C)	1070	1070	1070	1070	1070	1095	1095	1095	1095	1120	1120	1120
Starting material	A-190 + Fe + t	A-190 + Fe + t	A-190 + Fe + t	A-190 + Fe + t	A-190 + Fe + t	A-190 + Fe + t	A-190 + Fe + t	A-190 + Fe + t	A-190 + Fe + t	A-190 + Fe + t	A-190 + Fe + t	A-190 + Fe + t
Coexisting phases	mgt, plag, opx, liq	mgt, plag, opx, cpx, liq	mgt, plag, opx, cpx, liq	mgt, plag, opx, cpx, liq	mgt, plag, opx, cpx, liq	mgt, plag, opx, liq	mgt, plag, opx, cpx, liq	mgt, plag, opx, cpx, liq	mgt, plag, opx, liq	mgt, plag, opx, liq	mgt, plag, opx, liq	mgt, plag, opx, liq
Glass (wt. %)												
n	12	14	13	15	10	18	9	14	13	11	6	12
Na_2O	3.0(3)	3.6(2)	3.5(3)	3(1)	3.5(2)	3.5(2)	3.63(5)	3.51(4)	3.9(3)	3.73(4)	3.73(7)	3.73(6)
Al_2O_3	12.90(9)	13.4(1)	13.4(3)	14.1(5)	13.0(2)	14.1(2)	13.8(2)	13.60(2)	13.5(2)	14.7(2)	13.7(2)	13.90(7)
K_2O	2.86(7)	3.3(2)	3.7(2)	3.45(1)	3.85(7)	2.71(8)	2.97(8)	3.36(5)	3.13(9)	2.24(5)	2.6(1)	2.41(8)
CaO	4.4(2)	4.0(1)	3.1(2)	3.0(2)	2.5(1)	4.5(2)	4.3(2)	4.1(2)	3.5(2)	5.20(8)	5.0(3)	4.8(2)
P_2O_5	0.31(2)	0.37(4)	0.36(5)	0.33(6)	0.36(4)	0.30(3)	0.30(2)	0.36(4)	0.30(6)	0.26(3)	0.247(8)	0.25(4)
TiO_2	1.35(9)	1.01(7)	0.99(8)	1.1(1)	1.3(1)	1.05(6)	1.00(5)	1.31(8)	1.11(7)	0.92(2)	1.06(6)	1.04(6)
FeO*	7.9(4)	7.5(2)	4.6(2)	3.7(5)	3.2(1)	8.6(3)	6.02(1)	4.9(2)	4.0(2)	7.3(1)	5.4(5)	5.1(2)
MnO	0.131(8)	0.11(1)	0.09(1)	0.09(1)	0.06(1)	0.13(1)	0.12(1)	0.10(1)	0.09(2)	0.14(1)	0.12(1)	0.12(1)
MgO	1.97(7)	1.63(5)	1.40(6)	1.6(2)	1.37(6)	2.42(7)	2.17(9)	2.3(2)	2.0(1)	4.05(8)	3.8(3)	3.6(2)
SiO_2	63(1)	64.8(9)	69(1)	68.4(1)	71.5(7)	61.6(8)	64.9(4)	68.3(5)	68.0(8)	61.8(4)	64.2(9)	64.4(6)
Fe3+/Total Fe[a]	0.166(2)	0.229(3)	0.324(3)	0.43(2)	0.511(3)	0.243(3)	0.3180(5)	0.4270(6)	0.508(5)	0.364(1)	0.424(1)	0.499(1)
NBO/T[b]	0.24(1)	0.195(6)	0.113(6)	0.08(2)	0.070(3)	0.23(1)	0.170(7)	0.14(1)	0.107(6)	0.242(4)	0.22(2)	0.18(1)
Optical Basicity[c]	0.56	0.559	0.548	0.546	0.541	0.565	0.557	0.552	0.549	0.566	0.56	0.558
XFeO1.5[d]	0.0106	0.0136	0.0118	0.0125	0.0127	0.0166	0.0151	0.0162	0.0159	0.0206	0.0177	0.0198
XFeO[d]	0.0532	0.0459	0.0247	0.0168	0.0121	0.0518	0.0324	0.0218	0.0154	0.036	0.0241	0.0198
Mgt (wt. %)												
n	8	17	10	5	13	28	15	10	11	13	14	19
Al_2O_3	2.99(9)	3.06(8)	2.89(9)	3.2(2)	3.4(2)	3.9(1)	3.6(2)	3.6(3)	3.43(9)	5.5(1)	4.94(4)	4.78(8)
CaO	0.16(4)	0.12(3)	0.08(2)	0.10(4)	0.08(2)	0.08(3)	0.10(3)	0.08(2)	0.08(2)	0.11(2)	0.08(2)	0.10(4)
TiO_2	11.3(8)	8.3(2)	5.0(2)	3.0(2)	2.2(2)	6.7(2)	4.4(3)	2.8(1)	2.08(6)	3.10(6)	1.78(4)	1.83(4)
FeO*	74.6(6)	78.3(5)	81.5(4)	79(1)	78.4(4)	79.2(5)	80.5(4)	79.8(5)	78.0(5)	77.8(3)	75.2(3)	75.4(4)
MnO	0.32(2)	0.28(1)	0.36(3)	0.46(2)	0.56(2)	0.26(2)	0.31(1)	0.42(2)	0.50(2)	0.27(2)	0.40(1)	0.41(1)
V_2O_3	0.84(6)	0.43(2)	0.19(1)	< dl	< dl	0.37(2)	0.19(1)	0.064(8)	< dl	0.095(9)	< dl	< dl
Cr_2O_3	0.6(2)	0.13(8)	0.2(2)	0.05(3)	0.05(2)	0.4(1)	0.2(2)	0.12(4)	0.09(3)	0.17(7)	0.05(2)	0.06(1)
MgO	3.1(1)	2.65(6)	4.0(2)	6.6(2)	9.4(3)	3.4(1)	4.42(9)	6.8(2)	8.8(3)	6.4(1)	10.1(1)	10.1(2)
SiO_2	0.4(2)	0.30(9)	0.18(4)	0.14(4)	0.2(1)	0.18(4)	0.17(4)	0.15(5)	0.11(2)	0.19(4)	0.15(2)	0.16(7)
Mg#	0.130(7)	0.120(3)	0.192(9)	0.336(9)	0.47(1)	0.156(6)	0.217(4)	0.34(1)	0.45(2)	0.319(4)	0.511(5)	0.510(9)
$a Fe_3O_4$[e]	0.494	0.568	0.601	0.54	0.454	0.561	0.586	0.536	0.471	0.52	0.418	0.418
D(mgt/melt)												
D(Al)	0.232(7)	0.229(7)	0.216(8)	0.22(2)	0.26(1)	0.28(1)	0.26(2)	0.27(2)	0.253(8)	0.37(1)	0.362(5)	0.344(6)
D(Ti)	8.3(8)	8.2(6)	5.1(4)	2.7(4)	1.7(2)	6.4(4)	4.4(3)	2.1(2)	1.9(1)	3.4(1)	1.7(1)	1.8(1)
D(Mn)	2.5(2)	2.5(3)	3.9(6)	5.4(9)	9(1)	2.0(2)	2.7(3)	4.1(6)	6(1)	1.8(2)	3.4(4)	3.3(3)
D(Mg)	1.55(9)	1.62(6)	2.8(2)	4.2(5)	6.9(4)	1.38(6)	2.04(9)	3.0(2)	4.4(3)	1.59(4)	2.7(2)	2.8(2)

Table 2-3 continued

Experiment	RSM-6	RSM-11	RSM-21	RSM-9	RSM-19	RSM-15	RSM-12	RSM-18	RSM-16	RSM-3	RSM-17
log fO_2	-9.02	-8.02	-7.02	-6.31	-8.38	-7.68	-6.68	-5.98	-7.16	-6.36	-5.66
ΔFMQ	1	2	3	3.7	1.3	2	3	3.7	2.2	3	3.7
T (°C)	1070	1070	1070	1070	1095	1095	1095	1095	1120	1120	1120
Starting material	JA-1 + Fe	JA-1 + Fe	JA-1 + Fe	JA-1 + Fe	JA-1 + Fe	JA-1 + Fe	JA-1 + Fe	JA-1 + Fe + t	JA-1 + Fe	JA-1 + Fe	JA-1 + Fe
Coexisting phases	mgt, plag, liq	mgt, plag, liq	mgt, plag, liq	mgt, plag, opx, cpx, liq	mgt, plag, liq	mgt, plag, liq	mgt, plag, liq	mgt, plag, liq	mgt, plag, liq	mgt, plag, liq	mgt, plag, liq
Glass (wt. %)											
n	18	11	9	9	16	9	9	12	10	12	12
Na_2O	3.1(4)	2.9(2)	3.5(3)	3.2(3)	3.1(2)	3.0(5)	3.0(1)	2.9(4)	3.43(3)	3.4(3)	3.1(9)
Al_2O_3	11.80(9)	11.4(3)	11.1(2)	11.0(3)	12.8(2)	12.2(2)	11.80(1)	11.6(3)	14.5(3)	12.5(2)	12.5(3)
K_2O	0.94(6)	1.16(8)	1.13(9)	1.56(5)	0.89(5)	0.98(5)	1.24(8)	1.16(4)	0.85(5)	1.09(8)	1.08(6)
CaO	4.5(2)	4.6(2)	4.1(5)	3.0(1)	4.8(2)	4.9(3)	4.6(4)	3.3(2)	5.7(1)	4.4(2)	4.3(2)
P_2O_5	0.18(3)	0.21(2)	0.20(3)	0.24(2)	0.17(2)	0.19(2)	0.19(2)	0.16(2)	0.15(2)	0.17(3)	0.21(3)
TiO_2	1.04(3)	1.0(1)	1.0(1)	0.98(3)	0.96(4)	1.00(4)	1.1(1)	0.94(4)	0.87(3)	1.02(7)	0.98(3)
FeO*	10.3(5)	5.5(2)	4.3(6)	3.6(3)	10.2(5)	7.0(3)	5.0(5)	3.8(2)	8.4(3)	5.0(2)	4.6(2)
MnO	0.21(2)	0.21(2)	0.15(3)	0.11(1)	0.19(1)	0.20(1)	0.16(2)	0.118(8)	0.18(2)	0.14(2)	0.14(2)
MgO	2.1(1)	2.1(1)	1.8(2)	1.3(1)	2.0(1)	2.15(1)	1.8(2)	1.3(2)	1.82(9)	1.60(8)	1.50(7)
SiO_2	65.8(9)	72(1)	73(2)	76.8(7)	64(1)	68.3(1)	73(1)	74.2(8)	64.6(5)	71(1)	72.1(9)
Fe^{3+}/Total Fe[a]	0.205(4)	0.306(2)	0.419(5)	0.491(4)	0.225(2)	0.297(6)	0.408(3)	0.478(7)	0.3480(9)	0.404(3)	0.48(1)
NBO/T[b]	0.24(2)	0.16(1)	0.12(2)	0.064(9)	0.22(2)	0.17(2)	0.12(2)	0.06(1)	0.154(1)	0.11(1)	0.08(2)
Optical Basicity[c]	0.557	0.542	0.538	0.531	0.559	0.549	0.541	0.532	0.558	0.542	0.539
$XFeO_{1.5}$[d]	0.0169	0.0132	0.0142	0.0137	0.0185	0.0165	0.0159	0.0144	0.023	0.016	0.0174
XFeO[d]	0.0655	0.0299	0.0198	0.0142	0.0637	0.0391	0.0231	0.0157	0.0432	0.0236	0.019
Mgt (wt. %)											
n	13	8	10	11	3	10	9	16	12	16	20
Al_2O_3	3.45(9)	2.70(9)	2.5(2)	2.5(2)	3.7(1)	3.31(5)	2.77(7)	2.7(2)	4.6(3)	3.21(8)	3.0(1)
CaO	0.14(1)	0.16(2)	0.10(3)	0.10(3)	0.16(4)	0.12(1)	0.15(2)	0.10(2)	0.11(5)	0.06(1)	0.09(2)
TiO_2	5.1(2)	4.2(3)	2.43(1)	2.1(3)	4.4(1)	3.5(2)	2.5(1)	1.7(1)	2.2(1)	1.72(5)	1.59(7)
FeO*	81.2(3)	80.8(7)	80.8(4)	80.5(9)	82.3(4)	82.0(5)	81.7(5)	80.6(9)	83.2(7)	82.7(3)	82.1(3)
MnO	0.33(2)	0.56(2)	0.71(3)	0.91(9)	0.28	0.45(2)	0.62(2)	0.74(5)	0.33(2)	0.56(2)	0.63(2)
V_2O_3	0.226(9)	0.10(1)	0.044(8)	0.03(2)	0.18(2)	0.09(1)	0.038(6)	0.02(1)	0.06(1)	0.025(5)	0.01(1)
Cr_2O_3	0.06(2)	0.04(1)	0.12(1)	0.02(1)	0.21(2)	0.05(6)	0.05(5)	0.04(1)	0.12(2)	0.014(1)	0.05(3)
MgO	2.6(2)	4.2(2)	6.10(9)	7.6(3)	2.20(6)	3.6(1)	5.25(3)	6.5(4)	2.72(9)	4.8(2)	5.5(1)
SiO_2	0.4(1)	0.35(6)	0.18(6)	0.17(3)	0.3(1)	0.2(2)	0.26(9)	0.2(1)	0.2(1)	0.12(6)	0.2(1)
Mg#	0.126(7)	0.21(1)	0.316(5)	0.39(2)	0.103(5)	0.182(3)	0.271(3)	0.34(2)	0.142(4)	0.255(9)	0.291(7)
$a Fe_3O_4$[c]	0.634	0.616	0.581	0.531	0.658	0.641	0.615	0.579	0.678	0.638	0.617
D(mgt/melt)											
D(Al)	0.291(8)	0.24(1)	0.23(2)	0.23(2)	0.289(9)	0.272(5)	0.234(7)	0.23(2)	0.31(2)	0.256(8)	0.24(1)
D(Ti)	4.9(2)	4.1(6)	2.4(3)	2.1(3)	4.5(2)	3.5(2)	2.4(3)	1.8(2)	2.6(2)	1.7(1)	1.62(9)
D(Mn)	1.6(2)	2.7(3)	4.8(8)	8(1)	1.5(1)	2.2(2)	3.8(5)	6.2(6)	1.9(2)	3.9(5)	4.4(5)
D(Mg)	1.2(1)	2.0(1)	3.5(4)	5.9(7)	1.12(8)	1.67(9)	2.8(3)	4.9(6)	1.49(9)	3.0(2)	3.7(2)

Table 2-3 continued

Experiment	RSM-11	RSM-21	RSM-9	RSM-15	RSM-12	RSM-18	RSM-3	RSM-17
log fO_2	-8.02	-7.02	-6.31	-7.68	-6.68	-5.98	-6.36	-5.66
ΔFMQ	2	3	3.7	2	3	3.7	3	3.7
T (°C)	1070	1070	1070	1095	1095	1095	1120	1120
Starting material	JA-1	JA-1	JA-1	JA-1	JA-1	JA-1	JA-1	JA-1
Coexisting phases	mgt, plag, liq	mgt, plag, liq	mgt, plag, liq	mgt, plag, liq	mgt, plag, liq	mgt, plag, liq	mgt, plag, liq	mgt, plag, liq
Glass (wt. %)								
n	7	10	8	10	4	9	13	12
Na_2O	3.08(7)	3(1)	3.1(2)	2.9(1)	2.92(9)	2.9(2)	3.4(3)	3.28(6)
Al_2O_3	11.4(2)	11.4(2)	11.6(2)	12.3(1)	12.10(6)	12.10(9)	12.6(3)	12.6(1)
K_2O	1.12(3)	1.19(3)	1.50(8)	1.01(3)	1.19(9)	1.11(2)	1.07(7)	1.00(3)
CaO	4.0(2)	3.7(2)	3.6(3)	4.2(1)	4.0(2)	3.8(2)	4.2(1)	4.3(1)
P_2O_5	0.21(1)	0.21(3)	0.24(4)	0.19(2)	0.18(3)	0.20(4)	0.16(3)	0.20(2)
TiO_2	1.17(4)	1.19(4)	1.18(9)	1.06(2)	1.17(2)	1.15(3)	1.05(4)	1.06(3)
FeO*	7.0(3)	5.7(6)	4.1(5)	6.2(3)	6.1(6)	5.6(3)	6.4(4)	6.5(2)
MnO	0.22(2)	0.21(2)	0.20(4)	0.19(1)	0.20(2)	0.20(2)	0.19(1)	0.20(2)
MgO	2.2(1)	2.2(2)	2.0(4)	2.01(7)	2.1(1)	2.1(1)	1.92(8)	1.97(7)
SiO_2	69(1)	71(1)	73(1)	69.7(8)	72(1)	70.3(8)	69.0(5)	68.7(5)
Fe^{3+}/Total Fe[a]	0.299(1)	0.41(2)	0.490(4)	0.294(2)	0.395(1)	0.472(3)	0.396(3)	0.472(2)
NBO/T[b]	0.171(7)	0.13(2)	0.09(2)	0.141(8)	0.12(1)	0.10(1)	0.122(7)	0.104(7)
Optical Basicity[c]	0.547	0.542	0.537	0.544	0.542	0.541	0.547	0.546
$XFeO_{1.5}$[d]	0.0169	0.0183	0.0159	0.0145	0.0189	0.0212	0.0202	0.0244
XFeO[d]	0.0397	0.0268	0.0166	0.0349	0.0289	0.0237	0.0308	0.0274
Mgt (wt. %)								
n	1	6	11	6	1	10	3	4
Al_2O_3	3.15	2.77(5)	2.8(2)	3.49(5)	3.14	3.2(3)	3.5(1)	3.35(4)
CaO	0.18	0.132(5)	0.16(2)	0.17(1)	0.12	0.13(2)	0.08(2)	0.083(5)
TiO_2	3.41	2.62(7)	3.2(3)	3.9(2)	2.5	1.94(9)	1.47(9)	1.490(1)
FeO*	81.2	80.3(5)	79.0(9)	80.0(5)	82	78.6(7)	80.9(7)	81.90(6)
MnO	0.44	0.72(4)	0.86(7)	0.50(2)	0.54	0.86(6)	0.61(5)	0.60(2)
V_2O_3	0.1	0.06(2)	0.06(1)	0.13(1)	0.05	0.024(8)	0.023(6)	0.023(1)
Cr_2O_3	0.22	0.06(1)	0.06(2)	0.21(6)	0.28	0.05(3)	0.4(3)	0.16(1)
MgO	3.53	5.8(4)	6.7(4)	3.9(1)	4.64	7.1(4)	5.4(5)	5.11(6)
SiO_2	0.42	0.36(7)	0.31(8)	0.4(2)	0.37	0.3(1)	0.3(1)	0.15(4)
Mg#	0.18	0.30(2)	0.34(2)	0.197(5)	0.239	0.37(2)	0.28(3)	0.273(3)
$a Fe_3O_4$[e]	0.651	0.591	0.543	0.616	0.635	0.542	0.619	0.627
D(mgt/melt)								
D(Al)	0.28	0.243(6)	0.24(1)	0.283(5)	0.26	0.26(2)	0.28(1)	0.266(4)
D(Ti)	2.92	2.20(9)	2.7(3)	3.6(2)	2.14	1.69(1)	1.40(1)	1.40(4)
D(Mn)	1.98	3.5(4)	4.3(9)	2.6(2)	2.63	4.4(6)	3.3(4)	3.0(3)
D(Mg)	1.61	2.7(3)	3.4(7)	1.95(8)	2.23	3.3(3)	2.8(3)	2.59(9)

Table 2-4: Glass and titanomagnetite trace element composition determined using LA-ICP-MS and partition coefficients for trace elements

Experiment	RSM-20	RSM-6	RSM-11	RSM-21	RSM-19	RSM-15	RSM-12	RSM-18	RSM-4	RSM-17
log fO_2	-9.82	-9.02	-8.02	-7.02	-8.38	-7.68	-6.68	-5.98	-6.36	-5.66
ΔFMQ	0.2	1	2	3	1.3	2	3	3.7	3	3.7
T (°C)	1070	1070	1070	1070	1095	1095	1095	1095	1120	1120
Starting material	A-190 + Fe	A-190 + Fe	A-190 + Fe	A-190 + Fe	A-190 + Fe	A-190 + Fe	A-190 + Fe	A-190 + Fe	A-190 + Fe	A-190 + Fe
Glass (ppm)										
n	5	9	8	5	16	13	8	9	9	8
Sc	-	-	15(2)	16.1(9)	20(1)	22(1)	19(3)	19(1)	21(1)	19(2)
V	110(30)	88(7)	160(15)	250(26)	170(28)	200(17)	250(11)	290(25)	270(8)	230(16)
Co	-	-	6.7(5)	4.7(1)	13(1)	11.3(4)	6.3(6)	6.5(7)	11.8(6)	10.0(6)
Ni	-	-	1.5(5)	1.0(3)	2.4(3)	3.5(2)	1.4(3)	1.9(2)	3.0(4)	3.9(7)
Cu	-	-	3.8(4)	6(1)	2.8(2)	6.0(4)	6.2(9)	12(2)	17.8(6)	15.9(1)
Zn	-	-	12(3)	13(4)	5(2)	25(6)	10(4)	< dl	44(6)	31(6)
Ga	-	-	55(5)	83(6)	51(2)	48(2)	48(3)	70(19)	60(2)	38(3)
Zr	-	-	310(18)	230(26)	240(16)	250(24)	270(19)	220(20)	199(9)	200(15)
Nb	-	-	46(2)	35(4)	36(3)	39(4)	37(2)	36(5)	31(1)	31(4)
Mo	-	-	280(38)	40(9)	110(12)	130(28)	80(20)	80(23)	400(215)	21(5)
In	-	-	3.3(6)	1.1(2)	1.2(4)	3.6(4)	3.6(4)	5(1)	4(1)	3.0(4)
Hf	-	-	8.0(7)	5.8(8)	6.3(5)	6.6(9)	7(2)	5.8(4)	5.2(4)	5.1(4)
Ta	-	-	94(5)	73(8)	70(5)	77(7)	76(4)	80(14)	62(3)	64(6)
Mgt (ppm)										
n	8	17	4	9	10	5	8	4	15	10
Mean spot size (μm)	EPMA	EPMA	11.3	11.6	15.1	12	15.4	17.3	25.1	16.1
Sc	-	-	27(4)	30(4)	30(2)	28(3)	27(3)	24(2)	20(1)	22(2)
V	4200(570)*	2500(182)*	1,270(29)	400(24)	1,800(161)	1,000(184)	470(38)	130(18)	150(12)	160(22)
Co	-	-	170(18)	211(9)	141(10)	200(17)	200(17)	190(12)	203(9)	216(8)
Ni	-	-	210(42)	330(39)	130(15)	340(60)	350(81)	370(54)	280(35)	450(22)
Cu	-	-	< dl	9(1)	< dl	5(3)	7(2)	25(3)	18(2)	15(2)
Zn	-	-	120(49)	180(26)	13(5)	160(66)	130(51)	220(29)	290(50)	300(49)
Ga	-	-	43(5)	42(4)	39(5)	44(3)	43(5)	40(2)	47(3)	45(1)
Zr	-	-	24(3)	14(2)	29(3)	21(4)	14(3)	10(2)	7.2(7)	8(1)
Nb	-	-	4.5(7)	1.9(3)	6.0(7)	3.4(9)	1.9(2)	< dl	0.82(9)	1.0(1)
Mo	-	-	8(4)	< dl	7(1)	2(1)	< dl	< dl	< dl	< dl
In	-	-	20(11)	6(2)	3.0(9)	12.0(3)	15(4)	22(5)	12(5)	8.6(8)
Hf	-	-	0.8(4)	< dl	< dl	< dl	< dl	< dl	< dl	< dl
Ta	-	-	13(3)	5.3(4)	18(2)	9(1)	5.4(9)	< dl	2.9(2)	2.9(2)
D (mgt/melt)										
D(Sc)	-	-	1.8(3)	1.8(3)	1.5(1)	1.3(2)	1.4(3)	1.2(1)	0.97(8)	1.1(1)
D(V)	40(12)*	29(3)*	8.1(8)	1.6(2)	11(2)	5(1)	1.9(2)	0.44(7)	0.55(5)	0.7(1)
D(Co)	-	-	26(3)	45(2)	11(1)	18(2)	31(4)	30(4)	17(1)	22(2)
D(Ni)	-	-	140(52)	320(98)	52(9)	100(18)	250(75)	200(40)	90(17)	110(20)
D(Cu)	-	-	-	1.5(4)	-	0.8(4)	1.1(4)	2.0(3)	1.0(1)	0.9(1)
D(Zn)	-	-	10(5)	15(5)	3(1)	6(3)	13(7)	-	7(2)	10(2)
D(Ga)	-	-	0.8(1)	0.51(6)	0.8(1)	0.92(8)	0.9(1)	0.6(2)	0.78(6)	1.18(9)
D(Zr)	-	-	0.08(1)	0.06(1)	0.12(1)	0.08(2)	0.05(1)	0.05(2)	0.036(4)	0.042(7)
D(Nb)	-	-	0.10(2)	0.055(9)	0.17(2)	0.09(2)	0.053(5)	-	0.026(3)	0.031(6)
D(Mo)	-	-	0.03(1)	-	0.06(1)	0.014(9)	-	-	-	-
D(In)	-	-	5(3)	5(2)	3(1)	3.3(4)	4(1)	4(1)	3(1)	2.9(5)
D(Hf)	-	-	0.10(6)	-	-	-	-	-	-	-
D(Ta)	-	-	0.14(3)	0.073(1)	0.26(3)	0.11(2)	0.07(1)	-	0.046(4)	0.046(5)

*Titanomagnetite V content determined using EPMA < dl = measurement less than detection limit Error = 1 s.d. of multiple (n) analysis. Errors in D(mgt/melt) propagated from errors in magnetite and glass measurements

Table 2-4 continued

Experiment	RSM-11	RSM-21	RSM-9	RSM-19	RSM-15	RSM-12	RSM-18	RSM-4	RSM-17
log fO_2	-8.02	-7.02	-6.31	-8.38	-7.68	-6.68	-5.98	-6.36	-5.66
ΔFMQ	2	3	3.7	1.3	2	3	3.7	3	3.7
T (°C)	1070	1070	1070	1095	1095	1095	1095	1120	1120
Starting material	A-190 + Fe + t	A-190 + Fe + t	A-190 + Fe + t	A-190 + Fe + t	A-190 + Fe + t	A-190 + Fe + t	A-190 + Fe + t	A-190 + Fe + t	A-190 + Fe + t
Glass (ppm)									
n	10	9	8	16	14	15	7	11	10
Sc	130(18)	131(7)	130(16)	140(3)	158(6)	163(10)	139(10)	160(11)	163(7)
V	140(18)	280(38)	320(26)	170(11)	180(13)	270(28)	290(37)	280(21)	261(8)
Co	10.0(1)	7.5(6)	5.2(4)	21.9(5)	17(1)	12.1(7)	8.6(5)	17.0(9)	14.9(6)
Ni	1.6(2)	1.4(6)	1.2(2)	4.4(4)	4.2(7)	3.3(6)	2.2(2)	4.3(8)	4.3(7)
Cu	3.3(4)	7.7(7)	14(1)	5.0(2)	5.8(2)	10.2(7)	9.9(5)	24(2)	12.8(7)
Zn	11(3)	15(4)	21(5)	5(2)	18(6)	19(5)	23(1)	38(7)	30(7)
Ga	54(3)	65(8)	55(6)	65(3)	57(3)	56(3)	71(3)	56(2)	47(2)
Zr	520(43)	530(64)	470(47)	390(16)	440(31)	450(47)	380(32)	350(34)	370(22)
Nb	71(5)	70(7)	61(6)	52(2)	60(4)	60(6)	53(6)	51(5)	49(2)
Mo	400(48)	200(32)	240(16)	200(12)	270(28)	200(22)	200(27)	900(134)	160(21)
In	16(7)	50(12)	60(10)	10(2)	34(8)	44(8)	44(3)	50(12)	50(11)
Hf	200(20)	210(27)	190(20)	155(7)	180(14)	180(20)	150(12)	150(10)	151(8)
Ta	290(23)	310(38)	270(27)	235(9)	250(17)	260(26)	220(22)	210(15)	211(10)
Mgt (ppm)									
n	5	9	7	15	6	2	3	12	5
Mean spot size (μm)	11.8	15.9	13.7	18	12.8	19	11	21	12.8
Sc	250(23)	210(12)	220(13)	200(12)	220(12)	160(20)	170(13)	170(10)	170(14)
V	1,400(158)	710(50)	210(22)	2,400(184)	1,400(111)	490(31)	128(9)	144(9)	150(17)
Co	230(28)	270(11)	300(13)	210(13)	250(24)	310(33)	283(4)	280(23)	310(13)
Ni	190(21)	360(22)	390(35)	190(27)	340(57)	540(23)	400(56)	380(64)	490(53)
Cu	2(1)	6.8(9)	38(6)	1.5(9)	2.9(6)	14(2)	23.8(7)	22(1)	14(2)
Zn	50(9)	230(42)	400(103)	15(6)	90(42)	< dl	190(28)	260(51)	220(88)
Ga	62(9)	61(4)	62(5)	66(4)	65(4)	76(3)	67(9)	65(4)	64(4)
Zr	51(7)	30(2)	26(4)	50(3)	35(4)	35(2)	17(3)	14(1)	14(1)
Nb	10(2)	4.6(5)	3.3(9)	11(1)	6(1)	4.5(7)	1.9(5)	1.4(3)	1.7(3)
Mo	19(4)	2.2(9)	< dl	21(3)	8(2)	< dl	< dl	< dl	< dl
In	70(17)	230(23)	250(74)	20(7)	70(37)	26(3)	100(103)	150(37)	140(71)
Hf	31(5)	17(1)	14(2)	27(3)	21(3)	17(5)	8(1)	9.0(1)	10(1)
Ta	50(8)	25(1)	17(2)	66(5)	35(1)	30(2)	11(2)	9.9(8)	11(2)
D (mgt/melt)									
D(Sc)	2.0(3)	1.6(1)	1.7(2)	1.42(9)	1.39(9)	1.0(1)	1.2(1)	1.06(9)	1.06(1)
D(V)	11(2)	2.6(4)	0.65(9)	14(1)	7.5(8)	1.8(2)	0.44(6)	0.52(5)	0.58(7)
D(Co)	23(4)	36(3)	59(5)	9.4(6)	15(2)	25(3)	33(2)	17(2)	21(1)
D(Ni)	120(19)	300(119)	320(64)	44(7)	80(19)	160(29)	180(31)	90(22)	110(22)
D(Cu)	0.7(5)	0.9(1)	2.7(5)	0.3(2)	0.50(1)	1.3(2)	2.4(1)	0.91(9)	1.1(2)
D(Zn)	5(1)	16(5)	18(6)	3(1)	5(3)	-	8(1)	7(2)	7(3)
D(Ga)	1.2(2)	0.9(1)	1.1(2)	1.01(7)	1.12(9)	1.35(9)	0.9(1)	1.17(9)	1.4(1)
D(Zr)	0.10(1)	0.056(7)	0.05(1)	0.13(1)	0.079(1)	0.078(5)	0.045(8)	0.039(4)	0.038(4)
D(Nb)	0.15(3)	0.066(9)	0.05(2)	0.21(2)	0.09(2)	0.07(1)	0.036(1)	0.027(6)	0.034(7)
D(Mo)	0.05(1)	0.011(5)	-	0.10(2)	0.029(8)	-	-	-	-
D(In)	4(2)	5(1)	4(1)	2.1(9)	2(1)	0.6(1)	3(2)	3(1)	3(2)
D(Hf)	0.16(3)	0.08(1)	0.07(1)	0.17(2)	0.12(2)	0.09(3)	0.051(9)	0.062(8)	0.066(9)
D(Ta)	0.17(3)	0.08(1)	0.064(9)	0.28(2)	0.14(1)	0.12(2)	0.05(1)	0.048(5)	0.052(8)

Table 2-4 continued

Experiment	RSM-6	RSM-11	RSM-21	RSM-9	RSM-19	RSM-15	RSM-12	RSM-18	RSM-4
log fO_2	-9.02	-8.02	-7.02	-6.31	-8.38	-7.68	-6.68	-5.98	-6.36
ΔFMQ	1	2	3	3.7	1.3	2	3	3.7	3
T (°C)	1070	1070	1070	1070	1095	1095	1095	1095	1120
Starting material	JA-1 + Fe	JA-1 + Fe	JA-1 + Fe	JA-1 + Fe	JA-1 + Fe	JA-1 + Fe	JA-1 + Fe	JA-1 + Fe	JA-1 + Fe
Glass (ppm)									
n	9	6	7	2	4	12	10	9	11
Sc	-	-	49(7)	36(1)	-	43(3)	39(4)	37(3)	36(1)
V	129(8)	98(7)	150(21)	135(4)	150(13)	112(8)	130(15)	140(18)	136(8)
Co	-	-	3.0(4)	1.9(4)	-	6.7(4)	3.7(3)	2.4(4)	4.0(3)
Ni	-	-	0.6(2)	-	-	1.9(4)	0.8(3)	0.6(1)	0.6(1)
Cu	-	-	3.3(6)	3.9(3)	-	3.7(3)	4.7(5)	6(1)	5.5(2)
Zn	-	-	23(7)	21(2)	-	30(10)	22(5)	24(6)	21(3)
Ga	-	-	33(3)	17.6(8)	-	21(1)	18(2)	16(1)	18.7(7)
Zr	-	-	160(18)	120(17)	-	120(13)	120(16)	110(11)	98(5)
Nb	-	-	2.6(2)	2.0(2)	-	2.0(2)	1.8(3)	1.7(3)	1.55(8)
Mo	-	-	60(30)	140(94)	-	70(35)	70(23)	50(26)	1,000(149)
In	-	-	1.3(3)	2.6(8)	-	3.3(5)	1.6(3)	2.0(5)	0.042(6)
Hf	-	-	4.8(8)	3(1)	-	3.7(5)	3.4(7)	3.4(6)	2.8(2)
Ta	-	-	0.28(3)	0.2(1)	-	0.21(2)	0.19(4)	0.19(6)	0.21(3)
Mgt (ppm)									
n	13	8	2	3	3	2	8	5	8
Mean spot size (µm)	EPMA	EPMA	10.5	15	EPMA	12.5	10.2	12	22.5
Sc	-	-	51(3)	61(1)	-	47(6)	51(7)	43(4)	49(4)
V	1540(60)*	710(91)*	360(30)	170(37)	1200(118)*	560(89)	360(36)	88(5)	180(18)
Co	-	-	90.8(1)	90(8)	-	69(8)	94(8)	89(2)	89(5)
Ni	-	-	78(5)	98(10)	-	90(25)	130(14)	90(16)	59(8)
Cu	-	-	< dl	9(3)	-	0.5(4)	4(1)	14(6)	5.0(9)
Zn	-	-	170(26)	400(103)	-	100(114)	250(48)	280(53)	210(18)
Ga	-	-	27.4(2)	29.8(3)	-	30(3)	36(3)	31(4)	32(1)
Zr	-	-	4.8(6)	6(4)	-	6(3)	5(1)	4.5(6)	5.3(6)
Nb	-	-	< dl	< dl	-	< dl	< dl	< dl	< dl
Mo	-	-	< dl	< dl	-	5(6)	< dl	< dl	< dl
In	-	-	4.1(2)	10(3)	-	6(3)	4.6(7)	9(1)	0.15(4)
Hf	-	-	< dl	< dl	-	< dl	< dl	< dl	< dl
Ta	-	-	< dl	< dl	-	< dl	< dl	< dl	< dl
D (mgt/melt)									
D(Sc)	-	-	1.0(2)	1.67(6)	-	1.1(2)	1.3(2)	1.2(2)	1.4(1)
D(V)	11.9(9)*	7(1)*	2.3(4)	1.2(3)	8(1)*	5.0(9)	2.7(4)	0.61(8)	1.3(2)
D(Co)	-	-	31(4)	47(10)	-	10(1)	26(3)	36(6)	22(2)
D(Ni)	-	-	130(40)	-	-	50(15)	170(75)	150(43)	90(20)
D(Cu)	-	-	-	2.3(7)	-	0.12(1)	0.8(2)	2(1)	0.9(2)
D(Zn)	-	-	7(2)	18(5)	-	3(3)	12(3)	12(4)	10(2)
D(Ga)	-	-	0.82(7)	1.69(8)	-	1.4(2)	2.1(2)	1.9(3)	1.70(9)
D(Zr)	-	-	0.030(5)	0.05(3)	-	0.05(2)	0.04(1)	0.040(7)	0.054(7)
D(Nb)	-	-	-	-	-	-	-	-	-
D(Mo)	-	-	-	-	-	0.07(1)	-	-	-
D(In)	-	-	3.3(7)	4(2)	-	1.8(9)	2.8(7)	4(1)	3(1)
D(Hf)	-	-	-	-	-	-	-	-	-
D(Ta)	-	-	-	-	-	-	-	-	-

2.3.2 Titanomagnetite-melt partitioning

Magnesium, Mn, Zn, Co, and Ni are assumed to partition as divalent cations over the range of experimental conditions studied. Values of D(Mg), D(Mn), D(Zn), D(Co) and D(Ni) are well correlated with each other, suggesting that there is a common factor controlling their partitioning (Figure 2-5). Nickel is the most compatible divalent cation studied, followed by Co, Zn, Mn, then Mg. At constant ΔFMQ, the partition coefficients for divalent cations are greater at lower temperature (Figure 2-6). For fO_2 values between FMQ + 0.2 and FMQ + 3.7, titanomagnetite-melt partitioning of the divalent cations (e.g. Mg and Mn) increases with increasing fO_2, which is particularly pronounced at lower temperature (Figure 2-6A). This variation in the partitioning of these isovalent divalent cations with fO_2 cannot be attributed to a change in valence. Interestingly, an increase in partition coefficient for Mn, Co and Ni with increasing fO_2 was not observed in studies by Righter et al. (2006) and Toplis and Corgne (2002), who both investigated more mafic bulk systems ($SiO_2 \leq 49.5$ wt. %) (Figure 1-10).

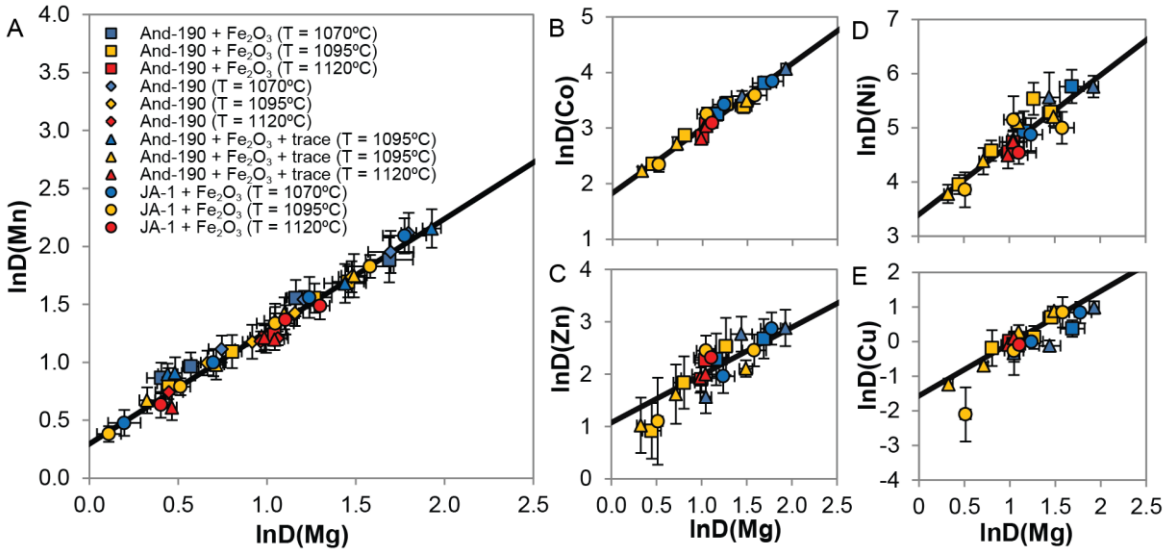


Figure 2-5: Natural log of titanomagnetite-melt partition coefficients of (A) Mn, (B) Co, (C) Zn, (D) Ni and (E) Cu as a function of the natural log of titanomagnetite-melt partition coefficient of Mg for And-190, And-190 + Fe_2O_3, And-190 + Fe_2O_3 + trace and JA-1 + Fe_2O_3 starting compositions. Lines are non-linear least-squared regression and their respective values of $a_M^0 and\ a_M^1$ are given in Table 5. Error bars = 1σ

Titanomagnetite-melt partitioning of Al shows no clear dependence on fO_2, but Al is more strongly partitioned into titanomagnetite at higher temperature (T > 1095°C) (Figure 2-6B). Nevertheless, the influence of temperature on D(Al) is weaker than for D(Mg), D(Mn), D(Zn), D(Co) and D(Ni). There is not a strong bulk compositional dependence with similar D(Al) values observed in ferrobasaltic (Toplis and Corgne, 2002), andesitic and dacitic bulk systems (this study) at comparable temperature and fO_2. Gallium is weakly compatible in titanomagnetite (D(Ga)

between 0.93 and 1.36), but exhibits no clear trend in titanomagnetite-melt partitioning with either fO_2 or temperature. The D(Ga) values obtained are somewhat lower than those reported for Cr-rich spinel at higher temperature by Horn et al. (1994) (D(Ga) > 2.49 at T > 1235°C), suggesting Ga is more strongly partitioned at higher temperature, although the higher D(Ga) could also be induced by the contrasting spinel composition.

Titanomagnetite-melt partitioning of Sc also shows no clear dependence on fO_2. No relationship between D(Ti) and D(Sc) is apparent in our data as previously reported by some studies (e.g. Horn et al. 1994 – Figure 1-8; Nielsen et al. 1994. Although Cr was detectable with EPMA analysis in titanomagnetite, Cr in the glass was below detection limit with LA-ICP-MS, which meant D(Cr) could not be determined.

Copper is moderately incompatible to compatible in titanomagnetite with D(Cu) ranging from 0.29 to 2.68. Similar to the divalent cations, at constant fO_2, D(Cu) is greater at lower temperature, and at constant T, D(Cu) increases with increasing fO_2. For example, at 1095°C, D(Cu) increases from 0.29 to 2.41 between FMQ + 1.3 < fO_2 < FMQ + 3.7 in the And-190 + Fe_2O_3 + trace bulk system. Our values for D(Cu) are in agreement with those reported for Cr, Al, and Fe spinels crystallised at pressure in a hydrous system (Liu et al., 2014; Liu et al., 2015) and also similarly exhibit an increase D(Cu) with increasing fO_2 and Fe^{3+} cpfu. However, there is no increase in D(Cu) with increasing Ti cpfu as was observed by Liu et al. (2015) and Simon et al. (2008) in dacitic and rhyolitic bulk compositions respectively.

At fO_2 < FMQ + 3, D(Ti) exhibits a strong decrease with increasing fO_2 (Figure 2-6C). At constant log fO_2, there is not significant change in D(Ti) with temperature. This finding differs from earlier studies which suggested that Ti is more strongly partitioned at higher temperature (e.g. Nielsen et al. 1994). Comparing results from this work with those from experiments using a more mafic starting material (e.g. Toplis and Corgne, 2002), shows a large degree of overlap suggesting that bulk composition does not have a significant effect on D(Ti). However, this breaks down at fO_2 < FMQ + 1, where Ti is more strongly partitioned in more silicic (andesitic-dacitic) bulk systems.

Vanadium is strongly compatible at low fO_2 (D(V) = 38.9 at fO_2 = FMQ + 0.2 and T = 1070°C using And-190 + Fe_2O_3)), but becomes incompatible at fO_2 > FMQ + 3 (D(V) = 0.65 at fO_2 = FMQ + 3.7 and T = 1070°C using And-190 + Fe_2O_3 + trace)) Thus, at constant temperature, D(V) decreases with increasing fO_2, exhibiting partitioning behaviour like Ti. There is also a slight increase in D(V) with decreasing temperature and constant fO_2. Although titanomagnetite crystals in experiments conducted at fO_2 ≤ FMQ + 1 were generally too small to analyse by LA-ICP-MS, because V contents increase strongly with decreasing fO_2 it was possible to measure the V content of titanomagnetite using EPMA for these experiments. The V contents of the glasses were

determined using LA-ICP-MS for some experiments at low fO_2 using And-190 + Fe_2O_3. The derived D(V) values are similar to those reported for the more mafic bulk compositions studied by Toplis and Corgne (2002) (Figure 2-6D). Similar to D(Ti), D(V) does not decrease significantly at fO_2 > FMQ + 3.

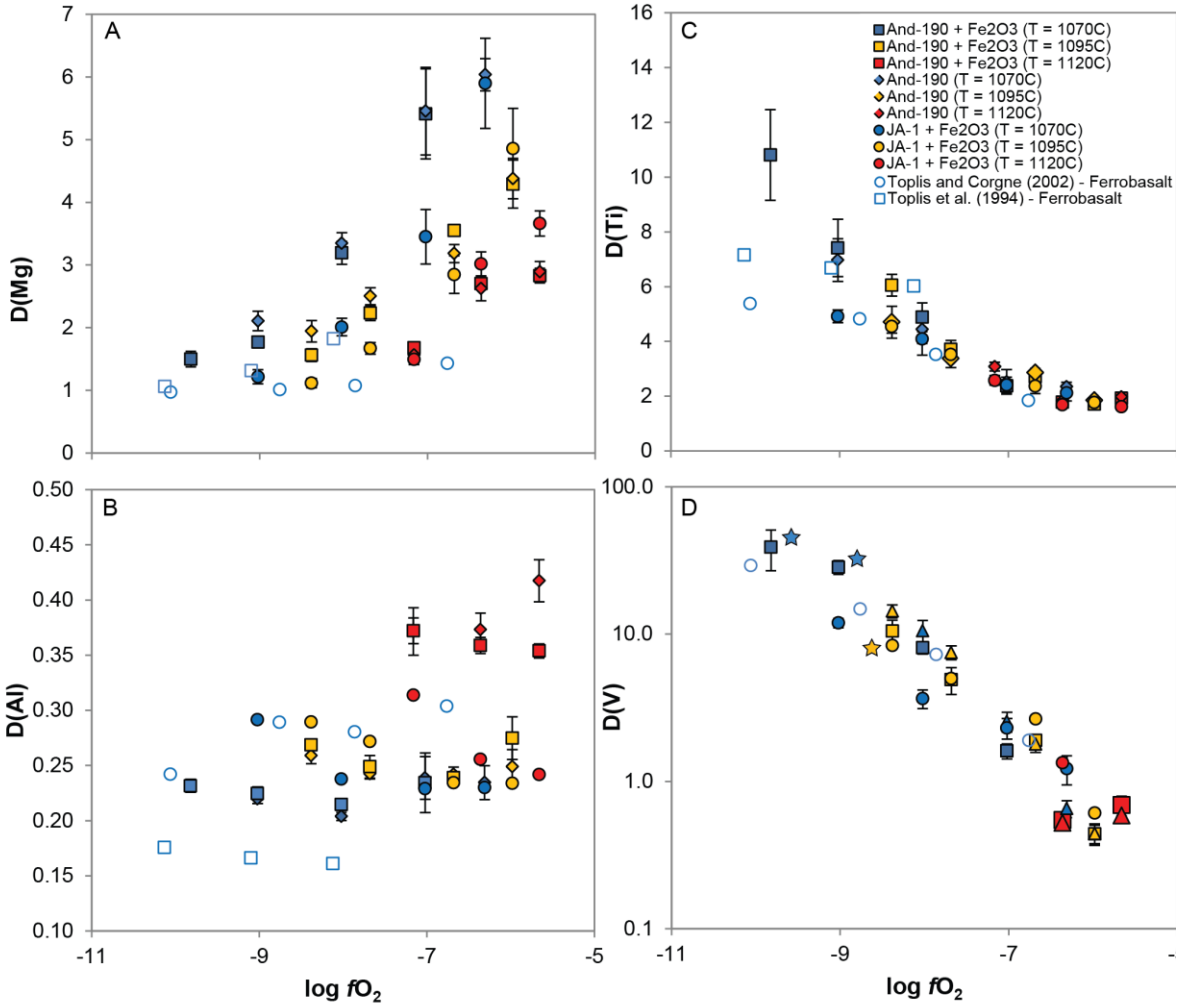


Figure 2-6: Titanomagnetite-melt partition coefficients of (A) Mg, (B) Al, (C) Ti and (D) V as a function of logfO_2. All partition coefficients for Mg, Al and Ti were determined using EPMA data; D(V) values determined using LA-ICP-MS data apart from those denoted with a star where V content was measured with EPMA due to small crystal size. Literature data from mafic bulk composition are included for comparison (Toplis et al., 1994; Toplis and Corgne, 2002) Error bars = 1σ.

The titanomagnetite-melt partition coefficients for the high-field strength elements (HFSE), Zr, Hf, Nb and Ta, all correlate positively (Figure 2-7). As for the divalent cations, this suggests a common factor controls their mineral-melt partitioning. Tantalum is the most compatible HFSE cation studied, followed by Nb, Hf, then Zr. With increasing fO_2, D(Zr)/D(Nb) and D(Hf)/D(Ta) increase, suggesting the incorporation of 4+ cations into titanomagnetite is increasingly favoured. For example, at T = 1095°C, D(Zr)/D(Nb) increases from 0.63 ± 0.088 at fO_2 = FMQ + 1.3 to 1.25 ± 0.39 at fO_2 = FMQ + 3.7 in experiments using And-190 + Fe_2O_3 + trace starting material. There is a linear correlation between D(Ta) and D(Nb), although Ta is slightly more compatible in

magnetite than Nb, despite the similarity in ionic radii and ionic charge (+5) of these two elements. Ta is also partitioned into titanomagnetite more strongly relative to Nb at higher temperature, with D(Nb)/D(Ta) decreasing from 0.82-0.85 at 1070°C to 0.57-0.65 at 1120°C in the And-190 + Fe_2O_3 + trace starting material. There is no significant variation in D(Nb)/D(Ta) with variation in fO_2. The results for the relative partition coefficients for the HFSEs contrast with earlier studies investigating spinel-melt partitioning in a more mafic bulk system (SiO_2 < 50 wt. %), which found these to be uniform (Nielsen et al., 1994; Horn et al., 1994) However, this work covers a relatively narrow range in spinel composition, with $Fe^{3+}/(Fe^{3+}+Al^{3+}+Cr^{3+}+(2*Ti^{4+})$ cpfu between 0.59 and 0.89.

Nielsen and Beard (2000) observed that the spinel composition, notably Al content, correlates with the partition coefficients for some elements. This is to be expected where the range of spinel compositions is large, due to the dependence of the activities of components in spinel with composition (e.g., O'Neill and Navrotsky, 1984). However, the thermodynamic model of O'Neill and Navrotsky (1984) suggests that this factor will be of minor importance over the limited compositional range of Fe_3O_4-rich spinels in this study; instead, empirical correlations with a factor such as Al in spinel can be explained by the response of Al partitioning to the same thermodynamic effects of melt composition, particularly $Fe^{2+}O_{melt}$, as other cations (see below).

Molybdenum was only present in titanomagnetite above the detection limit using LA-ICP-MS at fO_2 < FMQ + 3.7 at 1070°C, and fO_2 < FMQ + 3 at 1095°C. Despite the lack of data, it is clear that there is a decrease in D(Mo) with increasing fO_2 and increasing temperature. In experiments using And-190 + Fe_2O_3 + trace elements, at 1095°C, D(Mo) decreases from 0.103 ± 0.016 to 0.029 ± 0.008 between FMQ + 1.3 ≤ fO_2 ≤ FMQ + 2, and at 1070°C, D(Mo) decreases from 0.046 ± 0.012 to 0.011 ± 0.005 between FMQ + 2 ≤ fO_2 ≤ FMQ + 3. This trend of decreasing D(Mo) with increasing fO_2 was previously reported for spinel by Wijbrans et al. (2015) in a synthetic ultramafic bulk system, although D(Mo) was significantly lower in their experiments (D(Mo) = 0.0028 at T = 1220°C, fO_2 = FMQ + 2.1). The decrease in D(Mo) with increasing fO_2 could be explained by a change in valence state from Mo^{4+} to Mo^{6+}, suggesting that the tetravalent phase is more compatible. Nonetheless, like the other polyvalent elements such as Cu and V, Mo^{4+}, Mo^{5+} and Mo^{6+} could all be accommodated independent of fO_2 at high temperature via coupled exchange with Fe^{2+} and Fe^{3+}.

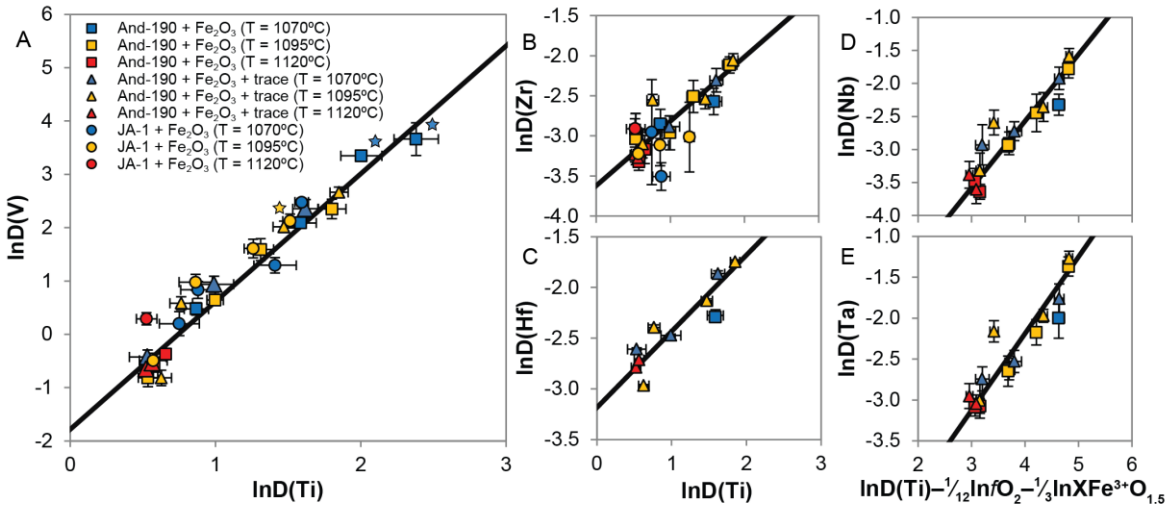


*Figure 2-7: Natural log of titanomagnetite-melt partition coefficients of (A) V, (B) Zr and (C) Hf as a function of lnD(Ti), and (D) lnD(Nb) and (E) lnD(Ta) as a function of lnD(Ti)-(1/12*lnfO$_2$)-(1/3*lnXFe^{3+}O$_{1.5}$). Ti concentrations determined using EPMA; all other concentration determined using LA-ICP-MS apart from three points labelled with a star, where V content was measured with EPMA due to small crystal size. Lines are non-linear least-squared regression and their respective values of a_M^0 and a_M^1 are given in Table 5. Error bars = 1σ*

2.4 Discussion

2.4.1 Prevailing valence states of elements in the melt

The oxidation states of a number of the trace elements studied namely, Fe, Cu, Mo and V, are redox-variable under natural conditions on earth. Copper can occur as both Cu^{+} and Cu^{2+}, but is predominantly Cu^{+} in the melt over the experimental conditions studied here, as suggested by the previous spinel-melt partitioning experiments by Liu et al. (2014, 2015) and the metal solubility study of Ripley and Brophy (1995). Molybdenum exists as 4+ and 6+ in silicate melts, but is likely to be Mo^{6+} in the melts studied here (O'Neill and Eggins, 2002). Moreover, although Ti^{3+} could occur at reduced conditions (fO_2 < FMQ - 2), Ti is expected to be present as Ti^{4+} in the melt in these experiments (Mallmann and O'Neill, 2009). Finally, V can occur in multiple valence states in silicate melts, but is likely to occur as V^{3+}, V^{4+} and V^{5+} in the melt studied here (Toplis and Corgne, 2002; Mallman and O'Neill, 2009).

2.4.2 Thermodynamic explanation of element partitioning

Thermodynamic principles show that an essential feature of any mineral-melt partitioning is the "stoichiometric control" described by the appropriate equilibrium reaction. Such reactions in general depend on the valence state of the partitioning element, the valence state of the element for which the partitioning element substitutes, hence the charge-balance mechanism, and the crystallographic site or sites on which the substitution takes place (e.g. O'Neill and Eggins, 2002).

In the case of magnetite, with its near random distribution of Fe^{2+} and Fe^{3+} over the two distinct cation sites, the details of site occupancy are less important than usual, but the stoichiometric control remains critical. In the case of polyvalent trace elements (e.g., Cu, V and Mo) in magnetite, there is also the additional complexity in the thermodynamics from the charge-transfer process.

2.4.2.1 Partitioning of divalent cations

The partitioning of divalent cations, such as Mg, Mn, Co, Ni and Zn, into magnetite can be described by the reaction:

$$M^{2+}O_{melt} + Fe^{2+}Fe^{3+}{}_2O_{4spinel} \rightleftharpoons M^{2+}\,Fe^{3+}{}_2O_{4spinel} + Fe^{2+}O_{melt} \qquad (2\text{-}3)$$

For which the equilibrium constant, K, is:

$$K = \frac{(aM^{2+}Fe^{3+}{}_2O_{4_{mgt}}) \times (aFe^{2+}O_{melt})}{(aFe^{2+}Fe^{3+}{}_2O_{4_{mgt}}) \times (aM^{2+}O_{melt})} \qquad (2\text{-}4)$$

By relating activities to the product of concentrations times activity coefficients in the usual way, and converting from mole fractions to concentrations by weight where appropriate, Eq. 2-4 can be rewritten as:

$$K_M{}^* = \frac{[M^{2+}]_{mgt}}{[M^{2+}]_{melt}} \times \frac{\gamma M^{2+}{}_{mgt}}{aFe_3O_{4_{mgt}}} \times XFe^{2+}O_{melt} \times \frac{\gamma Fe^{2+}O_{melt}}{\gamma M^{2+}O_{melt}} \qquad (2\text{-}5)$$

where $\gamma M^{2+}O_{melt}$ and $\gamma Fe^{2+}O_{melt}$ are the activity coefficients of the components $M^{2+}O$ and $Fe^{2+}O$ in the melt, and $\gamma M^{2+}{}_{mgt}$ is the activity coefficient of the $M^{2+}Fe^{3+}{}_2O_4$ component in the magnetite solid solution, which may, in principle, change with the major-element composition of the magnetite where this differs from pure Fe_3O_4 (in this study mainly solid solution towards Fe_2TiO_4). The weight ratio $[M^{2+}]_{mgt}/[M^{2+}]_{melt}$ is the partition coefficient $D(M^{2+})$, and K* is the equilibrium constant using a mix of concentrations-by-weights and mole fractions.

Rearranging gives:

$$D(M^{2+}) = K_M{}^* \times \frac{aFe_3O_{4_{mgt}}}{\gamma M^{2+}{}_{mgt}} \times \frac{1}{XFe^{2+}O_{melt}} \times \frac{\gamma M^{2+}O_{melt}}{\gamma Fe^{2+}O_{melt}} \qquad (2\text{-}6)$$

which shows that the magnetite-melt partition coefficients of divalent cations are strongly dependent on $XFe^{2+}O$, which is related to fO_2 by the reaction $Fe^{2+}O + ¼\ O_2 = Fe^{3+}O_{1.5}$. We may use Eq. 2-3 for comparing the partitioning behaviour of elements with 2+ cations independently of

variations in the activity of magnetite ($a\mathrm{Fe_3O_{4mgt}}$) by selecting one of the divalent cations as a reference. We chose Mg for this role, because it is in sufficient concentration in all experiments to be analysed precisely by EPMA, even in smaller magnetite crystals. By dividing Eq. 2-4 for Mg from Eq. 2-4 for another divalent cation, M, we obtain:

$$D(M^{2+}) = D(Mg) \times \frac{K_M{}^*}{K_{Mg}{}^*} \times \frac{\gamma M^{2+}O_{melt}}{\gamma Mg^{2+}O_{melt}} \times \frac{\gamma Mg_{mgt}}{\gamma M^{2+}{}_{mgt}} \qquad (2\text{-}7)$$

Hence plots of ln D(M^{2+}) vs. ln D(Mg) at a given temperature and pressure should produce straight lines with a slope of unity and an intercept of $\frac{K_M{}^*}{K_{Mg}{}^*} \times \frac{\gamma M^{2+}O_{melt}}{\gamma Mg^{2+}O_{melt}} \times \frac{\gamma Mg_{mgt}}{\gamma M^{2+}{}_{mgt}}$, regardless of $a\mathrm{Fe_3O_4}$ (magnetite composition), provided that both the ratios of activity coefficients, namely $\frac{\gamma Mg_{mgt}}{\gamma M^{2+}{}_{mgt}}$ and $\frac{\gamma M^{2+}O_{melt}}{\gamma Mg^{2+}O_{melt}}$ are constant. For the melt, there is a considerable body of experimental evidence addressing this question. The activity coefficients for the divalent cations (Mg^{2+}, Co^{2+}, Ni^{2+}, Fe^{2+}) have been investigated experimentally over a wide range of melt compositions (O'Neill and Eggins, 2002; O'Neill and Berry, 2006; Toplis, 2005; Doyle and Naldrett, 1987), and those of Mn^{2+} and Zn^{2+} have also been studied, albeit over a more limited range (Kohn and Schofield, 1994). The absolute variation in individual activity coefficients is only within a factor of two over a wide range of melt compositions, and although they do not correlate with any simple parameter such as melt chemistry or melt structural descriptor (O'Neill and Eggins, 2002), their ratios (e.g. $\gamma Mg^{2+}/\gamma Fe^{2+}$) remain almost constant, only exhibiting small dependences on silica content and concentration of alkalis (Toplis, 2005; O'Neill and Berry, 2006). Similarly, the systematics of thermodynamic mixing properties in complex spinel solid solutions indicate that the ratio $\frac{\gamma Mg_{mgt}}{\gamma M^{2+}{}_{mgt}}$ is likely to remain approximately constant within the rather limited range of spinel compositions covered by the $\mathrm{Fe_3O_4}$ –rich spinels of this study (or similar studies on "magnetite", because such systematics depend mainly on two fundamental properties of the cations themselves, their site preference energies and ionic radii (O'Neill and Navrotsky, 1984). The temperature range of this study (1070 to 1120ºC) is sufficiently small that the change of $K_M{}^*$ with temperature may be ignored as a first approximation. Nevertheless, Nielsen et al. (1994) have shown that spinel composition also correlates with mineral-melt partitioning of some trace elements. Therefore, it is important to emphasise that this model may not be applicable to magnetite-poor spinel crystallised in bulk compositions which contrast with the andesitic-dacitic system studied here.

Plots of ln D(M^{2+}) vs. ln D(Mg) are shown in (Figure 2-5) where M = Mn, Co, Ni and Zn. These data were fit by a global non-linear least-squares model to minimize chi-square:

$$x^2 = \sum_M \left(\frac{lnD(M)_{obs} - a_M^0 - a_M^1 lnD(Mg)_{calc}}{s(lnD(M))}\right)^2 + \left(\frac{lnD(Mg)_{obs} - lnD(Mg)_{calc}}{s\big(lnD(M)\big)}\right)^2 \quad (2\text{-}8)$$

where M = Mn, Co, Ni, Zn and also Cu, as discussed below, with uncertainties from Table 2-3 and 2-4. The results are summarised in Table 2-5. If the approximations just discussed are valid, the values of a_M^1 should be 1. For Mn, Co and Zn, a_M^1 is close to 1 with values 0.97, 1.16 and 0.91 respectively. The value of a_{Ni}^1 is somewhat higher (1.29). It is clear that the influence of melt composition, other than the all-important $Fe^{2+}O_{melt}$ (Eq. 2-3), is a rather minor input in the nearly order-of-magnitude variations in the partition coefficients of the divalent cations seen in this study.

2.4.2.2 Partitioning of Cu

Empirically, D(Cu) correlates quite well with D(Mg) as shown in Figure 2-5, but the slope of ln D(Cu) vs. ln D(Mg) at 1.51 (Table 2-5) is noticeably larger than unity. The valence state of Cu in silicate melts under the fO_2 regime of this study is predominantly 1+ (Ripley and Brophy, 1995; Liu et al., 2014, 2015), One distinctive crystal-chemical feature of magnetite trace-element partitioning compared to most other minerals is that in the magnetite, but not the melt, the valence states of redox-variable elements reflects the stoichiometry of magnetite through electron exchange reactions. Thus, the valence state of redox-variable elements in stoichiometric magnetite is independent of fO_2. For Cu, the electron-exchange could be written:

$$Cu^{1+} + Fe^{3+} = Fe^{2+} + Cu^{2+} \quad (2\text{-}9)$$

(e.g. O'Neill and Navrotsky, 1983, 1984).

The appropriate thermodynamic component is the fully oxidised end-member $Cu^{2+}Fe^{3+}{}_2O_4$, a well-known ferrite spinel (Nickel, 1973). The reasons for selecting this component rather than say $Cu^{1+}{}_{0.5}Fe^{3+}{}_{2.5}O_4$ (by analogy with $Li^{1+}{}_{0.5}Fe^{3+}{}_{2.5}O_4$) will be discussed further below. The partitioning equilibrium is then:

$$Cu^{1+}O_{0.5\,melt} + Fe_3O_{4\,spinel} + \frac{1}{4}O_2 = Cu^{2+}Fe^{3+}{}_2O_{4\,spinel} + Fe^{2+}O_{melt} \quad (2\text{-}10)$$

Using Eq. 2-1 and 2-2 (The $Fe^{2+}O + ¼\ O_2 = Fe^{3+}O_{1.5}$ and the $Fe^{2+}O + 2\ Fe^{3+}O_{1.5} = Fe_3O_4$ equilibria) to eliminate O_2, the comparison with the partitioning equilibrium for Mg to eliminate the effect of $a Fe_3O_{4mgt}$ gives:

$$Cu^{1+}O_{0.5_{melt}} + 1.5MgFe^{3+}{}_2O_{4_{spinel}} = Cu^{2+}Fe^{3+}{}_2O_{4_{spinel}} + Fe^{2+}O_{melt} + 1.5MgO_{melt} \qquad (2\text{-}11)$$

Hence:

$$lnD(Cu) = 1.5\ lnD(Mg) - lnXFe^{2+}O_{melt} - lnK(*) + \ln\frac{\gamma Mg_{mgt}}{\gamma Cu^{2+}{}_{mgt}} - ln\frac{\gamma Fe^{2+}O_{melt}(\gamma MgO_{melt})^{1.5}}{\gamma Cu^{1+}O_{0.5_{melt}}} \qquad (2\text{-}12)$$

Although we do find the slope of lnD(Cu) versus lnD(Mg) is near 1.5 (Figure 2-5E), this appears to be coincidental. If the expected effect of $XFe^{2+}O_{melt}$ is factored in, the relationship disappears: a plot of lnD(Cu) vs. {1.5lnD(Mg) - $lnXFe^{2+}O_{melt}$}gives a slope of 0.68 (Table 2-5); the discrepancy with theory presumably reflects a substantial change of the quotient of activity coefficients in the melt, $\frac{\gamma Fe^{2+}O_{melt}(\gamma MgO_{melt})^{1.5}}{\gamma Cu^{1+}O_{0.5_{melt}}}$, with melt composition.

The reasons for selecting $CuFe_2O_4$ rather than $Cu_{0.5}Fe_{2.5}O_4$ as the Cu-containing component in magnetite start with the observation that the phase relations in the system Cu-Fe-O show a continuous solid solution, with a smooth change of free energy along the binary join running from the spinel composition stable at the most oxidizing conditions achievable in this system, which is $Cu^{2+}Fe^{3+}{}_2O_4$, to that stable at the most reduced extreme, which is Fe_3O_4 (Jacob et al., 1977; Katayama et al., 1980; Katkov and Lykasov, 2003). The composition $CuFe_{2.5}O_4$ is simply the 50:50 composition. Its cationic configuration could in principle be anywhere between $Cu^{1+}{}_{0.5}Fe^{3+}{}_{2.5}O_4$ (all Cu as 1+, no Fe^{2+}) or $Cu^{2+}{}_{0.5}Fe^{2+}{}_{0.5}Fe^{3+}{}_2O_4$ (all Cu as 2+); these possibilities are related by the homogeneous equilibrium $Cu^{2+}Fe^{3+}{}_2O_4 + Fe_3O_4 = 2\ Cu^{1+}{}_{0.5}Fe^{3+}{}_{2.5}O_4$. Alternatively, this equilibrium could be expressed as the electron-exchange reaction $Cu^{2+} + Fe^{2+} = Cu^{1+} + Fe^{3+}$, as noted above. This electron-exchange reaction results in a large negative deviation from ideal mixing in the binary join $Cu^{2+}Fe^{3+}{}_2O_4$ - Fe_3O_4, due to the extra configurational entropy that it confers. Note that while the ratio of Cu^{1+}/Cu^{2+} in the spinel at a given Cu/Fe is expected to depend on temperature, it is independent of fO_2, being controlled, through the electron-exchange reaction, by the stoichiometry of the spinel. Although the thermodynamic properties of a component with stoichiometry $Cu_{0.5}Fe_{2.5}O_4$ could in principle be derived from the experimentally determined phase relations, they would depend on those of $CuFe_2O_4$ anyway. It is therefore simpler to stick with the latter.

2.4.2.3 Partitioning of trivalent cations

The partitioning of trivalent cations, such as Sc^{3+}, into magnetite can be described as follows:

$$M^{3+}O_{1.5melt} + ½\ Fe^{2+}Fe^{3+}{}_2O_4 \rightleftharpoons ½\ Fe^{2+}M^{3+}{}_2O_4 + FeO_{1.5melt} \quad (2\text{-}13)$$

Based on similar thermodynamic assumptions as for the partitioning of divalent cations, the partitioning of trivalent cations between magnetite and melt would be expected to follow the expression:

$$D_{M^{3+}(mgt-melt)} = K_M{}^* \times \frac{(aFe^{2+}Fe^{3+}{}_2O_{4_{mgt}})^{\frac{1}{2}}}{\gamma M^{3+}{}_{mgt}} \times \frac{1}{XFe^{3+}O_{1.5_{melt}}} \times \frac{\gamma M^{3+}O_{1.5_{melt}}}{\gamma Fe^{3+}O_{1.5_{melt}}} \quad (2\text{-}14)$$

Similar to the analyses of partitioning of divalent cations, the partitioning behaviour of 3+ cations can be compared to other trivalent cations as a reference. By dividing Eq. 2-14 for Al from Eq. 2-14 for another trivalent cation, M, we obtain the expression:

$$D(M^{3+}) = D(Al) \times \frac{K_M{}^*}{K_{Al}{}^*} \times \frac{\gamma M^{3+}O_{1.5_{melt}}}{\gamma Al^{3+}O_{1.5_{melt}}} \times \frac{\gamma Al_{mgt}}{\gamma M^{3+}{}_{mgt}} \quad (2\text{-}15)$$

Unlike the divalent cations, plots of lnD(Sc) and lnD(Ga) vs. lnD(Al) do not produce clear trends (Figure 2-8). In comparison to the divalent cations, there is not a large variation in the partitioning of trivalent cations in our dataset. It could be that the partitioning of the trivalent cations is more strongly controlled by spinel composition as a result of non-ideal mixing of Al, Fe^{3+} and Cr (Nielsen et al.,1994). This could explain the weak negative correlation between lnD(Sc) and lnD(Al). Alternatively, because Al is a major structural component of the melt, it is likely that the activity coefficients in the melt, $\frac{\gamma M^{3+}O_{1.5_{melt}}}{\gamma Al^{3+}O_{1.5_{melt}}}$, are not constant over the range of compositions and conditions studied here. Additionally, $K_M{}^*$ could be more sensitive to temperature for the trivalent cations than for the divalent cations.

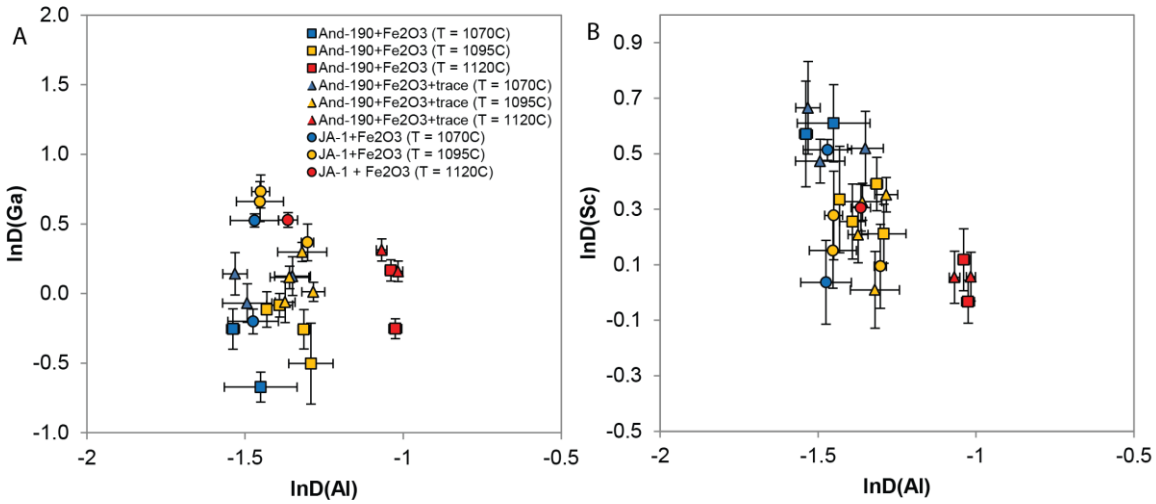


Figure 2-8: Natural log of titanomagnetite-melt partition coefficients of (A) Ga and (B) Sc as a function of the natural log of titanomagnetite-melt partition coefficient of Al for And-190 + Fe_2O_3, And-190 + Fe_2O_3 + trace and JA-1 + Fe_2O_3 starting compositions. Error bars = 1σ

2.4.2.4 Partitioning of tetravalent cations

The partitioning of tetravalent cations can be described by the reaction:

$$M^{4+}O_{2melt} + Fe^{2+}Fe^{3+}{}_2O_4 \rightleftharpoons Fe^{2+}{}_2M^{4+}O_4 + Fe^{3+}O_{1.5melt} + \tfrac{1}{4}\, O_2 \qquad (2\text{-}16)$$

Again, based on similar thermodynamic assumptions, the partitioning of tetravalent cations would be expected to follow the expression:

$$D(M^{4+}) = K_M{}^* \times \frac{(aFe^{2+}Fe^{3+}O_{4_{mgt}})}{\left(\gamma M^{4+}{}_{mgt}\right) \times (fO_2)^{\frac{1}{4}}} \times \frac{1}{XFe^{3+}O_{1.5_{melt}}} \times \frac{\gamma M^{4+}O_{2_{melt}}}{\gamma Fe^{3+}O_{1.5_{melt}}} \qquad (2\text{-}17)$$

In this case, the magnetite-melt partitioning of tetravalent cations is directly dependent on the fO_2. By dividing Eq. 2-17 for Ti from Eq. 2-17 for another tetravalent cation, M, we obtain:

$$D(M^{4+}) = D(Ti) \times \frac{K_M{}^*}{K_{Ti}{}^*} \times \frac{\gamma M^{4+}O_{2_{melt}}}{\gamma TiO_{2_{melt}}} \times \frac{\gamma Ti_{mgt}}{\gamma M^{4+}{}_{mgt}} \qquad (2\text{-}18)$$

Plots of $lnD(M^{4+})$ vs. lnD(Ti) are shown in (Figure 2-7) where M = Zr and Hf. These data were fit by a global non-linear least-squares model to minimize chi-square. These results are summarised in Table 2-5. The values of a^1_{Zr} and a^1_{Hf} are 0.80 and 0.75 respectively. This suggests that the ratio of the activity coefficients, $\frac{\gamma M^{4+}O_{2_{melt}}}{\gamma TiO_{2_{melt}}}$, also remains close to constant for the tetravalent cations. Similar to the partitioning of divalent cations, it is the $Fe^{3+}O_{1.5melt}$ and $Fe^{2+}O_{melt}$ (which is controlled by the fO_2) which dictates the primary control on the spinel-melt partitioning of tetravalent

cations. A plot of lnD(V) vs. lnD(Ti) does not have a slope close to unity (2.40), which would be expected given that the valence states of V in magnetite are, like those of Cu, controlled by stoichiometry through electron exchange reaction: $V^{3+} + Fe^{3+} = Fe^{2+} + V^{4+}$, with the thermodynamically convenient end-member being $Fe^{2+}V^{3+}{}_2O_4$ (O'Neill and Navrotsky, 1984). Thus, Eq. 2-16 does not suitably describe the partitioning of V into magnetite.

2.4.2.5 Partitioning of pentavalent cations

Pentavalent cations, such as niobian magnetite, have been shown to have solid solution towards the end-member $Fe^{2+}{}_{7/3}Nb^{5+}{}_{2/3}O_4$ (Turnock, 1966; Kitayama, 1987), hence the stoichiometry of the partitioning reaction is:

$$⅔\ M^{5+}O_{2.5melt} + Fe^{2+}Fe^{3+}{}_2O_4 \rightleftharpoons Fe^{2+}{}_{7/3}M^{5+}{}_{2/3}O_4 + ⅔\ Fe^{3+}O_{1.5melt} + ⅓\ O_2 \qquad (2\text{-}19)$$

Again, based on similar thermodynamic assumptions, the partitioning of tetravalent cations would be expected to follow the expression:

$$D(M^{5+}) = K_M{}^* \times \frac{(aFe^{2+}Fe^{3+}O_{4_{mgt}})}{\left(\gamma M^{5+}{}_{mgt}\right) \times (fO_2)^{\frac{1}{3}}} \times \frac{1}{(XFe^{3+}O_{1.5_{melt}})^{\frac{2}{3}}} \times \frac{\gamma M^{5+}O_{2.5_{melt}}}{(\gamma Fe^{3+}O_{1.5_{melt}})^{\frac{2}{3}}} \qquad (2\text{-}20)$$

By dividing Eq. 2-17 for Ti from Eq. 2-20 for another pentavalent cation, M, we obtain:

$$D(M^{5+}) = D(Ti) \times \frac{K_M{}^*}{K_{Ti}{}^*} \times \frac{\gamma M^{5+}O_{2.5_{melt}}}{\gamma TiO_{2_{melt}}} \times fO_2{}^{-\frac{1}{12}} \times XFe^{3+}O_{1.5}{}^{-\frac{1}{3}} \times \frac{\gamma Ti_{mgt}}{\gamma M^{5+}{}_{mgt}} \qquad (2\text{-}21)$$

After factoring in for the fO_2 and $XFe^{3+}O_{1.5}$ terms, D(Nb) and D(Ta) correlate with D(Ti), but with a slope of 1.01 and 0.94 respectively (Table 2-5), which suggests that $\frac{K_M{}^*}{K_{Ti}{}^*} \times \frac{\gamma M^{5+}O_{2.5_{melt}}}{\gamma TiO_{2_{melt}}} \times \frac{\gamma Ti_{mgt}}{\gamma M^{5+}{}_{mgt}}$ remains approximately constant within the experimental conditions studied. Notwithstanding this, the partitioning of HFSE also correlates with T, Al content of spinel and P (Nielsen and Beard, 2000), thus, the ratios of these activity coefficients may not be constant in spinel or melt outside the composition range studied here.

Table 2-5: Values of a_M^0 and a_M^1 from fitting titanomagnetite-melt partitioning for elements (M) to global non-linear least-squares model to minimize chi-square using the partitioning of another cation as a reference using data from this study (see Eq. 2-8)

Reference	lnD(M)	a_M^0	a_M^1
lnD(Mg)	lnD(Mn)	0.29	0.97
lnD(Mg)	lnD(Co)	1.82	1.17
lnD(Mg)	lnD(Ni)	3.39	1.29
lnD(Mg)	lnD(Zn)	1.07	0.91
lnD(Mg)	lnD(Cu)	-1.56	1.51
1.5lnD(Mg) - ln$XFe^{2+}O$(melt)	lnD(Cu)	-3.69	0.68
lnD(Ti)	lnD(V)	-1.79	2.40
lnD(Ti)	lnD(Zr)	-3.62	0.80
lnD(Ti)	lnD(Hf)	-3.19	0.75
lnD(Ti)	lnD(Nb)	-4.28	1.40
lnD(Ti)	lnD(Ta)	-3.73	1.25
lnD(Ti)-((1/12)*lnfO_2)-(⅓*ln$XFe^{3+}O_{1.5}$(melt))	lnD(Nb)	-6.61	1.01
lnD(Ti)-((1/12)*lnfO_2)-(⅓* ln$XFe^{3+}O_{1.5}$(melt))	lnD(Ta)	-5.94	0.94

2.4.2.6 Spinel thermodynamics and partitioning relations

Spinel-melt partitioning can be evaluated more directly if $a Fe_3O_{4mgt}$ can be calculated. O'Neill and Wall (1987) presented a model for calculating $a Fe_3O_{4mgt}$ in compositionally complex spinels in the system MgO-Al_2O_3-Cr_2O_3-TiO_2-Fe-O as a function of temperature and pressure. The $Fe^{2+}O$ concentration in the melt can be approximated from measured total Fe concentrations (i.e. FeO total) and fO_2 using the empirical parameterization of Kress and Carmichael (1991), which can then be converted into a mole fraction on a single cation basis ($XFe^{2+}O$), so that values of $XFe^{2+}O$ and $XFe^{3+}O_{1.5}$ can be calculated. As discussed earlier, the ratios of the activity coefficients for the divalent cations in melt and magnetite are expected to remain almost constant. Therefore, the partitioning of divalent cations would be expected to be linearly proportional to ($a Fe_3O_4$ in magnetite)/($XFe^{2+}O$ in liquid), which is observed in our data (Figure 2-9A-C).

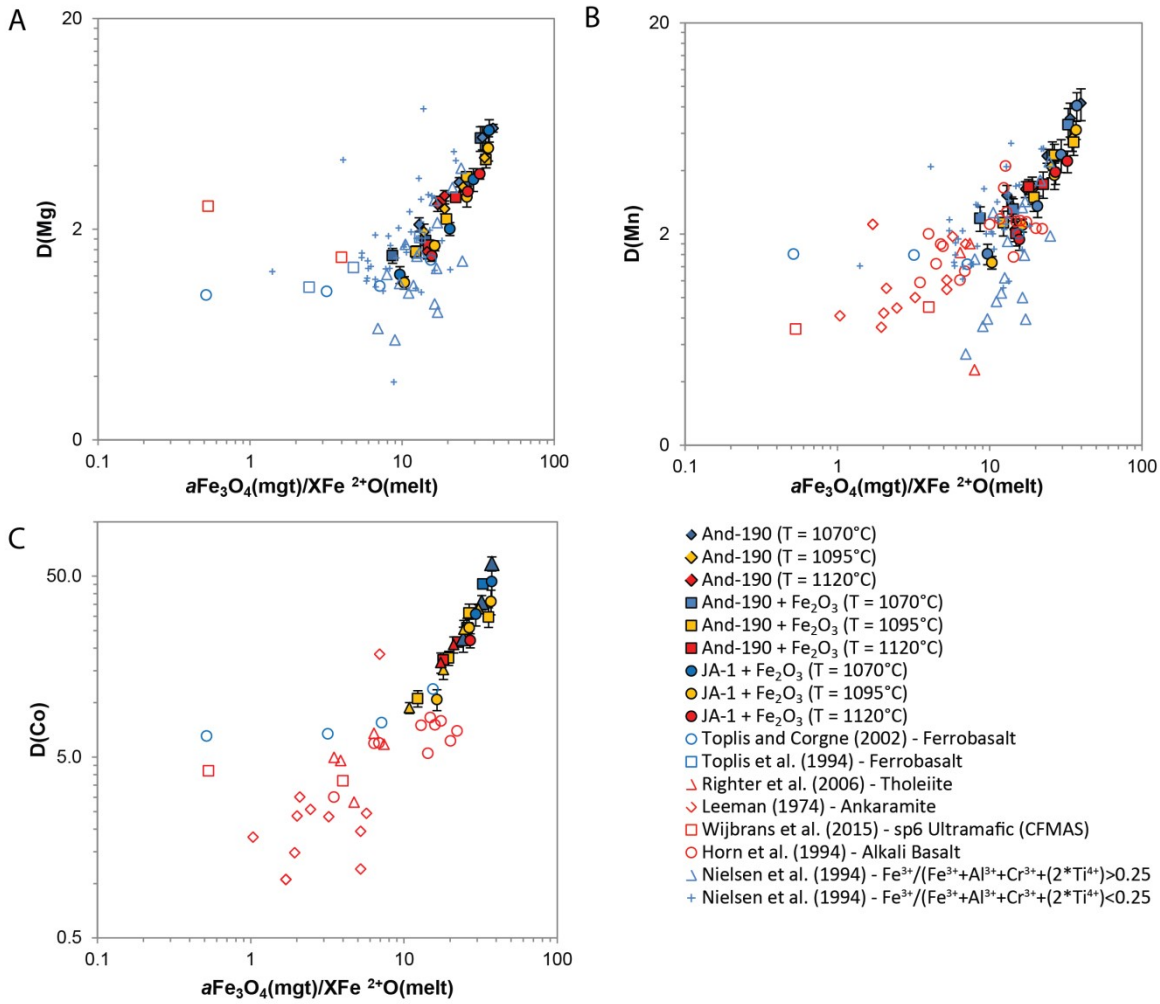


Figure 2-9: Titanomagnetite-melt partition coefficients of (a) Mg, (b) Mn and (c) Co plotted against $aFe_3O_4(mgt)/XFe^{2+}O(melt)$. $aFe_3O_4(mgt)$ approximated using model by O'Neill and Wall (1987), and mole fraction on single cation basis $XFe^{2+}O(melt)$ calculated from values approximated using Kress and Carmichael (1991). Literature data includes: Toplis and Corgne (2002), Toplis et al. (1994) and Nielsen et al. (1994) which were conducted at 1068-1130°C; and Righter et al. (2006), Leeman (1974), Horn et al. (1994) and Wijbrans et al. (2015) which were conducted between 1150°C and 1370°C. Error bars = 1σ

The linear trend for $D(M^{2+})$ as a function of $aFe_3O_4(mgt)/XFe^{2+}O(melt)$ is corroborated by literature data covering a variety of bulk compositions, but breaks down in some experiments, notably those conducted at lowest fO_2 by Toplis and Corgne (2002) and Toplis et al. (1994). These data are for particularly Ti-rich spinel with $Fe^{3+}/(Fe^{3+}+Al^{3+}+Cr^{3+}+(2*Ti^{4+}))$ cpfu of 0.11 to 0.30. Furthermore, data from Nielsen et al. (1994) with $Fe^{3+}/(Fe^{3+}+Al^{3+}+Cr^{3+}+(2*Ti^{4+}))$ cpfu > 0.25 agree well with the linear trend defined in this study, but those with $Fe^{3+}/(Fe^{3+}+Al^{3+}+Cr^{3+}+(2*Ti^{4+}))$ cpfu < 0.25 do not. Mg-rich spinel in experiments by Wijbrans et al. (2015) also have elevated D(Mg) relative to those studied here. Thus, it would seem that the model in terms of thermodynamic principles reliably explains magnetite-melt partitioning in magnetite-rich spinel, but breaks down for spinel with contrasting major element composition to those studied here. Thus, large changes in major element composition of the bulk system can

exert an additional control on spinel-melt partitioning, as expected from models of spinel solid-solution thermodynamics (O'Neill and Navrotsky, 1984). However, to establish this, the other relevant factors would first need to be accounted for. One of these is the change in the activity coefficients in the melt with the composition of the system.

In comparison to the andesitic-dacitic bulk composition studied here, in mafic bulk systems (e.g. Toplis and Corgne, 2002; Toplis et al., 1994; Righter et al., 2006), there is a stronger increase in the $a\mathrm{Fe_3O_4}$(mgt) over a similar range in $f\mathrm{O_2}$. This counteracts the decrease in $\mathrm{Fe^{2+}O}$(melt) with increasing $f\mathrm{O_2}$ and as a result there is significantly less variation in $a\mathrm{Fe_3O_4}$(mgt)/$\mathrm{XFe^{2+}O}$(melt) with $f\mathrm{O_2}$. Consequently, there is a lesser pronounced increase in $\mathrm{D(M^{2+})_{mgt\text{-}melt}}$ with increasing $f\mathrm{O_2}$ in mafic bulk systems in comparison to the silicic bulk compositions studied here (Figure 2-9).

There is a linear trend as a function of $a\mathrm{Fe_3O_4(mgt)^{0.5}/XFe^{3+}\ O_{1.5}}$(melt) for D(Sc), which is corroborated by literature data, investigating spinel-melt partitioning in different bulk compositions (Figure 2-10A). Similarly, plotting D(Ga) vs. $a\mathrm{Fe_3O_4(mgt)^{0.5}/XFe^{3+}\ O_{1.5}}$(melt) generates a linear trend when combined with data using the most Fe-rich starting composition studied by Wijbrans et al. (2015), however, this trend has a negative slope (Figure 2-10C). Plotting D(Al) vs. $a\mathrm{Fe_3O_4(mgt)^{0.5}/XFe^{3+}\ O_{1.5}}$(melt), also produces a poorly defined linear trend with a negative slope (Figure 2-10A). This could suggest there is large variation in the ratio of activity coefficients for Al and Ga relative to other 3+ cations in the melt with variation in bulk composition or temperature. This might be expected for Al given that it is a major component of the melt. It is also worth noting that spinels crystallised in studies included by Righter et al. (2006), Leeman (1976), Horn et al. (1994) and Wijbrans et al. (2015) have significantly higher Al cpfu (Al cpfu = 0.82 in data included from Wijbrans et al. (2015) in comparison to Al cpfu from 0.1 - 0.2 in this study), which could exert an additional control on spinel-melt partitioning through significantly altering the activity of the substituting cation.

Linear relationships can also be produced which describe the partitioning of tetravalent and pentavalent cations as a function of $(a\mathrm{Fe3O4_{mgt}})/(\mathrm{XFe^{3+}O_{1.5liq}}^{*}\ f\mathrm{O2^{0.25}})$ and $(a\mathrm{Fe3O4_{mgt}})/(\mathrm{XFe^{3+}O_{1.5liq}}^{2/3}\ *\ f\mathrm{O2}^{1/3})$ respectively (Figure 2-11). The linear trend for D(Ti) is corroborated by literature data covering different bulk compositions to that studied here. Data from Wijbrans et al. (2015) support the linear trend defined for D(Nb), however, data from Nielsen et al. (1994) do not. It is possible that the contrasting spinel composition effects the mineral-melt partitioning so that this model is only relevant for magnetite-rich spinel.

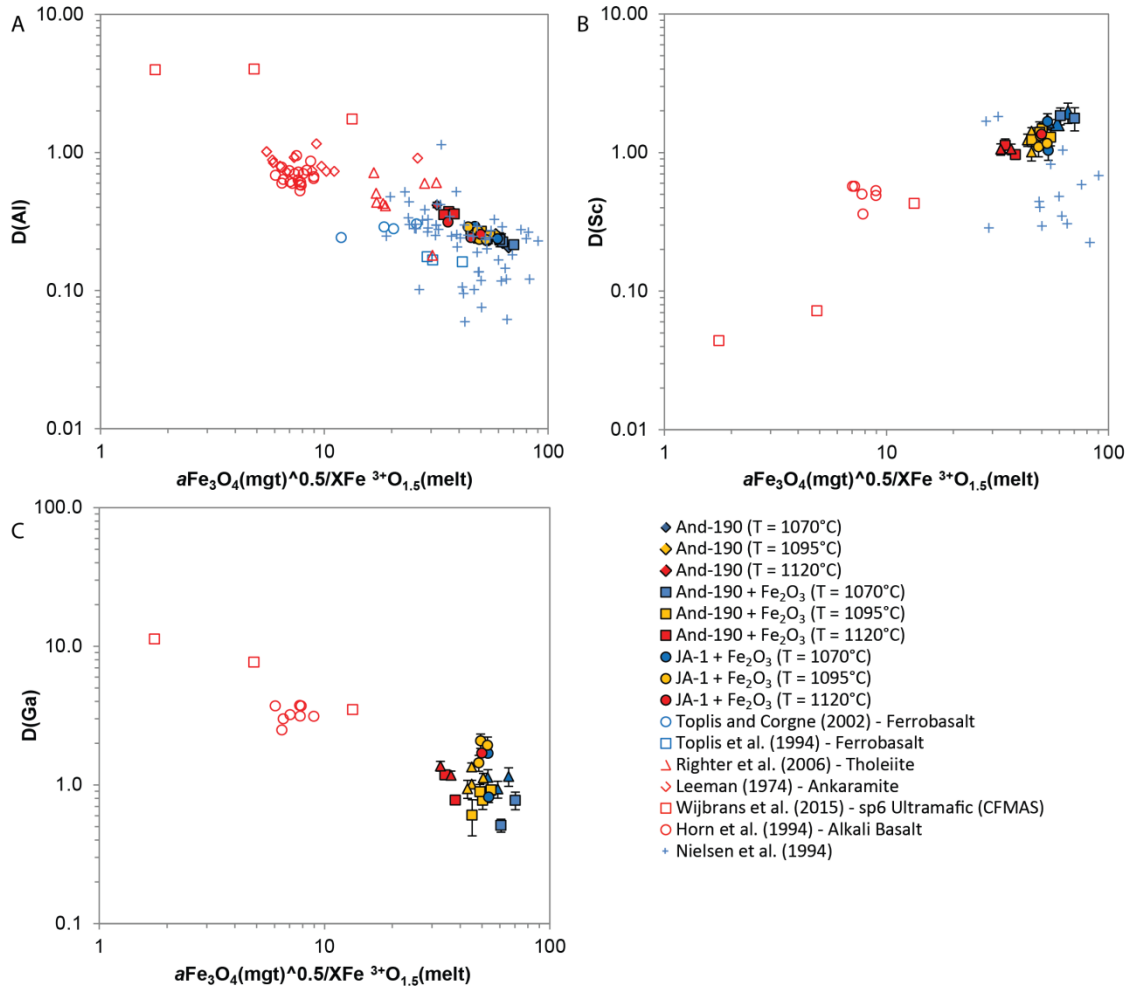


Figure 2-10: (A) D(Al), (B) D(Sc) and (C) D(Ga) as a function of aFe_3O_4(mgt)0.5/$XFe^{3+}O_{1.5}$(melt). aFe_3O_4(mgt) approximated using model by O'Neill and Wall (1987), and mole fraction on single cation basis $XFe^{3+}O_{1.5}$(melt) calculated from values approximated using Kress and Carmichael (1991). Literature data includes: Toplis and Corgne (2002), Toplis et al. (1994) and Nielsen et al. (1994) which were conducted at 1068-1130°C; and Righter et al. (2006), Leeman (1974), Horn et al. (1994) and Wijbrans et al. (2015) which were conducted between 1150°C and 1370°C. Error bars = 1σ

For the And-190 + Fe_2O_3 bulk composition, between FMQ + 0.2 and FMQ + 3, the maximum variation in aFe_3O_4(mgt)/$XFe^{3+}O_{1.5}$(melt) is between 42.5 and 54.3. The fO_2 expression, however, exhibits a much larger variation, and between FMQ + 0.2 < fO_2 < FMQ + 3, $1/(fO_2^{0.25})$ varies between 285.10 and 56.9. Clearly, the oxygen fugacity term ($fO_2^{0.25}$) dictates most influence on the partitioning of the tetravalent cations, which could explain the large degree of overlap between datasets for D(Ti) as a function of fO_2 (Figure 2-6C). In this premise, the partitioning of homovalent tetravalent and higher valence cations, should be easier to predict from the fO_2 alone, than cations with variable valence state. For example, V partitioning is often used as a proxy for fO_2 owing to its multivalent character. However, this mixed valency substantially complicates the dependence of its partitioning as a function of fO_2. In this premise, in comparison to V, the partitioning behaviour of homovalent tetravalent and pentavalent cations in response to fO_2 is

easier to predict, and therefore could offer an improved proxy for fO_2. Notwithstanding this, it is important to consider that the crystallisation of zircon will strongly influence the concentration of Zr and Hf in the melt, which would hinder the use of Zr and Hf titanomagnetite-melt partitioning as potential proxies for fO_2 in natural systems.

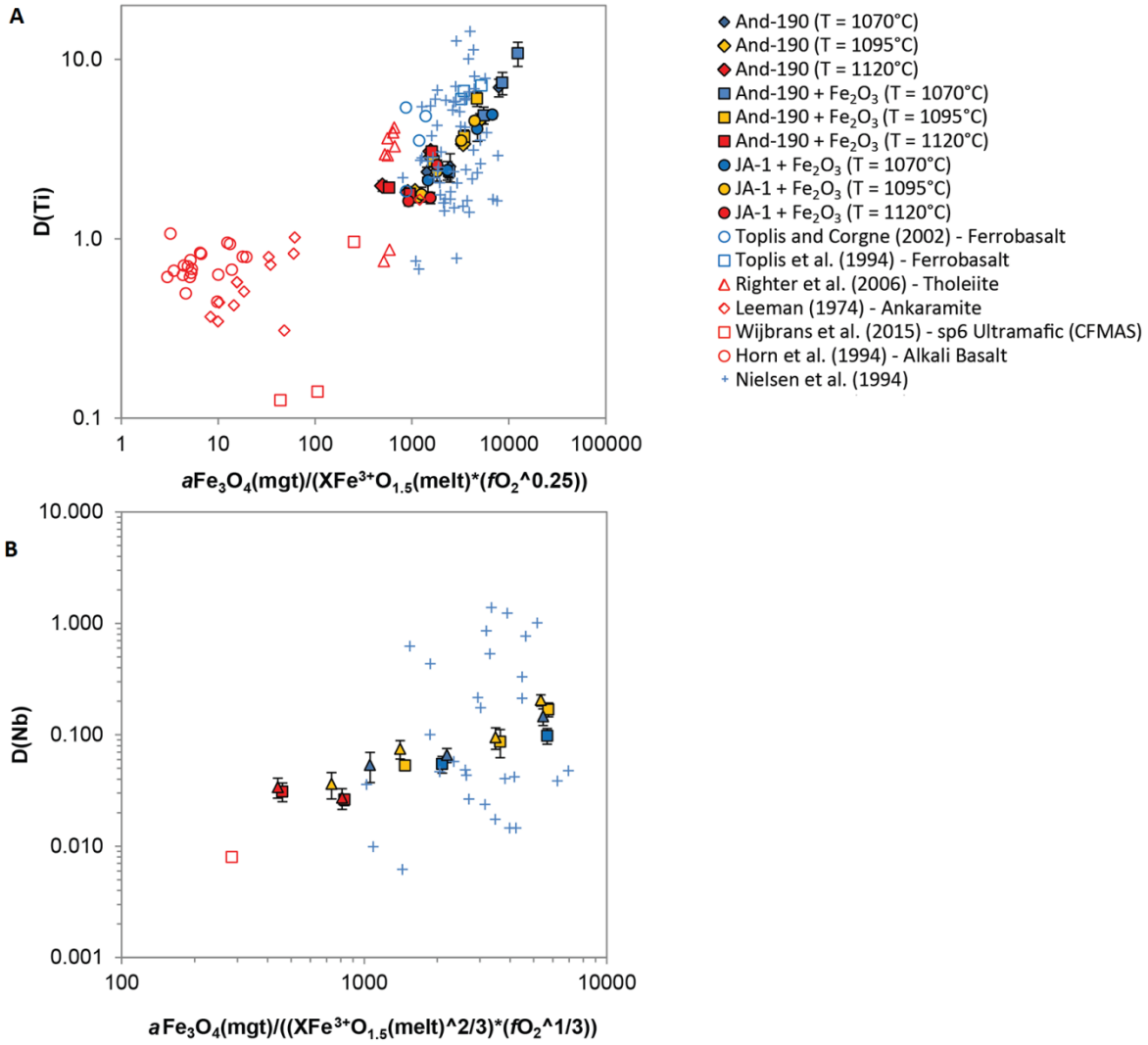


Figure 2-11: (A) D(Ti) plotted against $aFe_3O_4(mgt)/(XFe^{3+}O_{1.5}(melt)*(fO_2^{0.25}))$ and (B) D(Nb) as a function of $aFe_3O_4(mgt)/(XFe^{3+}O_{1.5}(melt)^{2/3})*(fO_2^{1/3})$. $aFe_3O_4(mgt)$ approximated using model by O'Neill and Wall (1987), and mole fraction on single cation basis $XFe^{3+}O_{1.5}(melt)$ calculated from values approximated using Kress and Carmichael (1991). Relevant literature data are included for comparison (Toplis et al., 1994; Toplis and Corgne, 2002; Nielsen et al., (1994); Righter et al., 2006; Leeman, 1974; Horn et al., 1994 and Wijbrans et al., 2015). Error bars = 1σ

In summary, thermodynamic principles predict linear relationships between titanomagnetite-melt partitioning and the aFe_3O_4 in titanomagnetite and $XFe^{3+}O_{1.5}$ and $XFe^{2+}O$ in the melt, which are supported by results in this study. Thus, for magnetite-rich spinel we conclude that titanomagnetite-melt partitioning is controlled to a first order by the chemical equilibria associated with a changing melt composition. Notwithstanding this, the activity coefficients, both

in spinel and the melt, are expected to vary with changes in the bulk composition of the system. This could exert an additional control on spinel-melt partitioning. Nevertheless, it is difficult to determine whether such changes in partitioning in contrasting bulk compositions to those studied here reflect changes in the activity coefficients in the crystal or melt (O'Neill and Eggins, 2002).

2.4.3 Melt polymerisation

A number of previous studies have identified that the degree of melt polymerisation exerts a strong control on the partitioning of elements between crystalline phases and melts (e.g. Kohn and Schofield, 1994; Toplis and Corgne, 2002; Kushiro and Mysen, 2002; Mysen, 2007). Melt polymerisation is frequently expressed as NBO/T (the molar ratio of non-bridging oxygens to tetrahedrally co-ordinated cations) which can be calculated from the melt composition. With increasing NBO/T, D(Mg), D(Mn), D(Ni), D(Co) and D(Zn) decrease forming well-defined trends, that are an exponential function of melt NBO/T (Figure 2-12A). When supplemented by data from Toplis and Corgne (2002), Righter et al. (2006), Leeman (1974), Horn et al. (1994) and Wijbrans et al. (2015), it is clear that this trend is particularly pronounced at NBO/T < 0.30, but flattens at higher values. In highly polymerised melts D(Mn) values up to 8.3 and D(Mg) up to 6.0 are observed; in this region of melt polymerisation, small increases in the degree of polymerisation (decreases in NBO/T) are accompanied by large increases in the partition coefficients.

As has been noted previously for several crystalline phases, $D(M^{2+})$ can be described by the equation $D(M^{2+}) = C \cdot (NBO/T)^{-X}$ where X and C are constants specific to the partitioning of each metal cation (Kohn and Schofield, 1994; Toplis and Corgne, 2002). Previous work cautioned the use of this equation at values of NBO/T < 0.08, however the results of this work suggest that this equation is still valid in this compositional range. Incorporating data from this study with that of previous work (Toplis and Corgne, 2002; Toplis et al., 1994; Righter et al., 2006; and Leeman, 1974), the following relationships have been derived to predict the titanomagnetite-melt partition coefficients for Mg and Mn:

$$D(Mg) = 0.52 \times (NBO/T)^{-0.82} \qquad R^2 = 0.78$$

$$D(Mn) = 0.77 \times (NBO/T)^{-0.77} \qquad R^2 = 0.81$$

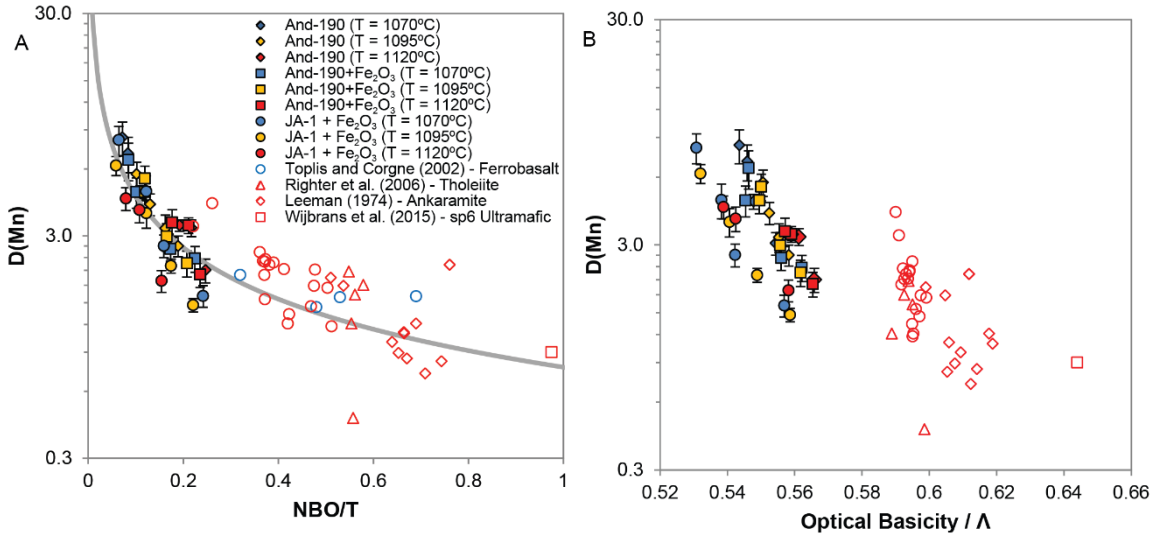


Figure 2-12: Titanomagnetite-melt partition coefficients of Mn versus (A) NBO/T (calculated as described in Toplis and Corgne, (2002)) and (B) optical basicity (Λ – calculated after Duffy, 1993). Relevant literature data are included for comparison (Toplis et al., 1994; Toplis and Corgne, 2002; Righter et al., 2006; Leeman, 1974; Horn et al., 1994; Wijbrans et al., 2015). Solid line represents fit to all data: D(Mn) = 0.77 x (NBO/T)-0.77 with an R^2 value of 0.81. Error bars = 1σ

The other divalent cations also have a similar trend in terms of NBO/T as could be inferred by the linear correlation of divalent cations with one another (Figure 2-5). It has been suggested that more polymerised melts contain fewer potential sites onto which network-modifying cations can partition (Toplis and Corgne, 2002). This could result in higher mineral-melt partition coefficients with increasing melt polymerisation for cations that act as network modifiers, notably the divalent cations. However, this does not explain why the relationship is exponential. Furthermore, there is not an adequate reason to account for the fact that the relationship with NBO/T is only observed for the divalent cations, and not the partitioning of other network modifying cations with different valence states.

The optical basicity (Λ) can be used as an alternative, and potentially superior, measure of melt structure because it distinguishes different cations with contrasting electron donor power (Duffy, 1993). Similar to plotting $D(M^{2+})$ vs. NBO/T, plotting $D(M^{2+})$ vs. Λ generates trends that are an exponential function of Λ (Figure 2-12B). This trend, however, diverges into two paths at $\Lambda < 0.56$, for the dacitic (JA-1) and andesitic (And-190) compositions investigated and does not form a single, well-defined trend as observed for NBO/T. The inability of Λ to fully describe the partitioning behaviour suggests melt polymerisation is not the dominant control on $D(M^{2+})$. Furthermore, NBO/T is a strong function of $Fe^{2+}O_{melt}$ (Figure 2-13), with a Pearson' correlation coefficient between the two variables of 0.72. Thus, the apparent correlation between the partitioning of divalent cations and NBO/T could in fact be an artefact of the change in $Fe^{2+}O_{melt}$ with increasing fO_2. For instance, with increased fO_2, there is an increase in the crystallisation of

titanomagnetite, which decreases the concentration Fe in the melt and hence of $Fe^{2+}O_{melt}$. There is also an increase in the concentration of SiO_2 in the melt with increasing NBO/T (Figure 2-13). The change in melt composition will therefore drive changes in melt structure and NBO/T which generates illusory correlations between partitioning and melt polymerisation. Although there is correlation between melt structure and partitioning, this does not imply causation. Instead, it is suggested that thermodynamic equilibria between mineral and melt and its associated changes in $a(Fe^{2+}O)$ and $a(Fe^{3+}O_{1.5})$ in the melt offers a more accurate explanation of partitioning.

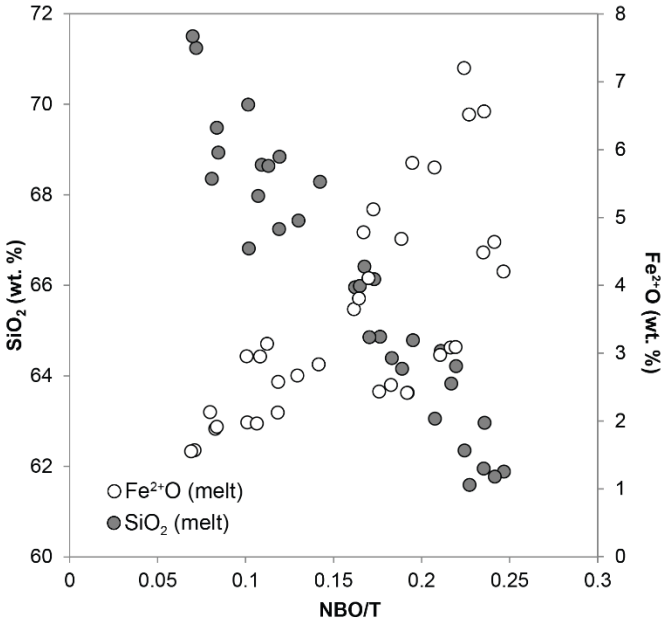


Figure 2-13: Melt $Fe^{2+}O$ (wt. %) and SiO_2 (wt. %) as a function of NBO/T (calculated as described in Toplis and Corgne, (2002). $Fe^{2+}O$ values approximated using Kress and Carmichael (1991).

2.4.4 Implications for studying natural systems

2.4.4.1 Evidence for redox sensitive partitioning of isovalent divalent cations in intermediate-silicic bulk systems

The relationship between fO_2 and melt composition has important implications for natural intermediate-silicic magmas. In silicic bulk systems, the increased crystallisation of magnetite with increasing fO_2 predominantly drives a decrease in $XFe^{2+}O_{melt}$, with only minor variation in aFe_3O_4 (Table 2-3). Consequently, the partitioning of divalent cations is indirectly sensitive to changes in fO_2, particularly between FMQ + 0.2 and FMQ + 3. The partitioning of divalent cations into other cocrystallising mafic phases, bearing a significant amount of ferrous iron, could also be indirectly sensitive to fO_2 for the same reasons. Fractionation of other phases, such as silicate phases, could also exert a control on melt composition although, because the crystallisation of magnetite occurs relatively abruptly in comparison to silicate phases and is particularly sensitive

to fO_2, magnetite crystallisation can trigger quite sudden changes in melt chemistry, particularly at high fO_2 (e.g. fO_2 > FMQ + 2).

There is evidence for a systematic increase in $D(M^{2+})$ with increasing fO_2 in natural intermediate-silicic rocks. Using the GEOROC database (Sarbas and Nohl 2008), data from titanomagnetite worldwide was filtered and sorted into categories based on host rock: basalt, andesite, dacite and rhyolite. Despite the complexity of its dependence, the partitioning of V into titanomagnetite has been shown to be a relatively good, qualitative proxy for the fO_2 ((e.g. this study; Righter et al., 2006; Toplis and Corgne, 2002). Plotting V content of magnetite as a redox proxy against divalent cations, such as Mn, indicates that at V contents less than approximately 1200 ppm, with decreasing V content, the MnO content of titanomagnetite increases in rhyolitic, dacitic and andesitic rocks. In titanomagnetite from basaltic rocks, however, there is no apparent increase in MnO content with decreasing V content. This suggests that Mn partitioning is indirectly sensitive to fO_2 as a result of the influence of fO_2 on magnetite crystallisation and its implications for $a Fe_3O_{4mgt}/XFe^{2+}O_{melt}$. It is interesting to note that the data from And-190 in this study follow a similar trend to natural titanomagnetite data from andesitic and dacitic rocks (Figure 2-14). Magnesium does not produce a trend of increasing titanomagnetite-melt partitioning with decreasing V content, but this is unsurprising given its incorporation as a major component in other crystallising phases. There is insufficient data in the GEOROC database to produce similar trends for other divalent cations at present.

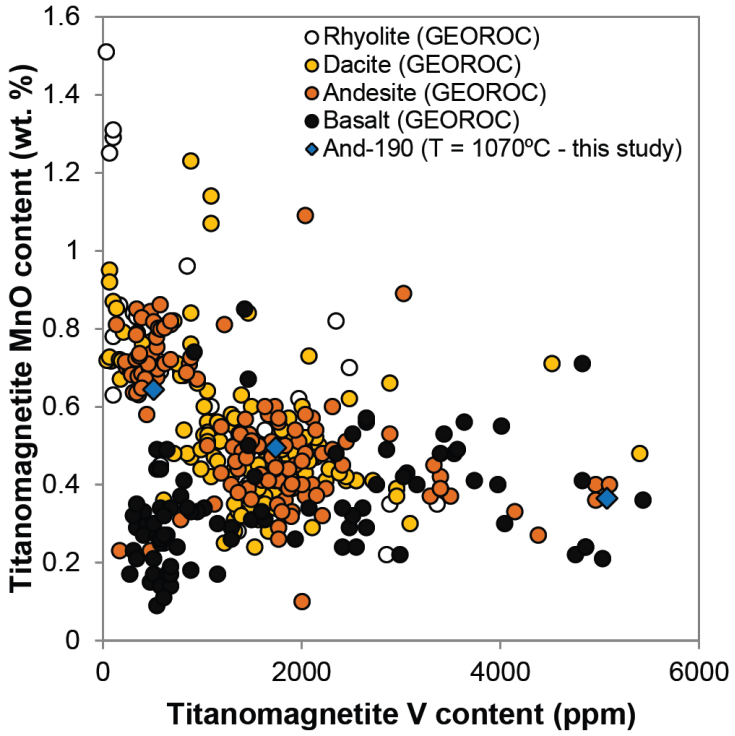


Figure 2-14: Titanomagnetite MnO vs. V contents for rhyolitic, dacitic, andesitic and basaltic rocks from GEOROC (Sarbas and Nohl 2008). Data using And-190 at 1070°C (this study) is included for comparison and mimics trend defined by andesite and dacite

2.4.4.2 Redox sensitive trace element ratios in magnetite

The relationships between fO_2 and our experimentally-determined titanomagnetite-melt partition coefficients of redox sensitive elements could be used to estimate the fO_2 of natural magmas, but only if the composition of the titanomagnetite and the melt from which it crystallised are known. Melt inclusions, hosted within a titanomagnetite grain, could be reasonably assumed to represent the melt from which the crystal grew. However, at magmatic temperatures, lattice diffusion through the host mineral has been shown to be sufficiently rapid to alter the original chemical composition of melt inclusions, including elements not compatible in the host minerals (Spandler et al., 2007; Spandler and O'Neill, 2010). In addition to this, melt inclusions are often difficult to find, or are too small to analyse using LA-ICP-MS. Collectively, this thwarts determination of the melt composition using melt inclusions.

Without an accurate means to measure the melt composition, relative redox indicators, using just the spinel composition alone, have been suggested as a means to estimate the fO_2 in natural systems (Wijbrans et al., 2015). For example, the ratio of a redox sensitive element to an element that does not change partitioning behaviour as a function of all other parameters (e.g. melt composition, crystal composition, temperature and fO_2) could be used. Furthermore, the bulk partition coefficients of the denominator element should be close to 1, so that its relative abundance is not strongly influenced by crystallisation of other mineral phases. On this basis, Wijbrans et al. (2015) suggested the use of Mo/Ga and V/Ni in spinel as possible relative redox monitors. In support of this, within the range of conditions studied here, the titanomagnetite-melt partitioning behaviours of Mo and V are redox sensitive, whereas the partitioning of Ga remains relatively insensitive to all parameters. In an intermediate-silicic bulk system, however, we have shown that the partitioning of Ni is sensitive to fO_2 and temperature. Furthermore, when including data from other studies, it is apparent that Ga is more strongly partitioned in Cr-rich spinel crystallised at higher temperature ($T > 1250°C$; e.g. Horn et al. (1994)), which negates the use of Ga in systems crystallising over a large range of compositions and temperatures. Notwithstanding this, Ga offers the best possible element for the denominator in a relative redox ratio and could be used in conjunction with redox sensitive elements such as V to qualitatively approximate the fO_2 in natural systems. In addition to V and Mo, titanomagnetite-melt partitioning of Nb and Ta is also sensitive to fO_2 whilst the concentration of Nb and Ta is relatively unaffected by fractionation of other co-crystallising phases in arc magmas; thus Nb/Ga and Ta/Ga in titanomagnetite may also be effective relative redox monitors for natural arc magmas. Nevertheless, the use of such relative redox indicator ratios is yet to be tested comprehensively in natural systems.

3 Diffusion and partition coefficients of minor and trace elements in magnetite as a function of oxygen fugacity

3.1 Introduction

Trace element concentrations in magnetite vary considerably between different deposit types (Dare et al., 2014; Nadoll et al., 2014) and can therefore be used as a tool for fingerprinting mineralisation styles and for interpreting primary conditions of crystallisation. Variations in trace element chemistry may be in part due to variation in parameters such as temperature, bulk composition, fO_2 and pressure, which dictate the equilibrium magnetite partitioning behaviour. However, partitioning of trace elements can also occur at disequilibrium. Diffusion (disequilibrium) processes can act to modify the original magnetite chemistry, particularly in igneous systems. Thus, in order to utilise magnetite as a petrogenetic tool, it is important to understand the transport properties of elements within the mineral so that the likelihood and timescales necessary for the trace element chemistry to be influenced by disequilibrium element partitioning can be assessed.

The formation of porphyry copper deposits involves an interplay of hydrothermal and magmatic processes which span a wide range of time periods. For example, the time period during interaction between a magma and hydrothermal fluid (e.g. 10^4-10^5 years for the lifetime of a hydrothermal system) will be much shorter than the crystallisation of a sub-volcanic magma chamber (typically greater than 10^6 years). In magnetite, diffusion coefficients for different elements can vary by more than 3 orders magnitude (Dieckmann et al., 1978, Dieckmann and Schmalzried, 1986; Aggarwal and Dieckmann, 2002). As a result, in igneous magnetite slower diffusing elements may provide a more robust indicator of the magmatic environment, whereas faster diffusing elements will be more susceptible to modification of the original magnetite chemistry, for example via interaction with a hydrothermal fluid.

The diffusion properties of some cations (Fe, Co, Cr, Al and Ni) in magnetite have been studied over a range physical conditions (Dieckmann et al., 1978; Dieckmann and Schmalzried, 1986; Aggarwal and Dieckmann, 2002). However, the diffusion properties for the lesser compatible trace elements are not well known. Consequently, the diffusion coefficients for >21 elements were investigated in natural magnetite as a function of oxygen fugacity (FMQ - 1 ≤ fO_2 ≤ FMQ + 4.89) at 1150°C and 1 bar, by equilibration with a synthetic silicate melt reservoir. In conjunction with presentation of diffusion coefficients, partition coefficients can also be calculated from the

concentration at the magnetite-melt interface and liquid concentration. Notably, transport properties for a number of elements in magnetite are presented, which until now have remained unexplored.

3.1.1 Cation diffusion in magnetite

Magnetite is a common mineral in igneous and metamorphic rocks, and has been studied extensively with regard to diffusion in relation to oxygen isotope thermometry. A large volume of early work investigated diffusion in magnetite, focusing on oxidation kinetics. In contrast to spinel, magnetite has a less ordered structure. At low temperature, magnetite has an inverse spinel structure, which allows both Fe^{2+} and Fe^{3+} to occupy the octahedral sites in equal proportions, and with Fe^{3+} being the sole component of the tetrahedral sites; at high temperature, the inverse spinel structure can be modified a little, shifting some Fe^{2+} onto the tetrahedral site, in essence moving the structure towards $[A_{1/3}B_{2/3}][A_{2/3}B_{4/3}]O_4$.

Magnetite is stable between the iron-magnetite and hematite-magnetite oxygen buffers. Although simple in terms of its structure and chemistry, the diffusion behaviour of magnetite is rather complex due to internal redox reactions. Under most conditions, magnetite has a slight cation defect ($\delta < 0.002$ in the formula $Fe_{3-\delta}O_4$), accommodated by vacancies on the normally occupied octahedral and/or tetrahedral cation sites. However, at low oxygen fugacities, where magnetite is at or near equilibrium with wustite, magnetite has a slight excess of cations at interstitial defects. As a result, an interstitial diffusion mechanism predominates at low oxygen fugacities, whereas a vacancy diffusion mechanism prevails under more oxidising conditions (Van Orman and Crispin, 2010).

Diffusion of iron has been studied using ^{59}Fe as a tracer (Himmel et al., 1953; Schmalzried, 1962; Dieckmann and Schmalzried, 1977). Iron diffusion has been shown to exhibit a concave-upwards trend with increasing fO_2, with a minimum at intermediate fO_2, as a consequence of a transition between interstitial- and vacancy-dominated mechanisms (Dieckmann and Schmalzried, 1977). At low fO_2, where the interstitial mechanism is dominant, the abundance of iron interstitials decreases with increasing fO_2, leading to a decrease in diffusivity of iron by an interstitial mechanism. Concomitantly, with increasing fO_2, vacancies form on the cation sublattices and, under sufficiently oxidising conditions, diffusion by a vacancy mechanism becomes predominant. After this point, the diffusivity of iron increases with increasing fO_2.

The dependence of point defect concentrations on fO_2 provides a convenient explanation for the diffusion mechanisms. The formation of cation vacancies (on octahedral and/or tetrahedral sites) by the addition of oxygen can be described by:

$$3Fe^{2+} + 2/3\ O_2 \leftrightarrow 2Fe^{3+} + V_{Fe} + 1/3Fe_3O_4 \qquad (3\text{-}1)$$

However, the abundance of cation vacancies is related to the formation of Fe^{2+} or Fe^{3+} interstitials by:

$$Fe^{n+} + V_I \leftrightarrow Fe_I^{n+} + V_{Fe} \qquad (3\text{-}2)$$

where V_{Fe} represents a vacant cation site, and V_I represents a vacant interstitial site (Dieckmann, 1998). Consequently, the addition of 2/3 of a mole of oxygen creates one mole of cation vacancies, but removes one mole of Fe^{2+} or Fe^{3+} interstitials. This offers an explanation for the dependence of iron diffusivity on fO_2, with diffusion rate increasing or decreasing with a slope of 2/3 or -2/3 respectively, around a minimum turning point where diffusion via interstitial and vacancy mechanisms is equally preferable.

Based on mass action, reaction 3-1 can yield the following by relating it to an equilibrium constant:

$$[V_{Fe}] = K_v([Fe^{2+}]^3/[Fe^{3+}]^2)(a_{O2}^{2/3}/\ a_{Fe3O4}^{1/3}) \qquad 3\text{-}3$$

In pure magnetite $a(Fe_3O_4) = 1$, and $[Fe^{2+}] = 1$ when $[Fe^{3+}]$ is 2, so, at conditions close to the stability of hematite, the expression can be simplified to:

$$[V_{Fe}] = (K_v/4) * a_{O2}^{2/3} \qquad 3\text{-}4$$

A similar expression can be written for iron interstitials based on mass action laws:

$$[Fe_I^{n+}] = 4\ K_I * a_{O2}^{-2/3} \qquad 3\text{-}5$$

Within this simple point defect framework described above, the diffusion coefficient for iron can be expressed as a sum of the diffusivities by interstitial and vacancy mechanisms. Dieckmann and Schmalzried (1977) used the following equation:

$$D_{Fe} = D_V \exp\left(\frac{-H_V}{RT}\right) a_{O_2}{}^{2/3} + D_I \exp\left(\frac{-H_I}{RT}\right) a_{O_2}{}^{-2/3} \qquad 3\text{-}6$$

D_{Fe} will reach a minimum for a given temperature, where the vacancy part of the expression is equal to the interstitial part. This expression also explains the temperature dependence of iron diffusion. The activation enthalpies for iron diffusion by vacancy and interstitial mechanism of

vacancies are -140 kJ/mol and 613 kJ/mol respectively. As temperature increases, diffusivity by the vacancy mechanism increases because the formation enthalpy is strongly negative, and has a larger value than the positive migration enthalpy. Thus, with increasing temperature, the concentration of cation vacancies decreases enough to inhibit diffusion by a vacancy mechanism, despite the fact that each vacancy is more mobile at higher temperature. For interstitials, however, both the formation and migration enthalpies are strongly positive. Therefore, both the concentration and mobility of interstitials increases with temperature, and diffusion by the interstitial mechanism therefore increases steeply with increasing temperature (Figure 3-1).

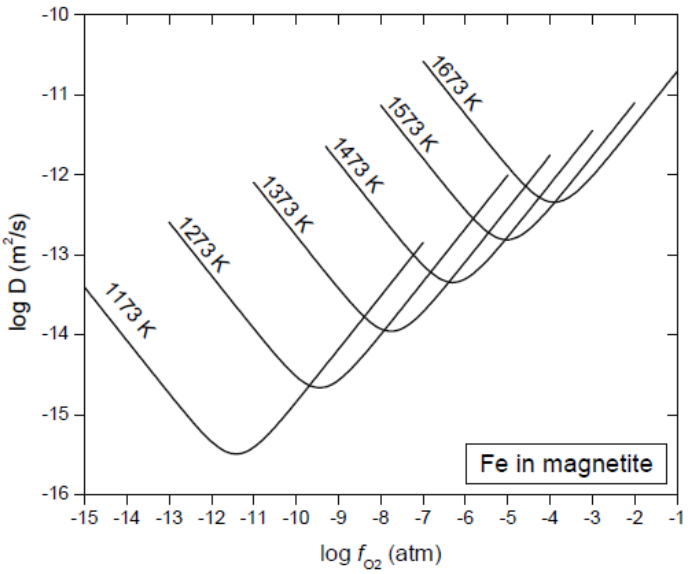


Figure 3-1: Variation of Fe diffusion coefficient in magnetite with fO_2, at different temperatures. Iron diffuses by a mechanism involving interstitials under reducing conditions, and by a vacancy mechanism under relatively oxidising conditions. Diffusion by interstitials is favoured at elevated T at a given fO_2 (From Van Orman and Crispin, 2010; data from Dieckmann and Schmalzried, 1977).

The rates of diffusion of iron and other cations by a vacancy mechanism depends on the concentration and diffusivity of cation vacancies. Based on a detailed study with Mossbauer spectra in magnetite at different temperatures and fO_2, Becker (1990) inferred that vacancy diffusion in magnetite involves the octahedral cation sublattice almost exclusively.

Diffusion coefficients for some other cations (Co, Mn, Cr, Al, Ni and Ti) have been investigated using radioactive isotopes (Dieckmann et al., 1978; Dieckmann and Schmalzried, 1986; Aggarwal and Dieckmann, 2002). All these cations behave similarly to Fe in their response to fO_2. The diffusivities of Co and Mn have been reported to be similar to Fe under all conditions, whereas those of Ti^{4+}, Al^{3+}, and Cr^{3+} are slower. Nickel, however, has been shown to diffuse faster under reducing conditions than Fe, Mn and Co, where the interstitial mechanism dominates, and is significantly slower than Fe, Mn and Co under oxidising conditions where a vacancy mechanism dominates (Figure 3-2)

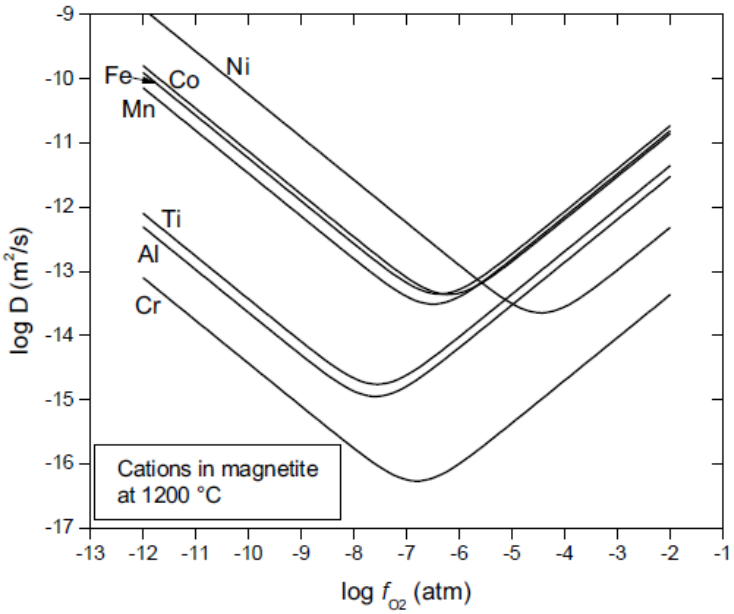


Figure 3-2: Variation of cation diffusion coefficients with fO_2 in magnetite for Fe, Co, Cr, Al and Ni at 1200°C (from Van Orman and Crispin, 2010; data from Dieckmann et al., 1978; Dieckmann and Schmalzried, 1986; Aggarwal and Dieckmann, 2002).

3.1.2 Experimental techniques for studying diffusion in minerals

Diffusion in minerals has been investigated using a variety of experimental techniques. To date, most work studying diffusion in magnetite has used radioactive tracers - such as Fe-59, Ti-44 and Co-60 - dropped in the form of aqueous solutions onto a polished disk of magnetite (e.g. Aggarwal and Dieckmann, 2002; Lu and Dieckmann, 1992). To determine tracer diffusion coefficients, the residual activity method is employed. Each of the radioactive tracers used emits γ-rays with specific energies which can be measured using a high-efficiency Ge detector. The initial activity is measured and compared with activities in subsequent slices of the material, sliced using diamod tools. Values for diffusion coefficient of the tracer species can be obtained using an equation which includes residual activity, activity at a specific distance from the interface, distance from the interface and time. Interdiffusion between titanomagnetite and magnetite has also been studied by solid-solid diffusion between single crystals of magnetite and a pressed pellet of powdered titanomagnetite, butt-jointed together and fired (e.g. Freer and Hauptman, 1978). Diffusion into each medium can be measured using EPMA, however, in order to analyse diffusion in the powdered medium, it must sinter during the experiment, which requires the experiments to be conducted at relatively high temperatures (e.g. > 800°C) (Freer and Hauptman, 1978).

A large volume of diffusion studies in silicate minerals has been obtained using Rutherford backscattering spectroscopy (RBS) (e.g. Cherniak and Watson, 1994; Cherniak et al., 2007). Samples are typically sectioned and polished, then ultrasonically cleaned to remove residual grit. The samples are then placed in Pt capsules surrounded by a mixture of oxide powders which provides a source of the diffusant of interest. The capsule can then be annealed at the specified

conditions. RBS is based on the measurement of energies of light ions, elastically scattered from atoms in the target material when exposed to an energetic beam, such as a beam of He ions. The spectra detected can be converted to a concentration profile with a computer code. The depth scale is determined by calculating the rate of energy loss for the ions travelling through the material before and after the scattering effects. Depth resolution is about 10 nm in the near-surface region, but degrades to approximately 50 nm by 1 μm depth in the sample. It is essential that all the diffusion-source material is completely removed from the mineral prior to RBS analysis because RBS can only investigate the outermost few microns of the sample. The presence of surface material can therfore dramatically degrade resolution, or at worst completely obscure the profile.

The novel experimental approach applied here, pioneered by Spandler and O'Neill (2010), consists of inserting a silicate melt inside a crucible made from a single crystal of magnetite, to form a diffusion couple between melt and magnetite. The magnetite crystals used have a restricted compositional range which is close to pure magnetite, as shown by the characterisation of multiple crystals by EPMA and LA-ICP-MS (see section 3.3.1). The composition of the silicate melt is designed to have a major-element composition in equilibrium with the magnetite under the experimental run conditions to ensure no nucleation or resorption of magnetite at the magnetite-melt interface occurs (see section 3.2.1.1). The melts were doped with > 21 trace elements, generating diffusion profiles in magnetite which can be measured using scanning LA-ICP-MS.

The experimental method applied here has a number of advantages over those previously employed to study diffusion in minerals. Firstly, the technique ensures a continuous diffusion couple since the melt completely wets the mineral surface, unlike methods involving solid-solid diffusion. Moreover, in comparison to methods using radioactive tracers, a considerably larger range of elements can be studied using LA-ICP-MS, since the analytical method is not limited to studying certain elements with radioactive isotopes. In comparison to techniques emplying RBS, it is possible to study significantly larger profiles using LA-ICP-MS. Furthermore, unlike RBS, no conversion factors are required to calculate the depth in the profile. Another benefit of the magnetite 'bucket' method is that in addition to measuring diffusion coefficients, equilibrium partition coefficients can also be obtained using the measured interface and liquid element concentrations. Despite its advantages, there are also some drawbacks of the experimental technique employed here. For example, the use of LA-ICP-MS to study diffusion necessitates the diffusion profiles to be large (> 10 micron). Nevertheless, this is not a problem for the study of diffusion in magnetite where diffusion is several orders of magnitude faster than in most common

silicates (see section 7.1.3.2). The method applied here is also limited to the study of magmatic temperatures which are necessary in order for the silicate mix to melt.

3.2 Experimental procedures

3.2.1 Experimental technique

A synthetic CaO-FeO-SiO_2 (CFS) melt was designed to have a major element composition which was in equilibrium with a natural magnetite (Mt-1) at the specified experimental run conditions. Other major elements, such as Al, Mg and Ti were chosen to be eliminated as major components in the melt because partitioning of such elements could alter the major element chemistry of magnetite, and therefore its structure and diffusion properties. The CFS melt was doped with Al, Co, Cr, Cu, Ge, Hf, In, Mg, Mn, Mo, Nb, Ni, Th, Ti, Sc, Sr, Ta, U, V, W, Y, Zn, Zr, Lu, Y in all experiments and Li for experiments at FMQ – 1, FMQ and FMQ + 4.89 and Ga in experiments at FMQ - 1) at concentrations of 200 ppm in order to produce measurable diffusion profiles in the magnetite.

3.2.1.1 Synthesis of trace-element doped melt

First, a primary CFS mix was prepared with FeO = 25% wt. %, CaO = 15 wt. % and SiO_2 = 60% from a mixture of synthetic oxides (SiO_2 and Fe_2O_3) and carbonates ($CaCO_3$). Oxides and carbonates were stored in a clean drying cabinet prior to mixing. Reagents were weighed on an electronic balance in their appropriate proportions and homogenized by grinding in an agate mortar with acetone for 30 minutes. The mixture was decarbonated at 600-1000°C for 5 h.

For each fO_2 studied, starting compositions were prepared which were designed to be sufficiently close to equilibrium with magnetite that there should be minimal dissolution/precipitation during the experiment. To do so, a small amount of the primary CFS mix was combined with finely ground magnetite and run at 1150°C and the specified fO_2 conditions for 12 hours, and then quenched into distilled water. The composition of the glass in equilibrium with the magnetite was analysed via EDS analysis. Separate starting compositions for each fO_2 conditions were then prepared from dried oxides and carbonates, and decarbonated as done for the primary starting material. Trace elements were added to each separate starting composition as inductively coupled plasma (ICP) standard solutions using a pipette in proportions necessary to dope the starting material at approximately 200 ppm for all trace elements. Each mixture was dried under a heat lamp, homogenized in an agate mortar, and denitrified at 500°C for 2 h.

3.2.1.2 Preparing magnetite crucibles

Euhedral magnetite crystals measuring more than 6 mm length and 6 mm in diameter were selected. SEM back-scattered electron (BSE) images confirmed that the magnetite crystals were

inclusion free and their compositions were checked via LA-ICP-MS. The crystals were mounted in epoxy resin and then carefully drilled with a diamond drill bit to produce a cylindrical cavity 1.25-2.5 mm in diameter and 3-4 mm long. The epoxy was then carefully removed with pliers by softening in an oven at 120°C, and each magnetite crucible was finally cleaned with ethanol and distilled water in an ultrasonic bath.

Each magnetite bucket was filled with the appropriate powdered starting material and hung by platinum wire in a 1-atm gas mixing furnace, with fO_2 conditions set to those required using a flowing CO_2/CO mixture. The magnetite was loaded into the furnace at 600°C, then the temperature was ramped at 200°C/h to 1150°C and left to anneal for the required duration of the experiment. Finally, the run product was mechanically drop quenched into distilled water, dried, mounted into epoxy and polished perpendicular to the cylindrical cavity for analysis.

3.2.2 Analytical technique

3.2.2.1 EPMA

A Cameca SX-100 electron microprobe, also at the Natural History Museum, London, was used to measure major element contents of the silicate glass. Calcium, Si and Fe were analysed. A 20 kV accelerating voltage, 2 nA sample current and a defocused (10-20 μm) beam was applied in order to minimise migration of alkalis.

3.2.2.2 LA-ICP-MS

Trace-element compositions of magnetite and glass were analysed using LA-ICP-MS at the Research School of Earth Sciences (RSES) at the Australian National University (ANU) and at the LODE Research Facility at the Natural History Museum, London. The LA-ICP-MS at ANU consists of an Agilent 7700x quadrupole ICP-MS coupled to a Resonetics 193nm excimer laser with a custom-built ablation chamber. At the LODE Research Facility, a New Wave Research 193nm excimer laser coupled is coupled to an Agilent 7700x quadrupole ICP-MS. Laser energy was regulated to provide a laser fluence at the sample site of 3.5J cm^{-2} (ANU)/3.2J cm^{-2} (LODE). The ICP-MS was tuned prior to analyses to ensure low backgrounds and low oxide production levels.

Rectangular ablation shapes can be used to improve the resolution of an element concentration profile to that obtained using conventional circular ablation shapes. Thus, for traverses, the laser was focused into a 100 x 6 micron rectangular beam oriented parallel to the magnetite/glass interface. After background counting for 30 s, the laser was switched on and the sample traversed continuously beneath the laser at a rate of 1 micron/second. All traverses were started in the interior of the magnetite crystal and ended by ablating clean glass; this avoided analyses of

previously ablated glass that could have been deposited at the magnetite-glass interface. The traverses were positioned as far from cracks as possible. Glass was analysed with a 50 micron laser spot size. Fe and Ca were used as an internal standard for the magnetite and glass analyses respectively, measured previously via EDS. BCR-2g was used as an external standard for magnetite analyses (other than Ge and In, for which GSD-1g was used) and NIST 610 for glass analyses. GSD-1g and GSE-1g were also measured for monitoring. All reference materials were analysed in the same fashion as the sample analysed. The isotopes analysed were ^{24}Mg, ^{27}Al, ^{29}Si, ^{31}P, ^{43}Ca, ^{45}Sc, ^{49}Ti, ^{51}V, ^{52}Cr, ^{55}Mn, ^{57}Fe, ^{59}Co, ^{60}Ni, ^{63}Cu, ^{65}Cu, ^{66}Zn, ^{69}Ga, ^{72}Ge, ^{75}As, ^{89}Y, ^{90}Zr, ^{92}Zr, ^{93}Nb, ^{95}Mo, ^{115}In, ^{175}Lu, ^{177}Hf, ^{181}Ta, ^{182}W, ^{208}Pb, ^{232}Th and ^{238}U. For the majority of analyses, Lu, Y and Th were measured using a 0.3 second dwell time on each element; the other elements had 0.1 second dwell times. Some slow diffusing elements (Sc, Ti, V, Ge, Zr, Nb, Hf, Ta) were also measured separately, thereby reducing the ICP-MS sweep time to 0.7 seconds which increased analytical precision. For most traverses, the sweep time for the ICP-MS was 2.0 seconds. Data generated at RSES-ANU were reduced using IOLITE software and data collected at the LODE Research facility were processed using in-house software, both in a 'natural' fashion, such that each individual ablation slice was processed individually. Results from the two LA-ICP-MS labs were consistent with one another (Appendix 3).

3.2.3 Experimental conditions

All experiments were conducted at 1 bar, 1150°C and FMQ - 1 ≤ fO_2 ≤ FMQ + 4.89. Twelve hours was sufficient time to generate diffusion profiles greater than 30 microns for most elements studied, which are sufficiently long to interpret reliable interface concentrations, initial concentrations and diffusion constants for the different elements. However, two experiments were run at longer durations (up to 7 days) in order to check for consistency with the 12 hour experiments (Table 3-1).

Table 3-1: Experimental conditions.

Experiment	T	fO_2 (ΔFMQ[a])	t (h)[b]
MB-3	1150°C	FMQ + 2.0	12.0
MB-2	1150°C	FMQ + 2.0	161.0
MB-9	1150°C	FMQ + 2.0	72.0
MB-7	1150°C	FMQ + 1.0	12.4
MB-14	1150°C	FMQ + 3.0	12.1
MB-21	1150°C	FMQ + 0.0	12.0
MB-23	1150°C	FMQ + 4.9	12.0
MB-24	1150°C	FMQ – 1.0	12.3

[a]ΔFMQ = log fO_2 (experiment) – log fO_2 (FMQ buffer); values were calculated using Hemingway (1990). [c]Time represents dwell time in hours after ramp up to final temperature.

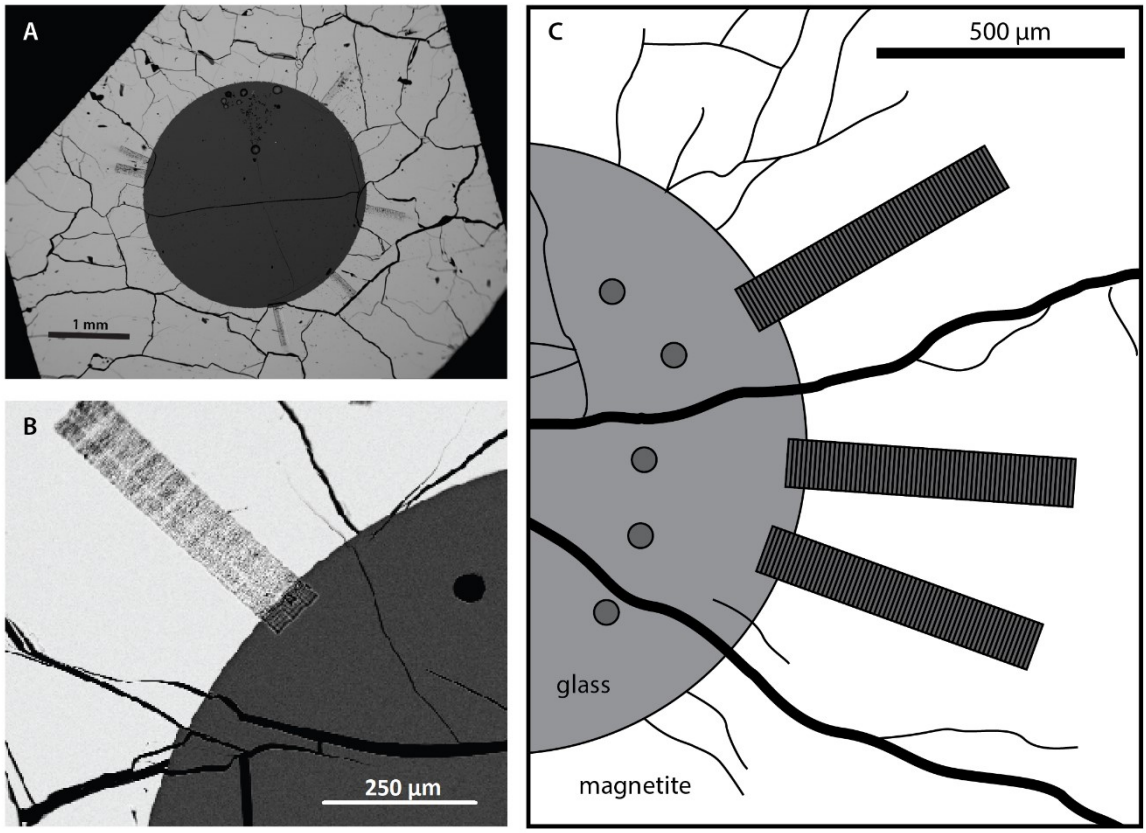


Figure 3-3: Geometry of experimental product and analytical procedure. (A) and (B) SEM Back-scattered electron images of magnetite crystal containing quenched glass post-analysis with LA-ICP-MS showing laser traverse profiles. (C) Cartoon of the magnetite-glass interface region showing laser-ablation profiles through magnetite and glass and laser ablation pits in glass.

3.2.4 Calculation of diffusion and partition coefficients

Diffusion is assumed to be comparable to that of one-dimensional diffusion into a semi-infinite medium with constant concentration boundary condition maintained at the magnetite-melt interface. This condition requires element diffusion in the melt to be instantaneous with respect to element diffusion in magnetite, which is deemed reasonable on account of very fast element diffusivities in silicate melts at high temperatures (Spandler and O'Neill, 2010). The solution to the diffusion equation under these conditions is (Crank, 1975):

$$\frac{c_i - c(x)}{c_i - c_0} = \mathrm{erf}\left(\frac{x}{2(D_M t)^{\frac{1}{2}}}\right) \qquad 3\text{-}7$$

Where D_M is the chemical diffusion coefficient (NB: D is denoted as diffusion coefficient and not partition coefficient for this chapter only), c(x) the concentration at distance x into the magnetite, c_i the concentration at the interface (x = 0), c_0 the initial concentration in magnetite and t is the duration of the experiment. This equation applies to element diffusion both into and out of the magnetite.

In order to obtain precise values of D_M, it is beneficial to produce profiles where there is a relatively large difference between c_o and c_i. Although this was ensured for most elements, some elements, e.g. Mg and Al, were doped at concentrations which were insufficient to alter the concentration of the magnetite. Similarly, particularly incompatible elements (e.g. Sr and Th) were not doped at sufficient concentrations to raise c_i above the limit of detection in most experiments.

Diffusion profiles across the inner edges of the magnetite crucibles into the glass evaluated by plotting element concentration versus distance. The position of the interface in each profile was determined by visual inspection of the ablated profile with an optical microscope, and from the abrupt change in concentrations of most elements in the profiles (Figure 3-4). It is worth noting that given the width of the rectangular laser beam (6 μm), the interface position could be inaccurate by up to 3 μm. The abrupt change in concentrations of most elements at the interface did vary for some analytical traverses by up to 5 microns, corresponding to 5 s of continuous analysis. More incompatible elements generally experienced an abrupt increase earlier than more compatible elements, probably indicating that this was due to incorporation of some glass in the analysis prior to reaching the magnetite-glass interface. In such cases, the last few microns of the profile was excluded, and this part of the profile at the edge of the magnetite was extrapolated to the interface using the remainder of the diffusion profile.

The data were fitted directly to the diffusion equation using the known values, c(x), x and t, and solving for c_i, c_o and D_M by using weighted multiple non-linear least squares. The accuracy of each fit was checked graphically comparing the calculated and measured diffusion profiles. Only diffusion profiles described well by the diffusion equation are included in this study. If a poor fit was found, which could occur for example if the profile was not taken close enough to being perpendicular to the interface, or if the profile was distorted by element diffusion from melt in a crack, the profile was rejected. Examples of the fits are given in Figure 3-4.

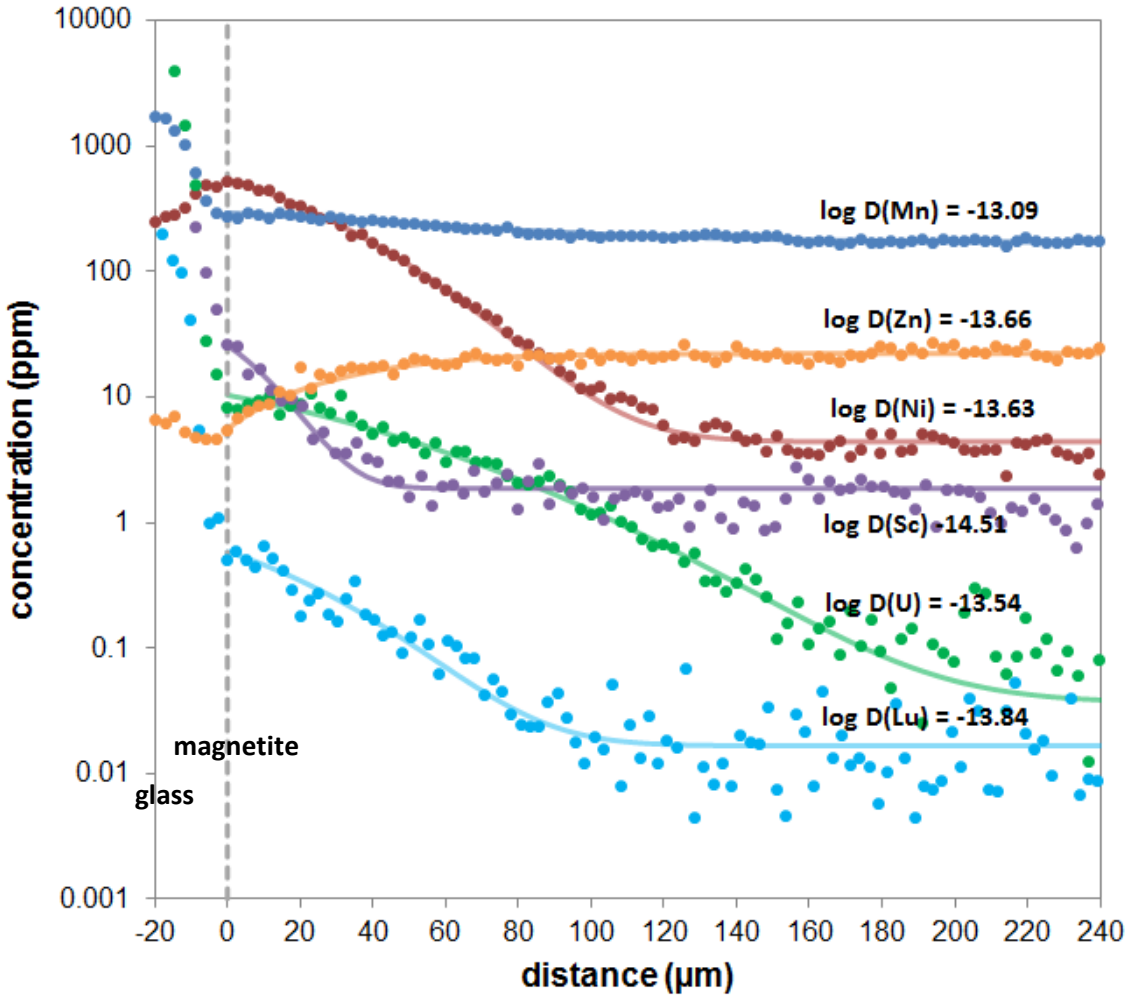


Figure 3-4: Representative diffusion profiles for Mn, Zn, Ni, Sc, U and Lu collected with LA-ICP-MS for experiment MB-7 at fO_2 = FMQ + 1, t = 12 hours. Solid curves represent the best fits to the data according to the diffusion equation. Dashed vertical line at 0 µm is the magnetite-glass interface.

C_i, c_o and D_M, were obtained separately for each element in each diffusion profile. Consistent values of D_M, c_i and c_0 for each element in each experiment provided a means to check the quality of the data. The standard deviation of multiple values was used to estimate the error associated with the values obtained. As an additional means of verification of the values of c_o, analyses using LA-ICP-MS with a 100 micron spot were conducted at the outside of the magnetite bucket and distal from the melt, in regions not influenced by element diffusion from the melt for most elements. Even with a 100 micron laser spot, a number of elements were not above the limit of detection. For these elements, the c_o was approximated as 0 ppm when solving for c_i and D_M.

Values of the magnetite/melt partition coefficients (K_M) can be calculated from $K_M = c_i/c_{liq}$, where c_{liq} is the concentration in the liquid, and c_i is the interface concentration (NB: Partition coefficient is denoted as K for this chapter only). The uncertainty in K_M for each element in each experiment was propagated from the standard deviations of multiple c_i and c_{liq} determinations. For some

analytical traverses, it was not possible to extract a viable diffusion profile whilst still being possible to interpret c_i. For example, in some analytical traverses pre-existing exsolution in the magnetite interrupted the diffusion profile meaning that it was not possible to accurately fit a diffusion profile and calculate D. However, it was still usually possible to interpret c_i, and thus calculate K_M.

3.3 Results

3.3.1 Mt-1 composition

Multiple analyses of several Mt-1 crystals prior to experiments indicate a relatively uniform major and trace element composition (Table 3-2). However, some minor exsolution for elements such as Mg and Ti, meant it was sometimes difficult to measure clean diffusion profiles for these elements. Most trace element contents are very low. Only Mg, Al, Si, P Sc, Ti, V, Cr, Mn, Co, Ni, Zn, Ga, Ge, and Mo were above the limit of detection with LA-ICP-MS using a 100 micron spot and GSD-1g as the external standard. The total trace element content of all elements detectable with LA-ICP-MS is generally less than 1000 ppm so that bulk magnetite diffusion mechanisms should apply.

Annealed magnetite crystals have trace element contents which, for all elements apart from Cu, Li and Si are in agreement with the initial composition of Mt-1 in the outer edge of the crucibles in regions unaffected by element diffusion. Furthermore, in all experiments, c_o values refined from least squared regressions are similar to the concentrations measured in the original magnetite for elements which are above the limit of detection. Values of c_i, c_0 and log D determined using LA-ICP-MS data generated at RSES and LODE were consistent for all elements analysed.

Table 3-2: Composition of magnetite crystal (Mt-1) composition prior to annealing which was used in experiments. Mean concentration of analyses of 4 separate crystals and 10 LA-ICP-MS analyses per crystal (Appendix 3).

Element	Mean Concentration (ppm)*	Element	Mean Concentration (ppm)*
Mg	260(71)	Ge	0.7(3)
Al	230(57)	Y	< dl
Si	230(38)	Zr	< dl
Ca	< dl	Nb	< dl
Sc	0.9(3)	In	< dl
Ti	230(56)	Hf	< dl
V	40(17)	Ta	< dl
Cr	10(7)	W	< dl
Mn	100(20)	Th	< dl
Co	2.0(3)	U	< dl
Ni	3.9(7)	Mo	0.02(1)
Cu	< dl	Ga	2.3(5)
Zn	26(3)	Li	0.91(3)

**Errors = 1 s.d. of 40 analysis (10 on each separate magnetite crystal*

3.3.2 Glass composition

The starting glass and final glass post-experiment are very similar in composition. For 12 hour experiments, the final glass varies from the initial composition by < 1.5 wt % for Ca, Fe and Si. This is important because it indicates that the composition of the melt remained relatively constant for the duration of experiments. Some experiments have rare crystals of magnetite and quartz nucleated within sections of the melt, the abundance of which increases with experiment duration. This resulted in a progressive decrease in FeO and SiO_2 concentrations, and concomitant increase in CaO concentrations in comparison to the starting composition with increasing experiment duration.

With increasing fO_2, there is a strong change in the major element chemistry of the melt which is in equilibrium with the magnetite. Between FMQ – 1 < fO_2 < FMQ + 4.89, the FeO content decreases from 61.95 wt. % to 27.91 wt. %, the CaO content increases from 7.09 wt. % to 22.90 wt. %, and the SiO_2 content increases from 30.95 wt. % to 49.19 wt. %.

Table 3-3: Starting composition and final glass compositions for experiments at fO_2 = FMQ + 2 and T = 1150°C. SiO_2, CaO and FeO were measured using EPMA. All data is given moderating total to 100%. Errors = 1σ is given in wt. %

	Starting mix	*Glass @ 12h*	*Glass @ 72h*	*Glass @ 161h*
SiO_2 (wt. %)	47.6	47.1(2)	46.3(1)	48.4(2)
CaO (wt. %)	18.6	18.0(1)	20.8(1)	23.7(2)
FeO (wt. %)	33.5	34.9(2)	32.9(1)	27.8(3)

3.3.2.1 Bulk loss of trace elements

Several elements could be susceptible to bulk loss during experiments due to their volatility. Bulk loss of trace elements could present problems when determining diffusion coefficients by distorting diffusion profiles as a result of decreasing c_i as the experiment progresses. Loss of trace elements from the melt could also impact the measured partition coefficients. Nevertheless, the interface concentration, used to calculate the partition coefficients here, is likely to rapidly re-equilibrate in response to changes in melt concentration, so would not be expected to have a significant effect on the reliability of the partition coefficients measured.

A number of elements, such as Sn, Cd, As, Sb and Pb, were deliberately omitted from the starting melt composition given their strong volatile behaviour. Some trace elements, however, which were added to the starting silicate material, are suggested to have been lost during the experiments. For example, although added at an initial concentrations > 200 ppm, the concentrations of Zn, Ge and In in the final glass were < 1.4 ppm, < 2.3 ppm, < 8.8 ppm respectively at fO_2 = FMQ - 1, and exhibited increasing loss with decreasing fO_2 and with increasing duration of the experiment. This is interpreted to be a result of volatile loss. For the case of In, it was clear that In was volatile at low fO_2 from the deviation in the fit of the diffusion profiles to equation 3-7. This effect was only apparent in experiments with low fO_2 ($fO_2 \leq$ FMQ + 1).

Copper concentrations in the glass are significantly lower than expected. This is not likely to be due to bulk loss of Cu to the Pt wire since only the outside of the magnetite crucible was in contact with the wire during experimental runs. It could be that Cu also underwent volatile loss during experiments. It is also possible that particularly fast diffusion for Cu meant a large amount of Cu was removed from the melt to the magnetite crucible during experimental runs; this interpretation is supported by the outside of the magnetite crucibles, in regions furthest from the melt reservoir, containing Cu contents above the average concentration of Mt-1. Chromium, V and Ni contents in the glass were also significantly less than 200 ppm. However, this is a result of loss to the magnetite crucible due to particularly high K values for these elements at some fO_2 conditions. Molybdenum and W could also be expected to undergo volatile loss during experiments, although their concentration remained well above 200 ppm in all experiments, indicating that any volatile loss of these elements was negligible.

For those elements interpreted to have undergone bulk loss during experiments, or exhibit volatile behaviour at certain fO_2 conditions, (e.g. Zn, Ge, Cu, In) the diffusion and partition coefficients derived from these experiments should be viewed with caution.

3.3.3 Partition coefficients

The results for c_i, c_{liq} and K_M are listed in Table 3-4. At least 3 values were measured for each element in each experiment, and the mean value of these was used to calculate K. In the realm of Henry's law, partition coefficients will be independent of the concentration of the trace element. It has been suggested that Henry's law will be satisfied as long as the concentrations in the crystal are less than 1 wt. % (Prowatke and Klemme, 2006), which is the case for the interface concentration of all trace elements in the magnetite crystals studied here.

Partition coefficients are in excellent agreement with literature data determined under similar conditions (FMQ + 2 and 1220°C; Wijbrans et al., 2015). Nevertheless, differences should be expected considering the different magnetite composition and temperature.

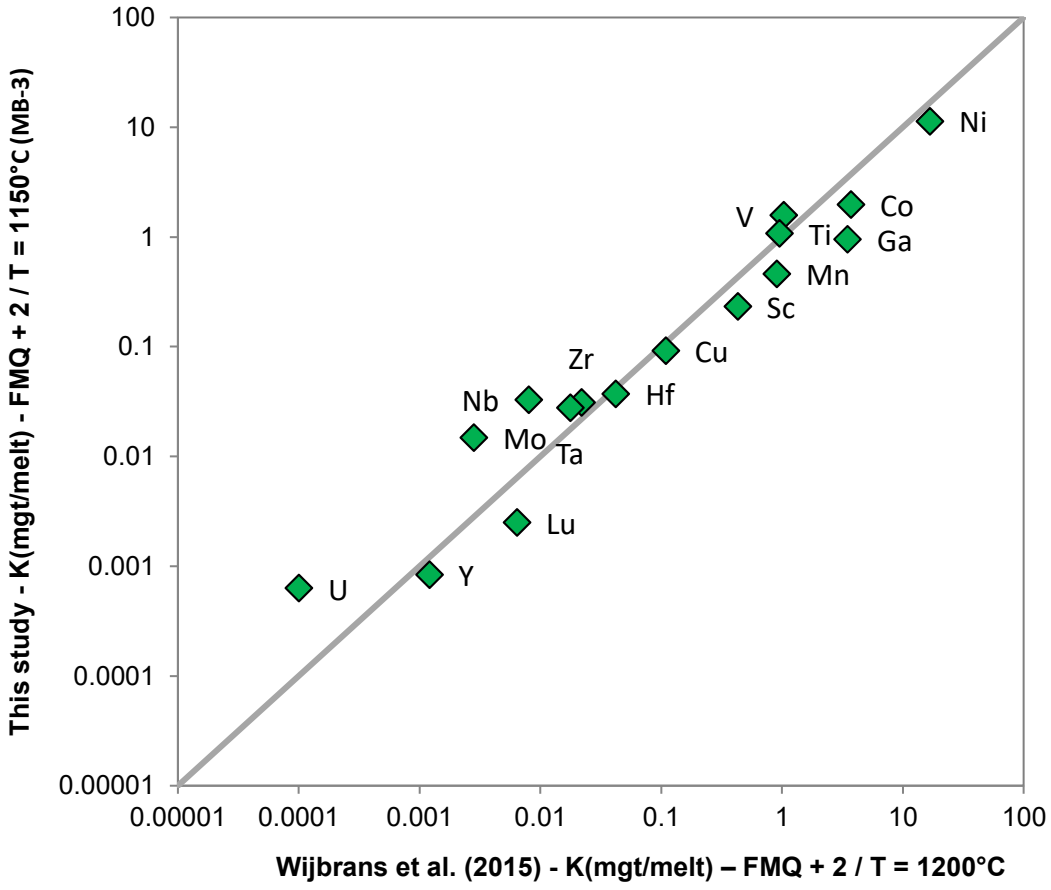


Figure 3-5: Data show relatively good consistency with partition coefficients recently reported by Wijbrans et al. (2015) at FMQ + 2 and 1220°C using sp6 starting material. Note, Wijbrans et al. (2015) studied spinel with a 54% magnetite, compared to 100% magnetite in this study. Grey line is 1:1

*Table 3-4: Calculated diffusion coefficients (D), concentration at the interface (c_i), initial concentration (c_0), measured concentration in glass, and partition coefficient (K) for all experiments. * is those C_0 which were set as original Mt-1 concentration.*

Experiment	**MB-3**	Element	log D (m^2/s)	n	C(i) (ppm)	n	C(O) (ppm)	n	C(melt) (ppm)	n	K(mgt/melt)
Furnace	**D**	Mg	-	0	330(26)	4	-	0	1,010(35)	15	0.33(3)
Internal Fe	**72.4**	Al	-	0	320(25)	3	-	0	980(18)	15	0.33(3)
***f*O$_2$**	**FMQ + 2**	Si	-	0	1,100(111)	3	-	0	292,000(1,506)	15	0.0039(4)
t (h)	**11.99**	Ca	-	0	70(30)	3	-	0	125,100(491)	15	0.0006(2)
T (°C)	**1150**	Sc	-14.23(8)	13	60(12)	13	2.9(4)	13	243(2)	15	0.23(5)
Line size	**100x6**	Ti	-14.7(1)	10	580(65)	10	160(38)	9	536(5)	15	1.1(1)
SM	**FMQ + 2 (1)**	V	-15.2(2)	17	310(51)	17	92(4)	17	197(3)	15	1.6(3)
		Cr	-15.8(3)	8	4,500(786)	5	< dl	1	125(6)	15	36(7)
		Mn	-13.5(1)	16	300(20)	16	119(6)	16	620(16)	15	0.48(3)
		Co	-13.51(5)	17	810(64)	17	4.6(6)	17	390(10)	15	2.1(2)
		Ni	-13.93(6)	17	1,600(107)	5	8.8(9)	5	132(4)	15	11.9(9)
		Cu	-11.6(4)	5	0.70(9)	5	< dl	5	7.6(3)	15	0.09(1)
		Zn	-14.7(1)	7	17(3)	7	25(2)	7	29.9(1)	15	0.6(1)
		Ge	-14.7(2)	14	22(8)	14	2(2)	14	18(2)	15	1.2(5)
		Y	-13.55(8)	5	0.20(3)	5	< dl	0	239(6)	15	0.0008(1)
		Zr90	-13.84(9)	15	7(1)	15	< dl	0	235(6)	15	0.031(6)
		Zr92	-13.9(1)	17	3.9(6)	17	< dl	0	129(4)	15	0.030(5)
		Nb	-14.05(8)	20	8(2)	20	< dl	0	238(7)	15	0.033(8)
		In	-13.56(9)	7	33(5)	7	< dl	0	45(1)	15	0.7(1)
		Hf	-14.3(1)	18	8(2)	18	< dl	0	209(6)	15	0.04(1)
		Ta	-14.7(1)	15	6(2)	16	< dl	0	210(6)	15	0.028(8)
		W	-	0	-	0	-	0	3.7(1)	15	-
		Th	-	0	-	0	-	0	170(5)	15	-
		U	-12.99(8)	10	3.6(5)	10	< dl	10	5,800(140)	15	0.00063(8)
		Ga	-13.9(1)	9	1.1(3)	9	3.5(2)	9	1.19(9)	15	0.9(3)
		Lu	-13.8(1)	7	0.52(5)	7	< dl	0	208(5)	15	0.0025(2)

Experiment	**MB-7**
Furnace	**D**
Internal Fe	**72.4**
fO_2	**FMQ + 1**
t (h)	**12.38**
T (°C)	**1150**
Line size	**100x6**
SM	**FMQ + 1**

Element	log D (m^2/s)	n	C(i) (ppm)	n	C(O) (ppm)	n	C(melt) (ppm)	n	K(mgt/melt)
Mg	-13.2	1	470(91)	7	450(67)	2	1,290(25)	15	0.36(7)
Al	-15.3	1	410(77)	4	406	1	1,020(30)	15	0.40(8)
Si	-	0	1,360(54)	3	-	0	269,000(1,328)	15	0.0050(2)
Ca	-	0	110(31)	2	-	0	91,500(304)	15	0.0012(3)
Sc	-14.6(1)	10	23(4)	10	1.6(2)	8	78.8(1)	15	0.30(5)
Ti	-15.1(1)	6	700(137)	6	120(20)	6	454(9)	15	1.6(3)
V	-15.5(3)	15	400(117)	14	32(6)	14	126(4)	15	3.3(9)
Cr	-16.0(2)	3	1,100(323)	4	4(1)	2	14(2)	15	70(25)
Mn	-13.1(1)	6	310(20)	17	170(15)	6	780(17)	15	0.40(3)
Co	-13.1(2)	8	550(64)	8	0.9(1)	8	332(7)	15	1.7(2)
Ni	-13.18(9)	6	1,000(103)	9	4(2)	8	98(3)	15	10(1)
Cu	-10.2(2)	3	1.1(7)	6	-	0	12.1(3)	15	0.09(6)
Zn	-13.8(1)	5	5(1)	6	21.8(7)	6	5.4(2)	15	1.0(3)
Ge	-15.0(1)	11	37(10)	11	2(2)	11	9(4)	15	4(2)
Y	-13.6(2)	2	0.18(2)	3	< dl	0	262(7)	15	0.00069(8)
Zr90	-14.3(2)	8	15(2)	8	< dl	0	285(8)	15	0.053(7)
Zr92	-14.4(2)	4	12(5)	6	< dl	0	352(9)	15	0.03(1)
Nb	-14.5(1)	3	21(3)	7	< dl	0	314(7)	15	0.07(1)
In	-13.8(2)	7	60(25)	9	< dl	0	33.7(9)	15	1.8(7)
Hf	-14.8(2)	5	17(2)	6	< dl	0	295(7)	15	0.058(6)
Ta	-15.1(1)	5	14(5)	6	< dl	0	242(5)	15	0.06(2)
W	-	0	-	0	-	0	2.81(7)	15	-
Th	-	0	-	0	-	0	190(3)	15	-
U	-13.33(5)	3	10(3)	9	< dl	0	6,300(77)	15	0.0016(5)
Mo	-15.2(2)	11	40(27)	11	0.1(1)	9	431(10)	15	0.10(6)
Ga	-13.6(3)	9	1.3(2)	9	2.9(1)	9	-	0	-
Lu	-14.0(1)	7	0.57(8)	7	< dl	0	239(5)	15	0.0024(3)

Experiment	**MB-14**	Element	log D (m^2/s)	n	C(i) (ppm)	n	C(O) (ppm)	n	C(melt) (ppm)	n	K(mgt/melt)
Furnace	**D**	Mg	-13	1	470(35)	9	790	1	1,060(19)	15	0.44(3)
Internal Fe	**72.4**	Al	-14.1(3)	3	430(54)	8	520(85)	3	1,970(34)	15	0.22(3)
fO_2	**FMQ + 3**	Si	-13.8	1	1,520(76)	5	1500	1	302,000(1,171)	15	0.0050(3)
t (h)	**12.12**	Ca	-13.6(3)	2	140(21)	2	< dl	0	145,100(518)	15	0.0009(1)
T (°C)	**1150**	Sc	-13.6(2)	9	13(2)	9	1.9(3)	9	68.9(9)	15	0.19(3)
Line size	**100x6**	Ti	-14.2(2)	8	540(45)	8	180(31)	8	770(16)	15	0.69(6)
SM	**FMQ + 3**	V	-14.7(2)	12	220(41)	12	49(3)	12	221(6)	15	1.0(2)
		Cr	-16.0(2)	5	6,000(1,138)	5	10(17)	5	136(10)	15	42(9)
		Mn	-13.0(1)	13	310(34)	13	170(14)	13	460(11)	15	0.68(8)
		Co	-13.2(1)	11	600(62)	11	4(2)	11	218(7)	15	2.8(3)
		Ni	-13.8(1)	12	1,400(301)	12	14(3)	12	78(4)	15	18(4)
		Cu	-11.8(3)	3	1.1(1)	4	< dl	0	4.5(2)	15	0.23(3)
		Zn	-13.8(4)	5	17.5(7)	5	25(1)	5	24.5(1)	15	0.71(4)
		Ge	-14.1(2)	9	18(4)	9	3(2)	9	90(11)	15	0.20(5)
		Y	-13.3(2)	3	0.19(2)	4	< dl	0	241(10)	15	0.00078(7)
		Zr90	-13.3(1)	9	4.2(4)	9	< dl	0	230(10)	15	0.018(2)
		Zr92	-13.3(2)	10	2.5(4)	10	< dl	0	240(10)	15	0.010(2)
		Nb	-13.4(2)	14	3.1(5)	14	< dl	0	250(10)	15	0.012(2)
		In	-13.0(1)	4	72(3)	4	< dl	0	127(3)	15	0.57(2)
		Hf	-13.8(2)	13	5.9(7)	13	< dl	0	280(10)	15	0.021(3)
		Ta	-14.1(2)	12	2.8(6)	12	< dl	0	217(8)	15	0.013(3)
		W	-	0	2.0(3)	2	< dl	0	620(21)	15	0.0032(5)
		Th	-	0	-	0	-	0	172(6)	15	-
		U	-12.8(2)	6	1.2(1)	6	< dl	0	4,300(149)	15	0.00029(3)
		Mo	-13.9(4)	4	2(1)	5	0.07(4)	5	249(9)	15	0.006(4)
		Ga	-13.5(2)	10	1.4(2)	10	4.2(2)	10	1.61(6)	15	0.9(2)
		Li	-12.0(4)	5	0.20(7)	5	0.9(1)	5	1.9(2)	15	0.11(4)
		Lu	-13.0(2)	5	0.59(4)	6	< dl	0	207(7)	15	0.0029(2)

Experiment	**MB-21**
Furnace	**D**
Internal Fe	**72.4**
fO_2	**FMQ**
t (h)	**11.99**
T (°C)	**1150**
Line size	**100x6**
SM	**FMQ**

Element	log D (m^2/s)	n	C(i) (ppm)	n	C(O) (ppm)	n	C(melt) (ppm)	n	K(mgt/melt)
Mg	-12.7(2)	4	390(20)	13	300(227)	12	2,110(13)	15	0.186(9)
Al	-15.0(1)	4	1,200(114)	4	345(5)	4	1,946(9)	15	0.61(6)
Si	-	0	910(86)	8	-	0	239,000(2,423)	15	0.0038(4)
Ca	-13.6(3)	6	23(3)	6	< dl	0	61,000(1,811)	15	0.00038(5)
Sc	-14.21(6)	5	51(6)	5	1.16(8)	5	114.5(5)	15	0.44(5)
Ti	-15.0(1)	10	1,900(224)	10	100(21)	10	728(3)	15	2.6(3)
V	-15.0(1)	5	910(95)	5	50.8(5)	5	113.4(8)	15	8.0(8)
Cr	-15.6(3)	11	2,100(483)	11	10(13)	9	13(1)	15	150(38)
Mn	-12.76(7)	5	222(3)	5	95.3(9)	5	915(6)	15	0.242(3)
Co	-12.41(2)	5	315(6)	5	2.9(3)	5	293(2)	15	1.08(2)
Ni	-12.45(1)	5	320(10)	5	5.3(3)	5	79.5(8)	15	4.0(1)
Cu	-11.0(3)	7	0.17(1)	8	< dl	0	10.75(8)	15	0.0159(1)
Zn	-12.79(3)	8	1.4(3)	8	29(1)	8	1.41(6)	15	1.0(2)
Ge	-15.0(1)	7	8(2)	7	4.22(4)	7	9.6(2)	15	0.8(2)
Y	-13.6(1)	10	0.34(5)	11	< dl	0	269.9(9)	15	0.0013(2)
Zr90	-14.53(6)	7	34(3)	8	< dl	0	235.0(9)	15	0.15(1)
Zr92	-14.76(6)	5	12(2)	6	< dl	0	398(3)	15	0.029(4)
Nb	-15.0(1)	9	70(16)	9	< dl	0	285(1)	15	0.24(6)
In	-14.00(4)	8	37(2)	8	< dl	0	32.0(2)	15	1.14(7)
Hf	-15.06(8)	8	46(4)	7	< dl	0	254(1)	15	0.18(2)
Ta	-15.6(2)	8	70(18)	6	< dl	0	317(2)	15	0.21(6)
W	-15.2(3)	4	16(4)	4	< dl	0	904(6)	15	0.017(4)
Th	-14.40(9)	3	0.03(2)	6	< dl	0	333(1)	15	0.00009(5)
U	-13.66(5)	8	24(1)	8	< dl	0	8,080(65)	15	0.0029(1)
Mo	-15.5(1)	7	340(62)	7	0.1(1)	6	612(5)	15	0.6(1)
Ga	-14.3(1)	8	0.80(5)	8	1.22(2)	8	1.16(3)	15	0.69(5)
Li	-11.5(1)	3	6(1)	3	0.91*	0	628(8)	15	0.009(2)
Lu	-13.61(5)	8	1.1(1)	7	< dl	0	238(1)	15	0.0047(6)

Experiment	**MB-23**	Element	log D (m^2/s)	n	C(i) (ppm)	n	C(O) (ppm)	n	C(melt) (ppm)	n	K(mgt/melt)
Furnace	**D**	Mg	-12.1(1)	4	940(59)	11	480(37)	4	1,420(25)	15	0.66(4)
Internal Fe	**72.4**	Al	-12.9(2)	4	300(17)	7	400(228)	4	2,630(31)	15	0.112(7)
fO_2	**FMQ + 4.89**	Si	-	0	1,000(170)	7	-	0	314,000(1,716)	15	0.0033(5)
t (h)	**12.00**	Ca	-12.4(1)	4	220(12)	7	< dl	0	163,000(2,157)	15	0.00137(8)
T (°C)	**1150**	Sc	-12.39(8)	10	8.2(5)	10	0.9(2)	10	69(1)	15	0.119(7)
Line size	**100x6**	Ti	-13.4	1	280(41)	12	496(6)	2	1,270(27)	15	0.22(3)
SM	**CO2**	V	-13.25(4)	3	30.8(5)	5	42.5(2)	3	280.3(9)	15	0.110(2)
		Cr	-14.74(9)	6	1,500(547)	6	3(3)	6	33(4)	15	50(17)
		Mn	-11.9(1)	8	175(3)	9	89(7)	8	162(2)	15	1.08(2)
		Co	-11.84(7)	7	240(19)	7	1.9(4)	7	52(3)	15	4.5(4)
		Ni	-12.39(5)	4	270(40)	4	7.1(3)	4	15(1)	15	18(3)
		Cu	-11.7(2)	4	2.0(4)	6	< dl	0	2.93(6)	15	0.7(1)
		Zn	-11.7(1)	2	23(1)	7	29.8(4)	2	12.9(3)	15	1.8(1)
		Ge	-12.7(2)	4	16(1)	4	0.7*	0	200(13)	15	0.077(7)
		Y	-12.0(1)	9	0.25(2)	14	< dl	0	491(5)	15	0.00051(5)
		Zr90	-12.0(2)	2	1.70(6)	6	< dl	0	271(3)	15	0.0063(2)
		Zr92	-12.12(6)	2	1.0(2)	6	< dl	0	468(6)	15	0.0022(4)
		Nb	-12.47(6)	6	0.636(9)	6	< dl	0	271(2)	15	0.00235(4)
		In	-12.0(2)	6	0.2(1)	6	< dl	0	110(3)	15	0.002(1)
		Hf	-12.62(2)	5	2.0(1)	5	< dl	0	276(3)	15	0.0073(4)
		Ta	-13.09(3)	6	0.62(2)	6	< dl	0	257(2)	15	0.00241(9)
		W	-	0	0.31(8)	4	-	0	870(12)	15	0.00036(9)
		Th	-14	1	0.00365	1	< dl	0	333(3)	15	0.00001
		U	-11.8(2)	6	0.8(2)	6	< dl	0	8,580(45)	15	0.00009(2)
		Mo	-13.0(3)	5	0.4(2)	7	0.03(4)	5	730(15)	15	0.0005(2)
		Ga	-12.26(6)	7	1.27(6)	7	1.73(7)	7	4.00(1)	15	0.32(2)
		Li	-12.0(2)	8	34(6)	9	0.91*	0	157.5(8)	15	0.22(4)
		Lu	-11.96(4)	4	0.54(1)	2	< dl	0	262(3)	15	0.0021(4)

Experiment	**MB-24**	Element	log D (m^2/s)	n	C(i) (ppm)	n	C(O) (ppm)	n	C(melt) (ppm)	n	K(mgt/melt)
Furnace	**D**	Mg	-12.2(5)	2	580(38)	2	510(57)	3	2,860(68)	15	0.20(1)
Internal Fe	**72.4**	Al	-14.3(4)	6	1,100(270)	6	460(54)	6	1,014(8)	15	1.1(3)
***f*O$_2$**	**FMQ - 1**	Si	-14.18(3)	2	960(88)	2	226.47784099578900(4)	6	196,000(1,826)	15	0.0049(5)
t (h)	**12.28**	Ca	-	0	19(4)	0	-	0	48,000(1,105)	15	0.00039(8)
T (°C)	**1150**	Sc	-13.3(2)	9	21(2)	9	0.93(6)	9	27.5(5)	15	0.75(6)
Line size	**100x6**	Ti	-14.69(5)	5	1,400(278)	5	110(28)	5	290(29)	15	5(1)
SM	**FMQ - 1**	V	-14.5(2)	6	600(121)	6	62(2)	6	36(6)	15	18(4)
		Cr	-15.1(2)	8	2,200(439)	8	32(1)	8	10(2)	15	230(66)
		Mn	-12.12(5)	9	104(3)	9	74.0(1)	9	434(5)	15	0.241(7)
		Co	-11.76(7)	7	110(5)	7	2.01*	0	117(2)	15	0.94(5)
		Ni	-11.86(7)	6	116(9)	6	3.93*	0	38(1)	15	3.0(3)
		Cu	-10(1)	4	0.13(3)	4	< dl	0	17.7(9)	15	0.007(2)
		Zn	-12.24(5)	8	0.9(4)	8	28(1)	8	1.4(6)	15	0.7(4)
		Ge	-14.7(4)	7	9(2)	7	4.4(2)	8	8.8(3)	15	1.0(2)
		Y	-13.0(2)	8	1.2(1)	8	< dl	0	469(3)	15	0.0026(3)
		Zr90	-13.9(2)	6	40(10)	6	< dl	0	120(2)	15	0.30(9)
		Zr92	-14.00(9)	4	12(3)	4	< dl	0	155(5)	15	0.07(2)
		Nb	-14.79(8)	6	47(6)	6	< dl	0	89.7(7)	15	0.52(7)
		In	-13.38(4)	4	3.0(8)	4	< dl	0	2.3(3)	15	1.3(4)
		Hf	-14.4(1)	5	55(8)	5	< dl	0	111(1)	15	0.50(7)
		Ta	-15.4(1)	5	35(8)	5	< dl	0	105(1)	15	0.33(8)
		W	-15.0(1)	3	17(5)	3	< dl	0	709(4)	15	0.024(7)
		Th	-13.4(2)	4	0.08(2)	4	< dl	0	325.4(1)	15	0.00024(5)
		U	-13.7(3)	2	49(10)	2	< dl	0	7,210(18)	15	0.007(1)
		Mo	-15.1(2)	7	600(123)	7	0.02*	0	200(13)	15	2.8(6)
		Ga	-13.4(2)	4	100(8)	4	2.5(5)	4	35.9(4)	15	2.8(2)
		Li	-9.5(9)	4	1.93(6)	4	0.91*	0	830(13)	15	0.00232(9)
		Lu	-12.97(4)	4	2.3(1)	4	< dl	0	238(1)	15	0.0098(5)

Experiment	**MB-9**	Element	log D (m^2/s)	n	C(i) (ppm)	n	C(O) (ppm)	n	C(melt) (ppm)	n	K(mgt/melt)
Furnace	**C**	Mg	-13.2(2)	3	550(67)	14	500(330)	3	1,580(22)	15	0.35(4)
Internal Fe	**72.4**	Al	-14.7(2)	4	290(49)	13	280(38)	4	1,072(8)	15	0.27(5)
***f*O$_2$**	**FMQ + 2**	Si	-	0	1,300(258)	10	-	0	287,000(659)	15	0.0047(9)
t (h)	**66.93**	Ca	-14.2(3)	10	100(32)	13	20(25)	9	144,400(546)	15	0.0007(2)
T (°C)	**1150**	Sc	-14.11(8)	17	15(4)	18	0.9(2)	18	62.2(6)	15	0.23(6)
Line size	**100x6**	Ti	-14.5(2)	9	650(57)	17	300(152)	11	540(5)	15	1.2(1)
		V	-15.0(1)	12	320(50)	12	37(5)	13	161(3)	15	2.0(3)
		Cr	-16.2(3)	7	3,100(423)	3	15(9)	7	34(1)	15	90(13)
		Mn	-	0	110(12)	8	-	0	204(4)	15	0.53(6)
		Co	-13.49(2)	11	360(19)	11	2.64(8)	12	166(3)	15	2.2(1)
		Ni	-12.6(2)	4	480(63)	4	7(4)	4	37.4(8)	15	13(2)
		Cu	-	0	1.1(1)	4	-	0	3.95(9)	15	0.27(3)
		Zn	-14.0(1)	8	4(1)	8	24.9(9)	8	3.7(8)	15	1.0(4)
		Ge	-14.7(1)	4	7(1)	4	4.4(2)	4	2.8(1)	15	2.6(4)
		Y	-13.5(1)	8	0.16(3)	9	< dl	0	229(6)	15	0.0007(1)
		Zr90	-13.7(3)	9	9(1)	10	< dl	0	272(7)	15	0.032(5)
		Zr92	-14.1(5)	7	9(4)	8	< dl	0	840(20)	15	0.011(5)
		Nb	-13.89(1)	11	7(2)	11	< dl	0	257(5)	15	0.028(7)
		In	-13.50(7)	7	11(2)	7	< dl	0	16.6(4)	15	0.7(1)
		Hf	-14.3(1)	11	11(3)	11	< dl	0	285(8)	15	0.038(9)
		Ta	-14.5(1)	10	5(1)	10	< dl	0	216(6)	15	0.025(5)
		W	-	0	-	0	-	0	580(15)	15	-
		Th	-	0	-	0	-	0	164(3)	15	-
		U	-	0	-	0	-	0	1.76(4)	15	-
		Mo	-14.9(2)	8	22(3)	8	0.04(2)	5	1,500(34)	15	0.015(2)
		Ga	-13.7(2)	5	1.76(2)	5	2.0(1)	5	-	0	-
		Lu	-13.68(6)	4	0.57(3)	4	< dl	0	206(5)	15	0.0028(2)

Experiment	**MB-2**	Element	log D (m^2/s)	n	C(i) (ppm)	n	C(O) (ppm)	n	C(melt) (ppm)	n	K(mgt/melt)
Furnace	**D**	Mg	-	0	-	0	-	0	1,180(19)	15	-
Internal Fe	**72.4**	Al	-	0	-	0	-	0	1,160(57)	15	-
***f*O$_2$**	**FMQ + 2**	Si	-	0	-	0	-	0	295,000(1,602)	15	-
t (h)	**161**	Ca	-	0	-	0	-	0	162,000(1,171)	15	-
T (°C)	**1150**	Sc	-14.37(2)	4	39(2)	4	0.73(9)	4	270(12)	15	0.143(9)
Line size	**100x6**	Ti	-15.0(2)	4	540(63)	4	230(17)	4	570(22)	15	0.9(1)
SM	**FMQ + 2 (1)**	V	-15.47(4)	3	230(30)	3	28.89(7)	3	163(8)	15	1.4(2)
		Cr	-	0	-	0	-	0	0.5(2)	15	-
		Mn	-13.89(6)	4	204(4)	4	110(3)	4	590(12)	15	0.35(1)
		Co	-13.47(4)	4	310(15)	4	0.2(4)	4	123(4)	15	2.5(1)
		Ni	-13.65(5)	4	220(11)	4	1(1)	4	8.2(6)	15	26(2)
		Cu	-	0	-	0	-	0	2.62(8)	15	-
		Zn	-13.8(1)	4	7.2(6)	4	24(1)	4	2.6(1)	15	2.8(3)
		Ge	-	0	-	0	-	0	0.18(8)	15	-
		Y	-	0	-	0	-	0	290(13)	15	-
		Zr90	-14.05(6)	4	6.5(2)	4	< dl	0	270(17)	15	0.024(2)
		Zr92	-14.08(5)	4	3.0(2)	4	< dl	0	151(9)	15	0.020(2)
		Nb	-14.29(4)	4	6.9(2)	4	< dl	0	290(15)	15	0.023(1)
		In	-13.89(4)	4	3.2(6)	4	< dl	0	4.4(2)	15	0.7(1)
		Hf	-14.57(4)	4	7.9(5)	4	< dl	0	240(16)	15	0.033(3)
		Ta	-14.93(8)	4	7.5(9)	4	< dl	0	250(14)	15	0.030(4)
		W	-	0	-	0	-	0	12.5(8)	15	-
		Th	-	0	-	0	-	0	200(11)	15	-
		U	-	0	-	0	-	0	7,300(448)	15	-
		Lu	-13.80(3)	8	0.54(6)	8	< dl	0	260(11)	15	0.0021(3)

3.3.3.1 Monovalent cations

Lithium partitioning into magnetite increases with increasing fO_2, particularly at fO_2 > FMQ (Figure 3-6A). Lithium was not added to the FMQ + 1, FMQ + 2 or FMQ + 3 starting materials, however, a trace amount was still present in these melts enabling K to be determined for FMQ + 3. In this experiment, Li diffused out instead of into magnetite. It was not possible to detect a diffusion profile for the experiments at FMQ + 1 or FMQ + 2.

Copper exhibits similar partitioning behaviour to Li, with a strong correlation between K(Cu) and K(Li) (Figure 3-13). This suggests that Cu is partitioned into magnetite in a similar fashion to Li. As mentioned previously, there was significant Cu loss during experimental runs, particularly at high fO_2. Notwithstanding this, it is considered that K(Cu) values are reliable because the c_i measured will be in equilibrium with the final melt composition at the end of each experiment, and the absolute concentration of Cu in the system does not matter.

3.3.3.2 Divalent cations

The magnetite-melt partitioning of Mn, Co, Ni and Mg all correlate suggesting a similar control on their behaviour (Figure 3-14). Nickel is most compatible, followed by Co, Mn and Mg. These divalent cations exhibit an increase in D with increasing fO_2; between FMQ – 1 ≤ fO_2 ≤ FMQ + 4.89, K(Mn) increases from 0.24 to 1.08, K(Co) increases from 0.94 to 4.50 (Figure 3-6B), K(Ni) increases from 3.01 to 18.41 and K(Mg) increases from 0.20 to 0.66.

It was generally difficult to measure accurate interface concentrations for Ca as a result of the large contrast between the Ca content of the melt (a major element in the melt composition) and the low concentration at the magnetite-melt interface. Consequently, K(Ca) values are not supported by as large a number of c_i as for other divalent cations, and should be viewed with caution. Nonetheless, where it was possible to calculate K(Ca), there is good correlation between K(Ca) and the other divalent cations. As mentioned previously, it was not possible to measure accurate c_i values for Zn, owing to excessive volatile loss of Zn during experimental runs, particularly at low fO_2 and K(Zn) values are thus not reported.

3.3.3.3 Trivalent cations

K-values for the trivalent cations, Sc, Al, Ga, Y and Lu correlate positively suggesting a similar control on their magnetite-melt partitioning behaviour (Figure 3-16). Gallium is the most compatible, followed by Al, Sc, Lu and Y. With increasing fO_2, there is a decrease in the partition coefficient for all trivalent cations. Between FMQ – 1 ≤ fO_2 ≤ FMQ + 4.89, K(Al) decreases from

1.05 to 0.11, K(Sc) decreases from 0.75 to 0.12 (Figure 3-6C), K(Ga) decreases from 2.79 to 0.32, K(Cr) decreases from 197 to 0.11, and K(Y) decreases from 0.0026 to 0.00051.

Cr is strongly compatible in magnetite, substantially higher than any other element studied, with a partition coefficient as high as 197.1. K(Cr) correlates positively with other trivalent cations which suggests Cr is partitioned as a trivalent cation. Between FMQ − 1 ≤ fO_2 ≤ FMQ + 3, there is a decrease in K(Cr) from 181.9 to 42.4, but no significant decrease at higher fO_2. Nevertheless, there are large errors associated with the K(Cr) values as a result of particularly slow diffusion which meant the exact concentration of Cr at the magnetite-melt interface was difficult to determine precisely.

Under the fO_2 range studied, Cr^{3+} is the dominant Cr species. However, Cr exhibits variable valence state as a function of fO_2 and the $Cr^{2+}/\Sigma Cr$ ratio has been shown to vary from 0.45 at FMQ + 0.61 (Ni-NiO fO_2 buffer) to 0.9 at FMQ - 3.1 (iron-wustite fO_2 buffer) in a basaltic melt at 1400°C (Berry and O'Neill, 2004). A minor amount of Cr^{6+} can also occur at particularly high fO_2 (FMQ + 4.38).

Although Ga was only added to starting compositions used in experiments MB-24, it was possible to measure the low concentration of Ga in the glass and at the magnetite-melt interface, as a result of low levels of Ga impurities in the other trace element solutions. Loss of indium due to volatility was evident, particularly at low fO_2, which produced hump shaped diffusion profiles as the concentration of In in the glass decreased during the experiments. Furthermore, In was not measured accurately in the secondary standard used during LA-ICP-MS analyses (GSD-1g) at ANU in 2016. Thus, K(In) values measured at fO_2 = FMQ -1 (MB-24); FMQ (MB-21) and FMQ + 4.89 (MB-23) are inaccurate and are not reported.

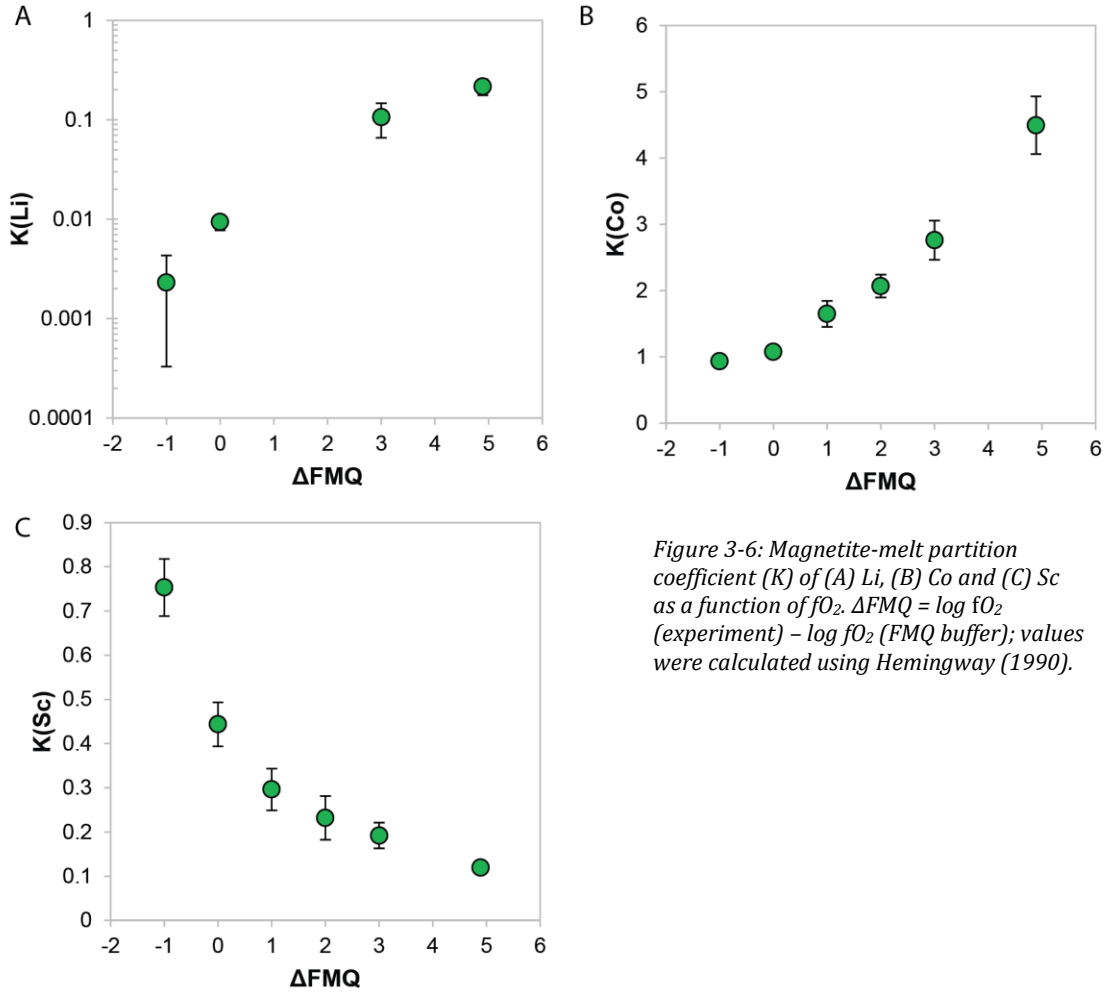


Figure 3-6: Magnetite-melt partition coefficient (K) of (A) Li, (B) Co and (C) Sc as a function of fO_2. ΔFMQ = log fO_2 (experiment) – log fO_2 (FMQ buffer); values were calculated using Hemingway (1990).

3.3.3.4 Tetravalent, pentavalent and hexavalent cations

Titanium and the HFSEs (Zr, Hf, Nb, and Ta) show similar partitioning behaviour and are decreasingly partitioned with increasing fO_2. Titanium ranges from being compatible at fO_2 < FMQ + 3 to incompatible at higher fO_2, whereas the HFSEs are incompatible over the range of fO_2 studied. Between FMQ – 1 ≤ fO_2 ≤ FMQ + 4.89, K(Ti) decreases from 4.97 to 0.22, K(Nb) decreases from 0.52 to 0.0024, K(Hf) decreases from 0.50 to 0.007, K(Ta) decreases from 0.33 to 0.0024 and K(Zr) decreases from 0.30 to 0.006. There is also excellent correlation between the partitioning of trivalent cations, Ti and HFSEs, although the range of partition coefficients does not vary as much for the trivalent cations as for Ti and the HFSEs. In comparison to the HFSEs, there is a paucity of data for Ti, which was a result of minor preexisting exsolution in the magnetite disturbing diffusion profiles for Ti. The HFSEs and other tetravalent, pentavalent and hexavalent cations, however, were much less frequently interrupted by exsolution. Furthermore, the minor increase in Ti content in exsolved sections did not affect the diffusion of other elements, as evinced by a good fit to the diffusion equation through exsolved regions. As a result of the large

contrast between the Si content of the melt (as a major constituent of the melt) and the low concentration at the magnetite-melt interface, it was often difficult to measure c_i for Si and so K(Si) values should be treated with caution. Nevertheless, there is a weak correlation between K(Ti) and K(Si) suggesting that Si is partitioned as a tetravalent cation.

Vanadium partitioning decreases with increasing fO_2 (Figure 3-7B) and, like Ti, changes from compatible at fO_2 < FMQ + 3 to incompatible at higher fO_2. Vanadium can occur in several possible valence states. Over the range of fO_2 conditions investigated, the abundance of V^{3+}, V^{4+} and V^{5+} varies. A number of previous studies have investigated magnetite-melt partitioning of V in detail (e.g. Righter et al., 2006; Toplis and Corgne, 2002; Canil, 1999). Most authors have inferred V^{3+} to be the dominant valence state incorporated into magnetite. K(V) values reported here follow a similar trend with fO_2, but are slightly offset to lower values to those reported by Toplis and Corgne (2002) for Ti-bearing ferrobasaltic system. It is likely the lower K(V) values are a result of the lower Ti contents of magnetite in this study (maximum Ti = 0.14 wt. %).

Uranium and W are highly incompatible and their partition coefficients decrease with increasing fO_2 (Figure 3-7C), correlating with Ti, HFSEs and V. Tungsten, although a polyvalent cation, has been shown to occur as W^{6+} in the fO_2 range studied (O'Neill et al., 2008), suggesting that W is incorporated into magnetite as a 6+ cation. Uranium can occur as either U^{4+}, U^{5+} or U^{6+} under conditions geologically relevant for Earth, although U^{4+} and U^{5+} are the most abundant species over the fO_2 range studied (Halse, 2014). It is therefore possible that U could be incorporated as either a 4+ or 5+ cation into magnetite. There were analytical problems when determining Ge for some analyses conducted at ANU. Furthermore, there was significant volatile loss of Ge during experimental runs, particularly at low fO_2.Thus, K(Ge) values are not reported. Thorium is strongly incompatible in magnetite with the lowest partition coefficient of any element investigated; the maximum K(Th) value in this study is 0.00023. It was only possible to measure discernible diffusion profiles in two experiments at fO_2 < FMQ + 1. Notwithstanding this, it is possible to infer that Th is partitioned as a 4+ cation and exhibits an increase in K(Th) with decreasing fO_2 like other tetravalent cations.

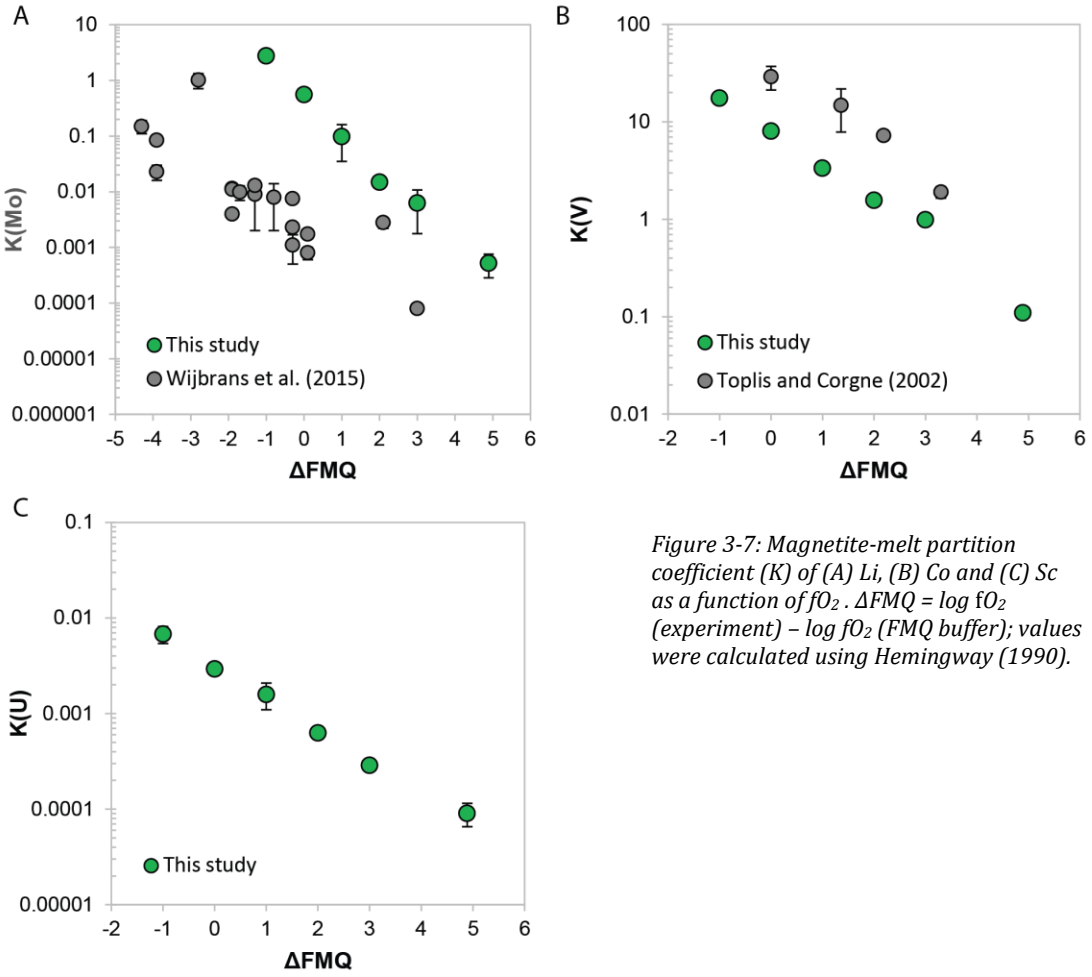


Figure 3-7: Magnetite-melt partition coefficient (K) of (A) Li, (B) Co and (C) Sc as a function of fO_2 . ΔFMQ = log fO_2 (experiment) – log fO_2 (FMQ buffer); values were calculated using Hemingway (1990).

Molybdenum partitioning decreases with increasing fO_2, but unlike other tetravalent, pentavalent and hexavalent cations previously reported, exhibits a more substantial decrease in magnetite-melt partitioning between FMQ – 1 and FMQ. Molybdenum is a 6+ cation under typical geological conditions, but has been shown to change valence to a 4+ cation slightly below the IW-1 buffer (FMQ – 4.33; Holzheid et al., 1994). There is not a linear correlation between K(Ti) and K(Mo) with a sharp increase in K(Mo) relative to K(Ti) between FMQ < fO_2 < FMQ – 1. It is possible that although Mo is predominantly incorporated into magnetite as a 6+ cation, there is an increase in the abundance of Mo^{4+} on approaching fO_2 = FMQ – 1. Mo^{4+} would be expected to be more compatible than Mo^{6+} thus explaining the substantial increase in K(Mo). Values of K(Mo) follow a similar trend with fO_2, but are generally higher than those reported by Wijbrans et al. (2015) who studied spinel-melt partitioning in more Cr-rich spinel (Figure 3-7A).

3.3.4 Diffusion coefficients

Chemical diffusion coefficients (D) are summarised in Table 3-4 and as a function of fO_2 in (Figure 3-12). For some traverses, it was sometimes not possible to interpret a diffusion coefficient because of features such as contamination of the diffusion profile from melt in a nearby crack. However, in these cases it was still possible to measure c_i. Thus, there are often more values for c_i for certain elements in some experiments than D values. Nonetheless, at least 3 or more D values were measured for each sample, and D values reported represent the mean of these repeat analyses. Diffusion coefficients are generally in good agreement with each other, with errors typically less than 0.2 log D units.

Most elements doped in the melt diffused into magnetite, with a concentration at the interface significantly greater than the initial background concentration. Only Li, Mg, Al, Si, Sc, Ti, V, Cr, Mn, Co, Ni, Zn, Ga, Ge, and Mo were above the limit of detection in the initial magnetite. Magnesium, Al, Si and Ti often have minor exsolution in parts of the magnetite crystal, which meant it was not always possible to fit a diffusion profile. Furthermore, the concentration of Al and Mg at c_i was often close to c_o which meant the profile was not as clear as for other elements. Spot analyses of the magnetite in regions furthest from the silicate melt reservoir were checked against the concentration in the original magnetite and used to verify c_0. For elements above the limit of detection in the initial magnetite crucible, apart from Li, most traverses reached c_0 and were within error of the concentration measured in the original magnetite. In some cases, however, where the analytical traverse did not reach c_0, the concentration determined from the spot analysis was used to identify c_0. For elements which were below the detection limit in the initial magnetite c_0 was set to 0. The variation in log D calculated using the limit of detection of spot analyses or a value of 0 as c_0 is less than 0.005 log units. Thus, c_0 for all elements not detectable in Mt-1 prior to annealing are reported as "< dl".

Copper diffusion was particularly fast, such that even at the furthest distance from the melt reservoir the Cu concentration was greater than the original magnetite (originally below detection limit); it was therefore not possible to determine D values for Cu for some experiments. Similarly, Li diffusion was also fast which meant that it was not possible to determine D values at fO2 < FMQ + 3. Silicon diffusion was sufficiently quick that flat profiles were produced in all 12-hour experiments, thus it was not possibly to accurately measure D(Si) in these experiments (Figure 3-8). This contrasts with Si diffusion in silicates, such as olivine, where Si is one of the slowest diffusing species (Dohmen et al., 2002).

For the twelve hour experiments, D values could be measured for elements with -16 < log D < -11.6, however, D values are most accurate for those in the middle of this range where the diffusion distance was not too short (< 12 microns) or too long (e.g. > 600 microns), in which case the diffusion profile appears flat (Figure 3-8). It was not possible to determine accurate D values for W and Th at fO_2 > FMQ + 1, where these elements were particularly incompatible.

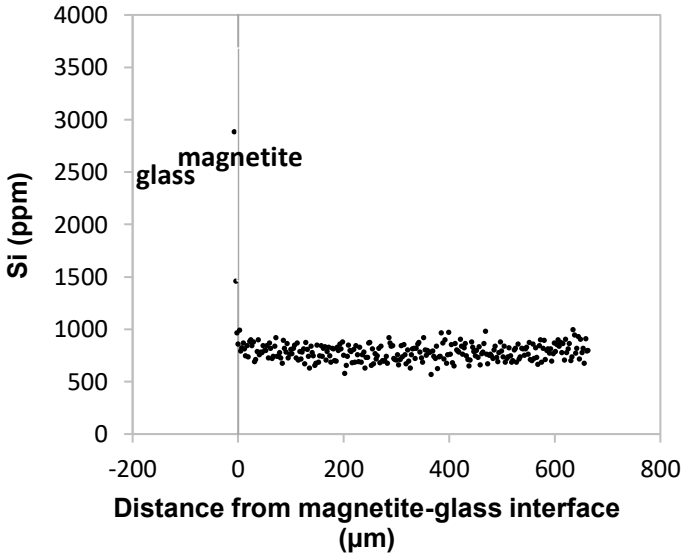


Figure 3-8: Analytical traverse for Si in experiment MB-23. Silicon diffusion produced flat profiles in all experiments from which it was not possible to calculate diffusion coefficients from.

Although there were difficulties determining K(Zn) owing to volatility of Zn, and K(Ge) and K(In) owing to analytical difficulties and volatile loss, it was possible to determine D values. Zinc was substantially lost from the melt during experimental runs so that diffusion profiles could be fitted for diffusion out of the crystal into the melt. Germanium and In were not present in the initial magnetite crystal above the limit of detection of LA-ICP-MS so diffusion still occurred into the crystal. However, there was sometimes evidence for a change in the interface concentration owing to progressive loss of the elements from the melt during runs. In cases where this occurred, the diffusion profile was only fitted for the initial part of the profile (Figure 3-9). Nevertheless, given that the concentration at the interface decreases slightly with time due to volatile loss, which would act to generate resistance to ion exchange at the interface. Consequently, in comparison to non-volatile elements, D values for these elements should be viewed with caution.

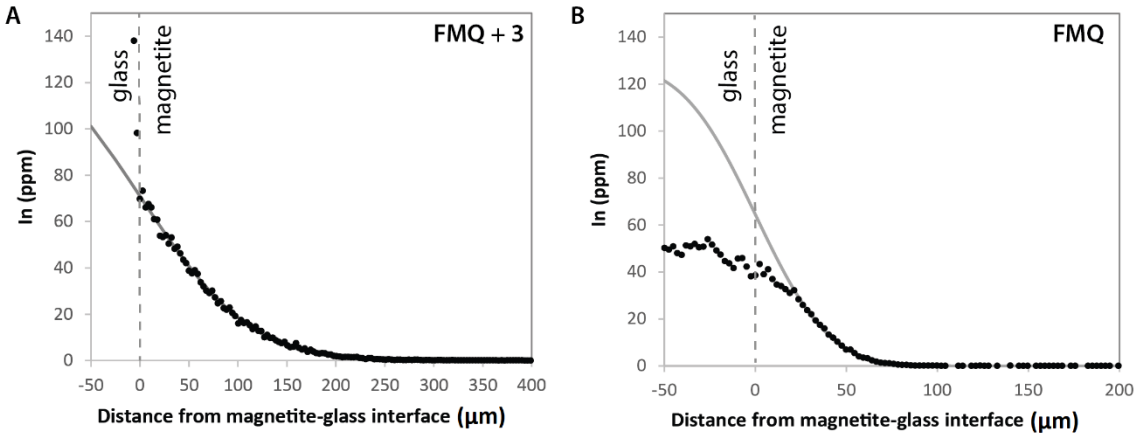


Figure 3-9: Analytical traverse for In in (A) experiment MB-21(FMQ) and (B) MB-14 (FMQ+3). Indium is clearly progressively lost due to volatility at low fO_2. Diffusion profile and diffusion coefficient is therefore calculated only for the start of the profile prior to substantial volatile loss. In volatility, however, does not pose a problem at higher fO_2.

3.3.4.1 Time-independent diffusion coefficients

Experiments MB-9 and MB-3 were conducted over the same fO_2 and T condition (FMQ + 2/1150°C), but MB-9 was annealed for 72.4 hours, whereas MB-3 was annealed for 12.0 hours. Despite the different experiment durations, diffusion coefficients from the two experiments are in agreement within error. This shows that diffusion coefficients are independent of experiment duration. Some elements, e.g. Mo, not added to the MB-3 starting composition, were added to the starting composition used in MB-9, so K and D values could only be interpreted from this experiment. Furthermore, diffusion profiles could only be fitted for Cr in MB-9, owing to its particularly slow diffusion, whereas some faster diffusing elements could not be measured in MB-9, since the concentration was raised above the original concentration for the whole crystal over the longer experiment duration.

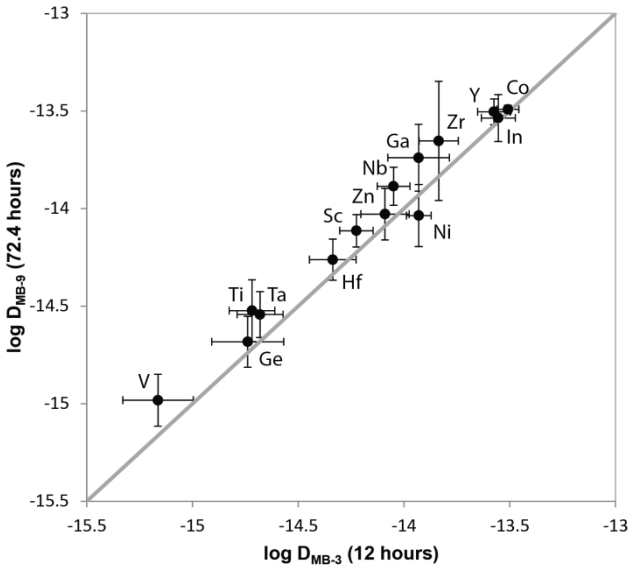


Figure 3-10: Comparison of log D values from two experiments at fO_2 = FMQ + 2 and T = 1150°C, but conducted over different experimental durations.

3.3.4.2 Cation diffusion

As reported by previous work, cation diffusion in magnetite exhibits a concave-upwards trend as a function of fO_2, with a minimum D at intermediate fO_2. This is a result of a transition between interstitial- and vacancy-dominated diffusion mechanisms. Here we extend this behaviour to > 20 elements. Dieckmann and Schmalzried (1977) derived the following equation to describe the diffusion coefficient for Fe as a function of fO_2, expressed as a sum of the diffusivities by interstitial and vacancy mechanisms:

$$D_{Fe} = D_V \exp\left(\frac{-H_V}{RT}\right) a_{O_2}{}^{2/3} + D_I \exp\left(\frac{-H_I}{RT}\right) a_{O_2}{}^{-2/3} \qquad 3\text{-}8$$

where D_{Fe}, D_V and D_I are diffusion coefficients for Fe, vacancy mechanism and interstitial mechanism respectively, H_V and H_I are the activation enthalpy for diffusion by a vacancy and interstitial mechanism respectively, R is ideal gas constant, T is temperature and a_{O2} is activity of oxygen. The diffusion of all other cations studied here exhibit a similar behaviour in their response to fO_2 as Fe. Thus, the same equation can also be used to explain cation diffusion for other species. The location of the minimum D point, however, in fO_2-D space varies between the different elements. Using the equation above, curves were fitted to the experimental data for each cation as a function of fO_2 using weighted least square regressions to solve for a vacancy constant ($D_V{}^0 = D_v\exp(-H_v/RT)$) and an interstitial constant ($D_I{}^0 = D_I\exp(-H_I/RT)$) with fixed exponents of fO_2 as 2/3 and -2/3 for the vacancy and interstitial terms respectively. These fits take account of the errors in D (Table 3-4); Figure 3-12C compares the fits for Sc, which has small errors in log D, and Cr, which has more significant errors in log D. The fit of the data to equation 3-8 is excellent for most elements. For certain elements, however, the fit is less good, for example the volatile elements In and Zn. The fit of the data is also less good for some polyvalent cations, such as U, and elements for which there are less data, such as Ti, where exsolution was a problem. Values for $D_V{}^0$ and $D_I{}^0$, as well as the minimum log D value (log D_X(min)) and log fO_2 at the minimum in the curve (log fO_2(min)) are given in Table 3-5.

3.3.4.3 Comparison with existing work

The diffusion coefficients for Co, Mn, Cr, Al, Ni and Ti as a function of fO_2 have previously been studied at 1200°C (Dieckmann et al., 1978; Dieckmann and Schmalzried 1986; Aggarwal an Dieckmann, 2002; Figure 3-2). The variation of Fe diffusion in magnetite with fO2 at different temperatures has also been investigated. Assuming the relationship between temperature and the diffusion coefficients of other cations is the same as for Fe, it is possible to predict the diffusion coefficients for the other cations at 1150°C so that they can be more readily compared to this

dataset (Figure 3-11). Using the approach, diffusion rates strongly agree with those predicted from the existing literature data suggesting that the diffusion coefficients determined here are robust and accurate, despite the different experimental method.

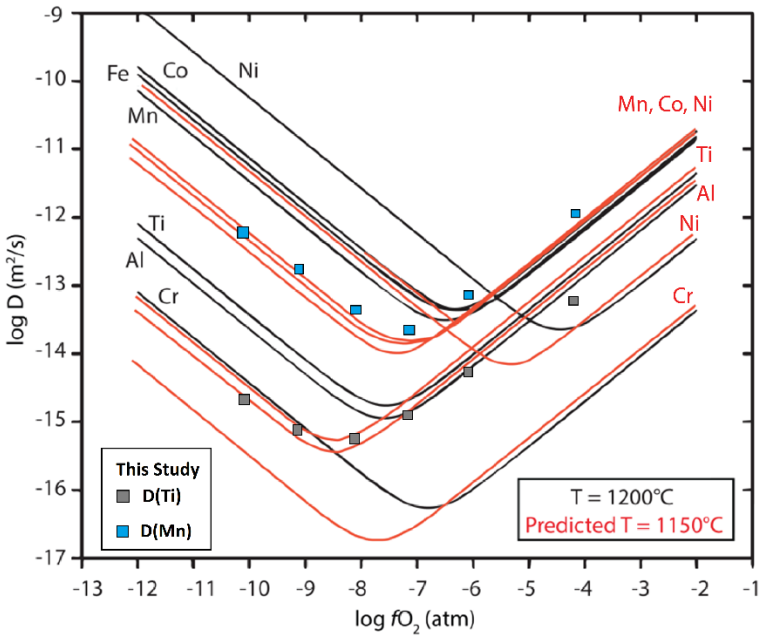
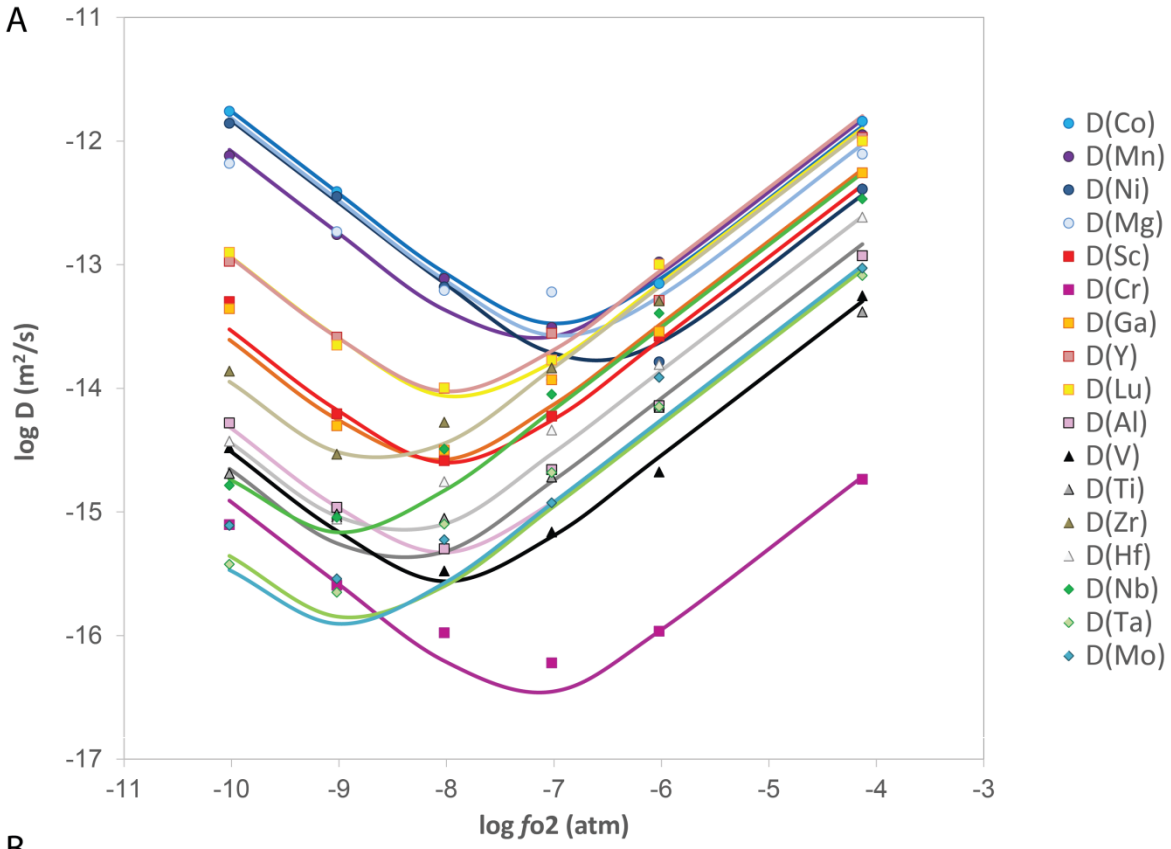
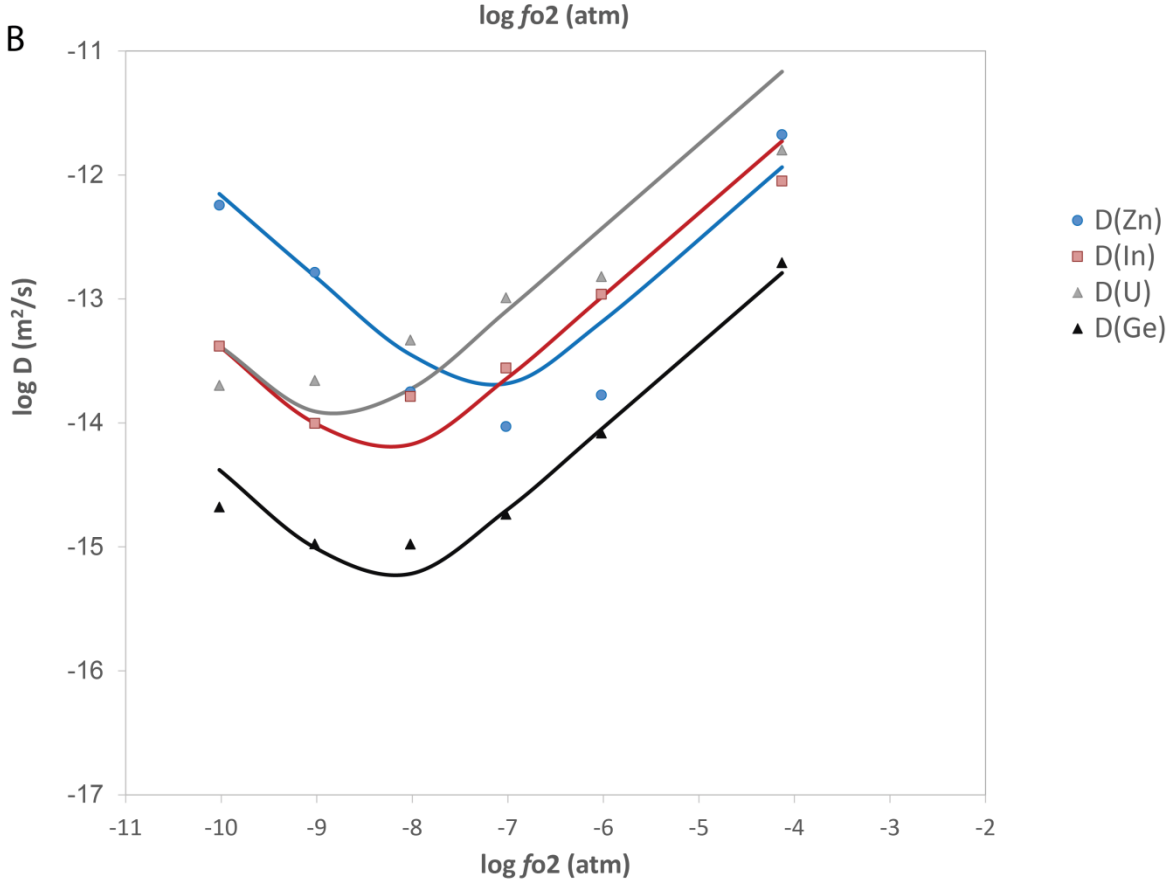


Figure 3-11: Variation of cation diffusion coefficients with fO_2 in magnetite for Fe, Co, Cr, Al and Ni at 1200°C (in black) and predicted at 1150°C (red), assuming the relationship between temperature and log D is the same as Fe for all other cations studied (modified from Van Orman and Crispin, 2010; data from Dieckmann et al., 1978; Dieckmann and Schmalzried, 1987; Aggarwal and Dieckmann, 2002).

The minimum log D (log D_{min}) varies significantly between the different elements. The relative speeds of diffusion, described by log D_{min} vary as follows: Cr < Mo ≈ Ta < V < Ti < Al < Ge < Hf ≈ Nb < Sc ≈ Zr90 ≈ Ga < In < Zr92 < Lu ≈ Y < Ni < U ≈ Zn < Mn ≈ Mg < Co. Silicon can be inferred to be the fastest diffusing cation generating flat profiles which were not possible to interpret diffusion constants from. Lithium and Cu can also be inferred to be particularly fast diffusing cations by their diffusion constants, which were only possible to measure at fO_2 ≥ FMQ + 2.

The location of the log D_{min} in fO_2 space describes the preference of different cations for a vacancy versus an interstitial mechanism of diffusion. The lower the fO_2 of the minimum log D, the greater the preference for a vacancy mechanism over an interstitial mechanism of diffusion. The fO_2 of the minimum D, i.e. the preference for a vacancy over an interstitial mechanism, increases as follows: Nb ≈ Mo < Ta < U < Zr90 ≈ Zr92 < Hf ≈ Ti < In < Ge < Ga ≈ Al < V < Sc ≈ Y < Lu < Mn ≈ Zn ≈ Cr < Co < Mg ≈ Ni. Given that it was only possible to measure D values for Li and Cu at fO_2 > FMQ + 2, it can be approximated that the preference for an interstitial over vacancy mechanism of diffusion is greatest for these elements. It is worth noting that at the highest fO_2 studied, there is convergence of D values, where the vacancy mechanism dominates. At the lowest fO_2, where the interstitial mechanism is dominant, there is more spread in the D values for the different cations.


A
log D (m²/s)
log fo2 (atm)
D(Co)
D(Mn)
D(Ni)
D(Mg)
D(Sc)
D(Cr)
D(Ga)
D(Y)
D(Lu)
D(Al)
D(V)
D(Ti)
D(Zr)
D(Hf)
D(Nb)
D(Ta)
D(Mo)


B
log D (m²/s)
log fo2 (atm)
D(Zn)
D(In)
D(U)
D(Ge)

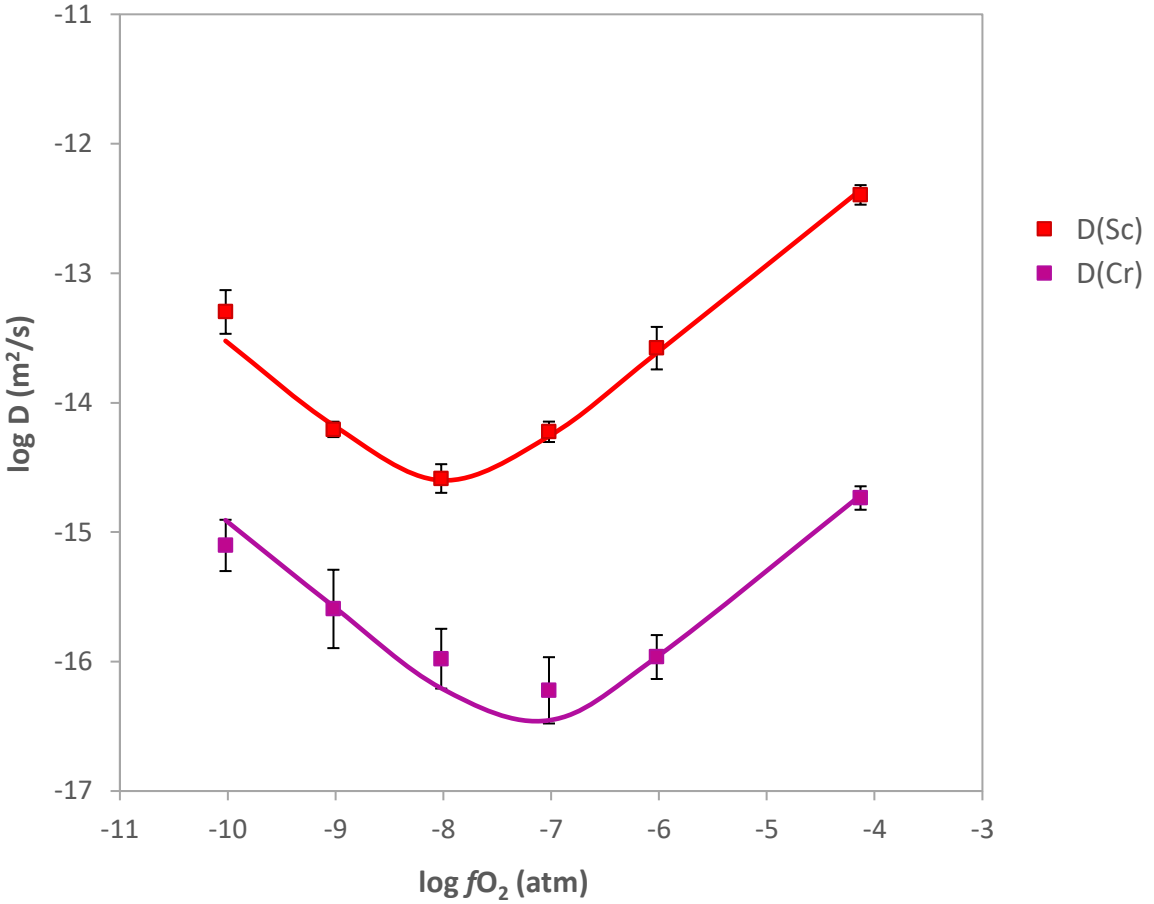


Figure 3-12: Variation in cation diffusion coefficients with fO_2 for A) Co, Mn, Ni, Mg,Sc, Cr, Ga, Y, Lu, Al, V, Ti, Zr, Hf, Nb, Ta, Mo, Zn; B) Zn, In, U, Ge. Elements prone to volatile elements (Zn, In, Ge) and the mixed valence of U could result in poor fit, so these elements were reported separately; C) Fit of cation diffusion coefficients for Sc and Cr, incuding errors, to equation 3-8 to solve for a vacancy constant ($D_V^0 = D_V exp(-H_V/RT)$ and interstitial constant ($D_I^0 = DIexp(-H_I/RT)$ with fixed exponents of fO_2 to 2/3 and -2/3 for the vacancy and interstitial terms respectively. Errors were not included in (A) and (B) for clarity.

Table 3-5: Values of D_v^0, D_i^0, minimum log fO_2 and D of fit to equation 3-8, and various physical parameters for cations in magnetite

Element	Charge	VI Radii (Å)[a]	Mass (g/mol)	OSPE (KJ[b]	Electronegativity (Pauling)	Charge density	K (FMQ-1)[c]	K (FMQ+4.89)[c]	log Dv^0 (0.67)[d]	log Di^0 (-0.67)[d]	Minimum log fO_2[e]	Minimum log D[e]
Li	1	0.76	6.94			0.544	-	0.216	-	-	-	-
Cu	1	0.77	63.5			0.523	-	0.676	-	-	-	-
Mn	2	0.83	54.9	45.0	1.83	0.835	0.241	1.08	-9.07	-18.8	-7.22	-13.61
Co	2	0.65	58.9	20.0	1.91	1.74	0.935	4.50	-9.13	-18.4	-6.94	-13.47
Ni	2	0.56	58.7	-28.0	1.90	2.72	3.01	18.4	-9.68	-18.5	-6.58	-13.79
Mg	2	0.72	24.3	20.0	1.31	1.28	0.204	0.660	-9.27	-18.5	-6.87	-13.58
Zn	2	0.74	65.4	53.0	1.81	1.18	0.667	1.77	-9.18	-18.8	-7.20	-13.71
Sc	3	0.745	45.0		1.54	1.73	0.753	0.119	-9.60	-20.2	-7.91	-14.60
Al	3	0.535	27.0	-36.0	1.61	4.68	1.05	0.112	-10.3	-21.0	-8.01	-15.33
Ga	3	0.62	69.7	-4.00	2.01	3.01	2.79	0.318	-9.48	-20.3	-8.07	-14.58
In	3	0.8	115		1.69	1.40	1.30	0.00199	-8.97	-20.1	-8.28	-14.22
Y	3	0.9	88.9		0.950	0.982	0.00257	0.000506	-9.04	-19.6	-7.89	-14.03
Cr	3	0.615	52.0	-160	1.55	3.08	234	45.9	-12.0	-21.6	-7.18	-16.47
Lu	3	0.861	175		1.25	1.12	0.00981	0.00207	-9.15	-19.6	-7.81	-14.07
V	3	0.78	50.9	-55.0		1.51	17.5	0.110	-10.5	-21.2	-7.94	-15.56
Si	4	0.4	28.1		1.90	14.9	0.00487	-	-	-	-	-
Ti	4	0.605	47.9	50.0	1.63	4.31	4.97	0.224	-10.1	-21.3	-8.40	-15.41
V	4	0.58	50.9		1.66	4.89	17.5	0.110	-10.5	-21.2	-7.94	-15.56
Ge	4	0.53	72.6	110		6.41	1.00	0.0774	-10.0	-21.1	-8.23	-15.25
Zr	4	0.72	91.2		1.22	2.56	0.304	0.00628	-9.17	-20.6	-8.56	-14.60
Hf	4	0.71	178			2.67	0.497	0.00725	-9.86	-21.1	-8.40	-15.18
U	4	0.89	238		1.30	1.35	0.00677	0.0000904	-8.23	-19.8	-8.63	-13.71
Nb	5	0.64	92.9		1.33	4.55	0.519	0.00235	-9.50	-21.4	-8.90	-15.17
Ta	5	0.64	181		1.27	4.55	0.334	0.00241	-10.3	-22.0	-8.77	-15.87
Mo	6	0.59	95.9		1.60	6.97	2.77	0.000520	-10.3	-22.2	-8.89	-15.91
W	6	0.6	184		1.30	6.63	0.0238	-	-	-	-	-

[a]*Ionic radii from Shannon (1976)*
[b]*Octahedral site preference energy from O'Neill and Navrotsky (1984)*
[c]*Magnetite-melt partition coefficients from this study (Table 3-4)*
[d]*$D_V^0 = D_v exp(-Hv/RT))$ and $D_I^0 = D_I exp(-H_I/RT)$ with fixed exponents of fO_2 as 2/3 and -2/3 following equation 3-8*
[e]*Minimum log fO_2 and log D are location of minimum in log fO_2-D space of fit to equation 3-8*

3.4 Discussion

3.4.1 Controls on magnetite-melt partitioning

As discussed in earlier experiments investigating magnetite-melt partitioning in an andesitic and dacitic bulk composition, magnetite-melt partitioning can be explained by a series of equilibrium reactions (section 2.4.2). For example, assuming both Li and Cu are partitioned in the same fashion, K(Cu) can be related to K(Li) by:

$$K(Cu^{+}) = K(Li^{+}) \times \frac{K_M^{*}}{K_{Li}^{*}} \times \frac{\gamma Cu^{+}O_{0.5melt}}{\gamma Li^{+}O_{0.5melt}} \times \frac{\gamma Li_{mgt}}{\gamma Cu^{+}{}_{mgt}} \qquad 3\text{-}9$$

Data for ln K(Cu^{+}) and ln K(Li) were fit by a non-linear least-squares regression to minimise chi-square. The results are summarised in Table 3-6. The value of a_M^1 is 0.95, which suggests that the activity coefficients, namely $\frac{\gamma Li_{mgt}}{\gamma Cu^{+}{}_{mgt}}$ and $\frac{\gamma Cu^{+}O_{0.5melt}}{\gamma Li^{+}O_{0.5melt}}$ remain constant over the range of experimental conditions studied.

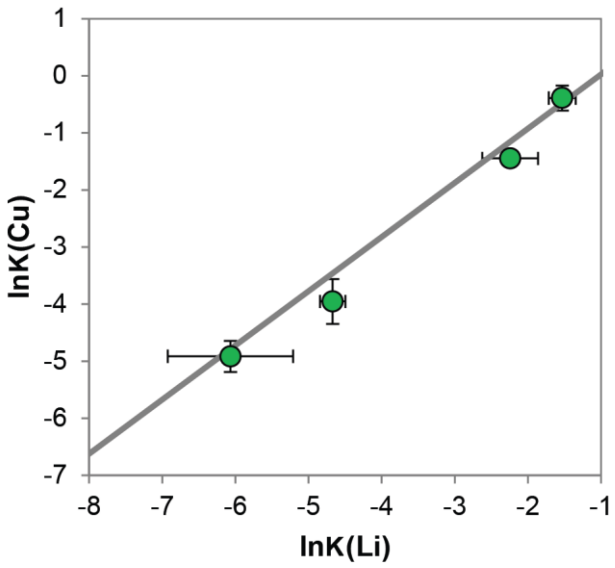


Figure 3-13: Natural log of magnetite-melt partition coefficient of Cu as a function of natural log of magnetite-melt partition coefficient of Li. Grey line is non-linear least-sqauredregression. Values of a_M^1 and a_M^0 are provided in Table. Error bars = σ.

Plotting lnK(M^{2+}) as a function of lnK(Mg), the results for the partitioning of Mn, Co, Ni and Zn from these experiments fit well using the non-linear least-squared regression previously calculated in an andesitic-dacitic bulk system (Figure 3-14). This suggests that the ratio of activity coefficients for divalent cations in the melt and spinel remains constant irrespective of the differing bulk compositions of the synthetic system studied here and more fractionated andesitic and dacitic compositions studied previously. It is important to note that the slope of

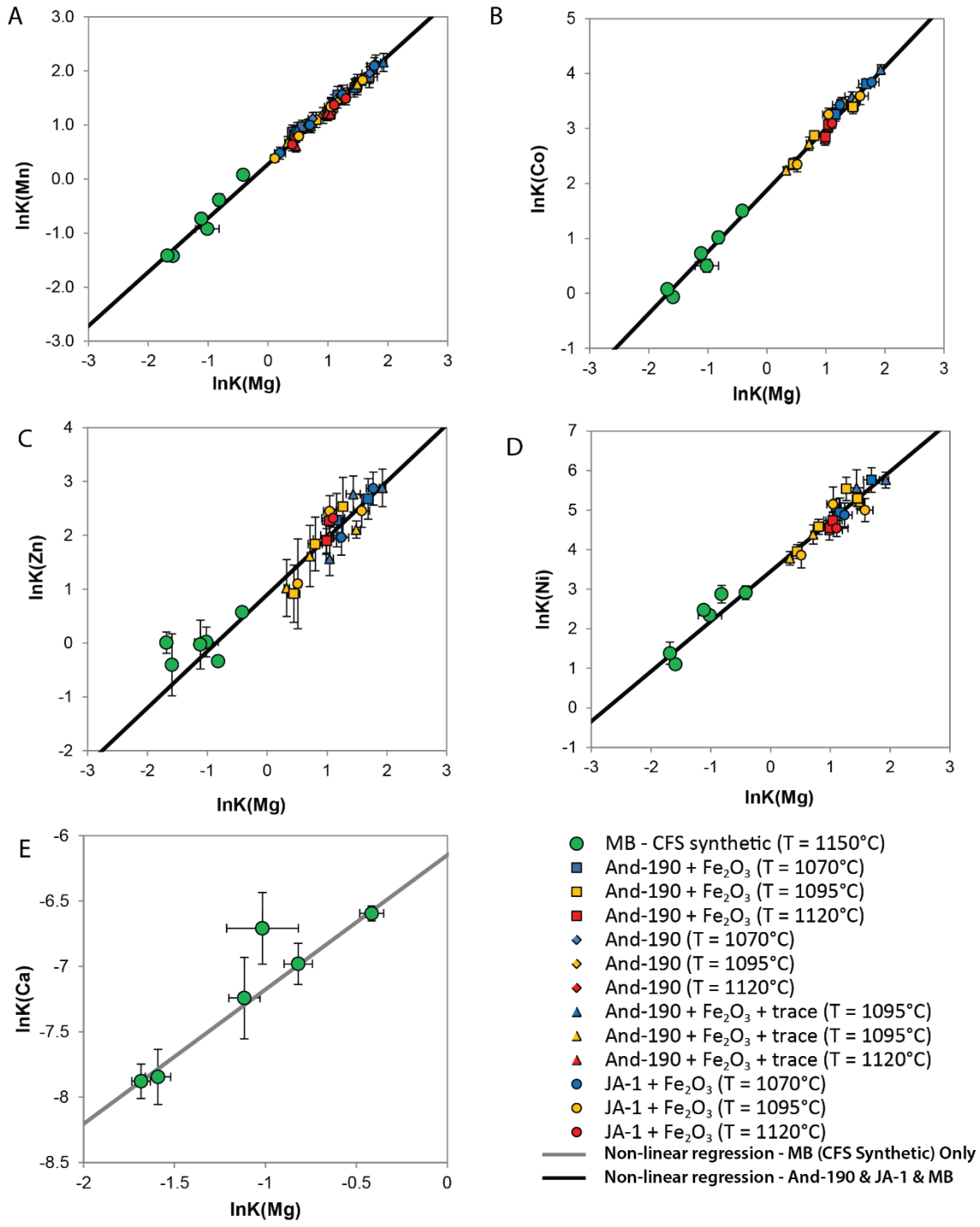


Figure 3-14: Natural log of magnetite-melt partition coefficient of (A) Mn, (B) Co, (C) Zn, (D) Ni and (E) Ca as a function of natural log of magnetite-melt partition coefficient of Mg for MB experiments in synthetic CFS composition and for experiments in andesitic-dacitic system (Chapter 2). Lines are fits of data to a non-linear least-squared regressions (Eq. 2-8) for MB experiments only (grey) or for MB and andesitic-dacitic experiments (black) and their respective values of $a_M^0 and\ a_M^1$ are given in Table 3-6. Value Error bars = σ.

the lines previously defined by the non-linear least-squared regression in an andesitic-dacitic bulk composition - which would be expected to be unity assuming the divalent cation of interest is partitioned in the same manner as Mg - does appear to be significant, with data from these experiments following the same slope. Including data from both these experiments in a synthetic CFS bulk composition with data from And-190 and JA-1 starting compositions in a non-linear least-squared regression generates values of a_M^1 which are similar to those calculated only using And-190 and JA-1 starting compositions (Table 3-6). The partitioning of Cu, however, follows a different trend to that previously defined by the non-linear least-squared regression in an andesitic-dacitic bulk composition (section 2.4.2.2); this suggests that there is significant variation in the ratio of activity coefficients in the melt as a function of bulk composition for Cu and Mg. Although partition coefficients for Ca should be viewed with caution, a plot of ln K(Ca) vs. ln K(Mg) produces a linear trend. Fitting a non-linear least squared regression to this data generates a value of a_M^1 of 1.02 (Table 3-6), which suggests that, like the other divalent cations, there is not a substantial change in the ratio of activity coefficients for Ca and Mg in these experiments.

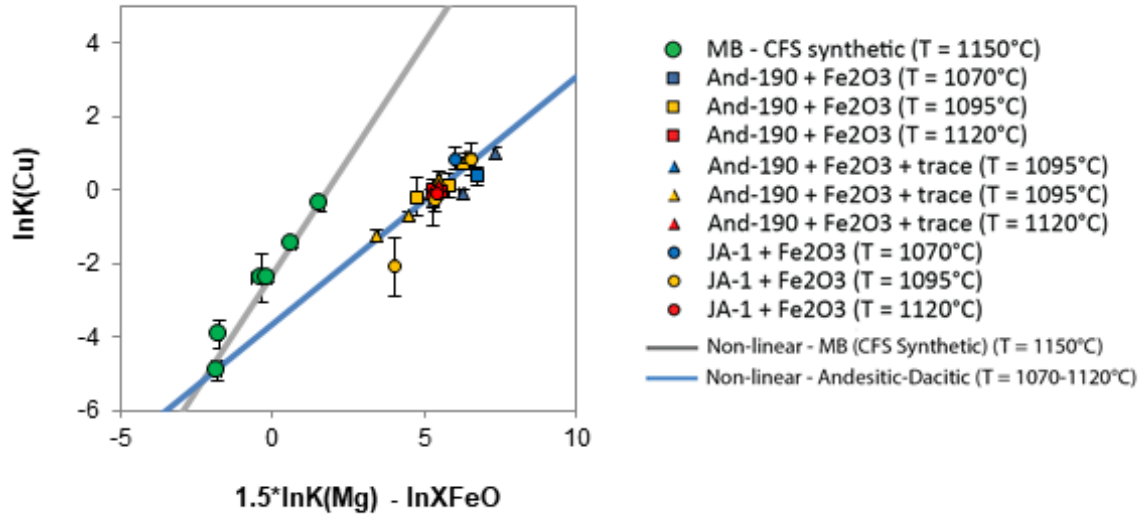


*Figure 3-15: Natural log of magnetite-melt partition coefficient of Cu as a function of natural log of magnetite-melt partition coefficient of 1.5*lnK(Mg)-lnXFeO for MB experiments in synthetic CFS composition and for experiments in andesitic-dacitic system (Chapter 2). Lines are fits to non-linear least-squared regression using equation 2-8 for MB experiments in a synthetic CFS bulk system (grey) and andesitic-dacitic experiments using JA-1 and And-190 starting compositions (blue). Values of $a_M^0 and\ a_M^1$ are given in Table 3-6. Value of Error bars = σ.*

lnK(Ga), lnK(Cr), lnK(Y), lnK(Lu) and lnK(Al) were plotted against lnK(Sc) producing linear trends. This data was fit using non-linear least squared models to minimise chi-square (Equation 2-8). The values of a_M^1 are highest for K(Al) at 1.27 and lowest for K(Y) at 0.84, but nevertheless are close to unity suggesting the ratios of the activity coefficients for these cations remains constant. Data from previous experimental work investigating magnetite-melt partitioning in an

andesitic-dacitic bulk system agrees with the linear trend for lnK(Ga) as a function of lnK(Al), but not for lnK(Sc). This could suggest that the ratio of activity coefficients for Ga and Al are similar in both of these experimental suites irrespective of the change in bulk composition, but differs for Sc and Al. Thus, the partitioning behaviour of Ga seems to follow that of Al.

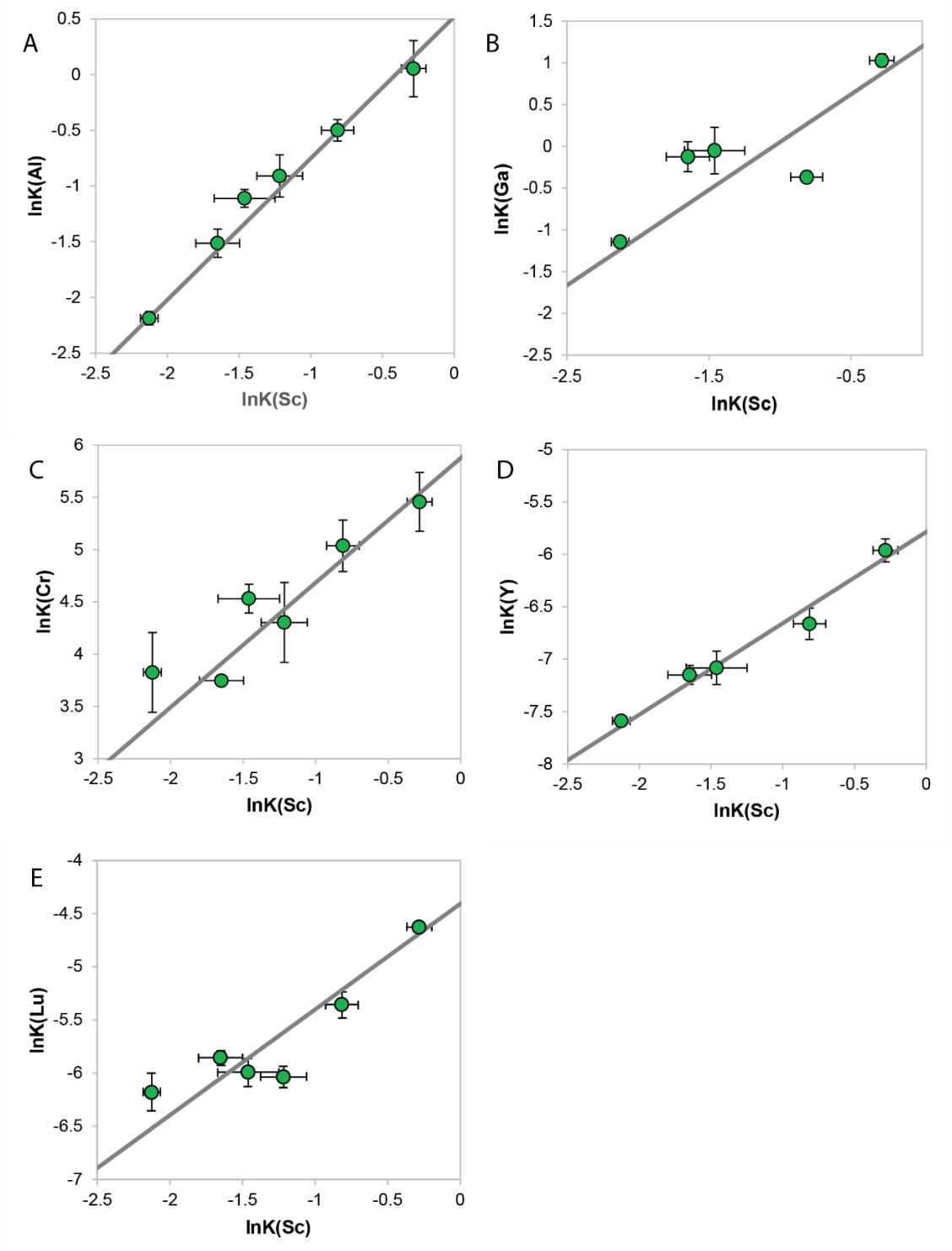


Figure 3-16: Natural log of magnetite-melt partition coefficient of (A) Al (B) Ga, (C) Cr (D) Y and (E)Lu as a function of natural log of magnetite-melt partition coefficient of Sc for MB experiments in synthetic CFS composition.

Grey lines are fits of data to a non-linear least-squared regression (Eq. 2-8) and their respective values of $a_M^0 and\ a_M^1$ are given in Table 3-6. Value Error bars = σ.

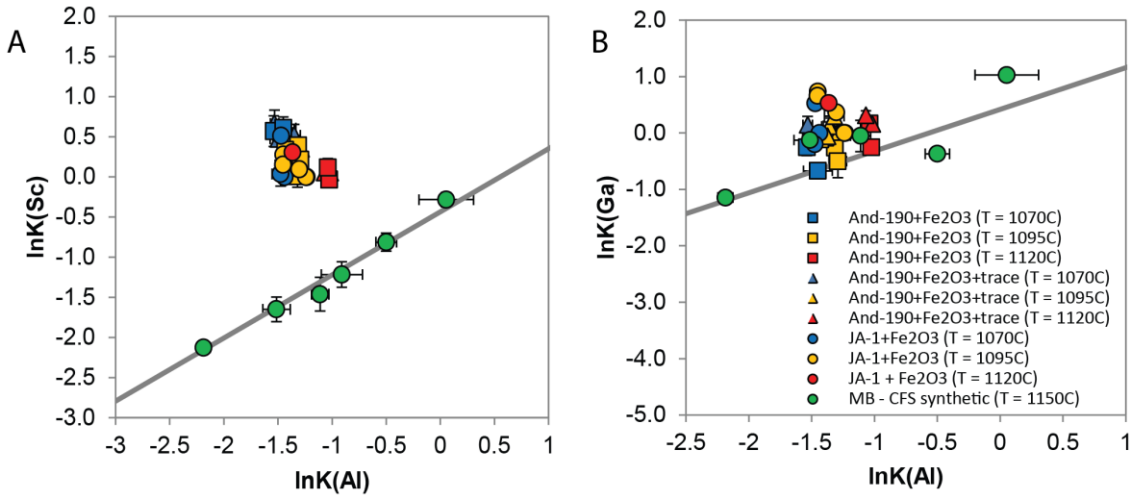


Figure 3-17: Natural log of magnetite-melt partition coefficient of (A) Sc and (B) Ga as a function of natural log of magnetite-melt partition coefficient of Al for MB experiments in synthetic CFS composition and for experiments in andesitic-dacitic system (Chapter 2). Grey lines are fits of MB data using a CFS synthetic starting composition to a non-linear least-squared regression (Eq. 2-8) and their respective values of $a_M^0 and\ a_M^1$ are given in Table 3-6. Value Error bars = σ.

Plotting lnK(V) vs. lnK(Ti) using data from these experiments produces a linear correlation, but with a shallower slope than that observed in an andesitic-dacitic bulk system, whereas plots of lnK(Zr), lnK(Hf) vs. lnK(Ti) produce linear trends with steeper slopes than in an andesitic-dacitic bulk system. Plots of lnK(Nb) and lnK(Ta) vs. lnK(Ti), after taking account for the fO_2 and $XFe^{3+}O_{1.5}$ terms, also produce linear fits with steeper slopes than in an andesitic-dacitic bulk system. This could suggest that there are significant differences in the ratios of activity coefficients, in the spinel or the melt, of these HFSE elements relative to Ti between the two suites of experiments in different bulk compositions. K(Zr) has been shown to have a strong inverse correlation with the concentration of Al in spinel (Nielsen et al., 1994; Wijbrans et al., 2015), possibly as a result of the miscibility gap between $(Fe,Mg)_2TiO_4$ and $(Mg,Fe)Al_2O_4$. As a result, the higher Al content in magnetite in an andesitic-dacitic system could explain the lower K(Zr).

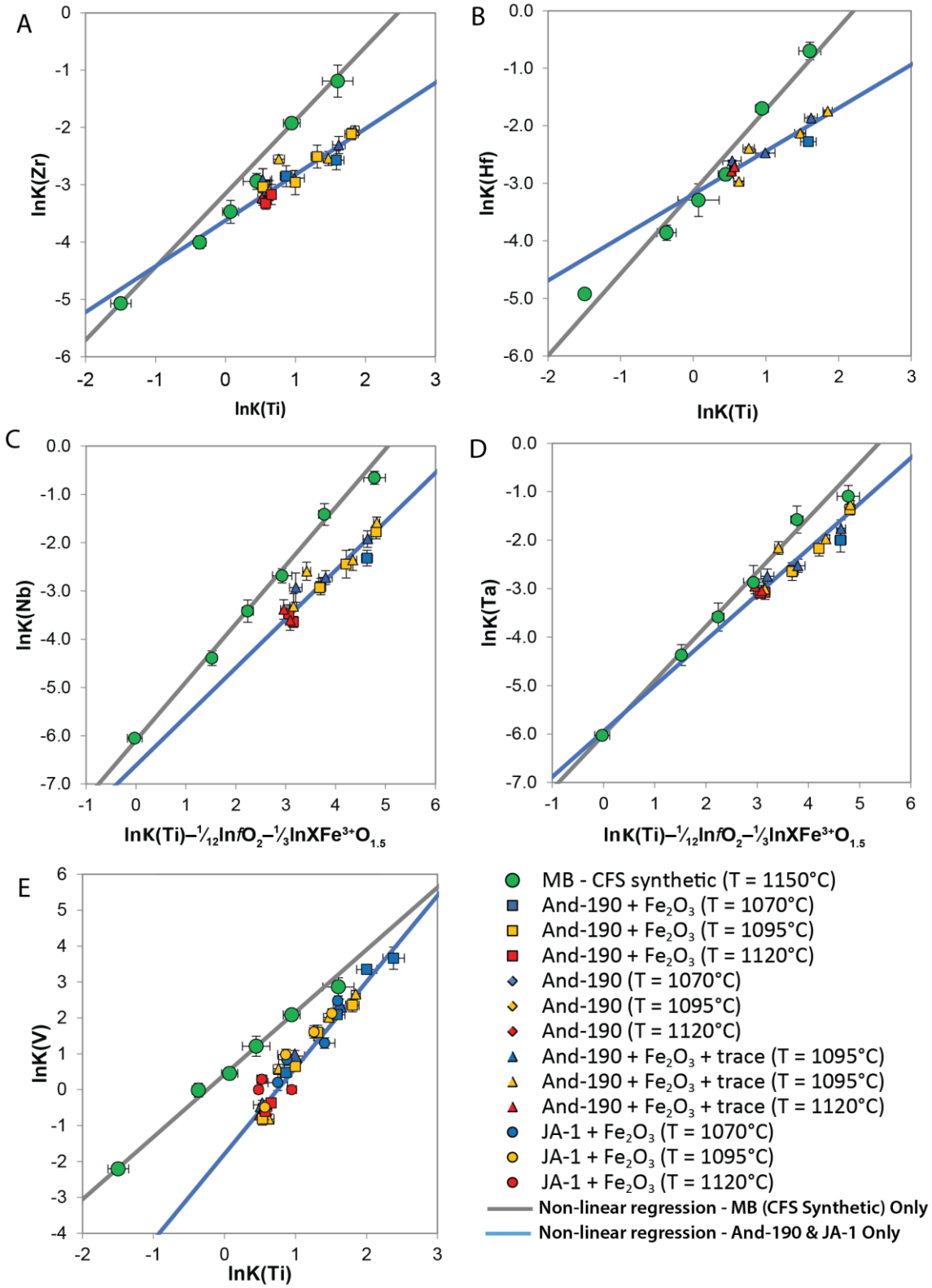


*Figure 3-18: Natural log of magnetite-melt partition coefficient of (A) Zr and (B) Hf as a function of natural log of magnetite-melt partition coefficient of Ti, (C) lnK(Nb) and (D)lnK(Ta) as a function of lnK(Ti)-(1/12*lnfO₂)-(1/3*lnXFe³⁺O₁.₅) and E) lnK(V) vs. lnK(Ti) for MB experiments in synthetic CFS composition and for experiments in andesitic-dacitic system (Chapter 2). Lines are fits of data to a non-linear least-squared regressions (Eq. 2-8) for MB experiments only (grey) or for andesitic-dacitic experiments (blue) and their respective values of* a_M^0 *and* a_M^1 *are given in Table 3-6. Error bars = σ.*

The reliability of Ge partition coefficients reported here suffered as a result of volatility and was not measured accurately during LA-ICP-MS analyses at ANU in 2016. lnK(W), lnK(U) and lnK(Mo) vs. lnK(Ti) were fit to non-linear least-squared regressions. The slopes are slightly above unity for U and W (Table 3-6), which suggests that these cations might be partitioned predominantly as tetravalent cations, like Ti. Notwithstanding this, because the slope is somewhat greater than unity, this could suggest that ratios of activity coefficients of these cations relative to Ti is not constant. The slope for lnK(Mo) as a function of lnK(Ti) is significantly greater than unity (Table 3-6), indicating Mo is partitioned in a different manner to Ti. This could be related to its partitioning as a 6+ cation. D(Mo) is also depressed in experiments by Wijbrans et al. (2015), who studied more Cr-rich spinel compositions (Figure 3-7). This could be a result of changes in activity coefficients, either in spinel and/or melt, with bulk composition.

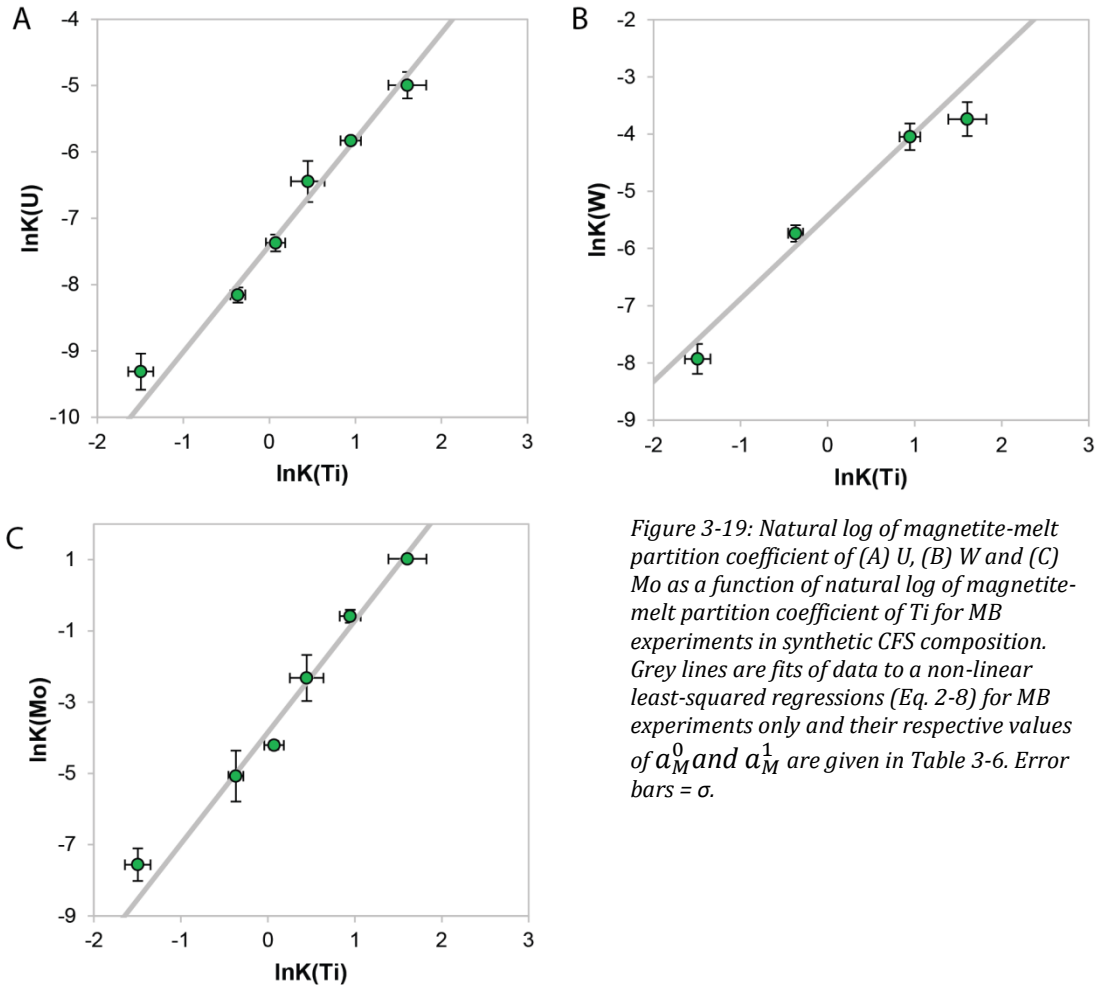


Figure 3-19: Natural log of magnetite-melt partition coefficient of (A) U, (B) W and (C) Mo as a function of natural log of magnetite-melt partition coefficient of Ti for MB experiments in synthetic CFS composition. Grey lines are fits of data to a non-linear least-squared regressions (Eq. 2-8) for MB experiments only and their respective values of a_M^0 and a_M^1 are given in Table 3-6. Error bars = σ.

Table 3-6: Values of a_M^0 and a_M^1 from fitting partitioning for elements (M) to global non-linear least-squares model to minimize chi-square using the partitioning of another cation as a reference using data from this study (see Eq. 2-8)

Reference	lnD(M)	Data included[a]	a_M^0	a_M^1
lnK(Li)	lnK(Cu)	MB	0.97	0.95
lnK(Mg)	lnK(Mn)	A-190, JA-1 and MB	0.28	1.00
lnK(Mg)	lnK(Co)	A-190, JA-1 and MB	1.89	1.12
lnK(Mg)	lnK(Ni)	A-190, JA-1 and MB	3.45	1.26
lnK(Mg)	lnK(Zn)	A-190, JA-1 and MB	0.90	1.05
lnK(Mg)	lnK(Mn)	MB	0.58	1.22
lnK(Mg)	lnK(Co)	MB	2.00	1.20
lnK(Mg)	lnK(Ni)	MB	4.07	1.75
lnK(Mg)	lnK(Zn)	MB	0.845	0.99
lnK(Mg)	lnK(Ca)	MB	-6.15	1.03
1.5lnK(Mg)-lnXFeO	lnK(Cu)	MB	-2.29	1.26
lnK(Sc)	lnK(Al)	MB	0.52	1.27
lnK(Sc)	lnK(Ga)	MB	1.2	1.14
lnK(Sc)	lnK(Cr)	MB	5.88	1.19
lnK(Sc)	lnK(Y)	MB	-5.78	0.87
lnK(Sc)	lnK(Lu)	MB	-4.41	0.99
lnK(Al)	lnK(Sc)	MB	-0.43	0.79
lnK(Al)	lnK(Ga)	MB	0.42	0.74
lnK(Ti)	lnK(V)	MB	0.43	1.74
lnK(Ti)	lnK(Zr)	MB	-3.15	1.28
lnK(Ti)	lnK(Hf)	MB	-3.14	1.43
lnK(Ti)	lnK(Nb)	MB	-3.48	1.90
lnK(Ti)	lnK(Ta)	MB	-3.57	1.75
lnD(Ti) - ((1/12)*lnfO_2) - (⅓*lnXFe$^{3+}O_{1.5}$(melt))	lnK(Nb)	MB	-6.09	1.21
lnD(Ti) - ((1/12)*lnfO_2) - (⅓*lnXFe$^{3+}O_{1.5}$(melt))	lnK(Ta)	MB	-6.01	1.12
lnK(Ti)	lnK(U)	MB	-7.41	1.60
lnK(Ti)	lnK(Mo)	MB	-3.84	3.13
lnK(Ti)	lnK(W)	MB	-5.43	1.45

[a]*MB represents data from magnetite-bucket experiments (reported in this Chapter). A-190 and JA-1 are starting materials used in Chapter 2.*

As discussed when interpreting the results of magnetite-melt partitioning in an andesitic-dacitic bulk system, the partition coefficients of elements into magnetite can be described in terms of simple thermodynamic principles (section 2.4.2.6), These predict linear correlations for partition coefficients based on functions related to aFe$_3$O$_4$(spinel), XFe^{2+}O(melt), XFe^{3+}O$_{1.5}$(melt) and fO$_2$. The results here agree with the linear trends defined by the earlier experiments for the divalent, tetravalent and pentavalent cations (Figure 3-20 to 3-22). A linear trend is also observed for K(Sc) as a function of aFe$_3$O$_4$^0.5/XFeO$_{1.5}$ which is supported by data from Wijbrans et al. (2015); this suggests that the partitioning of Sc is principally governed by thermodynamic equilibria associated with changes in spinel and melt composition and that there are not substantial changes in the activity coeffficients, either in the spinel or melt, with changes in bulk composition. The

partitioning of Al, however, is different. Whereas there is a weak negative correlation between K(Al) and $a Fe_3O_4$^0.5/$XFeO_{1.5}$ in an andesitic to dacitic bulk system, in these experiments there is a positive non-linear correlation. It is important to note that, unlike most natural silicate melts, Al is not a major network-forming component of the melt in these experiments. It could be that in normal Al-bearing silicate melts the activity-composition relations in the melt differ significantly. Alternatively, the partitioning of Al could be more sensitive to spinel composition (e.g. Al content) than other cations studied, possibly through altering the activity coefficients in spinel. In these experiments, however, with low-Al spinel, K(Al) is similar to the other trivalent cations and is dominantly dictated by thermodynamic equilibria between magnetite and melt species.

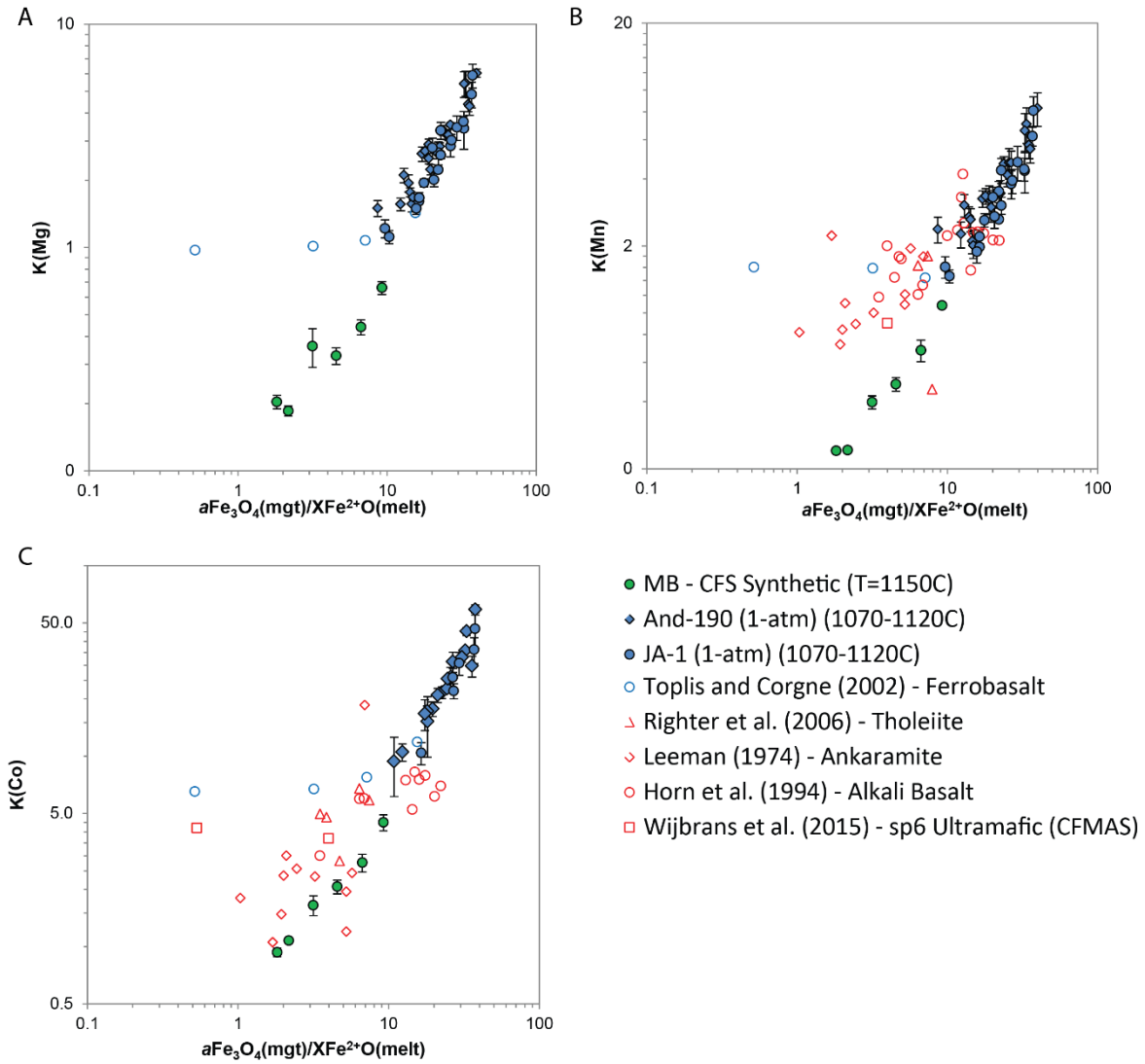


Figure 3-20: Magnetite-melt partition coefficients of (A) Mg, (B) Mn and (C) Co plotted against $aFe_3O_4(mgt)/XFe^{2+}O(melt)$. $aFe_3O_4(mgt)$ approximated using model by O'Neill and Wall (1987), and mole fraction on single cation basis $XFe^{2+}O(melt)$ and $XFe^{3+}O_{1.5}(melt)$ calculated from values approximated using Kress and Carmichael (1991). Data also included from 1-atm experiments in Chapter 2 (And-190 and JA-1). Literature data includes: Toplis and Corgne (2002) which were conducted at 1068°C; and Righter et al. (2006), Leeman (1974), Horn et al. (1994) and Wijbrans et al. (2015) which were conducted between 1150°C and 1370°C. Error bars = 1σ

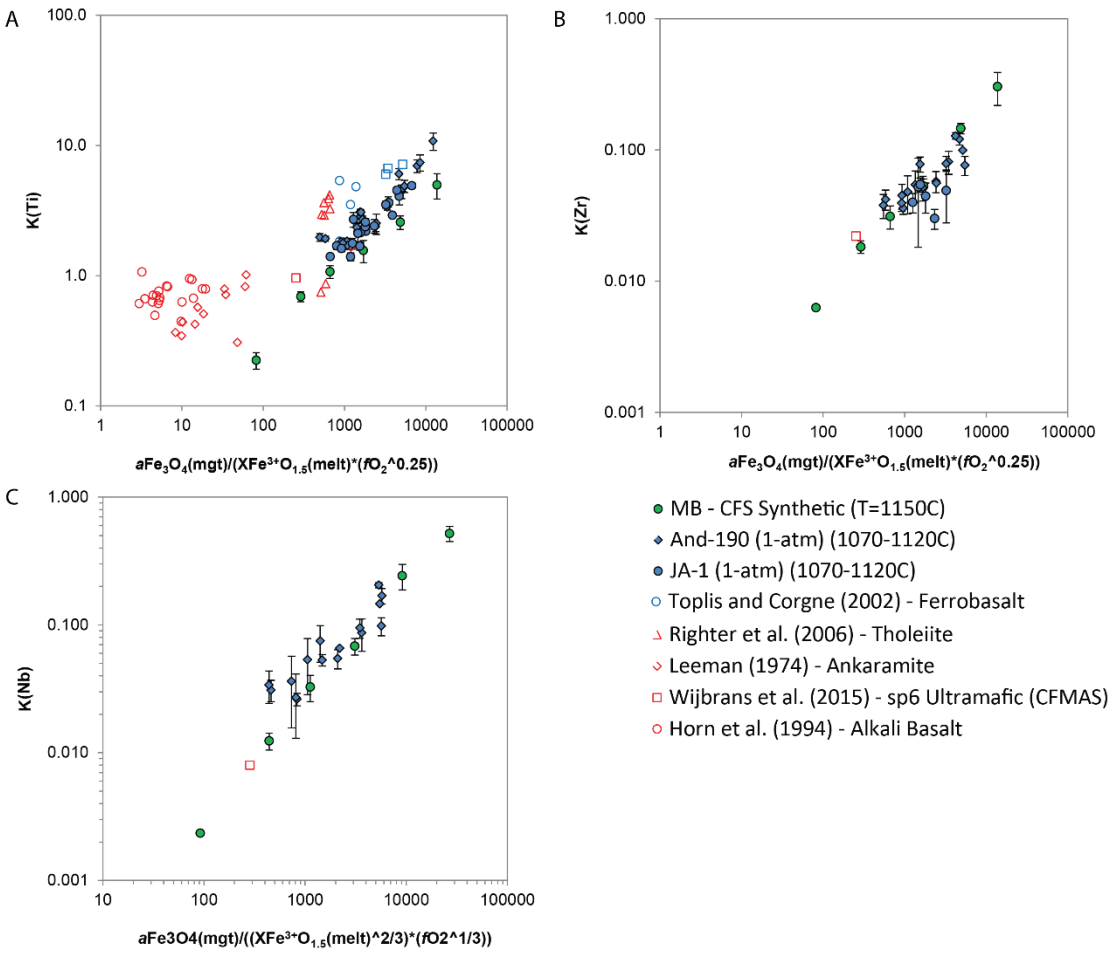


Figure 3-21: Magnetite-melt partition coefficients of (A) Ti and (B) Zr plotted against $aFe_3O_4(mgt)/(XFe^{3+}O_{1.5}(melt)*fO_2\text{^}0.25))$ and (C) D(Nb) vs. $aFe_3O_4(mgt)/(XFe^{3+}O_{1.5}(melt)\text{^}(2/3)*fO_2\text{^}(1/3))$. $aFe_3O_4(mgt)$ approximated using model by O'Neill and Wall (1987), and mole fraction on single cation basis $XFe^{2+}O(melt)$ and $XFe^{3+}O_{1.5}(melt)$ calculated from values approximated using Kress and Carmichael (1991). Data also included from 1-atm experiments in Chapter 2 (And-190 and JA-1). Literature data includes: Toplis and Corgne (2002), Toplis et al. (1994) which were conducted at 1068C; and Righter et al. (2006), Leeman (1974), Horn et al. (1994) and Wijbrans et al. (2015) which were conducted between 1150°C and 1370°C. Error bars = 1σ

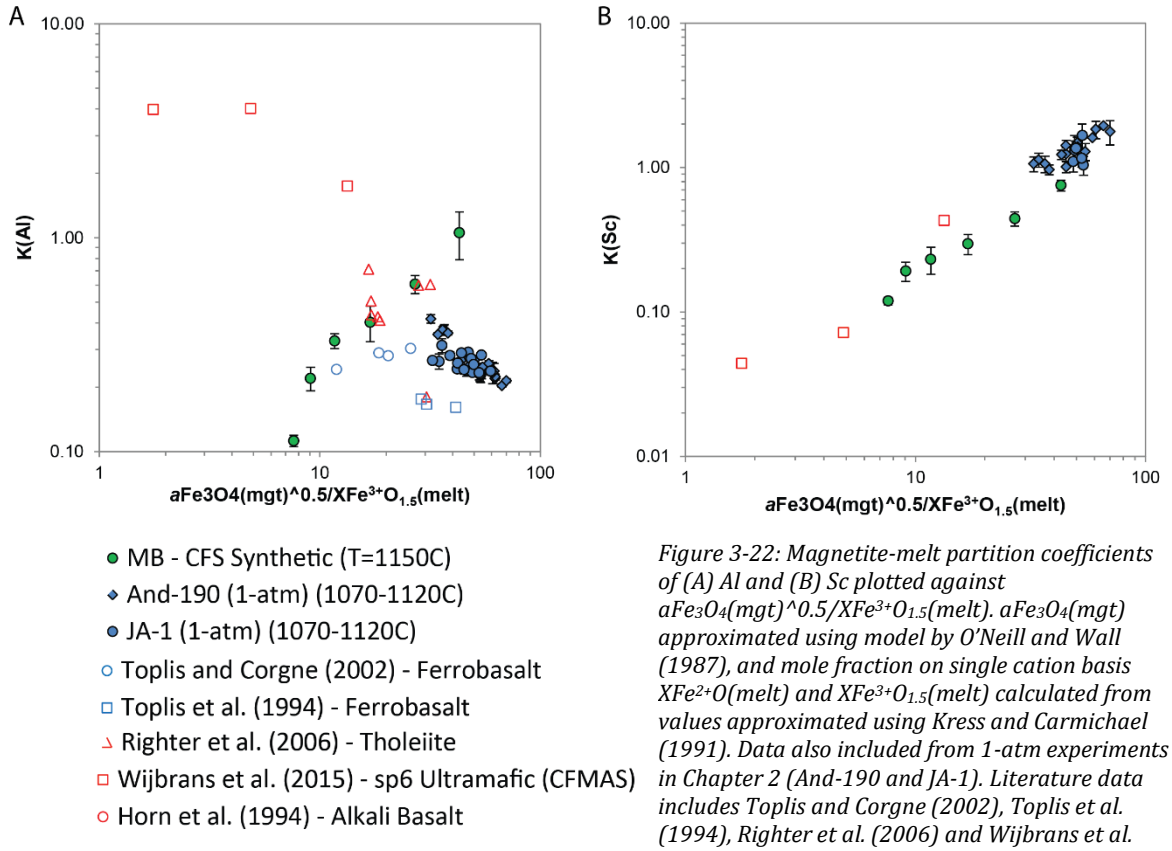


Figure 3-22: Magnetite-melt partition coefficients of (A) Al and (B) Sc plotted against $aFe_3O_4(mgt)^{0.5}/XFe^{3+}O_{1.5}(melt)$. $aFe_3O_4(mgt)$ approximated using model by O'Neill and Wall (1987), and mole fraction on single cation basis $XFe^{2+}O(melt)$ and $XFe^{3+}O_{1.5}(melt)$ calculated from values approximated using Kress and Carmichael (1991). Data also included from 1-atm experiments in Chapter 2 (And-190 and JA-1). Literature data includes Toplis and Corgne (2002), Toplis et al. (1994), Righter et al. (2006) and Wijbrans et al. (2015). Error bars = 1σ

3.4.1.1 Lattice strain models

The logarithm of partition coefficients plotted vs. ionic radius produces parabolic trends for suites of elements grouped by different valence states. The apices of these parabolic trends – known as Onuma diagrams (Onuma et al., 1968) – display the optimal size of the crystal site into which the cations substitute and the curvature indicates the elasticity of the surrounding lattice (Blundy and Wood, 1994). In magnetite, trivalent cations can occupy either the octahedral (B) or tetrahedral (A) site. All element radii used are for octahedral coordination since all elements in their octahedral coordination have an ionic radius closer to the radius of Fe in either the corresponding trivalent or divalent state, than for elements in tetrahedral coordination (Nadoll et al., 2014). This suggests that trace element substitution in magnetite occurs primarily in the octahedral (B) site. For the divalent and tetravalent cations only the right hand limb of the parabola is evident. Although V and U have been included with the tetravalent cations in Figure 3-23, plots of lnK(Ti) vs. lnK(U) and lnK(V) suggest that these elements are not partitioned solely as 4+ cations given that their slope is far from unity (Figure 3-23).

Some elements do not fit onto the parabolic trend for partition coefficients as a function of ionic radius in octahedral coordination. For example, Cr has a much higher partition coefficient than

would be expected based on the parabolic fit defined by the other trivalent cations. The other trivalent cations produce a well-defined parabola with a peak at approximately 0.63Å, suggesting this is the optimal trivalent site radius (r_0). The lattice-strain energy around a homovalent cation depends on the difference between the ionic radius of the cation (r_i) and r_0 and the young's modulus (E) of the host crystal:

$$\Delta G = 4\pi E N_A \left(\frac{r_O}{2}(r_i - r_O)^2 + \frac{1}{3}(r_i - r_O)^3\right) \qquad 3\text{-}10$$

where N_A is Avodgadro's number (Blundy and Wood, 1994). The mineral melt-partition coefficient for a cation can be related to the lattice-strain energy induced by its incorporation into a given crystal site using:

$$K_i = K_0 e^{-\Delta G/RT} \qquad 3\text{-}11$$

where K_i and K_0 is the partition coefficient of cation of interest and cation with optimal radius for the site respectively. Combining these equations, rearranging and converting to logarithms gives a linear relationship between mineral-melt partition coefficients (Ballard et al., 2002):

$$lnK_i = lnK_0 - \frac{4\pi E N_A}{RT}\left(\frac{r_i}{3} + \frac{r_0}{6}\right)(r_i - r_O)^2 \qquad 3\text{-}12$$

The trivalent cations (excluding Cr) can be plotted according to Eq. 3-12 using the suggested r_0 of 0.63Å. This produces straight lines from which both E and K_0 can be approximated as a function of fO_2 for these experiments. Using the identified K_0, E and r_0 values, parabolic trends can be drawn using Eq. 3-12 which can be used to predict K as a function of ionic radius. These fits are shown as a function of fO_2 in Fig. 3-23B and values of E and K_0 are provided in Table 3-7. Lattice strain models were not fitted to the divalent and tetravalent cations because only the right limb of the Onuma diagram was apparent and due to the possible mixed valence states for some elements.

Table 3-7: Approximated values of E and K_0 as a function of fO_2 for the trivalent cations (excluding Cr) using linear trends produced by plotting Eq. 3-12 assuming they are incorporated into the octahedral site.

Parameter	FMQ - 1	FMQ	FMQ + 1	FMQ + 2	FMQ + 3	FMQ + 4.89
E (GPa)	353.8	340.7	426.8	358.1	345.2	314.3
K_0	2.24	0.94	1.02	0.71	0.57	0.27

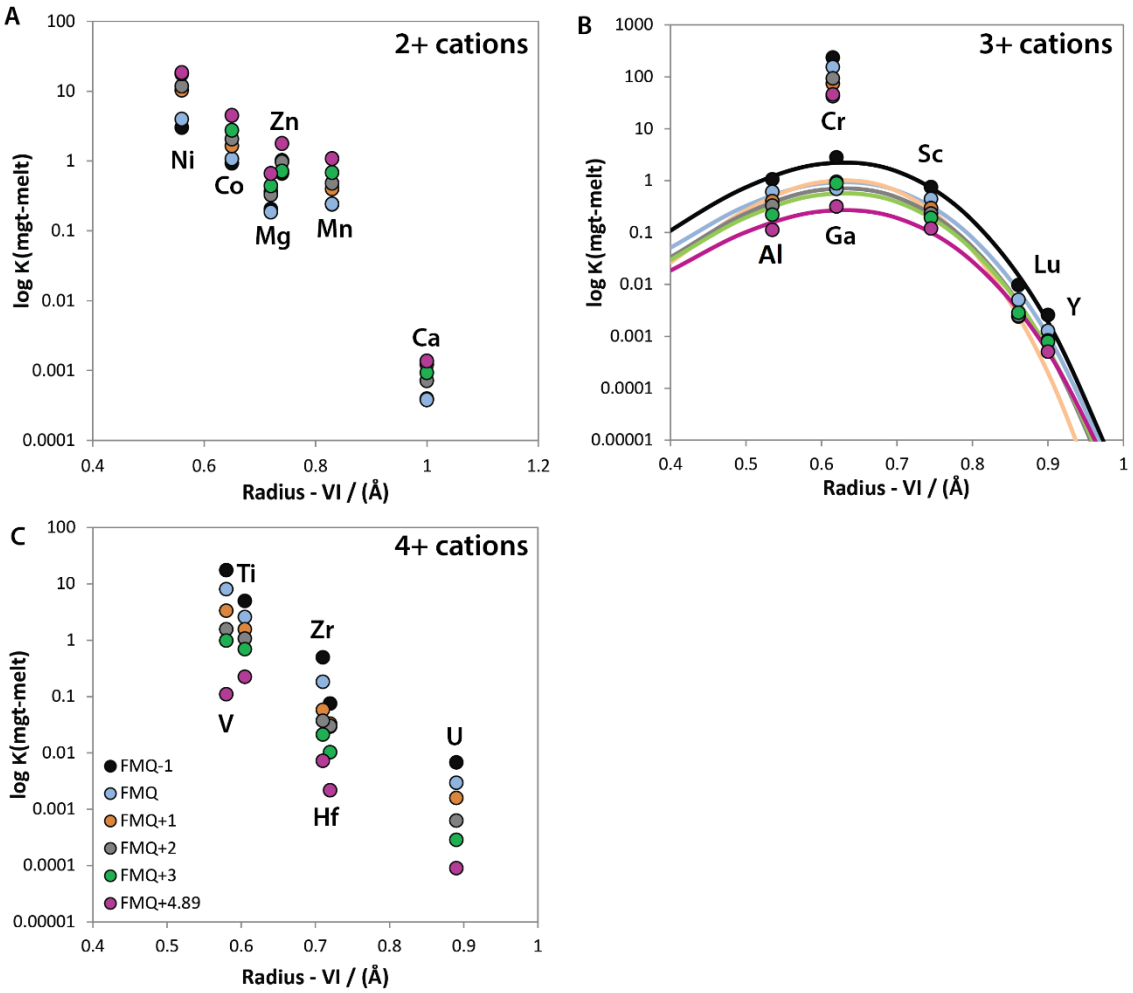


Figure 3-23: Magnetite-melt partition coefficients of (A) divalent, (B) trivalent and (C) tetravalent cations as a function of ionic radius for MB experiments in a synthetic CFS bulk system at 1150°C as a function of fO_2. The solid lines represent fit of trivalent cations to Eq. 3-12 taken from Blundy and Wood (1994). The optimum radius was fixed to be 0.63Å. The Young's modulus (E) and D_0 were approximated using Eq. 3-12, following method of Ballard et al. (2002).

3.4.2 Diffusion in magnetite as a function of fO_2

Lithium and Cu diffused rapidly, such that it was only possible to calculate D values for these elements at fO_2 = FMQ + 4.89. Copper and Li diffusion has been observed to be quick relative to higher valence cations in this study and in many other minerals (Seo and Heinrich, 2013). The ionic radius of Cu^{+} and Li^{+} are close to the middle of the range of other cations studied. However, these cations have the lowest valence state of all cations studied. Thus, it would seem that the low valence state is the characteristic which is most important in controlling the speed of diffusion. It could be that Cu diffusion was only measurable at fO_2 = 4.89 as a result of increased abundance of Cu^{2+}, which would be expected to diffuse slower than a monovalent cation. Similar to Cu and Li, Si diffusion was particularly fast such that it was not possible to interpret D values at any fO_2 studied (Figure 3-8). In comparison to all other cations studied, Si has the smallest ionic radius

(0.4Å for Si^{4+} in VI coordination; Shannon, 1976), which suggests the small ionic radii of silicon could be important in permitting such rapid diffusion.

For all other elements studied, it was possible to identify concave upward trends for cation diffusion as a function of fO_2. Using equation 3-8, curves could be fitted to the experimental data to solve for a vacancy constant ($D_V^0 = D_v exp(-H_v/RT)$) and an interstitial constant ($D_I^0 = D_I exp(-H_I/RT)$). In order to assess the relative controls of different parameters on vacancy and interstitial diffusion individually, values for the vacancy constant ($D_V^0 = D_v exp(-H_v/RT)$) and the interstitial constant ($D_I^0 = D_I exp(-H_I/RT)$) from Eq. 3-8 were studied separately. The following parameters were investigated: ionic radius (Shannon, 1976), charge density, K_M (reported here), site preference energy (O'Neill and Navrotsky, 1984), electronegativity, charge and atomic mass.

The majority of values for log D_V^0 exhibit less variation than values for log D_i^0 with all values ranging between -10.5 and -8.97 apart from U and Cr. There is an increase in log D_V^0 with increasing ionic radius and decreasing charge density for most cations, however, Cr and U are offset from the main trend. The observed relationship could be a result of cations with higher charge density having stronger interactions and forming stronger bonds with surrounding oxygen anions, so that they cannot jump between vacant sites as easily by a vacancy mechanism. The multiple possible valence states could explain why U does not fit on this trend. Log D_V^0 was also plotted against K at fO_2 = FMQ + 4.89 (most oxidising condition studied where vacancy mechanism is most dominant); this produced a relatively well defined linear trend for 3+, 4+, 5+ and 6+ cations, suggesting K could exert some control on vacancy diffusion (Figure 3-24D). It is important to note that this correlation aids in explaining the slower diffusion rate for Cr. This, however, does not seem to be the case for the divalent cations, which could reflect their higher affinity for interstitial diffusion (which might be less influenced by K) in comparison to higher valence cations. Site preference energies were determined for some cations in oxide spinels, relative to Fe^{3+} as a zero reference point (O'Neill and Navrotsky, 1984). Cations with a greater affinity for octahedral coordination have a more negative site preference energy. There is a trend of increasing log D_V^0 with increasing site preference energy (Figure 3-24C), indicating that cations with a greater affinity for octahedral coordination diffuse slower by a vacancy mechanism. No clear relationship is evident between D_V^0 and ionic charge (Figure 3-24E). No trend for log D_V^0 was found as a function of electronegativity or atomic mass.

There is generally more variation in values in log D_I^0 for the majority of cations. There are naturally more interstitial sites than vacancy sites in the lattice. This means that interstitial diffusion can usually reach faster rates than vacancy diffusion. For the trivalent, tetravalent,

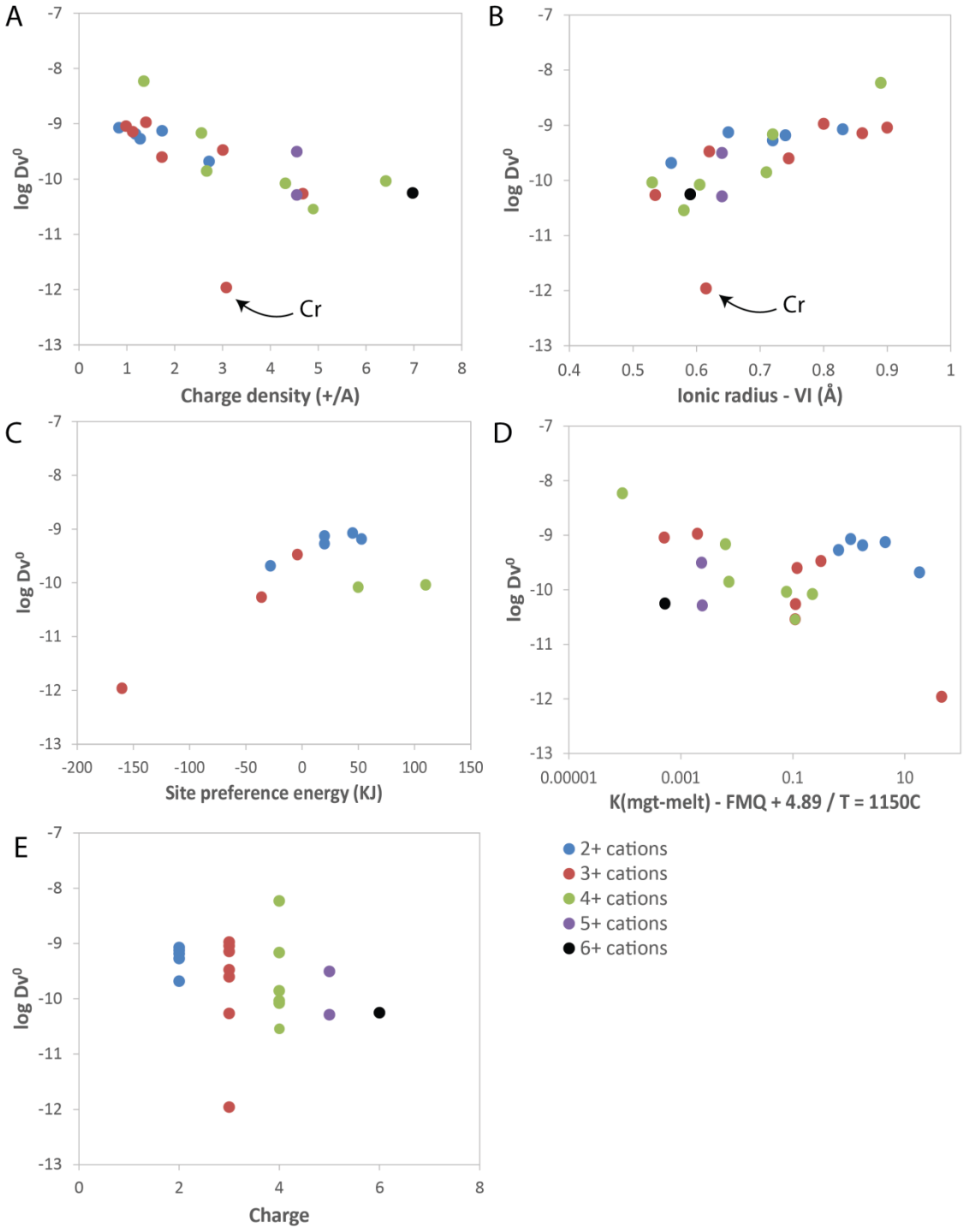


Figure 3-24: The logarithm of D_V^0 ($D_V^0 = D_V exp(-H_V/RT)$) for divalent (Mg^{2+}, Co^{2+}, Mn^{2+}, Ni^{2+} and Zn^{2+}), trivalent (Al^{3+}, Ga^{3+}, Sc^{3+}, In^{3+}, Y^{3+} and Lu^{3+}), tetravalent (Ti^{4+}, Ge^{4+}, Zr^{4+} and U^{4+}) pentavalent (Nb^{5+} and Ta^{5+}) and hexavalent (Mo^{6+}) as a function of (A) charge density, (B) ionic radius, (C) site preference energy, (D) K(mgt/melt) at FMQ + 4.89 and T = 1150°C (this study) and (E) charge. Site preference energy from O'Neill and Navrotsky (1984). Ionic radius in VI coordination sourced from Shannon (1976).

pentavalent and hexavalent cations, there is a general increase in log D_i^0 with increasing ionic radius and decreasing charge density (Figure 3-25), although the latter trend is more diffuse than that defined by logD_v^0 and varies over a greater range from -22.2 to -19.6. Unlike the trend

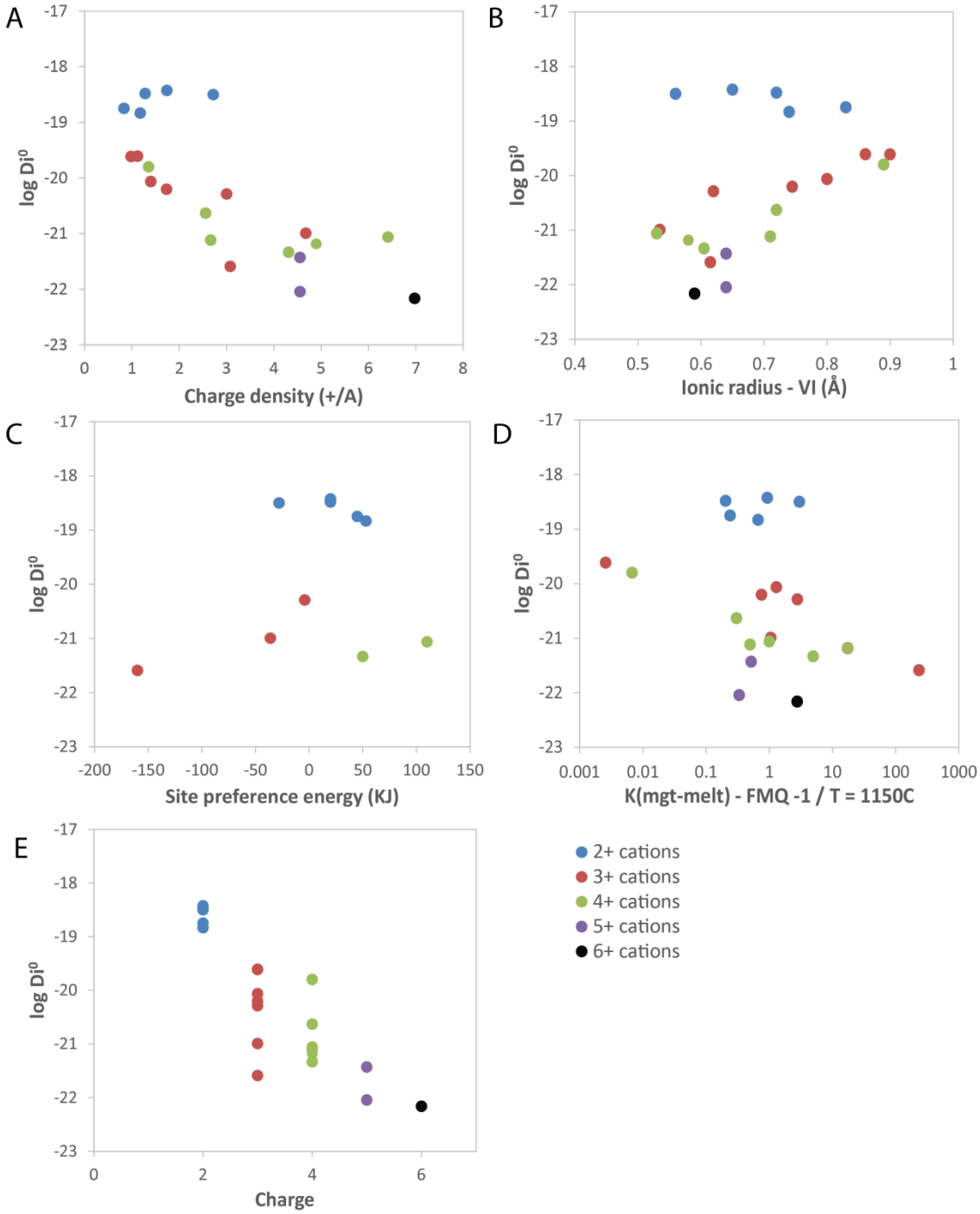


Figure 3-25: The logarithm of Di^0 ($D_i^0 = D_i exp(-H_V/RT)$) for divalent (Mg^{2+}, Co^{2+}, Mn^{2+}, Ni^{2+} and Zn^{2+}), trivalent (Al^{3+}, Ga^{3+}, Sc^{3+}, In^{3+}, Y^{3+} and Lu^{3+}), tetravalent (Ti^{4+}, Ge^{4+}, Zr^{4+} and U^{4+}) pentavalent (Nb^{5+} and Ta^{5+}) and hexavalent (Mo^{6+}) as a function of (A) charge density, (B) ionic radius, (C) site preference energy, (D) K(mgt/melt) at FMQ + 4.89 and T = 1150°C (this study) and (E) charge. Site preference energy from O'Neill and Navrotsky (1984). Ionic radius in VI coordination sourced from Shannon (1976).

defined by $logD_v^0$, the divalent cations do not exhibit a clear correlation between log D_i^0 with charge density or ionic radius (Figure 3-25). There is a relatively well-defined linear trend for the trivalent and tetravalent cations as a function of K at fO_2 = FMQ – 1 (most reducing condition where interstitial mechanism is most dominant), however, the 2+, 5+ and 6+ cations sit off this

trend (Figure 3-25). Unlike log D_V^0, there is a distinct decrease in log D_i^0 with increasing ionic charge, which suggests that this parameter is more important in controlling the interstitial over the vacancy mechanism of diffusion. No trend for log D_I^0 was found as a function of electronegativity or atomic mass.

Plotting log D_v^0 vs. log D_i^0 allows the preference for a vacancy relative to interstitial mechanism of diffusion to be assessed for each cation (Figure 3-26). Cations with a higher valence have increased preference for the vacancy over the interstitial mechanism of diffusion. Linear arrays can be defined on this plot for the 3+ and higher valence studied apart from Cr. The deviation in the behaviour of Cr could be explained by its higher K value and/or increased preference for octahedral coordination relative to the other trivalent cations studied. Vanadium plots along the lineation defined by the trivalent cations, which supports that V^{3+} is the diffusing species in magnetite. The divalent cations form a cluster offset from the dominant linear array defined by the 3+ and higher valence cations, possibly as a result of their lower charge. Within the divalent cations, those cations which plot furthest from the dominant linear array have strongest preference for octahedral coordination.

To summarise, interstitial diffusion relative to vacancy diffusion is primarily controlled by the concentration of interstitials relative to vacancies in the lattice which is predominantly influenced by fO_2 (Eq. 3-1). The preference and rate of interstitial diffusion are predominantly dictated by the ionic charge with increasing preference and rate of interstitial diffusion with decreasing ionic charge (Figure 3-26). In general, the value of ionic charge, whether positive or negative, has previously been shown to have a similar inhibiting effect on diffusion in most other minerals (Brady and Cherniak, 2010). Cations with greater preference for octahedral coordination also have an increased affinity for an interstitial over a vacancy mechanism of diffusion (Figure 3-25). Vacancy diffusion, however, is predominantly controlled by charge density and secondarily by the partition coefficient (which expresses how well it fits/binds to cation sites in the lattice) and site preference energy. Cations with a higher charge density, lower mineral-melt partition coefficient, and higher preference for octahedral coordination diffuse slower by a vacancy mechanism (Figure 3-24). These factors do not exert as strong an influence on the rate of interstitial diffusion. In spite of this, there are clearly further complications. For example, Nb and Ta have identical ionic radius, charge and similar partition coefficients, yet experience different rates of diffusion. Moreover, Si is the fastest diffusing, but also smallest cation studied, yet no trend of increasing rate of diffusion with decreasing ionic radius was observed for the other cations investigated.

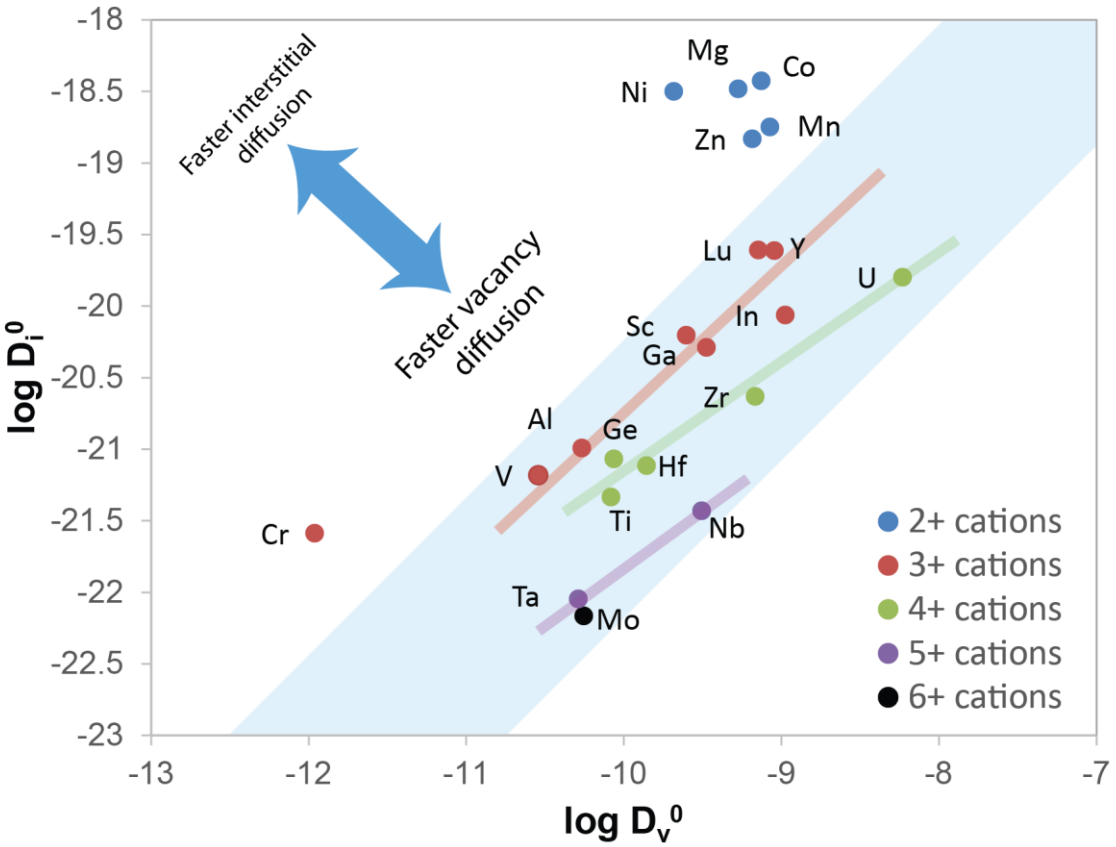


Figure 3-26: The logarithm of D_i^0 ($D_i^0 = D_i exp(-H_V/RT)$) vs. the logarithm of D_V^0 ($D_V^0 = D_V exp(-H_V/RT)$) for divalent (Mg^{2+}, Co^{2+}, Mn^{2+}, Ni^{2+} and Zn^{2+}), trivalent (Al^{3+}, Ga^{3+}, Sc^{3+}, In^{3+}, Y^{3+} and Lu^{3+}), tetravalent (Ti^{4+}, Ge^{4+}, Zr^{4+} and U^{4+}) pentavalent (Nb^{5+} and Ta^{5+}) and hexavalent (Mo^{6+}).

4 Titanomagnetite-melt partitioning at high-pressure and temperature in an andesitic hydrous bulk system

4.1 Introduction

The use of magnetite and Fe-Ti oxides as petrogenetic indicators requires a comprehensive understanding of the controls on element partitioning. In the previous chapters, two suites of experiments have been conducted to evaluate magnetite-melt partitioning, first in an andesitic-dacitic bulk composition and secondly in a synthetic, mafic Ca-Fe-Si bulk system. Although experiments at 0.1 MPa provide a general indication of how the trace element content of magnetite varies as a function of different parameters, it is necessary to assess the effect of pressure in order to be able to confidently apply results to natural systems. Furthermore, through performing experiments at pressure, it is possible to conduct experiments in a hydrous system, thus also testing for any sensitivity of partitioning behaviour to the presence of water. Piston-cylinder apparatus provide the capability to crystallise magnetite in a hydrous system at pressures representative of those at which porphyry systems form. Until now, there are only very few studies who have investigated titanomagnetite-melt partitioning experimentally at elevated pressure (e.g. Nielsen and Beard, 2000; Liu et al., 2015; Arato and Audetat, 2017a).

Here, the results of a series of piston-cylinder experiments are presented. These investigate titanomagnetite-melt partitioning of a wide range of trace elements using a natural calc-alkaline, andesitic bulk composition, comparable to magmas that form porphyry copper deposits. Experiments were conducted as a function of pressure (6-12 kbar), temperature (920-980°C) and fO_2 (at the Ni-NiO, Re-ReO_2 and and Fe_3O_4-Fe_2O_3 redox buffers) in a water-saturated system. An additional set of experiments were also conducted to study the effect of adding sulphur to the system to assess the influence of sulphide saturation on partitioning behaviour.

4.2 Experimental methods

4.2.1 Starting compositions

A natural andesitic lava, 'Andesite-190' (Henderson et al., 1985), doped with 5 wt. % Fe_2O_3, was used as an experimental starting material. Trace elements were added to this starting composition as inductively coupled plasma (ICP) standard nitrate solutions in the following amounts: 50 – 500 ppm for Co, Ge, Mo, Sc, W, Zn, Cr, Cu, Hf, In, Nb, Ni, Ta, Th, V, Y, Zr, Cd, Pb, and Sn (and Ga for experiments after PC-43); 500-1000 ppm for As, Sb, Lu). The mixture was then

dried under a heat lamp, homogenised in an agate mortar and pressed into a pellet, then denitrified at 500°C for 1 hour. A secondary starting material was also prepared by adding 2 wt. % FeS to the primary starting material. In order to check the bulk chemistry of the two starting materials, superliquidus experiments were conducted at a pressure (P) of 10 kbar and temperature (T) of 1500°C in Pt capsules, well above the liquidus of the andesite approximated using MELTS software (Ghiorso and Sack, 1995). The glasses produced were subsequently characterised by SEM-EDS and LA-ICP-MS. The compositions of the starting materials used with added trace elements are given in Table 4-1.

4.2.2 Addition of magnetite seeds

The development of LA-ICP-MS has significantly enhanced the ease by which the trace element composition of minerals can be determined. However, LA-ICP-MS analysis requires the crystal size to be relatively large (generally > 20 microns) and it is difficult in magnetite synthesis experiments to crystallise crystals of this size. This problem can be overcome by the addition of magnetite seeds to experiments.

During experimental runs, elements diffuse into the magnetite seeds, altering the initial composition of the magnetite. The concentration in the magnetite at the interface between the melt and the magnetite will be in equilibrium with the melt. Thus, this concentration determined using LA-ICP-MS, provides an alternative way of determing partition coefficients to analysing magnetite crystals nucleated during the experimental run. The interface concentration can be used to calculate a partition coefficient using D(X) = (wt. % X at magnetite interface)/(wt. % X in glass)).

Standard magnetite crystals (Mt-1) with a uniform major and trace element composition, as evinced by multiple analyses of several crystals (Table 3-2), were crushed using a pellet maker and a hydraulic press. The crystal fragments were separated according to size using a series of sieves. The 100-150 micron fraction was isolated and added to each starting composition in a ratio of 1:3 Mt-1:starting composition by weight.

Table 4-1: *Composition of experimental starting materials*

	SM 1 (n = 15)	SM 2 (n = 16)	SM2 + FeS (n = 17)
Na_2O	3.76(5)	3.83(1)	3.7(1)
MgO	2.97(1)	3.0(1)	3.0(1)
Al_2O_3	16.4(2)	16.6(2)	16.3(5)
SiO_2	55.6(4)	54.4(4)	53(1)
SO_3	-	-	1.2(1)
K_2O	5.0(1)	5.30(1)	5.18(9)
CaO	5.8(1)	6.1(1)	6.0(3)
TiO_2	0.87(1)	0.89(8)	0.9(1)
FeO*	9.5(3)	9.8(3)	10.6(2)
Trace elements (ppm)			
Sc	39.2(6)	64(1)	182(2)
V	251(5)	259(3)	264(7)
Cr	122(3)	150(9)	154(6)
Co	420(23)	530(10)	505(5)
Ni	140(19)	173(1)	141(3)
Cu	81(9)	220(14)	72(2)
Zn	134(3)	330(12)	345(7)
Ga	49(1)	189(2)	191(3)
Ge	259(7)	273(3)	278(6)
As	540(11)	656(9)	650(11)
Y	122(2)	119(2)	118(1)
Zr	208(4)	239(4)	239(3)
Nb	210(3)	377(4)	378(10)
Mo	199(2)	537(7)	540(20)
Cd	78(9)	87(9)	87(4)
In	87(4)	118(1)	114(2)
Sn	74(3)	84(1)	71(2)
Sb	800(17)	787(9)	700(14)
Lu	820(13)	820(18)	809(9)
Hf	92(2)	277(6)	273(3)
Ta	125(2)	92(2)	90(1)
W	500(81)	113(2)	130(17)
Pb	120(12)	160(11)	166(3)

SM 1 = And-190 + 5 wt. % Fe_2O_3 (used in all experiments until RSM-PC-41); SM 2 = And-190 + 5 wt. % Fe_2O_3 (used in all experiments after RSM-PC-43, apart from RSM-PC-51 and RSM-PC-52). Major elements were determined using SEM-EDS and trace elements were measured using LA-ICP-MS (processed using GSD-1g as the external standard). All data is given on an anhydrous basis. Precision (± 1σ) is given in wt. % or ppm respectively of multiple (n) analyses. FeO = total FeO assuming all Fe is FeO.*

4.2.3 Experimental technique

4.2.3.1 Experimental runs

Several suites of experiments were conducted (Table 4-2). The first investigated the influence of pressure on titanomagnetite-melt partitioning at T = 940°C and fO_2 = Re-ReO_2 under fluid-saturated (11-12 wt. % H_2O of the bulk composition) conditions. Another suite of experiments was conducted to investigate the influence of temperature on titanomagnetite-melt partitioning between 980°C and 920°C. Some of these experiments were repeated over longer (84 hours) and shorter (28 hours) durations than the standard experimental duration (48 hours) to assess whether the experimental dwell time was sufficient for equilibrium to be established. The third suite of experiments was designed to investigate the influence of fO_2 on titanomagnetite-melt partitioning at three fO_2 buffers (Ni-NiO, Re-ReO_2 Fe_3O_4-Fe_2O_3) within the limit of magnetite stability at both T = 920°C and 960°C at 12 kbar. An additional set of experiments was also conducted using the secondary starting material with 2 wt. % added FeS at the Ni-NiO and Fe_3O_4-Fe_2O_3 redox buffers at T = 920°C, 12 kbar and 11 wt. % water to determine the influence of the presence of sulphur and sulphide saturation on the titanomagnetite-melt partitioning.

4.2.3.1 Re-ReO_2 buffered capsules

Due to the insolubility of Re in silicate melt, Re-ReO_2 buffered experiments do not require a double capsule assembly to partition the buffer from the experimental starting material. First a mix of Re and ReO_2 was prepared in 15:85 by weight ratio. The capsules used were custom-designed cold-sealed 6.3x15.5mm Ag capsules with 2 mm-thick walls which have been shown to have a temperature variation of ± 5°C over the length of the capsule (Hack and Mavrogenes, 2006). Silver is relatively impermeable to H_2 in comparison to other noble metals (Data reported by Chou (1986), Ockwig and Nenoff (2007) and Uemiya (1999), suggested the following increase of H_2-permeation rates for pure metals: Au<Ag<Pt≤$Ag_{80}Pd_{20}$<Pd). The thick walls of the capsuled used here further ensured that H_2 losses during experiments were minimised. Approximately 0.065g of the Mt-1 and A-190+Fe+trace mix was packed into the capsules, sandwiched between the Re-ReO_2 mix (15:85 weight ratio) at the top and bottom of the capsules with a total weight of approximately 0.27g. Subsequently, approximately 11 wt. % of distilled H_2O was added using micro-syringe to ensure fluid-saturation at run conditions. 'Fluid present' melting helped the attainment of equilibrium, and enhanced melting at lower temperature experimental conditions which aided the generation of large melt fractions and crystal growth. After the capsules were loaded, separate lids were inserted and the capsules swaged by applying direct pressure using a

hydraulic press. This crimped the lip at the top of the capsule down over the lid to form a watertight, cold-seal.

Table 4-2: Summary of experimental conditions

Experiment	fO_2 buffer	log fO_2	T (°C)	Pressure (kbar)	Starting material	Time (hours)
Pressure series						
RSM-PC-32	RRO	-9.31	940	12	A-190+Fe+trace (SM1)	48
RSM-PC-39	RRO	-9.31	940	10	A-190+Fe+trace (SM1)	48
RSM-PC-40	RRO	-9.31	940	8	A-190+Fe+trace (SM1)	48
RSM-PC-41	RRO	-9.31	940	6	A-190+Fe+trace (SM1)	48
Temperature series						
RSM-PC-19	RRO	-8.72	980	12	A-190+Fe+trace (SM1)	48
RSM-PC-43	RRO	-9.01	960	12	A-190+Fe+trace (SM2)	48
RSM-PC-32	RRO	-9.31	940	12	A-190+Fe+trace (SM1)	48
RSM-PC-37	RRO	-9.63	920	12	A-190+Fe+trace (SM1)	48
Time series						
RSM-PC-46	RRO	-9.63	920	12	A-190+Fe+trace (SM2)	84
RSM-PC-37	RRO	-9.63	920	12	A-190+Fe+trace (SM1)	48
RSM-PC-36	RRO	-9.01	960	12	A-190+Fe+trace (SM1)	28
RSM-PC-43	RRO	-9.01	960	12	A-190+Fe+trace (SM2)	48
fO_2 series						
RSM-PC-47	NNO	-11.61	920	12	A-190+Fe+trace (SM2)	48
RSM-PC-37	RRO	-9.63	920	12	A-190+Fe+trace (SM1)	48
RSM-PC-49	MH	-7.04	920	12	A-190+Fe+trace (SM2)	48
RSM-PC-51	NNO	-11.61	920	12	A-190+Fe+trace+FeS	60
RSM-PC-52	MH	-7.04	920	12	A-190+Fe+trace+FeS	60
RSM-PC-31	NNO	-10.95	960	12	A-190+Fe+trace (SM1)	48
RSM-PC-43	RRO	-9.01	960	12	A-190+Fe+trace (SM2)	48
RSM-PC-30	MH	-6.33	960	12	A-190+Fe+trace (SM1)	48

H_2O content for all experiments was 11-12 wt. % of the starting composition. Abbreviations: RRO = Re=ReO_2; NNO = Ni-NiO; MH = Fe_3O_4-Fe_2O_3.

4.2.3.2 Ni-NiO and Fe_3O_4-Fe_2O_3 buffered capsules

Owing to the solubility of Ni and Fe in silicate melt, it was necessary to conduct experiments buffered by Ni-NiO and Fe_3O_4-Fe_2O_3 using a double capsule set-up, with a physical barrier to separate the solid redox buffer from the sample material. The fH_2 of the hydrous redox buffer is imposed on the inner capsule through hydrogen exchange across the physical barrier, thus controlling the fO_2. Platinum capsules were used for the inner capsule based on its high

permeability to hydrogen (Jakobsson 2012). Although Fe loss from the sample material to the Pt capsule could pose a problem, this is not likely to be significant given the relatively high oxidation state (fO_2 > FMQ + 1) and low temperature (T ≤ 960°C) of experimental runs. Approximately 0.02g of Mt-1 and A-190+Fe+trace mix (1:3 by weight) were sealed together into 2.0mm o.d./1.8mm i.d. Pt capsules with 11 wt. % distilled H_2O, added using microsyringe. The Pt capsules had one end triple crimped and welded, and the other single crimped and sealed by welding after the powdered starting material and H_2O had been added. The capsules were weighed before and after welding to ensure no weight loss occurred during welding. The capsules were then placed in a 200°C furnace and reweighed to ensure that they were fully sealed.

Mixes of Ni-NiO and Fe_3O_4-Fe_2O_3 in 50:50 and 15:85 ratios by weight were prepared. The sealed Pt capsules were loaded into custom-designed cold-sealed 9x23mm Ag capsules with 3mm-thick walls, together with the desired redox buffer and 30 µL distilled H_2O to ensure fluid saturation in the outer capsule. Care was taken to ensure the inner capsule was positioned centrally within the outer capsule. The outer Ag capsules were then cold-sealed in the same fashion as described above.

4.2.3.3 Piston-cylinder experiments

All piston-cylinder experiments were carried out using end-loaded piston cylinders at the Research School of Earth Sciences at the Australian National University. Both the single- and double-capsule configurations were loaded into a graphite furnace using a talc sleeve to isolate the capsule from the graphite heater, using MgO as a filler to ensure the capsules were positioned centrally. Two pressure-medium configurations were applied for the single- and double capsule assemblies (Figure 4-1). The smaller Re-ReO_2 buffered assemblies were enclosed in a pyrex sleeve, with an additional NaCl sleeve, surrounding the pyrex, to ensure that pressure was distributed evenly around the sample. The outer diameter of this assembly is 5/8 inch. The larger double capsule assemblies were inserted directly into a talc sleeve with an outside diameter of ¾ inch. The single- and double-capsule assemblies were wrapped in a thin teflon foil to minimise friction and inserted into 5/8 inch and ¾ inch pressure vessels respectively. A graphite disk was placed at the base of the assembly to improve the formation of a reliable heating circuit.

Experiments were performed using a "piston-out" routine. First, approximately 1.5 kbar was applied to the cell. Next, the sample was gradually heated at 50°C per minute to the desired temperature. Pressure was applied synchronously so that the final pressure was reached at 900°C, slightly lower than the desired temperature. Temperature was controlled using calibrated, type-C, $W_{95}Re_5$-$W_{74}Re_{26}$ thermocouples and a Eurotherm controller, which is accurate to within 3°C. The thermocouple was inserted axially into the assembly through a two-holed alumina

ceramic sleeve and the temperature was measured at the top of the capsule. The thermocouple fits into a pit drilled into the lid of the custom-designed capsule. A small amount of crushable alumina was packed into the base of this thermocouple recess to minimise drift due to contamination. Pressure was kept constant during runs to ±0.5 kbar by manual adjustment when necessary. Experiments were terminated by turning off the power to the apparatus, quickly quenching to below 200°C in less than 10 s and subsequently bleeding off the pressure over approximately 10 minutes.

After quenching, the entire capsules were mounted in epoxy resin. The resin was left to dry, after which the samples were carefully wet ground with a set of abrasive papers. All experiments yielded fluid upon opening the capsules. The samples were then polished with 9, 6, 3 and 1 µm diamond pastes consecutively in the absence of water.

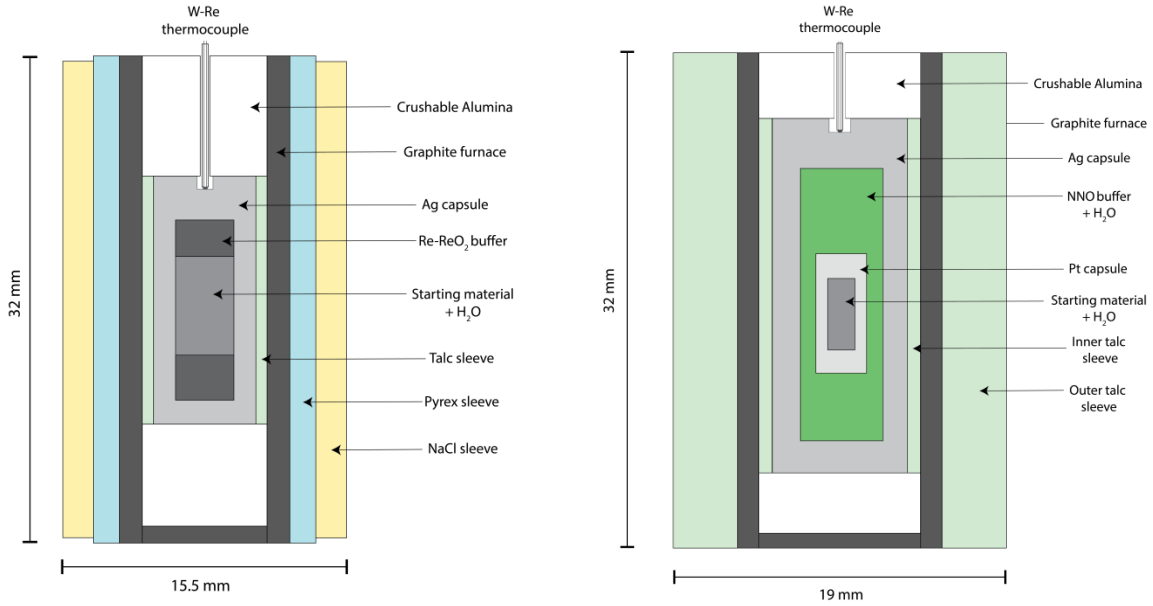


Figure 4-1: (A) The salt-pyrex assembly used in Re-ReO_2 buffered single-capsule experiments, showing the location of the sample within the graphite furnace, enclosed by a pyrex and NaCl sleeve; (B) the talc-only assembly used in NNO- and MH-buffered double-capsule experiments, showing the location of the sample in the inner Pt capsule within an outer Ag capsule containing redox buffer inside the graphite furnace, enclosed by a talc sleeve.

4.2.4 Analytical techniques

4.2.5 SEM

Run products were examined using a Zeiss EVO 15LS scanning electron microscope in the Imaging and Analysis Centre at the Natural History Museum, London. Electron-dispersive spectroscopy (EDS) analysis was used in conjunction with back-scattered electron (BSE) imaging to identify and determine the composition of the phases. Analytical conditions were 20 kV accelerating voltage, 3nA sample current and a 1 µm spot size.

4.2.5.1 EPMA

A Cameca SX-100 electron microprobe, housed at the Natural History Museum, London, was used to measure major and some trace element contents. Silicon, Al, Mg, Fe, Ca, P, Ti, Mn, Na, Cr, S, K and V were determined in both titanomagnetite and silicate glass. Alkali elements, such as Na and K, were included in the analysis of titanomagnetite to be sure no contamination by glass occurred. A 20 kV accelerating voltage, 10 nA sample current and focused electron beam with 1 μm spot size was used for magnetite analysis. In some experiments, traverses were conducted to measure the major element composition at the magnetite seed rim. Traverses started in the interior of magnetite seed and ended in silicate glass, with approximately 2 μm spacing between analyses. For glass analysis, analytical conditions were 20kV, 2nA and a defocused (10-20 μm) beam in order to minimise migration of alkalis.

4.2.6 LA-ICP-MS

The trace element compositions of magnetite and glass were analysed using LA-ICP-MS in the LODE Research Facility at the NHM, London using a New Wave Research 193nm excimer laser coupled to an Agilent 7700x quadrupole ICP-MS. Laser energy was regulated to provide a laser fluence at the sample site of 3.2 J/cm^2. The ICP-MS was tuned prior to analysis to ensure low backgrounds and low oxide production levels.

For magnetite analyses the laser was focused into a 50 x 3 micron rectangular beam oriented parallel to the magnetite-glass interface of a straight-sided magnetite seed. After background counting for 30s, the laser was switched on and the sample traversed continuously beneath the laser at a rate of 1 micron/second. All traverses were started in the interior of the magnetite crystal and ended by ablating glass or other phases around the magnetite seed (Figure 4-2); this avoided contamination by previously ablated glass that could be deposited at the magnetite-glass interface.

For glass analysis, the laser was operated with a 30-50 micron spot size, a pulse rate of 10 Hz, and a fluence of 3.5 J/cm^2. Fe and Ca were used as internal standards for the magnetite and glass analyses respectively, measured previously via EPMA. GSD-1g was used as the external standard for magnetite and glass analyses. GSE-1g and NIST 612 were used as secondary reference materials for monitoring for magnetite and glass analysis respectively.

The isotopes analysed were ^{23}Na, ^{24}Mg, ^{27}Al, ^{29}Si, ^{31}P, ^{39}K, ^{43}Ca, ^{45}Sc, ^{49}Ti, ^{51}V, ^{52}Cr, ^{55}Mn, ^{57}Fe, ^{59}Co, ^{60}Ni, ^{63}Cu, ^{65}Cu, ^{66}Zn, ^{69}Ga, ^{72}Ge, ^{75}As, ^{89}Y, ^{90}Zr, ^{93}Nb, ^{95}Mo, ^{115}In, ^{118}Sn, ^{121}Sb, ^{175}Lu, ^{177}Hf, ^{181}Ta, ^{182}W, ^{208}Pb, ^{232}Th and ^{238}U in both magnetite and glass. All isotopes were analysed using a 0.1 second dwell time, apart from As, Y, Sb, Lu and Th which were measured using a 0.3 second dwell time

on each isotope. For most traverses, element concentrations were recorded approximately every 2.5 seconds. Data were reduced using an excel spreadsheet developed in house, in a 'natural' fashion, such that each individual ablation slice was processed individually.

4.3 Experimental Results

4.3.1 Determining interface concentrations using LA-ICP-MS

An image of a magnetite seed, post-analysis with 50 x 3 μm LA-ICP-MS profile is provided in Figure 4-2).

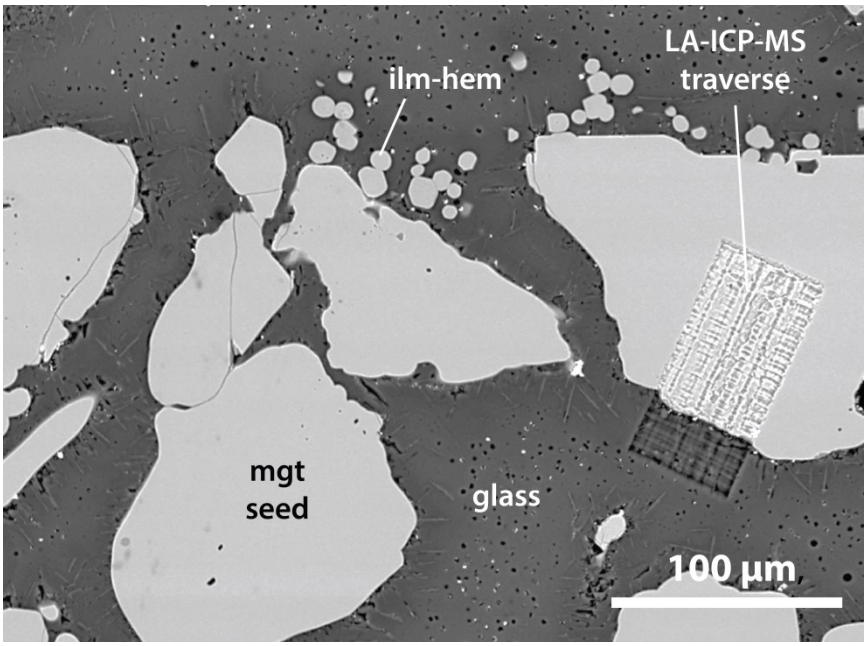


Figure 4-2: SEM Back-scattered electron image of magnetite from experiment RSM-PC-30 (fO_2 = MH, T = 960C, P = 12 kbar) post-analysis with LA-ICP-MS showing traverse of 50x3 micron profile.

The sharpness of the magnetite-melt interface was interpreted by studying the profiles of elements known to not partition strongly into magnetite but that were abundant in the melt, for example Na and Si. An example of a sharp, clear interface vs. a poor interface is given in Figure 4-3. Profiles which clearly underwent significant melt contamination close to the magnetite-melt interface as evinced in this manner were discarded.

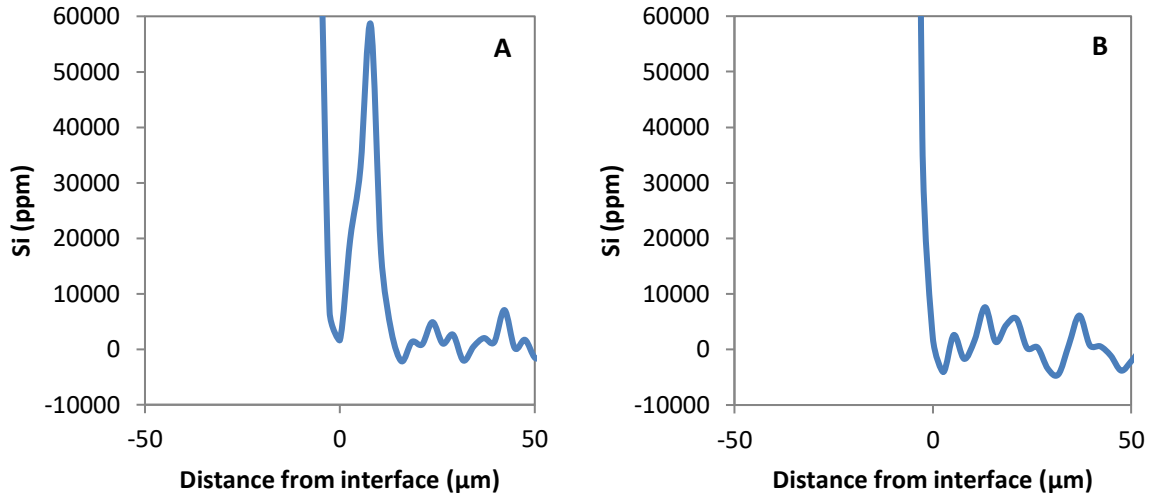


Figure 4-3: Si concentration with distance from the magnetite-melt interface measured using a LA-ICP-MS traverse across: (A) a less sharp interface contaminated by silicate melt (Experiment RSM-PC-37 – Line 2); and (B) a sharp, clean interface (RSM-PC-37 – Line 12). Shaded region is part of traverse within magnetite crystal, unshaded is part of traverse in glass.

Because the cut of each magnetite seed differed in 3D section, some profiles were flatter and some were steeper; thus profiles do not consistently fit the diffusion equation (Equation 3-7 in Chapter 3). Instead, linear trends projected through the magnetite concentration profile passing through the interface were considered the most reliable and consistent means to assess the interface concentration of the profile (Figure 4-4). The sensitivity of diffusion rate to fO_2 (see section 3.3.4) had an impact on the accuracy of estimating the concentration at the magnetite-melt interface. In the most oxidised experiments at fO_2 = MH, element diffusion is fastest so that the concentration of all elements was elevated further from the interface, typically 40 µm or more. Thus, the concentration at the interface could be projected over a greater distance of the LA-ICP-MS traverse at fO_2 = MH than in experiments conducted at lower fO_2.

This approach was generally successful, particularly for elements with a magnetite-melt partition coefficient greater than 1. However, for elements with partition coefficients less than 0.1, analysing the composition of the rim proved more taxing due to contamination from the glass. If the profile was projected to the interface over a sufficiently long distance, sometimes it was possible to ignore parts of the profile influenced by melt contamination and project through this region to the interface (Figure 4-5). Consequently, it was generally easier to measure a greater number of elements accurately at MH where diffusion was faster so it was possible to project to the interface using a substantial distance of profile (e.g. > 30 micron). If an element concentration fluctuated below 0 along the linear projection, the result was considered below detection limit. Arsenic and Sb could not be reliably measured above the detection limit in magnetite seeds in any experiments using this approach and are therefore not reported.

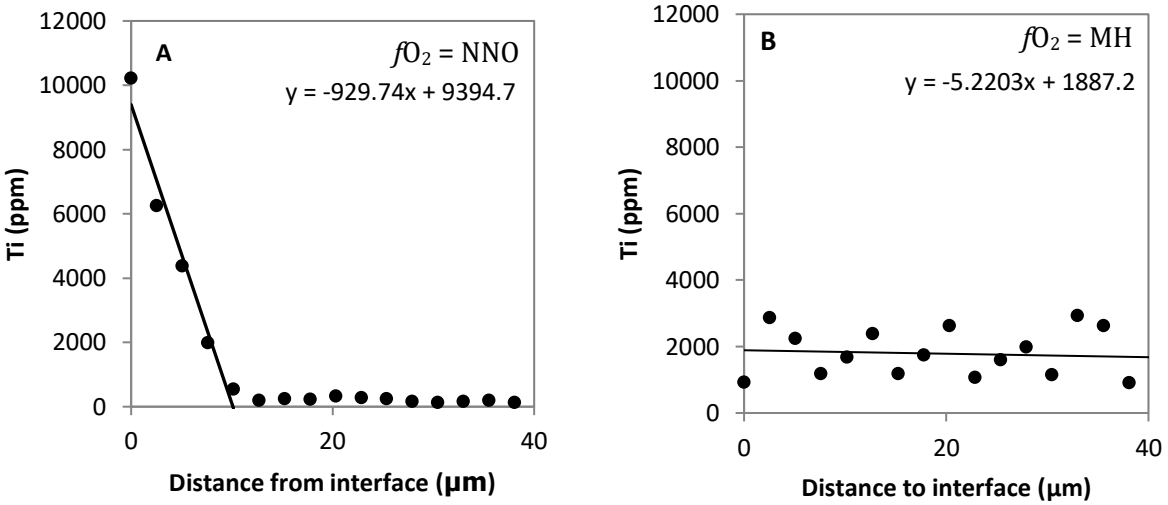


Figure 4-4: Ti concentration with distance from the magnetite-melt interface measured using a LA-ICP-MS traverse of magnetite seed from: a) Experiment RSM-PC-47 – Line 1 conducted at fO_2 = NNO, T = 920°C and 12 kbar; and b) RSM-PC-49 – Line 3, conducted at fO_2 = MH, T = 920°C and 12 kbar. The distance of the traverse to which the concentration at the interface was projected is > 40 microns for the experiment at MH, whereas this distance is substantially shorter (10 microns) for the experiment conducted at NNO, owing to slower diffusion at lower fO_2.

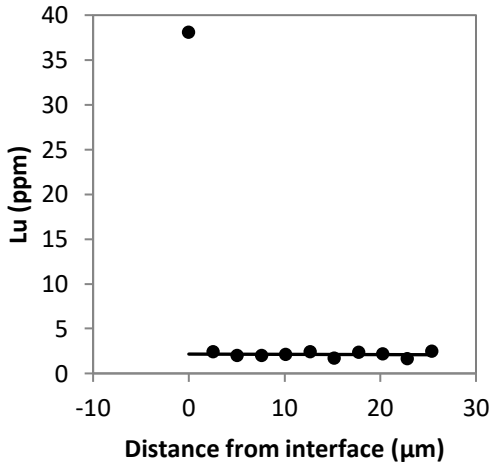


Figure 4-5: Lu concentration with distance from the magnetite-melt interface measureed using a LA-ICP-MS traverse (Line 4) of a magnetite seed in experiment RSM-PC-30. There is contamination from the melt close to the interface as a result of the large difference between the concentration of Lu in the melt and magnetite, thus this part of the traverse was ignored when projecting the concentration along the traverse to the magnetite-melt interface. Shaded region is part of traverse within magnetite crystal, unshaded is part of traverse in glass.

4.3.2 Demonstrating that magnetite seed rim concentration is at equilibrium

Experiments buffered at Re-ReO_2 contained both magnetite seeds and magnetite crystals which nucleated during the experiment. Although the latter were too small to analyse reliably with LA-ICP-MS, it was possible to check the compositions determined using LA-ICP-MS at the rim of the magnetite seeds against that of the nucleated crystals determined using EPMA for elements detectable using both techniques. For most experiments, there is good agreement between the chemical composition of the magnetite seeds determined using LA-ICP-MS and the nucleated magnetite crystals using EPMA. Assuming that the nucleated magnetite crystals are in

equilibrium with the melt, this supports the assumption that magnetite at the rim of the magnetite seeds is also in equilibrium with the melt. Furthermore, this strong correlation between EPMA and LA-ICP-MS for those elements detectable by both techniques supports the accuracy of the LA-ICP-MS data (Figure 4-6).

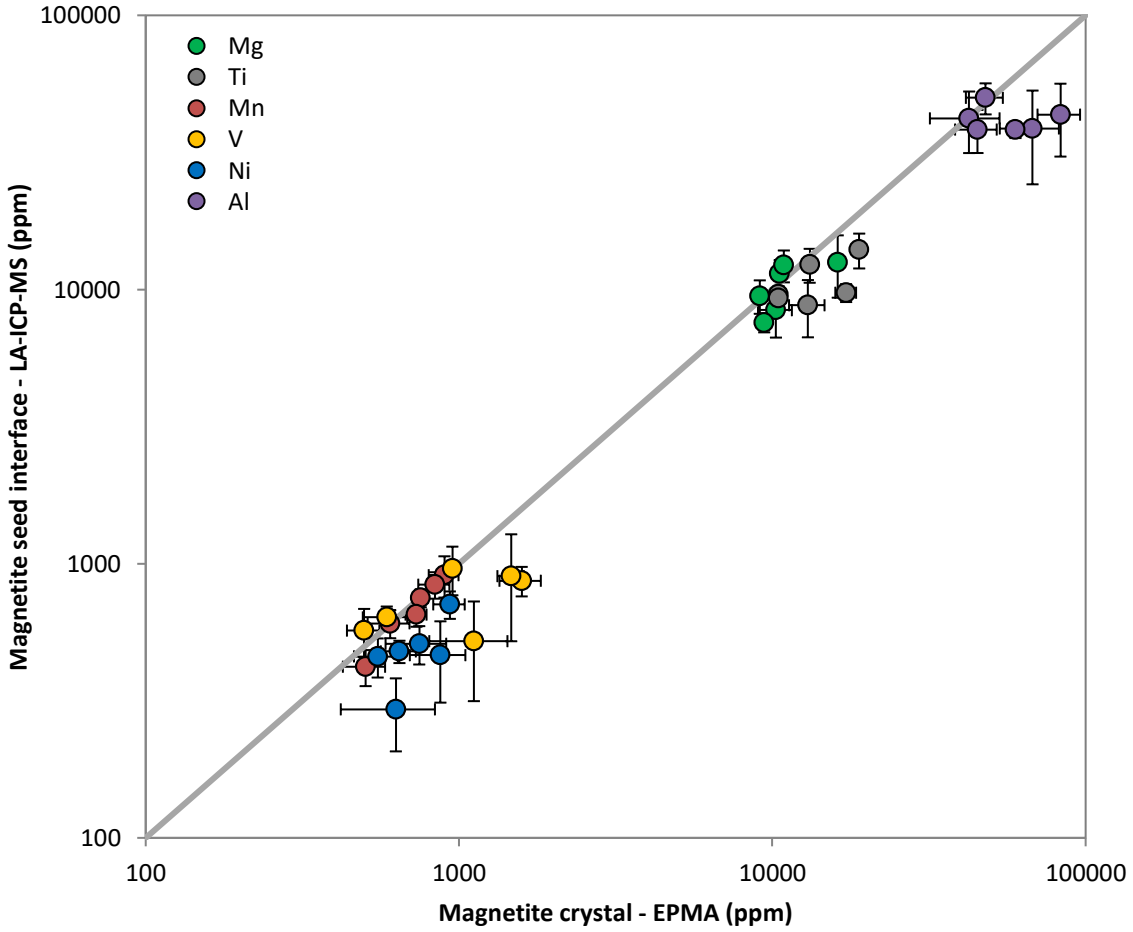


Figure 4-6: Concentration in magnetite crystal nucleated during experimental run determined using EPMA vs. concentration at the magnetite-melt interface of magnetite seed determined using LA-ICP-MS for a suite of elements detectable by both analytical techniques for experiments conducted at Re-ReO_2. Grey line is 1:1 and error bars represent ± 1σ.

4.3.3 Time series

Two experiments were conducted at fO_2 = Re-ReO_2, T = 920°C, P = 12 kbar and 11-12 wt. % over different timescales, one for the standard experiment duration of 48 hours (RSM-PC-37) and the other for 84 hours (RSM-PC-46). Additionally, two experiments were conducted over different timescales at RRO, 12 kbar and 960°C, one for the standard duration of 48 hours (RSM-PC-43) and one for 28 hours (RSM-PC-36). Experimental run products consisted of magnetite seeds + nucleated magnetite crystals + glass. Magnesium, Ti, Mn and Al could be determined using EPMA in nucleated magnetite crystals and glass in all experiments so that partition coefficients could be

determined for these elements. In the first set of experiments conducted at 920°C, RRO and 12 kbar, the partition coefficients of these elements do not vary significantly between 48 and 84 hours, less than one standard deviation for D(Ti) and D(Mn) and less than two standard deviations for D(Mg) and D(Al). In the second set conducted at RRO, 960°C and 12 kbar, partition coefficients vary by less than one standard deviation for Mg, Ti and Mn, and less than two standard deviations for Al, for experiments conducted over 28 hours and 48 hours. This suggests that a close approach to equilibrium was attained by 28 hours, substantially within the standard experiment duration of 48 hours.

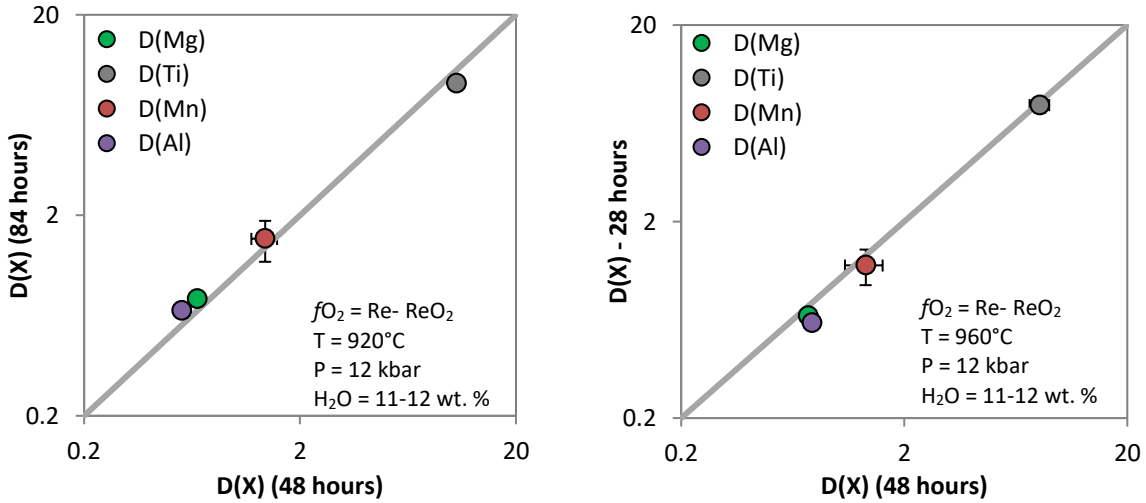


Figure 4-7: Comparison of experimentally determined partition coefficients (D) from EPMA analyses of titanomagnetite nucleated during the experiments and glass for two sets of experiments conducted at the same fO_2, T, P and H_2O content, but over different timescales. Experimental conditions are given in the bottom right of each plot. Grey line is 1:1 and error bars = 1σ.

4.3.4 Loss of elements to capsule

Some elements were evidently lost during the experiments and could present issues when determining equilibrium partition coefficients. There was clearly Cu loss during experiments as evinced by < 12 ppm in the glass despite initial doping of the starting composition at 100 ppm and its moderately incompatible behaviour in magnetite. Notwithstanding this, Cu loss does not seem to have a significant effect on the calculated magnetite-melt partition coefficients for Cu in this study, producing results which are similar to those reported in Liu et al. (2015). Some other elements were variably lost as a function of fO_2. For example, Sn, In, As and Sb were abundant in the melt in experiments at RRO and MH, but were strongly depleted at NNO such that the concentration in the glass was commonly below the detection limit of LA-ICP-MS. There is a transition in the dominant valence state from Sn^{4+} to Sn^{2+} in peraluminous haplogranitic melts at FMQ + 2.4 (Linnen et al., 1994), which could be responsible for the bulk loss of Sn observed at NNO.

4.3.5 Pressure series

All experiments in this series were conducted at T = 940°C, fO_2 = Re-ReO_2 and 11-12 wt. % bulk H_2O, but variable pressure between 12-6 kbar. Experiments consist of magnetite seeds + nucleated magnetite crystals + glass ± orthopyroxene ± clinopyroxene (Table 4-3).

A glass phase was abundant in all experiments. The difference between the EPMA analytical total and 100% can be used to estimate the amount of dissolved water in the melt. With decreasing pressure, there is a general increase in glass total from 88.4% to 93.3% between 12 and 6 kbar which suggests that the H_2O content dissolved in the melt decreased with decreasing pressure (Figure 4-8), consistent with expected melt water solubility behaviour. This supports the assumption of fluid saturation for all experiments. Saturation in an aqueous fluid phase is important to reach the fO_2 imposed by the external buffer. Glass compositions are relatively homogeneous with a standard deviation < 15% for all major elements. Texturally, glasses were relatively vesicular. Some larger vesicles show evidence of crystal inclusions, which could imply that the vesicles were stable at high pressure and not simply a product of degassing upon quenching (Figure 4-10). Some experiments showed minor evidence for quench crystallisation, in the form of sub-micron particles scattered throughout the glass (e.g. Figure 4-10D). Unfortunately, this is difficult to avoid in Fe-rich starting compositions like those used in this study. However, it is important to emphasise that the amount of quench crystallisation was only minor and therefore unlikely to significantly modify the glass composition. All melt compositions are granitic, with SiO_2 content from 65-69% when normalised to 100% on an anhydrous basis.

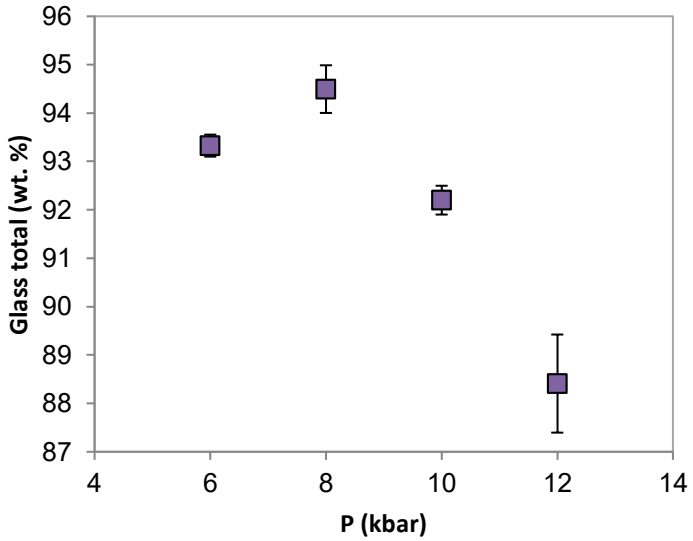


Figure 4-8: Analytical total for glass phase determined using EPMA as a function of P between 6 and 12 kbar in experiments conducted at fO_2 = RRO and T = 940°C. Dissolved H_2O content in the melt phase during experiments can be inferred by difference in total and 100%. This suggests that H_2O content dissolved in the melt decreases with decreasing pressure.

Both Re and ReO_2 were present in the run products at the end all RRO experiments indicating that all experiments remained buffered (Figure 4-9).

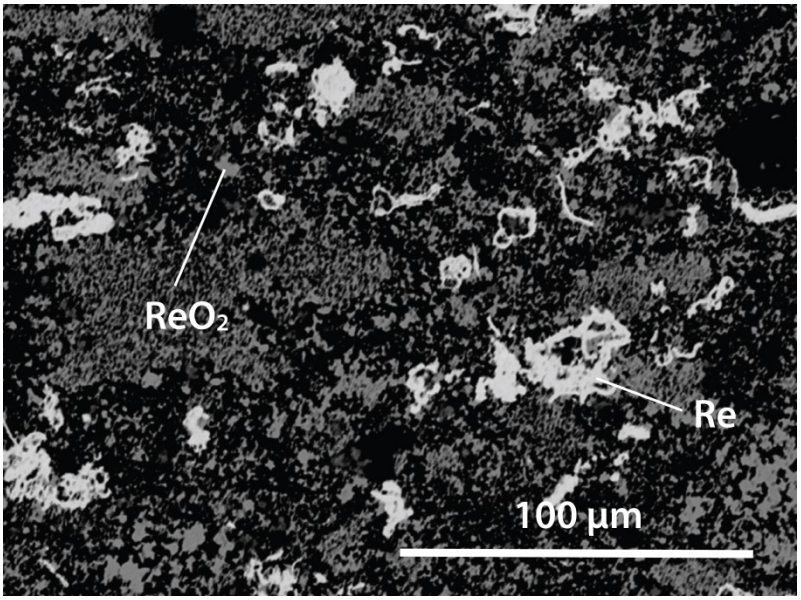


Figure 4-9: Back-scattered electron image showing the presence of both Re (bright grey) and ReO_2 (dark grey) buffer phases in the run products from experiment RSM-PC-32 (940/Re-ReO_2/12kbar/fluid-saturated)

Magnetite seeds generally have sharp boundaries, suggesting that there has not been significant crystallisation or resorption at their boundaries. Titanomagnetite crystals nucleated during experiments are typically 10-15 µm across and rounded in shape. Titanomagnetite contain a significant Al component (Al cpfu ~ 0.4). With decreasing pressure between 12 and 6 kbar, there is a progressive increase in Al cations per formula unit (cpfu) in nucleated titanomagnetite crystals, increasing from 0.34 ± 0.02 to 0.65 ± 0.12. Although there is some variation in the number of Mg, Ti and Mn cations per formula unit this is not large and does not show a progressive change with pressure. Notwithstanding this, there is a small decrease in the $a Fe_3O_4$ in nucleated titanomagnetite grains with decreasing pressure, decreasing from 0.62 at 12 kbar to 0.56 at 6 kbar.

Orthopyroxene formed only in experiments at 12 kbar and 8 kbar and comprises tabular crystals 100 µm in length. Compositionally orthopyroxenes are predominantly enstatite-ferrosilite in composition with a dominant enstatite component (62-66%) and lesser ferrosillite component (34-38%). Orthopyroxenes also have a small Al component. Clinopyroxene was only observed in RSM-PC-40 at 8 kbar and is present as smaller (< 20 µm), subhedral grains. All clinopyroxenes are aegerine-augite with a high Ca-Mg-Fe (QUAD) component (X_{QUAD} > 70% - Morimoto et al., 1988). With decreasing pressure, there is a general increase in crystallisation, accompanied by a decrease in grain size of crystalline phases.

Table 4-3: Table describing phases present in experiments from pressure series (conducted at fO_2 = RRO, T = 940°C between 12 and 6 kbar), fO_2 series (conducted at fO_2 = NNO, RRO and MH at P = 12 kbar and T = 960°C and 920°C) and two experiments with added FeS to starting material at fO_2 = NNO and MH, P = 12 kbar and T = 920°C

Experiment	T (°C)	fO_2	Pressure (kbar)	Phases
Pressure series				
RSM-PC-32	940	RRO	12	Mgt Seeds, Mgt crystals, Glass, OPX
RSM-PC-39	940	RRO	10	Mgt Seeds, Mgt crystals, Glass
RSM-PC-40	940	RRO	8	Mgt Seeds, Mgt crystals, Glass, OPX, CPX
RSM-PC-41	940	RRO	6	Mgt Seeds, Mgt crystals, Glass
fO_2 series				
RSM-PC-31	960	NNO	12	Mgt Seeds, Glass, CPX, Biotite
RSM_PC-43	960	RRO	12	Mgt Seeds, Mgt crystals, Glass, OPX
RSM-PC-30	960	MH	12	Mgt Seeds, Hem-Ilm, Glass, CPX
RSM-PC-47	920	NNO	12	Mgt Seeds, Glass, CPX, Biotite
RSM_PC-37	920	RRO	12	Mgt Seeds, Mgt crystals, Glass
RSM-PC-49	920	MH	12	Mgt Seeds, Hem-Ilm, Glass, CPX
fO_2 series with added FeS				
RSM-PC-51	920	NNO	12	Mgt Seeds, Glass, CPX, Biotite, Amphibole, FeS
RSM-PC-52	920	MH	12	Mgt Seeds, Hem-Ilm, Glass, CPX

Abbreviations: RRO = Re=ReO_2; NNO = Ni-NiO; MH = =Fe_3O_4-Fe_2O_3.

In most cases, partition coefficients calculated using the rim of the magnetite seeds and the nucleated titanomagnetite crystals are within 1 standard deviation (σ) the same for all elements detectable by both EPMA and LA-ICP-MS. This breaks down for Al and Ti in experiments at 8 and 6 kbar, where D(Ti) and D(Al) calculated using the rim of the magnetite seed are instead within 2σ of those calculated using nucleated titanomagnetite crystals.

Mg, Ti, Mn and Al could be detected by EPMA in magnetite nucleated during the experiment and glass so that partition coefficients for these elements could be determined (Table 4-4). D(Mg) and D(Al) are slightly greater at 6 and 8 kbar (0.96 ± 0.12 and 1.47 ± 0.15 respectively for Mg and 1.10 ± 0.23 and 0.82 ± 0.09 respectively for Al) than at 10 and 12 kbar (0.81 ± 0.014 and 0.86 ± 0.030 respectively for Mg and 0.60 ± 0.003 and 0.53 ± 0.039 respectively for Al). This variation, however, is not substantial and approximately 2σ. Conversely, D(Ti) is slightly less at 6 and 8 kbar than 10 and 12 kbar, however, this variation is less substantial and also within 2σ. D(Mn) does not vary by more than 1σ between 12 and 6 kbar.

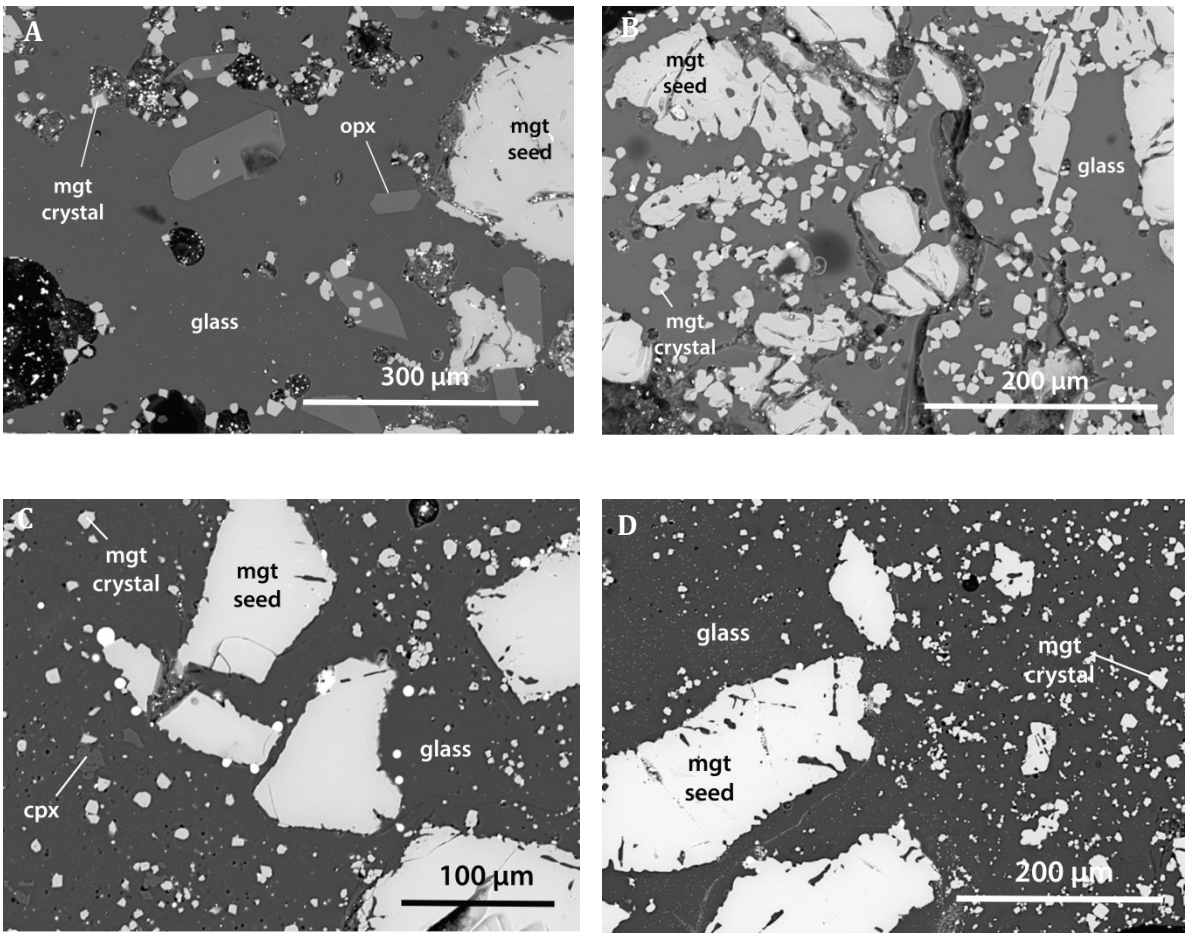


Figure 4-10: Back-scattered electron images of experiments in the pressure series at T = 940 °C, fO_2 = Re-ReO_2 and 11-12 wt. % bulk H_2O and variable pressure at (A) 12 kbar (RSM-PC-32), (B) 10 kbar (RSM-PC-39), (C) 8 kbar (RSM-PC-40) and (D) 6 kbar (RSM-PC-41).

In this set of experiments the following elements could be consistently analysed at the rim of magnetite seeds using LA-ICP-MS: Mg, Al, Sc, Ti, V, Mn, Co, Ni, Cu, Zn, Ga, In and Sn (Table 4-5). Scandium exhibits similar partitioning behaviour to Al and is greater at 6-8 kbar than 10-12 kbar, however, again this variation is not substantial. Conversely, V is increasingly partitioned into magnetite at higher pressure, but the variation in D(V) between 6 and 12 kbar is less than 2σ. Similar to the partitioning of Mn, D(Co), D(Ga), D(Sn) and D(Cu) do not vary by more than 1σ over the range of pressures investigated, however, D(Ni) is generally greater at higher pressure (D(Ni) = 87.9 ± 11.3 at 12 kbar) than at lower pressure (D(Ni) = 34.4 ± 12.0 at 6 kbar). D(Zn) and D(In) are greatest at 8 kbar, but otherwise do not vary by more than 1σ for experiments conducted at 6, 10 and 12 kbar. Zirconium, Nb, Hf, Ta, Ge and Lu, were also analysed at the rim of magnetite seeds, however, owing to the low partition coefficients of these elements, the partition coefficients should be viewed with caution. Nevertheless, the partition coefficients for these elements do not vary by more than 2σ over the range of pressures investigated indicating that pressure does not exert a strong control on the magnetite-melt partitioning. Furthermore, given

that the melt H_2O content varies from approximately 11.6 wt. % to 6.7 wt. % it can be inferred that the effect of water content also has a negligible effect on magnetite-melt partitioning within this range. The water content has also been shown to have no effect on the magnetite-melt partitioning of vanadium (Arato and Audetat., 2017a). All other elements not reported were consistently below the detection limit using the analytical approach.

4.3.6 fO_2 series

4.3.6.1 Experiments without added FeS

The first set of the fO_2 series experiments were conducted at 960°C, H_2O-saturation, 12 kbar and three fO_2 buffers: Ni-NiO (NNO), Re-ReO_2 (RRO) and Fe_3O_4-Fe_2O_3(MH) which correspond to FMQ + 0.72, FMQ + 2.66 and FMQ + 5.34 at 960°C (fO_2 values converted to ΔFMQ values using Hemingway (1990) for FMQ buffer). Ni and NiO, Re and ReO_2, and Fe_3O_4 and Fe_2O_3 were present in the run products at the end all experiments indicating that all experiments remained buffered (Figure 4-11). Experimental run products consist of magnetite seeds ± nucleated magnetite crystals + glass ± orthopyroxene ± clinopyroxene ± biotite ± hematite-ilmenite (Table 4-3).

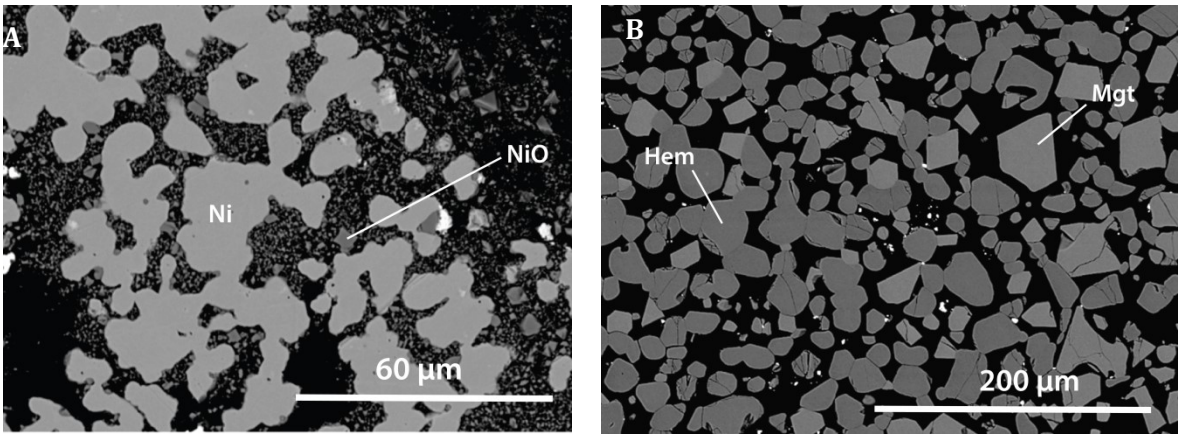


Figure 4-11: Back-scattered electron images showing the presence of (A) Ni (light grey) and NiO (dark grey) buffer phases in the run products from experiment RSM-PC-31 (960°C/NNO/12 kbar/fluid-saturated); and (B) both Fe_3O_4 (mgt) (light grey) and Fe_2O_3 (hem) (dark grey) buffer phases in the run products from experiment RSM-PC-30 (960°C /MH/12 kbar/fluid-saturated).

Magnetite seeds have variable morphology at different fO_2. At NNO, magnetite seeds are strongly resorbed and generally have more undulated boundaries. Although it appears there may be nucleated titanomagnetite crystals at NNO, it is likely that these are in fact remnants from resorbed magnetite seeds based on their variable composition. With increased fO_2, the stability of titanomagnetite increases and, at RRO, magnetite seeds have sharp, straight boundaries, suggesting that the original shape of the seeds has not been modified. At the highest fO_2, although the magnetite seeds remain a stable phase, ilmenite-hematite solid solutions represent the only Fe-Ti phase nucleated during the experiment. These nucleate both throughout the glass and

around the rims of existing magnetite seeds. Thus, when laser ablation profiles were measured, profiles were chosen where ilmenite-hematite crystals were not nucleated on the magnetite seed boundary.

Titanomagnetite crystals nucleated during the runs were only present at RRO. These contain a dominant magnetite component ($a Fe_3O_4$ = 0.82-0.61), and minor ulvospinel (Ti) and hercynite (Al) components. At T = 960°C, with increasing fO_2 there is a progressive increase in Mg cpfu and Mn cpfu. Fe^{3+} cpfu decreases between NNO and RRO, but increases between RRO and MH. Similarly, the $a Fe_3O_4$ decreases from 0.82 at NNO to 0.61 at RRO, then increases to 0.76 at MH. Conversely, Al increases between NNO and RRO and decreases between RRO and MH. Fe^{2+} and Ti cpfu remain relatively constant between NNO and RRO, but decrease between NNO and MH.

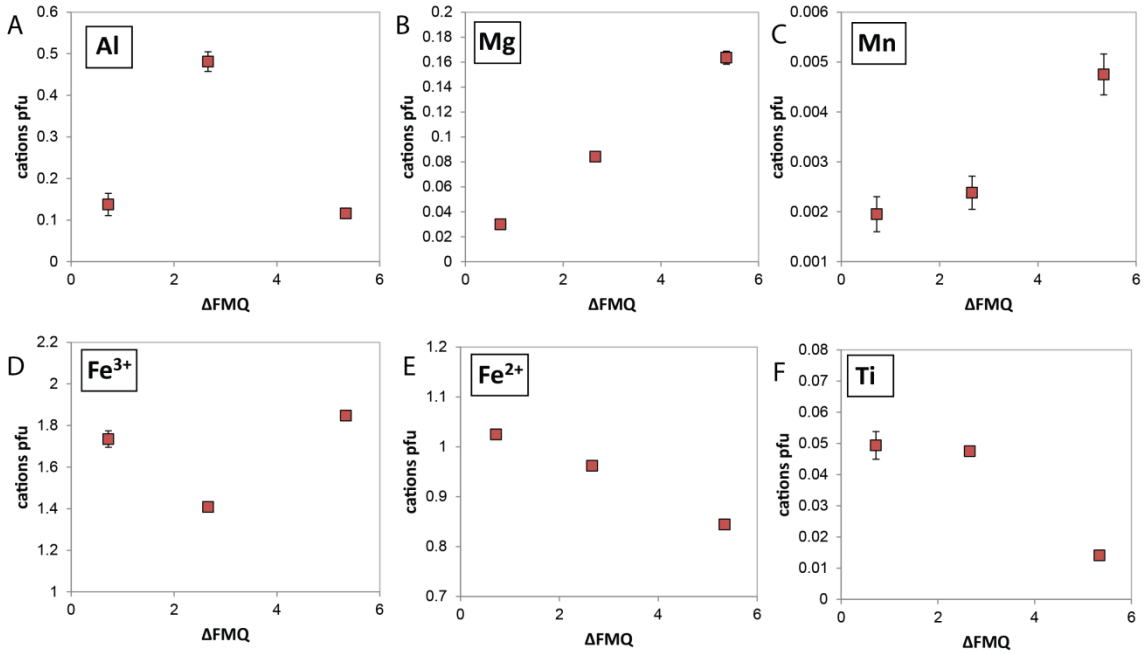


Figure 4-12: Titanomagnetite cations per formula unit for (A) Al, (B) Mg, (C) Mn, (D) Fe^{3+}, (E) Fe^{2+} and (F) Ti as a function of fO_2 in experiments at T = 960°C, P = 12 kbar and H_2O-saturated.

Ilmenite-hematite crystals nucleated at MH were generally small (< 15 µm) and rounded in shape. They contain a dominant hematite component (50%), significant ilmenite component (47-48%) and a minor Mg component ($MgTiO_3$) (<2%). They were not large enough to accurately analyse with LA-ICP-MS.

Clinopyroxene is a minor phase in experiments at NNO and MH. At MH, it is present as small (< 10 µm, subhedral grains, whereas at NNO there are some larger (~20 µm), sub-euhedral grains. All clinopyroxenes have a dominant Ca-Mg-Fe (QUAD) component (0.74-0.9) and small aegerine component (0.06-0.17) (Fe3+ after Droop, 1987; site assignment after Morimoto et al., 1988).

Orthopyroxene was identified in the experimental run products at fO_2 = RRO and T = 960°C, but was not apparent in experiment RSM-PC-37 conducted at fO_2 = RRO, but at 920°C. However, it is worth noting that experiment RSM-PC-37 was difficult to prepare for analysis and a large amount of material was lost during post-run sample preparation (Figure 4-16), thus it is likely that orthopyroxene could have been missed during inspection of the run products.

Biotite occurs as small (< 20 μm), subhedral grains and was present in all runs at NNO, and one experiment at MH (RSM-PC-52 – contained added FeS). Biotites are binary annite-phlogopite solid solutions in composition. At NNO, they have a slightly more dominant Fe-component (46-49%) and lesser Mg-component (45%), whereas at MH, biotite has a dominant Mg-component (60%) and significantly lesser Fe-component (29%). There is also a trace Ti- and Ca- component (< 2%).

Glass compositions are relatively homogeneous with a standard deviation < 10% for all major elements apart from Mg (Table 4-4). Texturally, glasses were relatively vesicular, with some larger vesicles showing evidence of crystal inclusions; again, the presence of vesicles suggests that fluid saturation was attained during experiments. Some experiments show minor evidence for quench crystallisation, particularly in RSM-PC-31 (Figure 4-15A), where sub-micron particles were scattered throughout some larger pools of glass. Notwithstanding this, the amount of quench crystallisation was only minor and therefore unlikely to significantly modify the glass composition upon quenching.

Mg, Mn, Al and Ti were detectable in both magnetite and glass with EPMA (Table 4-4). The partition coefficients for the divalent cations do not correlate and exhibit different trends with increasing fO_2. With increasing fO_2, there is not a significant change in D(Mg) between NNO and RRO, but an increase between RRO and MH. D(Mn), however, increases progressively with increasing fO_2 between NNO and MH (Figure 4-13). It is important to note the concentration of Mg in the glass at NNO is relatively heterogeneous compared to other elements, which could be a result of quench crystallisation of Mg-bearing phases in the experiment at NNO. This alters the precision of the partition coefficient for Mg at NNO. With increasing fO_2, D(Al) increases from NNO to RRO, then decreases between RRO and MH (Figure 4-14). D(Ti) decreases progressively with increasing fO_2 between NNO and MH (Figure 4-14).

All other elements were determined by analysing the rim composition of the magnetite seeds with LA-ICP-MS (Table 4-5). Like D(Mg), there is not a significant change in D(Co) between NNO and RRO, then an increase with increasing fO_2 between RRO and MH (Figure 4-13). Nickel and Zn, however, behave like Mn, with a progressive increase in their partitioning with increasing fO_2

(Figure 4-13). Between NNO and MH, Copper also is increasingly partitioned with increasing fO_2 between NNO and MH (Figure 4-13).

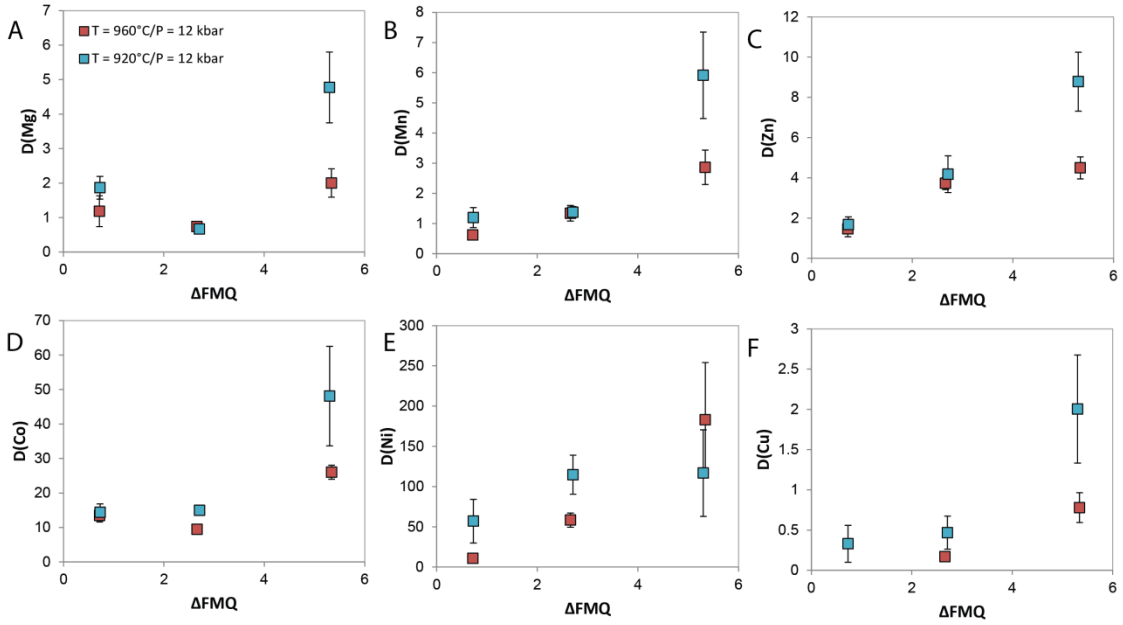


Figure 4-13: Effect of fO_2 on the magnetite-melt partition coefficients of (A) Mg, (B) Mn, (C) Zn, (D) Co, (E) Ni and (F) Cu at P = 12 kbar, T = 960°C and 920°C in H_2O saturated conditions. ΔFMQ is deviation in log fO_2 from the fayalite-magnetite-quartz buffer (calculated using Hemingway (1990)).

Scandium exhibits no significant variation in partitioning with fO_2 (Figure 4-14). Like D(Al), D(Ga) increases between NNO and RRO, increasing from 1.16 ± 0.20 to 3.46 ± 0.43, then decreases between RRO and MH to 0.16 ± 0.05 in experiments at T = 960°C (Figure 4-14). D(In), however, exhibits a slight decrease in partitioning at T = 960°C between RRO and MH, although there is no significant variation between NNO and MH at T = 920°C (Figure 4-14). There is no discernible variation in D(Lu) with increasing fO_2 (Figure 4-14). Cr could not be accurately measured in magnetite with EPMA, where there were large errors in the measurements, or with LA-ICP-MS where slow diffusion made it difficult to accurately determine the interface concentrations.

Like Ti, V exhibits a decrease in titanomagnetite-melt partitioning with increasing fO_2 from 84.5 ± 18.2 at NNO to 1.81 ± 0.25 at MH in experiments at T = 960°C (Figure 4-14). The HFSEs (Zr, Nb, Hf and Ta) all decrease with increasing fO_2, particularly between NNO and RRO for Nb and Ta (Figure 4-14). There is not a significant variation in the ratios of D(HFSE) to one another with fO_2 between NNO and MH, thus variable titanomagnetite-melt partitioning will affect the abundances of HFSE in the melt, but not their ratios to one another. Notwithstanding this, the partition coefficients for the HFSE are less than 1 and should therefore be viewed with caution, particularly at fO_2 = NNO, where slow diffusion meant the interface concentration was projected over a shorter distance. D(Mo) decrease with increasing fO_2, to such an extent that Mo was not

detectable at the interface of the titanomagnetite seeds at MH. In most cases, it was not possible to determine accurate Pb concentrations at the interface of the magnetite seeds. Nevertheless, in experiments where Pb could be measured there is no clear variation in D(Pb) with increasing fO_2. Cadmium was only detectable in titanomagnetite at MH, which suggests that its partitioning increases with increasing fO_2. Tin is compatible in titanomagnetite at RRO (D(Sn) = 1.0 ± 0.07) and MH (D(Sn) = 0.93 ± 0.15), showing no variation in partitioning over this range in fO_2, however, D(Sn) could not be determined at NNO owing to inferred element loss to the noble metal capsule.

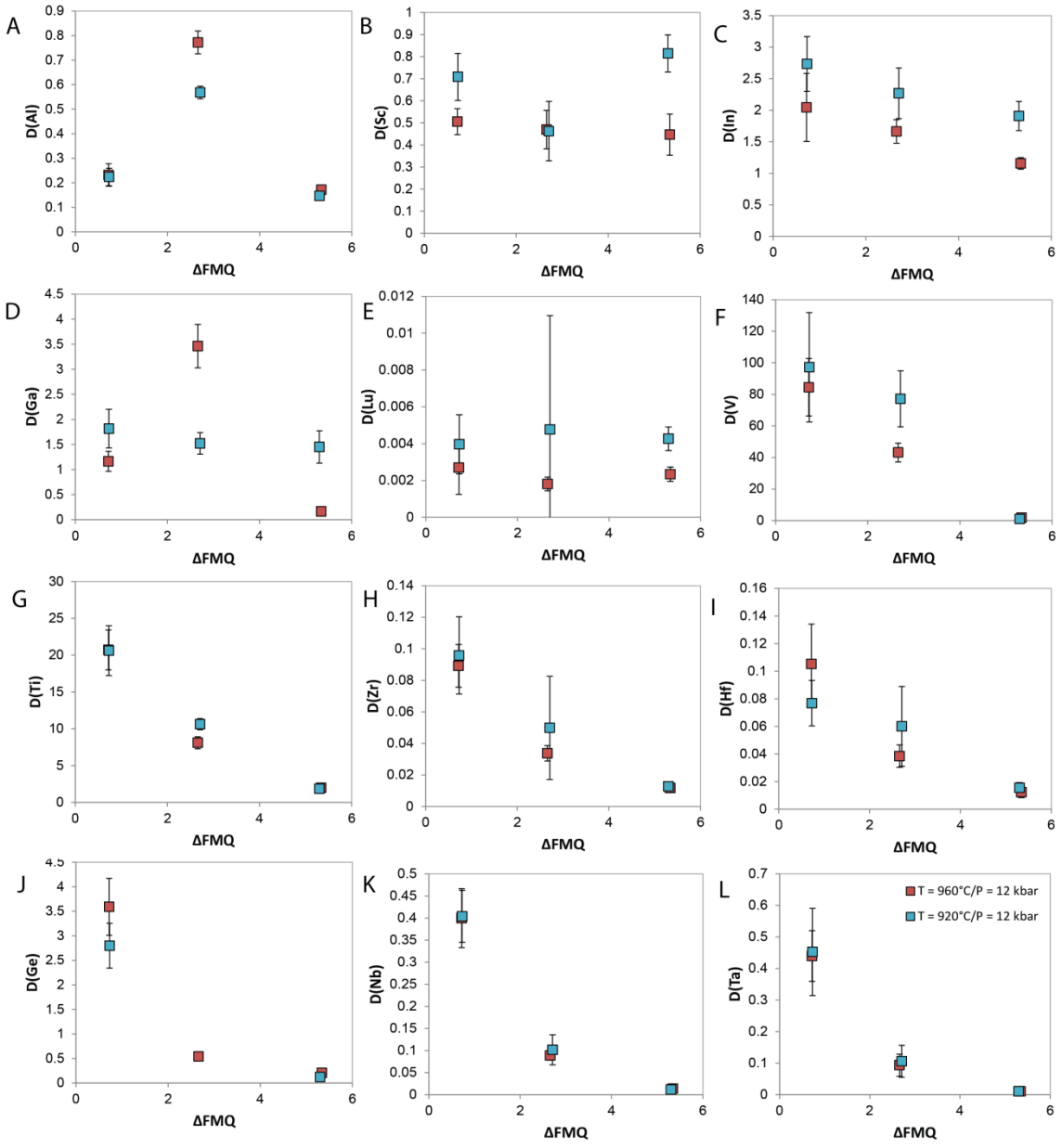


Figure 4-14: Effect of fO_2 on the magnetite-melt partition coefficients of (A) Al, (B) Sc, (C) In, (D) Ga, (E) Lu, (F) V, (G) Ti, (H) Zr, (I) Hf, (J) Ge (K) Nb and (L) Ta at P = 12 kbar, T = 960°C and 920°C in H_2O saturated conditions. ΔFMQ is deviation in log fO_2 from the fayalite-magnetite-quartz buffer (calculated using Hemingway (1990)).

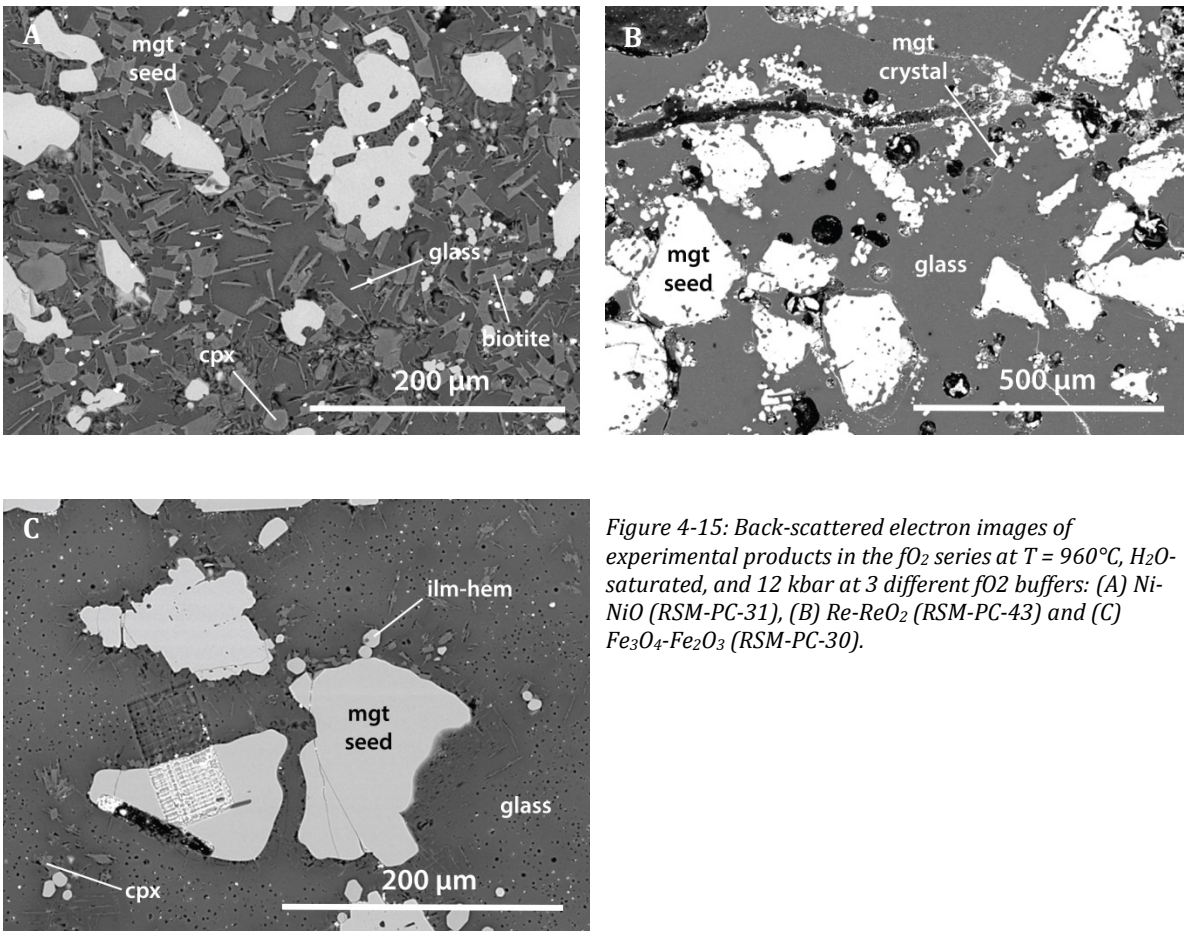


Figure 4-15: Back-scattered electron images of experimental products in the fO_2 series at T = 960°C, H_2O-saturated, and 12 kbar at 3 different fO2 buffers: (A) Ni-NiO (RSM-PC-31), (B) Re-ReO_2 (RSM-PC-43) and (C) Fe_3O_4-Fe_2O_3 (RSM-PC-30).

4.3.6.2 Experiments with added FeS to starting material

Experiments consist of magnetite seeds + glass ± amphibole + clinopyroxene + biotite ± hematite-ilmenite ± sulphide phase.

Magnetite seeds in experiments with added sulphur have a similar morphology to those in the experiments without added sulphur. However, at NNO, magnetite seeds were more strongly resorbed leaving only a few grains of skeletal magnetite that were too small to analyse with LA-ICP-MS. Ilmenite-hematite, clinopyroxene and biotite compositions are similar to those in experiments without added FeS at their respective fO_2. In the experiment with added FeS at NNO, a sulphide phase formed. This is Fe-rich (59.53 wt. % Fe), but also contains appreciable Co (0.79 wt %), Ni (0.30 wt. %) and Cu (0.12 wt. %). Amphibole was also observed in the run products of the experiment with added FeS at NNO.

Glass compositions are broadly similar in experiments with and without added FeS (Table 4-4). However, in the sulphur-rich experiments, MgO is higher in the melt at NNO; CaO is approximately 1-2 wt. % higher at NNO and MH; TiO_2 is slightly higher at both NNO and MH in experiments with

added FeS (up to 0.26 wt. % higher at NNO); and FeO is elevated by approximately 1 wt. % at MH with added FeS, but is raised by 2.76 wt. % at NNO. Collectively, these observations suggest that ferromagnesian phases, mostly magnetite, are somewhat destabalised by the addition of FeS at NNO.

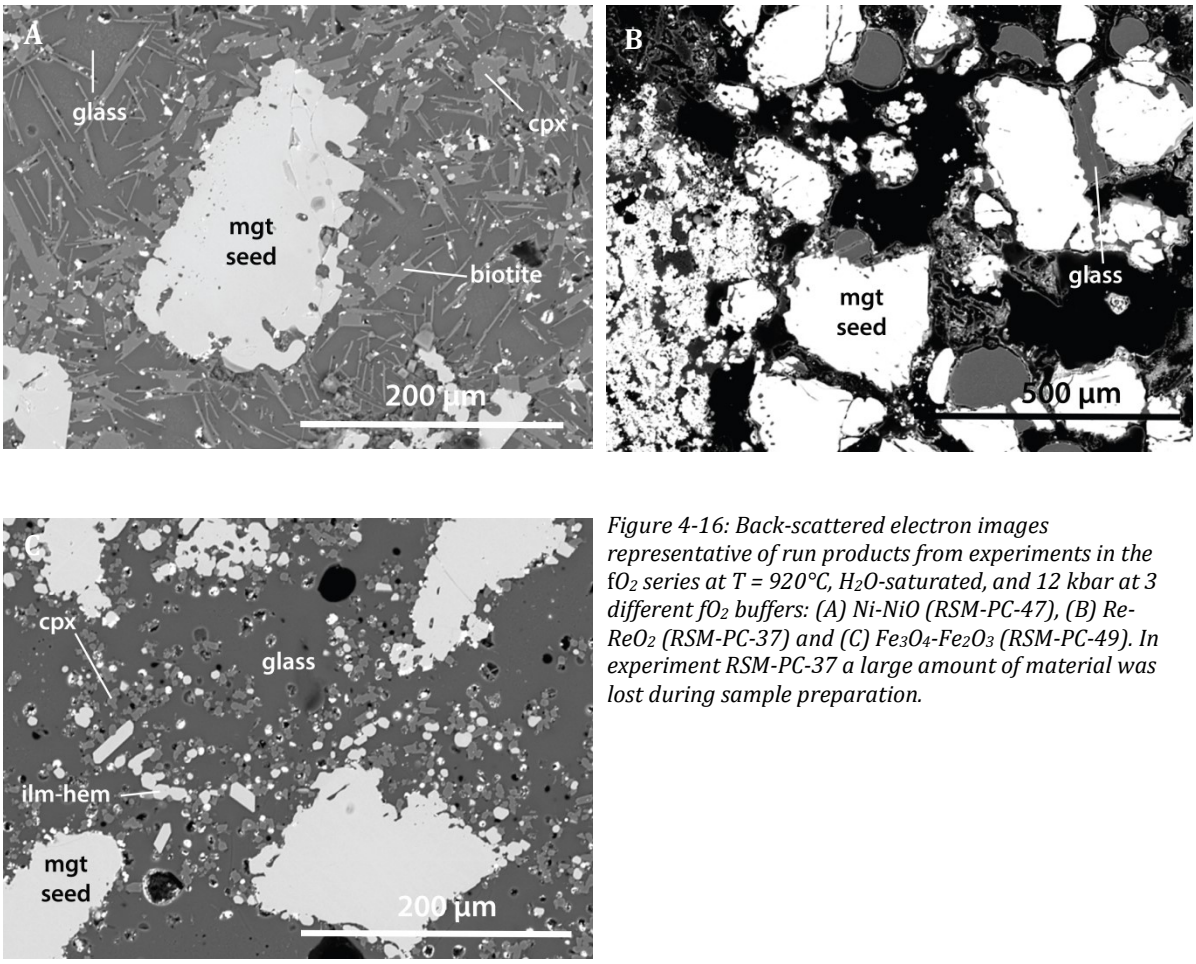


Figure 4-16: Back-scattered electron images representative of run products from experiments in the fO_2 series at T = 920°C, H_2O-saturated, and 12 kbar at 3 different fO_2 buffers: (A) Ni-NiO (RSM-PC-47), (B) Re-ReO_2 (RSM-PC-37) and (C) Fe_3O_4-Fe_2O_3 (RSM-PC-49). In experiment RSM-PC-37 a large amount of material was lost during sample preparation.

For the most part, the major element chemistry of the rim of the magnetite seeds, determined using EPMA, is within error the same in experiments at NNO and T = 920°C with or without added FeS (Table 4-4). Titanium, however, is lower in experiments with added FeS (1.78 ± 0.19 wt % in RSM-PC-51, but 5.53 wt. % ± 0.70 in RSM-PC-47). There are generally only minor variations in magnetite-melt partitioning associated with adding FeS. At NNO, D(Mg) is slightly lower (0.71 ± 0.05 at NNO/920°C/added FeS compared with 1.86 ± 0.33 at NNO/920°C/without added FeS), but there is no change in adding FeS at MH. D(Ti) is unaffected by adding FeS at NNO, although there is a slight increase in partitioning with added FeS at MH (D(Ti) = 3.62 ± 0.48 at MH/920°C/added FeS compared with D(Ti) = 1.84 ± 0.17 at MH/920°C/without added FeS). D(Mn) and D(Al) are unaffected by adding FeS at both NNO and MH. Vanadium, like Ti, is more

strongly partitioned into magnetite with added FeS (D(V) = 4.41 ± 0.88 at MH/920°C/added FeS compared with D(V) = 1.04 ± 0.23 at MH/920°C/without added FeS). Magnetite seeds were too small to analyse with LA-ICP-MS at NNO, so that element partitioning of additional trace elements, not detected with EPMA, could not be determined. However, magnetite seeds could be analysed using LA-ICP-MS in both experiments with and without added FeS at MH. The partitioning of Sc, Co, Ni, Cu, Zn, Ga, Ge, Cd, Sn, Lu, Zr, Hf, Nb and Ta remain unaffected by the addition of FeS, whereas there is a minor increase in the partitioning of In in magnetite with experiments with added FeS (D(In) = 2.97 ± 0.41 at MH/920°C/with added FeS compared with D(In) = 1.91 ± 0.23 at MH/920°C/without added FeS) (Table 4-5).

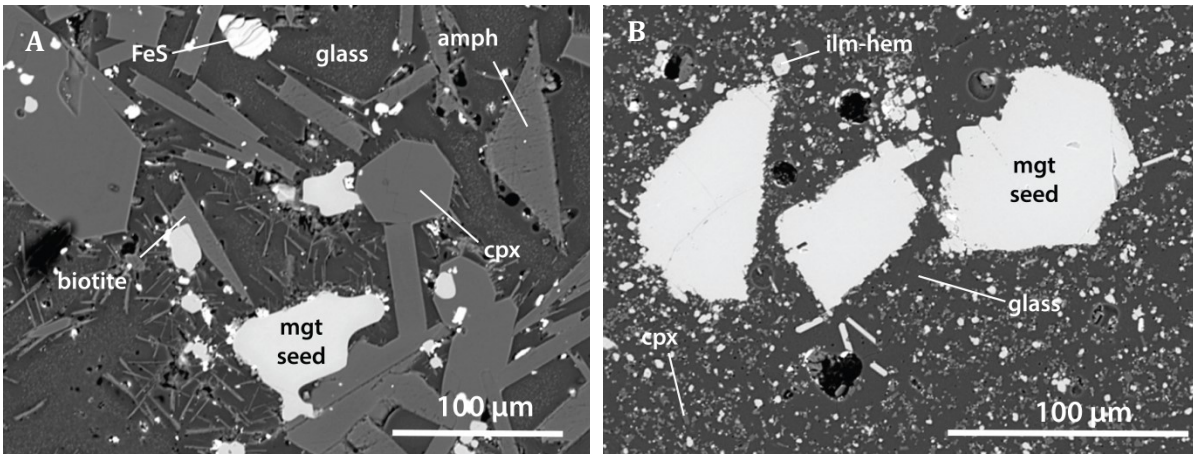


Figure 4-17: Backscattered electron SEM image of run products of experiments using starting material with added FeS at T = 920°C, P = 12 kbar and (A) fO_2 = NNO (RSM-PC-51) and (B) fO_2 = MH (RSM-PC-52). Phase assemblage is similar in experiments with and without added FeS at fO_2, but at fO_2 = NNO, there is an FeS phase in experiments with added FeS and magnetite seeds are more strongly resorbed.

4.3.7 Temperature series

Partition experiments were determined using LA-ICP-MS in experiments between T = 920°C and 960°C at fO_2 = NNO, RRO, and MH, and P = 12 kbar (Table 4-5) and using EPMA in experiments between T = 920°C and 980°C at fO_2 = RRO and P = 12 kbar (Table 4-4). Magnetite-melt partition coefficients of Mg, Al, Sc, Ti, V, Cr, Co, Ni, Cu, Zn, Ga, Ge, Zr, Nb, In, Sn, Ta do not vary by more than 2σ between T = 920°C and 960°C at each respective fO_2 buffer. Partition coefficients for Mo, Pb, U, Hf, Cd, Ge could not be measured in all experiments at RRO in this suite owing to low concentrations of these elements in magnetite seeds. Notwithstanding this, where partition coefficients could be determined for these elements, partition coefficients do not vary by more than 2 σ between 920°C and 960°C at their respective fO_2. Thus, there are generally not large variations magnetite-melt partitioning with temperature over the experimental conditions studied.

Table 4-4: Glass and titanomagnetite major element composition determined using EPMA and partition coefficients

Experiment	RSM-PC-32	RSM-PC-39	RSM-PC-40	RSM-PC-41	RSM_PC-19
fO_2 buffer[f]	RRO	RRO	RRO	RRO	RRO
T	940	940	940	940	980
Pressure (kbar)	12	10	8	6	12
Starting material	A-190+Fe+trace	A-190+Fe+trace	A-190+Fe+trace	A-190+Fe+trace	A-190+Fe+trace
Time (hours)	48	48	48	48	48
Glass (wt. %)					
n	13	10	10	10	16
Na_2O	1.4(1)	1.1(2)	1.65(8)	0.95(6)	0.86(6)
MgO	2.04(4)	2.23(2)	1.8(2)	1.76(3)	2.36(7)
P_2O_5	0.20(2)	0.19(1)	0.22(2)	0.22(2)	0.20(1)
K_2O	1.90(5)	1.66(6)	2.2(2)	1.28(4)	1.3(1)
CaO	4.26(4)	3.55(5)	3.3(6)	2.04(6)	3.5(1)
SO_3	< dl	< dl	< dl	< dl	< dl
TiO_2	0.28(2)	0.24(2)	0.3(1)	0.26(4)	0.28(1)
V_2O_5	0.01(1)	0.01(1)	0.01(1)	0.004(8)	0.01(1)
MnO	0.072(7)	0.065(1)	0.05(1)	0.051(7)	0.071(1)
FeO	5.4(2)	6.61(6)	4.7(3)	7.4(1)	7.4(6)
Al_2O_3	15.1(2)	15.00(6)	15.5(6)	14.2(2)	15.2(2)
SiO_2	57.7(7)	61.5(2)	64.7(9)	65.2(3)	58.9(7)
H_2O (fluid)[a]	11.6	7.80	5.50	6.67	9.91
Fe^{3+}/Total Fe[b]	0.255(3)	0.257(3)	0.290(2)	0.276(1)	0.219(2)
$XFe^{3+}O_{1.5}$[c]	0.00676	0.00955	0.00840	0.0120	0.00845
$XFe^{2+}O$[c]	0.0198	0.0276	0.0205	0.0315	0.0301
Mgt (wt. %)					
n	10	4	10	12	15
Seed rim/Crystal	Crystal	Crystal	Crystal	Crystal	Crystal
MgO	1.75(5)	1.81(2)	2.68(9)	1.7(2)	1.46(3)
CaO	0.06(2)	0.08(2)	0.10(2)	0.06(1)	0.06(1)
TiO_2	3.2(1)	2.19(6)	2.9(2)	2.2(3)	2.15(2)
V_2O_5	0.28(4)	0.17	0.26(3)	0.20(6)	0.11(1)
Cr_2O_3	0.09(5)	0.06(2)	0.06(1)	0.051(1)	0.21(5)
MnO	0.12(1)	0.098(5)	0.11(1)	0.07(1)	0.076(7)
FeO	80.4(7)	80.5(2)	75(1)	75(3)	80.5(3)
Al_2O_3	8.0(6)	9.06(3)	13(1)	16(3)	9.1(2)
SiO_2	0.13(3)	0.3(2)	0.21(7)	0.23(1)	0.3(1)
Mg#[d]	0.088(3)	0.0920(8)	0.132(4)	0.084(8)	0.075(1)
$a Fe_3O_4$[e]	0.618	0.630	0.552	0.560	0.631
D(mgt/melt)					
D(Mg)	0.86(3)	0.81(1)	1.5(2)	1.0(1)	0.62(2)
D(Ti)	11(1)	9.2(7)	9(1)	8(1)	7.8(4)
D(V)	100(103)	30(73)	30(42)	0(106)	20(59)
D(Mn)	1.6(2)	1.5(2)	2.4(8)	1.3(3)	1.1(2)
D(Al)	0.53(4)	0.603(3)	0.83(1)	1.1(2)	0.59(1)

[a] H_2O (fluid) represents an estimate of the total H_2O in the fluid-vapour phase and hydrous melt prior to quenching, as approximated from making up the low totals from EPMA of the hydrous glass to 100%
[b] Fe^{3+}/Total Fe in melt calculated using Kress and Carmichael (1991)
[c] Number of moles of $Fe^{3+}O_{1.5}$ and $Fe^{2+}O$ on a single cation basis as described in O'Neill and Eggins (2002)
[d] Mg# is Mg/(Mg + Fe^{2+}). Fe^{2+} calculated from stoichiometry
[e] Activity of Fe_3O_4 in titanomagnetite calculated using model from O'Neill and Wall (1987)
[f] Abbreviations: RRO = Re=ReO_2; NNO = Ni-NiO; MH = Fe_3O_4-Fe_2O_3; < dl = less than limit of detection. Errors are 1 s.d. of multiple (n) analyses.

Experiment	RSM_PC-46	RSM_PC-36	RSM-PC-47	RSM_PC-37	RSM-PC-49
fO_2 buffer	RRO	RRO	NNO	RRO	MH
T	920	960	920	920	920
Pressure (kbar)	12	12	12	12	12
Starting material	A-190+Fe+trace	A-190+Fe+trace	A-190+Fe+trace	A-190+Fe+trace	A-190+Fe+trace
Time (hours)	84	28	48	48	48
Glass (wt. %)					
n	8	12	6	14	10
Na_2O	0.64(5)	0.78(8)	2.2(3)	0.73(4)	2.1(1)
MgO	2.10(8)	2.20(8)	0.36(6)	2.26(5)	0.7(1)
P_2O_5	0.22(2)	0.19(1)	0.27(3)	0.20(1)	0.24(1)
K_2O	1.2(2)	1.4(2)	3.7(5)	1.30(7)	5.6(1)
CaO	3.2(2)	3.2(2)	7.4(5)	3.79(5)	4.6(3)
SO_3	< dl	< dl	< dl	< dl	< dl
TiO_2	0.18(1)	0.27(1)	0.09(2)	0.16(1)	0.17(1)
V_2O_5	0.009(8)	0.004(9)	0.00(1)	0.006(9)	0.04(1)
MnO	0.055(9)	0.07(1)	0.07(1)	0.069(8)	0.031(7)
FeO	6.2(4)	6.7(7)	7.0(8)	5.7(2)	3.6(2)
Al_2O_3	15.0(2)	15.1(4)	14.9(6)	15.0(2)	16.8(1)
SiO_2	60.6(6)	59(1)	55(1)	59.9(4)	57.7(3)
H_2O (fluid)[a]	10.7	11.0	9.17	10.8	8.47
Fe^{3+}/Total Fe[b]	0.234(2)	0.225(3)	0.156(5)	0.242(2)	0.593(3)
$Fe^{3+}O_{1.5}$[c]	0.00732	0.00761	0.00578	0.00694	0.0114
$Fe^{2+}O$[c]	0.0240	0.0263	0.0314	0.0217	0.00783
Mgt (wt. %)					
n	13	19	6	9	6
Seed rim/Crystal	Crystal	Crystal	Seed rim	Crystal	Seed rim
MgO	1.61(5)	1.5(1)	0.67(4)	1.51(5)	3.17(6)
CaO	0.03(1)	0.04(1)	0.06(3)	0.05(2)	0.06(3)
TiO_2	1.59(3)	2.10(9)	1.8(2)	1.75(5)	0.32(2)
V_2O_5	0.09(1)	0.14(1)	0.17(5)	0.09(1)	0.038(8)
Cr_2O_3	0.07(3)	0.13(5)	0.09(6)	0.20(5)	0.07(4)
MnO	0.08(1)	0.08(1)	0.08(2)	0.094(7)	0.183(8)
FeO	80.4(7)	80.7(6)	87(1)	81.5(4)	86.7(7)
Al_2O_3	10.0(5)	9.2(5)	3.3(5)	8.5(4)	2.5(2)
SiO_2	0.16(7)	0.20(4)	0.3(1)	0.17(3)	0.09(2)
Mg#[d]	0.084(3)	0.075(5)	0.036(2)	0.079(2)	0.176(3)
$a Fe_3O_4$[e]	0.638	0.633	0.805	0.655	0.756
D(mgt/melt)					
D(Mg)	0.77(4)	0.66(6)	1.9(3)	0.67(3)	5(1)
D(Ti)	9.1(7)	7.8(7)	21(3)	10.6(8)	1.8(2)
D(V)	10(10)	30(71)	0(154)	20(23)	1.0(4)
D(Mn)	1.5(4)	1.2(2)	1.2(3)	1.4(2)	6(1)
D(Al)	0.67(3)	0.61(4)	0.22(4)	0.57(3)	0.15(1)

Experiment	RSM-PC-51	RSM-PC-52	RSM-PC-31	RSM_PC-43	RSM-PC-30
fO_2 buffer	NNO	MH	NNO	RRO	MH
T	920	920	960	960	960
Pressure (kbar)	12	12	12	12	12
Starting material	A-190+Fe+trace+FeS	A-190+Fe+trace+FeS	A-190+Fe+trace	A-190+Fe+trace	A-190+Fe+trace
Time (hours)	60	60	48	48	48
Glass (wt. %)					
n	11	12	7	15	10
Na_2O	2.8(2)	2.5(1)	2.2(2)	0.72(3)	2.2(1)
MgO	0.97(6)	0.60(8)	0.5(2)	2.11(2)	1.5(3)
P_2O_5	0.24(2)	0.17(2)	0.24(2)	0.21(2)	0.20(2)
K_2O	4.2(2)	5.5(1)	2.0(2)	1.11(3)	4.9(2)
CaO	5.6(3)	3.51(1)	8.6(3)	2.95(4)	5.9(3)
SO_3	< dl	0.42(3)	< dl	< dl	< dl
TiO_2	0.35(4)	0.077(1)	0.08(1)	0.215(7)	0.255(1)
V_2O_5	0.01(1)	0.02(1)	0.02(1)	0.00(1)	0.03(1)
MnO	0.09(1)	0.035(7)	0.099(7)	0.058(7)	0.053(9)
FeO	9.7(3)	2.5(2)	10.2(8)	7.40(1)	4.7(3)
Al_2O_3	15.4(2)	16.9(1)	13.4(1)	14.60(9)	15.5(2)
SiO_2	52.3(3)	59.8(4)	53(1)	58.7(4)	57.6(5)
H_2O (fluid)[a]	8.19	7.88	9.31	11.9	7.19
Fe^{3+}/Total Fe[b]	0.147(2)	0.591(3)	0.142(2)	0.2180(6)	0.592(4)
$Fe^{3+}O_{1.5}$[c]	0.00780	0.00809	0.00768	0.00789	0.0158
$Fe^{2+}O$[c]	0.0455	0.00561	0.0465	0.0282	0.0109
Mgt (wt. %)					
n	11	12	8	14	11
Seed rim/Crystalc	Seed rim	Seed rim	Seed rim	Crystal	Seed rim
MgO	0.69(3)	2.17(4)	0.54(6)	1.56(7)	3.0(1)
CaO	0.07(4)	0.05(2)	0.06(1)	0.05(2)	0.06(2)
TiO_2	5.5(7)	0.26(1)	1.8(2)	1.75(7)	0.51(1)
V_2O_5	0.5(1)	0.07(2)	0.17(5)	0.11(2)	0.056(7)
Cr_2O_3	0.1(2)	0.03(2)	0.12(8)	0.2(1)	0.05(3)
MnO	0.12(2)	0.23(1)	0.06(1)	0.08(1)	0.15(1)
FeO	84(1)	87.2(5)	87.7(7)	78(2)	87.1(4)
Al_2O_3	3.2(5)	2.7(2)	3.1(6)	11.3(7)	2.66(8)
SiO_2	0.14(5)	0.1(1)	0.4(1)	0.16(5)	0.12(5)
Mg#[d]	0.0335(1)	0.121(2)	0.028(3)	0.081(3)	0.162(5)
$a Fe_3O_4$[e]	0.698	0.799	0.823	0.610	0.762
D(mgt/melt)					
D(Mg)	0.71(5)	3.6(5)	1.2(4)	0.74(3)	2.0(4)
D(Ti)	16(3)	3.4(4)	21(3)	8.1(8)	2.0(2)
D(V)	50(49)	3(2)	10(10)	0(137)	2.0(8)
D(Mn)	1.3(2)	7(1)	0.6(1)	1.3(3)	2.9(6)
D(Al)	0.21(3)	0.16(1)	0.23(5)	0.77(5)	0.172(6)

Table 4-5: Glass and titanomagnetite trace element compositions determined using LA-ICP-MS and partition coefficients for trace elements

Experiment	RSM-PC-32	RSM-PC-39	RSM-PC-40	RSM-PC-41	RSM_PC-43	RSM-PC-47	RSM_PC-37	RSM-PC-49	RSM-PC-52	RSM-PC-31	RSM-PC-30
fO_2 buffer	RRO	RRO	RRO	RRO	RRO	NNO	RRO	MH	MH	NNO	MH
T	940	940	940	940	960	920	920	920	920	960	960
Pressure (kbar)	12	10	8	6	12	12	12	12	12	12	12
Starting material	A-190 +Fe+trace	A-190 +Fe+trace	A-190 +Fe+trace	A-190 +Fe+trace	A-190 +Fe+trace	A-190 +Fe+trace	A-190 +Fe+trace	A-190 +Fe+trace	A-190 +Fe+trace+FeS	A-190 +Fe+trace	A-190 +Fe+trace
Time (hours)	48	48	48	48	48	48	48	48	60	48	48
Glass (ppm)											
n	7	10	3	5	11	2	12	4	4	5	12
Sc	34.8(8)	35(1)	34(4)	39(2)	62.7(5)	43(1)	36.0(9)	28(2)	42(4)	32(2)	31(2)
V	23.4(6)	16(2)	40(13)	21(4)	15(2)	10.0(7)	7.4(7)	184(5)	90(11)	10.8(9)	150(7)
Cr	1.0(4)	3.6(4)	20(11)	8(4)	2(3)	< dl	2(1)	< dl	< dl	< dl	< dl
Co	181(5)	87(4)	78(3)	88(5)	119(3)	37.3(8)	102(7)	32.0(9)	23(3)	33(6)	41(4)
Ni	8.1(2)	5.6(1)	10(5)	9(2)	8.2(9)	2.5(9)	4.0(3)	2(1)	6(8)	15(9)	2.1(6)
Cu	11.7(7)	8.2(6)	9.8(9)	11.8(5)	9.0(2)	2.52(7)	5.7(8)	5(1)	5.4(6)	1.9(3)	10(2)
Zn	78(3)	69(5)	47(3)	56(2)	161(4)	196(6)	56(3)	81(2)	75(10)	80(20)	50(4)
Ga	38(2)	37(3)	45(6)	18.6(9)	91(2)	158(9)	23.3(9)	148(4)	180(18)	19(2)	123(7)
Ge	300(11)	260(12)	290(25)	345(9)	310(14)	42.3(1)	250(17)	260(12)	230(12)	27(2)	270(12)
Zr	252(7)	249(10)	240(12)	250(28)	293(5)	271(5)	241(9)	242(6)	210(13)	210(18)	220(17)
Nb	168(7)	143(4)	150(11)	140(15)	46.6(6)	40.7(9)	129(3)	38(3)	33(3)	120(11)	141(10)
Mo	13(1)	13(1)	150(50)	20(16)	33(1)	399(7)	2.4(3)	460(34)	550(46)	160(17)	210(14)
Cd	41(1)	32(1)	29.9(1)	31.8(1)	48(2)	60(4)	39(3)	67(6)	70(12)	42(9)	70(14)
In	80(2)	58(2)	53(7)	50(1)	90(4)	4.1(3)	57(3)	53(4)	38(3)	4.0(2)	60(3)
Sn	64(2)	46(2)	46(3)	44(3)	56(3)	< dl	47(2)	13(5)	10(2)	< dl	35(2)
Lu	890(27)	900(42)	910(69)	990(69)	920(17)	950(12)	970(23)	730(28)	490(47)	970(56)	940(74)
Hf	110(3)	113(5)	109(3)	100(14)	341(6)	301(10)	109(3)	280(7)	240(19)	93(8)	97(6)
Ta	400(183)	152(7)	150(19)	150(11)	109(2)	89(1)	230(7)	84(3)	72(6)	114(8)	128(7)
Pb	98(3)	80(3)	74(3)	69(2)	128(2)	209(10)	93(4)	190(14)	180(15)	150(15)	144(6)
U	16.8(4)	16.1(8)	21(2)	15(2)	3,200(493)	2,320(75)	15.9(4)	3,800(217)	2,600(704)	21(3)	21(1)

Experiment	RSM-PC-32	RSM-PC-39	RSM-PC-40	RSM-PC-41	RSM_PC-43	RSM-PC-47	RSM_PC-37	RSM-PC-49	RSM-PC-52	RSM-PC-31	RSM-PC-30
fO_2 buffer	RRO	RRO	RRO	RRO	RRO	NNO	RRO	MH	MH	NNO	MH
T	940	940	940	940	960	920	920	920	920	960	960
Pressure (kbar)	12	10	8	6	12	12	12	12	12	12	12
Starting material	A-190 +Fe+trace	A-190 +Fe+trace	A-190 +Fe+trace	A-190 +Fe+trace	A-190 +Fe+trace	A-190 +Fe+trace	A-190 +Fe+trace	A-190 +Fe+trace	A-190 +Fe+trace+FeS	A-190 +Fe+trace	A-190 +Fe+trace
Time (hours)	48	48	48	48	48	48	48	48	60	48	48
Mgt (LA-ICP-MS)											
n	4	6	4	4	7	5	5	8	9	6	8
Sc	15(4)	19(3)	26(3)	28(6)	29(5)	30(4)	17(5)	23(2)	35(8)	16(2)	14(3)
V	900(107)	1,000(193)	900(379)	500(206)	640(61)	1,000(338)	600(114)	190(43)	390(77)	900(179)	270(37)
Cr	230(63)	100(107)	200(152)	120(60)	200(143)	700(250)	300(218)	90(71)	60(58)	< dl	-
Co	2,400(230)	1,200(141)	1,100(166)	800(168)	1,120(88)	540(91)	1,500(110)	1,500(460)	1,900(291)	440(52)	1,060(66)
Ni	710(82)	510(82)	500(152)	290(88)	480(45)	140(37)	460(75)	290(60)	600(194)	160(45)	380(45)
Cu	3.7(8)	3(1)	10(5)	4(3)	1.5(3)	0.8(6)	3(1)	9(2)	8(3)	< dl	8(1)
Zn	290(44)	280(54)	300(39)	180(47)	600(49)	330(75)	230(50)	700(117)	860(92)	120(30)	230(26)
Ga	53(9)	46(6)	70(35)	32(2)	310(39)	290(61)	35(5)	210(47)	230(39)	22(3)	20(6)
Ge	180(41)	240(41)	220(49)	130(24)	170(28)	120(19)	< dl	32(7)	42(9)	100(15)	56(7)
Zr	7(3)	11(4)	10(7)	20(17)	10(1)	26(7)	12(8)	3.1(5)	4(1)	18(3)	2.6(6)
Nb	14(2)	20(4)	18(4)	20(10)	4.1(5)	17(2)	13(4)	0.4(2)	0.8(3)	47(8)	1.9(3)
Mo	< dl	< dl	< dl	< dl	6.4(7)	300(131)	< dl	< dl	< dl	120(17)	< dl
Cd	< dl	< dl	< dl	< dl	< dl	< dl	< dl	10(3)	8(4)	< dl	8(3)
In	150(29)	130(24)	170(27)	90(12)	150(16)	11(1)	130(22)	100(12)	110(15)	8(2)	69(5)
Sn	94(6)	80(11)	120(41)	60(12)	57(4)	< dl	80(10)	17(4)	12(3)	< dl	33(5)
Lu	0.9(2)	1.9(2)	2.0(5)	2.3(8)	1.7(3)	4(2)	5(6)	3.1(5)	1.5(3)	3(1)	2.2(4)
Hf	< dl	7(2)	7(2)	20(11)	13(3)	23(5)	7(3)	4(1)	3.4(4)	10(3)	1.2(4)
Ta	14.7(6)	15(2)	12(4)	23(7)	10(4)	40(12)	20(12)	0.9(2)	1.1(4)	50(9)	1.4(3)
Pb	< dl	< dl	< dl	< dl	< dl	1.4(2)	< dl	< dl	2.0(6)	5(2)	2.1(6)
U	< dl	< dl	< dl	< dl	< dl	14(10)	< dl	< dl	< dl	0.15(4)	< dl

Experiment	RSM-PC-32	RSM-PC-39	RSM-PC-40	RSM-PC-41	RSM_PC-43	RSM-PC-47	RSM_PC-37	RSM-PC-49	RSM-PC-52	RSM-PC-31	RSM-PC-30
fO_2 buffer	RRO	RRO	RRO	RRO	RRO	NNO	RRO	MH	MH	NNO	MH
T	940	940	940	940	960	920	920	920	920	960	960
Pressure (kbar)	12	10	8	6	12	12	12	12	12	12	12
Starting material	A-190 +Fe+trace	A-190 +Fe+trace	A-190 +Fe+trace	A-190 +Fe+trace	A-190 +Fe+trace	A-190 +Fe+trace	A-190 +Fe+trace	A-190 +Fe+trace	A-190 +Fe+trace+FeS	A-190 +Fe+trace	A-190 +Fe+trace
Time (hours)	48	48	48	48	48	48	48	48	60	48	48
D(Mgt/melt)											
D(Sc)	0.4(1)	0.55(8)	0.8(1)	0.7(2)	0.47(9)	0.7(1)	0.5(1)	0.81(8)	0.8(2)	0.51(6)	0.45(9)
D(V)	37(5)	60(13)	20(11)	24(10)	43(6)	100(35)	80(18)	1.0(2)	4.4(9)	80(18)	1.8(3)
D(Cr)	200(151)	40(30)	11(10)	14(8)	80(96)	-	200(161)	-	-	-	-
D(Co)	13(1)	14(2)	15(2)	9(2)	9.5(8)	14(2)	15(1)	50(14)	80(14)	14(2)	26(2)
D(Ni)	90(11)	90(22)	50(19)	30(12)	58(9)	60(27)	120(24)	120(54)	110(61)	11(4)	180(71)
D(Cu)	0.32(8)	0.4(1)	1.1(5)	0.3(3)	0.17(3)	0.3(2)	0.5(2)	2.0(7)	1.5(5)	-	0.8(2)
D(Zn)	3.7(6)	4.1(8)	6.4(9)	3.1(9)	3.7(3)	1.7(4)	4.2(9)	9(1)	11(1)	1.5(4)	4.5(5)
D(Ga)	1.4(2)	1.3(2)	1.4(8)	1.7(1)	3.5(4)	1.8(4)	1.5(2)	1.5(3)	1.3(2)	1.2(2)	0.16(5)
D(Ge)	0.6(1)	0.9(2)	0.8(2)	0.36(7)	0.54(9)	2.8(5)	-	0.12(3)	0.18(4)	3.6(6)	0.21(3)
D(Zr)	0.03(1)	0.04(2)	0.04(3)	0.08(7)	0.034(5)	0.10(2)	0.05(3)	0.013(2)	0.019(7)	0.09(1)	0.012(3)
D(Nb)	0.08(1)	0.14(3)	0.12(3)	0.17(7)	0.09(1)	0.40(6)	0.10(3)	0.012(4)	0.025(1)	0.40(7)	0.014(2)
D(Mo)	-	-	-	-	0.20(2)	0.9(3)	-	-	-	0.8(1)	-
D(Cd)	-	-	-	-	-	-	-	0.14(5)	0.11(6)	-	0.11(4)
D(In)	1.9(4)	2.1(4)	3.2(5)	1.8(2)	1.7(2)	2.7(4)	2.3(4)	1.9(2)	3.0(4)	2.0(5)	1.16(9)
D(Sn)	1.47(9)	1.8(2)	2.6(9)	1.4(3)	1.01(7)	-	1.7(2)	1.3(4)	1.3(3)	-	0.9(2)
D(Lu)	0.0010(2)	0.0021(2)	0.0022(5)	0.0023(8)	0.0018(4)	0.004(2)	0.005(6)	0.0043(6)	0.0031(6)	0.003(1)	0.0023(4)
D(Hf)	-	0.06(2)	0.06(2)	0.1(1)	0.039(8)	0.08(2)	0.06(3)	0.016(4)	0.014(2)	0.11(3)	0.012(4)
D(Ta)	0.041(2)	0.10(1)	0.08(3)	0.15(4)	0.09(3)	0.5(1)	0.11(5)	0.011(2)	0.016(6)	0.44(8)	0.011(2)
D(Pb)	-	-	-	-	-	0.0065(8)	-	-	0.011(3)	0.03(1)	0.015(5)
D(U)	-	-	-	-	-	0.006(4)	-	-	-	0.008(2)	-

4.4 Discussion

4.4.1 Titanomagnetite-melt partitioning as a function of fO_2 at elevated pressure

As outlined in section 2.4.2.6, spinel-melt partitioning can be explained in terms of thermodynamic equilibria between magnetite and melt by plotting against terms including the $a Fe_3O_4$ - calculated using the model by O'Neill and Wall (1987) - and values of $XFe^{2+}O$ and $XFe^{3+}O_{1.5}$ – approximated using the empirical parameterization of Kress and Carmichael (1991). For example, the partitioning of divalent cations, Mg^{2+}, Mn^{2+}, Co^{2+} and Ni^{2+} has previously been shown to be linearly proportional to $a Fe_3O_4$(mgt)/$XFe^{2+}O$(melt) for the 1-atm experiments conducted so far. These expressions derived from thermodynamic principles can be used to explain the relative variations in magnetite-melt partitioning as a function of fO_2.

The relationship between $D(M^{2+})$ and $a Fe_3O_4$(mgt)/$XFe^{2+}O$(melt) can be used to explain the increase in titanomagnetite-melt partitioning of divalent cations with increasing fO_2. Data from these experiments, conducted at higher pressure and lower temperature plot along a linear trend which is offset to lower $D(M^{2+})$, but is parallel to those defined by the experiments at 1-atm (-Figure 4-18). This suggests that the partition coefficients for these divalent cations are slightly depressed at higher-pressure and lower-temperature. D(Mg) and D(Mn) at elevated pressure and lower temperature are offset from the linear trend defined by experiments at 1-atm to a greater degree than D(Co) and D(Ni). It is important to note that these experiments were also conducted in a hydrous environment. The water content of the melt phase has been taken into account when calculating $XFe^{2+}O$, assuming the H_2O content of the melt makes up the difference between the low total of the glass phase analysed by EPMA and 100%. Data from Nielsen and Beard (2000) agrees well with the trend defined here for D(Mn) as a function of $a Fe_3O_4$(mgt)/$XFe^{2+}O$(melt), however, their values for D(Mg) are substantially higher than those reported here. Partition coefficients for Mg and Ni reported by Liu et al. (2015) for magnetite and titanomagnetite agree relatively well with those defined by these experiments, supporting that the partition coefficients for these cations is depressed at higher pressure and lower temperature. Spinels crystallised in the study by Liu et al (2014), however, do not follow the same linear trend defined by these data, which could be expected given the contrasting spinel composition they studied which contained significantly higher Al, Mg and Cr content than the titanomagnetite studied here (spinel in experiments by Liu et al. (2014) has $a Fe_3O_4 < 0.36$, whereas those in this study have $a Fe_3O_4 > 0.55$).

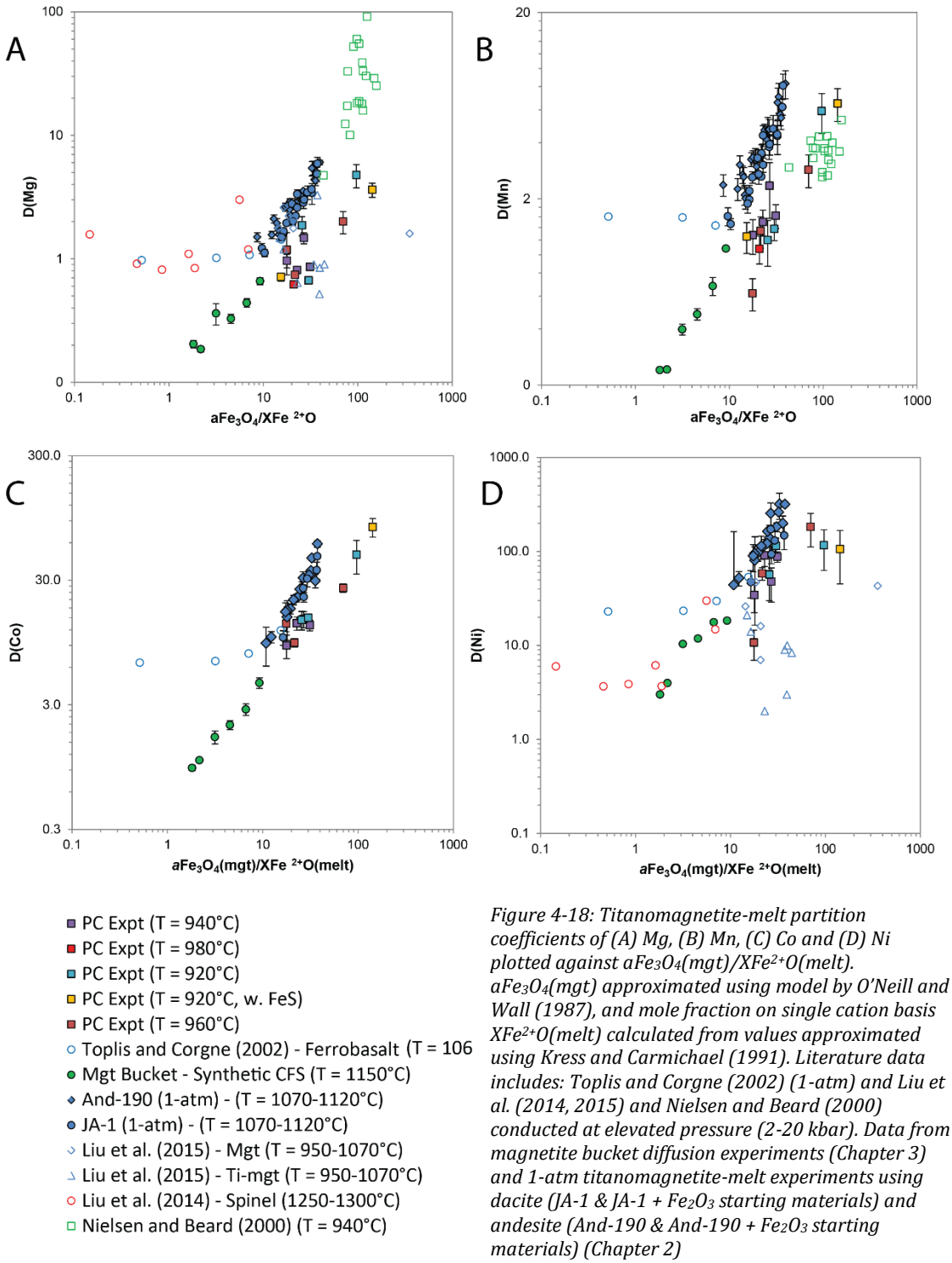


Figure 4-18: Titanomagnetite-melt partition coefficients of (A) Mg, (B) Mn, (C) Co and (D) Ni plotted against aFe_3O_4(mgt)/$XFe^{2+}O$(melt). aFe_3O_4(mgt) approximated using model by O'Neill and Wall (1987), and mole fraction on single cation basis $XFe^{2+}O$(melt) calculated from values approximated using Kress and Carmichael (1991). Literature data includes: Toplis and Corgne (2002) (1-atm) and Liu et al. (2014, 2015) and Nielsen and Beard (2000) conducted at elevated pressure (2-20 kbar). Data from magnetite bucket diffusion experiments (Chapter 3) and 1-atm titanomagnetite-melt experiments using dacite (JA-1 & JA-1 + Fe_2O_3 starting materials) and andesite (And-190 & And-190 + Fe_2O_3 starting materials) (Chapter 2)

An increase in D(Cu) with increasing fO_2 has been reported by Liu et al. (2014, 2015) for magnetite and Cr- and Al-rich spinel, but not for Ti-rich magnetite (> 10 wt. % Ti). Liu et al. (2015) attributed this increase to coupled substitution of Cu^{+} + Fe^{3+} for 2 Fe^{2+} in magnetite. However, it is proposed here that this increase is driven by thermodynamic equilibria. Assuming Cu is partitioned as a 1+ cation, the partitioning of Cu can be described by the reaction:

$$Cu^{1+}O_{0.5\,melt} + Fe_3O_{4\,spinel} + \frac{1}{4}O_2 = Cu^{2+}Fe^{3+}{}_2O_{4\,spinel} + Fe^{2+}O_{melt}$$

Thus, the partitioning of Cu would be expected to be linearly proportional to (aFe$_3$O$_4$(mgt)*(fO$_2^{0.25}$))/XFe^{2+}O(melt). Data from the 1-atm experiments in an andesitic-dacitic system, the 1-atm experiments in a synthetic CFS bulk system and these experiments at elevated pressure show a broad correlation on a plot of D(Cu) vs. (aFe$_3$O$_4$(mgt)*(fO$_2^{.25}$))/XFe^{2+}O(melt) (-Figure 4-19) consistent with this hypothesis. Plotting D(Cu) against aFe$_3$O$_4$(mgt)/XFe^{2+}O(melt) does not produce a linear correlation indicating that Cu is unlikely to exist predominantly as a divalent cation in the melt. This trend is corroborated by data for magnetite-rich spinel from Liu et al. (2015) and Wijbrans et al. (2015), but not Ti-rich magnetite (Liu et al. (2015) – where there is a general decrease in D(Cu) with increasing fO$_2$ or Cr- and Al-rich spinel (Liu et al. (2014). Therefore, it would seem that this equation describing the partitioning of Cu into magnetite-rich spinel is not appropriate for Cr- and Al-rich spinel or Ti-rich magnetite (> 10 wt. % Ti).

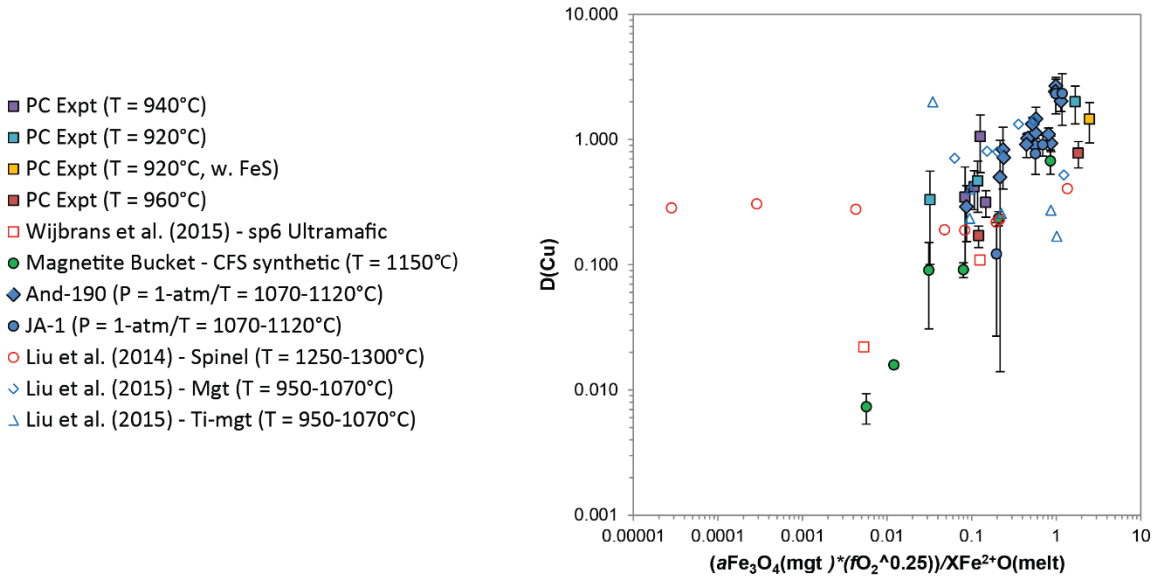


Figure 4-19: Titanomagnetite-melt partition coefficients of Cu plotted against aFe3O4(mgt)fO$_2$^0.25/XFe^{2+}O (melt). aFe$_3$O$_4$(mgt) approximated using model by O'Neill and Wall (1987), and mole fraction on single cation basis XFe^{2+}O(melt) calculated from values approximated using Kress and Carmichael (1991). Literature data includes: Wijbrans et al. (2015) (1-atm) and Liu et al. (2014, 2015) conducted at elevated pressure (5-20 kbar). Data from magnetite bucket diffusion experiments (Chapter 3) and 1-atm titanomagnetite-melt experiments at T = 1070-1120°C using dacite (JA-1 + Fe$_2$O$_3$ starting materials) and andesite (And-190 + Fe$_2$O$_3$ and And-190 + Fe$_2$O$_3$ + trace starting materials) (Chapter 2).*

Linear trends can also be defined by the data from these experiments for D(M^{4+}) as a function of aFe$_3$O$_4$(mgt)/(XFe^{3+}O$_{1.5}$(melt))*(fO$_2$^0.25)) and D(M^{5+}) as a function of aFe$_3$O$_4$(mgt)/(XFe^{3+}O$_{1.5}$(melt)^(2/3))*(fO$_2$^(1/3))), which account for a decrease in magnetite-melt partitioning for these elements with increasing fO$_2$. It is interesting to note that whereas D(Ti) from these higher pressure and lower temperature experiments plots along the same linear

trend defined by the experiments at 1-atm, data for D(Zr) and D(Nb) plot along a separate linear trend, lower but parallel to that defined by the 1-atm data. This is corroborated from existing experiments conducted at high-pressure by Nielsen and Beard (2000) and Liu et al. (2015) for magnetite. Data for Ti-mgt – containing more than 10 wt. % Ti – from Liu et al. (2015) plot higher that the linear field defined by magnetite-rich spinel. Data from Liu et al. (2014) for spinel ($a Fe_3O_4$ < 0.36) also plot higher than the linear trend defined by experiments which crystallised magnetite-rich spinel. This might be expected given the contrasting spinel compositions in these experiments to those studied here, which could alter the ratios of activity coefficients for these elements either in the crystal or in the melt.

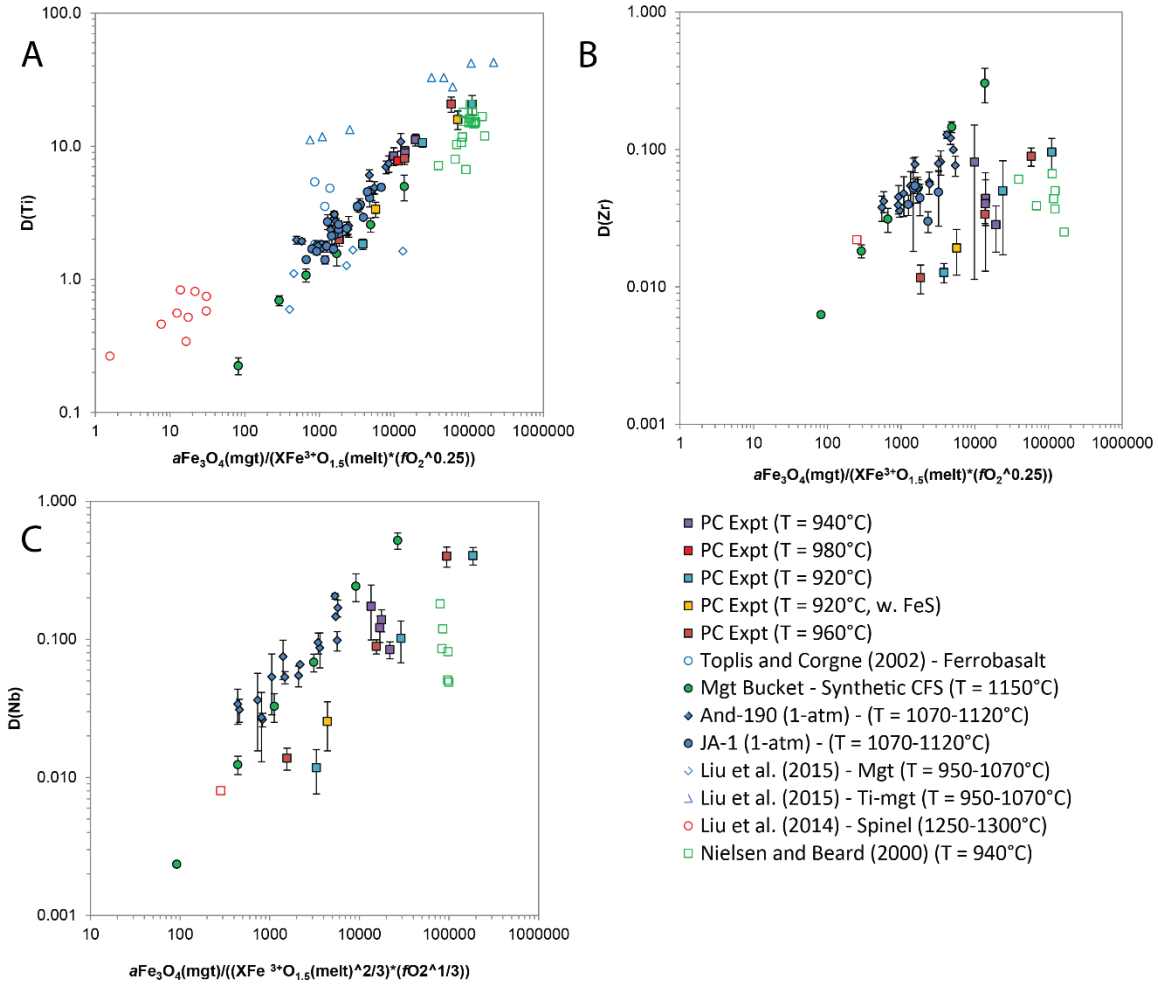


Figure 4-20: Titanomagnetite-melt partition coefficients of (A) Ti and (B) Zr plotted against $aFe_3O_4(mgt)/(XFe^{3+}O_{1.5}(melt)*fO_2\text{^}0.25)$ and (C) D(Nb) plotted against $aFe_3O_4(mgt)/(XFe^{3+}O_{1.5}(melt)\text{^}(2/3)*fO_2\text{^}(1/3))$. $aFe_3O_4(mgt)$ approximated using model by O'Neill and Wall (1987), and mole fraction on single cation basis $XFe^{3+}O_{1.5}(melt)$ calculated from values approximated using Kress and Carmichael (1991). Literature data includes: Toplis and Corgne (2002) (1-atm) and Liu et al. (2014, 2015) and Nielsen and Beard (2000) conducted at elevated pressure (2-20 kbar). Data from magnetite bucket diffusion experiments (Chapter 3) and 1-atm titanomagnetite-melt experiments using dacite (JA-1 & JA-1 + Fe_2O_3 starting materials) and andesite (And-190 & And-190 + Fe_2O_3 starting materials) (Chapter 2).

Nielsen and Beard (2000) have previously shown that partition coefficients for the HFSEs: Zr, Hf, Nb and Ta, are depressed relative to D(Ti) at higher pressure and lower temperature relative to those determined at 1-atm. Data from these experiments support this result (Figure 4-21) Moreover, it is interesting to note that in experiments conducted at T = 940°C, but over a range of pressure between 6 and 12 kbar, there is a progressive shift further away from the linear trend for lnD(HFSE) as a function lnD(Ti) at 1-atm (Figure 4-21).

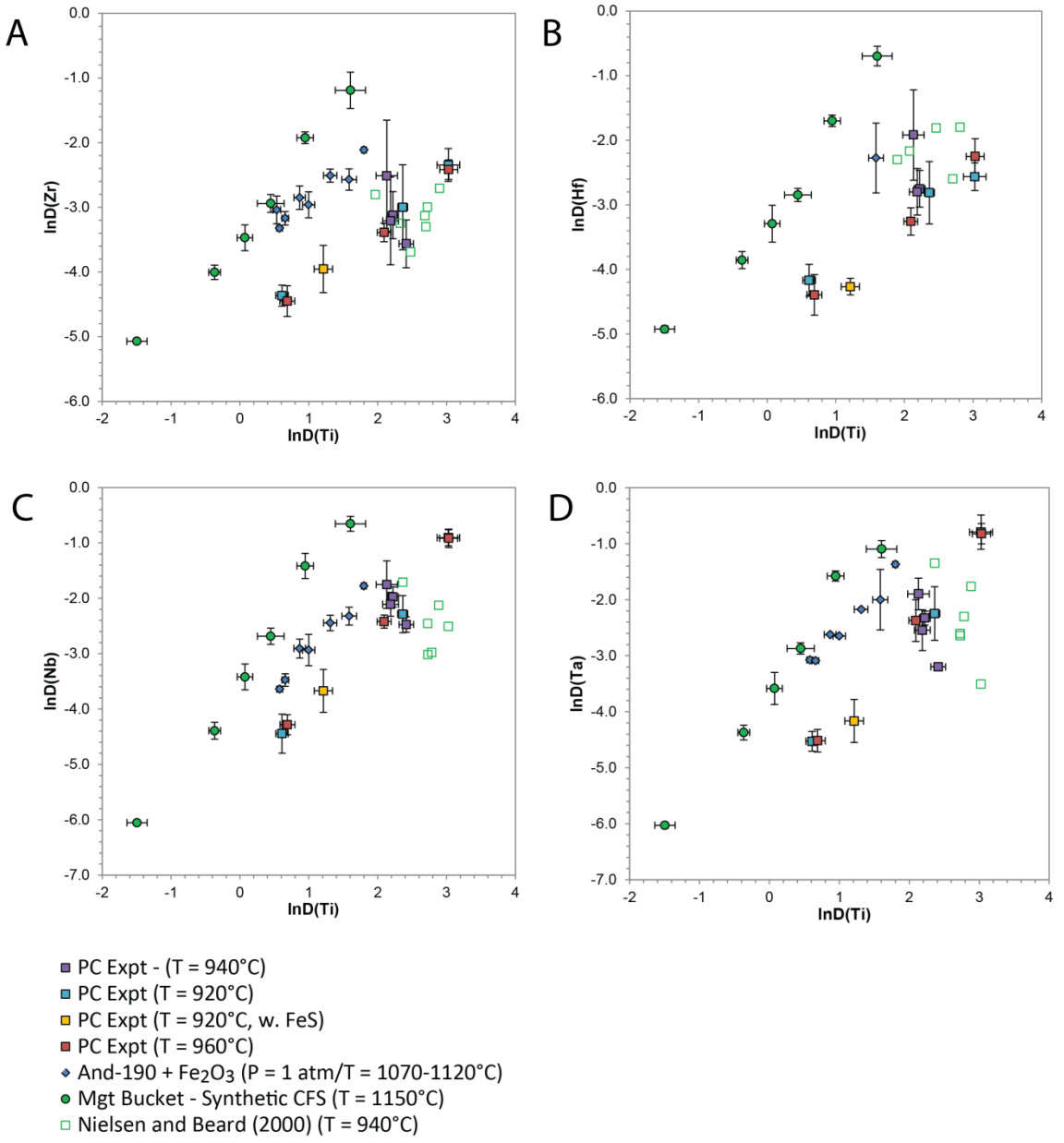


Figure 4-21: Natural log of titanomagnetite-melt partition coefficient of (A) Zr, (B) Hf, (C) Nb and (D) Ta as a function of the natural log of titanomagnetite-melt partition coefficient of Ti for piston cylinder experiments using And-190 + Fe_2O_3 and And-190 + Fe_2O_3 + FeS starting materials. Literature data from Nielsen and Beard (2000) conducted at elevated pressure (2-5 kbar) also provided for comparison, along with other experimental data in this PhD from magnetite bucket diffusion experiments, and 1-atm titanomagnetite-melt partitioning experiments at 1-atm using And-190 + Fe_2O_3 starting material.

There is only a small variation in $a Fe_3O_4(mgt)^{0.5}/XFe^{3+}O_{1.5}(melt)$ over the experimental conditions studied here, which can account for the limited variation in D(Sc) observed with fO_2 (Figure 4-22). Plotting D(Sc) against $a Fe_3O_4(mgt)^{0.5}/XFe^{3+}O_{1.5}(melt)$ does not define a linear trend as previously observed for experiments at 1-atm in a synthetic mafic bulk system (Figure 3-22B). Rather, the results from these experiments plot in a cluster, similar to those derived from experiments in an andesitic-dacitic bulk system at 1-atm (Chapter 2), but offset to lower D(Sc). This suggests D(Sc) is depressed with increasing pressure. There is no clear relationship between D(Al) and $Fe_3O_4(mgt)^{0.5}/XFe^{3+}O_{1.5}(melt)$. When combined with existing work studying spinel-melt partitioning in Al-bearing silicate bulk systems (e.g. Wijbrans et al., 2015; Righter et al., 2006; Toplis and Corgne, 2002; Toplis et al., 1994; Nielsen and Beard, 2000; Liu et al., 2014, 2015), there is a weak negative correlation between and $a Fe_3O_4{}^{0.5}/XFeO_{1.5}$, as previously highlighted in experiments investigating magnetite-melt partitioning at 1-atm in an andesitic-dacitic bulk system (Figure 2-10A).

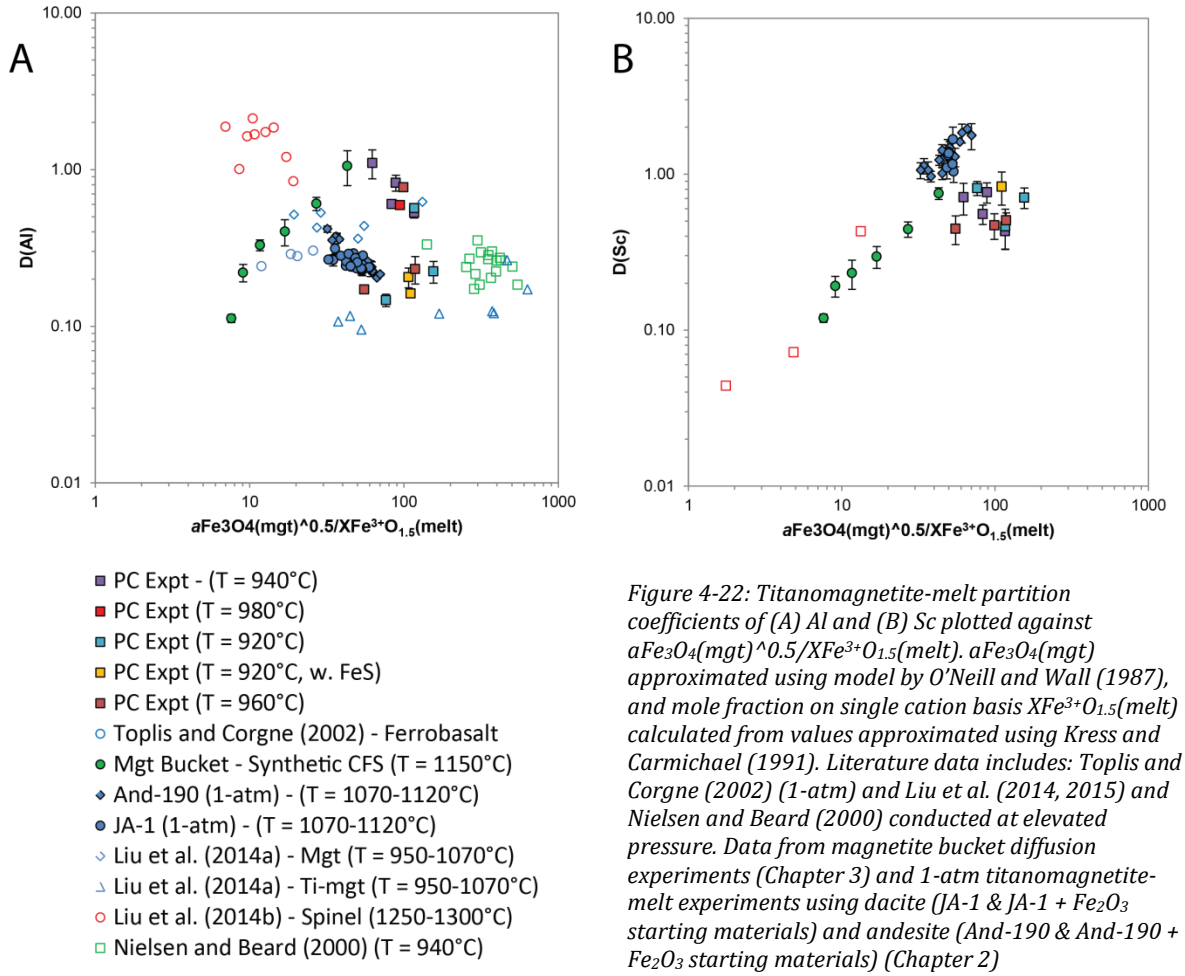


Figure 4-22: Titanomagnetite-melt partition coefficients of (A) Al and (B) Sc plotted against $aFe_3O_4(mgt)^{0.5}/XFe^{3+}O_{1.5}(melt)$. $aFe_3O_4(mgt)$ approximated using model by O'Neill and Wall (1987), and mole fraction on single cation basis $XFe^{3+}O_{1.5}(melt)$ calculated from values approximated using Kress and Carmichael (1991). Literature data includes: Toplis and Corgne (2002) (1-atm) and Liu et al. (2014, 2015) and Nielsen and Beard (2000) conducted at elevated pressure. Data from magnetite bucket diffusion experiments (Chapter 3) and 1-atm titanomagnetite-melt experiments using dacite (JA-1 & JA-1 + Fe_2O_3 starting materials) and andesite (And-190 & And-190 + Fe_2O_3 starting materials) (Chapter 2)

There is no clear relationship between D(Al) and T or fO_2, although there is a slight increase in D(Al) observed at RRO at elevated pressure. As suggested in section 2.4.2.6, it appears that in normal, Al-bearing, silicate melts the partitioning of Al between magnetite and silicate melt is strongly controlled by some other factor, related to bulk compositional, as well as thermodynamic equilibria. This contrasts with experiments using a synthetic CFS melt composition in which Al is present as a trace component in the magnetite, where the partitioning behaviour of Al is more similar to the other trivalent cations.

The partitioning of V has been shown by precursor experiments (see Chapters 2 and 3) and by existing work in the literature (e.g. Toplis and Corgne, 2002) to offer a relatively good proxy for melt oxidation state, with a strong decrease in magnetite-melt partitioning with increasing fO_2. At elevated pressure and lower temperature, there is also a decrease in D(V) with increasing fO_2, however, the absolute partition coefficients for V are greater by an order of magnitude relative to experiments conducted at 1-atm (Figure 4-23). This is supported by experimental work by Arato and Audetat (2017a), who have developed an oxybarometer based on vanadium partitioning between magnetite and silicate melt.

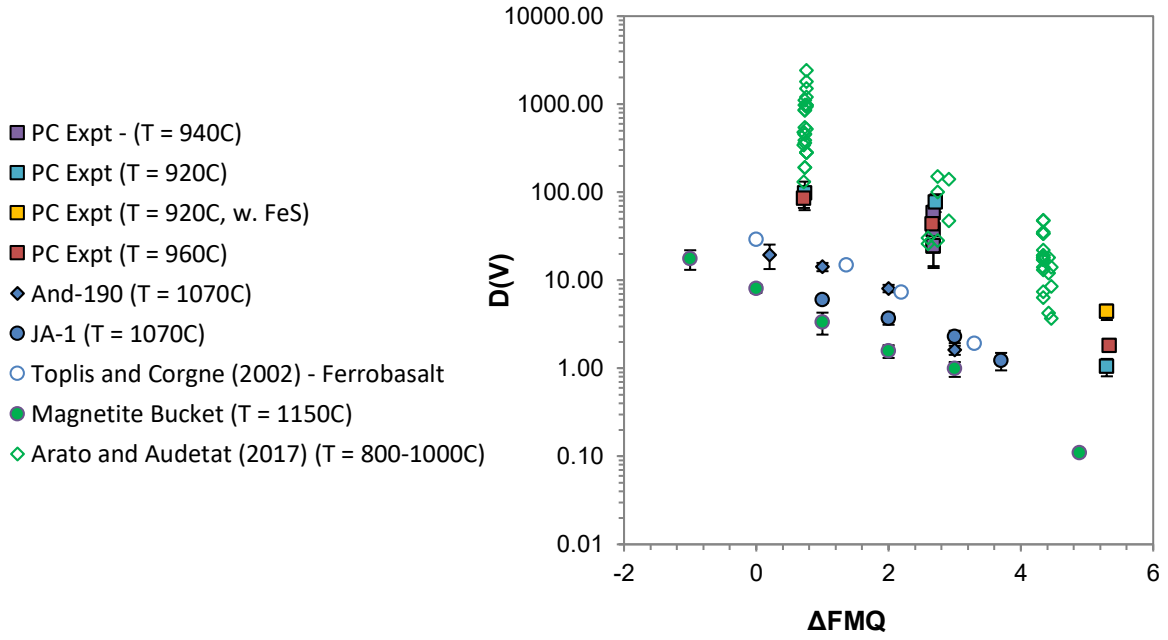


Figure 4-23: Titanomagnetite-melt partition coefficient for V as a function of fO_2. Partition coefficients for V were determined using LA-ICP-MS data. Literature data from Toplis and Corgne (2002) conducted at 1-atm and Arato and Audetat (2017a) at elevated pressure (1 – 5 kbar) are provided along with data from 1-atm experiments at T = 1070°C using JA-1 (JA-1 + Fe_2O_3 starting material) and And-190 (And-190 + Fe_2O_3 starting materials) for comparison.

Arato and Audetat (2017a) derived the following equation to describe the dependence of $D(V)_{mgt\text{-}melt}$ on fO_2, temperature and melt composition:

$$logD(V)_{mgt-melt} = 0.3726 \times \frac{10{,}000}{T} + 2.0465 \times ASI - 0.4773 \times \Delta FMQ - 2.1214$$

Where temperature is given in K, ASI is the aluminium saturation index of the melt calculated as molar $Al_2O_3/(CaO + Na_2O_3 + K_2O)$ and ΔFMQ refers to the difference in log fO_2 from FMQ. This equation predicts D(V) relatively accurately for experiments conducted at NNO and MH, however, D(V) measured in RRO experiments have poor agreement with those predicted. It is unlikely that the lower D(V) values measured in experiments at RRO are a consequence of not reaching equilibrium because these experiments were conducted at similar temperatures. Furthermore, diffusion of V in magnetite is slower at NNO than RRO (section 3.3.4), as also evinced by shorter diffusion profiles at NNO relative to experiments conducted at higher fO_2. Instead, the elevated D(V) predicted is a result of higher ASI in experiments at RRO (ASI = 1.25-2.13), relative to experiments at NNO and MH (ASI = 0.62-1.03), which probably reflects the lack of biotite and clinopyroxene as coexisting phases. No additional phases coexisted with magnetite and glass in experiments by Arato and Audetat (2017a). This suggests that the relationship derived by Arato and Audetat (2017a) is not accurate in all cases and particularly the dependence on ASI may require modification.

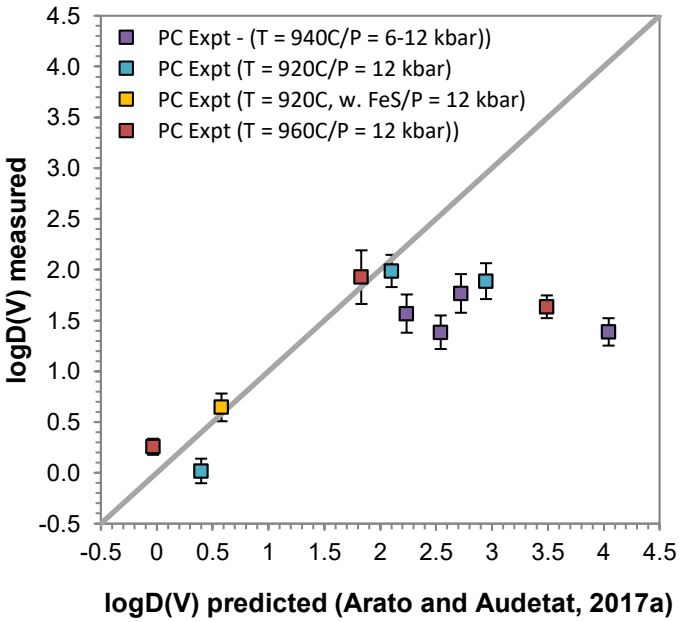


Figure 4-24: Comparison of measured D(V)(mgt-melt) with corresponding values predicted by equation derived by Arato and Audetat (2017a). Grey line represents 1:1.

4.4.2 Titanomagnetite-melt partitioning at elevated pressure

The divalent cations define linear trends in magnetite-melt partition coefficients as a function of $a Fe_3O_{4mgt}/XFe^{2+}O_{melt}$, but are displaced downward by approximately 1-2 $D(M^{2+})$ values at elevated pressures. Nickel and Co are displaced less than Mn and Mg from the trend defined by experiments at 1-atm (Figure 4-18). Similarly, the linear trends previously defined for Zr^{4+}, Nb^{5+}, Hf^{4+}, Ta^{5+}, in terms of $a Fe3O4_{mgt}$, $XFe^{3+}O_{1.5}$ and fO_2 are depressed with lower partition coefficients relative to experiments at 1-atm (Figure 4-20). Titanium, however, is not displaced significantly from the linear trend in terms of $aFe_3O_4(mgt)/(XFe^{3+}O_{1.5}(melt)*(fO_2\text{^}0.25))$ defined by the 1-atm experiments (Figure 4-20). These results are supported by experiments of Nielsen and Beard (2000), who previously identified that the HFSEs become incompatible relative to Ti at higher pressures and/or lower temperatures. It is possible that at higher pressures, the Young's modulus decreases, thereby decreasing the elasticity of the lattice site. Consequently, the lattice strain parabola tightens, which decreases the partition coefficient for cations which do not have the optimal radius of the site (r_0). This effect will be strongest for those cations with a larger difference between r_i and r_0 which could explain why there is not a significant depression in the partition coefficients for elements closest in size to r_0 (e.g. Ni^{2+} and Ti^{4+}).

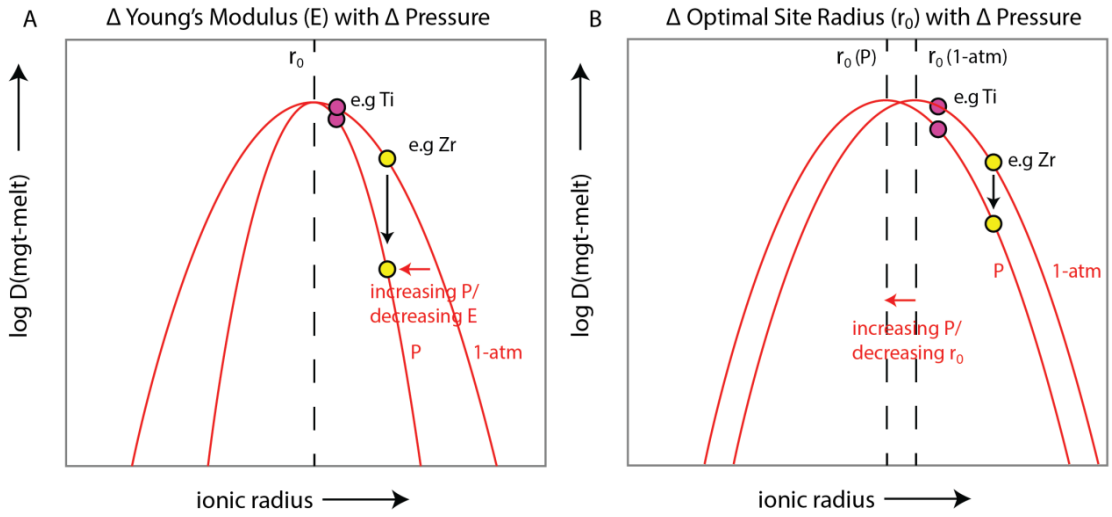


Figure 4-25: Schematic diagram illustrating the possible effect of increasing pressure on (A) decreasing Young's Modulus (E) of the lattice site or (B) decreasing the optimal site radius (r_0). Both decreasing E and r_0 with increasing pressure could result in a decrease in D(mgt/melt) with increasing pressure for cations which do not have an ionic radius (r_i) close to r_0. This effect would be strongest for those with greatest $r_i - r_0$. For example, this could explain why D(HFSE) are depressed relative to D(Ti) at elevated pressure.

Alternatively, it could be that the size of the optimal radius of the site (r_0) onto which the cations partition decreases or that the difference between the ionic radius of the cation and r_0 increases thereby decreasing the partition coefficient. Again, this effect will be strongest for those cations with a larger difference between r_i and r_0. This could also explain the increase in D(V) in

experiments at elevated pressure, with a decrease in r_0 bringing it closer to the ionic radius of V. These possible explanations for the change in mineral-melt partitioning with elevated pressure are illustrated in Figure 4-24.

4.4.3 Effect of adding sulphur on magnetite-melt partitioning

Addition of FeS to the starting material resulted in no change in the phases present at MH, however, at NNO, a sulphide phase crystallised. Furthermore, the saturation of a sulphide phase does not have a large effect on the major element chemistry of magnetite.

For elements detectable with EPMA, only Ti was significantly lower in experiment RSM-PC-51 (at NNO/920°C/12 kbar) which had a sulphide phase present in the run products. This suggests that sulphide saturation cannot be traced in natural magnetite using the major element chemistry of magnetite.

Addition of FeS at NNO destabilised magnetite so that only very few strongly resorbed magnetite seeds were present in the run products. These were too small to analyse their rim concentration with LA-ICP-MS. For elements detectable with EPMA, there was no significant difference in element partitioning at NNO and MH for most elements. Exceptions to this were Mg, which was approximately a factor of 2 higher in experiments without added FeS. It is possible that this result is actually an artefact of increased quench crystallisation in the experiment without added FeS; increased quench crystallisation of Mg-bearing phases could act to decrease the Mg content of the melt, thus increasing the measured D(Mg). Notwithstanding, the difference in D(Mg) between the two experiments is not substantial and does not differ by more than 3σ. The partition coefficients for D(Ti) and D(V) were also higher in experiments with added FeS at MH. In the experiment at MH with added FeS, $XFe^{3+}O_{1.5}$ is lower (0.0081 with added FeS compared with 0.0114 without added FeS), which results in an increase in Fe_3O_4(mgt)/($XFe^{3+}O_{1.5}$(melt))*(fO_2^0.25)). Given the linear relationship between Fe_3O_4(mgt)/($XFe^{3+}O_{1.5}$(melt))*(fO_2^0.25)) and D(Ti) (Figure 4-20A) and D(V), this could explain the higher D(Ti) in the experiment with added FeS. Nevertheless, the difference between the partition coefficients in experiments with and without added FeS is only slightly higher than 3 σ and within 3σ for Ti. In summary, addition of FeS to the starting composition does not have a significant effect on the magnetite-melt partitioning for elements measured with EPMA, whether sulphide saturation does or does not occur. In spite of this, it was not possible to interpret whether sulphide saturation influences the magnetite-melt partitioning for trace elements detectable with LA-ICP-MS.

5 Developing a method for LA-ICP-MS analysis of natural magnetite

5.1 Introduction

LA-ICP-MS has revolutionised our ability to determine major, minor and trace element concentrations in individual minerals at high spatial resolution, thereby providing valuable information on a variety of rock-forming processes. Element analysis using LA-ICP-MS is fast and comparatively non-destructive compared to sample digestion and solution chemistry. Moreover, LA-ICP-MS offers lower limits of detection than EPMA and is far cheaper, and can determine a much wider spectrum of elements than secondary ion mass spectroscopy.

There has recently been a surge in the use of LA-ICP-MS to study the chemistry of a variety of mineral phases, including magnetite, in efforts to elucidate processes involved in the formation of ore deposits (Mao Mao et al., 2016, Belousova et al., 2002, Nadoll et al., 2014, Canil et al., 2016, Dare et al., 2014). However, such studies are commonly hampered by the lack of well-developed analytical protocols. Thus, prior to embarking on collection of a large geochemical dataset of magnetite compositions in this study, it was important to develop a consistent and reliable method for analysis of natural magnetite via LA-ICP-MS. Various factors, such as exsolution phenomena, alteration and impurities, create complications and uncertainties that are quite specific to the analysis of Fe-Ti oxides. Thus, a study was conducted to research and develop a method which optimises the use of LA-ICP-MS to accurately and precisely measure their composition.

LA-ICP-MS involves the ablation of a small volume of target material with a focussed laser beam. The aerosol produced is then transferred in a gas stream normally to a quadrupole ICP-MS for isotopic analysis. To quantify major and trace element abundances, the technique requires bracketing samples with standards of known composition (external standards). Additionally, the concentration of one element in the unknown sample is required for calibration; this is known as the internal standard. This is usually determined independently using a different analytical technique, for example using EPMA or energy dispersive spectroscopy using a scanning electron microscope (SEM-EDS). Recently, alternative calibration methods, such as the assumption of a maximum stoichiometric amount of Fe, have been proposed, which obviate the requirement for analysis using another technique prior to LA-ICP-MS analysis (Pisiak et al., 2017). Notwithstanding this, analysis by some other external technique provides the most accurate method to obtain the internal standard whilst concurrently allowing for cross comparison of a range of major elements for quality control purposes.

In this chapter, a method for determining the internal standard concentration in Fe-Ti oxides with strong exsolution features is presented. In addition, the results of a study into the effect of varying laser spot size and an assessment of the suitability of various standard reference materials as external standards are discussed. A quality control flow chart to define the workflow needed to identify analyses contaminated by mineral inclusions is also described. During an interruption of studies from my PhD to conduct research for Rio Tinto Exploration, a brief study investigating the optimal isotope choice to minimise isotopic interferences when analysing some elements was conducted. A summary of this study is provided in Appendix 1 (section A1.1.1).

5.2 Analysing grains with exsolution features

Oxidative 'exsolution' in Fe-Ti oxides commonly occurs as result of oxidation of ulvöspinel-rich magnetite(ss) (titanomagnetite) at high temperature (> 600°C), typically forming ilmenite-hematite(ss) along {111} cubic spinel planes (Haggerty, 1976). Textures produced are usually dictated by crystallographic structure. Further metasomatism often results in replacement of the titanomagnetite-ilmenite assemblage to form titanite. Typically, titanite replacement is restricted to ilmenite-rich exsolution lamellae, but titanite can also form through metasomatism of magnetite. Because porphyry copper deposits are associated with magmatic-hydrothermal phenomena, this form of oxidative exsolution and metasomatism is particularly common as a result of interaction with hydrothermal fluids.

In order to best approximate the initial composition of titanomagnetite prior to the formation of exsolution features, previous work using LA-ICP-MS has employed a large laser beam size (50-80 μm), which incorporates exsolution lamellae into the analysis (e.g. Dare et al., 2012, Pisiak et al., 2017). However, this does not address the determination of the internal standard necessary to quantify LA-ICP-MS data for a composite grain made up of two phases with different compositions.

5.2.1 Determining the internal standard for LA-ICP-MS

Typically, the Fe content of magnetite is used as an internal standard and is determined prior to LA-ICP-MS analysis using SEM-EDS or EPMA. Although it is acceptable to analyse a mixture of phases using LA-ICP-MS analysis (assuming the mixed phase results can be deconvolved), it is generally not satisfactory to analyse a mixture of phases using electron beam spectroscopy, as a result of differences in the way the electron beam interacts with the different phases. To overcome this problem for titanomagnetite grains with exsolution features, the required internal standard for the mixed LA-ICP-MS analysis can be approximated from separate SEM-EDS analyses of both phases, coupled with an estimate of their proportions.

Sample R-S-8, a coarse granite from the Schultze batholith, Arizona, USA – thought to represent the source magma to the Resolution porphyry copper deposit – contains numerous titanomagnetite crystals with abundant ilmenite exsolution in a 'trellis' form dictated by the crystallographic structure (Figure 5-1).

5.2.1.1 Method

Titanomagnetite grains extracted from R-S-8 were mounted in epoxy and prepared for SEM-EDS and LA-ICP-MS analysis. Three grains from this sample were analysed as follows: (1) separate SEM-EDS analyses of both 'clean' (exsolved) titanomagnetite and exsolution lamellae were acquired using a Zeiss EVO 15LS scanning electron microscope at the Natural History Museum, London using 20kV accelerating voltage, 3nA sample current and < 1 μm beam size; (2) a backscattered electron image of part of the composite grain was acquired; (3) a subsection of the BSE image was cropped and processed using *ImageJ* (Schneider et al., 2012) to generate a binary image separating ilmenite exsolution lamellae from titanomagnetite using the default settings and the respective areas were then calculated using the 'Analyse' function in *ImageJ*; (4) finally, the "bulk" Fe concentration was calculated using the Fe concentrations measured for ilmenite and magnetite and their respective areas:

Bulk Fe concentration = (Fe concentration in magnetite * modal % of magnetite) + (Fe concentration in exsolution lamellae * modal % of exsolution lamellae)

Although not conventional for SEM-EDS analysis, three separate analyses were also conducted rastering the beam over a 40x40 μm of area of a composite grain, thus analysing exsolution lamellae and exsolved titanomagnetite together.

The concentrations of elements present above the limit of detection using SEM-EDS were also determined using LA-ICP-MS on the same grain using a laser spot size of between 40 and 60 μm, fluence of 3.5 J/cm^2 and laser repetition rate of 5 Hz. All analyses were carried out using a New Wave Research 193nm excimer laser coupled to an Agilent 7700x quadrupole ICP-MS in the LODE Laboratory at the Natural History Museum, London. Reference material USGS GSD-1g was used as the primary calibration standard and USGS GSE-1g was used as a secondary reference material for monitoring. Each of the reference materials was measured three times at the beginning and after each 15-18 analysis with a spot size of 50 μm. The Fe content, determined from either the *ImageJ* processing or rastered SEM-EDS analysis, was used as the internal standard. Analysis duration was 90 s, with the first 30 s monitoring a gas blank prior to ablation. The isotopes analysed were ^{7}Li, ^{23}Na, ^{24}Mg, ^{27}Al, ^{29}Si, ^{31}P, ^{39}K, ^{43}Ca, ^{45}Sc, ^{49}Ti, ^{51}V, ^{52}Cr, ^{55}Mn, ^{57}Fe, ^{59}Co, ^{60}Ni, ^{63}Cu, ^{65}Cu, ^{66}Zn, ^{71}Ga, ^{72}Ge, ^{75}As, ^{88}Sr, ^{89}Y, ^{92}Zr, ^{93}Nb, ^{95}Mo, ^{115}In, ^{118}Sn, ^{121}Sb, ^{139}La, ^{140}Ce, ^{175}Lu, ^{177}Hf, ^{181}Ta,

^{182}W, ^{208}Pb, ^{209}Bi, ^{232}Th and ^{238}U. Data were reduced using ExLAM (Zacharias and Wilkinson, 2007).

This full procedure was repeated for two more titanomagnetite grains from sample R-S-8.

5.2.1.2 Results

Iron, Mn and Ti are present at concentrations above the limit of detection of EDS analysis. In all grains studied, the mean concentrations of Fe, Mn and Ti measured by rastering the electron beam over a mixture of phases are, within error, the same as the bulk concentrations determined using the image processing method (Table 5-1). Thus, the internal standard determined using the *ImageJ* processing or rastered SEM-EDS analysis does not significantly effect the resulting concentrations determined using LA-ICP-MS. Furthermore, the mean concentrations of Mn and Ti determined using LA-ICP-MS are in better agreement with those determined from rastered SEM-EDS analyses than image processing, suggesting that the former technique is more accurate for the determination of bulk concentrations in admixed Fe-Ti oxides.

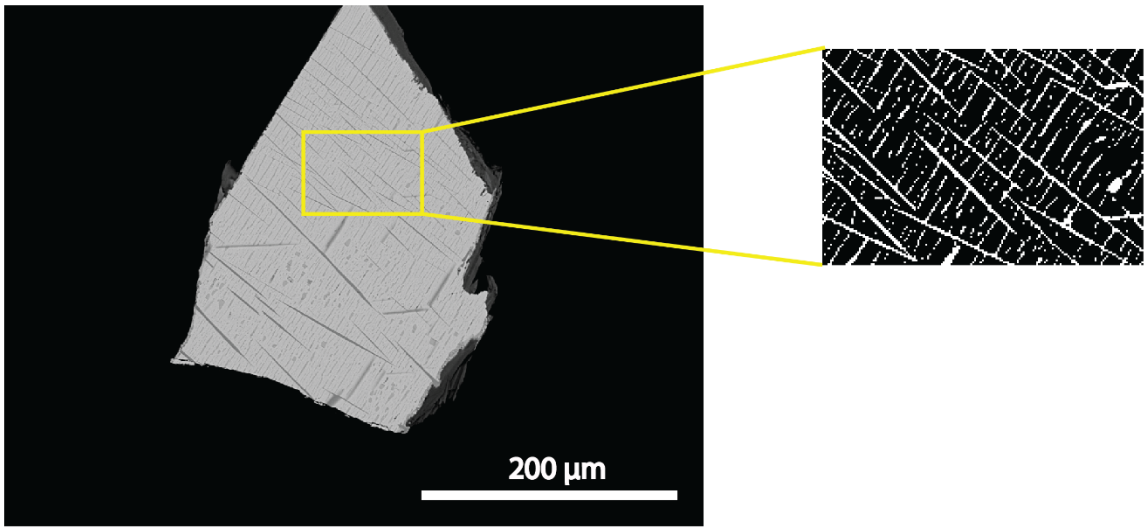


Figure 5-1: BSE image of grain 13 from sample R-S-8 (Schultze Granite, USA) and binary image generated in ImageJ that separates ilmenite exsolution lamellae from residual titanomagnetite.

Table 5-1: Mean concentrations of major elements within exsolved ilmenite lamellae and residual titanomagnetite in 3 separate grains, and the bulk composition of the composite grains estimated from: (1) the separate SEM-EDS analyses and phase proportions derived from image processing, (2) rastering the electron beam over a 40x40 µm area; and (3) LA-ICP-MS with a 40 µm spot, with GSD-1g as the external standard and the internal standard value for Fe derived from the image processing method. Errors are ±1σ of multiple analyses.

	Exsolved ilmenite (SEM-EDS) (n = 3)	Titanomagnetite (SEM-EDS) (n = 3)	Bulk grain (*ImageJ*) (n=3)	Bulk grain (EDS raster) (n=3)	Bulk grain (LA-ICP-MS) (40-60 µm spot n = 3, Int std = GSD-1g)
Grain 13					
Area (%)	16.9	83.1	-	-	
Ti (wt. %)	29.46 ± 0.69	7.23 ± 0.71	10.99 ± 1.11	11.26 ± 0.33	10.55 ± 0.32
Mn (wt. %)	6.56 ± 0.82	0.58 ± 0.16	1.59 ± 0.49	1.06 ± 0.22	0.90 ± 0.17
Fe (wt. %)	32.40 ± 0.52	61.07 ± 0.42	56.21 ± 0.98	56.60 ± 0.93	56.21
Grain 10					
Area (%)	12.4	88.6	-	-	
Ti (wt. %)	31.2 ± 1.53	7.29 ± 0.28	10.27 ± 0.43	11.15 ± 0.51	10.47 ± 0.28
Mn (wt. %)	9.55 ± 1.77	0.60 ± 0.21	1.72 ± 0.53	0.66 ± 0.18	0.81 ± 0.14
Fe (wt. %)	29.12 ± 0.96	61.29 ± 1.16	57.30 ± 1.02	56.56 ± 0.27	57.30
Grain 4					
Area (%)	18.7	81.3	-	-	
Ti (wt. %)	28.03 ± 1.55	7.36 ± 0.57	11.20 ± 0.76	10.35 ± 0.52	9.76 ± 0.66
Mn (wt. %)	5.76 ± 0.33	0.67 ± 0.22	1.62 ± 0.24	1.45 ± 0.09	1.28 ± 0.06
Fe (wt. %)	33.32 ± 1.30	59.91 ± 1.12	54.94 ± 1.15	55.90 ± 0.09	54.94

5.2.1.3 Discussion

Several factors could have contributed to inaccuracies when approximating the bulk grain composition using the image processing method. Firstly, it is likely that boundary pixels introduce a significant error, possibly by overestimating the lamellae width, when analysing fine exsolution features so that the modal area estimate for these is inaccurate. The contrasting densities of the two phases was also not taken into account when calculating the bulk concentrations so that volume (using area as a proxy) proportions rather than mass proportions were considered.

Although matrix corrections are generally considered to be problematic where intricate phase mixtures are concerned, this does not seem to have a practical impact on the analysis of titanomagnetite containing exsolution lamellae. Possibly the difference in matrix corrections between the two phases are negligible or that because the exsolved phase is generally distributed evenly throughout the area analysed – as opposed to one large inclusion for example – the mixture can be treated as being close to homogeneous. Irrespective, it appears to be the case that rastering the electron beam over an area of titanomagnetite with trellis exsolution offers a superior method

for the estimation of the bulk grain Fe concentration for use as an internal standard when processing LA-ICP-MS data.

5.2.2 Incorporating exsolution into LA-ICP-MS analysis

An experimental study applying a range of different beam sizes for laser ablation was conducted to identify the minimum beam size necessary to adequately incorporate exsolved phases in the analysis of composite grains. Four grains from sample R-S-8 (Coarse Schultze granite) were chosen for the study.

5.2.2.1 Method

On each grain, LA-ICP-MS analyses were conducted with 10, 20, 30, 40, 50 and 60 μm diameter laser spot sizes. The analytical method was the same as in section 5.2.1.1, however, the internal standard used was measured solely by rastering the beam over a 40x40 μm area of unexsolved magnetite and exsolution.

5.2.2.2 Results and Discussion

Mg, Al, Sc, Ti, V, Cr, Mn, Co, Ni, Cu, Zn, Ga, Sr, Y, Zr, Nb, Mo, In, Sn, Hf, and Ta were consistently above the limit of detection with LA-ICP-MS using the analytical conditions specified at spot sizes greater than 20 μm (Full data in Appendix 3). The majority of elements present above the detection limit exhibit a trend with increasing spot size of decreasing variability between grains, resulting in a convergence towards a more homogeneous concentration (Figure 5-2). This is particularly clear for Al, Ti, Ni, Mo and In (Figure 5-2). It is likely that these elements represent those which show greatest concentration contrast between residual titanomagnetite and the ilmenite exsolution lamellae. It is evident from these results that analytical variability is markedly reduced above 30 μm suggesting that a spot size greater than this is sufficient to adequately incorporate exsolution features into the analysis, thus best representing the original composition of the titanomagnetite prior to subsolidus exsolution.

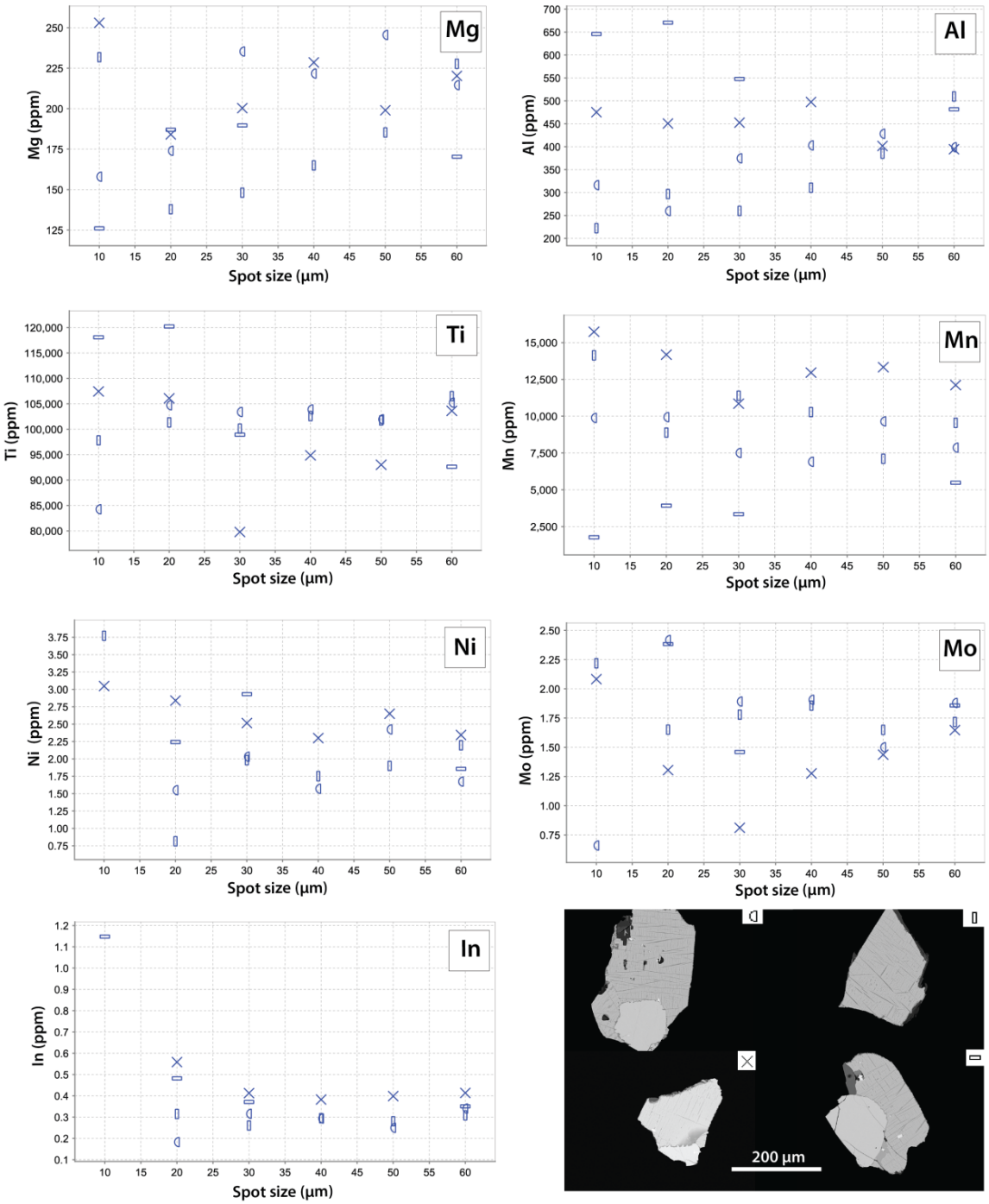


Figure 5-2: Spot size vs. element concentration for Mg, Al, Ti, Mn, Ni, Mo and In determined using LA-ICP-MS on four grains of titanomagnetite with strong ilmenite exsolution from sample R-S-8. BSE-SEM images of the four grains studied are shown in the bottom right of the figure with a key to the symbols in the plot. Grain 10 has semicircle symbol, Grain 13 has vertical rectangle, Grain 4 has X, Grain 3 has horizontal rectangle. Note that due to contamination from zircon inclusions, it was not possible to process the analyses of grain 3 completed with 40 and 50 µm laser spots.

5.2.3 Effect of laser spot size and use of different external standards

In LA-ICP-MS analysis, it is preferable to employ an external standard with a matrix which is close to that of the analysed substance. This ensures more similar ablation behaviour and laser-induced elemental fractionation in both the reference material and the sample analysed. Nevertheless, numerous studies have shown that matrix-matched external standards are not required to produce reliable results in magnetite for a wide range of elements (e.g. Nadoll and Koenig, 2011, Dare et al., 2012). Here, four different reference materials (USGS GSE-1g, USGS GSD-1g, NIST 610 and BCR-2g) were assessed as potential external standards for the analysis of natural magnetite. BC28, a well- characterised titanomagnetite from the Bushveld Complex (see Dare et al., 2012), was selected for the study. BC28 is generally devoid of exsolution features and has been demonstrated previously to be homogeneous in composition for most elements (Dare et al., 2012).

5.2.3.1 Method

Ten LA-ICP-MS analyses of BC28 were conducted using spot sizes of 10, 25, 50, 75 and 100 μm. Each set of BC28 analyses with varying spot size was bracketed by three analyses of each of the standard reference materials using the same respective spot size as for magnetite. Fe was employed as the internal standard using a concentration of 57.2 wt.% as reported by Dare et al. (2014) for BC28. Otherwise, analytical method was the same as in section 5.2.1.1.

5.2.3.2 Results

Mg, Al, Sc, Ti, V, Cr, Mn, Co, Ni, Cu, Zn, Ga, Zr, Nb, Mo, Sn, Hf, and Ta were found to be consistently above their detection limits in BC28 at all spot sizes using the analytical conditions specified. The concentrations of these elements vs. spot size are presented in Figure 5-3 and compared with results from Dare et al. (2012). Full results are provided in Appendix 3.

With increasing spot size, there is a decrease in the variability of the determined element concentration as might be expected. Noticeably, there is significant variability when using a 10 μm spot, however, this variability decreases substantially with a spot size of 25 μm and greater. Because this magnetite is largely devoid of exsolution features, the variability at the smallest spot size is due to low signal:noise ratios and possibly particle transport effects related to low ablation rates. When using a spot size greater than 10 μm and GSD-1g or GSE-1g as the external standard, the majority of results for Sc, Ti, V, Cr, Mn, Co, Ni, Cu, Zn, Ga, Zr, Nb, Mo, Sn, Hf and Ta are within error of those determined by Dare et al. (2012) (Figure 5-3). Mg and Al concentrations determined using any of the four standards are generally higher than those measured by Dare et al. (2012). Using NIST 610 to process data generally produces slightly higher values than when

using GSD-1g or GSE-1g; this is most notable for Al, Co, Ni, Zn, Ga, Zr, Nb, Sn, Hf and Ta. Using BCR-2g to process the data generates significantly higher values for Ni. Furthermore, some elements, such as Sn and In, are not reported in the certificate value for BCR-2g, thus it was not possible to determine these concentrations using this as the calibration standard. As observed by Dare et al. (2012), Cu concentrations appear to be highly variable in BC28; this could be due to the presence of Cu-bearing sulphide microinclusions heterogeneously distributed throughout the magnetite or just to compositional zoning in this element.

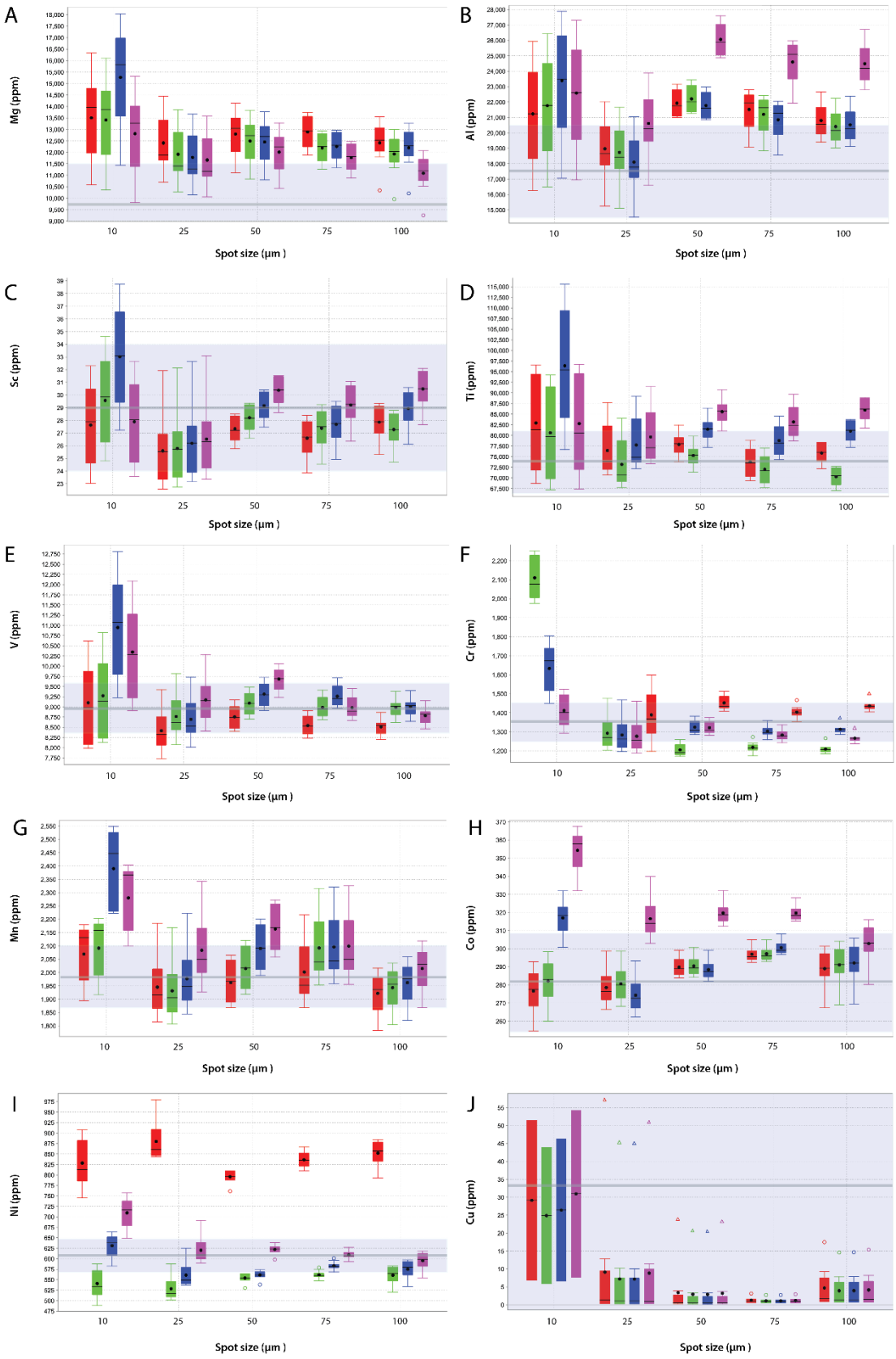
5.2.3.1 Discussion

In summary, GSD-1g and GSE-1g generate results which are in best agreement with those previously reported by Dare et al. (2012). GSE-1g and GSD-1g have 15 elements within 25% of the concentrations reported by Dare et al. (2014) for spot sizes between 25 and 100 micron (Figure 5-3). BCR-2g does not have reported values for several elements commonly detected in magnetite, such as Ge and Sn. Furthermore, only 11 elements are within 25% of those reported by Dare et al. (2014), when using a spot size between 25 and 100 micron (Figure 5-3). In particular, Mg, Ni and Zr are inaccurately measured using BCR-2g. Thus, BCR-2g is the least preferable choice as an external standard.

In spite of the low concentration of Fe in NIST 610, the results generated using this standard are generally in good agreement with those using GSD-1g and GSE-1g. When using a spot size between 25 and 100 micron, 14 elements are within 25% of the concentrations reported by Dare et al. (2014) (Figure 5-4). Furthermore, there are some elements certified in NIST 610 which are not reported in GSD-1g and GSE-1g, such as Re. Consequently, NIST 610 appears to be a viable standard for magnetite, particularly to quantify elements not reported in the other standards.

On balance, it is suggested that GSD-1g is the best option as the primary reference standard because its composition is most comparable to those of natural magnetites. In addition, GSE-1g and NIST 610 could be used as the secondary reference materials for monitoring.

Varying the laser spot size during the analysis of BC28 produced a comparable result to that observed when varying the spot size in the analysis of Fe-Ti oxides with exsolution features (section 5.2.2). With increasing spot size there is a decrease in the variability of the concentrations obtained. The scatter diminishes at spot sizes greater than 25 μm, so spot sizes greater than 25 μm are recommended even for magnetite grains without exsolution textures. However, Fe-Ti oxides commonly have micro-inclusions, inhomogeneities or zoning, thus it not advisable to use a laser spot greater than 50 μm in order to avoid contamination from other phases.


A
Mg (ppm)
Spot size (µm)
B
Al (ppm)
Spot size (µm)
C
Sc (ppm)
Spot size (µm)
D
Ti (ppm)
Spot size (µm)
E
V (ppm)
Spot size (µm)
F
Cr (ppm)
Spot size (µm)
G
Mn (ppm)
Spot size (µm)
H
Co (ppm)
Spot size (µm)
I
Ni (ppm)
Spot size (µm)
J
Cu (ppm)
Spot size (µm)

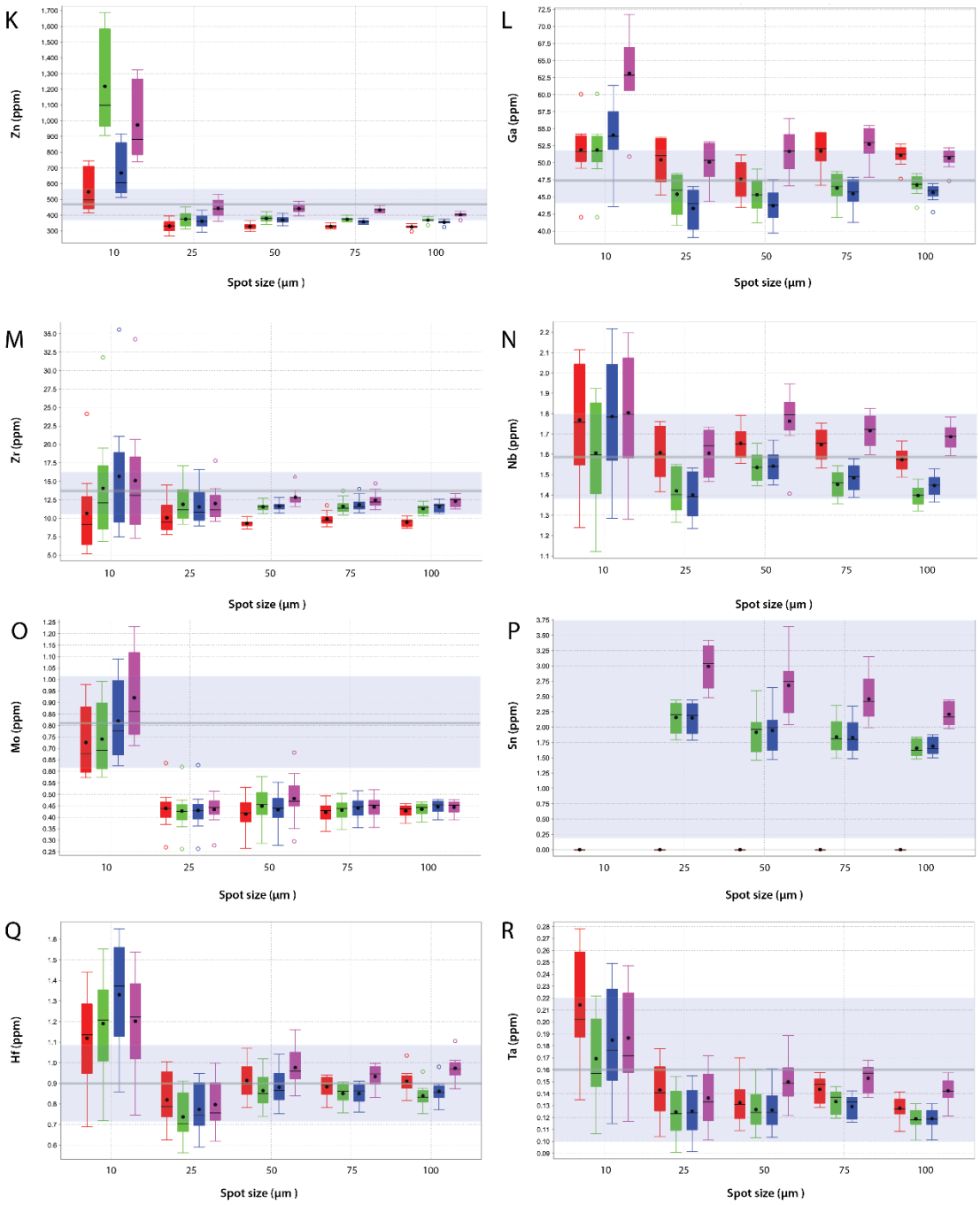


*Figure 5-3: Element concentrations in BC28 vs. spot size, for (A) Mg, (B) Al, (C) Sc, (D) Ti, (E) V, (F) Cr, (G) Mn, (H) Co, (I) Ni, (J) Cu, (K) Zn, (L) Ga, (M) Zr, (N) Nb, (O) Mo, (P) Sn, (Q) Hf, (R) Ta determined using LA-ICP-MS using four different reference materials as calibration standards. Central box is the middle 50% of data from Q1 to Q3. An circle outlier is further than 1.5 * (Q3-Q1) from the box and a triangle outlier is further than 3.0 * (Q3-Q1) from the box. The whiskers are the extreme values which are not outliers. The different colours correspond to data processed with BCR-2g (red), GSD-1g (green), GSE-1g (blue) and NIST 610 (magenta). Grey line indicates concentration reported by Dare et al. (2012) and shaded region shows their reported error range, calculated as 1 σ of multiple analyses. Note results from Dare et al. (2012) were processed using GSE-1g as the external standard.*

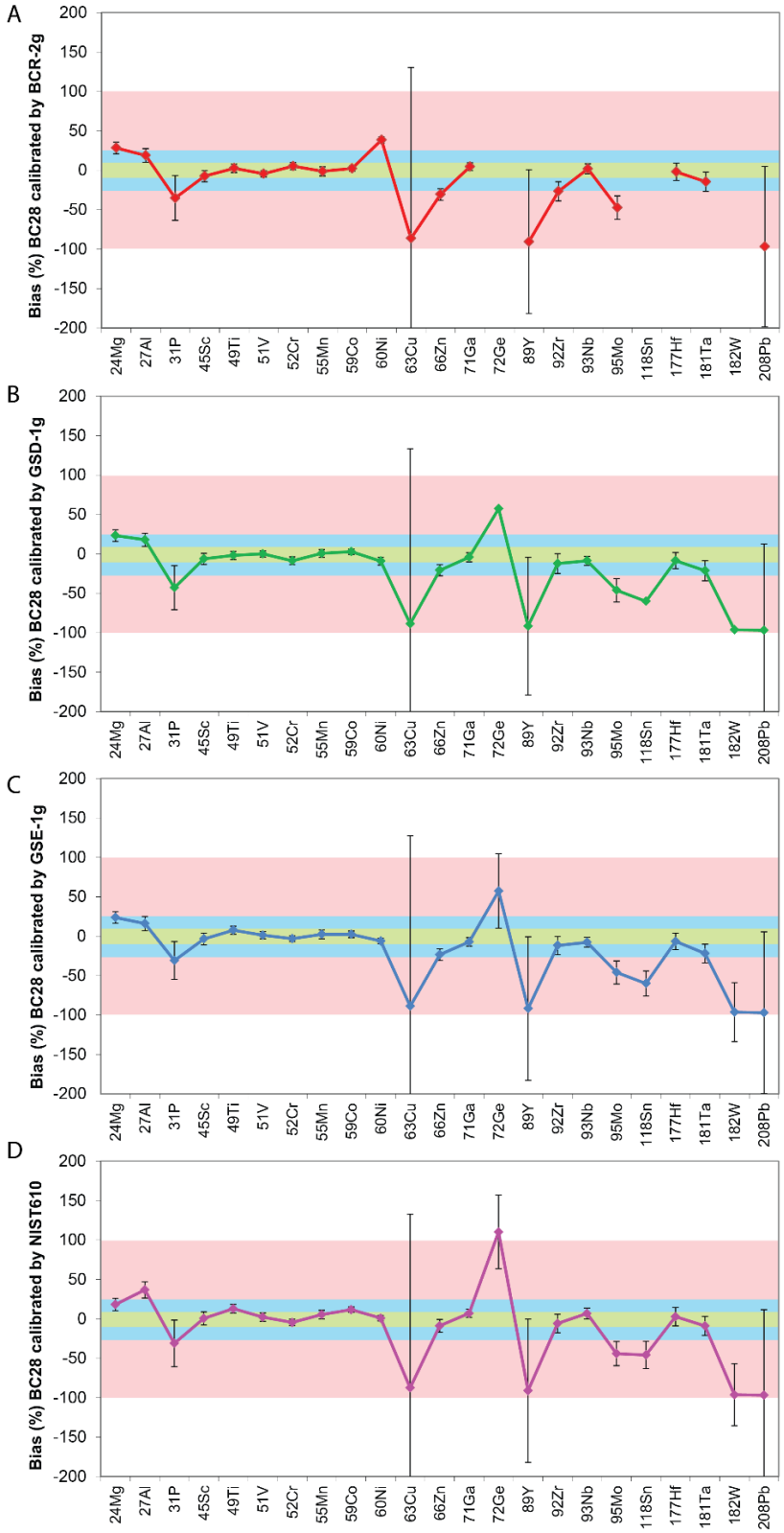


Figure 5-4: Bias for concentrations in BC28 determined using laser spot size between 25-100 µm and various external standards: (A) BCR-2g, (B) GSD-1g, (C) GSE-1g and (D) NIST610 relative to concentrations reported by Dare et al. (2012). Bias is calculated as (concentration measured-reported concentration)/reported concentration. Error bars are relative standard deviation (%) determined as 100(1σ/mean concentration for multiple analyses). Green band is ±10%, Blue band is ±25% and Red band is ±100% bias.*

5.2.4 Filtering contamination from other phases

Natural samples commonly host inclusions and inhomogeneities which can contaminate LA-ICP-MS analysis. Therefore, prior to analysis, all Fe-Ti oxides should undergo petrographic examination to identify alteration phases and inclusions, so that areas with obvious mineral inclusions at the surface can be avoided. In spite of this, inclusions can still be intersected at depth by the laser. As a result, it is important to monitor some isotopes specifically to highlight common mineral inclusions. Examples of other phases which commonly occur as inclusions in magnetite include apatite, zircon, REE-phosphate, K-feldspar and chalcopyrite. Thus, elements such as Na, P, Ca, REEs and K should be included in the analyte list when analysing magnetite. During processing, laser ablation data should be carefully checked to exclude any parts of the spectrum contaminated by mineral inclusions (e.g. Figure 5-5). In some cases, where contamination is particularly frequent or influences the whole spectrum, the analysis had to be discarded.

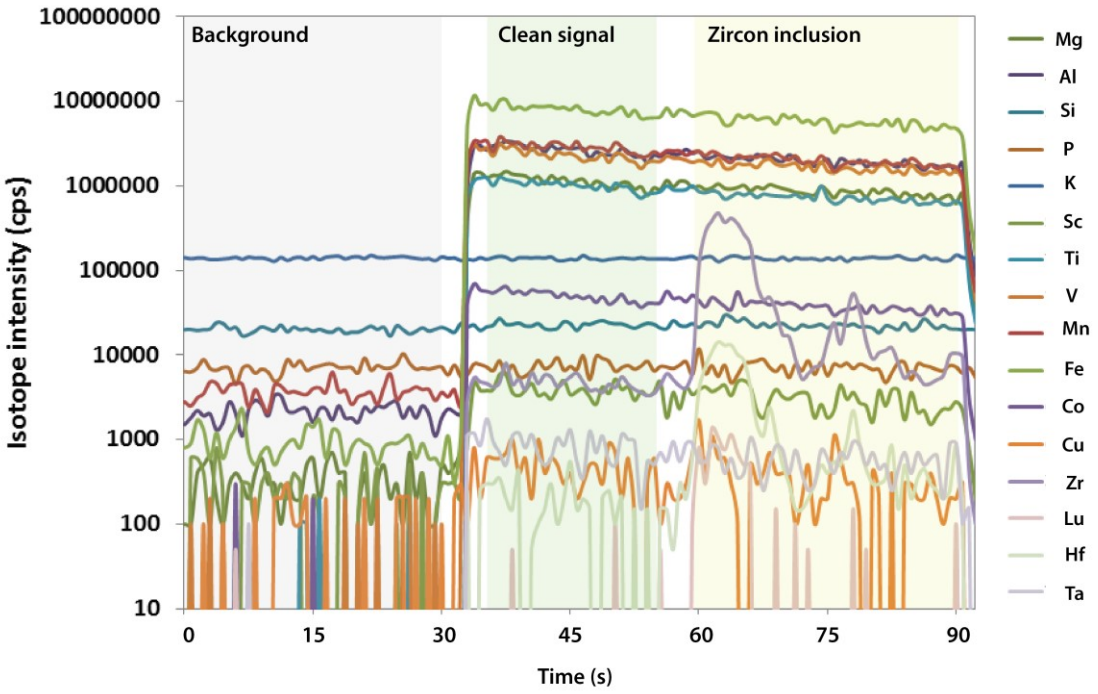


Figure 5-5: LA-ICP-MS spectra for a selection of elements illustrating the effect of a zircon inclusion in magnetite. As well as an increase in Zr, there are simultaneous increases in Hf and Lu, which also occur in elevated concentrations in zircon. In this case, only the start of the ablation signal from ~35-55 s should be processed. Analysis is titanomagnetite in OR.11(2)-RP_10_1 (JL03C20).

Despite such screening procedures, it is inevitable that some contaminated analyses are processed and make it into the dataset. By plotting certain elements, present as a major component in possible inclusions, against one another and evaluating data distributions using normal probability plots it is possible to filter out analyses which are significantly contaminated. For example, plotting K vs. Si can be used to identify analyses contaminated by K-feldspar; a steep,

positive trend towards 2:1 Si:K by weight likely indicates such a problem. Analyses which clearly follow this trend should be rejected, typically appearing as a tail protruding from a cloud of data points with no clear trend (Figure 5-6A), with a natural break resolvable on a probability plot usually at K ~ 1000 ppm. If all analyses with K > 1000 ppm are removed, K-feldspar could only represent a maximum of approximately 0.67% of the total wt. % of the analysis, assuming all K is due to such contamination.

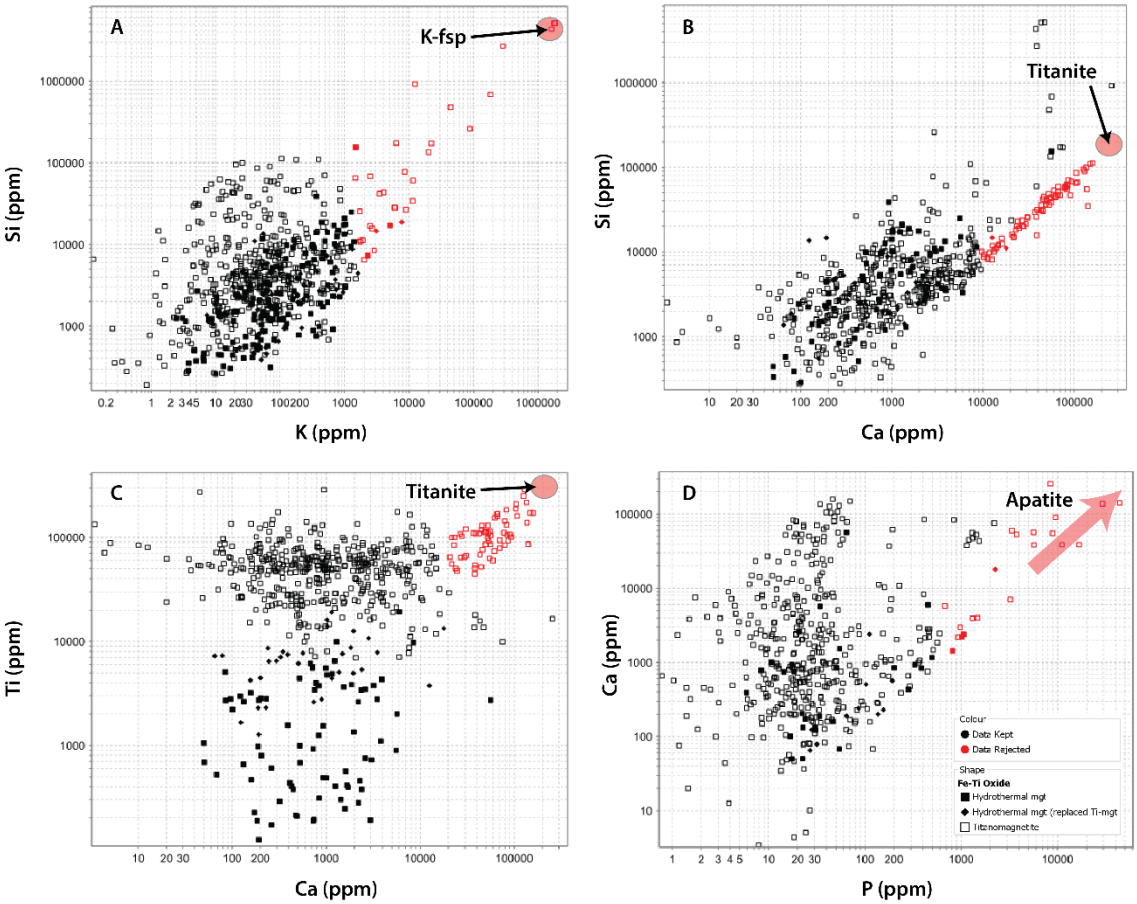


Figure 5-6: Scatter plots for a series of elements measured in magnetite by LA-ICP-MS which are susceptible to contamination from various mineral phases: A) Si vs. K contents in magnetite indicate contamination from K-feldspar; B) Si vs. Ca and C) Ti vs. Ca contents in magnetite highlight contamination from titanite; and D) Ca vs. P indicates contamination from apatite. Red circles indicate approximate composition of contaminant phases. Data derived from analyses of hydrothermal (solid symbols) and igneous (open symbols) magnetite collected in this study and that of Fry (2017). See section 6.4.1 for classification of hydrothermal and igneous magnetite. Red symbols indicate those data points clearly showing evidence for contamination and which should be rejected.

Titanite contamination is also common in magnetite, sometimes occurring as inclusions, but also frequently as replacement of exsolved lamellae in the host magnetite, formed by a process known as sphenitization. Sphenitization occurs by metasomatic introduction of CaO and SiO_2, thus grains containing titanite-altered lamellae cannot have their bulk composition reconstructed by the methods described earlier. Neither Ca nor Si are typically observed in high concentrations (e.g. > 1 wt. %) in magnetite. By plotting Ca vs. Si, a positive linear trend with a gradient of approximately 4:3 Ca:Si can be used to identify contamination from titanite (Figure 5-6B). Such analyses, typically with a Ca > 500 ppm, should be rejected. A 1:1 correlation between Ca and Ti can be used to corroborate that this contamination is due to titanite (Figure 5-6C). Assuming all Ca is from titanite, removing all analyses with Ca > 500 ppm limits the possible contamination by titanite to 0.25% of the total wt. % analysed.

Similarly, contamination from zircon inclusions can be filtered by plotting Zr vs. Si. However, no clear post-processing zircon contamination was observed in datasets studied during this PhD project, possibly because it is more easily screened during visual inspection of the ablation signals.

Apatite, a particularly common inclusion in magnetite, can be screened by plotting Ca vs. P. Analyses with apatite contamination can be identified by a linear spread in the data towards 2:1 Ca:P by weight (Figure 5-6D). Data along this trend, typically with a P > 100 ppm should be rejected. If all data with P > 100 ppm are removed, apatite contamination could only make up a maximum of 0.05% of the total wt. % of the analysis.

Finally, to assess the potential presence of REE-phosphate inclusions, such as monazite, REE can also be plotted against P. However, like zircon, parts of the ablation signal with anomalously high REE are usually easily recognised and are therefore excluded from the processed signal.

A flow chart summarising how to filter analyses with significant contamination from a dataset of magnetite chemistry determined by LA-ICP-MS is provided below.

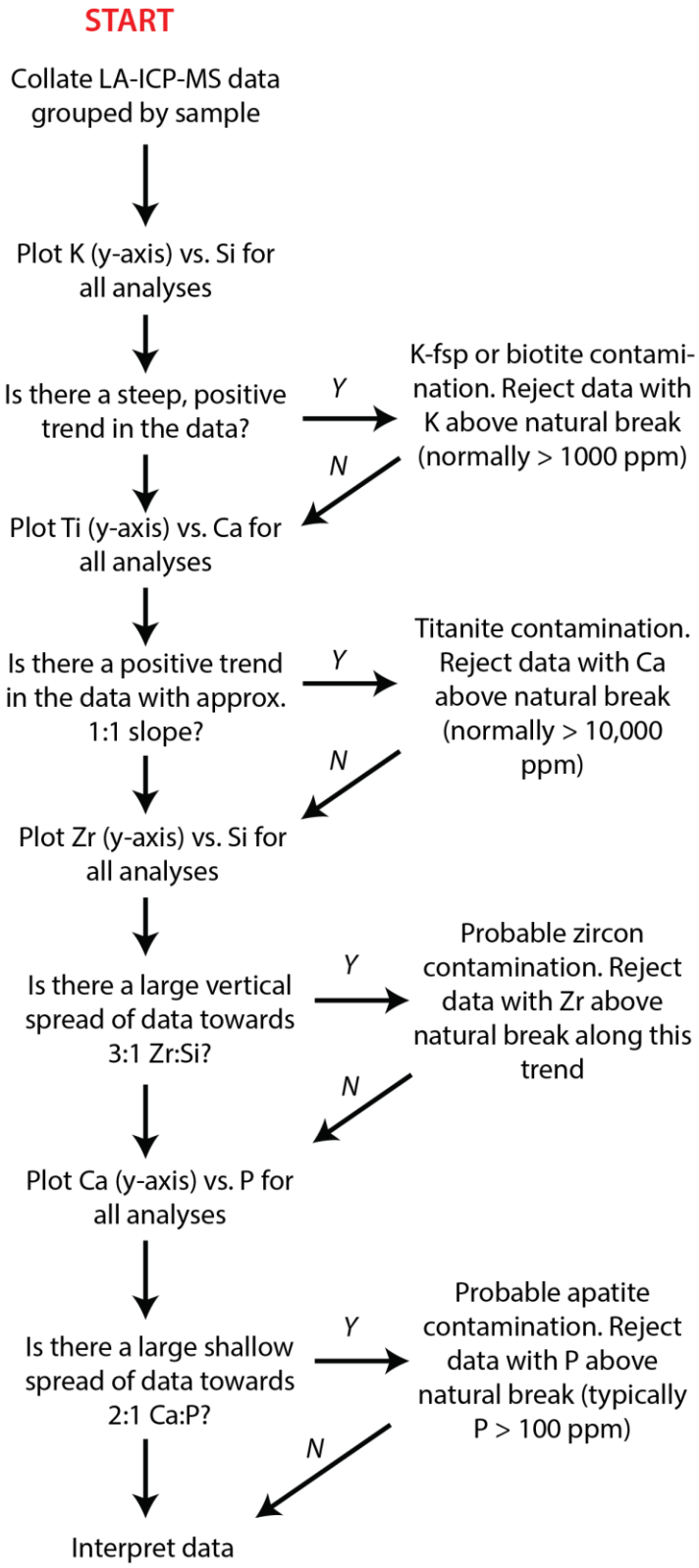


Figure 5-7: Flow chart describing how to filter analyses with significant contamination from other mineral phases.

5.3 Summary of recommended analytical method

With regard to analysing Fe-Ti oxides with strong exsolution features, the data presented here show that the internal standard, necessary for quantification of LA-ICP-MS data, can be determined using SEM-EDS by rastering the beam over the area of magnetite to be analysed. For grains with such exsolution, a spot size greater than 30 μm is able to homogenize the bulk composition, effectively representing the original composition of the Fe-Ti oxide prior to exsolution. For grains devoid of significant exsolution, there is considerable analytical variability at spot sizes less than 25 μm and several elements are below the limit of detection, thus a spot size greater or equal to 25 μm is preferred for accurate results. Spot sizes greater than 50 μm will be more prone to contamination from mineral inclusions and are therefore not recommended. Although not investigated here, the LODE research facility generally applies a 5 Hz laser repetition rate for analysis of Fe-Ti oxides, lower than the standard 10 Hz used for silicates. This is because Fe-Ti oxides ablate faster, so using a lower frequency limits the speed with which the laser drills through the sample.

GSD-1g is the recommended primary external standard, with GSE-1g as a secondary standard for monitoring, based on reliable results which are consistent with those generated in other labs (e.g. Dare et al., 2014). NIST 610, despite its low Fe concentration relative to magnetite, also generates relatively accurate results and also contains some elements not reported in GSD-1g and GSE-1g. Thus, NIST 610 could also be used as secondary standard. The importance of including a number of elements, not typically present in Fe-Ti oxides but high in concentration in possible mineral inclusions, is emphasised, as well as the importance of careful visual screening of the laser ablation spectra to avoid contamination of the analysis when signal processing. A flow chart is also presented to illustrate a suitable, post-processing, data filtering workflow. Finally, the recommended isotopes for determination of Zr, Ga and Cu are ^{92}Zr, ^{71}Ga and ^{63}Cu, based on minimal interference from other species and their isotopic abundance (see Appendix 1 – section A1.1.1).

A summary of the recommended analytical method for LA-ICP-MS analysis of magnetite is provided in Table 5-2.

Table 5-2: Recommended analytical conditions for LA-ICP-MS of natural magnetite

Parameter	**Condition**
Spot size	25-50 µm (no exsolution) 35-50 µm (with exsolution)
Laser frequency	5 Hz
Laser fluence	3.5 J/cm^2
Analysis	30 s gas blank, 60 s signal
Internal standard	Fe – use EDS and raster beam over area of exsolved mixed phases to be analysed by LA-ICP-MS
External standard	Primary: GSD-1g Secondary: GSE-1g Tertiary: NIST 610 (contains additional elements)
Isotopes	^{7}Li, ^{23}Na, ^{24}Mg, ^{27}Al, ^{29}Si, ^{31}P, ^{39}K, ^{43}Ca, ^{45}Sc, ^{49}Ti, ^{51}V, ^{52}Cr, ^{55}Mn, ^{57}Fe, ^{59}Co, ^{60}Ni, ^{63}Cu, ^{66}Zn, ^{71}Ga, ^{72}Ge, ^{75}As, ^{88}Sr, ^{89}Y, ^{92}Zr, ^{93}Nb, ^{95}Mo, ^{107}Ag, ^{111}Cd, ^{115}In, ^{118}Sn, ^{121}Sb, ^{139}La, ^{140}Ce, ^{175}Lu, ^{177}Hf, ^{181}Ta, ^{182}W, ^{185}Re, ^{195}Pt, ^{197}Au, ^{205}Tl, ^{208}Pb, ^{209}Bi, ^{232}Th and ^{238}U. Important to include Na, P, K, Ca, Cu, and REE to monitor for inclusions

6 Geochemistry of magnetite from porphyry Cu systems

6.1 Introduction

Magnetite shows good potential as a tool to fingerprint mineralisation. Pioneering work by Dupuis and Beaudoin (2012), Dare et al. (2014) and Nadoll et al. (2014) has highlighted how specific formation conditions associated with various mineral deposits and their host rocks is reflected in the chemistry of magnetite. Some studies have also investigated the chemistry of magnetite specifically from porphyry copper systems (e.g. Nadoll et al., 2015; Canil et al., 2016; Pisiak et al., 2016). However, until now there has been no work comparing the chemistry of magnetite from various sizes or types of porphyry copper system, or categories of alteration type. Notably, the ability to distinguish magnetite chemistry from mineralised and less mineralised systems could be particularly valuable for mineral exploration.

Porphyry copper deposits are associated with hydrous, intermediate to felsic (> 56 wt. % SiO_2) silicate magmas. However, within this class there are a range of possible magma compositions and emplacement conditions which may influence metal abundances and ratios in the final deposit. They are commonly grouped according to the economically dominant metals, e.g. Cu-Mo vs. Cu-Au (see section 1.2.1.2iii), and size of deposit in terms of contained Cu.

A very wide range of cations can be incorporated into igneous magnetite as illustrated by experimental studies (see chapters 2, 3 and 4). The partition coefficients between magnetite and silicate melt are largely influenced by the charge and ionic radius of the cations, but also by fO_2, mineral and melt composition, temperature, and pressure (see chapters 2, 3 and 4). The chemistry of magnetite can also be modified by post-crystallization diffusion which varies widely between different elements as a function of temperature and fO_2 (chapter 3). Thus, magnetite-melt partitioning relationships can be used to infer possible variations in parameters such as oxygen fugacity (fO_2) and temperature of the coeval melt, whereas diffusion coefficients can potentially be used to interpret the temperature and time scales of later disequilibrium processes.

A large proportion of magnetites derived from intrusions intimately associated with porphyry copper deposits are hydrothermal in origin, precipitated from an aqueous fluid as opposed to crystallising from a silicate melt at high temperature. Although the preceding experimental work has investigated magnetite-melt partitioning and diffusion at magmatic conditions, first-order principles suggest that the same factors could apply to lower temperature hydrothermal magnetite (Nadoll et al., 2014). Notwithstanding this, it is important to consider how some

factors, less relevant when studying the magmatic environment, may control the chemical composition of hydrothermal magnetite. For example, salinity and pH control the concentration and mobility of various elements in hydrothermal fluids and could therefore exert a strong influence on the partitioning of such elements into hydrothermal magnetite.

In this Chapter, the composition of magnetite from a variety of rocks associated with porphyry copper deposits with various metal associations (Cu-Au/Cu-Mo/Cu-Mo-Au) and mineralised to different degrees is evaluated to see how the different formation environments are reflected in the arising magnetite chemistry. Because rocks associated with porphyry copper systems commonly bear both hydrothermal and igneous magnetite (titanomagnetite), attention is also paid to distinguishing these contrasting forms based on texture and chemistry. The main objectives are to:

(1) explore whether hydrothermal magnetite from different alteration domains has characteristic alteration-related chemistry
(2) discriminate the different styles of porphyry deposit with different metal associations
(3) distinguish systems with different intensity or extent of mineralisation.

Discrimination diagrams developed using discriminant projection analysis (DPA) are used to subdivide populations of hydrothermal magnetite based on a range of elements commonly detectable with LA-ICP-MS. The veracity of these discrimination methods is tested using other magnetite datasets from porphyry copper deposits. This work suggests that the geochemical composition of hydrothermal magnetite can be used to discriminate well-mineralised from less-mineralised ore forming environments, which could thereby offer a valuable tool to assist in mineral exploration. Igneous magnetite, however, is particularly susceptible to having its chemistry modified by hydrothermal fluids and commonly undergoes oxy-exsolution, which alters its chemistry. Thus, the chemistry of magnetite from hydrothermally altered intrusive rocks is difficult to use to petrogenetically study the magmatic environment.

6.2 Analytical method

6.2.1 Sample selection and preparation

A total of 65 magnetite-bearing samples of intermediate-felsic igneous rock associated with 34 different porphyry copper systems were studied. The samples include both plutonic and volcanic rocks and cover a range of the different alteration types associated with porphyry copper systems (see section 1.2.1.2i). The majority of samples are derived from the inferred causative porphyry intrusion in the mineralised zone, however, some samples come from areas in the propylitic halo,

more distal to mineralisation. Samples were selected to cover a range of metal associations and sizes of porphyry copper system. Additionally, some samples of altered barren porphyry and unaltered porphyritic rocks were investigated. Samples were primarily sourced from the Ore Collection at the Natural History Museum, London, and Rio Tinto Exploration.

Samples from the Ore Collection at the Natural History Museum were rock samples. A hand magnet was used to assess whether the sample contained magnetite during sample selection. A number of these samples were collected on a field trip across Romania, Serbia and Bulgaria studying porphyry and epithermal deposits in part of the Tethyan metallogenic belt. Typically, ore collections predominantly consist of samples of strongly mineralised rock from well-known giant deposits, however, several of these samples collected on the field trip were from relatively small porphyry copper deposits and altered barren porphyry intrusions, which are important for assessing whether mineralisation tenor can be fingerprinted using magnetite chemistry. Representative sections of the chosen samples were cut using a diamond saw, mounted in epoxy and polished.

All samples supplied by Rio Tinto Exploration were magnetite separates. A random selection of grains from each separate was mounted in epoxy and polished. Although it was not possible to petrographically study the rock from which the magnetite grains originated, Rio Tinto Exploration provided a broad range of information pertaining to the rock from which the magnetite was derived, including detailed petrographic descriptions.

Each sample was categorised according to lithology, deposit type, alteration style and phase of mineralisation (pre/syn/post), if known. Relevant information pertaining to the various porphyry copper systems was researched and used to classify the samples into the following categories:

- Porphyry CuAu giant (PoCuAu-giant) – Porphyry Cu-Au deposits with approx. > 3Mt contained Cu
- Porphyry CuAu large (PoCuAu-large) – Porphyry Cu-Au deposits with approx. 1-3 Mt contained Cu
- Porphyry CuAu small (PoCuAu-small) – Porphyry Cu-Au deposits with approx. < 1Mt contained Cu
- Porphyry CuMo giant (PoCuMo-giant) – Porphyry Cu-Mo deposits with approx. > 3Mt contained Cu
- Porphyry CuMo large (PoCuMo-large) – Porphyry Cu-Mo deposits with approx. 1-3 Mt contained Cu
- Porphyry CuMoAu giant (PoCuMoAu-giant) – Porphyry Cu-Au deposits approx. > 3Mt contained Cu
- Porphyry CuMoAu large (PoCuMoAu-large) – Porphyry Cu-Au deposits with approx. 1-3 Mt contained Cu

- Porphyry Cu-prospect – Porphyry Cu prospects with no resource reported
- Background – Unaltered and not associated with porphyry mineralisation

For some porphyry copper systems, there are several samples (as many as 8 from Chuquicamata), whereas for others, only one sample was available. Although magnetite was present in all samples, its abundance varied which limited the number of analyses per sample. A total of 1833 individual LA-ICP-MS analyses were conducted of which 1273 were successfully processed. The deposits and samples with the number of successful LA-ICP-MS analyses of hydrothermal (low-Ti) and igneous (high-Ti) magnetite (classified below in section 6.4.1), are provided in Table 6-1. Figure 6-1 shows the locations of the samples analysed in this study.

Table 6-1: List of deposits and samples studied with lithology, alteration and number of successful magnetite analyses on each sample

Porphyry Cu System	Deposit	Samples[a]	Lithology	Alteration	Successful magnetite analyses	
					Hydrothermal[b]	Igneous[b]
PoCuAu-giant	Panguna	OR.2180-PAN	Quartz Diorite	Potassic-Phyllic	14	
		OR.2179-PAN	Quartz Diorite w. mgt vein	Potassic-Phyllic	18	
		OR.2174-PAN	Andesite	Propylitic	19	
		OR.2169-PAN	Andesite	Potassic	19	
	Majdanpek	OR.16(3)-MAJ	Granodiorite Porphyry	Potassic-Propylitic	11	
	Grasberg	OR.1122-GRAS	Andesitic Intrusion	Propylitic	13	14
	Far South-East/Lepanto	OR.1766-LEP	Dacite	Unaltered		14
PoCuAu-large	Dizon	OR.835-DIZ	Andesitic Intrusion	Propylitic		16
	Elatsite	OR.12(5)-ELAT	Granodiorite Porphyry	Potassic	17	3
		OR.12(4)-ELAT	Granodiorite	Potassic	22	
		OR.12(3)-ELAT	Granodiorite Porphyry	Potassic-Propylitic	5	
		OR.12(2)-ELAT	Granodiorite Porphyry	Potassic	14	1
	Placetas	RTX-3372047-PLAC	Monzodiorite Porphyry	Potassic	15	
	Rosia Poieni	OR.11(1)-RP	Andesite	Argillic-intermediate		22
		OR.11(2)-RP	Andesite	Propylitic		19
	Rovina Valley Project	OR.13(1)-ROV	Microdiorite	Potassic-Propylitic	4	16
		OR.13(2)-ROV	Microdiorite	Potassic-Phyllic	4	
	Veliki Krivelj	OR.18(2)-VK	Andesite	Unaltered		52
		OR.18(3)-VK	Andesite	Potassic-Propylitic	6	11
		OR.18(1)-VK	Andesite	Phyllic	5	
PoCuAu-small	Arroyo de las Minas	RTX-3372033-AR	Granodiorite Porphyry	Potassic-Phyllic	22	
	Valea Morii	OR.14(1)-VM	Andesite	Potassic-Propylitic	14	
		OR.14(3)-VM	Dacite	Phyllic	11	
		OR.14(2)-VM	Dacite	Phyllic	9	
	GRP 314	RTX-10047184-GRP	Quartz Monzonite Porphyry	Potassic	12	
PoCuMo-giant	Chuquicamata	OR.750(2)-CHUQ	Granodiorite	Potassic	13	
		OR.750(1)-CHUQ	Granodiorite	Potassic	13	
		OR.6271o-ESTE-CHUQ	Monzonite Porphyry	Potassic	12	
		OR.6271n-BANCO-CHUQ	Monzonite Porphyry	Potassic	6	

		OR.6273p-ES-CHUQ	Monzonite Porphyry	Potassic	26	
		OR.6273p-EL-CHUQ	Granodiorite	Potassic	29	
		OR.6273n-ES-CHUQ	Monzonite Porphyry	Potassic	28	
		OR.6273l-CHUQ-ES	Monzonite Porphyry	Potassic	52	
	La Granja	RTX-3372032-LG	Early Dacite Porphyry	Potassic	21	
		RTX-3372037-LG	Early Dacite Porphyry	Argillic-intermediate	22	
		RTX-3372030-LG	Dacite Porphyry	Potassic	23	
	Los Bronces	OR.6271k-LOS	Quartz Monzonite	Potassic	14	2
	Resolution	R-S-13	Porphyritic Granite	Unaltered		20
		R-S-8	Coarse Granite	Unaltered		19
		R-SX-1	Mafic Xenolith in Granite	Unaltered		40
	Zaldivar	RTX-6759114-ZAL	Feldspar-Biotite Porphyry	Potassic-Propylitic	18	20
PoCuMo-large	Lomas Bayas	RTX-6759101-LB	Granodiorite	Potassic	19	
		RTX-6759104-LB	Dacite porphyry	Propylitic	14	
PoCuMoAu-giant	Bingham	RTX-40100928-BING	Hybrid Monzonite	Potassic-Propylitic	18	
		RTX-40100946-BING	Quartz Latite Porphyry	Propylitic	19	
PoCuMoAu-large	La Voluntad	RTX-3372038-LV	Tonalite	Potassic	5	
	Michiquillay	OR.8(6)-MICH	Granodiorite	Potassic	6	
		OR.8(9)-MICH	Granodiorite	Potassic		13
		OR.8(7)-MICH	Andesite	Unaltered		10
	Taca Taca Bajo	RTX-3372037-TACA	Dacite Porphyry	Potassic-Phyllic	9	3
PoCu-prospect	Copper Cliff	RTX-10049733-CC	Latite Porphyry	Potassic	11	1
	Flagstaff Stock	RTX-40105538-FLAG	Granodiorite	Propylitic	4	29
	Valeo Stock	RTX-40105539-VAL	Granodiorite	Propylitic	45	
	White Pine	RTX-40105533-WP	Quartz Monzonite Porphyry	Phyllic	10	
		RTX-40105534-WP	Quartz Monzonite Porphyry	Phyllic	22	
	Red River	OR.19(2)-RED	Diorite Porphyry	Propylitic		26
		OR.19(1)-RED	Diorite Porphyry	Propylitic	3	20
	Cerro Blanco	RTX-3372048-CB	Quartz-Diorite porphyry	Argillic-intermediate	29	2
	Chelopech (porphyry)	OR.23(2)-CHEL	Diorite Porphyry	Potassic		19
	Range Front (nr. Resolution)	R-RF-G	Granodiorite Porphyry	Potassic		5
	Alta Stock	RTX-40105536-AL	Granodiorite	Unaltered	18	
		RTX-40105535-ALT	Granodiorite	Unaltered	36	
Background	Clayton Peak Stock	RTX-40105537-CLAY	Diorite	Unaltered	46	
	Little Cottonwood Stock	RTX-40105532-LILC	Porphyrytic granite	Unaltered	31	
Total					876	397

[a]*Samples with prefix "OR" were provided by the Natural History Museum and those with prefix "RTX" and "R" were provided by Rio Tinto Exploration.*

[b]*Discriminating hydrothermal from igneous magnetite is described in section 6.4.1; hydrothermal magnetite includes both vein/disseminated and replacement.*

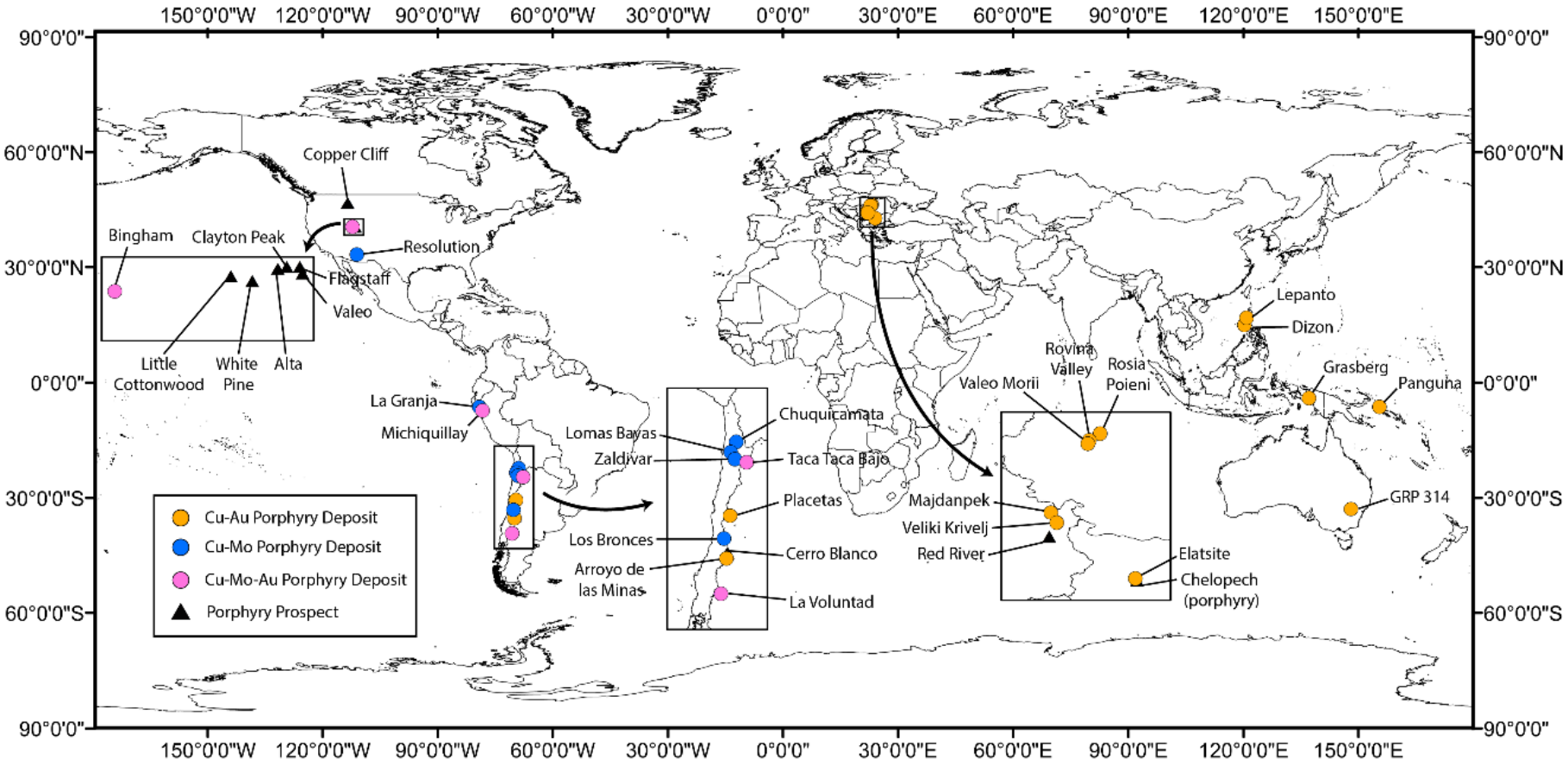


Figure 6-1World map showing location of samples used in this study.

6.2.2 SEM-EDS analysis

Prior to analysing magnetite grains with LA-ICP-MS, it is important to petrographically study the texture of the grains to be analysed in detail. This can highlight whether certain types of alteration could result in specific chemical enrichments. Moreover, in the case of hydrothermal magnetite which can be formed by a variety of possible processes (Nadoll et al., 2014), textural information can be used to better constrain the processes and stages involved in the formation of the magnetite. Petrography is also important to allow targeting of areas which are least altered and thus best approximate the environment in which the Fe-Ti oxides originally formed. All samples were studied using a Zeiss EVO 15LS SEM at the Natural History Museum, London. Textural characteristics, such as exsolution features, alteration phases and inclusions pertaining to each magnetite grain studied were documented using back-scattered electron SEM imaging. For samples sourced from the NHM where samples of rock, as opposed to mineral separates, were available, petrographic descriptions were also made documenting the abundances of other minerals and textural relationships.

SEM-EDS analyses of magnetite were conducted with an accelerating voltage of 20kV, a beam current of 3 nA. For magnetite grains with strong exsolution, the electron beam was rastered over a 40 x 40 micron square covering the area to be analysed by LA-ICP-MS in order to take account of the exsolution. Grains devoid of exsolution were analysed with a < 1 micron spot size.

6.2.3 LA-ICP-MS analysis

Magnetite was analysed by LA-ICP-MS at the LODE laboratory at the Natural History Museum, London, using a New Wave Research 193 nm excimer laser coupled with an Agilent 7700x quadrupole ICP-MS. Between 10 and 60 magnetite grains per sample were analysed, depending on the abundance of suitable magnetite grains. Grains with least exsolution, alteration and fracturing were targeted for analysis to minimise contamination from other phases.

The analytical method follows those recommended in section 5.3. The laser was operated with 5 Hz pulse frequency, a fluence of 3.5 J cm^{-2}, and a spot size between 35 and 50 microns for grains with exsolution, or 25 and 50 microns for grains without exsolution, however, in some cases (55/1833 analyses) a spot size between 15 and 25 microns was applied where grains were very small. The Fe concentration, determined by SEM-EDS, was used as the internal standard, making sure the same analytical spot was targeted with both SEM-EDS and LA-ICP-MS. The background was analysed for 30 s, followed by 90 s of ablation. The masses analysed were: ^{7}Li, ^{23}Na, ^{24}Mg, ^{27}Al, ^{29}Si, ^{31}P, ^{39}K, ^{43}Ca, ^{45}Sc, ^{49}Ti, ^{51}V, ^{52}Cr, ^{55}Mn, ^{57}Fe, ^{59}Co, ^{60}Ni, ^{63}Cu, ^{66}Zn, ^{71}Ga, ^{72}Ge, ^{75}As, ^{88}Sr, ^{89}Y, ^{92}Zr, ^{93}Nb, ^{95}Mo, ^{107}Ag, ^{111}Cd, ^{115}In, ^{118}Sn, ^{121}Sb, ^{139}La, ^{140}Ce, ^{175}Lu, ^{177}Hf, ^{181}Ta, ^{182}W, ^{185}Re, ^{195}Pt, ^{197}Au,

^{205}Tl, ^{208}Pb, ^{209}Bi, ^{232}Th and ^{238}U. Each batch of 15-18 magnetite analyses was bracketed by three analyses of a primary calibration standard (GSD-1g) and a secondary standard (GSE-1g) with a spot size of 50 μm. Each batch of magnetite analyses also included one analysis of a natural Ti-rich magnetite (BC28) studied by Dare et al. (2012). In some batches, two analyses of a tertiary standard (NIST 610) were also conducted. The Th/ThO+ ratio was optimized to be less than 0.2%.

Based on repeat analyses of GSE-1g, the analytical precision (calculated as 100*[measure-true]/true) is better than 5% for all elements studied apart from P, Cr, Zn, Cd, Pt, Au, Tl and Th (Figure A1-1). Chromium, Cd, Tl and Th have precisions between 5 and 10%; Zn, Sn and Tl between 10 and 15%; and P and Au at 20 to 25%. The precision in comparison to the composition reported by Dare et al. (2014) for BC28 is better than 10% for Cr, Ni, Sc, Co, Nb, Ti, Ga, Ti, Al, Mg and V; between 10 and 20% for Mn, Hf, Zr, Ta, P and Zn; 30 to 40% for Mo, Si; but varied by more than 66% for Pb, Ge, Sn, Y and Cu (Figure A1-1). However, some elements, such as Y and Cu, with high RSD values may well be heterogeneous in the natural magnetite, so that this feature may not necessarily reflect poor analytical precision. Detection limits were calculated following the method of Longerich et al. (1996), as three times the standard deviation of the gas background signal that contains zero analyte. Analyses below the limit of detection are provided as the detection limit with a "<" as a prefix.

Data were reduced using in-house software (ExLAM 2000) with careful attention paid to the exclusion of areas affected by contamination from mineral inclusions when processing. Further screening following the flow chart procedure outlined in section 5.2.4 was also conducted to remove any remaining contaminated analyses.

6.3 Results

6.3.1 Petrography

The magnetite studied exhibit a variety of textures, morphologies, alteration and inclusions. Notably, there are distinct differences between high-Ti magnetite (Ti > 1 wt. %), which is likely to be igneous in origin, and low-Ti magnetite (Ti < 1 wt. %), which is probably hydrothermal.

High-Ti magnetite typically forms subhedral-euhedral individual crystals or large glomerocrysts intergrown with other igneous phases. This form of magnetite commonly exhibits oxy-exsolution typically forming abundant ilmenite-rich lamellae along cubic spinel planes known as 'trellis' texture (Figure 6-2A). This decreases the Ti content in the residual unexsolved regions of the magnetite. Titanite can also form through replacement of these lamellae during metasomatism by late-stage hydrothermal fluids. Although less common, titanite can also form through

metasomatism of magnetite, which can produce a mottled appearance in SEM-BSE image (Figure 6-2F); this alteration is focused along fractures and grain boundaries which increase effective porosity and are favourable for fluid infiltration. Ilmenite exsolution can also occur replacing larger areas of the precursor titanomagnetite, producing a striped texture (Figure 6-2D), although this form of exsolution is less common than 'trellis' exsolution. Samples which were relatively unaltered and volcanic, as opposed to plutonic, more commonly contained magnetite devoid of complex exsolution and alteration (Figure 6-2B). Titanomagnetite grains are often poikilitic, containing inclusions other phases, including apatite (Figure 6-2E), zircon, chalcopyrite (Figure 6-2B) and silicate phases, such as K-feldspar. Mineral inclusions commonly occur in a concentric manner, suggesting a stage of growth in which magnetite and the included phases were co-crystallising (Figure 6-2E). Some particularly unusual textures were observed sporadically, such as the lamellae of high-Ti magnetite overprinting trellis exsolved magnetite (Figure 6-2C).

Low-Ti magnetite (Ti < 1 wt. %), generally occurs in veins or in voids, but is often disseminated. Magnetite with Ti < 1 wt. % often resembles the euhedral-subhedral morphology of igneous magnetite and in some cases hydrothermal magnetite displays evidence for transitional replacement of titanomagnetite (Figure 6-4). Less commonly, this form of magnetite was observed progressively replacing silicate phases, such as biotite. Low-Ti magnetite does not typically show oxy-exsolution forming Ti-rich lamellae, possibly as a result of its low-Ti concentrations not permitting the formation of Ti-rich exsolution phases. Notwithstanding this, some low-Ti magnetite replacing titanomagnetite or resembling a crystal habit like titanomagnetite does exhibit signs of relic trellis exsolution (Figure 6-4B). Magnetite with low-Ti commonly exhibits recrystallization textures with 120° triple junctions (Figure 6-3A). This has been attributed to fluid assisted recrystallization in the presence of Si-rich hydrothermal fluids by Hu et al. (2015). Some rare low-Ti magnetite shows oscillatory zoning with Si-inclusion rich zones suggesting precipitation from Si-saturated hydrothermal fluids (Figure 6-3B). Martitization (hematite after magnetite) was frequently observed in low-Ti magnetite, as evinced by a lower SEM-EDS total of 87-89 wt. % in comparison to magnetite with a total of 91-94 wt.% and lower Fe content, with 66-68 wt. % Fe in martite in comparison to 70-72 wt.% Fe typically measured in magnetite (Figure 6-3C). Martite also appears a slightly different grey in SEM-BSE images. Although it was often difficult to discriminate martite from magnetite in SEM-BSE images, these phases could be clearly distinguished on the RL camera used for navigation during LA-ICP-MS, with magnetite appearing a darker grey relative to martite in RL (Figure 6-3E and F). Martitization is caused by alteration by an oxidising or acidic fluid (Ohmoto, 2003). Areas with greatest effective porosity are more prone to martitization, such as heavily fractured grains (Figure 6-3F), or along grain boundaries (Figure 6-3E).

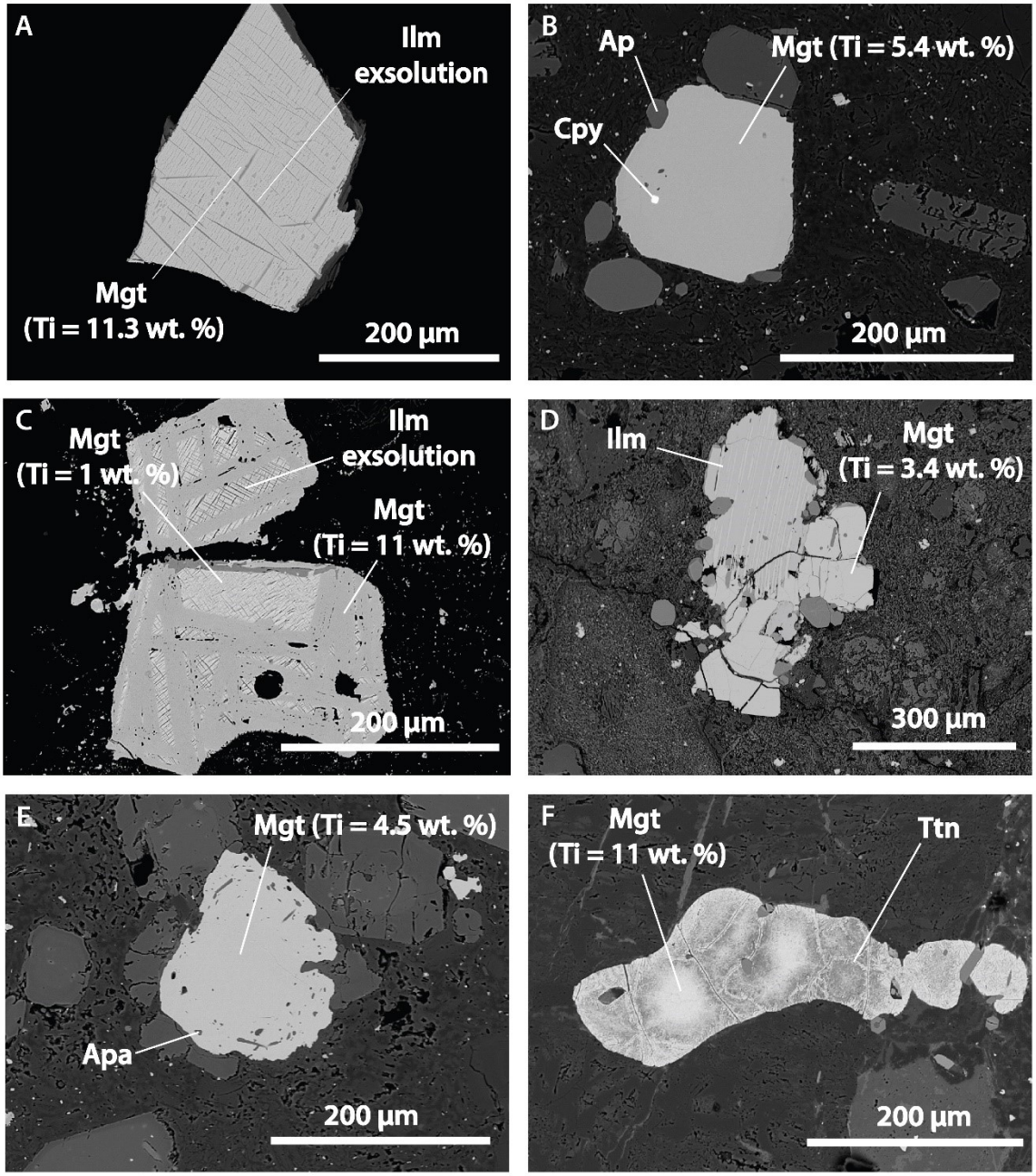


Figure 6-2: BSE images showing examples of textures observed in magnetite with Ti > 1 wt. %. (A) Subhedral titanomagnetite with ilmenite 'trellis' lamellae (R-S-8). (B) Euhedral titanomagnetite devoid of exsolution and with chalcopyrite inclusion (OR8(7)-MICH). (C) Magnette with 'trellis' exsolution overprinted with thick lamellae of high-Ti titanomagnetite (Abinico formation, C. Chile – Fry, 2017). (D) Subhedral glomerocryst of fractured titanomagnetite with stripes of ilmenite exsolution (OR.835-DIZ). (E) Subhedral titanomagnetite with a concentric rim with several apatite inclusions (OR8(7)-MICH). (F) Subhedral fractured titanomagnetite with titanite alteration concentrated along fractures and at the rim (Farrellones formation, C. Chile – Fry, 2017). Abbreviations: Mgt = magnetite; Ttn = titanite; Ilm = ilmenite; Cpy = chalcopyrite.

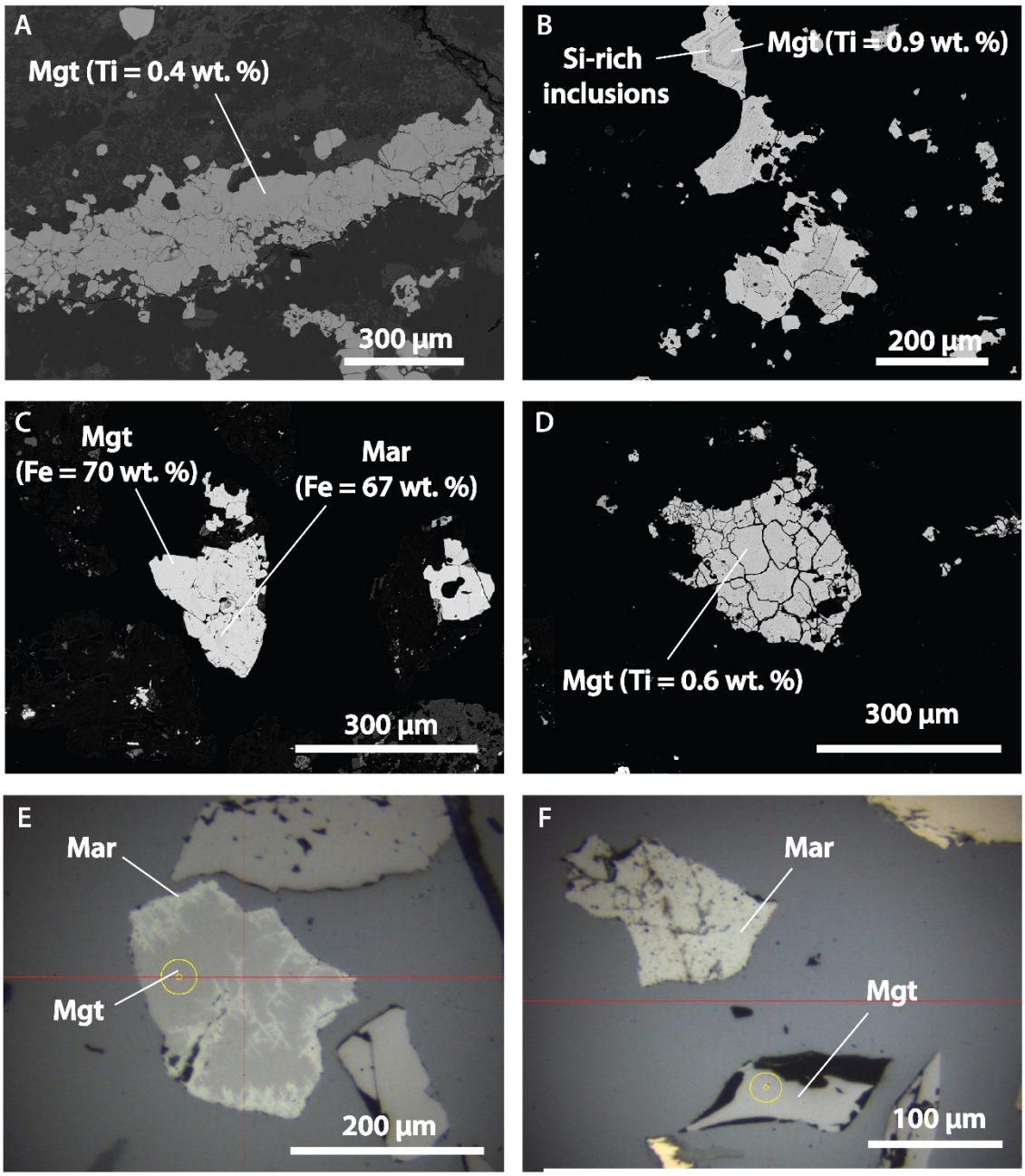


Figure 6-3: BSE and RL images showing textures observed in magnetite with Ti < 1 wt. % which occurs as veins or in voids. (A) BSE image of vein magnetite recrystallized with 120° triple junctions (OR.16(3)-MAJ). (B) BSE image of oscillatory zoning in magnetite with Si inclusion-rich zones (La Granja). (C) BSE image of partially martitized magnetite; martitization is less obvious in BSE than in RL (RTX-40105539-VAL). (D) BSE image of void magnetite with recrystallized texture (La Granja). (E) RL image of magnetite with martitization concentrated along fractures and rim (RTX-3372047-PLAC). (F) RL image of magnetite (dark grey) and martitized magnetite (light grey) (RTX-3372030-LG).

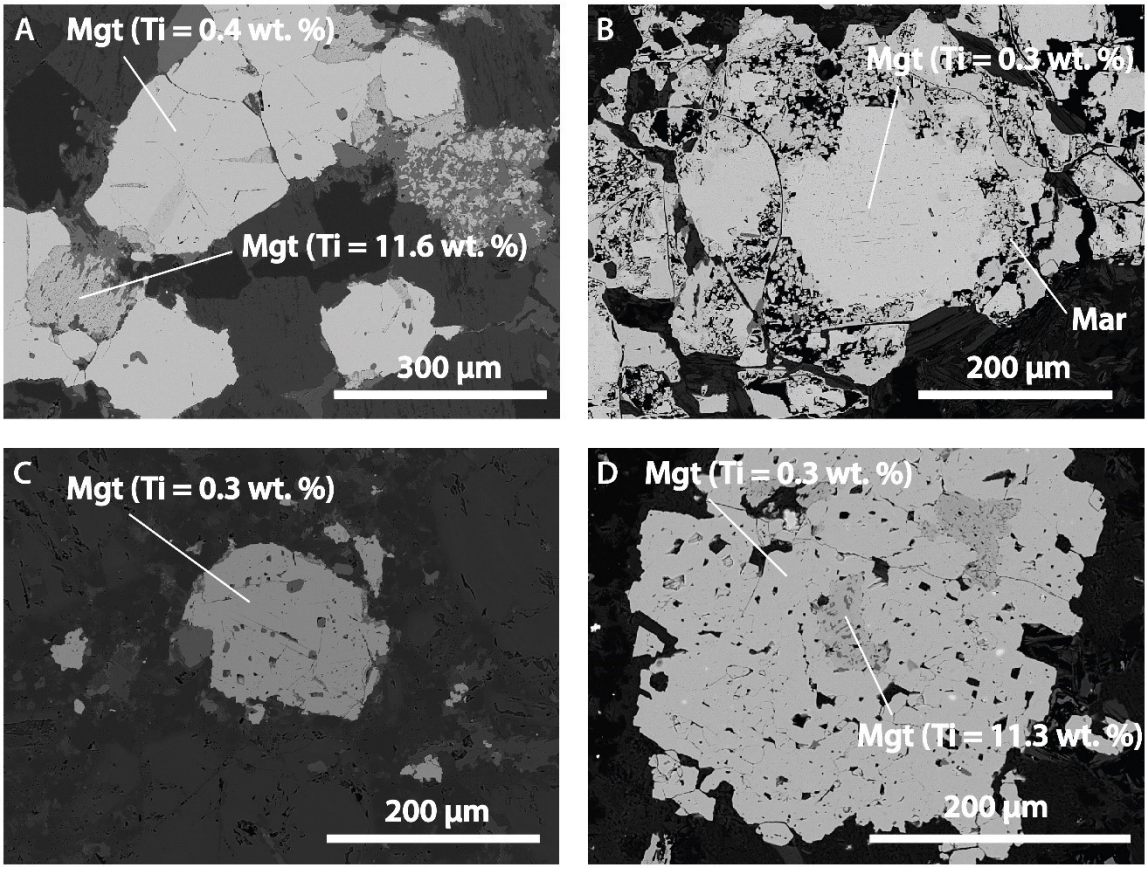


Figure 6-4: BSE images showing textures observed in magnetite with Ti < 1 wt. % which replaces other phases. (A) Low-Ti magnetite with recrystallized texture partially replacing existing high-Ti magnetite with ilmenite exsolution (OR.6271-LOS). (B) Subhedral core of low-Ti magnetite with relic 'trellis' exsolution, which has likely replaced Ti-rich magnetite, and overgrowth with martite alteration (OR.2179-PAN). (C) Subhedral low-Ti magnetite resembling the morphology of igneous magnetite with apatite inclusions (Sample OR.14(1)-VM) (D) Low-Ti magnetite with relic 'trellis' exsolution replacing igneous magnetite with trellis exsolution, still present in the core (OR.1122-GRAS).

6.3.2 Chemistry of magnetite

The complete raw dataset of all SEM-EDS and LA-ICP-MS analyses is provided in Appendix 3. There are two distinct varieties of magnetite in the dataset, one with elevated Ti (generally Ti > 1.5 wt. %) and one with lower Ti contents (generally Ti < 0.5 wt. %), which correspond to igneous titanomagnetite and hydrothermal magnetite respectively. The method used to discriminate igneous and hydrothermal magnetite based on texture and chemistry is provided in section 6.4.1. Hydrothermal magnetite is close to pure stoichiometric Fe_3O_4, with only a minor amount of some other elements, such as Al, Ti, Mn and V. Minor element concentrations are typically less than 0.5 wt. % and may not be reliable given they are close to the detection limit of SEM-EDS. Igneous magnetite are dominated by a magnetite (Fe_3O_4) component, but also have significant Ti (up to 13.3 wt. %), Mg (up to 3.6 wt. %), Al (up to 4.8 wt. %), Cr (up to 13.3 wt. %), Mn (up to 1.9 wt. %) and minor V.

6.3.2.1 Comparison of analytical methods

Some trace elements, such as Ti, Mg and Al, could be detected by both SEM-EDS and LA-ICP-MS providing data for cross-comparison between the two analytical techniques. Titanium was the most frequently detected trace element using SEM-EDS. The Ti concentrations determined using both techniques are generally in very good agreement, with a robust simple regression yielding an $R^2 = 0.9976$ (Figure 6-5). However, this breaks down at values determined using SEM-EDS with Ti < 0.1 wt. % which likely represents the approximate value of the detection limit of this technique. Significant scatter concentrated above a 1:1 reference line for Ti in magnetite measured using EMP and LA-ICP-MS (Pisiak et al., 2017) was attributed to an undersampling of Ti-rich exsolution lamellae when using electron-beam based techniques, owing to the small electron beam size in comparison with laser spot sizes. This is not apparent in this dataset, probably as a result of using a rastered 40 x 40 micron electron beam when analysing grains with strong exsolution.

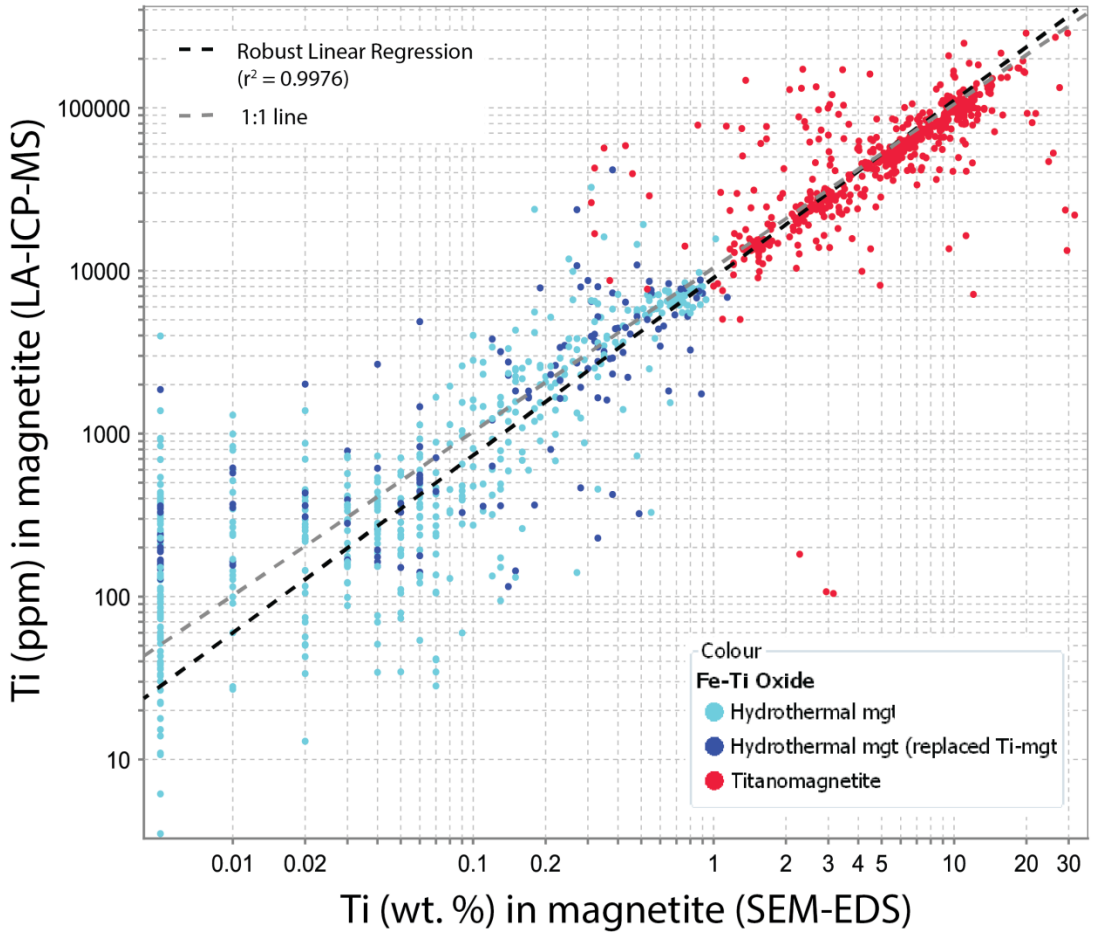


Figure 6-5: Comparison of Ti in magnetite determined using LA-ICP-MS and SEM-EDS. A good correlation is observed between the two techniques, however, this breaks down < 0.1 wt. % Ti close to the detection limit of SEM-EDS. Classification of hydrothermal and titanomagnetite is provided in section 6.4.1. Grey dashed line is 1:1 and black dotted line is robust simple regression which has an $R^2 = 0.9976$.

6.3.2.2 Hydrothermal magnetite

A summary of the hydrothermal magnetite content in each sample is provided in Appendix 3. For analyses of hydrothermal magnetite, Mn, Al, Mg, V, Zn, Ti, Co, Ni, Ga, Cr, Ge were above the limit of detection in more than 93% of the analyses; Sn, Sc, Zr were detected in 70-79% of all analyses and Si, Mo and Sr were detected in 51-60% of the analyses. All other elements were detected in less than 50% of the analyses. The proportion of successful LA-ICP-MS analyses above the limit of detection for each element analysed are provided in Table 6-2.

All elements were plotted against one another to examine bivariate relationships. Scandium, V, Cr, Co, Ni, Ga, W and U do not have strong correlations with any other element (< 0.45 Pearson correlation coefficient). Notably, there is relatively little variation in Ga and V compared to other elements commonly above the limit of detection (Figure 6-6C). The partitioning of V has been suggested to be controlled by the redox state (Toplis and Corgne, 2002; Righter et al., 2006, chapters 2, 3 and 4), which could suggest that there is relatively small variability in the oxygen fugacity of hydrothermal fluids in the magnetite-stable domain of porphyry copper systems.

Studies on natural hydrothermal magnetite suggest that Ga is controlled by temperature (Nadoll et al., 2014). The narrow range in Ga therefore implies that magnetite does not precipitate from porphyry-related fluids over a very wide range in temperature, consistent with its spatial distribution (section 1.2.1.2). In contrast, experimental work does not indicate that Ga partitioning between melt and magnetite is sensitive to temperature over the limited temperature range studied (section 2.3.2).

Mg shows strong correlation with Al with a Pearson correlation coefficient of 0.74 (Figure 6-6D); the relative proportions of these elements suggest that this could be attributed to contamination from inclusions of biotite although, given the variable content of Mg and Fe in biotite, this is difficult to verify. Alternatively, this could be related to a coupled substitution of Mg with Al in spinel. There is a positive correlation between Ti and Al (Figure 6-6A) (Pearson correlation coefficient of 0.78) and Ti and Mn (Figure 6-6B) (Pearson correlation coefficient of 0.47) which has been noted in hydrothermal magnetite by Canil et al. (2015). There is also a good correlation between Mn and Zn (Figure 6-6E) (Pearson correlation coefficient of 0.69), suggesting that the behaviour of these elements is coupled. Molybdenum and Zr are particularly strongly correlated with a Pearson linear correlation coefficient of 0.96 (Figure 6-6F); it is possible that this could arise due to an isotopic interference given that there are several possible isotopes of Zr (section A1.1.1) which could form molecules with the same mass as ^{95}Mo.

Table 6-2: Proportion of analyses above the limit of detection of LA-ICP-MS for each element analysed in hydrothermal magnetite

Element	% Above LOD in Hydrothermal Mgt
Mn	100
Al	99.9
Mg	99.8
V	99.5
Zn	99.4
Ti	99.3
Co	98.7
Ni	98.5
Ga	98.5
Cr	94.2
Ge	93.7
Sn	78.6
Sc	73.9
Zr	69.6
Mo	59.9
Si	57.0
Sr	50.8
Ce	49.3
Pb	41.2
Cu	40.6
U	39.3
La	38.8
Y	34.5
Nb	30.3
P	26.0
K	25.7
Th	25.7
W	23.4
Ba	20.2
Li	18.4
In	17.0
Ta	14.6
Tl	14.4
Na	12.2
Ca	11.6
As	11.4
Lu	8.6
Sb	8.3
Ag	7.1
Hf	7.0
Bi	6.5
Pt	3.0
Cd	2.9
Au	2.3

Copper was generally highly heterogeneous within samples with RSD within sample greater than 150% for several samples. High Cu variability was also observed whilst analysing BC28 (section 5.2.3) and could be attributed to nano-inclusions of Cu-bearing minerals in magnetite.

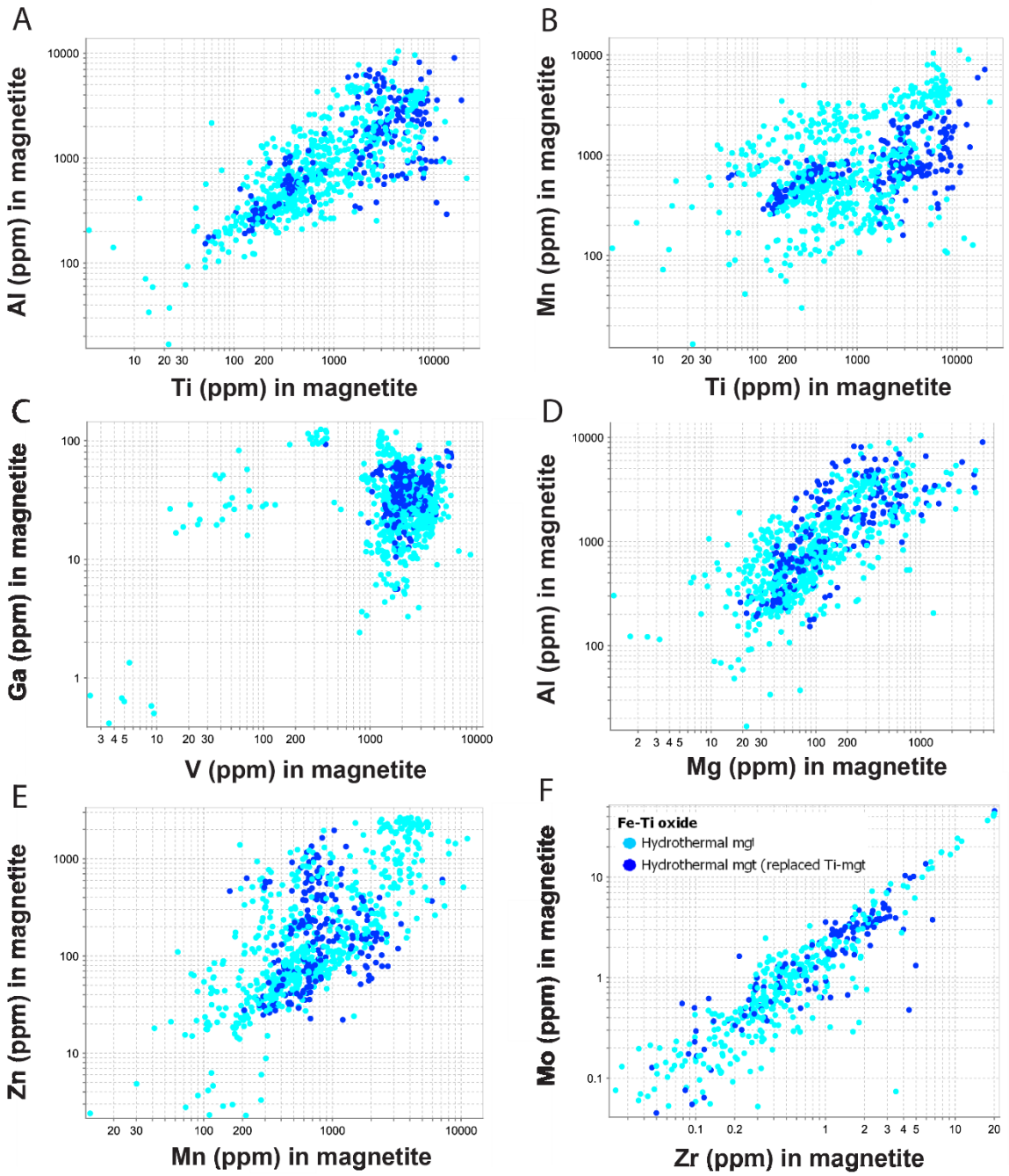


Figure 6-6: Scatterplots for hydrothermal magnetite compositions. (A) Al vs. Ti; (B) Mn vs. Ti; (C) Ga vs. V; (D) Al vs. Mg; (E) Zn vs. Mn; and (F) Mo vs. Zn.

6.3.2.3 Igneous magnetite

A summary of the igneous magnetite content in each sample is provided in Appendix 3. The percentage of analyses less than the limit of detection is less than 10% for Ti, V, Cr, Mn, Ni, Ga, Mg, Al, Zr, Sc, Co, Sn, Zn, Nb, Sr and Cu (Table 6-3). Molybdenum, Ta, Hf, Si, Y, Ge, Ce and In were detected in 71-86% of analyses, and U, La, W and Li were present above the limit of detection in 51-69% of analyses.

Table 6-3: Proportion of analyses above the limit of detection of LA-ICP-MS for each element analysed in igneous magnetite.

Element	% Above LOD in Igneous Mgt
Ti	100
V	100
Cr	100
Mn	100
Ni	100
Ga	100
Mg	100
Al	100
Zr	99.7
Sc	99.5
Co	98.7
Sn	97.2
Zn	96.9
Nb	95.9
Sr	94.3
Cu	93.0
Mo	85.6
Ta	84.5
Hf	79.4
Si	78.4
Y	78.1
Ge	75.5
Ce	74.7
In	71.1
U	68.7
La	67.0
W	60.6
Li	51.9
Pb	45.1
Ba	43.9
Th	42.8
Lu	35.8
P	33.8
Sb	30.9
Au	29.2
As	26.0
K	25.3
Ca	24.7
Na	12.4
Tl	11.0
Bi	9.3
Cd	8.0
Ag	7.2
Pt	1.7

All elements analysed were plotted against one another to examine for significant correlations. Copper and Ga do not exhibit strong correlation with a Pearson correlation coefficient greater than 0.5 with any other elements. Magnesium has a distinct positive correlation with Co, suggesting that the behaviour of these elements is similar (Figure 6-7A); titanomagnetite data collected by Fry (2017) in a master's project related to this PhD project (Appendix 4) also follow the same correlation. Magnesium and Co are both divalent cations with similar geochemical behaviour which could explain the association. As previously observed for hydrothermal magnetite, there is also relatively little variation in Ga and V in igneous magnetite (Figure 6-7B). Moreover, the concentrations of these elements are similar in both igneous and hydrothermal magnetite. It could be that the concentrations of V and Ga are largely dictated by the fO_2 and temperature, respectively, under which the magnetite formed. There is also a positive correlation between Cr and Ni (Figure 6-7C), which, like Mg and Co, follows the same trend defined by titanomagnetite from volcanics in Central Chile (Fry, 2017 - Appendix 4). It is possible that this correlation is controlled by variable contamination of another phase which bears both Cr and Ni. Alternatively, this correlation could reflect the coupled behaviour of Ni and Cr in calc-alkaline magmas. Nickel and Cr are both strongly compatible in magnetite (e.g. section 3.3.3), so will decrease in the melt with progressive magnetite fractionation.

A particularly strong correlation (Pearson Linear Correlation Coefficient = 0.94) was observed between Nb and Ta (Figure 6-8A). These elements are characteristically high in ilmenite relative to magnetite (Figure 6-9). Ilmenite trace element data are available from 22 successful LA-ICP-MS analyses performed on six samples (OR8(9)-MICH, OR.1766 – LEP, OR8(7) – MICH, OR.835 – DIZ, OR.13(2)-ROV, OR.14(1)-VM) using the same analytical method as for LA-ICP-MS of magnetite. These ilmenite analyses cluster at the high Nb and Ta end of the linear trend, suggesting that this trend could represent variable incorporation of ilmenite contamination in the analyses. Data from titanomagnetite with variable exsolution from Central Chile volcanics (Fry, 2017) also plot along a similar trend. Textural analyses of the magnetite grains analysed also confirmed that those at the high Nb and Ta end of the linear trend have particularly strong ilmenite exsolution, whereas those at the low Nb and Ta end have little to no exsolution (Figure 6-8A).

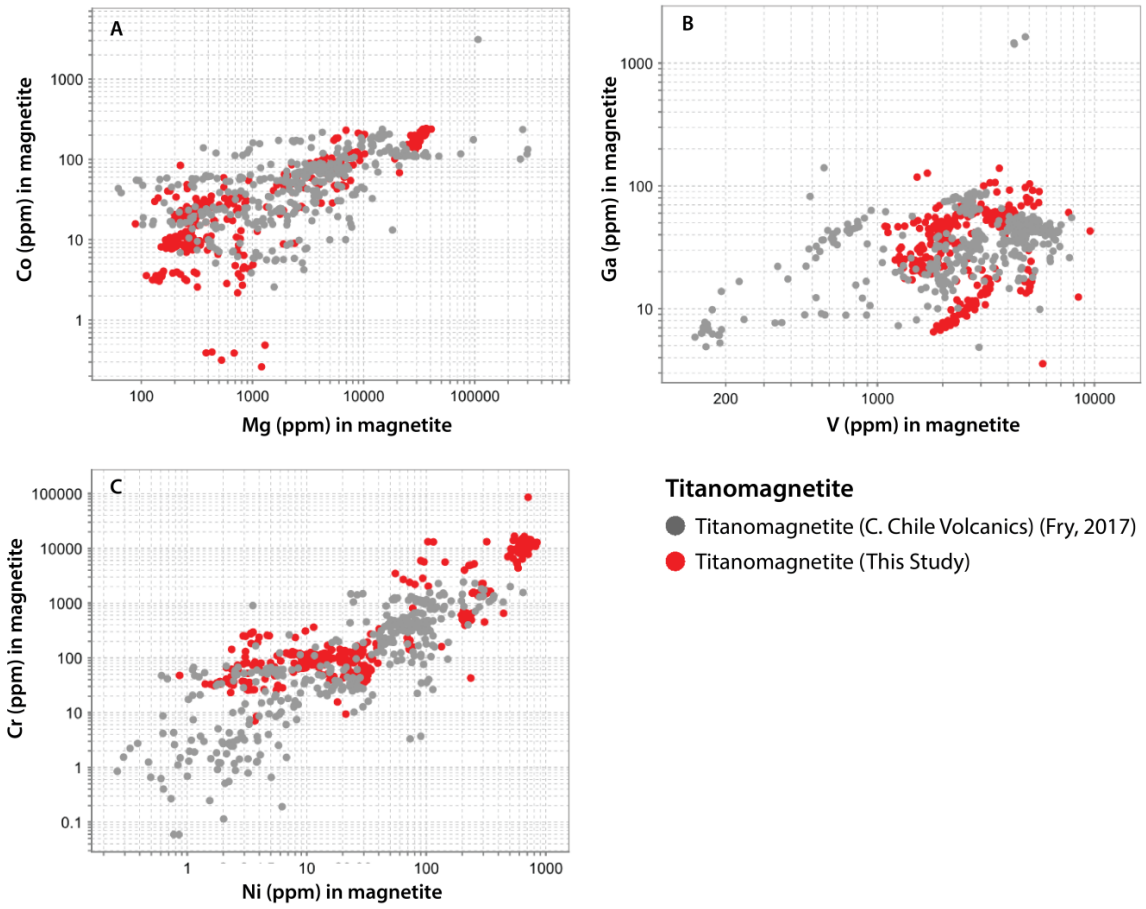


Figure 6-7: Scatterplots for igneous magnetite compositions. (A) Co vs. Mg; (B) Ga vs. V; and (C) Ni vs. Cr.

The composition of magnetite (hydrothermal and igneous) was compared with ilmenite using box and whisker diagrams to assess which elements have the largest difference in concentration between magnetite and ilmenite. Scandium, Ti, Zr, Nb, In, Hf and Ta occur at higher concentrations in ilmenite relative to magnetite (Figure 6-9); the extreme upper values in titanomagnetite, represented by the upper whisker, are comparable to the composition of ilmenite. Gallium was the only element observed with substantially lower concentrations in ilmenite relative to magnetite (Figure 6-9). Plotting Zr vs. Ti (elements with large concentration difference between magnetite and ilmenite), defines two positive linear trends, which converge towards the composition of ilmenite (Figure 6-8B); titanomagnetite data from central Chile volcanics further support this trend (Fry, 2017). Similarly, plotting Sc vs. Ta, shows a positive linear trend towards the composition of ilmenite (Figure 6-8C). Furthermore, data acquired from titanomagnetite with strong exsolution cluster together with ilmenite on this diagram.

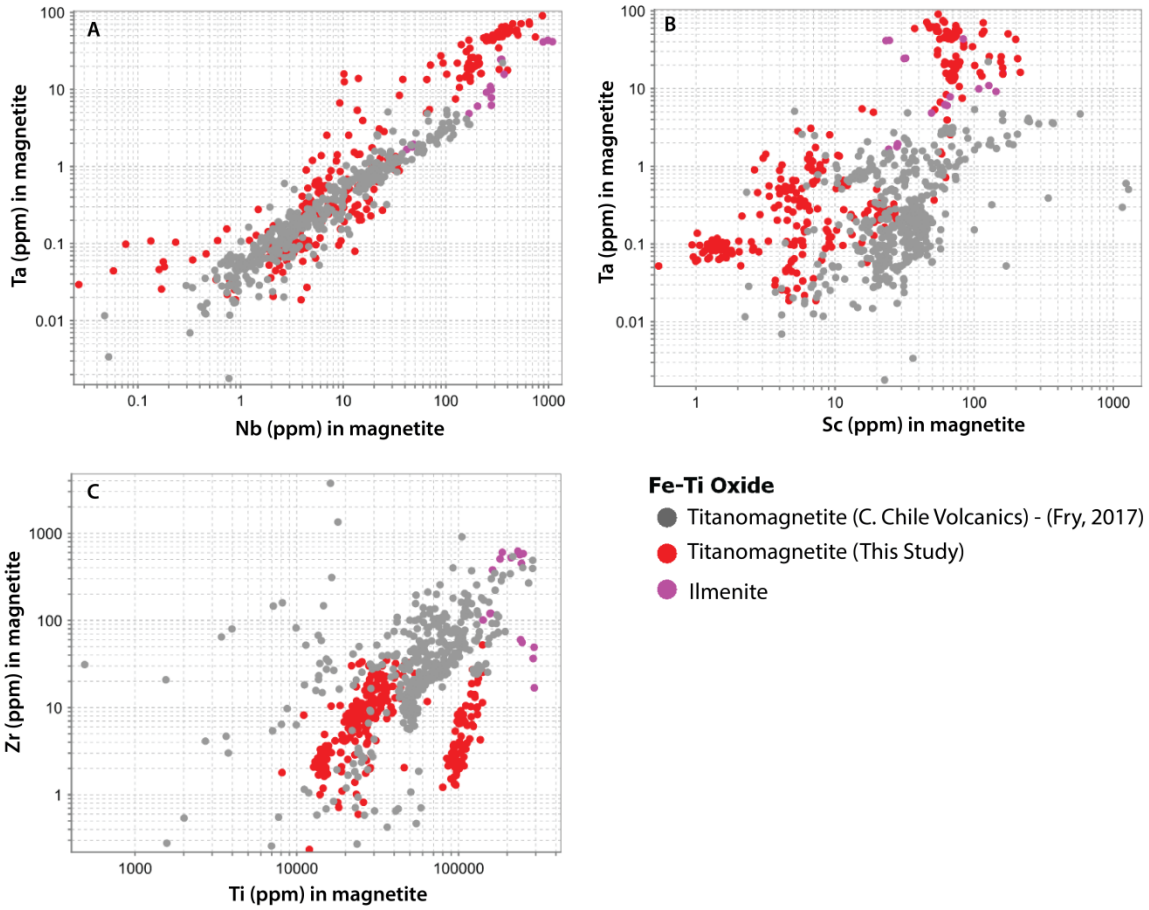


Figure 6-8: Scatterplots for igneous magnetite compositions. (A) Ta vs. Nb; (B) Ta vs. Sc; and (C) Zr vs. Ti.

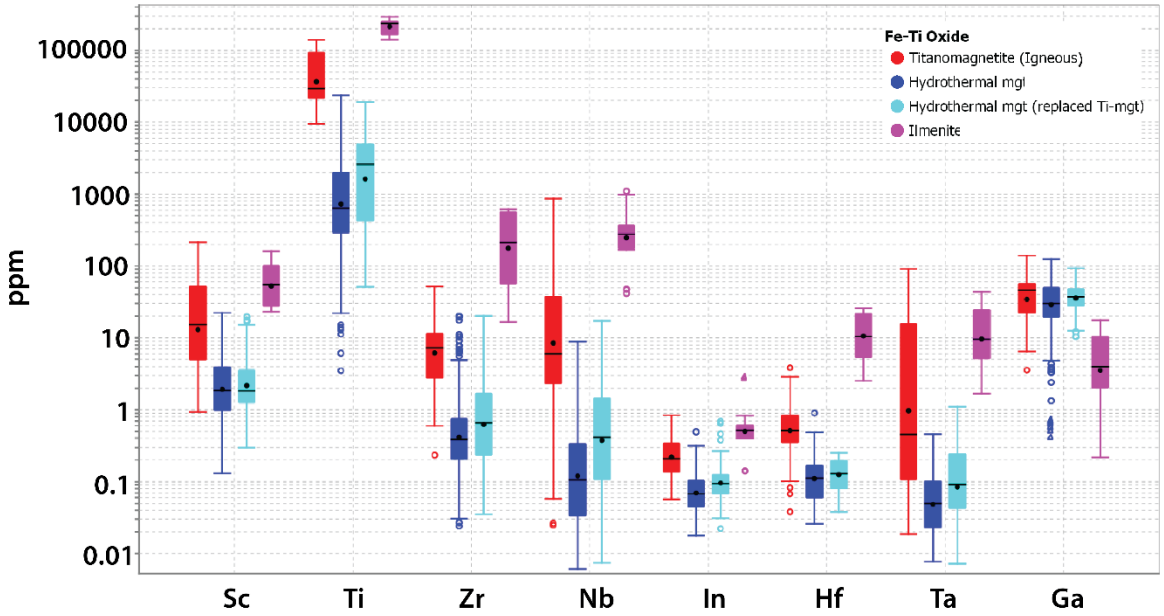


*Figure 6-9: Box and whisker plot comparing element concentrations which are substantially different in ilmenite relative to hydrothermal and igneous magnetite. Central box is the middle 50% of data from Q1 to Q3. Outliers are shown by circles (greater than 1.5 * (Q3-Q1) from the box) and triangles (greater than 3.0 * (Q3-Q1) from the box). The whiskers represent the extreme values which are not outliers on the basis given above.*

6.3.2.4 Effect of Hydrothermal Alteration on Chemistry of Igneous Magnetite – Rosia Poieni Case Study

Most samples studied were from intermediate-felsic igneous rocks with hydrothermal alteration. As a result, samples were generally richer in hydrothermal magnetite than igneous titanomagnetite (Table 6-1). Moreover, in the samples which predominantly contain igneous magnetite, the titanomagnetite is strongly altered as evinced from petrographic observation. If we are to use igneous titanomagnetite as a petrogenetic indicator to interpret conditions pertaining to magmatic environments, it is important to understand what effect different styles of hydrothermal alteration have on its chemistry.

Samples OR11(1)-RP and OR11(2)-RP from Rosia Poieni (Figure 6-10) are both from the same andesitic unit (Middle Miocene andesite). Both samples similarly contain large amphibole (1-2 mm) and plagioclase (1-3 mm) phenocrysts in a finer grained matrix. However, OR11(1)-RP has undergone moderate argillic alteration to form fine-grained clay whereas OR11(2)-RP has undergone weak propylitic alteration forming a pervasive darker green colour (Figure 6-10). Igneous titanomagnetite is present in both samples, so the effect of these two forms of alteration can be evaluated. Titanomagnetites in both samples are slightly poikilitic with inclusions of apatite, zircon, K-feldspar and chalcopyrite, have minor trellis exsolution and, sometimes, thicker stripes of ilmenite exsolution (Figure 6-10).

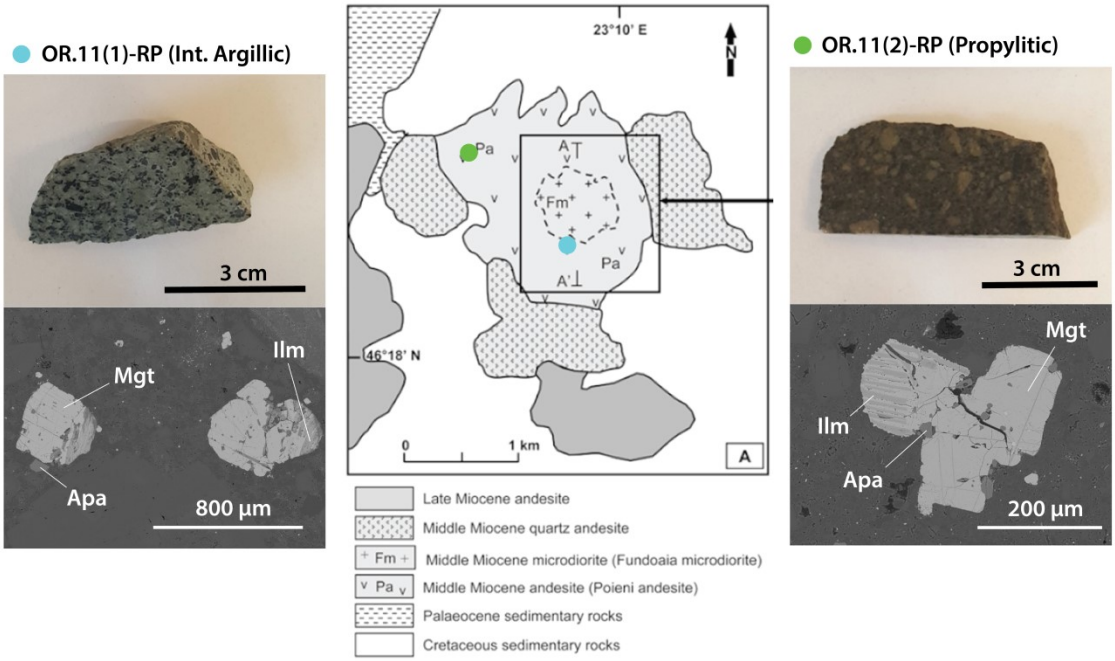


Figure 6-10: Map showing the geology of Rosia Poieni area and locations of samples OR.11(1)-RP and OR.11(2)-RP, with photographs of hand specimens and SEM-BSE images of titanomagnetite in both samples.

During alteration of igneous magnetite to hydrothermal magnetite the Ti content decreases, as observed in both samples (e.g. Figure 6-11). This is likely due to the re-equilibration of igneous magnetite with a hydrothermal fluid carrying a low concentration of Ti in comparison to a silicate melt. Titanomagnetite in OR.11(2)-RP (propylitic) appears to have been re-equilibrated less (Ti content between 2.7 and 4.5 wt. %) than OR11(1)-RP (intermediate-argillic) which has a somewhat lower Ti content, between 1.4 and 3.4 wt. %, consistent with the relative intensity of alteration.

The variations in a range of elements with decreasing Ti content were evaluated to assess how the chemistry overall is modified with progressive alteration. With decreasing Ti content, there is a linear decrease in Sc, Sn, Cr and Sr in both samples indicating that both alteration types lead to depletion in these elements (Figure 6-11).

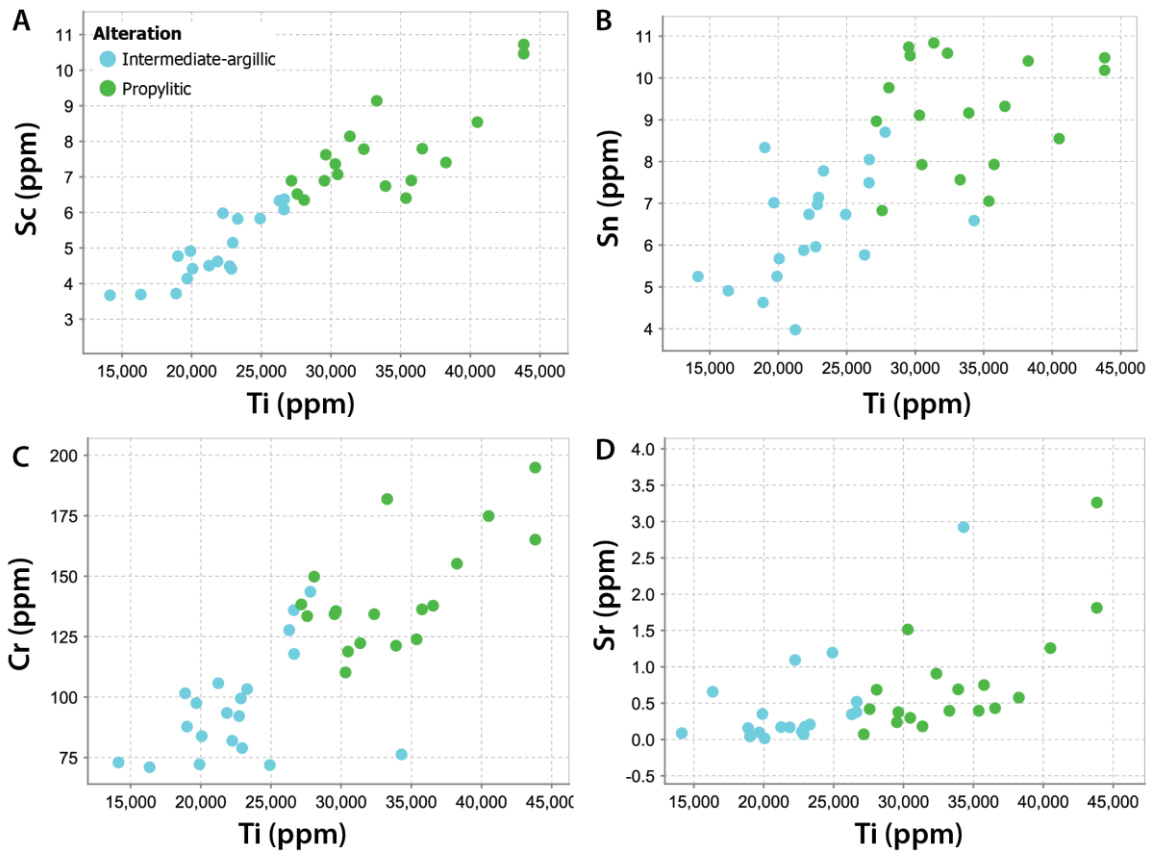


Figure 6-11: (A) Sc, (B) Sn, (C) Cr and (D) Sr vs. Ti content in igneous magnetite for samples OR11(1)-RP (intermediate argillically-altered) and OR11(2)-RP (propylitically-altered) andesite associated with the Rosia Poieni porphyry copper deposit. Both forms of alteration cause a progressive decrease in these elements in titanomagnetite.

The high field strength cations (Zr, Nb, Hf and Ta) show different trends in the two styles of alteration. In the propylitically-altered andesite, Zr and Nb exhibit a slight increase with decreasing Ti in titanomagnetite, whereas Hf shows little change in concentration and Ta exhibits

are slight decrease with decreasing Ti (Figure 6-12). This suggests that propylitic alteration results in an addition of Zr and Nb, but no change in Hf and removal of Ta. However, in the intermediate-argillically altered andesite, Zr, Nb, Hf and Ta all decrease with decreasing Ti (Figure 6-12).

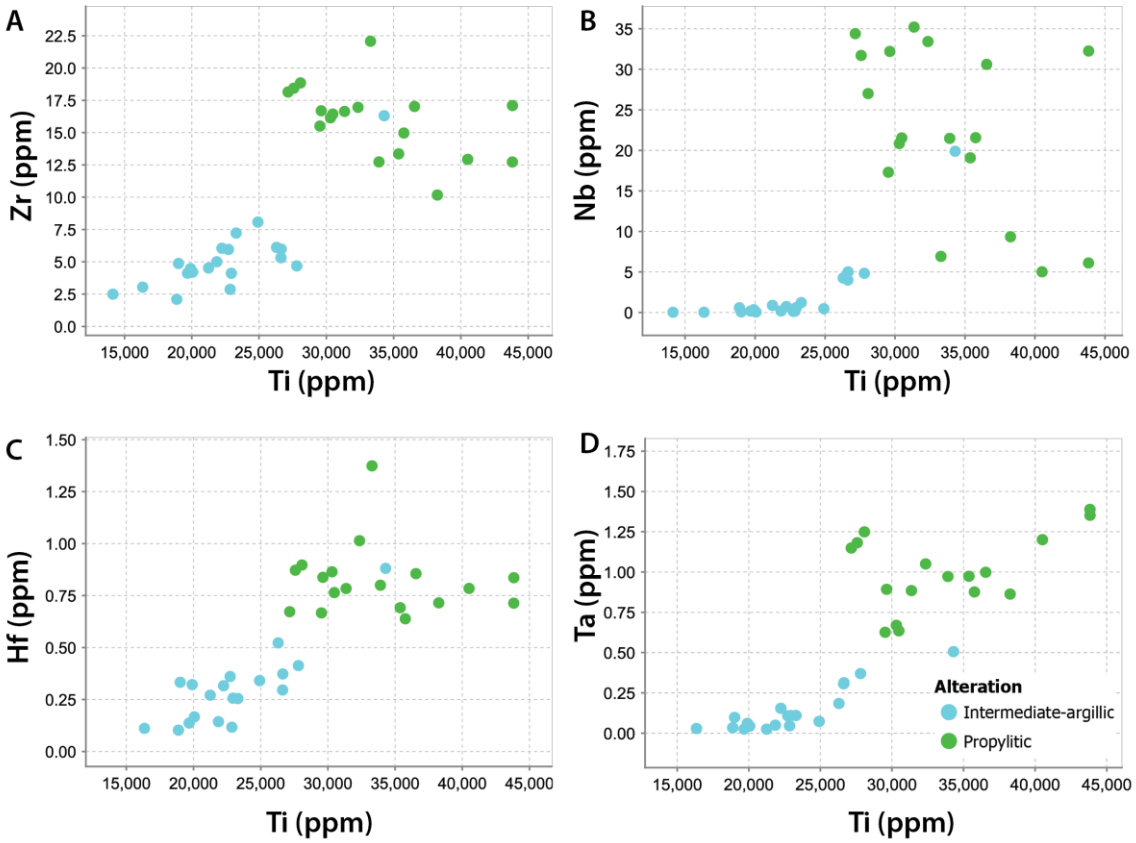


Figure 6-12: (A) Zr, (B) Nb, (C) Hf and (D) Ta vs. Ti content in igneous magnetite for samples OR11(1)-RP (intermediate argillically-altered) and OR11(2)-RP (propylitically-altered) andesite associated with the Rosia Poieni porphyry copper deposit.

Magnesium, Al and Co increase with decreasing Ti in titanomagnetite in the propylitically-altered andesite (Figure 6-13). Al decreases with Ti in titanomagnetite in intermediate argillically-altered andesite, however, no clear trend is apparent for Mg and Al in this sample (Figure 6-13).

Zinc, Mn and Cu decrease with decreasing Ti in titanomagnetite in the propylitically-altered sample, whereas Ni shows no significant change with decreasing Ti (Figure 6-14). The concentrations of Zn, Mn and Cu in igneous magnetite from the intermediate argillically-altered andesite are higher than propylitically-altered samples with the lowest Ti. Nickel concentration, however, is generally lower in argillically- altered than in propylitically-altered igneous titanomagnetite (Figure 6-14).

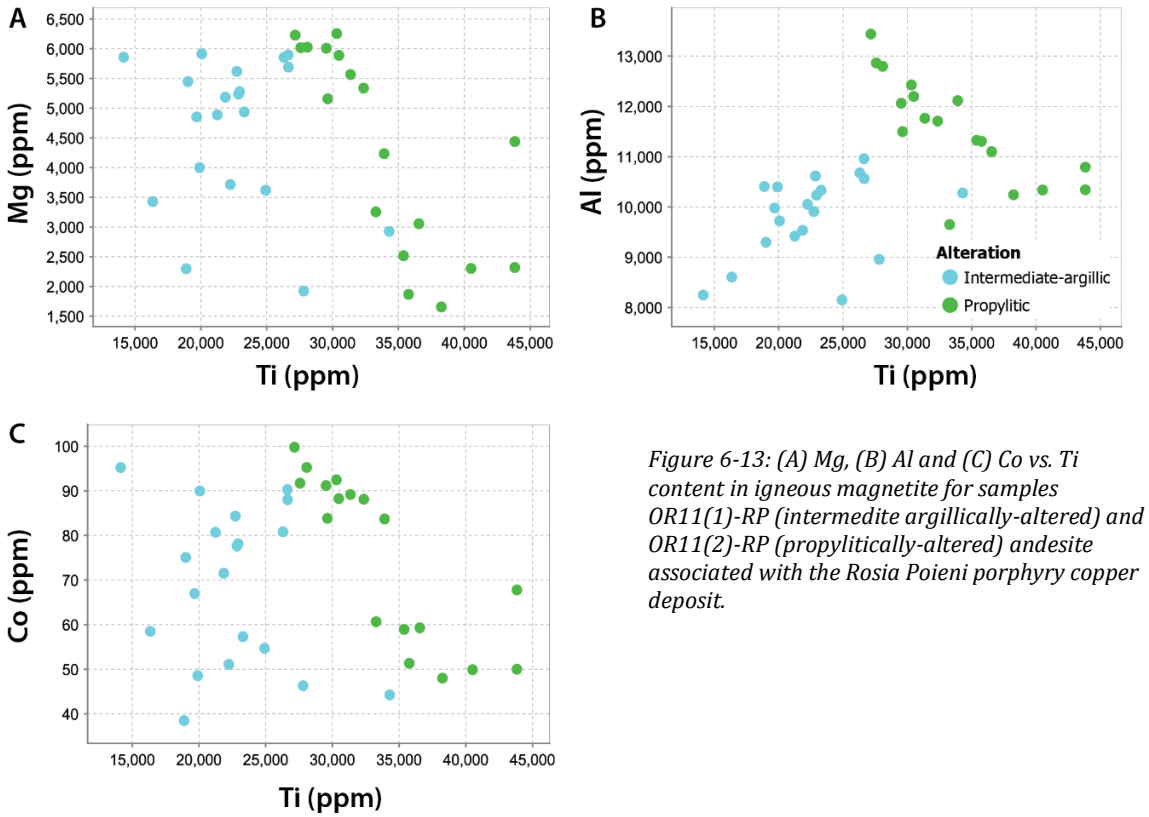


Figure 6-13: (A) Mg, (B) Al and (C) Co vs. Ti content in igneous magnetite for samples OR11(1)-RP (intermedite argillically-altered) and OR11(2)-RP (propylitically-altered) andesite associated with the Rosia Poieni porphyry copper deposit.

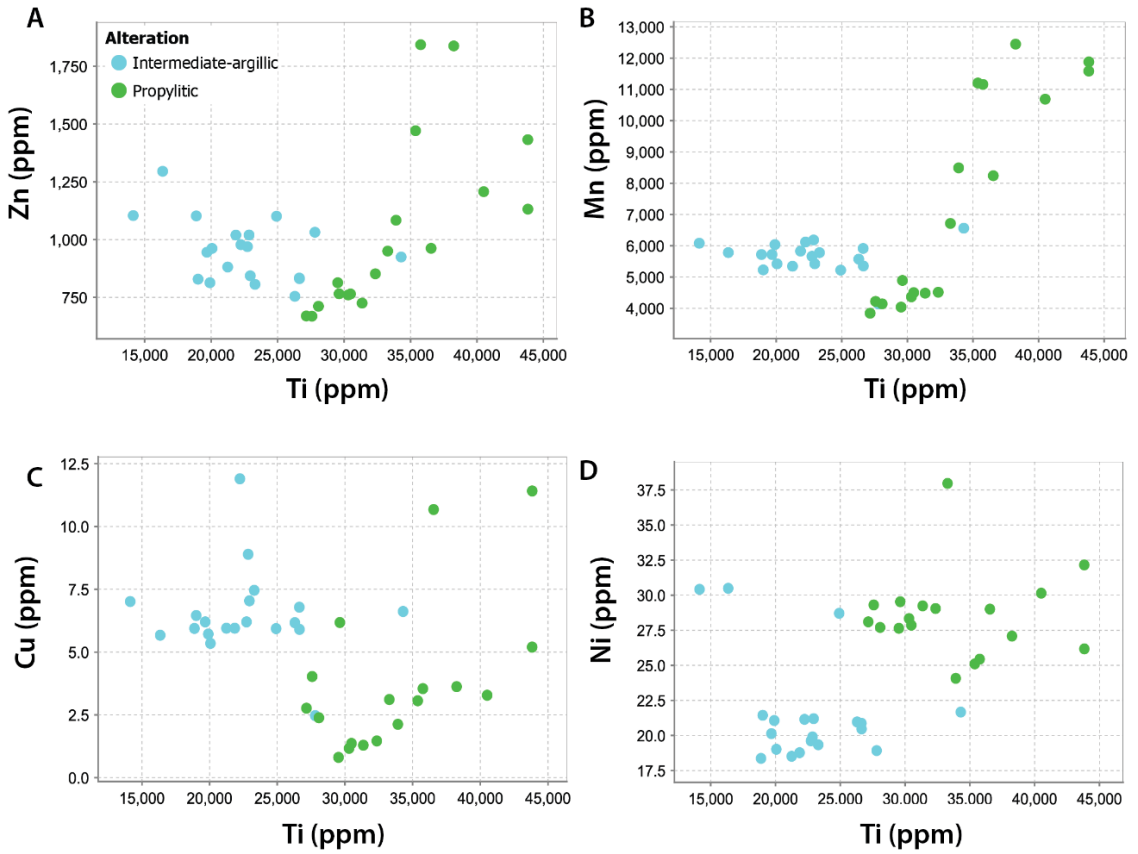


Figure 6-14: (A) Zn, (B) Mn, (C) Cu and (D) Ni vs. Ti content in igneous magnetite for samples OR11(1)-RP (intermediate argillically-altered) and OR11(2)-RP (propylitically-altered) andesite associated with the Rosia Poieni porphyry copper deposit.

There is not a large change in Ga, Ge, V or Mo with decreasing Ti in igneous magnetite from argillic and propylitic altered rocks. Notwithstanding this, V and Mo are slightly elevated in concentration in propylitically- relative to argillically-altered igneous magnetite (Figure 6-15).

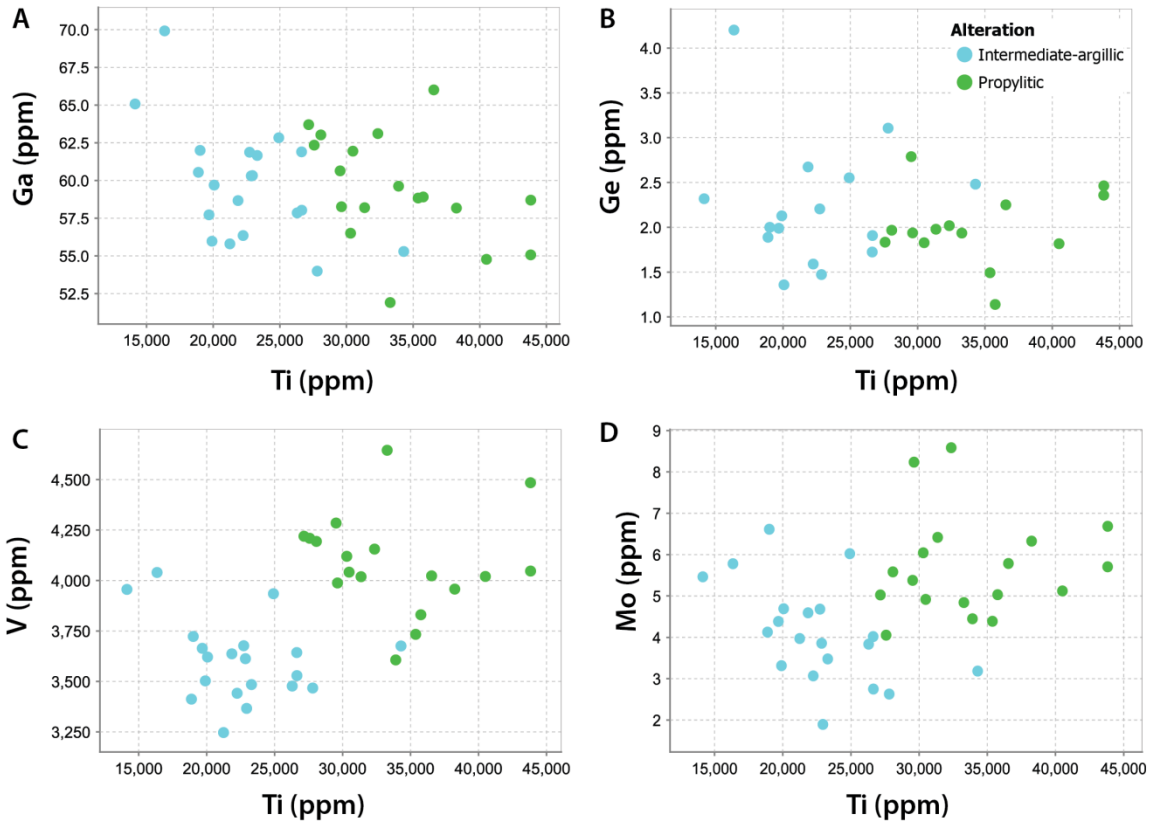


Figure 6-15: (A) Ga, (B) Ge, (C) V and (D) Mo vs. Ti content in igneous magnetite for samples OR11(1)-RP (int-argillic altered) and OR11(2)-RP (propylitic altered) andesite associated with Rosia Poieni porphyry copper deposit.

6.4 Discussion

6.4.1 Hydrothermal vs. Igneous magnetite

Hydrothermal magnetite is most easily distinguished from magmatic magnetite based on Ti content, with lower contents of Ti typically observed in hydrothermal magnetite (< 0.5 wt. % TiO_2), in comparison to magmatic magnetite (>1.5 wt. % TiO_2). Consequently, magnetite analyses were first classified as hydrothermal if Ti < 1 wt. % and igneous if Ti > 1 wt. %. An additional type of hydrothermal magnetite was also identified with the aid of petrographic observations, where low-Ti magnetite was observed to be replacing high-Ti magnetite.

A normal distribution probability plot can be used to assess magnetite populations based on Ti content. Distinct populations in the data derived in this study are indicated by linear slope segments (Figure 6-16). The first population has Ti < 600 ppm, a second population has 600 < Ti

< 20000 and there are three further Ti-rich populations with Ti > 20000 ppm. Zooming in to the region around 1 wt. % Ti shows that there is an apparent break in the dataset just above 1 wt%.

Nevertheless, there are evidently several populations of hydrothermal and igneous magnetite with one passing through the 1 wt. % threshold. Thus, the 1 wt. % cut-off may not be universally applicable as a discriminator of hydrothermal vs. igneous magnetite. To investigate the distinction in more detail, normal distribution probability plots of magnetite Ti content were generated for individual subsets of samples from separate deposits which contained magnetite with a wide range of Ti contents.

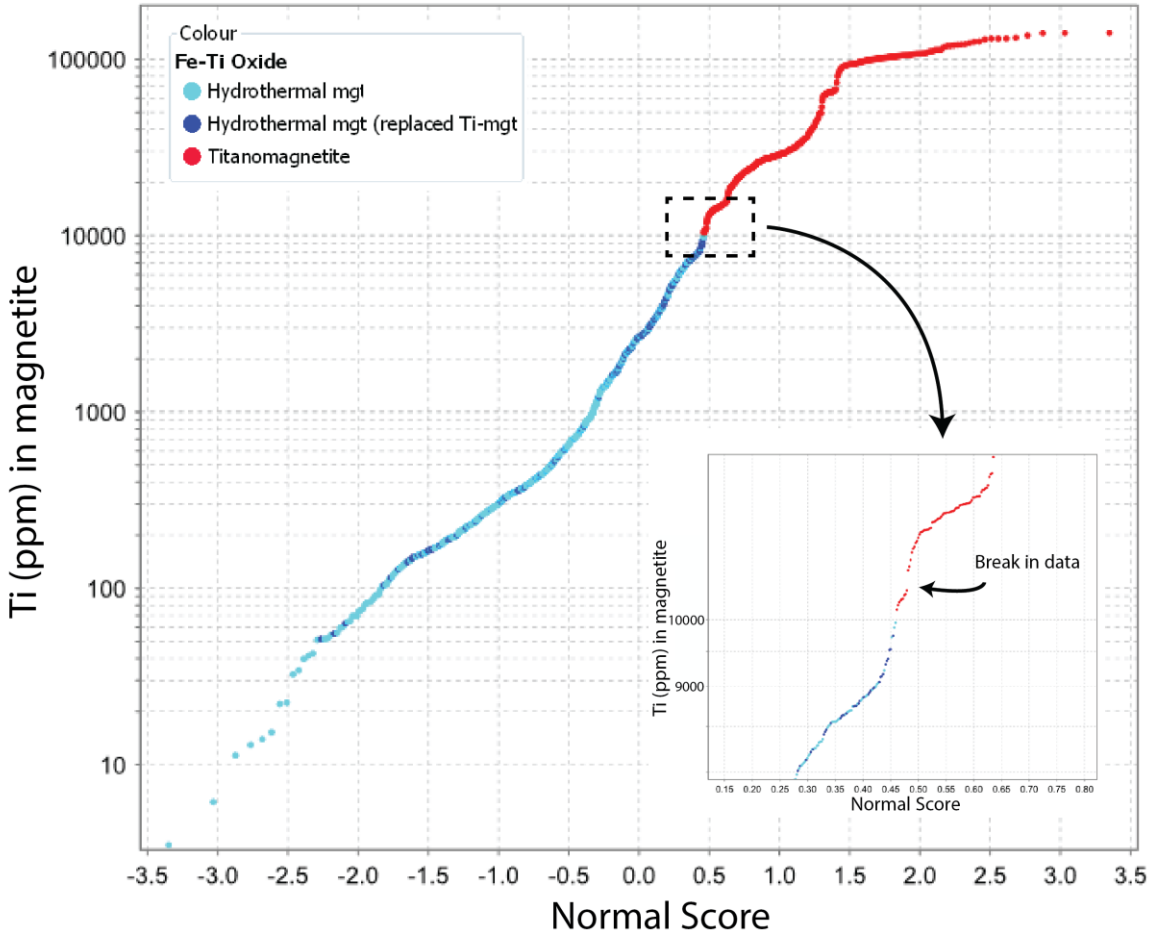


Figure 6-16: Normal probability plot for Ti in magnetite using all LA-ICP-MS data from this study.

In sample RTX-6759114-ZAL, a feldspar-biotite porphyry from the Zaldivar Cu-Mo deposit, there are two distinct populations of magnetite. One of these has Ti > 8 wt. % and the other has Ti < 1000 ppm indicating that the 1 wt. % cut-off is appropriate in this case (Figure 6-17A). Similarly, in sample OR.1122-GRAS, an andesitic intrusion from Grasberg, there is a clear break separating

igneous and hydrothermal magnetite, including some hydrothermal magnetite which was classified as replaced titanomagnetite based on its texture (Figure 6-17B). Clear breaks in the Ti content distinguishing a high-Ti magnetite population (> 1 wt. %) and a low-Ti population (Ti < 5000 ppm) were also observed in samples RTX-3372037-TACA and OR.6271-LOS (Figure 6-25).

In samples OR.13(1)-ROV and OR.13(2)-ROV from the Rovina Valley Project (Cu-Au porphyry system), there are three populations of magnetite, one with Ti < 10000 ppm, one with 10000 ppm < Ti < 20000 ppm and one with Ti > 20000 ppm. On reassessment of BSE images of those grains with Ti between 10000-20000 ppm, they were found to exhibit evidence for replacement of pre-existing minerals and recrystallization textures, typical of hydrothermal magnetite. Thus, these analyses were reclassified as hydrothermal magnetite (replaced), despite having a Ti > 1 wt. % (Figure 6-17C). Similarly, a number of analyses from Panguna, e.g. sample OR.2180-PAN, were classified as igneous using a 1 wt. % cut-off, but visibly showed evidence for replacement of strongly altered and exsolved titanomagnetite in BSE images (Figure 6-17D); thus, these grains were also reclassified as hydrothermal replacement type.

Samples OR.19(1)-RED and OR.19(2)-RED, diorite porphyries from the Red River porphyry-Cu prospect, display a dominant population with Ti > 20000 ppm but also yielded grains with distinctly lower Ti than the rest of the sample set (Figure 6-17E). These grains are intergrown with apatite and have the general appearance of igneous titanomagnetite but are highly altered. Thus, these grains are thought to be hydrothermally overprinted igneous magnetite and were classified as hydrothermal replacement type.

Subsets of the samples from individual deposits were studied in this fashion for the rest of the dataset. Most samples had either one clear population of low-Ti (hydrothermal) magnetite with Ti < 0.5 wt. % (e.g. Placetas, Majdanpek, White Pine, Valeo Stock, Little Cottonwood Stock, GRP 314, Clayton Peak Stock, Cerro Blanco, Alta Stock, La Granja, Valea Morii) or high-Ti (igneous) magnetite with Ti > 1.5 wt % (e.g. Far South-East, Dizon, Chelopech, Rosia Poieni). However, as above, there were a few cases where magnetites with Ti content greater than 1 wt. % were reclassified as hydrothermal replacement magnetite based on probability plots and visual inspection of the magnetite textures. There were no cases where hydrothermal magnetite was reclassified as titanomagnetite.

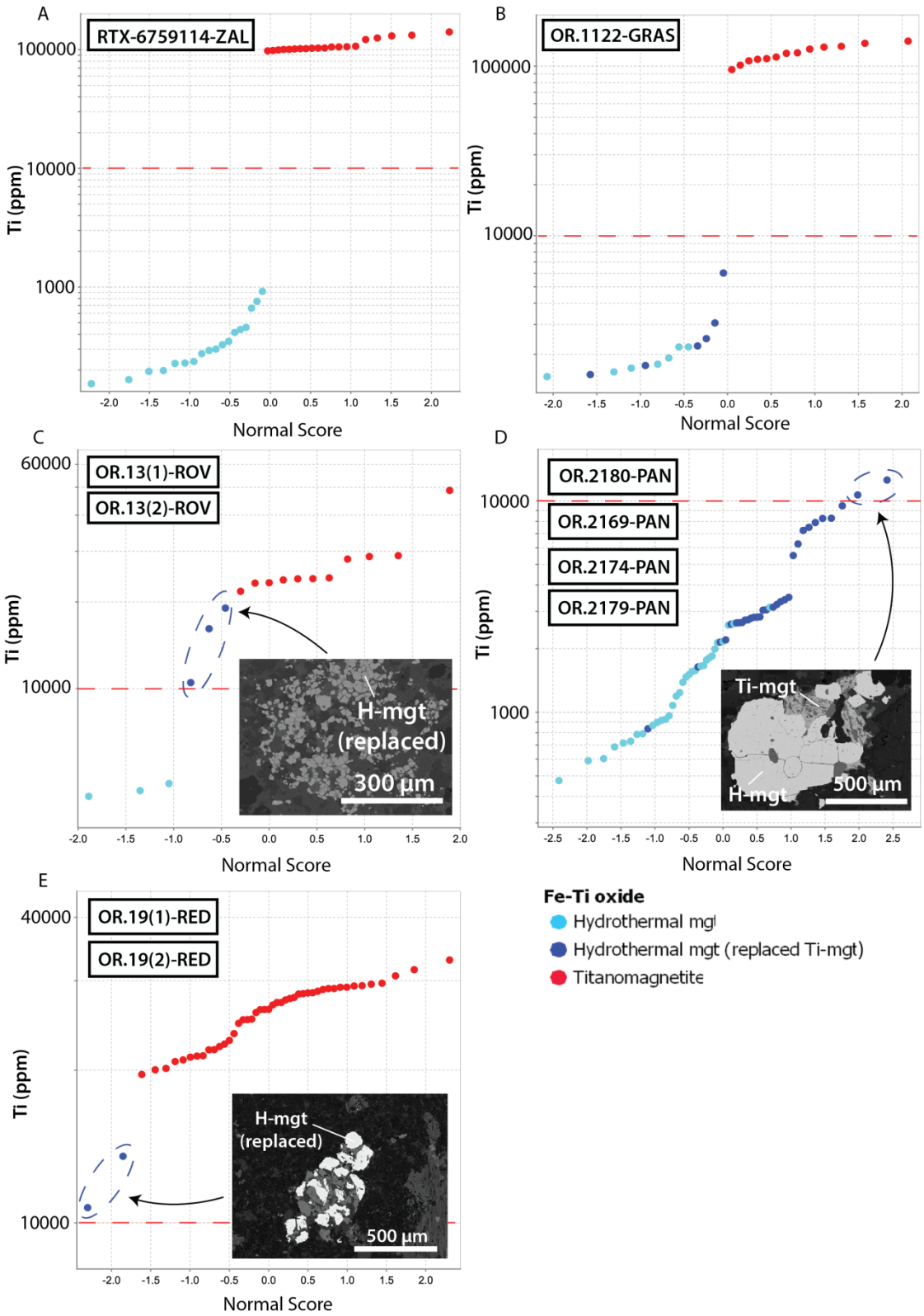


Figure 6-17: Normal probability plot for Ti for a subset of samples from porphyry copper systems: (A) Zaldivar, Chile; (B) Grasberg; (C) Rovina Valley Project; (D) Panguna; (E) Red River. Boxes in top-left indicate samples included in plot. Data circled in C-E would be classified as igneous magnetite based on 1 wt. % cut-off (shown with dashed red line), but have been reclassified as hydrothermal magnetite (replaced) based on textural study and Ti content which forms a separate population closer to the composition of hydrothermal magnetite. BSE-SEM images of the grains from which these data were derived are shown in the bottom-right of the plots.

In summary, for the vast majority of magnetite data, there is a distinct break in the Ti content which discriminates hydrothermal from igneous types. This is clearly apparent when studying subsets of samples from individual localities. In the majority of cases, a 1 wt. % cut-off is appropriate to distinguish the two varieties of magnetite. Notwithstanding this, there are rare cases where hydrothermal magnetite can have a Ti content higher than 1 wt. %, particularly when it is replacing an earlier generation of Ti-rich magnetite. Thus, it is suggested that standard procedure should be to generate normal distribution plots on a deposit by deposit basis. This can be used to identify occurrences of hydrothermal magnetite with Ti > 1 wt. %, aided by the use of petrographic observations.

6.4.2 Comparing the chemistry of igneous and hydrothermal magnetite

The chemistry of igneous, hydrothermal and hydrothermally replaced igneous magnetites was compared using box and whisker plots (Figure 6-18 to 6-21). The concentrations of Li, Mg, Al, Ti, Cu, As, Zr, Nb, Mo, In, Sn, Hf and Ta are higher in igneous titanomagnetite than hydrothermal magnetite, and hydrothermal magnetite observed to be replacing a precursor igneous phase is transitional in concentration between igneous magnetite and vein- and disseminated-type hydrothermal magnetite. Scandium, Mn, Zn, Sb, Ba and Pb are similar in concentration in both forms of hydrothermal magnetite but are higher in igneous magnetite. The concentrations of V, Cr, Co, Ni, Ga, Sr, Lu, W, Th and U are similar in both igneous and hydrothermal magnetite. Bismuth is the only element with a higher concentration in hydrothermal magnetite.

Of all the elements studied, the clearest distinction between hydrothermal and igneous magnetite is offered by Ti, HFSEs (Zr, Nb, Hf, Ta), Mn and Sc. Hydrothermal magnetite is thought to contain low Ti due to the limited solubility of Ti in most hydrothermal fluids (e.g. Van Baalen, 1993). The behaviour of the HFSE typically correlates with Ti (Chapters 2, 3 and 4), which could explain why these elements are also enriched in Ti-rich magnetite and are low in hydrothermal magnetite.

Given that the chemistry of hydrothermal replacement-type magnetite is transitional in composition between igneous and hydrothermal magnetite (Figure 6-18), it could be suggested that rejection of these data would help to emphasise distinctions between igneous and hydrothermal magnetite. However, hydrothermal and hydrothermal replacement magnetite are more similar in composition to each other than to igneous titanomagnetite. Furthermore, it is often not obvious petrographically whether magnetite is replacing precursor phases, particularly when studying mineral separates as opposed to rock samples. Thus, it was considered more practical to group both types of hydrothermal magnetite identified here together during interpretation of magnetite data.

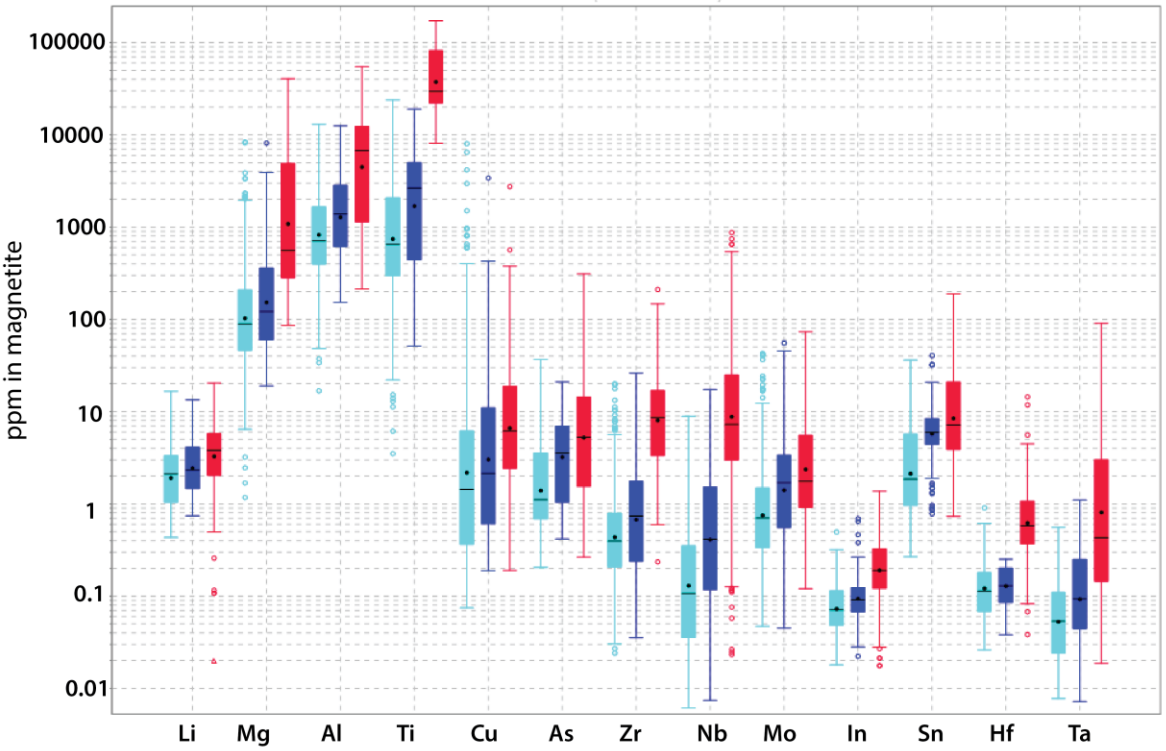


*Figure 6-18: Box and whisker plot showing elements that are present at high concentrations in igneous titanomagnetite and intermediate concentrations in hydrothermal magnetite replacing titanomagnetite. Central box is the middle 50% of data from Q1 to Q3. Outliers are shown by circles (greater than 1.5 * (Q3-Q1) from the box) and triangles (greater than 3.0 * (Q3-Q1) from the box). The whiskers represent the extreme values which are not outliers on the basis given above.*

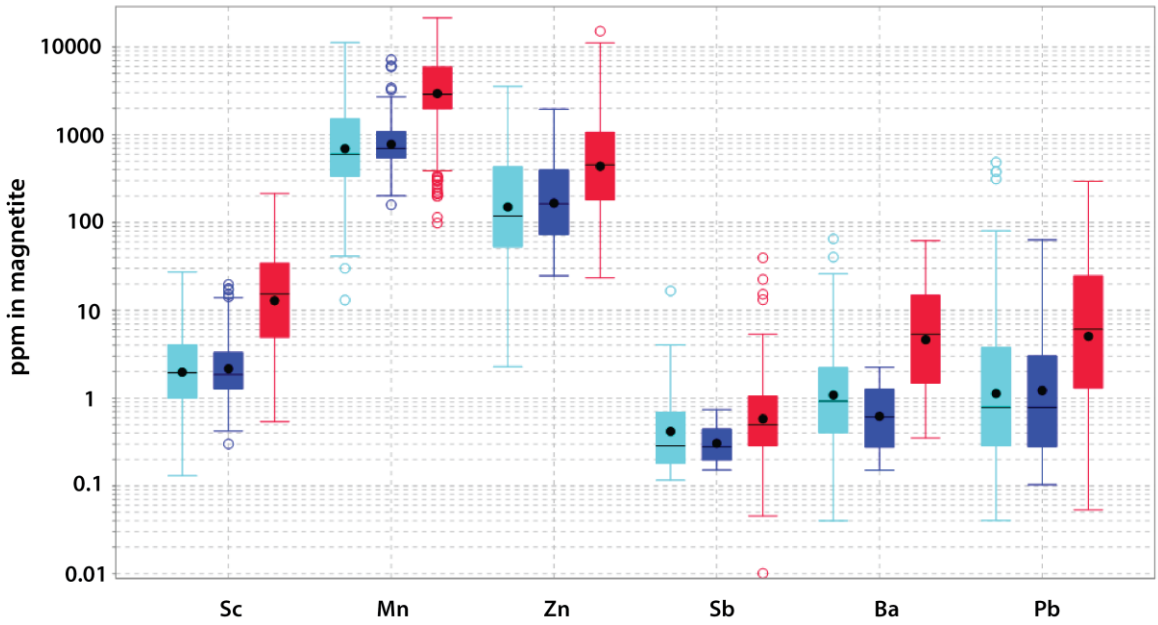


Figure 6-19: Box and whisker plot showing elements that are higher in titanomagnetite, but similar in replacement hydrothermal magnetite and primary magnetite.

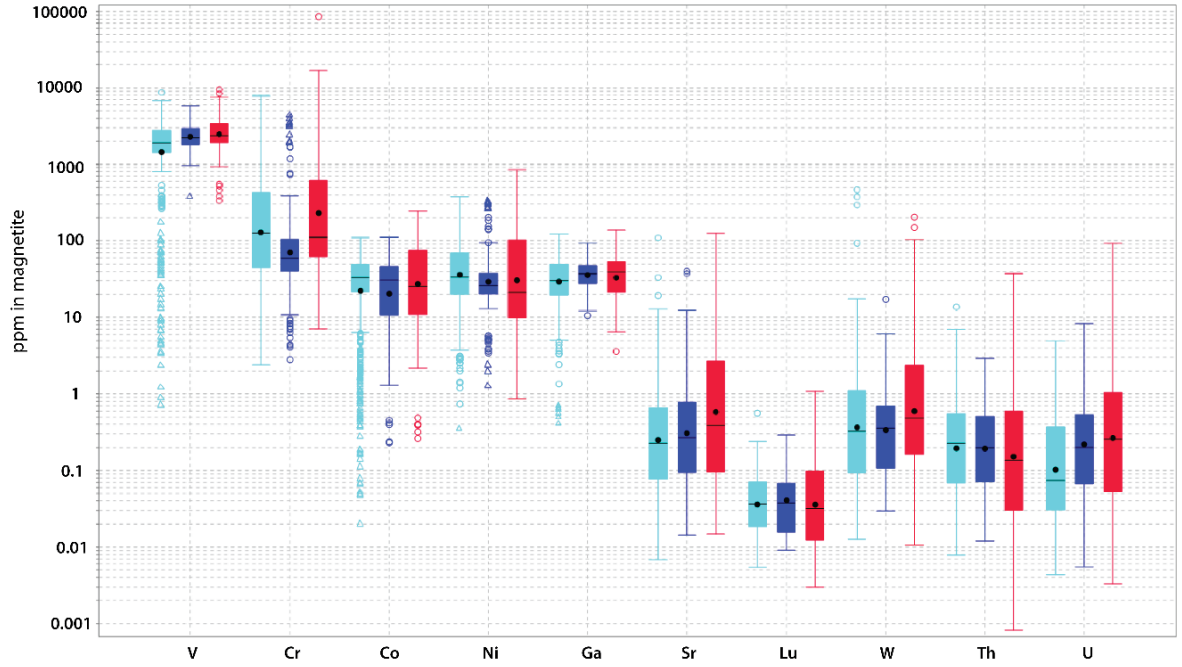


Figure 6-20: Box and whisker plot showing elements that have broadly comparable compositional ranges in hydrothermal and igneous magnetite.

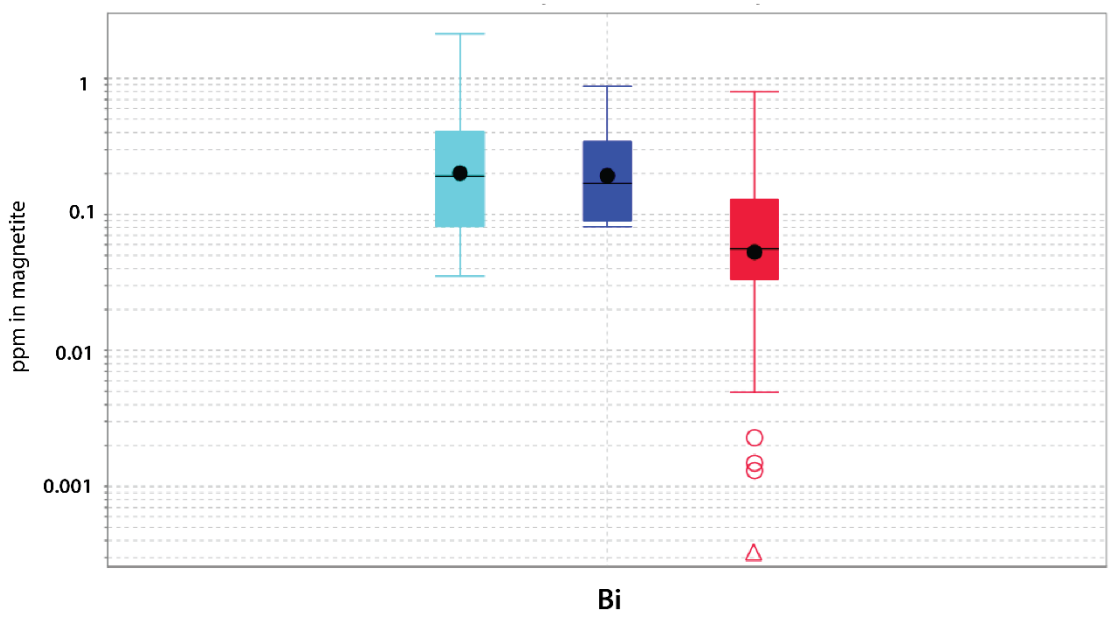


Figure 6-21: Box and whisker plot illustrating the Bi compositional range of hydrothermal and igneous magnetite. Bismuth is the only element to show greater concentrations (on average) in hydrothermal and hydrothermal replacement-type magnetite.

The observation that igneous magnetite contains higher concentrations of most elements than hydrothermal magnetite was previously reported by Nadoll et al. (2014). However, Nadoll et al. (2014) noted that mean V and Cr were lower and Co higher in porphyry-related hydrothermal magnetite relative to igneous magnetite. This is not apparent in the dataset reported here, with similar concentrations of these elements observed in both hydrothermal and igneous magnetite. Nadoll et al. (2014) also reported that Mg shows less variability in igneous magnetite than hydrothermal magnetite, whereas the converse was observed in this study (Appendix 3).

6.4.3 Comparison with literature data

The Ca + Al + Mn vs. Ti + V plot was developed by Dupuis and Beaudoin (2011) to distinguish magnetite derived from porphyry, iron-oxide Cu-Au, skarn, Kiruna-type, Fe-Ti and V deposits, and Banded Iron Formations. Calcium contributes only negligible amounts to the overall cation sum (typically 1-2 orders of magnitude less than the concentrations of Al and Mn) and was often below the detection limit of LA-ICP-MS in this study, thus Ca was omitted from the y-axis term, as previously done by Nadoll et al. (2014). The modified Al + Mn vs. Ti + V diagram effectively classifies a large proportion of the hydrothermal magnetite analysed here as porphyry-related, although there is a marked spread into the neighbouring Kiruna-type magnetite field (Figure 6-22). Essentially, all the Kiruna-type magnetite analysed by Dupuis and Beaudoin (2011) overlaps with the wider porphyry hydrothermal compositional domain defined here. All igneous titanomagnetites plot in the Fe-Ti and V deposits field. This can be explained by the fact that Dupuis and Beaudoin (2011) did not include analyses with more than 2 wt. % of any element when creating their classification diagram, with the exception of Cr, Ti, and V for Cr, Fe-Ti and V deposits. Because most igneous magnetite has Ti greater than 2 wt. %, it cannot plot in the porphyry field which is restricted to analyses with less than 2 wt. % of any element.

A plot of Ga vs. Sn was developed by Nadoll et al. (2014) to discriminate magnetite from different types of deposit. Variations in Ga and Sn in magnetite appear to be partly temperature controlled based on the groupings of the magnetite populations according to various deposit types (Nadoll et al., 2014). The magnetite analysed here plots broadly in the same region as the porphyry-related magnetite analysed by Nadoll et al. (2014), although spreading over a significantly greater range, mainly to lower values (Figure 6-23). Igneous magnetite generally has higher Sn contents, whereas the Ga contents in hydrothermal and igneous magnetite are broadly similar.

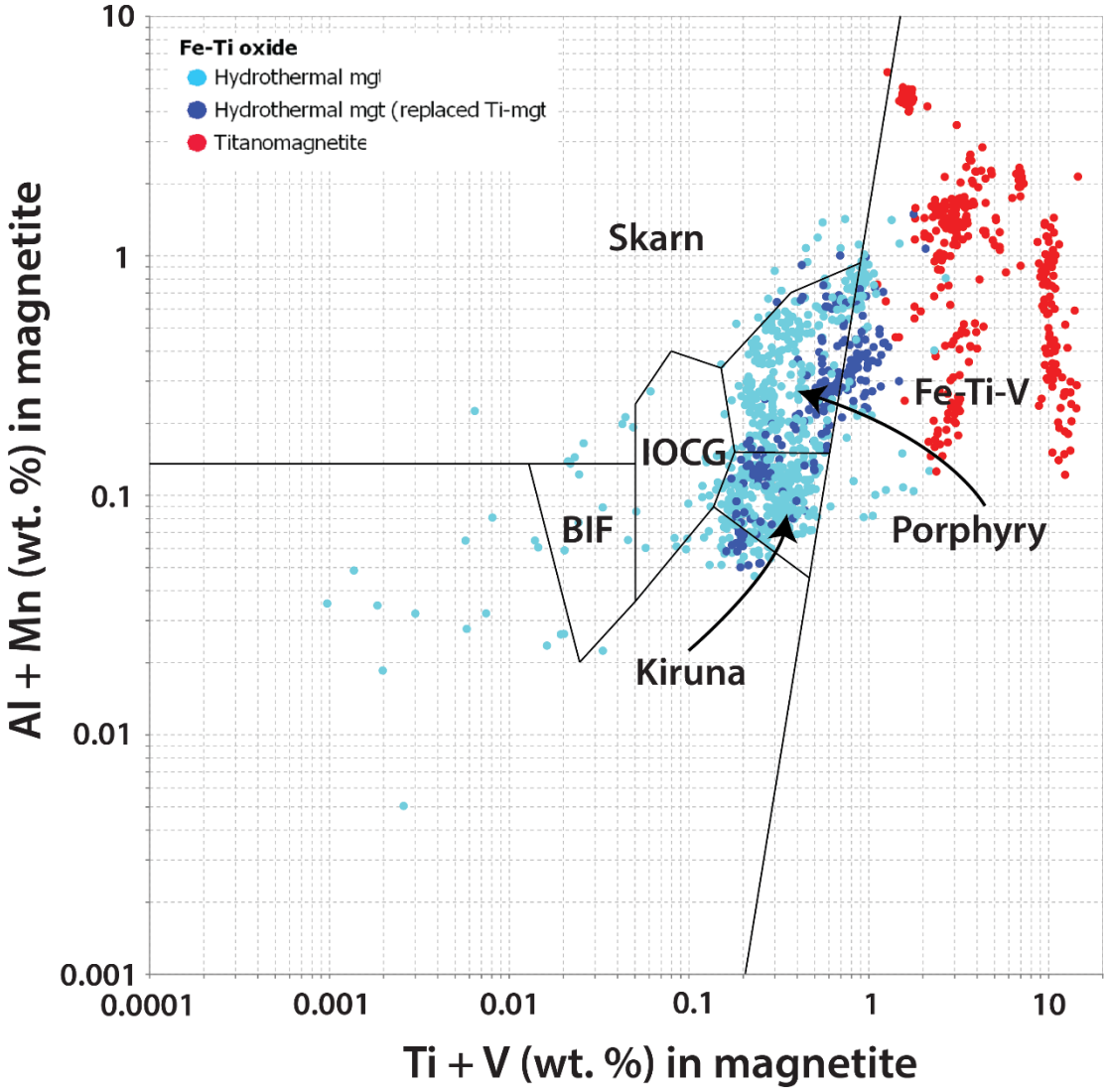


Figure 6-22: Diagram for the discrimination of magnetite from different deposit types (after Dupuis and Beaudoin, 2011). Ca has been omitted from the Al + Mn term because it was rarely above the limit of detection of LA-ICP-MS and contributes a negligible amount to this.

Dare et al. (2014) employed a plot of Ti vs. Ni/Cr to distinguish hydrothermal from igneous magnetite. However, the results from this study show that the plot is not effective for porphyry-related magnetite, classifying the majority of hydrothermal magnetite studied here as igneous (Figure 6-24). Separate examples where this plot misidentifies hydrothermal magnetite visibly replacing titanomagnetite confirm that this diagram should not be used (Figure 6-25).

Dare et al. (2014) used the Ni/Cr parameter to distinguish igneous magnetite from hydrothermal magnetite in felsic host rocks based on the premise that Ni and Cr are coupled in silicate magmas but decoupled in hydrothermal settings, leading to enrichment of Ni over Cr in the latter. However, the low-Ti magnetite listed as igneous by Dare et al. (2014) can be reinterpreted based on the results presented here as a hydrothermal replacement of precursor igneous magnetite.

This form of magnetite tends to have a low Ni/Cr, possibly as a result of high Cr inherited from the precursor igneous magnetite owing to its slow diffusion (section 3.3.4.2). This contrasts with new growth hydrothermal magnetite which displays high Ni/Cr and which does fall within the hydrothermal magnetite field defined by Dare et al. (2014) (Figure 6-25).

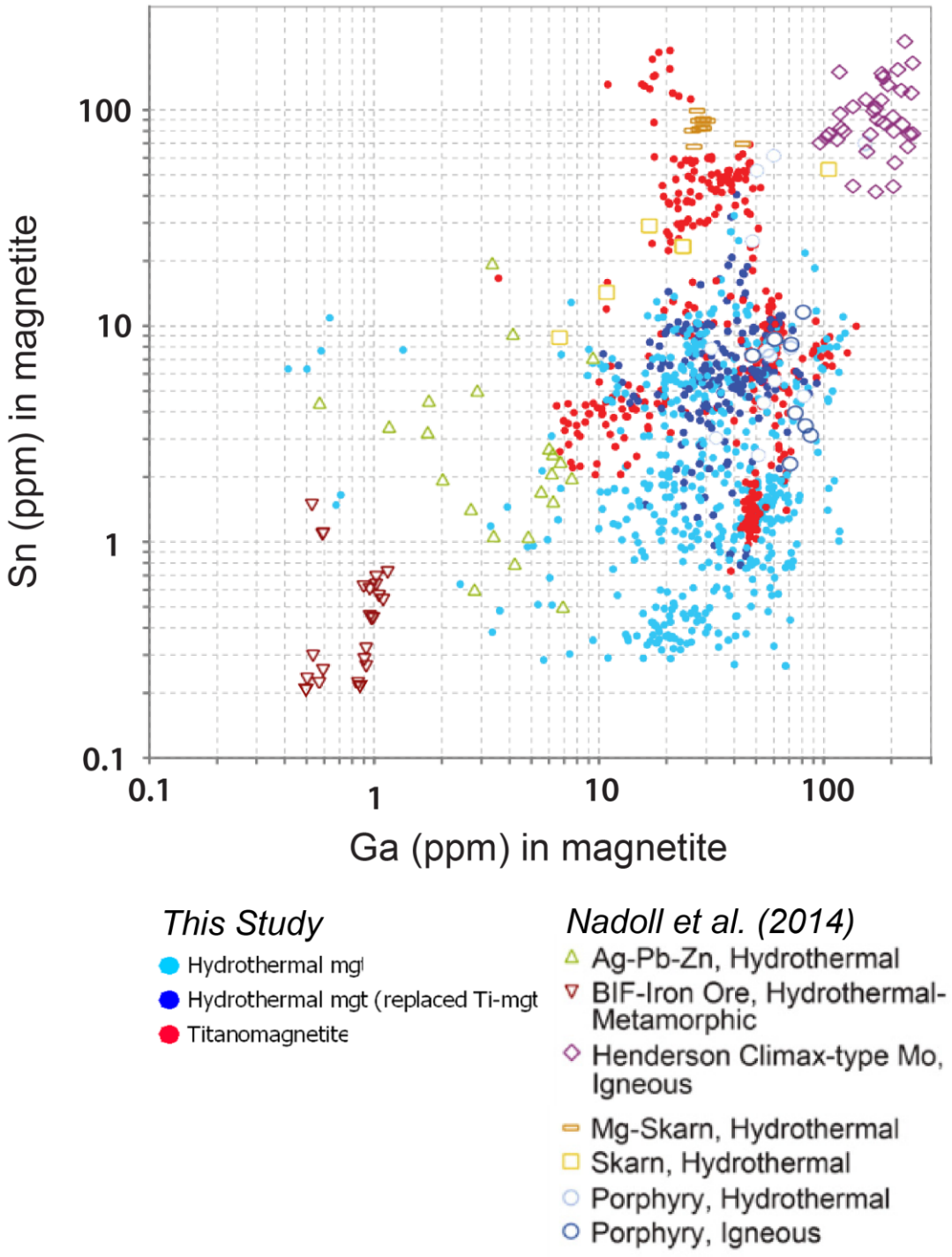


Figure 6-23: Plot of Sn vs. Ga for magnetite discrimination. From Nadoll et al. (2014).

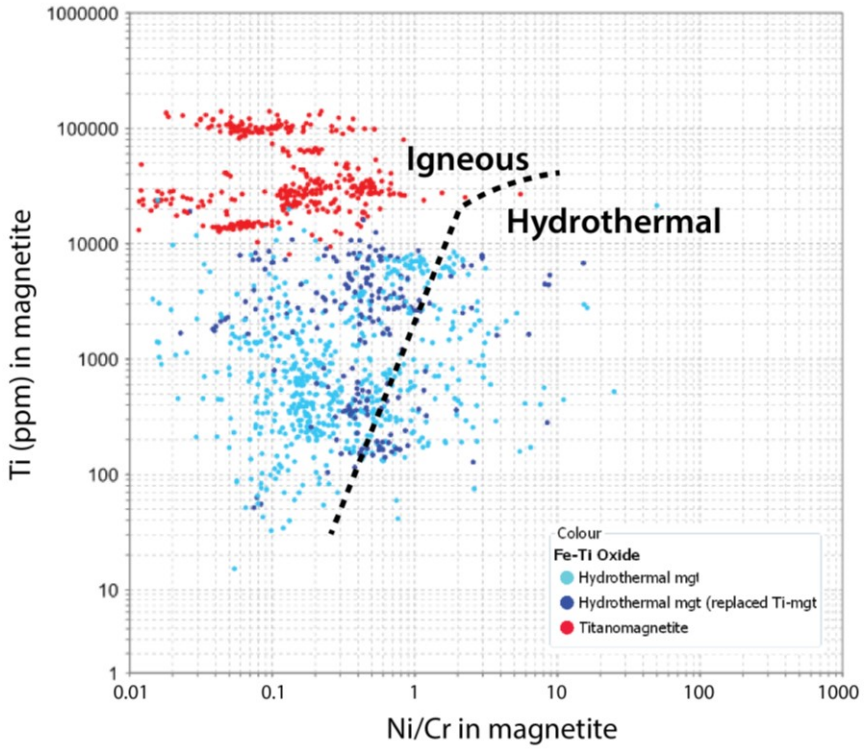


Figure 6-24: Plot of Ti vs. Ni/Cr in magnetite for the discrimination of igneous and hydrothermal magnetite in this study. From Dare et al. (2014).

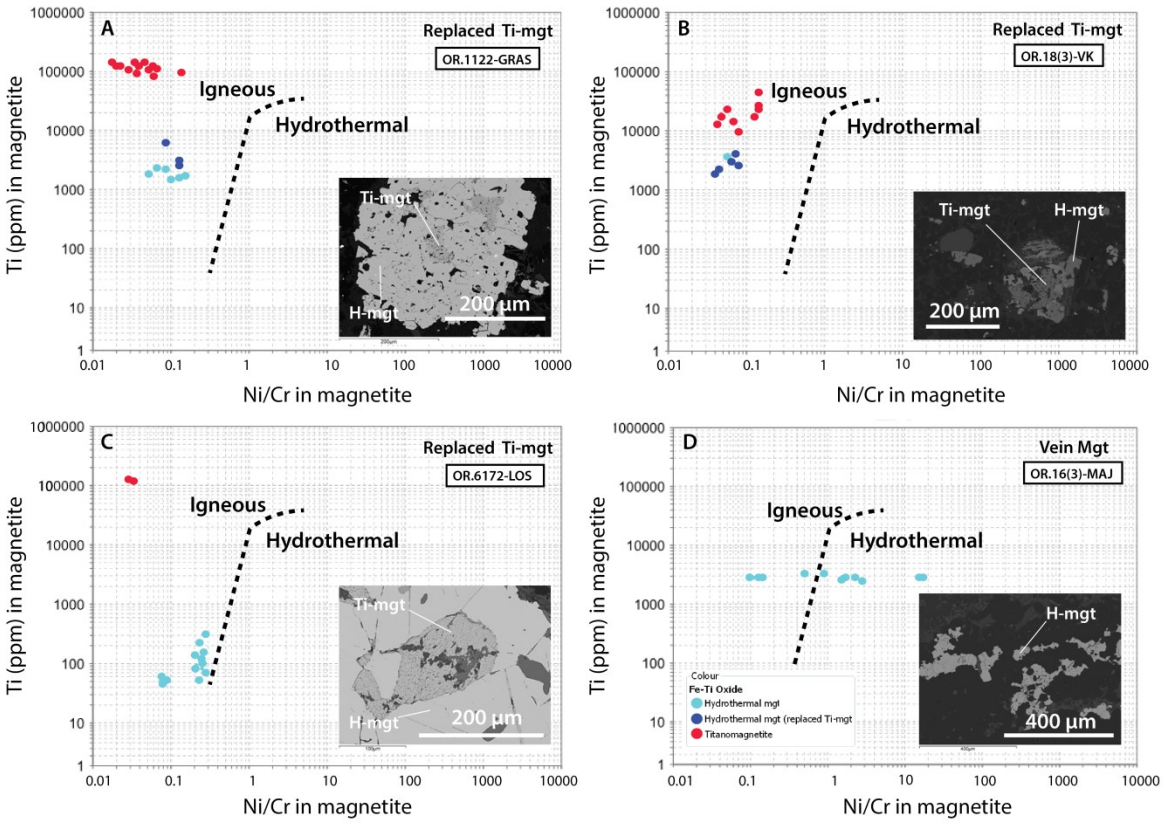


Figure 6-25: Examples illustrating the failure of the Ti vs. Ni/Cr diagram to effectively discriminate igneous from hydrothermal magnetite. (A-C) Ti vs. Ni/Cr for samples containing hydrothermal magnetite petrographically seen to be replacing titanomagnetite (OR.1122-GRAS; OR.18(3)-VK; OR.6172-LOS) (D) Ti. Vs Ni/Cr for hydrothermal magnetite precipitated in veins and voids (OR.16(3)-MAJ).

6.4.4 Discriminant projection analysis

Simple two-dimensional bivariate plots are not effective for discrimination of various populations of hydrothermal magnetite. Instead multi-element discrimination diagrams have been shown to offer a more powerful tool for the classification of specific minerals into various groups pertaining to the environment in which it formed (e.g. Mao et al., 2016; Pisiak et al., 2017). The approach used here was to apply discriminant projection analysis (DPA).

Discriminant projection analysis (DPA) is a multivariate statistical method used to find an optimum projection of multivariate data into a lower dimensional space which separates two or more classes of objects. DPA is similar to Principal Component Analysis (PCA) in that both techniques look for linear combinations of variables which best explain the data. However, DPA also maximises the separation between multiple classes of data. Whereas PCA can be described as an 'unsupervised' algorithm because it does not take into account class labels, DPA is 'supervised' and computes linear discriminants that represent axes which maximise separation between multiple classes. Explicitly, the linear functions calculated by the DPA maximise the ratio of the within-groups to between-groups sum-of-squares matrices. These discriminant functions, or projections, can be plotted in the discriminant space so that the group separation can be visualised and examined (Mao et al., 2016). Structure coefficients, calculated during the analysis, indicate which of the selected variables carry most weight in the linear functions and are most critical for distinguishing the groups. Increasingly, discriminant analysis has been applied as a statistical method in earth sciences to separate and classify data from various classes using multivariate inputs (e.g. Tahmasebi et al., 2010; Mao et al., 2016; Pisiak et al., 2017).

In this study, discriminant projection analysis was applied to define different populations of magnetite based on multiple major and trace element variables. The projections generated can then be used to classify unknown magnetite into various categories, such as alteration association, porphyry system type, or system size. The method relies on the data being separated into predefined groups which can be used as a training dataset for discriminant analysis.

ioGAS®, a geochemical software package, was used to perform the discriminant projection analysis. Discriminant analysis requires values for all inputs. Thus, only a selection of elements frequently above the limit of detection were included for each analysis. This selection of elements was then assessed for correlations in the dataset using a correlation matrix. Elements without a bivariate correlation with any other element with a Pearson Correlation Coefficient greater than 0.4 were excluded. PCA analysis was also conducted using all variables to confirm that none of the elements, excluded based on their lack of bivariate correlation with individual elements, exhibit correlations with one the first three principal components of the data.

DPA assumes normally distributed data. However, geochemical data are often skewed and/or contain outliers. Moreover, compositional data are closed to a constant sum of 100%, which violates the assumption of variable independence (Pisiak et al., 2017). Therefore, to minimise deviations from normality and prevent the effects of data closure, all discriminant projection analyses were transformed into log-space, using the log-10 of the concentration values (Davis, 2002). ioGAS® was then used to perform the DPA using an inbuilt function. The report generated from the DPA describes which elements have the greatest discriminating power.

6.4.4.1 Discriminant Projection Analysis with Hydrothermal Magnetite

Although there are some differences in the concentrations of elements in hydrothermal magnetite that has replaced pre-existing phases compared with vein or disseminated hydrothermal magnetite, the chemistry is largely similar. Thus, these two forms of hydrothermal magnetite have been grouped together for the purpose of discrimination studies.

i Alteration style

There are a range of alteration assemblages commonly associated with porphyry copper systems, both within ore zones and extending into a larger volume (>10 km^3) of adjacent rock (see section 1.2.1.2i). Alteration assemblages are significant because they can be used to approximate the physico-chemical conditions of the hydrothermal environment and provide a broad zonation that is useful for exploration. The sample set studied here includes hydrothermal magnetite derived from four types of alteration zone associated with porphyry copper systems: potassic, phyllic, propylitic and intermediate-argillic. The first DPA was designed to discriminate hydrothermal magnetite from these alteration types.

Samples which are described in the database as "transitional" in alteration type were not included in the DPA. Eleven elements (Mn, Al, Mg, V, Zn, Ti, Co, Ni, Ga, Cr and Ge) which were detected above the limit of detection of LA-ICP-MS in more than 93% of hydrothermal magnetite analyses were initially selected for the study. All these elements have bivariate correlations with at least one other element in the group with a Pearson linear correlation coefficient greater than 0.4, apart from V, Co and Ge.

A robust principal component analysis was also conducted using these eleven elements using ioGAS® software. Vanadium and Co have a good correlation (> 0.5 Pearson correlation coefficient) with two of the first three principal components, whereas Ge does not exhibit a clear correlation with any of the first three principal components (>0.4 Pearson correlation coefficient). Thus, V and Co were retained but Ge omitted from the subsequent analysis. Discriminant projection analysis was then conducted using log10-equivalent concentrations of

Mg, Al, Ti, V, Cr, Mn, Co, Ni, Zn and Ga in hydrothermal magnetite (n = 670) from the four alteration types using ioGAS® (DPA-A). Table 6-4 summarises the results and structure coefficients of the DPA-A.

The discriminant projection scores obtained as follows:

DP-A-1: 0.15787359 * (LOG(MG_PPM) - 2.119107) + -1.9978564 * (LOG(AL_PPM) - 3.0406623) + -0.17315072 * (LOG(TI_PPM) - 2.9809196) + 0.4894688 * (LOG(V_PPM) - 3.1441414) + 0.5509781 * (LOG(CR_PPM) - 1.8329765) + -0.536126 * (LOG(MN_PPM) - 2.8402503) + 1.3019744 * (LOG(CO_PPM) - 1.3458353) + -1.1050482 * (LOG(NI_PPM) - 1.5002421) + -0.22972353 * (LOG(ZN_PPM) - 2.1608531) + 1.0562601 * (LOG(GA_PPM) - 1.4850951)

DP-A-2: -1.039425 * (LOG(MG_PPM) - 2.119107) + 0.032450106 * (LOG(AL_PPM) - 3.0406623) + -0.40893596 * (LOG(TI_PPM) - 2.9809196) + 1.0749936 * (LOG(V_PPM) - 3.1441414) + 0.032513715 * (LOG(CR_PPM) - 1.8329765) + 1.0280559 * (LOG(MN_PPM) - 2.8402503) + -1.6357617 * (LOG(CO_PPM) - 1.3458353) + -0.6050455 * (LOG(NI_PPM) - 1.5002421) + 0.021400755 * (LOG(ZN_PPM) - 2.1608531) + 0.32237798 * (LOG(GA_PPM) - 1.4850951)

DP-A-3: 0.5163468 * (LOG(MG_PPM) - 2.119107) + -0.06941627 * (LOG(AL_PPM) - 3.0406623) + -0.7270639 * (LOG(TI_PPM) - 2.9809196) + 0.9762744 * (LOG(V_PPM) - 3.1441414) + -0.057321295 * (LOG(CR_PPM) - 1.8329765) + 0.94384724 * (LOG(MN_PPM) - 2.8402503) + -0.031971 * (LOG(CO_PPM) - 1.3458353) + 1.8603135 * (LOG(NI_PPM) - 1.5002421) + -0.11629289 * (LOG(ZN_PPM) - 2.1608531) + -3.0176082 * (LOG(GA_PPM) - 1.4850951)

The greatest influence on DP-A-1 are Al, Co and Mg and on DP-A-2 are Co, V and Mg. A discriminant plot of DP-A-1 vs. DP-A-2 separates magnetite derived from the different alteration facies (Figure 6-26). Using ioGas®, an auto-domain classification diagram tool can be used to objectively construct linear boundaries which separate the various groups within the discriminant space (Figure 6-26). Using this approach, data from intermediate argillic associated magnetite are well separated from the remaining groups. Similarly, most of the data from propylitic-associated magnetite are discriminated well, apart from a few points which spread into the potassic and phyllic fields. There is, however, more overlap of data between potassic- and phyllic-associated samples which could reflect the close spatial association of these alteration types and the likelihood of overprinting of phyllic alteration on hydrothermal magnetite that was originally formed during an earlier potassic phase. In such cases, the rock alteration classification based on hand specimen observation may be misleading.

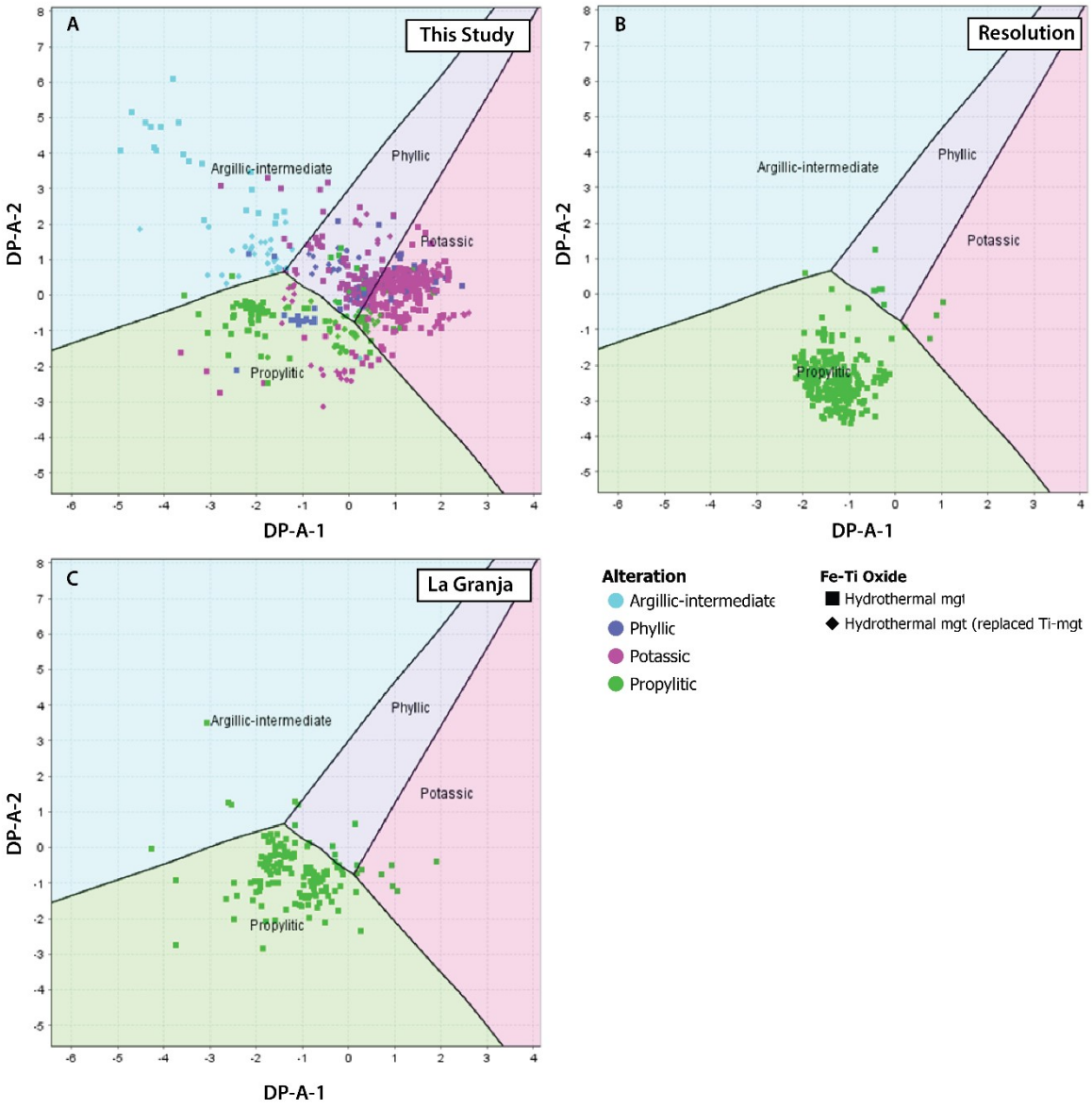


Figure 6-26: Discrimination diagrams (DP-A-2 vs. DP-A-1) for hydrothermal magnetite from various alteration styles developed using DPA-A. Linear boundaries were constructed using the auto-domain classification diagram tool in ioGAS®. (A) Data used in construction of DPA-A, (B) Hydrothermal magnetite from propylitically altered rocks at La Granja porphyry copper system, Peru and (C) Hydrothermal magnetite from propylitically altered rocks at Resolution porphyry copper system, USA.

In general, DP-A-1 separates potassic-associated magnetite at high loadings from phyllic and propylitic at intermediate DP-A-1, from intermediate-argillic at more negative loadings. Thus, DP-A-1 could represent, at least in part, a temperature control given that potassic and intermediate-argillic occur at higher and lower temperatures respectively (Seedoorf et al., 2005). Magnetite from potassically-altered rocks typically has lower Al and Mg contents and higher Co than that from phyllic, propylitic and intermediate argillic-altered rocks.

DP-A-2 principally separates intermediate-argillic associated magnetite at high DP-A-2 loadings from potassic and phyllic at moderate DP-A-2 and propylitic at low DP-A-2. Magnetite from propylitically-altered rocks has higher concentrations of Mg, Co and Ni and lower V and Mn relative to magnetite from intermediate-argillic altered rocks. DP-A-1 and DP-A-2 do not show any significant correlation (> 0.4 Pearson linear correlation coefficient) with any other element analysed, which were not used in DPA-A.

Table 6-4: Results of Discriminant Projection Analysis to categorise magnetite according to alteration style

DPA-A (Alteration)			
Category	n		
Intermediate argillic	50		
Phyllic	74		
Potassic	367		
Propylitic	179		
Total	670		
Structure Coefficients			
	DP-A-1	DP-A-2	DP-A-3
Mg	**-0.59**	**-0.55**	-0.08
Al	**-0.77**	-0.27	-0.28
Ti	-0.38	0.16	-0.14
V	0.38	**0.57**	0.14
Cr	0.24	0.22	0.39
Mn	-0.24	0.21	0.10
Co	**0.61**	**-0.57**	0.02
Ni	-0.17	-0.27	0.58
Zn	-0.30	0.24	-0.04
Ga	0.03	-0.02	-0.58
Eigenvalues	1.122	0.6854	0.1606
Cumulative %	57.01	91.84	100

Structure coeffiecients indicate which of the selected variables carry most weight discriminant functions out of a total of +/- 1. Eigenvalues show the amount of variance explained by the discriminant function. Cumulative % is the percentage of variance added by each function.

The discriminant plot of DP-A-1 vs. DP-A-2 was tested by applying it to magnetite datasets that were not used to create the discriminant functions. The test was successful in that it effectively classified hydrothermal magnetite data from propylitically-altered rocks associated with the Resolution porphyry Cu-Mo deposit, Arizona, USA, with 96% success (Figure 6-26C). It was also effective for the classification of hydrothermal magnetite from propylitically-altered rocks from La Granja porphyry Cu-Mo deposit, Peru, where correctly attributed 88% of the data (Figure 6-26B). It remains to be tested whether other types of alteration associations of magnetite can be reliably categorised using this diagram.

ii Metal Association

The sample set studied here covers predominantly Cu-Au and Cu-Mo deposits in approximately equal proportions and also comprises some Cu-Mo-Au systems. Porphyry Cu-Au and porphyry Cu-Mo deposits are generally associated with different lithologies and types of arc settings (section 1.2.1.2iii).

Because the chemistry of hydrothermal magnetite from different alteration domains in porphyry copper systems is distinct (Figure 6-26), an assessment of whether hydrothermal magnetite chemistry from various metal associations of porphyry copper system can be distinguished requires the study of samples from individual alteration facies.

The majority of hydrothermal magnetite data are from potassically-altered porphyritic intrusions from all three main classes of deposit (Cu-Au, Cu-Mo and Cu-Mo-Au). Thus, this subset provides a viable group for the establishment of discrimination functions for porphyry system type. DPA-B was carried out using log10-equivalent concentrations of Mg, Al, Sc, Ti, V, Cr, Mn, Co, Ni, Zn, Ga and Ge in hydrothermal magnetite (n = 310) from potassically-altered rocks only. Sample RTX-6759101-LB (PoCuMo) and OR.2169-PAN (PoCuAu) were excluded from the analysis to allow testing of the discriminant plot generated. Because there are only two potassically-altered samples from PoCuMoAu deposits with hydrothermal magnetite in the study, no samples from PoCuMoAu deposits were excluded. No elements from the suite present above the limit of the detection in more than 93% of analyses were omitted from the DPA because they all either show strong correlation (>0.4 Pearson correlation coefficient) with another element or with one of the first three principal components of a robust PCA. The results from DPA-B are summarised in Table 6-5.

The discriminant projection scores are calculated:

DP-B-1: -0.61106694 * (LOG(MG_PPM) - 1.8545424) + -1.909574 * (LOG(AL_PPM) - 2.801582) + 0.033855073 * (LOG(TI_PPM) - 2.7904518) + -1.3947856 * (LOG(V_PPM) - 3.324835) + -0.8387977 * (LOG(CR_PPM) - 1.9028754) + -0.8690916 * (LOG(MN_PPM) - 2.8334093) + -0.8379736 * (LOG(CO_PPM) - 1.4788158) + 2.0924146 * (LOG(NI_PPM) - 1.4499941) + -0.5705431 * (LOG(ZN_PPM) - 2.096529) + 1.7945036 * (LOG(GA_PPM) - 1.4726648) + -2.8670897 * (LOG(GE_PPM) - 0.7208343)

DP-B-2: 0.63047373 * (LOG(MG_PPM) - 1.8545424) + 0.98554665 * (LOG(AL_PPM) - 2.801582) + 1.592911 * (LOG(TI_PPM) - 2.7904518) + -1.2429285 * (LOG(V_PPM) - 3.324835) + 0.43379048 * (LOG(CR_PPM) - 1.9028754) + 0.061072774 * (LOG(MN_PPM) - 2.8334093) + -1.2398416 * (LOG(CO_PPM) - 1.4788158) + 2.159406 * (LOG(NI_PPM) - 1.4499941) + -0.486784 * (LOG(ZN_PPM) - 2.096529) + -1.1980897 * (LOG(GA_PPM) - 1.4726648) + 0.6299349 * (LOG(GE_PPM) - 0.7208343)

Table 6-5: Results of Discriminant Projection Analysis to categorise hydrothermal magnetite from potassically alterated rocks according to metal association of porphyry copper deposit

DPA-B (Porphyry deposit type - Potassic alteration facies samples only)		
Category	n	
PoCuAu	63	
PoCuMo	225	
PoCuMoAu	22	
Total	310	
Structure Coefficients		
	DP-B-1	DP-B-2
Mg	-0.27	0.36
Al	**-0.49**	0.32
Ti	**-0.55**	**0.47**
V	-0.23	-0.23
Cr	0.03	**0.49**
Mn	**-0.51**	-0.24
Co	-0.22	**-0.56**
Ni	**0.57**	0.29
Zn	-0.38	-0.17
Ga	-0.23	-0.30
Ge	**-0.65**	-0.08
Eigenvalues	1.585	1.082
Cumulative %	59.43	100

The first two discriminant components represent all the variation in the dataset. In general, DP-B-1 separates PoCuAu systems from PoCuMo and PoCuMoAu, whereas DP-B-2 distinguishes PoCuMoAu from PoCuMo and PoCuAu. The discriminant plot of DP-B-1 vs. DP-B-2 correctly classifies 95% of PoCuAu data, 95% of PoCuMo and 77% of PoCuMoAu (Figure 6-27). Hydrothermal magnetite from potassically-altered rocks from PoCuAu deposits generally contains higher concentrations of Ge, Ti, Al, and Mn, but the lowest concentrations of Ni relative to hydrothermal magnetite from PoCuMoAu and PoCuMo deposits. PoCuMoAu can be distinguished from PoCuMo and PoCuAu deposits by elevated concentrations of Cr and Ti and lower levels of Co. Vanadium is the least important discriminatory element with a structure coefficient < ±0.3 for both DP-B-1 and DP-B-2. The concentrations of Mg, Al, Ti, V, Cr, Mn, Co, Ni, Zn, Ga, and Ge in hydrothermal magnetite from potassically-altered rocks in the PoCuAu, PoCuMo and PoCuMoAu deposits studied here are compared using box and whisker diagrams in Figure 6-28.

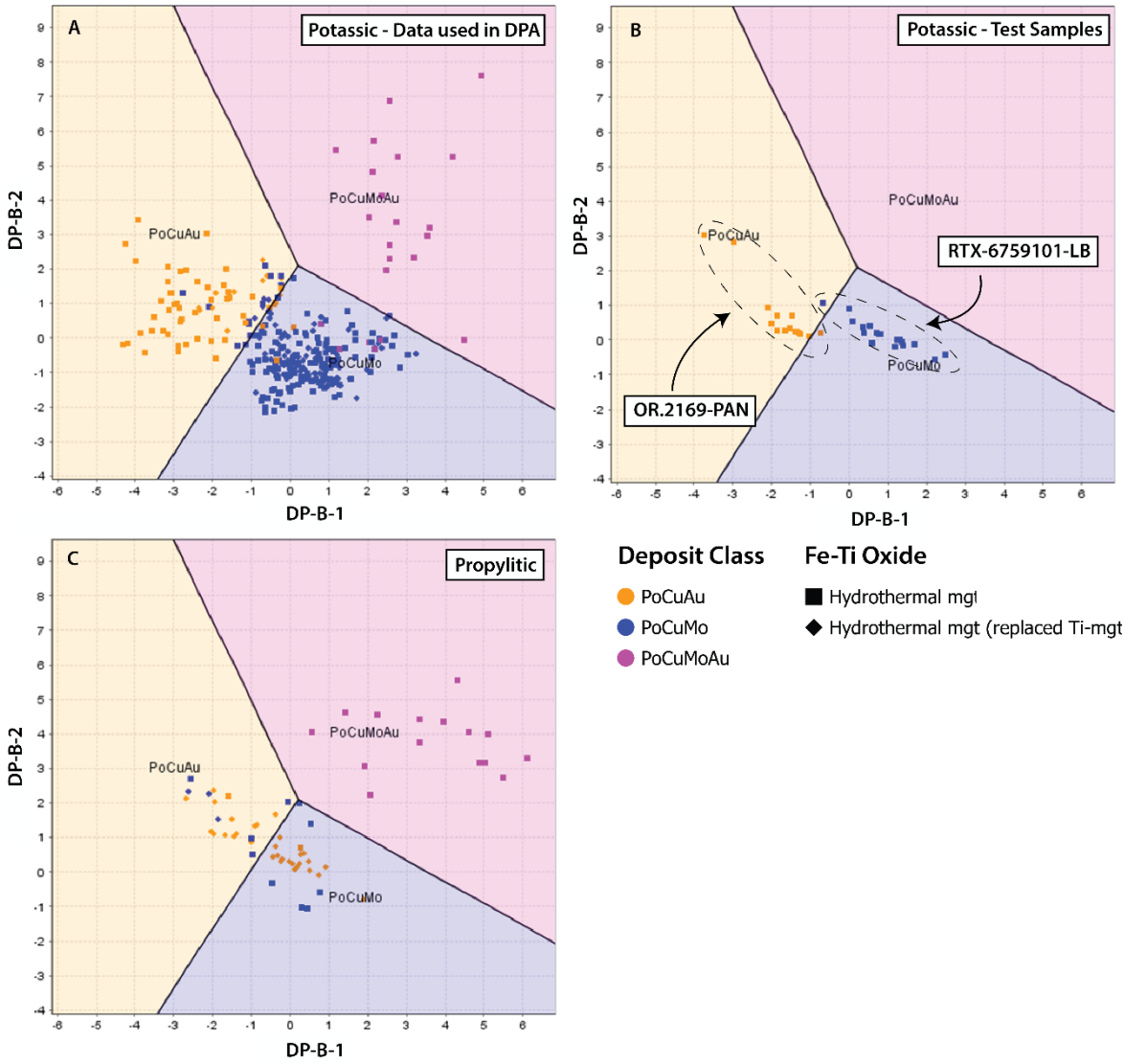


Figure 6-27: (A) Discrimination diagram (DP-B-2 vs. DP-B-1) for hydrothermal magnetite from potassically-altered rocks from different porphyry copper deposit types. (B) Hydrothermal magnetite from RTX-6759101-LB, potassically-altered granodiorite from Lomas Bayas, classified as PoCuMo with 94% accuracy and OR.2169-PAN, potassically-altered andesite from Panguna, classified as PoCuAu with 93% accuracy. (C) Hydrothermal magnetite from propylitically-altered rocks from PoCuMo and PoCuAu systems is significantly misclassified, whereas hydrothermal magnetite from propylitically-altered rocks in PoCuMoAu systems are categorised accurately using DPA-B.

Correlations between DP-B-1 and DP-B-2 with other elements less frequently detected in hydrothermal magnetite (which were not included in the DPA) were also evaluated. The most significant correlations are a negative correlation between DP-B-1 and Li content (-0.71 Pearson linear correlation coefficient; Figure 6-29A), and a positive correlation between DP-B-2 and Sb (0.88 Pearson's linear correlation coefficient; Figure 6-29B). Lithium contents are higher in hydrothermal magnetite from Cu-Au relative to Cu-Mo and Cu-Mo-Au systems, although Li was not detected in the latter. Hydrothermal magnetite from Cu-Mo-Au systems has the highest Sb content, whereas Sb is lowest in hydrothermal magnetite from Cu-Mo systems.

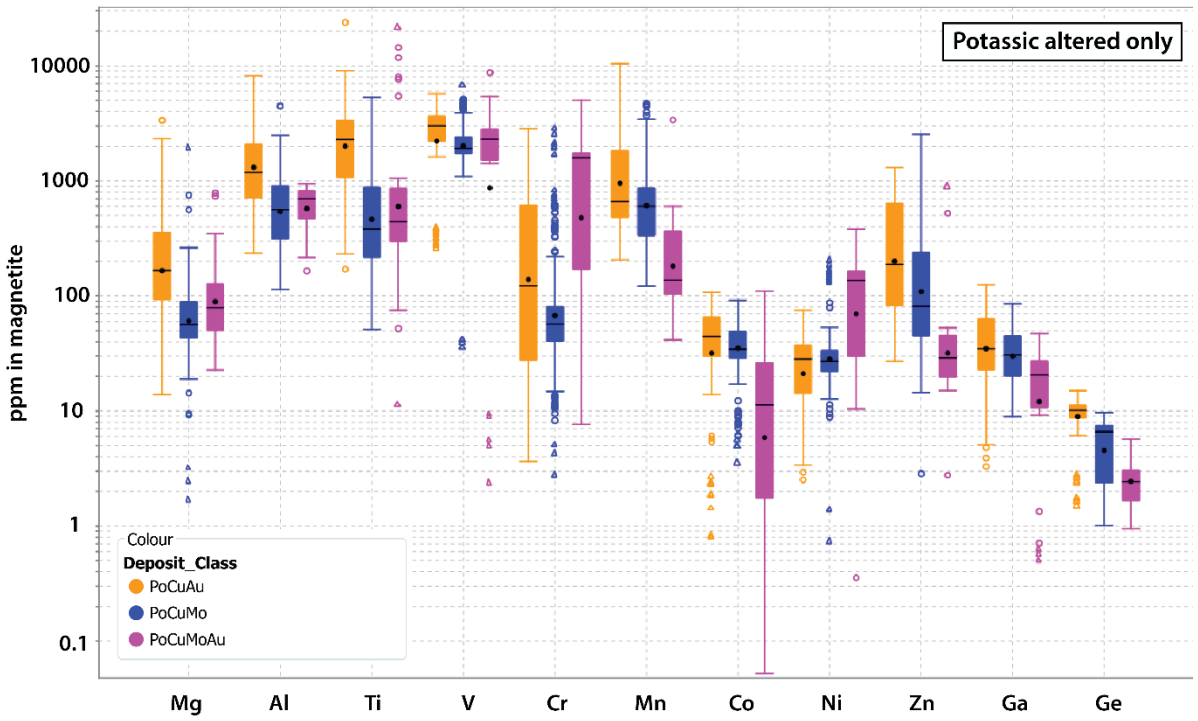


Figure 6-28: Box and whisker plot comparing the concentrations of Mg, Al, Ti, V, Cr, Mn, Co, Ni, Zn, Ga and Ge in hydrothermal magnetite from potassically-altered rocks from PoCuAu, PoCuMo and PoCuMoAu deposits. Germanium, Ti, Al, Mn and Zn are key elements for discriminating PoCuAu deposits from PoCuMo, and Cr, Ni and Co are important for discriminating PoCuMoAu from PoCuMo and PoCuAu deposits.

The efficacy of the DP-B-1 vs. DP-B-2 plot for discriminating porphyry system type using hydrothermal magnetite chemistry was evaluated using two samples omitted from the DPA. Hydrothermal magnetite from RTX-6759101-LB, a potassically-altered granodiorite from Lomas Bayas PoCuMo deposit is classified with 94% accuracy and hydrothermal magnetite from OR.2169-PAN, a potassically-altered andesite from Panguna is classified with 93% accuracy (Figure 6-27B). However, the plot does not accurately categorise hydrothermal magnetite from PoCuMo and PoCuAu deposits from propylitically-altered rocks, but can discriminate PoCuMoAu hydrothermal magnetite from propylitically altered rocks (Figure 6-27C).

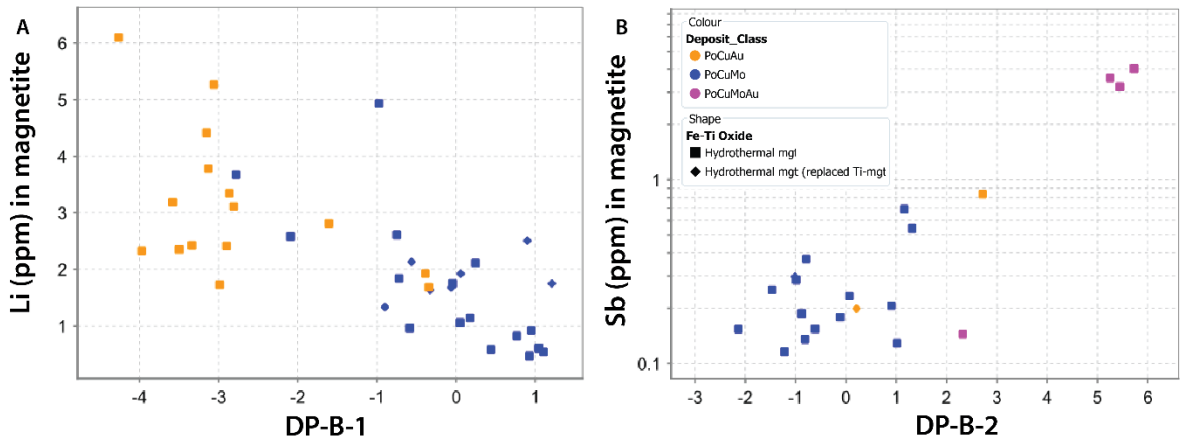


Figure 6-29: A) Li content in hydrothermal magnetite vs. DP-B-1. B) Sb content in hydrothermal magnetite vs. DP-B-2.

To assess whether hydrothermal magnetite populations could be categorised irrespective of the style of associated alteration, an additional DPA was conducted using all alteration types. DPA-C was performed using log-10 equivalents of Mg, Al, Ti, Cr, Mn, Co, Ni, Zn, Ga and Ge in hydrothermal magnetite from all types of alteration in the sample set (n = 510). V was omitted because it showed no significant correlation with any other element investigated, or with any of the first three principal components of a robust PCA. The results of DPA-C are summarised in Table 6-6.

The discriminant projection scores are calculated using:

DP-C-1 (59.7%): - -0.3090831 * (LOG(MG_PPM) - 2.0580661) + -1.7427504 * (LOG(AL_PPM) - 2.9681275) + -1.1161519 * (LOG(TI_PPM) - 2.953542) + -0.49341318 * (LOG(CR_PPM) - 1.8443148) + -0.6300958 * (LOG(MN_PPM) - 2.8227508) + -1.4317976 * (LOG(CO_PPM) - 1.3242936) + 2.005782 * (LOG(NI_PPM) - 1.4107196) + 0.40148297 * (LOG(ZN_PPM) - 2.1176283) + 0.9914991 * (LOG(GA_PPM) - 1.4810339) + -0.7008887 * (LOG(GE_PPM) - 0.62964386)

DP-C-2 (40.3%): 1.5562353 * (LOG(MG_PPM) - 2.0580661) + -0.2659164 * (LOG(AL_PPM) - 2.9681275) + 1.0386591 * (LOG(TI_PPM) - 2.953542) + -0.0859585 * (LOG(CR_PPM) - 1.8443148) + -1.6732788 * (LOG(MN_PPM) - 2.8227508) + -1.0739928 * (LOG(CO_PPM) - 1.3242936) + 2.1001596 * (LOG(NI_PPM) - 1.4107196) + -0.0067679235 * (LOG(ZN_PPM) - 2.1176283) + 0.120914 * (LOG(GA_PPM) - 1.4810339) + 1.0092776 * (LOG(GE_PPM) - 0.62964386)

Table 6-6: Results of Discriminant Projection Analysis to categorise hydrothermal magnetite from all alteration types according to metal association of porphyry copper deposit

DPA-C (Porphyry deposit type - All alteration associations)		
Category	n	
PoCuAu	179	
PoCuMo	292	
PoCuMoAu	39	
Total	510	
Structure Coefficients		
	DP-C-1	DP-C-2
Mg	**-0.50**	**0.62**
Al	**-0.61**	**0.43**
Ti	**-0.76**	**0.34**
Cr	0.09	0.05
Mn	**-0.49**	-0.40
Co	-0.23	**-0.51**
Ni	**0.49**	0.14
Zn	-0.38	-0.18
Ga	-0.34	-0.09
Ge	-0.27	-0.05
Eigenvalues	1.139	0.7689
Cumulative %	59.69	100

Similar to DPA-B, the first discriminant function of DPA-C largely separates PoCuMo and PoCuMoAu from PoCuAu, whereas the second discriminates PoCuMoAu from PoCuAu and PoCuMo (Figure 6-30). PoCuAu hydrothermal magnetite has higher contents of Ti, Al, Mg, Mn, Zn and Ga, but lower contents of Ni in comparison to PoCuMo and PoCuMoAu. This is a similar set of elements to those that most strongly influence DP-B-1, apart from Ge. Incorporating all alteration styles, hydrothermal magnetite from PoCuMoAu deposits has higher Mg, Al and Ti contents, but lower Co and Mn relative to PoCuMo and PoCuAu deposits. This contrasts with DPA-B, where Cr and Ni exert most influence on DP-B-2.

The efficacy of this plot was examined using available data from La Granja PoCuMo deposit in Peru and the Resolution PoCuMo deposit in the USA. Hydrothermal magnetite from propylitically-altered rocks from Resolution are classified quite well with a success rate of 87.7% (Figure 6-30B). However, those from La Granja are not effectively categorised as PoCuMo, with success rate of just 5.3% (Figure 6-30C). It is possible that the plot is not very effective because it was constructed using propylitically-altered samples predominantly from PoCuAu deposits but is

dominated overall by potassically-altered samples. Furthermore, there is some uncertainty regarding the classification of La Granja because it contains some Au (and Ag) in addition to Cu and Mo so could be regarded as a CuMoAu system. In conclusion, more data should be collected and an additional DPA performed to produce an improved discrimination diagram for porphyry system type using the chemistry of hydrothermal magnetite from a more even distribution of alteration styles.

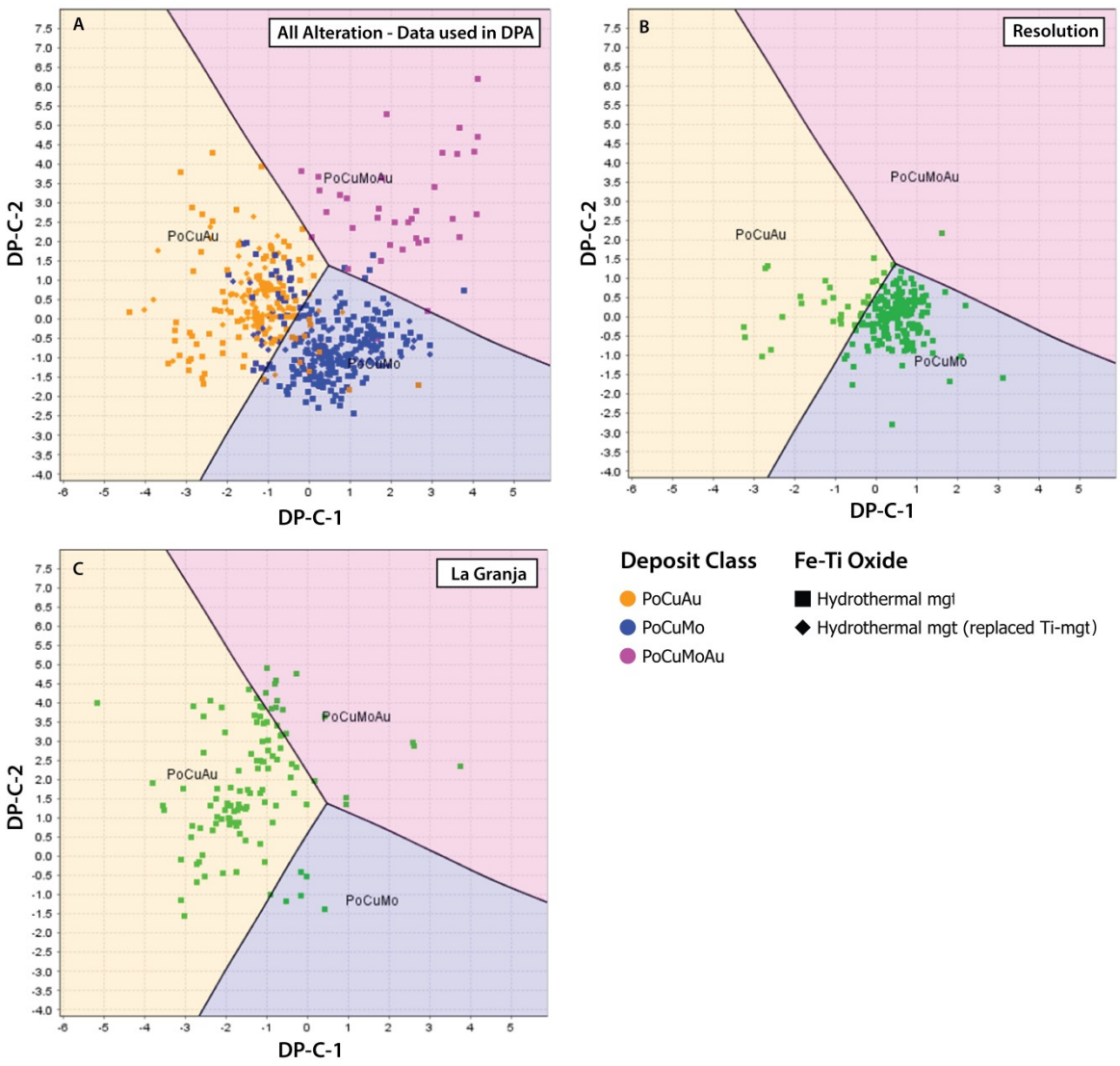


Figure 6-30: A) Discrimination diagram using DP-C-1 and DP-C-2 to categorise porphyry system type based on hydrothermal magnetite from all alteration styles. B) DP-C-1 vs. DP-C-2 for hydrothermal magnetite data from propylitically-altered rocks surrounding the Resolution porphyry copper deposit, Arizona, USA. C) DP-C-1 vs. DP-C-2 for hydrothermal magnetite data from propylitically-altered rocks at La Granja porphyry copper deposit, Peru.

iii Fertility Assessment in the Central Wasatch Mountains and Bingham Canyon, Utah, USA

The central Wasatch Mountains, southeast of Salt Lake City, Utah, USA (Figure 6-31) host several mineral deposits, including Ag-Pb-Zn ± Cu ± Au replacement and vein deposits, a low-grade porphyry Cu-Au deposit, Cu-bearing skarns, a quartz monzonite porphyry Mo deposit, and high-sulphidation Au deposits (John , 1989). These deposits are associated with an east-west-trending mid-Tertiary igneous belt, consisting of high-K, calc-alkaline porphyry stocks and cogenetic volcanic rocks that formed approximately 41-30 Ma. The deposits of the central Wasatch Mountains are dwarfed by the giant Bingham Canyon porphyry Cu-Mo-Au deposit, also associated with late Eocene igneous rocks that are similar in age and composition to those of the Wasatch igneous belt, which is located approximately 20 km west of the central Wasatch Mountains (Figure 6-31 and 6-34).

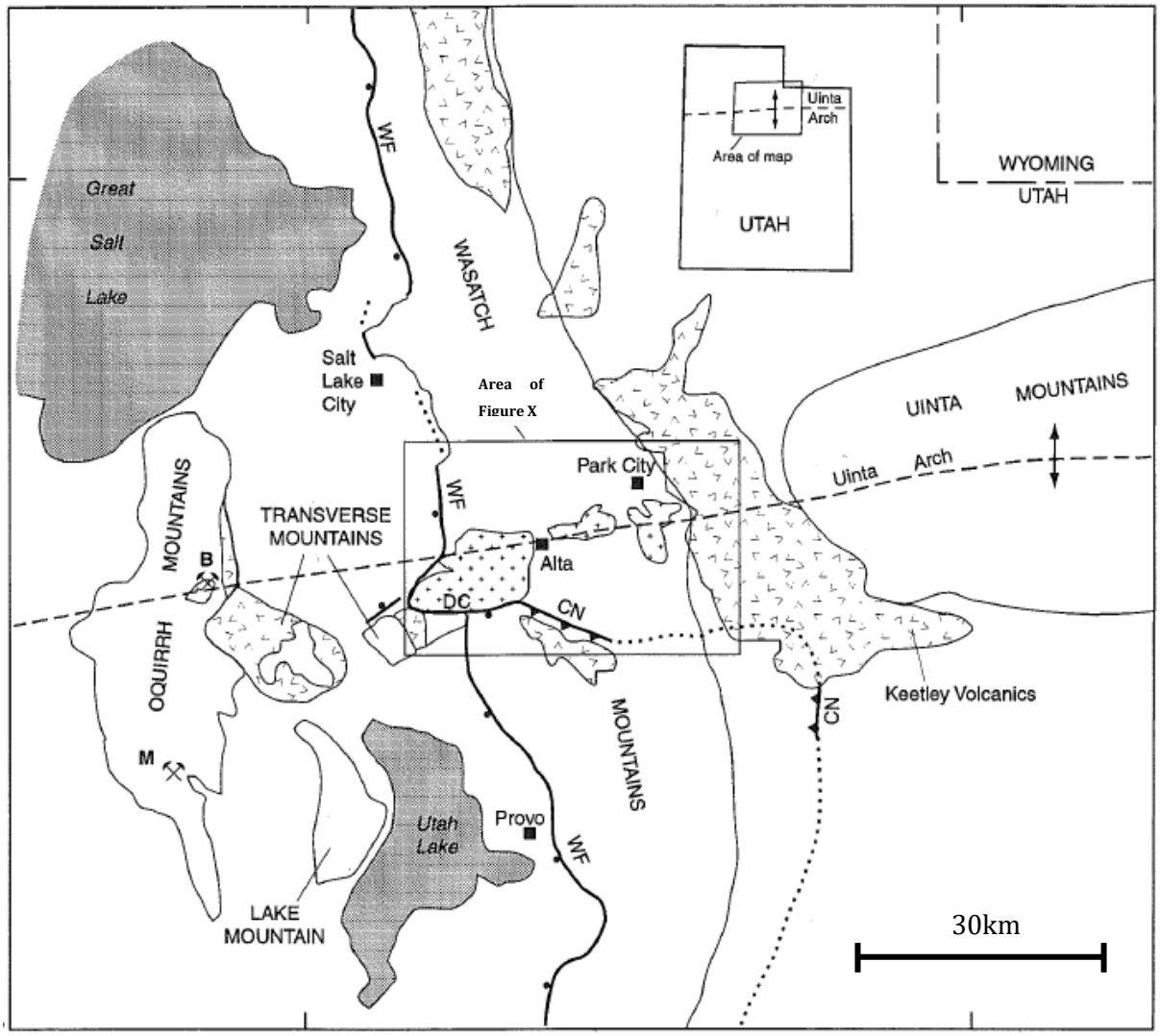


Figure 6-31: Map showing the location of the central Wasatch Mountains and Tertiary igneous intrusions in north-central Utah. Location of the Bingham Canyon Mine is denoted by "B". (From John, 1997)

Eastward tilting of the central Wasatch Mountains during Late Cenozoic Basin-and-Range extension resulted in progressively deeper levels of exposure from east to west, from <1 km to about 11 km (John, 1997; Figure 6-32). This has exposed a variety of mineral deposit types across the range, from replacement and vein deposits that formed at 1-2 km depth in the east, to deeper plutonic porphyry Mo deposits in the west which formed at about 6 km paleodepth (John, 1997; Figure 6-34).

The sample set used in the present study comprises several intrusions in the central Wasatch Mountains, including altered but barren porphyritic rocks and 'unaltered' background samples, as well as samples of mineralised porphyry intrusions from Bingham Canyon, which are all of a similar age and composition (Table 6-1). Thus, this subset of samples provides an opportunity to assess variations in the chemistry of hydrothermal magnetite in mineralised and less mineralised rocks in a specific region.

This subset includes two samples from the giant Bingham Canyon porphyry Cu-Mo-Au deposit: RTX-40100928-BING, a potassic-propylitic altered hybrid monzonite; and RTX-40100946-BING, a propylitic altered quartz latite porphyry. There are two samples from White Pine intrusion, a low-grade Mo-mineralised porphyry intrusion, hosted within the Little Cottonwood Stock, of which there is also one sample: RTX-401005533-WP and RTX-401005533-WP, both phyllic altered leucocratic quartz monzonite from adjacent to the Mo-mineralisation at White Pine with 5% and 1% pyrite respectively; and RTX-401005532-LILC, an 'unaltered' porphyritic biotite-hornblende granite. Alta Stock and the adjacent Clayton Peak Stock are located in the central part of the range and association with polymetallic (Ag-Pb ± Zn ± Cu) replacement and fissure and Cu-bearing skarn deposits. Samples RTX-40105535-ALT, an 'unaltered' equigranular granodiorite and RTX-40105536-ALT, an 'unaltered' porphyritic granodiorite, are from Alta Stock, and RTX-40105537-CLAY, an 'unaltered' mafic granodiorite is from Clayton Peak Stock. Samples RTX-40105538-FLAG and RTX-40105539-VAL are from the Flagstaff and Valeo Stocks respectively in the eastern part of the range. Propylitic alteration is widespread in both these stocks, although they are not associated with significant mineralisation. The locations of the samples in the Central Wasatch mountains is shown in Figure 6-33.

The samples all contain similar, subhedral, slightly poikilitic and fractured hydrothermal magnetite. RTX-40105538-FLAG is the only sample that contains igneous magnetite.

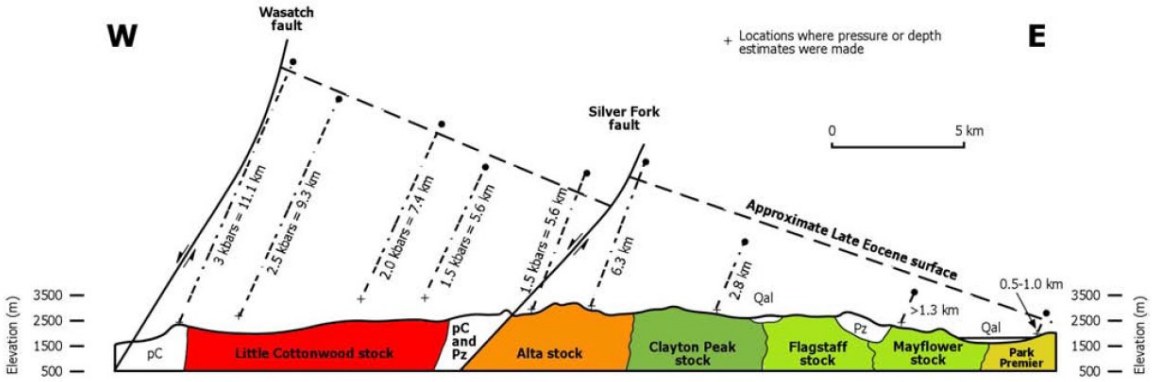


Figure 6-32: East-West cross section across the Central Wasatch mountains displaying the locations of the various intrusions, tilting and estimated depths of emplacement (from Cooke et al., 2012).

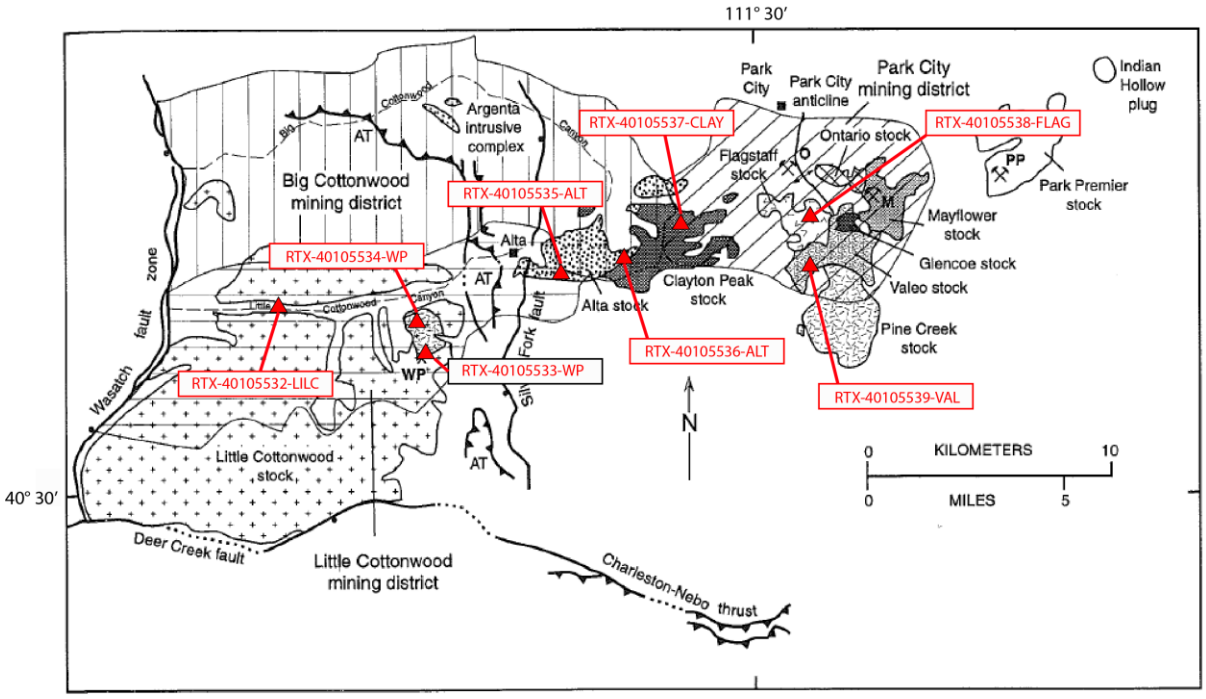


Figure 6-33: Geological map of the central Wasatch Mountains showing locations of samples studied, intrusive units and major structural features. Modified after John (1997).

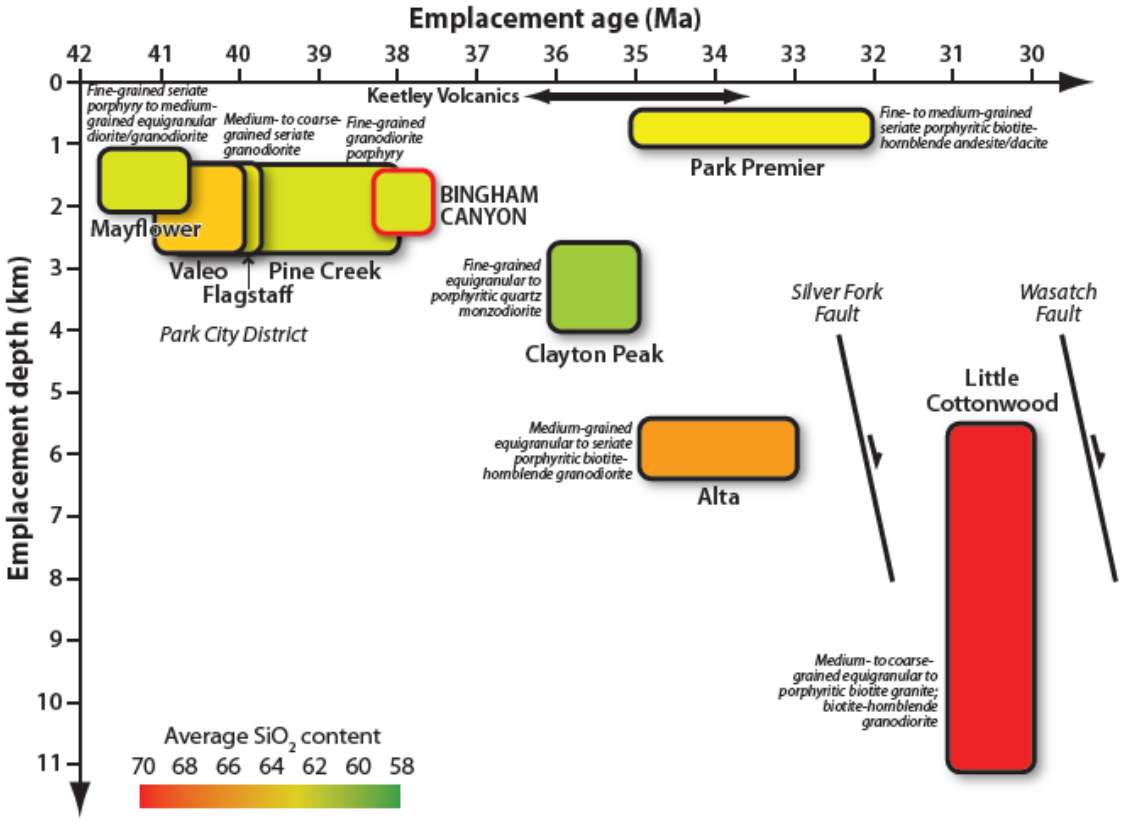


Figure 6-34: A summary of the estimates of depth and geochronology of various intrusions in the Central Wasatch mountains (data from John, 1989; John, 1997; Vogel et al., 1997 and sources therein) and Bingham Canyon deposit (data from Redmond et al., 2004; Von Quadt et al., 2011) (From Cooke et al., 2012)

None of the samples in the central Wasatch mountains are from intrusions associated with a porphyry deposit with a well-defined resource. As a result, the porphyry system types (metal associations) that could be present are unknown. Thus, hydrothermal magnetite data from the central Wasatch Mountains dataset were plotted using the metal association plot developed in DPA-C (Figure 6-30) in order to assess possible metal associations.

The data from White Pine plot in the PoCuMo field (Figure 6-35), which is consistent with the presence of uneconomic, low-grade Mo mineralisation at the White Pine Fork porphyry Mo deposit. Data from the Little Cottonwood intrusion, which itself contains no mineralisation but encloses the White Pine intrusion (Figure 6-35), also classify this as a PoCuMo system. Data from the Alta stock spreads across the boundary between PoCuMo and PoCuAu fields, but is mostly within the PoCuMo field. There are Fe-Cu skarn deposits associated with Alta stock, hornblende-, magnetite-, biotite- and K-feldspar-bearing veins, quartz-sericite-pyrite veins and some molybdenite- and Cu-sulphide mineralisation, indicative of at least weak, porphyry-style

phenomena (John, 1997). Hydrothermal magnetite from Clayton Peak straddles the boundary between the PoCuMo and PoCuMoAu fields. The Clayton Peak stock is the most alkalic of the western stocks which could explain its closer affinity to the PoCuMoAu field, because alkalic magmas often generate more Au-rich porphyry copper deposits (Seedorff et al., 2005). A number of polymetallic vein and replacement style deposits (Cu-Au-Ag-Pb) are associated with this intrusion, however, no porphyry-style mineralisation has yet been identified. Data from the Flagstaff and Valeo stocks, associated with Au-Ag-Pb-Zn-Cu mineralisation, plot predominantly in the PoCuAu field; however, these samples are both propylitically-altered which may result in an inaccurate classification as noted above. Notwithstanding this, these intrusions are more shallowly emplaced than those in the west and have quartz diorite to syenodiorite compositions, features which are consistent with a stronger Cu-Au character (Muntean and Einaudi, 2000; Seedoorf et al., 2005). Samples from the Bingham porphyry copper deposit plot within the PoCuMoAu field, which is unsurprising given that these data were used in DPA-C (Figure 6-35).

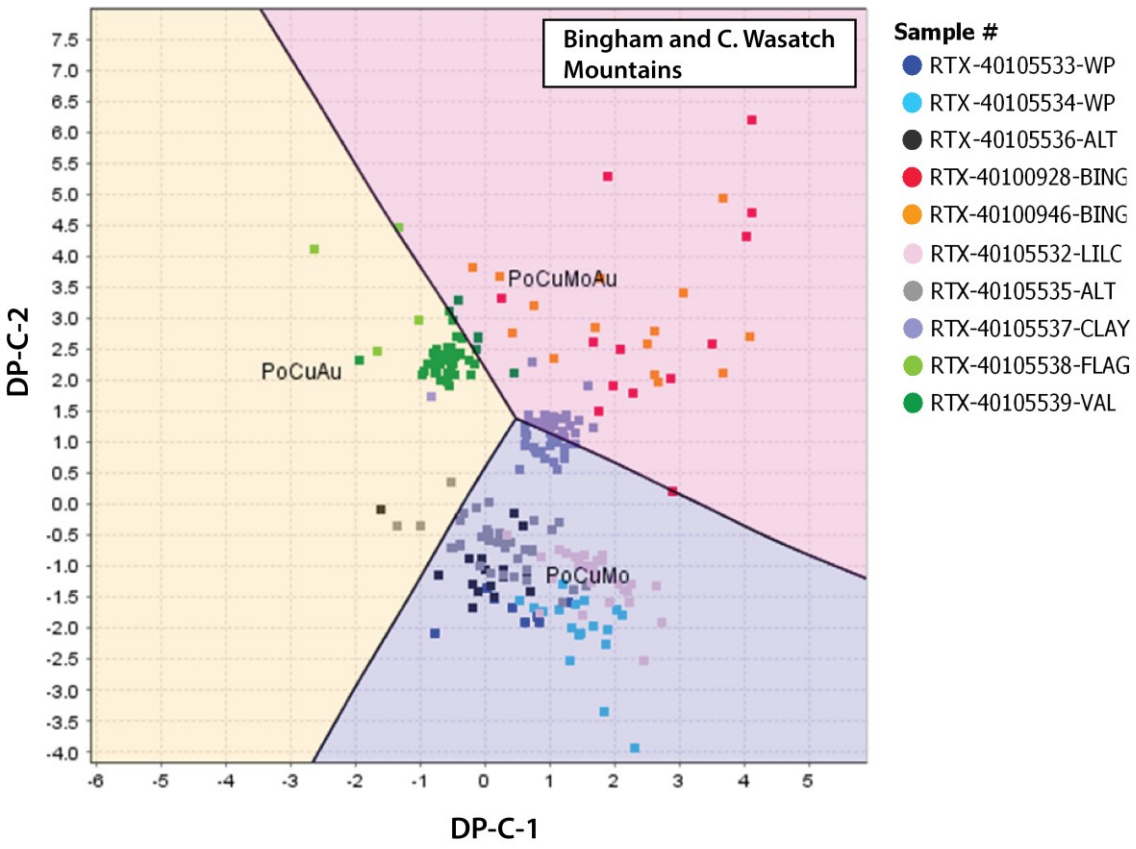


Figure 6-35: Discrimination diagram using DP-C-1 and DP-C-2 to categorise metal association of porphyry copper system using hydrothermal magnetite from samples in central Wasatch Mountains and Bingham Canyon.

Based on the hydrothermal magnetite compositions derived from this region, a discrimination diagram was developed for the assessment of porphyry endowment. Samples from Bingham Canyon, a giant porphyry copper system, were classified as strongly mineralised. Alta, White Pine, Valeo, Flagstaff and Clayton Peak stocks are all associated with some mineralisation, albeit containing no known significant resource. Thus, these samples were classified as weakly mineralised. There is no known mineralisation associated with the Little Cottonwood intrusion, so this sample was classified as background. Since this sub-set of samples covers a range of alteration styles (Table 6-1), it was not possible to study each alteration type separately. The top 11 elements (Mg, Al, Ti, V, Cr, Mn, Co, Ni, Zn, Ga and Ge) above the limit of detection in more than 93% of LA-ICP-MS analyses of hydrothermal magnetite all have bivariate correlation with at least one other element and/or are associated with other elements in the first 3 components or a robust PCA analysis, so were all used in the DPA. The results this DPA (DPA-D) are summarised in Table 6-7.

The discriminant projection scores are calculated as follows:

DP-D-1: -0.9861734 * (LOG(MG_PPM) - 1.9726304) + 1.1509104 * (LOG(AL_PPM) - 2.8748922) + -0.6750864 * (LOG(TI_PPM) - 2.8142824) + 1.7386996 * (LOG(V_PPM) - 3.1983712) + 0.36975327 * (LOG(CR_PPM) - 2.4804828) + 1.8147185 * (LOG(MN_PPM) - 2.9227726) + 1.439655 * (LOG(CO_PPM) - 1.4270712) + -2.8354099 * (LOG(NI_PPM) - 1.8826731) + 1.3652382 * (LOG(ZN_PPM) - 2.2814634) + -3.136737 * (LOG(GA_PPM) - 1.4776456) + 1.947997 * (LOG(GE_PPM) - 0.7814821)

DP-D-2: -1.8682051 * (LOG(MG_PPM) - 1.9726304) + -0.35669214 * (LOG(AL_PPM) - 2.8748922) + -1.5017225 * (LOG(TI_PPM) - 2.8142824) + -3.228667 * (LOG(V_PPM) - 3.1983712) + 1.1192244 * (LOG(CR_PPM) - 2.4804828) + 0.6341536 * (LOG(MN_PPM) - 2.9227726) + -1.21472 * (LOG(CO_PPM) - 1.4270712) + 2.0542614 * (LOG(NI_PPM) - 1.8826731) + 0.77115685 * (LOG(ZN_PPM) - 2.2814634) + -0.39418185 * (LOG(GA_PPM) - 1.4776456) + 0.03790842 * (LOG(GE_PPM) - 0.7814821)

Most of the hydrothermal magnetite from strongly mineralised, weakly mineralised and background samples are discriminated from one another in a plot of DP-D-1 vs. DP-D-2, although a few data from weakly mineralised samples spread into the background field (Figure 6-36). The principal elements controlling DP-D-1 are Co, Mn, V, Cr, Ge and Mg, whereas the key elements influencing DP-D-2 are Ti, Ga and Al. DP-D-1 predominantly separates data from strongly mineralised rocks from weakly mineralised and background samples and DP-D-2 distinguishes background from weakly mineralised samples.

Hydrothermal magnetite from Bingham contains more Mg, but less Co, Mn, V, Ge and Cr relative to other samples used in DPA-D and these features are the key discrimination characteristics of the strongly mineralised system. Hydrothermal magnetite in weakly mineralised samples contains more Ti, Ga and Al relative to “background” hydrothermal magnetite. Nevertheless,

there is only one background sample and one strongly mineralised sample used in DPA-D, so more data are needed to determine whether this is a general characteristic of "background" and "strongly mineralised" hydrothermal magnetite.

Table 6-7: Results of Discriminant Projection Analysis to categorise hydrothermal magnetite from central Wasatch mountains and Bingham Canyon according to porphyry endowment.

DPA-D (Bingham and central Wasatch Mountains area)		
Category	n	
Background	31	
Strongly mineralised	29	
Weakly mineralised	172	
Total	232	
Structure Coefficients		
	DP-D-1	DP-D-2
Mg	**-0.44**	-0.39
Al	-0.33	**-0.52**
Ti	-0.17	**-0.65**
V	**0.57**	-0.35
Cr	**0.40**	0.19
Mn	**0.63**	-0.24
Co	**0.84**	-0.20
Ni	0.12	-0.04
Zn	0.33	-0.34
Ga	-0.08	**-0.60**
Ge	**0.46**	0.13
Eigenvalues	4.442	1.523
Cumulative %	74.46	100

The concentrations of some elements less frequently above the limit of detection in the hydrothermal magnetite analyses were also compared in the different domains defined in DPA-D. Notably, the content of Cu in hydrothermal magnetite is fairly consistently highest in strongly mineralised samples (Figure 6-36A). Tin and W contents are also highest in strongly mineralised samples and lowest in background samples (Figure 6-36B and C), therefore these elements appear to reflect intensity of mineralisation, possibly related to temperature, pH and metal budget of the hydrothermal fluids.

To assess whether this plot could be extended to assess mineralisation potential worldwide, all hydrothermal magnetite from the full dataset was plotted, apart from the data used to make the

discriminant plot. The result is that most samples are classified as weakly mineralised (Figure 6-37) meaning that, globally, the plot is not effective for discrimination of hydrothermal magnetite from weakly and strongly mineralised settings. What it does indicate is that Bingham hydrothermal magnetite is distinct from all other hydrothermal magnetite in the database, and also that the background data from the Little Cottonwood stock is unique. Nonetheless, the plot could aid exploration for another Bingham-like deposit in the Wasatch Mountains area.

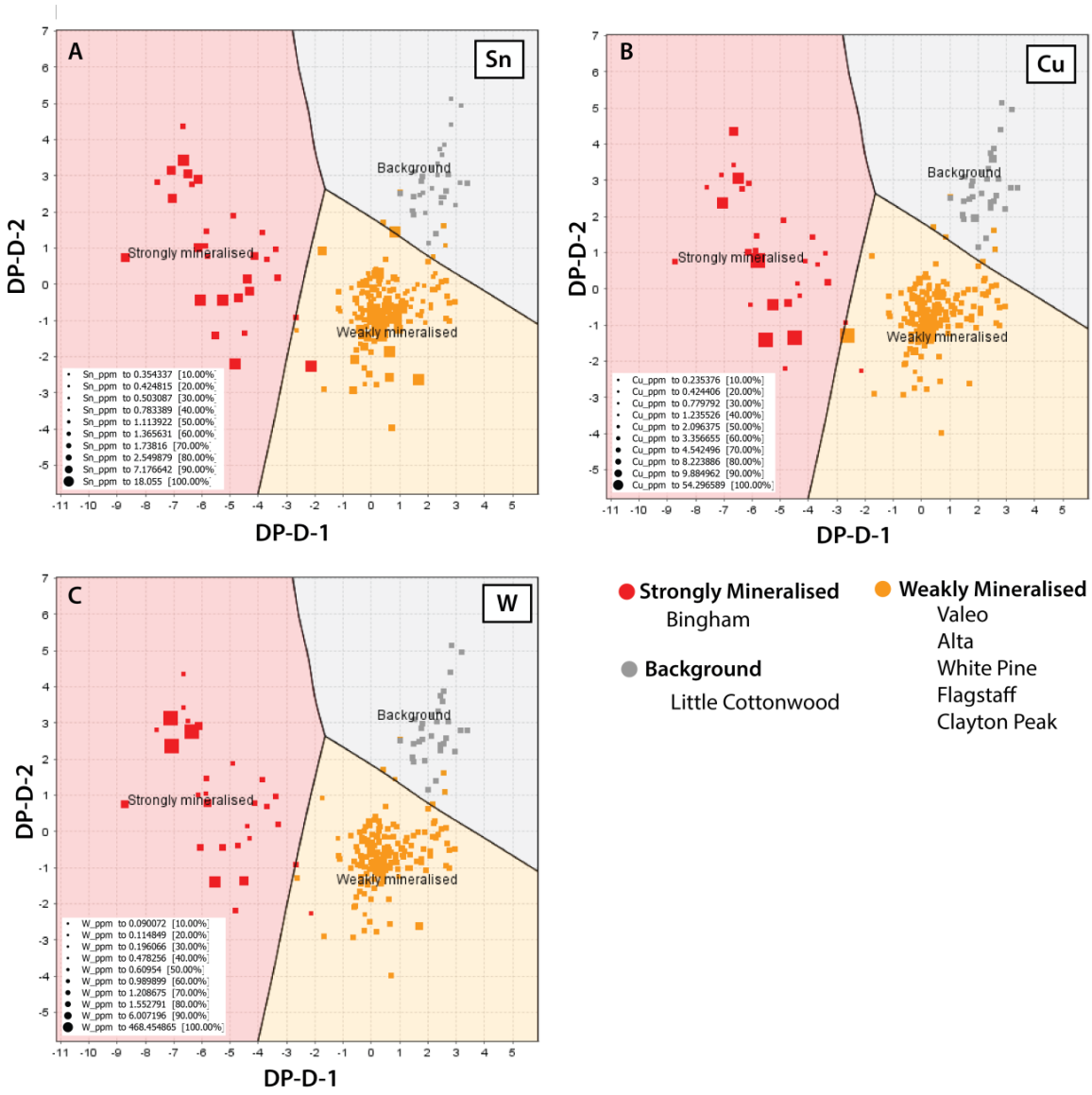


Figure 6-36: Discrimination diagram using DP-D-1 and DP-D-2 to categorise endowment of porphyry copper systems using hydrothermal magnetite from samples in central Wasatch Mountains and Bingham Canyon. (A) Sn content in magnetite; (B) Cu content in magnetite, and (C) W content in magnetite indicated by symbol size.

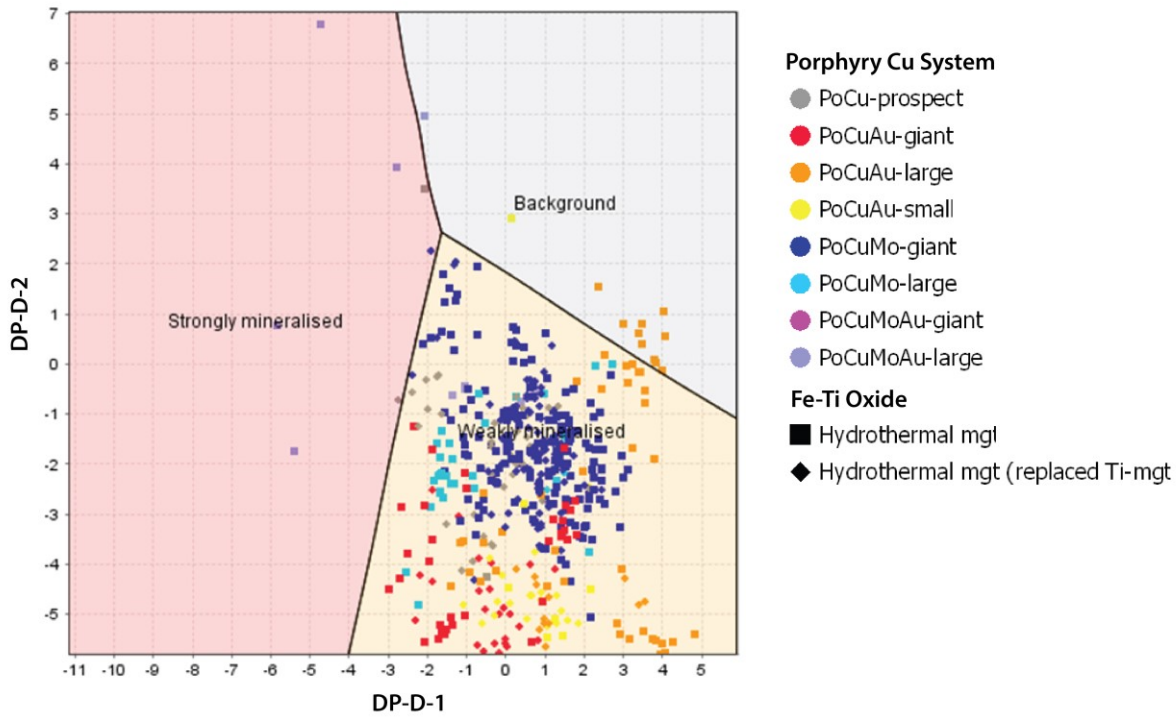


Figure 6-37: Discrimination diagram using DP-D-1 and DP-D-2 to categorise endowment of porphyry copper systems for all hydrothermal magnetite analysed in this study, apart from that data used to create the discriminant plot.

iv Global Fertility Assessment

Finally, discrimination diagrams were constructed in an attempt to develop a tool for the assessment of porphyry system fertility worldwide. The dataset includes samples from a number of PoCu prospects which have no porphyry copper resource associated with them. Albeit that the mineralisation potential of these systems is strictly unknown, the samples have been assumed unprospective for porphyry copper deposits given that no significant porphyry mineralisation has been identified to date. Still, it is important to bear in mind that one or more of these could be prospective and that this might emerge in the results.

The style of alteration influences the chemistry of hydrothermal magnetite, therefore magnetite from individual alteration domains needs to be studied separately. The majority of the hydrothermal magnetite in the sample set is from potassically-altered samples, so this alteration facies was chosen for the fertility study. Moreover, potassic alteration occurs in the core of porphyry copper systems, thus largely eliminating possible variations in chemistry that are related to distance from the mineralised centre, controlled by parameters such as temperature. A number of samples from PoCu prospects have been described as unaltered in petrographic descriptions yet, given that they contain hydrothermal magnetite, they must come from a

relatively proximal alteration zone (most likely potassic). Additionally, several samples are described as a hybrid between various alteration styles.

The procedure adopted was to use the alteration plot, developed using DPA-A, to classify the alteration association of hydrothermal magnetite. The potassically-associated subset of the data (Figure 6-38) was then used for the global fertility assessment.

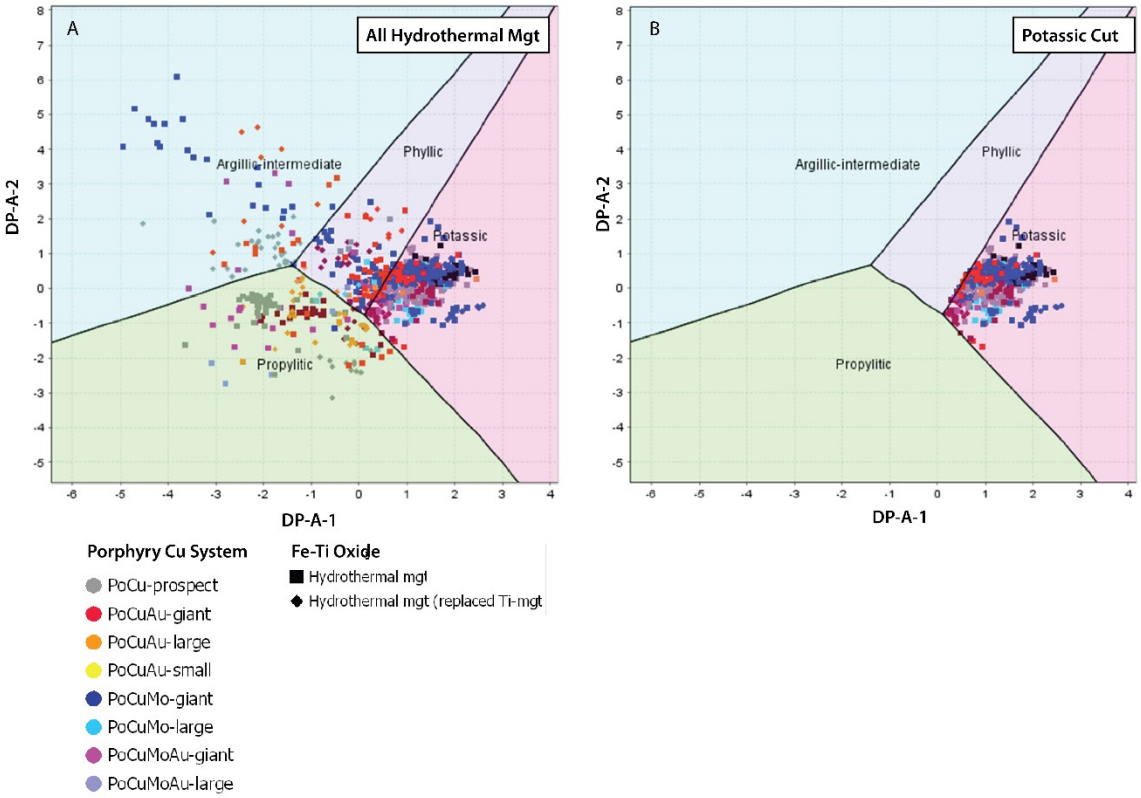


Figure 6-38: Discriminant diagram developed in DPA-A (DP-A-2 vs. DP-A-1) to categorise magnetite according to alteration style. (A) All hydrothermal magnetite analysed in this study (B) Cut-off of hydrothermal magnetite classified as potassically altered by this discriminant plot.

Because there are also distinct differences between the chemistry of hydrothermal magnetite from PoCuAu systems and PoCuMo systems (Figure 6-27), separate fertility assessments were developed for these two system types. The discrimination diagram for potassically-altered rocks developed using DPA-B was used to separate the potassically-associated magnetite data for PoCu prospects into PoCuMo and PoCuAu sub-types for the purposes of the DPA (Figure 6-39).

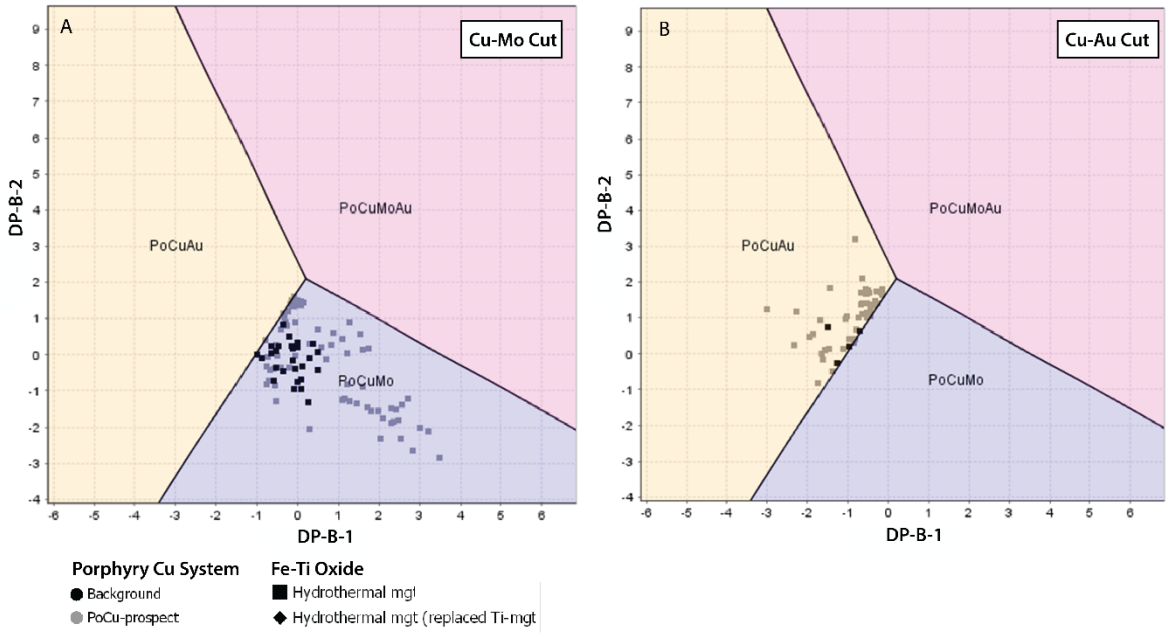


Figure 6-39: Discriminant diagram developed in DPA-B (DP-B-2 vs. DP-B-1) to categorise potassically altered hydrothermal magnetite according to metal association of porphyry copper system. (A) Hydrothermal magnetite from background and PoCu-prospects classified as PoCuMo (B) Hydrothermal magnetite from background and PoCu-prospects classified as PoCuAu.

Porphyry Cu-Mo fertility discrimination

The first global fertility diagram was generated to discriminate hydrothermal magnetite from potassic-associated PoCuMo samples into the following groups: PoCuMo-giant, PoCuMo-large, PoCuMo-prospect and PoCuMo-background. To perform the DPA, Mg, Al, Ti, Cr, Mn, Co, Ni, Zn, Ga and Ge were used. V was omitted from those elements detected in more than 93% of LA-ICP-MS analyses of hydrothermal magnetite because it showed no significant bivariate correlation (> 0.4 Pearson Correlation coefficient) with any other element or any of the first 3 principal components of a robust PCA. Samples RTX-6759114-ZAL, from the Zaldivar deposit (PoCuMo-giant), and RTX-40105537-CLAY, from the Clayton Peak stock (PoCu-prospect) were omitted from the DPA to allow subsequent testing of the effectiveness of the discrimination diagram. No samples from PoCuMo-large and background categories were omitted since these two groups were both made up of just one sample. The results of this DPA (DPA-E) are summarised in Table 6-8.

The discriminant projection scores are calculated as follows:

DP-E-1 (57.8%): -1.577791 * (LOG(MG_PPM) - 1.7186809) + -1.1233599 * (LOG(AL_PPM) - 2.6269314) + -0.909711 * (LOG(TI_PPM) - 2.5385325) + 1.1422858 * (LOG(CR_PPM) - 2.0550625) + 2.6073306 * (LOG(MN_PPM) - 2.8012526) + -2.62727 * (LOG(CO_PPM) - 1.5975003) + 0.35530856 * (LOG(NI_PPM) - 1.5122458) + 1.9548465 * (LOG(ZN_PPM) - 1.9530544) + -1.5083662 * (LOG(GA_PPM) - 1.4471908) + 1.3944522 * (LOG(GE_PPM) - 0.69399995)

DP-E-2 (27.8%): -2.7181911 * (LOG(MG_PPM) - 1.7186809) + 1.5287856 * (LOG(AL_PPM) - 2.6269314) + 1.7478461 * (LOG(TI_PPM) - 2.5385325) + 1.4998516 * (LOG(CR_PPM) - 2.0550625) + -1.9639455 * (LOG(MN_PPM) - 2.8012526) + 2.9273198 * (LOG(CO_PPM) - 1.5975003) + 0.33090279 * (LOG(NI_PPM) - 1.5122458) + 0.6001399 * (LOG(ZN_PPM) - 1.9530544) + -2.5913205 * (LOG(GA_PPM) - 1.4471908) + -1.329152 * (LOG(GE_PPM) - 0.69399995)

DP-E-3 (14.4%): 0.38210276 * (LOG(MG_PPM) - 1.7186809) + 3.7489038 * (LOG(AL_PPM) - 2.6269314) + -0.20584753 * (LOG(TI_PPM) - 2.5385325) + -0.4922048 * (LOG(CR_PPM) - 2.0550625) + -0.64899033 * (LOG(MN_PPM) - 2.8012526) + 0.9554364 * (LOG(CO_PPM) - 1.5975003) + 2.4890609 * (LOG(NI_PPM) - 1.5122458) + -1.3205098 * (LOG(ZN_PPM) - 1.9530544) + -2.7416232 * (LOG(GA_PPM) - 1.4471908) + 2.817361 * (LOG(GE_PPM) - 0.69399995)

The majority of the data included in DPA-E from PoCuMo-giant, PoCuMo-large and PoCu-prospects are effectively discriminated from one another using a plot of DP-E-1 vs. DP-E-2 (Figure 6-40A). All background samples included in DPA-E are discriminated from the other groups in this plot.

Table 6-8: Results of Discriminant Projection Analysis to categorise hydrothermal magnetite classified as potassically altered and as PoCuMo according to size of porphyry copper system.

DPA-E (PoCuMo fertility)			
Category	n		
Background	27		
PoCu-prospect	51		
PoCuMo-giant	179		
PoCuMo-large	23		
Total	280		
Structure Coefficients			
	DP-E-1	DP-E-2	DP-E-3
Mg	**-0.42**	-0.22	0.15
Al	**-0.59**	0.09	-0.18
Ti	**-0.66**	0.19	-0.10
Cr	**0.50**	**0.62**	0.15
Mn	**0.44**	-0.31	-0.29
Co	0.20	0.01	-0.13
Ni	**0.48**	0.28	0.31
Zn	0.31	-0.11	-0.58
Ga	-0.31	-0.28	-0.52
Ge	**0.41**	**-0.44**	0.57
Eigenvalues	2.094	1.01	0.5228
Cumulative %	57.75	85.59	100

The first function, DP-E-1 has strong positive loadings for Cr, Ni, Mn and Ge and negative loadings for Ti, Al and Mg. The second function, DP-E-2, is most strongly influenced by positive Cr and negative Ge. DP-E-1 predominantly separates background samples at high DP-E-1, from PoCuMo-

prospect and PoCuMo-giants at moderate DP-E-1, and from PoCuMo-large deposits at low DP-E-1. DP-E-2 primarily discriminates hydrothermal magnetite from PoCuMo-giant samples from the other system types. Accordingly, hydrothermal magnetite from background samples has the lowest Ti, Al and Mg contents, but higher contents of Cr, Ni, Mn and Ge.

The plot of DP-E-1 vs. DP-E-2 correctly classifies most of the hydrothermal magnetite analysed from samples RTX-6759114-ZAL and RTX-40105537-CLAY (Figure 6-40B), which were omitted from the DPA. Although data from RTX-6759114-ZAL straddle the boundary between the PoCuMo-giant and PoCuMo-large fields, Zaldivar is relatively small compared to most other PoCuMo-giant deposits included in the sample set. This test lends support to the effectiveness of this diagram for distinguishing hydrothermal magnetite from strongly mineralised PoCuMo systems from weakly mineralised and background samples. Notwithstanding this, because just one sample was used to define each of the PoCuMo-large and background fields, these fields should be refined by a new DPA with more data. Hydrothermal magnetite from mineralised PoCuAu and PoCuMoAu systems are not effectively discriminated from hydrothermal magnetite in less mineralised samples using this discriminant plot, emphasizing the need for a porphyry system type specific tool.

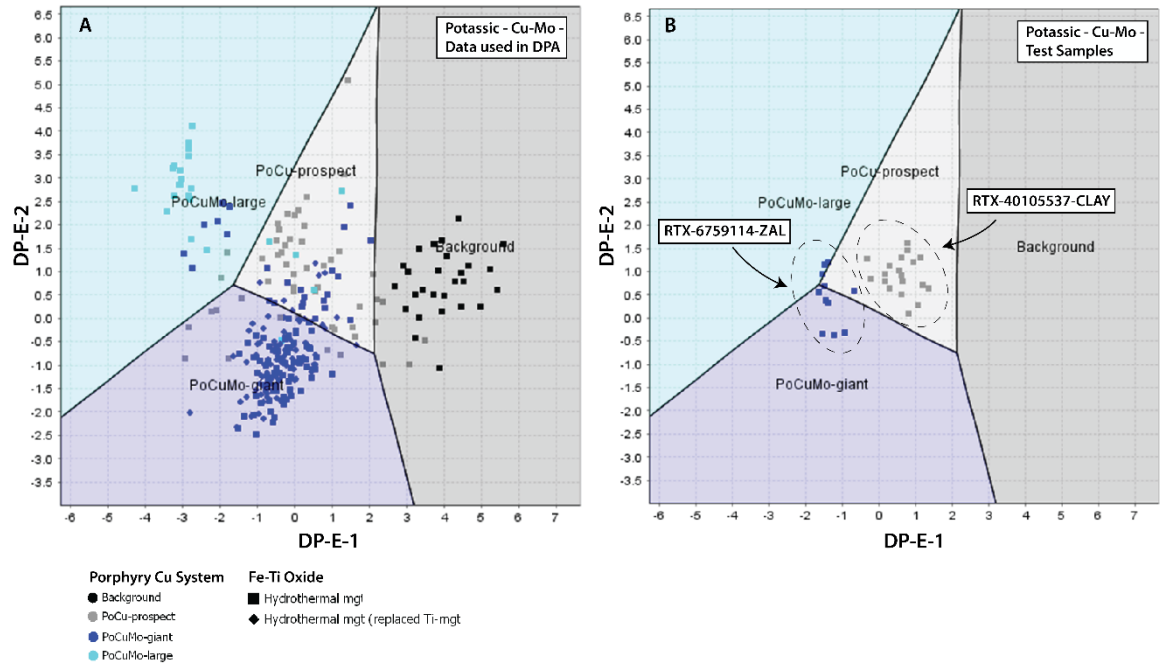


Figure 6-40: Discrimination diagram (DP-E-1 vs. DP-E-2) to classify hydrothermal magnetite from potassically-altered rocks classified as PoCuMo according to size of porphyry copper deposit. (A) All hydrothermal magnetite classified as potassically altered and as related to a PoCuMo system used in developing the discriminant diagram. (B) Hydrothermal magnetite from RTX-20105537-CLAY and RTX-6759114-ZAL, which were omitted for testing the accuracy of the discriminant plot.

Porphyry Cu-Au fertility discrimination

The second global fertility DPA was designed to separate hydrothermal magnetite from the potassic domains of PoCuAu systems according to the following categories: PoCuAu-giant, PoCuAu-large, PoCuAu-small, PoCuAu-prospect and PoCuAu-background. Mg, Al, Ti, V, Mn, Co, Ni, Zn, Ga and Ge were used in this DPA (DPA-F). Chromium was omitted from the DPA because it showed no significant bivariate correlation (> 0.4 Pearson Correlation coefficient) with any other element or with any of the first 3 principal components of a robust PCA. Data from the Alta stock (PoCu-prospect), Grasberg deposit (PoCuAu-giant), Veliki Krivelk deposit (PoCuAu-large) and GRP 314 deposit (PoCuAu-small) were omitted to test the efficacy of the discrimination diagram generated. No samples classified as background were omitted since this group is made up of only one sample. A summary of the results of DPA-F is provided in Table 6-9.

The discriminant projection scores are calculated as follows:

DP-F-1: 3.176464 * (LOG(MG_PPM) - 2.1569164) + -3.2186153 * (LOG(AL_PPM) - 2.9564817) + -0.63245404 * (LOG(TI_PPM) - 3.0366302) + 2.945844 * (LOG(V_PPM) - 3.3580995) + -2.100925 * (LOG(MN_PPM) - 2.8372986) + -1.2785054 * (LOG(CO_PPM) - 1.6081579) + 6.8908787 * (LOG(NI_PPM) - 1.572407) + -1.2321868 * (LOG(ZN_PPM) - 2.1803522) + 4.1936607 * (LOG(GA_PPM) - 1.4748714) + -2.8970563 * (LOG(GE_PPM) - 0.85877204)

DP-F-2: -0.25701106 * (LOG(MG_PPM) - 2.1569164) + -5.228648 * (LOG(AL_PPM) - 2.9564817) + 1.6190693 * (LOG(TI_PPM) - 3.0366302) + -2.3074532 * (LOG(V_PPM) - 3.3580995) + 1.707964 * (LOG(MN_PPM) - 2.8372986) + -1.4774252 * (LOG(CO_PPM) - 1.6081579) + 3.749079 * (LOG(NI_PPM) - 1.572407) + 1.9144936 * (LOG(ZN_PPM) - 2.1803522) + 0.18726623 * (LOG(GA_PPM) - 1.4748714) + 1.3695296 * (LOG(GE_PPM) - 0.85877204)

DP-F-3: 0.6905302 * (LOG(MG_PPM) - 2.1569164) + -4.8886943 * (LOG(AL_PPM) - 2.9564817) + 1.5868068 * (LOG(TI_PPM) - 3.0366302) + -0.36823067 * (LOG(V_PPM) - 3.3580995) + 0.86326844 * (LOG(MN_PPM) - 2.8372986) + 0.5248041 * (LOG(CO_PPM) - 1.6081579) + 0.36249685 * (LOG(NI_PPM) - 1.572407) + 0.7457394 * (LOG(ZN_PPM) - 2.1803522) + 0.2018219 * (LOG(GA_PPM) - 1.4748714) + -3.452041 * (LOG(GE_PPM) - 0.85877204)

DP-F-4: 0.7499787 * (LOG(MG_PPM) - 2.1569164) + 2.3191235 * (LOG(AL_PPM) - 2.9564817) + -4.45644 * (LOG(TI_PPM) - 3.0366302) + 0.20367861 * (LOG(V_PPM) - 3.3580995) + 2.579986 * (LOG(MN_PPM) - 2.8372986) + 0.060124148 * (LOG(CO_PPM) - 1.6081579) + -1.2585597 * (LOG(NI_PPM) - 1.572407) + 1.4437518 * (LOG(ZN_PPM) - 2.1803522) + -2.2597158 * (LOG(GA_PPM) - 1.4748714) + -1.1853002 * (LOG(GE_PPM) - 0.85877204)

The majority of the data are effectively separated into the different classes on a plot of DP-F-1 vs. DP-F-2 (Figure 6-41A). DP-F-1 is most strongly influenced by positive loadings for Ni and V and a negative loading for Zn, whereas DP-F-2 is most affected by positive loadings for Ge and Ni, and negative loadings for Al and Mg. Hydrothermal magnetite from mineralised systems has low DP-F-1 and DP-F-2 values relative to PoCu-prospects and background samples. These relationships indicate that hydrothermal magnetite from the potassic zone of mineralised PoCuAu systems has

high Zn, Al and Mg and lower Ni and V relative to hydrothermal magnetite from background and less mineralised samples.

The discriminant diagram, DP-F-1 vs. DP-F-2, was tested using data omitted from DPA-F (Figure 6-41B). Hydrothermal magnetite from the Alta PoCu-prospect classifies as background. Although Alta is a PoCu-prospect in that porphyry-style mineralised veins are present, the intensity of veining is weak suggesting that a large hydrothermal system did not develop. Bearing in mind that background is only defined by one sample, the distinction between background and prospects is probably not very robust.

Grasberg did not yield any analyses with all 10 elements used in DPA-F above the LOD so could not be plotted on the diagram. Data from GRP 314, classified as PoCuAu-small, plot within the PoCuAu-giant field. Although GRP 314 is classified as PoCuAu-small with respect to contained Cu, it could be considered a larger deposit using the lower grade 0.3% Cu cut-off, which is not currently included in the resource model (Pacey A., personal communication). This could explain why it plots within the PoCuAu-giant field. Data from Veliki Krivelj, classified as PoCuAu-large, plots in the PoCuAu-small field.

Table 6-9: Results of Discriminant Projection Analysis to categorise hydrothermal magnetite classified as potassically altered and as PoCuAu according to size of porphyry copper system.

DPA-F (PoCuAu fertility)				
Category	n			
Background	4			
PoCu-prospect	27			
PoCuAu-giant	30			
PoCuAu-large	34			
PoCuAu-small	7			
Total	102			
Structure Coefficients				
	DP-F-1	DP-F-2	DP-F-3	DP-F-4
Mg	0.04	**-0.46**	0.04	-0.21
Al	-0.19	**-0.58**	-0.09	-0.09
Ti	-0.39	-0.33	0.29	**-0.48**
V	**0.44**	-0.14	0.12	0.01
Mn	-0.27	0.29	**0.57**	0.11
Co	-0.21	0.01	**0.54**	0.10
Ni	**0.73**	**0.55**	-0.16	0.14
Zn	**-0.55**	0.02	0.03	0.11
Ga	-0.11	-0.21	0.18	-0.15
Ge	-0.20	**0.66**	-0.59	-0.20
Eigenvalues	8.932	3.52	0.6321	0.4569
Cumulative %	65.96	91.96	96.63	100

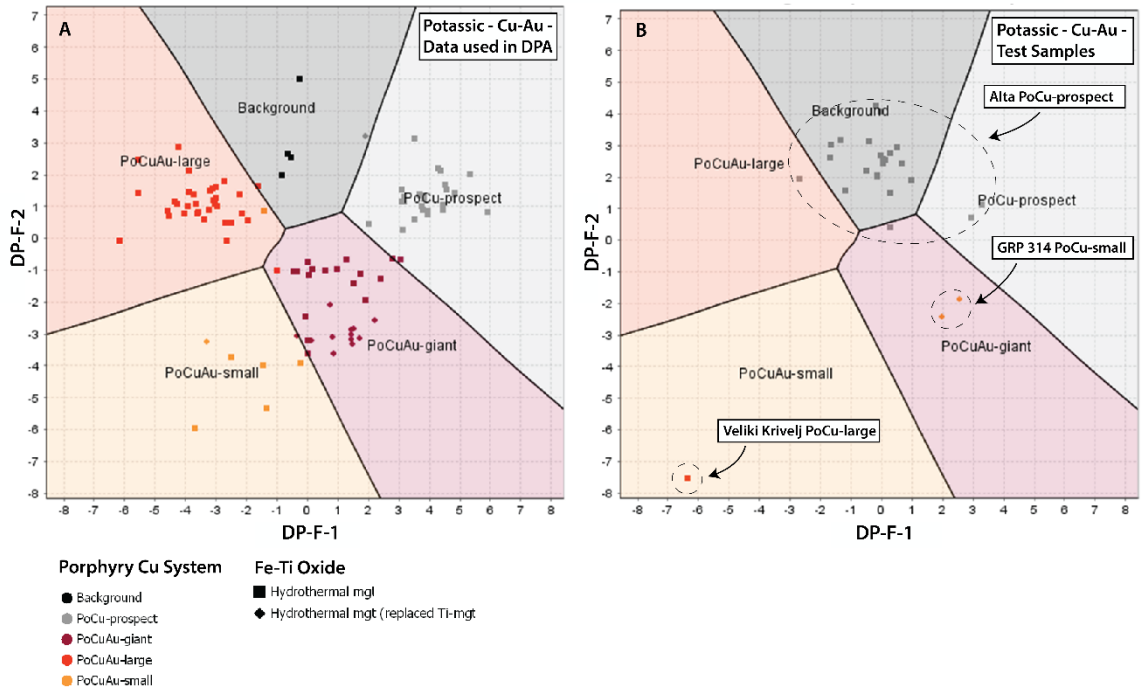


Figure 6-41: Discrimination diagram (DP-F-1 vs. DP-F-2) to classify hydrothermal magnetite classified as potassically-altered rocks and as PoCuAu according to size of porphyry copper deposit. A) All hydrothermal magnetite classified as potassically altered and from PoCuAu systems used in developing the discriminant diagram. B) Hydrothermal magnetite classified as potassically altered and related to a PoCuAu system from Alta Stock, Veliki Krivelj and GRP 314 which were omitted for testing the accuracy of the discriminant plot.

Collectively, this suggests that this plot can discriminate hydrothermal magnetite associated with mineralised PoCuAu systems from that associated with less mineralised or background samples. However, the discriminant diagram cannot effectively separate hydrothermal magnetite according to size, in terms of contained Cu, of PoCuAu systems.

Some elements in hydrothermal magnetite, less commonly above the limit of detection, were compared from PoCuAu-small, PoCuAu-large and PoCuAu-giant systems to evaluate progressive variations with size of deposit. Lithium, Sc, Sr, Y, Zr, Mo, Lu and Th all show a progressive decrease in concentration with increasing size of PoCuAu deposit (Figure 6-42). The middle 50% of hydrothermal magnetite data from PoCuAu-giant deposits have Li = 0.7-2.4 ppm, Sc = 1.3-2.7 ppm, Sr = 0.05-0.4 ppm, Y = 0.04-0.56 ppm, Zr = 0.03-0.43 ppm, Mo = 0.04-0.67 ppm, Lu = 0.03-0.06 ppm, and Th = 0.01-0.53 ppm, thus comparable concentrations of these elements could be used to identify giant PoCuAu systems from hydrothermal magnetite composition.

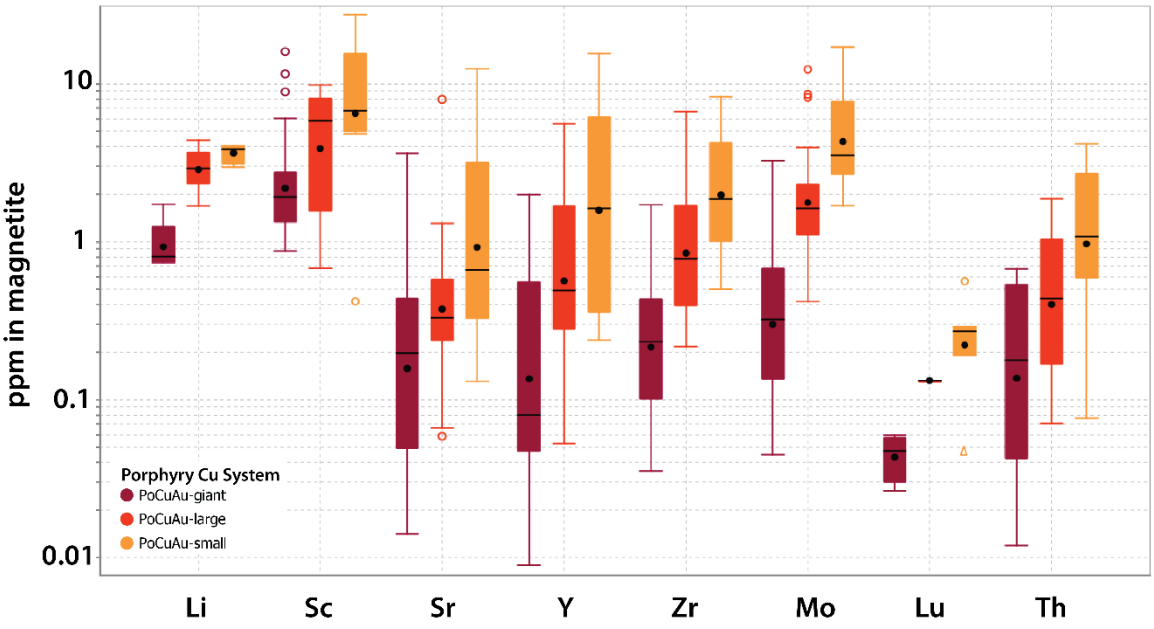


Figure 6-42: Box and whisker plot comparing the concentrations of Li, Sc, Sr, Y, Zr, Mo, Lu and Th in hydrothermal magnetite from potassically-altered rocks from PoCuAu-small, PoCuAu-large and PoCuAu-giant systems. The concentrations of these elements all generally decrease with increasing size of PoCuAu deposit in terms of contained Cu.

6.4.4.2 Discriminant Projection Analysis with Igneous Magnetite

Discriminant projection analyses to categorise different styles of alteration association and porphyry system type were attempted using igneous magnetite in the same fashion as for hydrothermal magnetite, but without success. The 16 elements above the detection limit in more than 93% of titanomagnetite analyses were omitted from the DPA if they showed no significant correlation (>0.4 Pearson correlation coefficient) with any other element or with any of the first three components of a robust PCA.

A plot was designed to classify various types of titanomagnetite as potassic-associated, propylitic-associated or unaltered (no titanomagnetites were analysed from phyllically-altered rocks and only one intermediate argillic sample had more than 2 titanomagnetite analyses), but it could not correctly classify samples omitted from the DPA for testing. Furthermore, titanomagnetite data from propylitically-altered rocks from Resolution and La Granja were not effectively classified, with data spreading beyond the boundaries of the plot generated with data from this study.

When attempting to classify metal association, it was not possible to individually study specific types of alteration separately because there was just one potassically-altered sample from PoCuMoAu sytems which contained titanomagnetite and no propylitically-altered samples from PoCuMo systems containing titanomagnetite. A DPA was performed attempting to categorise titanomagnetite from PoCuMo, PoCuAu and PoCuMoAu systems using samples from all alteration

types, but again without success. When testing this plot with titanomagnetite data from propylitically-altered samples from La Granja and Resolution, data spread across all metal association fields and extended far beyond the limits of the DP1 vs. DP2 plot.

Igneous titanomagnetite was plotted on some of the discrimination diagrams designed to separate various populations of hydrothermal magnetite. The plot developed during DPA-A to categorise hydrothermal magnetite according to style of alteration is not effective in classifying titanomagnetite (Figure 6-43A). The discriminant diagram designed to separate hydrothermal magnetite from potassically-altered rocks according to porphyry system type also does not effectively categorise titanomagnetite, plotting all data within the PoCuAu field. However, the relative positions of PoCuMoAu, PoCuAu and PoCuMo titanomagnetite is similar in DP-C-1 and DP-C-2 space to the boundaries defined for hydrothermal magnetite, but offset to lower DP-C-1 values (Figure 6-43B). DP-C-1 is strongly negatively loaded for Ti, Al, Mg and Mn (Table 6-6), which are all elevated in titanomagnetite relative to hydrothermal magnetite. Given that the titanomagnetite data are organised in a similar manner to hydrothermal magnetite, this could suggest that the titanomagnetites have been variably altered towards the composition of hydrothermal magnetite. With progressive alteration, the titanomagnetite data would be expected to move to higher DP-C-1, towards the composition of hydrothermal magnetite, as Ti, Al, Mg and Mn contents are decreased. This is further supported by the observation that hydrothermal magnetite, texturally observed to be replacing titanomagnetite, generally has concentrations of Ti, Al and Mg transitional between titanomagnetite and hydrothermal magnetite (vein or disseminated) (Figure 6-18).

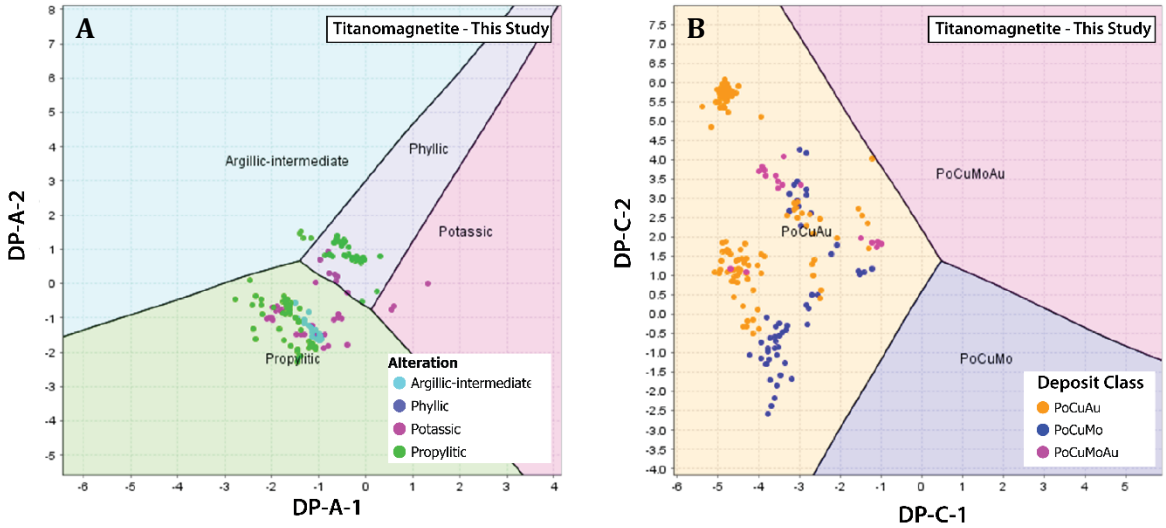


Figure 6-43: (A) All titanomagnetite data plotted on discriminant diagram (DP-A-1 vs. DP-A-2) developed to classify hydrothermal magnetite according to style of alteration. (B) All titanomagnetite data plotted on discriminant diagram (DP-C-1 vs. DP-C-2) developed to classify hydrothermal magnetite from all alteration types according to metal association of porphyry copper system.

6.4.5 Analysing igneous magnetite with exsolution

Data from igneous magnetite create linear trends between elements strongly incorporated into ilmenite relative to magnetite, e.g. Nb vs. Ta (Figure 6-8). This suggests that these linear arrays could represent variable incorporation of ilmenite exsolution in the analysis. Several authors have suggested that sampling the magnetite and exsolution together can be used to approximate the original composition of titanomagnetite prior to subsolidus exsolution (Dare et al., 2012; Pisiak et al. 2016). It is possible that exsolution occurs as a closed system process, so the abundance of ilmenite exsolution is limited by the original composition of the titanomagnetite. However, these linear arrays suggest other elements, not strongly incorporated into ilmenite, could be metasomatically removed during the exsolution process, thereby generating lineations towards the composition of ilmenite. If this is the case, grains with exsolution should not be used as a petrogenetic indicator to interpret magmatic conditions. Elements with large differences in concentration between hydrothermal and igneous magnetite (Figure 6-9) will be particularly susceptible to contamination from ilmenite exsolution. Oxidative exsolution of igneous magnetite is particularly common in plutonic rocks and hydrothermally-altered rocks, therefore titanomagnetite from unaltered and volcanic rocks should be targeted for petrogenetic work. Nevertheless, it is not possible to validate whether the original magnetite composition governs the abundance of ilmenite exsolution here given that the original composition of the magnetite prior to exsolution is unknown.

6.4.6 Effect of Hydrothermal Alteration on Chemistry of Igneous Magnetite

Differing styles of hydrothermal alteration modify the chemistry of igneous magnetite in different ways. The effect of propylitic and intermediate-argillic alteration on the chemistry of igneous magnetite was compared in igneous magnetite crystallised from the same andesitic unit at Rosia Poeini, Romania.

Titanium, Sn, Sc, Cr and Sr are all strongly depleted by both propylitic and intermediate-argillic alteration, particularly in intermediate-argillic alteration. Intermediate-argillic alteration is generally a more intense form of alteration than propylitic alteration. Moreover, magnetite is not typically formed in intermediate-argillic alteration so is likely more destabalised in this alteration zone. Zirconium and Nb increase, whereas Hf and Ta exhibit no significant change during propylitic alteration. Because the behaviour of these elements is similar in response to changing parameters such as fO_2, T and mineral composition it is possible that the differing behaviour reflects decoupled transport of these elements in hydrothermal fluids. Magnesium, Al and Co also increase during propylitic alteration, whereas Zn and Mn decrease. Again, because cations with similar physical properties and partitioning behaviour do not behave in the same fashion, this

suggests that addition or removal of these elements during alteration reflects variations in the composition of hydrothermal fluids with which they reequilibrate.

Gallium, Ge, V and Mo do not change significantly during intermediate-argillic and propylitic alteration. Because the concentrations of these elements do not vary much in concentration in magnetite between the two alteration styles and do not change with decreasing Ti content, this could indicate that these elements can see through alteration, offering the best chance to interpret conditions pertaining to the magmatic environment in which the titanomagnetite crystallised, prior to hydrothermal alteration. However, if this is the case, it does not seem that the resistance of these elements to having their chemistry modified is controlled by diffusion in magnetite, since these elements cover a range of diffusivities (Figure 3-12).

In summary, this study shows that during hydrothermal alteration, there are progressive changes in most elements which act to modify the original composition of the titanomagnetite from that which crystallised in the magmatic environment. Igneous titanomagnetite from hydrothermally-altered rocks has its chemistry overprinted, forming a hybrid composition between the original igneous composition and hydrothermal magnetite. The speed of diffusion (as inferred from magmatic studies) does not ostensibly limit the ease with which different elements have their chemistry modified, since Cr, one of the slowest diffusing species, exhibits large changes in its concentration with progressive hydrothermal alteration. Therefore, if we are to use igneous magnetite as a petrogenetic indicator to interpret conditions of the magmatic environment forming porphyry copper systems, it is important to work with unaltered samples, which have not undergone alteration.

6.4.7 Using Igneous Magnetite as a Petrogenetic Indicator in Unaltered Volcanic Rocks

The principal conclusion here is that if we are to use igneous magnetite as a petrogenetic indicator to identify conditions pertaining to the magmatic environment, unaltered samples must be targeted. Moreover, volcanic rocks more frequently contain titanomagnetite devoid of exsolution because they have cooled rapidly, not allowing oxy-exsolution to form at higher temperatures (> 600°C). Unfortunately, there are very few unaltered volcanic samples in the sample set studied here. Samples OR8(7)-MICH, OR.835-DIZ, OR.1766-LEP and OR.18(2)-VK are considered the least altered volcanic samples containing igneous magnetite.

OR8(7)-MICH, a fresh unaltered andesite associated with the Michiquillay porphyry Cu-Mo-Au deposit, Peru, contains subhedral, poikilitic magnetite intergrown with clean ilmenite (Figure 6-44A). Titanomagnetite in this sample commonly contains inclusions of apatite and also

chalcopyrite, suggestive of saturation of magmatic sulphide (Figure 6-2B). Sample OR.835-DIZ, from the Dizon Cu-Au deposit, Phillipines, is a contact between two porphyritic andesites, one slightly more mafic than the other. Although the sample is relatively unaltered, it does have a very weak propylitic alteration to a slight green colour. This sample hosts subhedral, clean titanomagnetite, commonly intergrown with ilmenite with a striped lamellae pattern (Figure 6-44C). OR.1766-LEP, an unaltered porphyritic dacite, associated with the Far-South East/Lepanto porphyry and high sulphidation Cu-Au system, contains abundant subhedral, poikilitic, clean titanomagnetite grains with abundant apatite inclusions (Figure 6-44B). Titanomagnetite is also intergrown with clean ilmenite. Lastly, OR.18(2)-VK is an unaltered late-stage andesite with large (up to 5 mm) amphibole phenocrysts and slightly poikilitic, but generally clean, titanomagnetite phenocrysts. This sample contains no ilmenite and appears to be the most mafic rock of this selection of least altered volcanic samples containing igneous magnetite.

6.4.7.1 "Two-oxide" oxybarometry

The "two-oxide method" for oxybarometric investigations, originally proposed by Buddington and Lindsley (1964), is based on equilibrium constants for the mineral redox reactions between components of solid solutions that include ferrous and ferric iron. The method remains one of the most common approaches for estimation of fO_2 in igneous rocks. Calculation of the fO_2 requires a simultaneous estimate of the temperature. The "two-oxide method" uses experimental data for equilibria between magnetite-ulvospinel and hematite-ilmenite solid solutions. Assuming that the compositions of coexisting ilmenite-hematite and magnetite-ulvospinel solid solutions are known, the reaction:

$$FeTiO_3\ (ilm) + Fe_3O_4\ (mt) = Fe_2O_3\ (hem) + Fe_2TiO_4\ (ulv)$$

can be used to estimate the temperature. A redox reaction, such as:

$$4Fe_3O_4\ (mt) + O_2 = 6Fe_2O_3\ (hem)$$

may then be used as an oxygen barometer. Several revisions have since applied more elaborate thermodynamic models to refine the Fe-Ti oxide geothermometer and oxygen barometer.

Experimental studies have shown that Fe-Ti oxides re-equilibrate quickly in response to changes in the temperature and/or fO_2 (e.g. Frost et al., 1988). In order to minimise error, it is best to analyse adjacent Fe-Ti oxides which share a common boundary, thereby ensuring equilibrium crystallisation conditions are more likely and re-equilibration effects are minimised (Blundy et al., 2006). Furthermore, the ease of re-equilibration during slow cooling of intrusive rocks means

that Fe-Ti oxides are generally not useful as an oxybarometer for plutonic assemblages. Thus, two-oxide geothermobarometry is best applied when studying volcanic or hypabyssal rocks.

Geothermometry and oxybarometry were performed using coexisting titanomagnetite-ilmenite pairs in these three unaltered volcanic samples. ILMAT, an excel worksheet created by Lepage (2003) was used for the calcuations. This takes account of various models for geothermobarometry and calculates an average based on all methods (e.g. Anderson and Lindsley, 1985; Stormer, 1983; Spencer and Lindsley, 1981). The composition of magnetite-ilmenite pairs were determined using SEM-EDS and used to approximate the temperature and fO_2 at which the Fe-Ti oxides co-crystallised in OR8(7)-MICH, OR.835-DIZ and OR.1766-LEP (Table 6-10).

Table 6-10: Temperature and log fO_2 calculated from coexisting ilmenite-magnetite pairs in three relatively unaltered volcanic samples.

Sample	Ilm-Mgt pairs	T (°C)	log fO_2	ΔFMQ[a]	ΔNNO[b]
OR.8(7)-MICH	3	875 ± 6	-11.47 ± 0.16	1.69 ± 0.24	0.95 ± 0.27
OR.835-DIZ	2	871 ± 23	-10.64 ± 0.27	2.59 ± 0.71	1.86 ± 0.7
OR.1766-LEP	1	954	-9.38	2.39	1.67

[a]log fO_2 relative to FMQ buffer calculated using Hemingway (1990). [b]log fO_2 relative to NNO buffer calculated using O'Neill & Pownceby (1993).

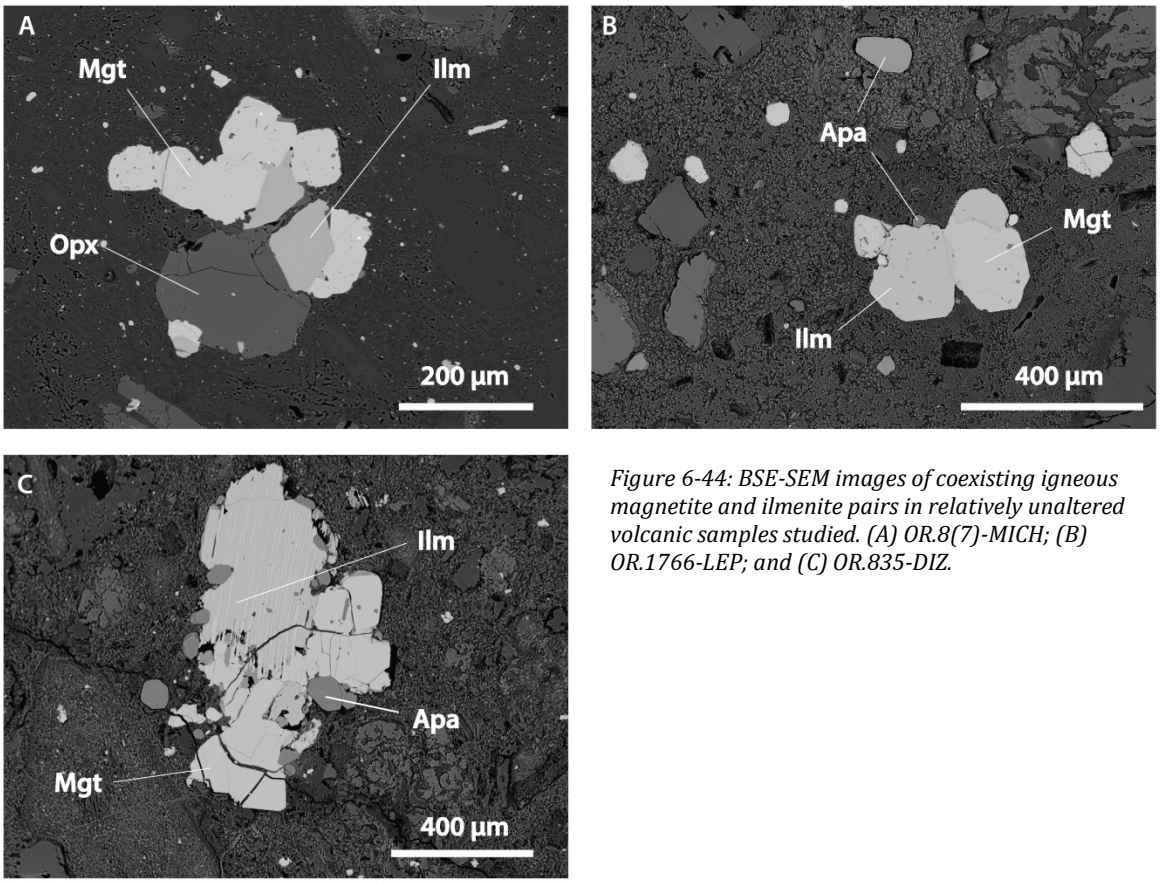


Figure 6-44: BSE-SEM images of coexisting igneous magnetite and ilmenite pairs in relatively unaltered volcanic samples studied. (A) OR.8(7)-MICH; (B) OR.1766-LEP; and (C) OR.835-DIZ.

The T-fO_2 results suggest that porphyry Cu-Au forming magmas are more oxidised than those forming Cu-Mo-Au deposits. This is consistent with previous work which suggested that magmas associated with porphyry Cu-Au deposits are oxidised relative to those forming Cu-Mo systems (Seedorff et al., 2005). In samples OR.8(7)-MICH and OR.1766-LEP, ilmenite and titanomagnetite crystals are subhedral and appear to have co-crystallised in the magma. In OR.835-DIZ, however, ilmenite forms over large areas intergrown with titanomagnetite, but is intermixed with fine lamellae of titanomagnetite. It is possible that the ilmenite in OR.835-DIZ is not magmatic, but in fact formed during subsolidus cooling. Thus, the T-fO_2 calculated for OR.835-DIZ may not represent equilibrium magmatic conditions.

6.4.7.2 Relative redox ratios

Relative redox ratios, using just the spinel composition alone, have been proposed as a means to estimate fO_2 in natural systems (e.g. Wijbrans et al., 2015). In section 2.4.4.2, V/Ga, Mo/Ga, Nb/Ga and Ta/Ga were suggested as possible relative redox ratios, where lower values correspond to higher fO_2. In the four samples investigated, the same relative variations are observed for most of the ratios (Figure 6-45). V/Ga, Mo/Ga, Nb/Ga and Ta/Ga are lowest in OR.1766-LEP, suggesting that this sample formed in the most oxidised system. However, these ratios are higher (but similar) in OR.8(7)-MICH and OR.835-DIZ, suggesting these samples formed under more reducing conditions. This is supported by the two-oxide geothermobarometry calculations for OR.8(7)-MICH, but not for OR.835-DIZ, although as previously noted, the two-oxide geothermobarometry in OR.835-DIZ may be inaccurate. OR.18(2)-VK has consistently low values for these ratios suggesting it is relatively oxidised. This could also explain the lack of ilmenite in this sample, since ilmenite crystallises under more reducing conditions than magnetite.

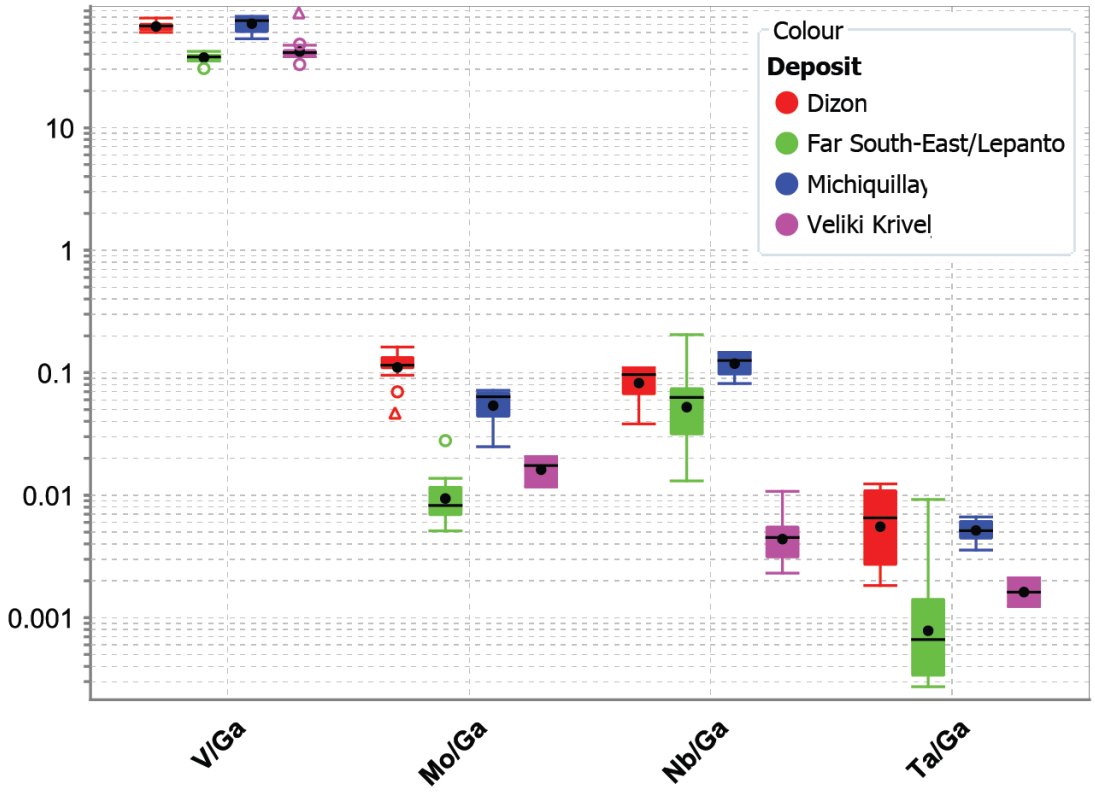


Figure 6-45: Box and whisker plots of relative redox ratios: V/Ga, Mo/Ga, Nb/Ga and Ta/Ga, for titanomagnetite from OR.1766-LEP (Far South-East/Lepanto), OR.8(7)-MICH (Michiquillay), OR.835-DIZ (Dizon) and OR.18(2)-VK (Veliki Krivelj).

6.4.7.3 Minor and trace element variations

Nickel and Cr contents of titanomagnetite are significantly lower in the dacitic sample (OR.1766-LEP) than the andesitic samples (OR.8(7)-MICH, OR.835-DIZ and OR.18(2)-VK (Figure 6-46). Both Ni and Cr are compatible and therefore decrease in concentration during fractionation of a magma. Thus, Ni and Cr contents in titanomagnetite may track changes in the concentrations of these elements during arc magma differentiation. Gallium and Sn have been suggested to be sensitive to temperature based on observations in natural samples, with higher contents in magnetite at higher temperature (Nadoll et al., 2014). Experimental studies have also shown Al to be increasingly incorporated into magnetite at higher temperatures (section 2.3.2). The contents of Al and Ga are a little higher in OR.1766-LEP (Figure 6-46), which appears to have formed at a temperature approximately 70°C higher than OR.8(7)-MICH and OR.835-DIZ based on the geothermometry calculations. Tin, however, is lower in OR.1766-LEP, which suggests that the concentration of Sn in magnetite may not be temperature sensitive in magmatic magnetite, despite being apparently sensitive to temperature in hydrothermal magnetite.

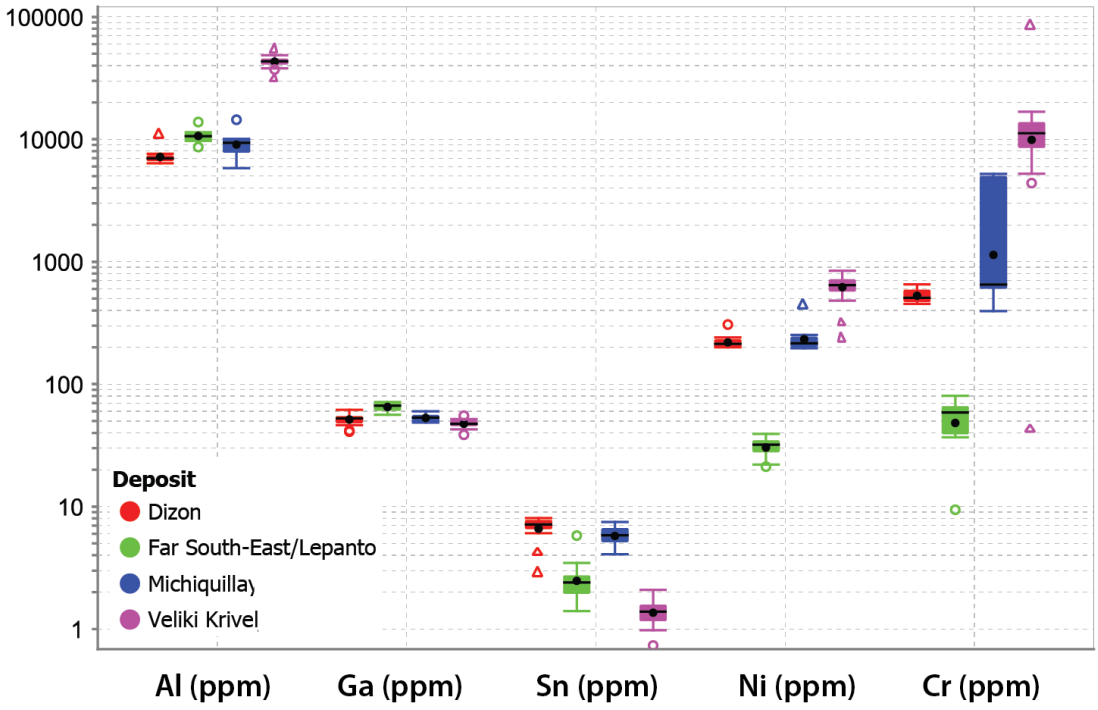


Figure 6-46:, Box and whisker plot for Al, Ga, Sn, Ni and Cr contents of igneous magnetite from OR.1766-LEP (Far South-East/Lepanto), OR.8(7)-MICH (Michiquillay), OR.835-DIZ (Dizon) and OR.18(2)-VK (Veliki Krivelj).

6.4.7.4 Estimating Cu contents of silicate melts using igneous magnetite

The fO_2 is the physical parameter which drives most change on the partitioning of Cu in igneous magnetite (section 4.4.1). Assuming the fO_2 is known, the Cu contents of the melt in equilibrium with titanomagnetite can be estimated. The fO_2 values approximated using "two-oxide" oxybarometry are considered to be reliable for OR.1766-LEP and OR.8(7)-MICH (Table 6-10). Given the relative redox ratios for OR.18(2)-VK and OR.835-DIZ are most similar to OR.1766-LEP and OR.8(7)-MICH respectively (Figure 6-45), similar fO_2 values can be assumed for these samples. Partition coefficients for Cu derived from experiments can then be used to approximate melt Cu contents. D(Cu) was assumed to vary linearly between fO_2 values for which D(Cu) is reported so D(Cu) values at the relevant fO_2 for the samples could be approximated. Separate estimates of melt Cu contents were calculated using partition coefficients reported for 1-atm and piston cylinder experiments using And-190 + Fe + trace starting material (Table 6-11). Melt Cu contents generate similar results irrespective of using partition coefficients from each experimental set. The Cu contents estimates are within a range reasonable for andesitic melts (e.g. Richards, 2015), however, there is no clear correlation between Cu content of melt and size or grade of porphyry copper deposit. Assuming that these volcanics are the volcanic equivalents of the intrusives which form the associated porphyry copper system, this suggests that melt Cu

contents are not imperative for the the formation of porphyry copper deposits, as has been suggested by previous work (e.g. Cline and Bodnar, 1991). It could be that the low Cu contents approximated for melts at Veliki Krivelj and Far South-East could reflect sequestration of Cu in a magmatic sulphide phase, which has been considered to promote mineralisation by some authors (e.g. Halter et al., 2002; Keith et al., 1997; Wilkinson, 2013). However, Cu-bearing sulphide inclusions were present in titanomagnetite from OR.8(7)-MICH indicating that there was a magmatic sulphide phase present, although the estimate of Cu content of the melt is this highest of those studied. Instead, it has been suggested that large volumes of sulphide (> 1 %) would be necessary to significantly scavenge a large proportion of dissolved Cu in the melt (Richards, 2009), which may not be the case in this sample.

Table 6-11: Estimate of Cu contents of silicate melts in equilibrium with titanomagnetite in a selection of unaltered volcanic rocks associated with porphyry copper deposits

Sample	Cu in magnetite (ppm)	ΔFMQ estimate	D(Cu) estimate (1-atm)[c]	D(Cu) estimate (PC)[d]	Cu (melt) estimate (1-atm)	Cu (melt) estimate (PC)	Deposit Cu Grade	Deposit Class
OR.835-DIZ	45.3±20.3	1.7[b]	0.41	0.40	110.5	113.7	0.3-0.5%	PoCuAu-large
OR.18(2)-VK	21.9±7.6	2.4[b]	0.83	0.45	26.4	48.9	0.5-1%	PoCuAu-giant
OR.1766-LEP	12.1±3.3	2.4[a]	0.83	0.45	14.6	27.0	0.3-0.5%	PoCuAu-large
OR.8(7)-MICH	48.5±13.5	1.7[a]	0.41	0.40	118.3	121.7	0.5-1%	PoCuAu-large

[a]fO_2 approximated using two-oxide oxybarometry
[b]fO_2 approximated by comparing relative redox ratios
[c]D(Cu) estimated using And-190 + Fe + trace starting material at T = 1095°C (RSM-19 and RSM-15) and projecting linearly between fO_2 values where D(Cu) reported
[d]D(Cu) estimated using And-190 + Fe + trace starting material at T = 920°C/P = 12 kbar (RSM-PC-47 and RSM-PC-37) and projecting linearly between fO_2 values where D(Cu) reported

7 Discussion

7.1 Using magnetite as a petrogenetic indicator

Magnetite shows significant potential as a petrogenetic indicator. In particular, the use of LA-ICP-MS allows determination of a plethora of elements that can be employed for petrogenetic studies. For example, in the natural magnetite analysed here, in addition to Fe, 28 elements were detected in >50% of LA-ICP-MS analyses of igneous magnetite and 17 elements were detected in >50% of LA-ICP-MS analyses of hydrothermal magnetite. Experimental work indicates that the composition of magnetite is sensitive to a number of physico-chemical parameters under which it formed, particularly fO_2. Despite the viability of magnetite as a petrogenetic tool, studies on natural magnetite indicate that the chemistry of magnetite is easily altered, particularly in comparison to silicate phases. Moreover, diffusion is fast in magnetite relative to other common silicate phases. This means that the chemistry of magnetite is relatively easily reset, for example during subsolidus re-equilibration or interaction with hydrothermal fluids. This can present some difficulties when trying to unravel the conditions under which certain magnetites crystallised.

In this section, the method for discriminating igneous and hydrothermal magnetite is examined. Then, the application of igneous magnetite as a petrogenetic indicator is discussed, which includes a synthesis of the results of experimental work investigating magnetite-melt partitioning (Chapters 2, 3 and 4). A new oxybarometer based on magnetite-melt partitioning relationships in terms of thermodynamic equilibria is also presented. Finally, the use of hydrothermal magnetite as a petrogenetic indicator is discussed. This includes an assessment of possible controls on the composition of hydrothermal magnetite, as well as the use of diffusion gradients in hydrothermal magnetite to interpret the timescales of ore-forming processes in porphyry copper systems. Section 7.2 recommends how the chemistry of magnetite, both igneous and hydrothermal, could be used as an exploration tool for porphyry copper deposits. A comparison of magnetite with other possible indicator minerals for porphyry copper systems is also presented.

7.1.1 Discriminating igneous and hydrothermal magnetite

A particularly important consideration when using magnetite as a petrogenetic tool is the distinction between igneous and hydrothermal magnetite (section 6.4.1). These two varieties form in contrasting environments so it is important that these two forms are accurately discriminated. Hydrothermal magnetite is most easily distinguished from magmatic magnetite based on Ti content (section 6.4.1). Hydrothermal magnetite typically has Ti < 0.5 wt. %, whereas igneous magnetite has Ti > 1.5 wt. %. A complicating factor is that hydrothermal magnetite can

also be formed through replacement of precursor igneous magnetite (Figure 6-4). During this process, the Ti content is reduced in igneous magnetite and its chemistry progressively changes towards a composition more diagnostic of the hydrothermal environment. The effect on Ti is probably due to re-equilibration with hydrothermal fluids with relatively low content of Ti in comparison to a silicate melt, owing to the limited solubility of Ti in hydrothermal fluids (Van Baalen, 1993; Hu et al., 2015).

Whilst studying the chemistry of natural magnetite, a 1 wt. % Ti cut-off was initially used to broadly segregate igneous and hydrothermal magnetite populations using chemistry alone. The accuracy in using this cut-off was investigated using normal distribution probability plots of Ti content in magnetite from sub-sets of samples from individual localities (Figure 6-17). Where a magnetite population straggled across the 1 wt. % cut-off, back-scattered electron SEM images of the grains were consulted to examine their texture. Some magnetite analyses with Ti > 1 wt. % exhibit textures characteristic of low-Ti hydrothermal magnetite, or evidence for transitional replacement of a precursor igneous phase. Thus, these were reclassified as hydrothermal magnetite. Nevertheless, only 22 analyses with Ti > 1 wt. %, out of 876 successful LA-ICP-MS analyses of hydrothermal magnetite, were reclassified as hydrothermal magnetite. Although studying normal distribution plots of Ti on a case by case basis and consulting petrographic observations is suggested as the optimal method to identify hydrothermal magnetite, given that a 1 wt. % cut-off is reliable in 97.5% of instances, this cut-off could offer a simple, yet accurate, means to discriminate the two varieties of magnetite.

7.1.2 Igneous magnetite

The evidence presented in Chapter 6 shows that the composition of igneous magnetite, at least that sampled from the proximal parts of porphyry environments, is frequently altered by sub-solidus exsolution and/or later hydrothermal fluids. Previous work has employed a large spot size when analysing with LA-ICP-MS, incorporating both exsolution lamellae and residual magnetite in order to best approximate the original composition of the magnetite (e.g. Dare et al., 2014; Pisiak et al., 2017). Ilmenite is the most common phase formed through oxy-exsolution, typically forming a trellis texture. However, in magnetite with significant ilmenite exsolution, the chemistry is dominated by the composition of the ilmenite. This is evinced by linear trends towards the composition of ilmenite on bivariate plots of elements with a large concentration difference between magnetite and ilmenite (Figure 6-8). It is possible that the oxy-exsolution process does not occur in a closed system and elements which are less compatible in ilmenite are expelled in the process. As a result, incorporating exsolution into the analysis may not accurately represent the original composition of magnetite prior to subsolidus exsolution. However, it was

not possible to verify this, given that the original composition of magnetite prior to exsolution was not known.

Consequently, when using igneous magnetite as a petrogenetic indicator, it is important to focus on samples which are not hydrothermally altered and where magnetite grains do not display exsolution features. Oxy-exsolution typically forms during sub-solidus cooling at temperatures greater than 600°C, so is more common in plutonic than in volcanic rocks. Magnetite included in other minerals more resilient to alteration, such as quartz and zircon, could be protected from alteration and more suitable for petrogenetic purposes (Figure 7-3 and 7-10). Thus, it is suggested that unaltered volcanic rocks are targeted preferentially where igneous magnetite is to be used as a petrogenetic indicator.

7.1.2.1 Controls on the composition of igneous magnetite

i Controls on magnetite-melt partitioning in igneous magnetite

In chapters 2, 3 and 4, the influence of a range of parameters on element partitioning between magnetite and silicate melts was investigated, including fO_2, T, bulk composition, pressure and water content. Oxygen fugacity drives most change in titanomagnetite-melt partitioning in intermediate-silicic bulk compositions, with strong decreases in D values for 4+ and higher valence cations with increasing fO_2. There are also strong increases in the magnetite-melt partitioning of divalent cations and Cu with increasing fO_2. This contrasts with titanomagnetite-melt partitioning in mafic bulk compositions. There is only a minor variation in magnetite-melt partitioning with T. Nevertheless, the T range studied was relatively limited by the constraint of keeping magnetite on the liquidus whilst also maintaining large melt fractions. Thus, the T range may not have been substantial enough to evaluate the effect of T on magnetite-melt partitioning. The magnetite-melt partitioning of some elements is depressed at elevated pressure and lower temperature, which could be related to $r_i - r_0$ (section 4.4.2). However, this factor is less important in controlling magnetite-melt partitioning than fO_2. The relationship between magnetite-melt partitioning and fO_2 can be explained in terms of thermodynamic equilibria associated with a change in aFe_3O_4(spinel), $XFe^{2+}O$(melt), $XFe^{3+}O_{1.5}$(melt) and fO_2 (e.g. section 2.4.2.6). Some elements are strongly controlled by an additional factor, possibly related to changing activity coefficients either in spinel or melt with changes in the bulk composition of the system. This effect is particularly strong for Al and Ga.

Table 7-1 summarises the principal controls on magnetite-melt partitioning for all elements studied for magnetite-rich spinel in equilibrium with an andesitic-dacitic melt. This is primarily based on experiments conducted using natural andesitic-dacitic bulk compositions and

comparisons with experimental data from the literature (e.g. Toplis and Corgne, 2002; Nielsen et al., 1994; Nielsen and Beard, 2000). Although the partitioning behaviour was also investigated between pure magnetite and a synthetic mafic Ca-Fe-Si bulk composition, this is considered less representative of natural conditions – mafic lithologies usually crystallise Ti-rich spinel at low fO_2. Thus, for elements where partitioning behaviour could only be deduced from these experiments, the 'expected' controls are reported based on couplings in partitioning behaviour with other elements and the physical properties of the cation. Temperature does not exert a strong control on magnetite-melt partitioning over the experimental conditions studied. Notably, there is not a significant variation in magnetite-melt partitioning (> 2σ) with temperature for any elements studied in piston-cylinder experiments, although some elements show minor variation with temperature in experiments at 1-atm. It is considered that temperature control is more accurate in 1-atm experiments, thus variation in D values with temperature is only based on experiments conducted at 1-atm. The range of D values observed in each set of experiments indicates which elements are compatible (D > 1) or incompatible (D < 1) in magnetite (Figure 7-1). This is useful since it demonstrates which elements will increase or decrease as a result of magnetite fractionation during the evolution of arc magmas.

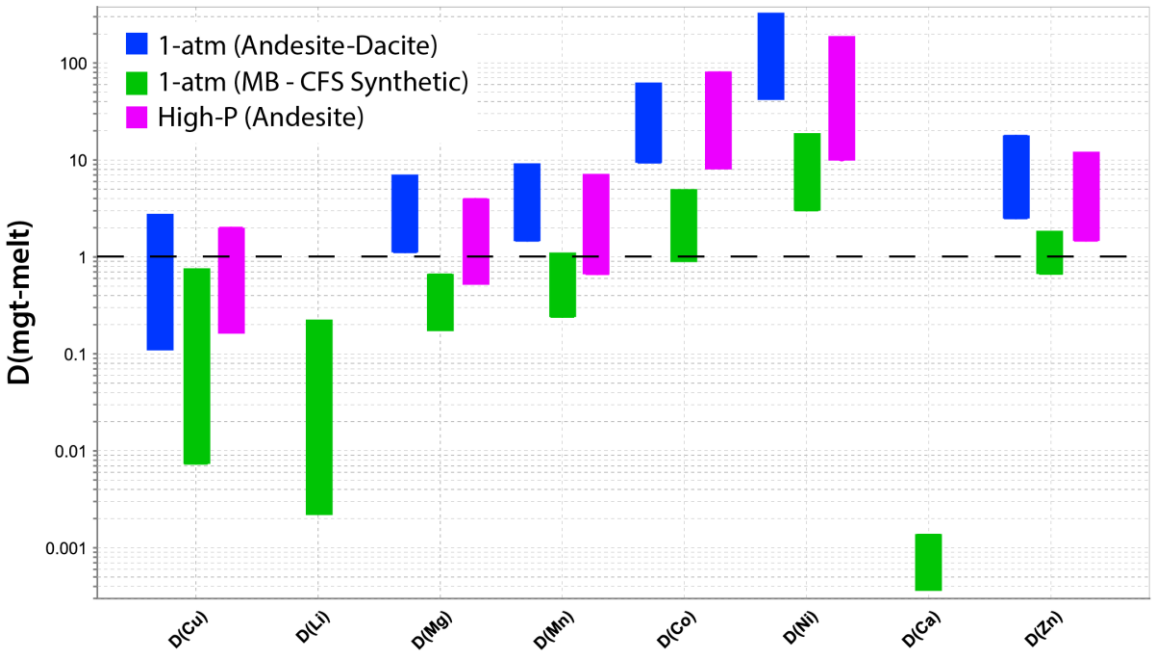
Table 7-1: Controls of magnetite-melt partitioning in system crystallising magnetite-rich spinel from an andesitic-dacitic melt as determined from experiments in chapters 2, 3 and 4 conducted at T = 920 and 1150°C, P = 1-atm to 12 kbar.

Element	**D(mgt-melt)[a]**	***Increasing fO2*[b]**	**Increasing T[c]**	**Increasing P[d]**	**Bulk composition[e]**
Li	0.0023-0.22 (MB)	Unknown (Expected D(Li) ⬆ like D(Cu)	Unknown	Unknown (Expected insensitive like D(Cu)	Unknown
Mg	0.66-4.77 (PC) 0.20-0.66 (MB)	D(Mg) ⬆	D(Mg) slight ⬇	D(Mg) slight ⬇	Moderately (Not fO_2 sensitive in natural mafic bulk compositions)
Al	0.15-1.10 (PC) 0.11-1.05 (MB)	Insensitive	D(Al) slight ⬆	Insensitive	Strongly (D(Al) ⬆ with increasing Al-content of bulk composition)
Ca	0.00039-0.0014 (MB)	Unknown (Expected D(Ca) ⬆ like D(Mg)	Unknown	Unknown (Expected ⬇ - large $r_i - r_0$)	Unknown
Sc	0.43-0.83 (PC) 0.12-0.75 (MB) 0.97-1.95 (1-atm)	Insensitive	D(Sc) slight ⬇	D(Sc) slight ⬇	Insensitive
Ti	1.84-20.71 (PC) 0.22-4.97 (MB)	D(Ti) ⬇	Insensitive	Insensitive	Insensitive
V	1.04-97.19 (PC) 0.11-17.51 (MB) 0.44-19.40 (1-atm)	D(V) ⬇	Insensitive	D(V) ⬆	Insensitive
Cr	-	Unknown (Expected insensitive like D(Sc) or D(Al))	Unknown	Unknown	Unknown
Element	**D(mgt-melt)[a]**	**Increasing fO_2 [b]**	**Increasing T[c]**	**Increasing P[d]**	**Bulk composition[e]**

Mn	0.62-6.50 (PC) 0.24-1.08 (MB)	D(Mn) ⬆	D(Mn) slight ⬇	D(Mn) slight ⬇	Moderately (Not fO_2 sensitive in natural mafic bulk compositions)
Co	8.97-80.2 (PC) 0.94-4.50 (MB) 9.36-58.7 (1-atm)	D(Co) ⬆	D(Co) slight ⬇	Insensitive	Moderately (Not fO_2 sensitive in natural mafic bulk compositions)
Ni	10.75-183.04 (PC) 3.01-18.40 (MB) 43.9-317 (1-atm)	D(Ni) ⬆	D(Ni) slight ⬇	Insensitive	Moderately (Not fO_2 sensitive in natural mafic bulk compositions)
Cu	0.17-2.00 (PC) 0.0073-0.68 (MB) 0.122-2.68 (1-atm)	D(Cu) ⬆	D(Cu) slight ⬇	Insensitive	Moderately (Not fO_2 sensitive in natural mafic bulk compositions)
Zn	1.46-11.43 (PC) 0.67-1.77 (MB) 2.50-17.80 (1-atm)	D(Zn) ⬆	D(Zn) slight ⬇	D(Zn) slight ⬇	Moderately (Not fO_2 sensitive in natural mafic bulk compositions)
Ga	0.16-3.46 (PC) 0.32-2.79 (MB) 0.511-2.08 (1-atm)	Insensitive	Insensitive	Insensitive	Moderately (D(Ga) ⬆ with increasing Al-content of bulk composition)
Ge	0.12-3.59 (PC)	D(Ge) ⬇	Unknown	Unknown (Expected insensitive - small $r_i - r_0$)	Unknown
Y	0.00051-0.0026 (MB)	Unknown (Expected insensitive like D(Lu))	Unknown	Unknown	Unknown
Zr	0.0063-0.30 (MB) 0.012-0.096 (PC) 0.030-0.128 (1-atm)	D(Zr) ⬇	Insensitive	D(Zr) ⬇	Moderately (D(Zr) ⬇ with increasing Al-content of bulk composition?)
Nb	0.0023-0.52 (MB) 0.012-0.40 (PC) 0.026-0.21 (1-atm)	D(Nb) ⬇	Insensitive	D(Nb) ⬇	Moderately (D(Nb) ⬇ with increasing Al-content of bulk composition?)
Mo	0.20-0.86 (PC) 0.00052-2.77 (MB) 0.011-0.10 (1-atm)	D(Mo) ⬇	D(Mo) slight ⬇	Unknown (Expected insensitive - small $r_i - r_0$)	Unknown
Cd	0.10-0.14 (PC)	Unknown (Expected D(Cd) ⬆)	Unknown	Unknown	Unknown
In	1.15-3.19 (PC) 0.56-1.80 (MB) 0.60-5.2 (1-atm)	Insensitive	Unknown	Unknown	Unknown
Sn	0.92-2.54 (PC)	Unknown (no change between RRO and MH)	Unknown	Unknown	Unknown
Lu	0.0010-0.0048 (PC) 0.0029-0.0097 (MB)	Insensitive	Unknown	Unknown (Expected ⬇ - large $r_i - r_0$)	Unknown
Hf	0.012-0.15 (PC) 0.0073-0.50 (MB) 0.051-0.17 (1-atm)	D(Hf) ⬇	Insensitive	D(Hf) ⬇	Moderately (D(Hf) ⬇ with increasing Al-content of bulk composition?)
Element	**D(mgt-melt)[a]**	**Increasing fO_2 [b]**	**Increasing T[c]**	**Increasing P[d]**	**Bulk composition[e]**

Ta	0.011-0.45 (PC) 0.0024-0.33 (MB) 0.046-0.28 (1-atm)	D(Ta) ⬇	Insensitive	D(Ta) ⬇	Moderately (D(Ta) ⬇ with increasing Al-content of bulk composition?)
W	0.00036-0.024 (MB)	Unknown (Expected D(W) ⬇ like D(Ti))	Unknown	Unknown - Expected insensitive (small $r_i - r_0$)	Unknown
Th	0.000095-0.00024 (MB)	Unknown (Expected D(Th) ⬇ like D(Ti))	Unknown	Unknown - Expected ⬇ (large $r_i - r_0$)	Unknown
U	0.000090-0.0067 (MB)	Unknown (Expected D(U) ⬇ like D(Ti))	Unknown	Unknown - Expected ⬇ (large $r_i - r_0$)	Unknown

[a]Range of D values reported in 1-atm andesitic-dacitic experiments (1-atm), magnetite-bucket experiments (MB) and piston cylinder (PC) experiments
[b]fO_2 control determined from experiments investigating titanomagnetite-melt partitioning in an intermediate-dacitic bulk composition. Because MB experiments are not representative of natural silicate melts, expected fO_2 is provided based on results of these experiments
[c]No elements showed strong T sensitivity over the experimental conditions investigated (920-980°C for PC experiments, 1070-1120°C for 1-atm experiments). Only some elements showed significant variation with temperature in 1-atm experiments in andesitic-dacitic bulk system, so only results from these experiments are expressed here
[d]D values for some elements are suppressed at elevated temperature and lower temperature. This could be related to $r_i - r_0$. Where effect of pressure could not be measured, expected effect of increasing pressure on D value is provided.
[e]Effect of bulk composition deduced by comparison with literature data for spinel-melt partitioning in different bulk systems.



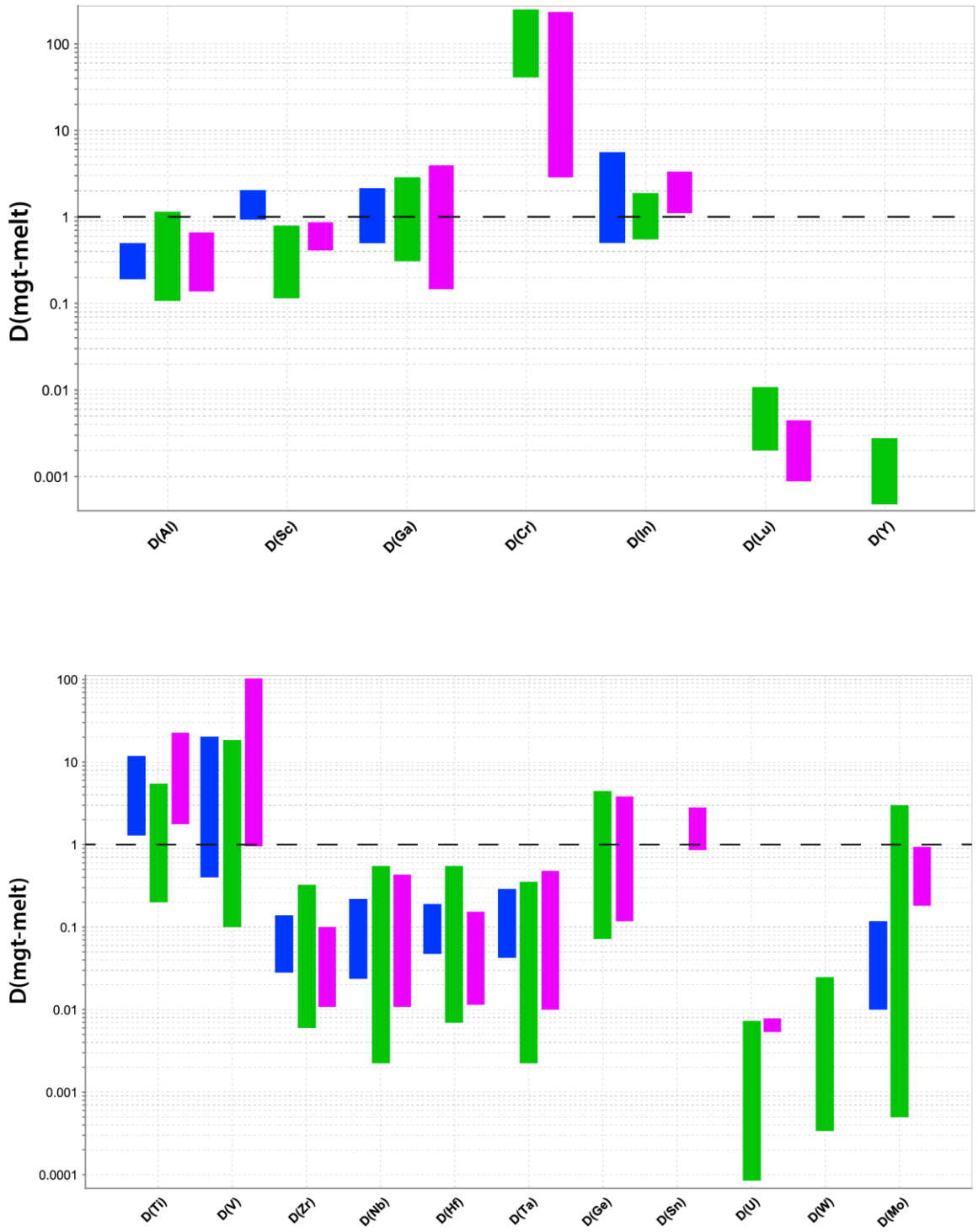


Figure 7-1: Compilation of magnetite-melt partition coefficients (D(mgt-melt) from experiments investigating titanomagnetite-melt partitioning in an andesitic-dacitic bulk systemat 1-atm (Chapter 2- blue); magnetite-melt partitioning in a synthetic Ca-Fe-Si bulk system at 1-atm (Chapter 3 - green); and titanomagnetite-melt partitioning in an andesitic bulk system at 6-12 kbar (Chapter 4 – pink). Dashed line is D(mgt-melt) = 1.

ii Controls on element availability in arc magma systems

The mineral assemblage coexisting with magnetite will variably fractionate different elements from the melt, thus dictating their availability to be incorporated into magnetite. Furthermore, the concentrations of various elements in a magma will increase or decrease during its evolution depending on their bulk partition coefficient. For example, elements with a bulk partition coefficient greater than 1 will be sequestered from the residual melt, whereas those which are incompatible (D<1) will be enriched. Elements with higher partition coefficients in magnetite would be expected to mimic changes in their melt concentration most reliably.

Evidence for a bulk composition control on the chemistry of igneous magnetite was apparent in the study by Fry (2017) (Appendix 4). With increasing whole-rock silica content there is a decrease in Ni, V, and Co in magnetite. This likely reflects a decrease in the concentration of these elements in the residual melt with magmatic evolution. In fact, it is probable that this decrease is chiefly induced by magnetite fractionation given the high compatibility of these elements in magnetite (Figure 7-1) and the bulk compositional range over which this effect was observed (50-72% SiO_2). In more mafic compositions, prior to magnetite fractionation, other phases, such as olivine and pyroxene will control the concentrations of these elements in the residual melt (Mallman and O'Neill, 2009).

7.1.2.1 Application of igneous magnetite as a petrogenetic indicator in arc magmas

Once igneous magnetite devoid of alteration or exsolution has been identified and analysed, the experimentally-determined partition coefficients reported here (Table 7-1) can be used to predict the trace element evolution of silicate magmas fractionating magnetite. Assuming the physical magmatic conditions (e.g. T, P and fO_2) can be estimated, the partition coefficients can be used to approximate the trace element composition of the melt from the chemistry of magnetite. For magnetite-rich spinel in equilibrium with intermediate-silicic melts, given the relatively limited effect on partitioning by magma bulk composition, temperature, pressure and water content, it is really only the fO_2 that needs to be constrained reasonably accurately for such modelling to be viable. Experiments conducted here provide partition coefficients for a number of elements, such as Mo, U, W, Y, Lu and Li, which until now have not been investigated comprehensively. It is important, however, to be wary of elements which are highly incompatible in magnetite in comparison to possible inclusion phases in petrogenetic studies.

Magnetite-rich spinel typically appears as a late-stage crystallising end-member of the spinel solid solution series, which starts with Cr-spinel in primitive basaltic magmas, followed by Ti-rich

magnetite (generally Ti > 10 wt. %) in andesites, and later magnetite-rich spinel (generally Ti < 10 wt. %) in dacites (e.g. Richards et al., 2006; Tollan et al., 2012). Porphyry copper deposits form from a relatively limited range of intermediate-felsic bulk compositions (section 1.2.1), thus the magnetite formed is typically magnetite-rich, as observed in Chapter 6. Notwithstanding this, evidence for both of the latter two varieties of igneous magnetite is apparent in the data presented in Chapter 6, for example in Figure 6-8C, where two lineations towards the composition of ilmenite are apparent, one with Ti > 10 wt. % and the other with Ti > 1.5 wt. %. These two types of magnetite could be used to investigate magmatic controls on the formation of porphyry copper deposits at different stages in the evolution of arc magmas.

As observed in experimental work in Chapters 2 and 4, there is only a minor variation in partitioning between magnetite-rich spinel and andesitic-dacitic melts with T. Nevertheless, the T range studied was relatively limited by the constraint of keeping magnetite on the liquidus. In natural systems this constraint could also expected to apply, so that magnetite-rich spinel will only crystallise over a relatively narrow T range (e.g. 100°C). Thus, T is not likely to exert a strong control on the composition of igneous magnetite in natural arc magmatic systems.

Although magnetite-melt partitioning of most elements can be explained in terms of thermodynamic equilibria associated with a changing magnetite and melt composition, some elements are also controlled by an additional factor, apparently related to changes in bulk composition. This effect is particularly strong for Al and Ga. Thus, large variations in the chemistry of these elements could be used to infer changes in the bulk composition, induced for example by magma mixing. Bulk compositional controls on magnetite-melt partitioning were also observed in experiments by Simon et al. (2008), with a correlation between Ti-content of magnetite and the incorporation of Au and Cu in magnetite. Nevertheless, because porphyry copper deposits are associated with a relatively limited range of intermediate-felsic compositions, the magnetite formed is typically magnetite-rich, so is not likely to exercise a strong control on magnetite-melt partitioning.

The fO_2 is a particularly important variable in controlling the metal contents of arc magmas, because it affects the stability of sulphide phases, which act to sequester ore-metals from the melt (section 1.2.2). Notwithstanding this, the ideal fO_2 for magmas generating porphyry copper deposits is a matter of debate. Whereas some have inferred an oxidised magma is necessary to limit sequestration to magmatic sulphides (e.g. Mungall, 2002), others have suggested that the formation of a magmatic sulphide phase could act to form highly enriched regions of ore-metals, which if subsequently destroyed could release high concentrations of ore-metals and thereby

promote mineralisation (e.g Halter et al., 2005; Wilkinson, 2013). The onset of magnetite crystallisation has also been suggested to be a trigger for sulphide saturation because of its effect on the Fe^{3+}/Fe^{2+} ratio, and therefore oxidation state of the remaining melt (section 1.2.2.2; Jenner et al., 2010). Contrary to this, Fe^{3+}/Fe^{2+} ratios and ΔFMQ in arc magmas have been shown to increase with differentiation, suggesting oxidation occurs with progressive magnetite fractionation (Richards, 2006; 2013).

The fO_2 is the physical parameter which drives most variation in magnetite-melt partitioning in magnetite-rich spinel. Wijbrans et al. (2015) proposed that element ratios in spinel could be used to qualitatively constrain fO_2 variations. The ratio of a redox-sensitive element relative to an element with behaviour largely unaffected by changing parameters of the magmatic system and with a bulk partition coefficient close to 1 can be used. This normalises for the effects of non-redox related processes. Suggested redox sensitive elements include V, Mo, Nb or Ta. Based on experimental results presented here, Ga is a good choice for the denominator (section 2.4.4.2). Furthermore, Ga was found to be largely insensitive to changes in whole rock compositions by Fry (2017) (Appendix 4), indicating that its concentration in magnetite and in silicate melt does not change significantly during fractionation of arc magmas. Relative redox ratios, V/Ga, Nb/Ga, Ta/Ga and Mo/Ga for igneous magnetite were plotted against whole rock MgO using data from Fry (2017) to assess changes in the oxidation in arc magmas with differentiation (Figure 7-2). With differentiation (decreasing whole rock MgO), there is a weak trend of decreasing V/Ga, but an increase in Ta/Ga and Nb/Ga. There is no clear trend for Mo/Ga as a function of whole rock MgO. Assuming that these relative redox ratios are controlled by fO_2, the variation in V/Ga suggest an increase in fO_2 with differentiation, while Ta/Ga and Nb/Ga indicate a decrease in fO_2. In fact, it is probable that these ratios are not tracking fO_2, but relative changes in element availability in the melt. With progressive fractionation of magnetite, V, which is highly compatible in magnetite (Figure 7-1), is likely to decrease, whereas Nb and Ta, which are strongly incompatible (Figure 7-1), should increase in the melt. Thus, if these ratios are to be used to assess relative variations in fO_2, it is suggested that samples with similar bulk compositions be compared.

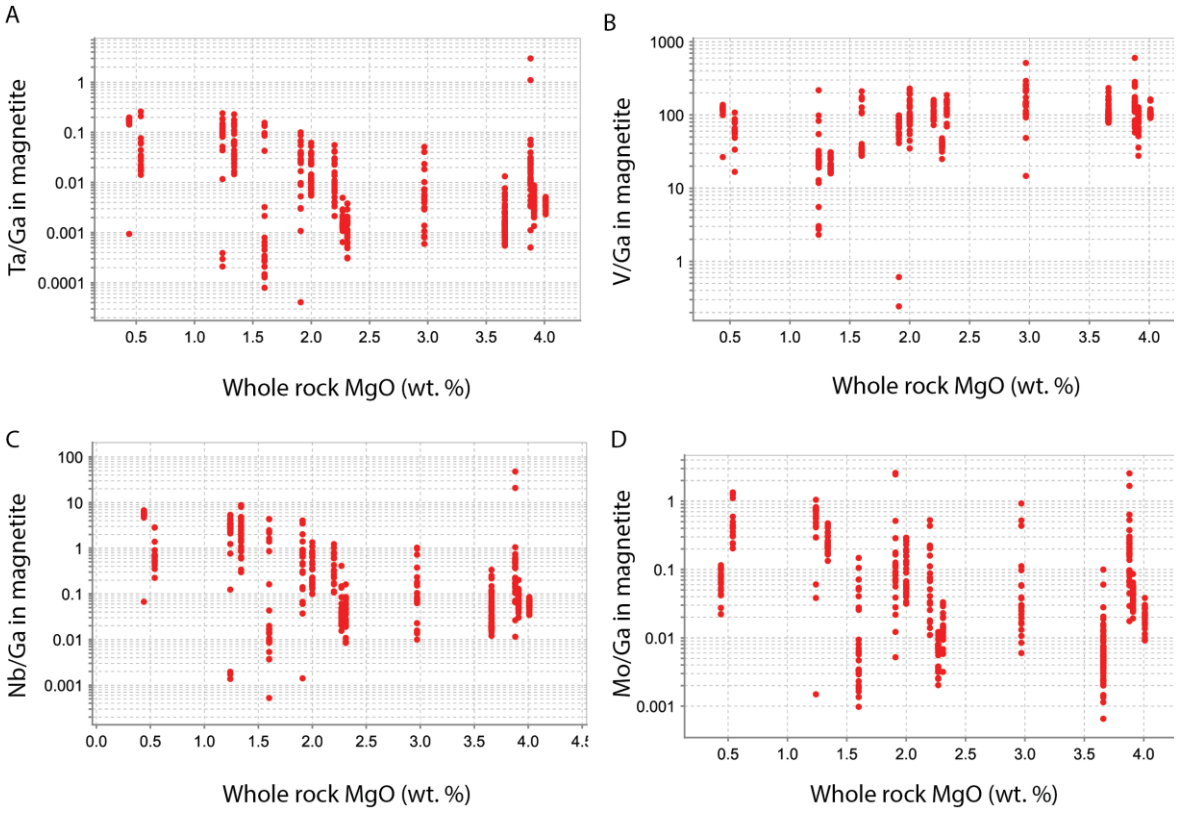


Figure 7-2: Relative redox ratios (A) Ta/Ga, (B) V/Ga, (C) Nb/Ga and (D) Mo/Ga in magnetite vs. whole rock MgO (wt. %) for igneous magnetite from volcanics in Central Chile (data from Fry, 2017).

i Chemistry of igneous magnetite from volcanics in Central Chile

The majority of the natural samples studied in this PhD were altered intrusive rocks. Consequently, few samples were suitable for the application of magnetite chemistry to the interpretation of the magmatic environment. However, Fry (2017) conducted a Master's project related to this PhD in which the trace element chemistry of igneous magnetite from a suite of relatively unaltered volcanics in Central Chile (the location of the El Teniente, Rio Blanco-Los Bronces and Los Pelambres giant deposits) was studied. These samples cover a wide age range (125 to 5 Ma) spanning the period prior to, during, and after mineralisation. The whole-rock chemistry of these samples has previously been documented in detail by Hollings et al. (2005) and their geochronology is relatively well understood. The aim of this project was to use magnetite as a petrogenetic indicator to trace the temporal evolution of the magmatic system.

Approaching the age range of mineralisation over the period 30-5 Ma, there is evidence for a decrease in the oxidation state of the magmas that infilled the pre-mineralisation volcanic basins, as evinced by the relative redox ratio V/Ga. It is possible that this could have been caused by magnetite crystallisation itself, as this process results in removal of Fe^{3+} from the residual melt

(Richards, 2015). Concomitantly, there is a decrease in the Pb, As and Sb concentrations in magnetite, inferred to reflect loss of highly fluid-mobile elements from the melt, due to an increasingly abundant magmatic volatile phase. There is also an increase in the contents of Co, Cu and Ni in magnetite in the period preceding mineralisation, followed by a decrease during the period of mineralisation. This is attributed to an increase in the concentration of these elements in the melt as a result of typical igneous fractionation processes during the build-up to mineralisation, with the drop related to the attainment of sulphide saturation. It is suggested that subsequent destruction of these highly enriched, sulphidic regions could release a high concentration of ore metals to form metal-rich fluids, thereby promoting mineralisation (e.g. Halter et al., 2002; Keith et al., 1997; Wilkinson, 2013)

Despite the interesting results of this study, some samples analysed contained igneous magnetite which is substantially altered, including the presence of strong trellis exsolution or titanite alteration. Thus, the chemistry of some grains may have been modified by metasomatic alteration. Furthermore, a number of samples contained hydrothermal magnetite, which indicates that sub-solidus overprinting has occurred, despite them appearing relatively unaltered in hand specimen. Moreover, partition coefficients for As and Sb could not be determined for magnetite in experiments in Chapter 4, despite high concentrations in the melt (> 500 ppm). This, suggests D(Sb) and D(As) are very low (i.e. D < 0.001). Since hydrothermal fluids can have substantially higher concentrations of As, Pb and Sb in comparison to silicate melts (Noll et al., 1996; Ulrich et al., 1999) the high concentrations of As and Sb in magnetite analysed by Fry (2017) could be a result of reequilibration of igneous magnetitite with hydrothermal fluids. It is suggested that before further interpretation of the data, the results should be filtered more stringently for alteration effects and contamination from mineral inclusions using the flow chart in section 5.2.4. If the same trends are still apparent then more reliable interpretations could be made from the results.

ii Development of a new oxybarometer based on magnetite-melt partitioning

As shown by experimental work, changing fO_2 drives most variation in magnetite-melt partitioning behaviour. Thus, magnetite shows excellent promise as a tool for the estimation of the paleoredox state of magmas. The traditional method to estimate fO_2 is the 'two-oxide' method, first developed by Buddington and Lindsley (1964). Several iterations of this technique have since improved this calibration (e.g. Stormer, 1983; Anderton and Lindsley, 1988), some of which were applied to estimate the T-fO_2 of some samples in section 6.4.7. However, two-oxide oxybarometry requires that the chemistry of Fe-Ti oxides has not been altered, which in the case of hydrothermally-altered intrusive rocks is a rarity. Moreover, it relies on having coexisting

magmatic ilmenite and magnetite, thus placing further restrictions on samples suitable for the technique.

Arato and Audetat (2017a) have developed a new oxybarometer for use in silicic rocks based on magnetite-melt partitioning of V. The technique is designed for use on magnetite present as inclusions within quartz phenocrysts, so shielded from the effects of subsolidus alteration. It also requires the quartz phenocryst to contain silicate melt inclusions so that a partition coefficient for V can be determined (Figure 7-3). The calibration of the oxybarometer is dependent on the ASI, which can be measured in the melt inclusions, and T, which can also be approximated from the melt chemistry via the zircon saturation temperature (e.g. Hanchar and Watson, 2003). This technique was applied in Chapter 4, but was not accurate in experiments conducted at fO_2 = RRO. It would seem that the dependence on ASI is not correct.

In experiments conducted here, it is shown that the magnetite-melt partitioning of a range of elements can be explained in terms of thermodynamic equilibria associated with changes in $a Fe_3O_4$(spinel), $XFe^{2+}O$(melt) and $XFe^{3+}O_{1.5}$(melt). The numerous possible valence states of V complicate the dependence on these factors, so it is difficult to predict changes in its partitioning behaviour in response to fO_2. Instead, based on experiments conducted here, a new technique to estimate fO_2 is postulated based on magnetite-melt partition coefficients for a suite of homovalent elements, with partitioning controlled to a first order by chemical equilibria associated with changes in $a Fe_3O_4$, $XFe^{2+}O$(melt) and $XFe^{3+}O_{1.5}$(melt). Similar to the method of Arato and Audetat (2017a), magnetite and silicate melt inclusions in quartz phenocrysts could be targeted and partition coefficients determined for the range of elements detectable using LA-ICP-MS. The $a Fe_3O_4$ could be calculated using model of O'Neill and Wall (1987) and the ΣFe content measured in the silicate melt. The relationships derived for the divalent cations in terms of $a Fe_3O_4$(spinel)/$XFe^{2+}O$(melt) and trivalent cations as a function of $a Fe_3O_4$(spinel)/$XFe^{3+}O_{1.5}$(melt), and calculated $a Fe_3O_4$, could be used to approximate values for $XFe^{2+}O$(melt) and $XFe^{3+}O_{1.5}$(melt). Using the Total Fe concentration measured in the silicate melt inclusion, values for Fe^{2+}/Total Fe could then be approximated. Given the T, which could be estimated using zircon saturation temperature (Hanchar and Watson, 2003), and P, which could be estimated using a geobarometer such as Al-in-hornblende (Johnson and Rutherford, 1989), an empirical parameterisation could be used to estimate fO_2 from the Fe^{2+}/Total Fe estimate (e.g. Kress and Carmichael, 1991). It is important to note that some elements, such as Al and Ga where partitioning is strongly controlled by changes in bulk composition, should not be used. Furthermore, it would not be possible to determine fO_2 using partition coefficients for homovalent 4+ and 5+ cations, which depend on $a Fe_3O_4/(XFe^{3+}O_{1.5} * fO_2^{0.25})$ and $a Fe_3O_4/(XFe^{3+}O_{1.5}^{2/3} * fO_2^{1/3})$, thereby requiring two unknowns to be solved for. Although there are

possible variations in the activity coefficients for the divalent cations and Sc with changes in bulk composition, these do not appear to be significant as shown by the single linear trend for data derived from andesitic-dacitic and synthetic mafic CFS bulk systems (e.g. Figure 3-20 and 3-22).



Figure 7-3: Magnetite and coeval melt inclusion within a quartz phenocryst from the air fall tuff, Pine Grove, Utah, USA (from Arato and Audetat, 2017b)

Robust linear regressions were generated for D(Mg), D(Mn), D(Co), D(Ni) and D(Zn) as a function of $a\mathrm{Fe_3O_4}$(spinel)/$\mathrm{XFe^{2+}O}$(melt) and D(Sc) as a function of $a\mathrm{Fe_3O_4}$(spinel)$^{0.5}$/$\mathrm{XFe^{3+}O_{1.5}}$(melt) (Figure 7-4). Robust (least median of squares) linear regressions downweight outliers to create a more representative fit to the data (Rousseeuw and Leroy, 1988). This is useful where some data may be anomalous; for example, some D(Zn) values determined in magnetite bucket experiments at low fO_2 where volatile loss is thought to have been significant. Data were not included from piston cylinder experiments in these plots because of variations in partitioning as a function of pressure, and the larger error bars on this dataset in comparison to the 1-atm experiments (see section 4.3). The equations for these robust linear regressions can be used to predict $a\mathrm{Fe_3O_4}$(spinel)/$\mathrm{XFe^{2+}O}$(melt) using D(M^{2+}) or $a\mathrm{Fe_3O_4}$(spinel)$^{0.5}$/$\mathrm{XFe^{3+}O_{1.5}}$(melt) from D(Sc) and are provided below:

$$\log(a\mathrm{Fe_3O_4}(\text{spinel})/\mathrm{XFe^{2+}O}(\text{melt})) = (0.7628 \times \log D(\mathrm{Co})) + 0.32$$

$$\log(a\mathrm{Fe_3O_4}(\text{spinel})/\mathrm{XFe^{2+}O}(\text{melt})) = (0.6724 \times \log D(\mathrm{Ni})) - 0.04869$$

$$\log(a\mathrm{Fe_3O_4}(\text{spinel})/\mathrm{XFe^{2+}O}(\text{melt})) = (0.5452 \times \log D(\mathrm{Zn})) + 0.8817$$

$$\log(a\mathrm{Fe_3O_4}(\text{spinel})/\mathrm{XFe^{2+}O}(\text{melt})) = (0.7385 \times \log D(\mathrm{Mg})) + 1.0139$$

$$\log(a\mathrm{Fe_3O_4}(\text{spinel})/\mathrm{XFe^{2+}O}(\text{melt})) = (0.7681 \times \log D(\mathrm{Mn})) + 0.9142$$

$$\log(a\mathrm{Fe_3O_4^{0.5}}(\text{spinel})/\mathrm{XFe^{3+}O_{1.5}}(\text{melt})) = (0.7736 \times \log D(\mathrm{Sc})) + 1.5899$$

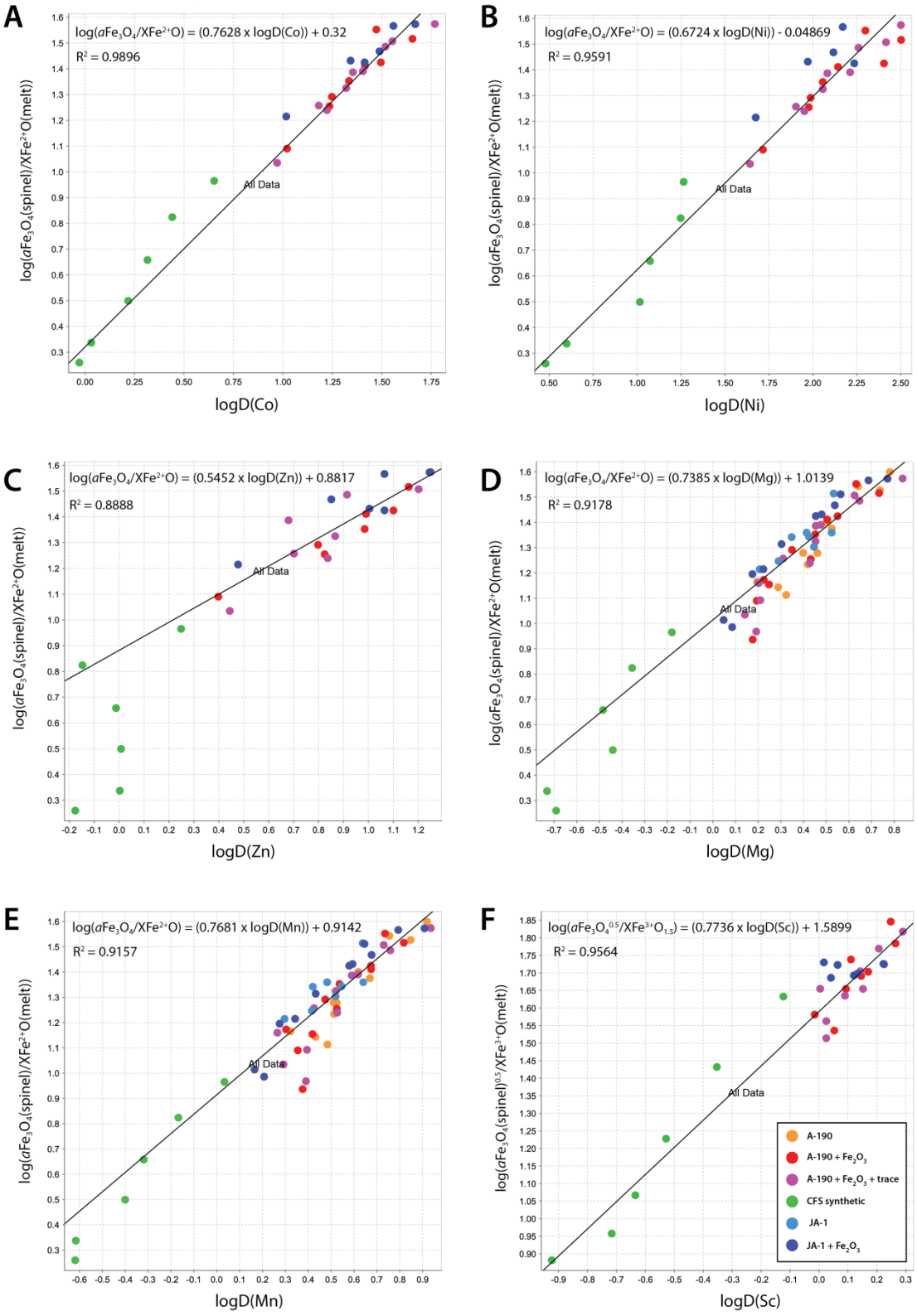


Figure 7-4: Results of robust linear regressions of (A) D(Co),(B) D(Ni),(C) D(Zn),(D) D(Mg) and (E) D(Mn) as a function of aFe_3O_4(spinel)/$XFe^{2+}O$(melt) and F) (D(Sc) as a function of aFe_3O_4(spinel)$^{0.5}$/$XFe^{3+}O_{1.5}$(melt) using data from 1-atm experiments using And-190 and JA-1 starting materials at T = 1070-1120°C and 1-atm experiments using synthetic Ca-Fe-Si bulk composition at T = 1150°C. Equation of regression provided in top-left of each plot along with R^2 value.

An advantage of this technique is that several values of Fe^{2+}/Total Fe could be approximated based on the partitioning of several elements, providing a means to cross-check the values determined. It remains to be tested whether this could offer a reliable means of oxygen barometry in natural rocks. An ideal suite of samples to test this would be those used in Arato and Audetat, 2017b).

7.1.3 Hydrothermal magnetite

Hydrothermal magnetite has a 'cleaner' texture and less commonly has exsolution features and inclusions than igneous magnetite (Figure 6-3). Thus, detailed textural assessment prior to interpreting its chemistry is less complex and successful LA-ICP-MS analyses devoid of contamination are obtained more frequently. Furthermore, the composition of hydrothermal magnetite is close to stoichiometric Fe_3O_4 such that the internal standardisation value for Fe can be assumed to be that of pure magnetite (Fe = 72.4 wt. %), without significant detriment to the accuracy of LA-ICP-MS data.

7.1.3.1 Controls on the composition of hydrothermal magnetite

Various populations of hydrothermal magnetite show distinct chemical differences according to the environment in which they formed. However, due to the limited experimental work investigating the controls on the chemistry of hydrothermal magnetite (Buddington and Lindsley, 1964; Ilton and Eugster, 1989; Simon et al., 2004) there are few constraints on what controls these variations. Nevertheless, first-order principles could suggest that the factors controlling partitioning between igneous magnetite and silicate melt at high temperature (600-1200°C), for example fO_2, T, P and matrix (melt/fluid) composition, will also influence partitioning between hydrothermal magnetite and hydrothermal fluids at lower temperatures (200-650°C). As for igneous magnetite, cation radius and charge (Goldschmidt, 1954) and crystal chemical conditions in the spinel structure (O'Neill and Navrotsky, 1984) will place constraints on possible substitutions into hydrothermal magnetite. It is probable that the partitioning relations in response to chemical equilibria associated with changing aFe_3O_4, $XFe^{2+}O$(fluid), $XFe^{3+}O_{1.5}$(fluid) and fO_2, will also be important in controlling the chemistry of hydrothermal magnetite. However, the major element chemistry of hydrothermal magnetite is typically close to pure magnetite, thus aFe_3O_4 in spinel is close to 1. Therefore, the $XFe^{2+}O$, $XFe^{3+}O_{1.5}$ and fO_2 of hydrothermal fluids will be relatively more important (see section 2.4.2).

Element availability in hydrothermal fluids will contrast significantly with that in igneous silicate melts. This adds an additional layer of complexity when understanding controls on the chemistry

of hydrothermal magnetite. Some fluid-mobile elements, such as As, Pb, Sb, Zn and Cu, can be highly enriched in hydrothermal fluids relative to their concentrations in igneous melts (Audetat et al., 2000; Ulrich et al., 1999). Furthermore, magnetite-hydrothermal fluid partition coefficients are likely to differ to magnetite-silicate melt partition coefficients. For example, stronger bonding with elements in solution might mean that the elements are more mobile in the fluid so that they partition more readily into the fluid, thereby decreasing the concentration in magnetite. Several factors could be important in controlling the composition of hydrothermal fluids and partitioning of various elements between magnetite and hydrothermal fluid, which will be described below.

The abundance of various complexing ligands, such as Cl^- or F^-, will influence element concentrations in hydrothermal fluids and could also affect magnetite-fluid partition coefficients (Zajacz et al., 2008). For example, the concentration of Mn in fluids increases with chlorinity (Ilton and Eugster, 1989), so that with increasing Cl^- concentrations, Mn is likely to be increasingly partitioned into the fluid relative to magnetite (Canil et al., 2016). The behaviour of Zn is similar to Mn in both hydrothermal magnetite (Figure 6-6) and igneous magnetite altered by hydrothermal fluids (Figure 6-14), suggesting that the behaviour of Mn and Zn is likely to be coupled. Both of these elements behave similarly to Pb in hydrothermal fluids (another strongly Cl^-complexed element), so a similar partitioning effect might be anticipated. Other elements that are strongly complexed by chloride ions in solution (e.g. Li, Na, K, Rb, Cs) are also likely have relatively small $D_{magnetite\text{-}fluid}$ values. It is interesting to note that Mg and Co exhibit different trends to Mn and Zn in igneous magnetite altered by hydrothermal fluids (Figure 6-13). Because these divalent cations would be expected to partition in a similar manner into magnetite (e.g. Figure 2-5), their contrasting behaviour during alteration likely reflects a decoupling of their transport in hydrothermal fluids.

The oxidation state and pH affect the stability of various species in hydrothermal fluids so will also be important to consider in attempts to understand the composition of hydrothermal magnetite. For example, the partitioning of Mo into hydrothermal fluids from silicate melt is favoured under more reduced and acidic conditions in porphyry systems (Seo et al., 2012). The pH also affects the solubility of Al in hydrothermal fluids, with increasing solubility as pH decreases. This has been suggested as a control on Al incorporation in hydrothermal quartz (Rusk et al., 2008).

Titanium is typically considered insoluble in hydrothermal fluids (Mysen, 2012, Van Baalen, 1993), which could explain the low concentration of Ti in hydrothermal magnetite. Notwithstanding this, recent work has indicated that TiO_2 is not insoluble in Cl- and F-rich brines (e.g. Rapp et al., 2010). The substitution of Ti into magnetite has been shown to be favoured at

high temperature in ulvospinel-magnetite solid solutions (Buddington and Lindsley, 1964). Thus, it is possible that Ti in magnetite is strongly influenced by temperature (Canil et al., 2016). Nevertheless, there is not a significant effect on magnetite-melt partitioning observed with temperature in experiments conducted as part of this PhD, although this could be a result of the rather limited temperature range investigated (920-1150°C). The Ti + V vs. Al + Mn diagram, modified by Nadoll et al. (2014) after Dupuis and Beaudoin (2011) to categorise magnetite populations from various ore forming settings (Figure 6-22), displays a possible temperature trend. Generally, hydrothermal magnetite forming at higher temperatures displays higher Ti + V and higher Al + Mn relative to that forming at lower temperatures. Titanium and Al are generally present at higher concentrations than V and Mn in hydrothermal magnetite so dictate most of the variation in this plot. This lends support to the contention that Ti, and also Al, are temperature-controlled in hydrothermal magnetite.

The solubility of many elements in hydrothermal fluids is controlled by temperature because of the prograde solubility behaviour of most rock-forming minerals. Based on empirical evidence from natural magnetite, it is suggested that lower temperature hydrothermal magnetite generally contains lower levels of trace elements. For example, hydrothermal magnetite from porphyry systems has higher contents of Sn and Ga than that from banded iron formations (BIF) (Nadoll et al., 2014), which could be a thermal effect. Aluminium, Ti, V and Mn contents are all distinctly elevated in hydrothermal magnetite associated with porphyry Cu-Au systems relative to Cu-Mo or Cu-Mo-Au systems (see 6.4.4.1ii). It could be that hydrothermal magnetite associated with Cu-Au systems is stabilised and crystallises at higher T than in Cu-Mo and Cu-Mo-Au systems.

During the re-equilibration of igneous magnetite to form hydrothermal magnetite, the Ti-content is strongly reduced. Given that Ti is typically viewed as an immobile element in hydrothermal systems (Van Baalen, 1993) it is interesting to consider where the Ti is sequestered. Most probably the Ti is lost to hydrothermal fluids and is transported elsewhere where it may form secondary Ti-rich phases, such as rutile. This exemplifies the open system nature of the hydrothermal environment, with assorted element gains and losses at various stages.

The V content of igneous magnetite has been recognised to be strongly redox controlled, with V increasingly incorporated into magnetite at low fO_2 (Chapters 2, 3 and 4; Toplis and Corgne, 2002; Arato and Audetat, 2017a). Conversely, hydrothermal fluids exsolved from a more reduced magma may be depleted in V as a result of its earlier incorporation in magnetite. The opposite effect might also apply, that V concentrations in fluids exsolved from highly oxidised magmas may be relatively enriched in V. This is consistent with the occurrence of the vanadium mica, roscoelite, in porphyry Cu-Au systems such as Porgera (Richards et al., 1997).

The concentrations of V and Ga in hydrothermal magnetite studied in Chapter 6 was shown to be relatively homogeneous, both within sample (generally < 15% RSD) and across all porphyry copper systems (Appendix 3). The V content of hydrothermal magnetite does not have bivariate correlation with Ti or Al, suggesting that V is not controlled by temperature. Similar to V, Ga abundances in hydrothermal magnetite are homogeneous both within samples and across all porphyry copper systems. Interestingly, and unlike most elements, the V and Ga contents of igneous and hydrothermal magnetite from porphyry copper systems are comparable (Figure 6-7).

Elements which partition strongly into coexisting mineral phases, could be important in controlling the chemistry of magnetite through influencing element availability. For example chalcophile elements, such as Cu, will preferentially partition into coexisting sulphide phases (e.g. Dare et al., 2012; Simon et al., 2008), whereas lithophile elements, such as Mg or Al, will be strongly incorporated into silicates (Nadoll et al., 2014). Possibly the V and Ga contents in magnetite are largely dictated by the coexisting mineral assemblage (e.g. biotite, K-feldspar) limiting the availability of these elements.

Extensive fluid-host rock interaction has been attributed to explain the enrichment of a number of elements, e.g. Mg, Al, Mn, Co, Ni and Zn, in hydrothermal magnetite associated with skarns (Nadoll, 2011; Meinert, 1987; Nadoll et al., 2014). Ni/Cr ratios in hydrothermal magnetite in BIF from the Brockman Iron Formation have also been shown to resemble that of the underlying mafic host rocks, suggesting that the magnetite composition reflects hydrothermal fluids which have interacted with these mafic rocks (Pecoits et al., 2009). The composition of the source magma, will also exert a strong control on the composition of the hydrothermal fluids exsolved. Ni and Cr were shown to be enriched in hydrothermal magnetite from potassically altered porphyry intrusions associated with Cu-Mo-Au systems. It is possible that this could be a result of fluid exsolution from a more mafic magma in samples from Cu-Mo-Au relative to Cu-Au and Cu-Mo systems. Alternatively, this could reflect interaction between hydrothermal fluids and highly mafic host rocks in the Cu-Mo-Au systems studied. Hydrothermal magnetite from propylitically altered rocks has high Mg and Co contents relative to those from other alteration styles. There is also an increase in Mg and Co with progressive propylitic alteration of igneous magnetite, which is not apparent for other divalent cations (Figure 6-13). Mafic rocks are particularly prone to propylitic alteration, thus the high Mg and Co in propylitic hydrothermal magnetite could be controlled by the host rock.

In summary, understanding the composition of hydrothermal magnetite is a complex problem. As well as the same factors that control magnetite-melt partitioning in igneous systems, it is

necessary to consider an array of additional parameters that can influence the composition of hydrothermal fluids and magnetite-fluid partitioning behaviour. Moreover, hydrothermal magnetite forming in porphyry copper systems may be subject to numerous successive stages of alteration, which could continually alter its chemical makeup. In comparison to the igneous environment, hydrothermal conditions are less likely to be representative of equilibrium and may be associated with a range of element gains and losses during various stages of hydrothermal activity. As a result, it is more difficult to accurately replicate the natural hydrothermal environment experimentally. Fluid inclusion data that provide insights into the complex chemical composition of hydrothermal fluids is becoming increasingly available (e.g. Rusk et al., 2004) and could be valuable for constraining magnetite-fluid partition coefficients. It would be interesting to see how these compare to partition coefficients between magnetite and silicate melt derived experimentally (e.g. Chapters 2, 3 and 4; Toplis and Corgne, 2002), or empirically using natural samples (e.g. Ewart and Griffin, 1994).

7.1.3.2 Geospeedometry

Diffusion modelling of chemical gradients in minerals is frequently applied as a chronological tool to constrain the timescales of geological processes. Diffusion speedometry requires thermal histories and diffusion rates which are neither too short and/or slow to produce a measurable concentration profile, nor so long and/or fast that the diffusion gradient is not discernible. Diffusion is significantly faster in magnetite than other silicate minerals. For example, Table 7-2 compares the diffusion rates of Mg at 1150°C in some silicate phases, relative to magnetite. Thus, magnetite may not be so well suited for tracking the timescales of higher temperature magmatic processes, where rapid diffusion is likely to generate flat, completely relaxed diffusion profiles. On the other hand, magnetite could be useful in tracing the timescales of lower temperature hydrothermal processes, generating broader diffusion profiles for a range of elements which would not be easily detectable in minerals with slower diffusion.

Table 7-2: Literature values for the diffusion rates of Mg at 1150°C in some silicate phases, compared with magnetite (this study)

Mineral	Orientation	ΔFMQ[a]	T (°C)	log D(Mg)	Reference
Diopside (1.8% Fe)	Parallel to c axis	FMQ - 3.6	1150	-19.30	Zhang et al. (2009)
Olivine - (Fo(100) - Synthetic)	Parallel to c axis	FMQ - 3.0	1150	-17.27	Chakraborty et al. (1994)
Garnet (Alm-Pyr)	Isotropic	FMQ - 0.8	1150	-17.90	Perchuk et al. (2009)
Magnetite	Isotropic	FMQ + 1	1150	-13.22	This study

[a]fO_2 values converted to ΔFMQ values using Hemingway (1990) for FMQ buffer, Ulmer and Luth (1991) for graphite and O'Neill and Pownceby (1993) for IW

The trace element contents of hydrothermal magnetite are commonly heterogeneous on the grain scale (Cook et al., 2016), exhibiting oscillatory zoning (e.g. Knipping et al., 2015, Figure 6-3) and multiple stages of dissolution and reprecipitation (Hu et al., 2015). Zoning and intracrystal variability in the chemistry of magnetite could be studied in conjunction with the diffusion coefficients reported in Chapter 3 to study the rates of processes associated with mineralisation. Owing to its cubic symmetry, magnetite does not exhibit variation in diffusivity with crystallographic orientation, thereby removing an additional aspect of complication in using magnetite for diffusion speedometry relative to anisotropic phases. The diffusion rates of various trace elements in magnetite cover a broad range of nearly four orders of magnitude, offering a range of possible elements to cross check the timescales of processes. Although there are strong variations in diffusion rates with fO_2, porphyry copper deposits typically form over a relatively narrow range of fO_2 between FMQ + 1 and FMQ + 3 (Ballard, 2002; Richards, 2015).

Mercer et al. (2015) applied diffusion modelling of Ti gradients in quartz to investigate the formation and cooling time scales of quartz from porphyry dyke intrusions and hydrothermal veins associated with porphyry copper mineralisation at Butte, Montana. The brightness in SEM cathodoluminescence (CL) images was shown to correlate positively with Ti concentration in quartz so that the CL gradient could be calibrated as a proxy for Ti gradients. This technique allowed multiple Ti gradients to be determined from high spatial resolution CL images, over distances as short as 2 μm, and also minimised the need for time-consuming and costly EPMA analyses. Titanium diffusion in quartz is significantly slower than all elements studied here in magnetite; Ti diffusion in quartz has log D = -17.7 ± 0.4 at 1150°C parallel to the c axis (Cherniak et al., 2007), over an order of magnitude slower than Cr in magnetite. Like quartz, magnetite formed in hydrothermal environments commonly shows multiple generations of formation and stages of growth. However, because diffusion is significantly faster in magnetite than quartz, the boundaries over which the concentration could be modified by diffusion would be significantly greater. For example, using the formula $x = (Dt)^{0.5}$, the diffusion distance (x) for Ti at 1150°C, assuming fO_2 = FMQ + 1 (log D(Ti) = -15.05, Table 3-4), will be approximately 530 μm over a timescale of 10 years. In quartz, however, Ti would diffuse over a distance of just 25 μm under the same conditions in 10 years (using log D(Ti) = -17.7, Cherniak et al., 2007). Thus, diffusion gradients in magnetite could be amenable to analysis by LA-ICP-MS, even at temperatures relevant for the magmatic-hydrothermal transition (approximately 700°C), where diffusion could be expected to be approximately 3-4 orders of magnitude slower. Magnetite could thereby be used to trace the timescales of pulses of hydrothermal fluids associated with precipitation of magnetite in an ore-forming system.

7.2 Advice on how to use magnetite chemistry as an exploration tool for porphyry copper deposits

7.2.1 Hydrothermal vs. Igneous magnetite

In the majority of cases, hydrothermal magnetite can be discriminated from igneous magnetite by its Ti content, with hydrothermal magnetite typically having Ti < 1 wt. %. Identifying hydrothermal magnetite alone could be useful in itself, when exploring for magmatic-hydrothermal ore deposits, providing evidence for proximal hydrothermal alteration. Pisiak et al. (2017) studied the chemistry of magnetite in till samples surrounding the Mt. Polley porphyry copper deposit in British Columbia, Canada. Linear discriminant analysis (LDA) was performed on a compilation of magnetite compositions to distinguish the composition of hydrothermal magnetite related to porphyry copper systems from igneous magnetite associated with barren or mineralised rocks. The LDA model was subsequently applied to categorise magnetite in the till samples. More than 90% of the magnetite was identified to be from igneous bedrock sources, however, there is an increase in the abundance of hydrothermal porphyry magnetite identified proximal to the porphyry copper system. The results are compared with the proportions of hydrothermal magnetite determined using the Ti-Ni/Cr diagram developed by Dare et al., (2014). If the system had been unknown, an understanding of the ice-flow history in this glaciated terrain could have been used in conjunction with hydrothermal magnetite abundance to vector towards its source.

Using data from Pisiak et al. (2017), there is a good agreement between the percentage of magnetite identified as hydrothermal magnetite using the Ti-Ni/Cr diagram (after Dare et al. 2014) and using a 1 wt. % Ti in magnetite cut-off, which supports that the Ni/Cr term is not useful (Figure 7-4). There is less agreement between the percentage of magnetite identified as hydrothermal magnetite using a 1 wt. % cut-off and the proportion of hydrothermal porphyry magnetite identified using the LDA models (Figure 7-4); although, this might be expected given that this discriminant plot was developed to discriminate hydrothermal magnetite specifically related to porphyry copper deposits, whereas the 1 wt. % cut-off is proposed to distinguish all hydrothermal magnetite from igneous magnetite occurrences.

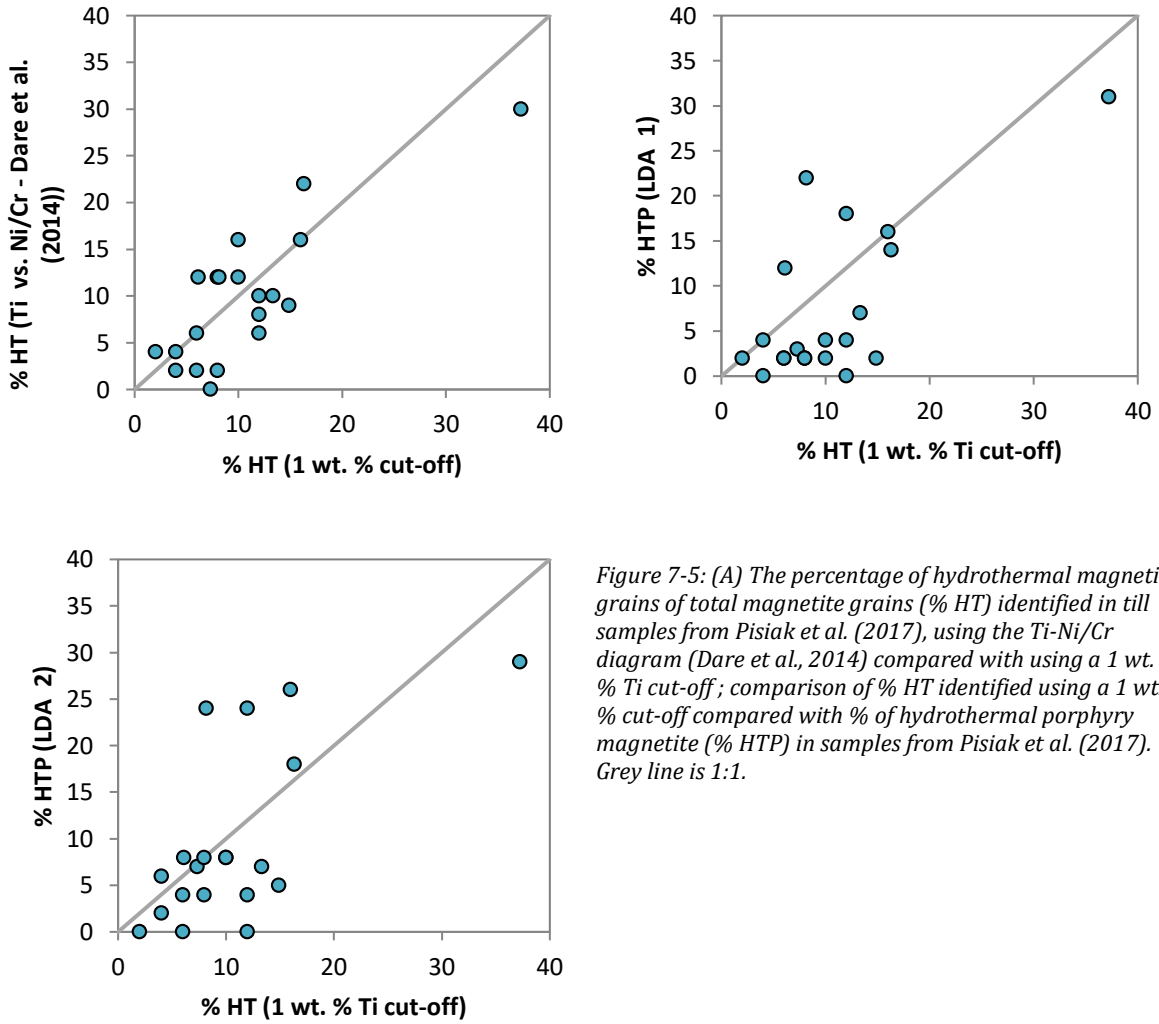


Figure 7-5: (A) The percentage of hydrothermal magnetite grains of total magnetite grains (% HT) identified in till samples from Pisiak et al. (2017), using the Ti-Ni/Cr diagram (Dare et al., 2014) compared with using a 1 wt. % Ti cut-off ; comparison of % HT identified using a 1 wt. % cut-off compared with % of hydrothermal porphyry magnetite (% HTP) in samples from Pisiak et al. (2017). Grey line is 1:1.

A similar approach to that applied by Pisiak et al. (2017) could be used to distinguish hydrothermal magnetite, but using a simpler 1 wt. % cut-off. Magnetite could be analysed from surface samples or drill core in the propylitic zone and the relative amount of hydrothermal to igneous magnetite mapped to guide towards a hydrothermal system. Alternatively, this approach could also be used on magnetite grains separated from stream sediments. The proportion of hydrothermal magnetite in such samples could be mapped out in different catchments to identify those draining from a potential hydrothermal centre.

Additionally, because the Ti content of magnetite is lowered during hydrothermal alteration, the Ti content of igneous magnetite could offer a direct vector towards a porphyry copper system. Thus, the statistical distribution of magnetite compositional information, such as its Ti content, could indicate samples that contain a higher proportion of more proximal magnetite grains. For the samples studied by Pisiak et al. (2017), the percentage of hydrothermal porphyry magnetite determined using the LDA models was plotted against the mean Ti content of igneous magnetite

- discriminated from hydrothermal magnetite using a 1 wt. % Ti cut-off. There is a negative correlation which indicates that samples containing more hydrothermal porphyry magnetite contain igneous magnetite with lower Ti content (Figure 7-5). This supports that the Ti content of igneous magnetite could offer a vector towards mineralisation. Because only Ti content is required for these vectoring techniques, a large volume of grains could be analysed relatively simply using SEM-EDS or EPMA analysis alone, negating the need for more expensive and time-consuming LA-ICP-MS analysis. Nevertheless, although hydrothermal alteration is inherently associated with porphyry copper mineralisation, hydrothermal alteration can occur without mineralisation. Thus, this technique could recognise an occurrence of hydrothermal alteration, but does not necessarily identify the presence of economic mineralisation.

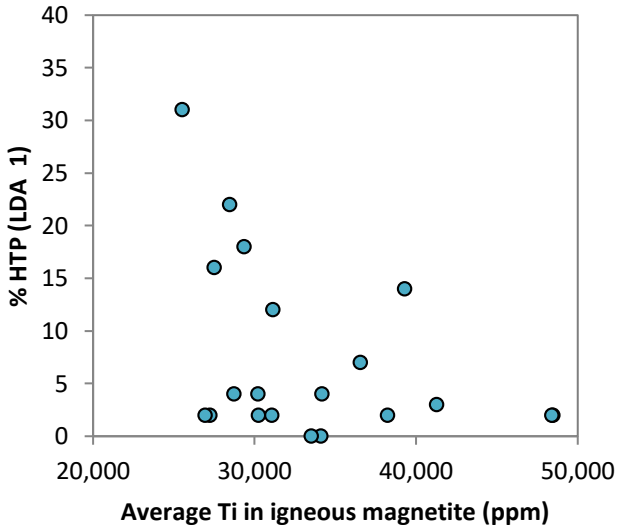


Figure 7-6: (A) The percentage of hydrothermal porphyry magnetite grains of total magnetite grains (% HTP) identified in till samples from Pisiak et al. (2017) vs. Ti content of igneous magnetite (discriminated from hydrothermal magnetite using a 1 wt. % cut-off).

Taking this to the next level, LA-ICP-MS can be used to determine the minor and trace element chemistry and this used to categorise hydrothermal magnetite pertaining to various characters, such as style of alteration, metal association and deposit size, using the discriminant projection tools developed in section 6.4.4. The minor and trace element chemistry of magnetite thereby offers a superior tool to that based on major element composition alone.

7.2.2 Analytical method

Prior to interrogating a large geochemical dataset, it is important to understand how the analytical technique used can influence the resulting concentrations. Laser spot size has a particularly strong influence on the analysis. When analysing grains with exsolution, it is recommended that a spot size greater than 30 microns is used to homogenise the bulk composition, whereas for grains devoid of exsolution, a spot size greater than or equal to 25 microns is preferred to substantially reduce analytical variability. Notwithstanding this, with

future advances in technology and sensitivity of LA-ICP-MS systems, it may become possible to analyse with smaller spot sizes.

The method for determining the internal standard can influence resulting concentrations determined by LA-ICP-MS. Pisiak et al. (2017) assessed the validity of three different techniques for approximating the internal standard: the EMP method, where Fe is measured independently using a different analytical technique; the stoichiometric calibration method, where the maximum stoichiometric Fe (72%) is assumed; and a technique known as the AYCF method, which calibrates to the total counts per second in each analysis. The latter two methods negate the requirement for an additional analytical step. Nevertheless, it is considered that predetermining the Fe using a different analytical technique is important because, in addition to providing the most accurate means to calculate the internal standard, it offers a means to cross check the reliability of LA-ICP-MS data with concentrations determined using a different analytical technique (e.g. Figures 2-3 and Figure 6-5)

When comparing data obtained from electron beam instruments with LA-ICP-MS data it is important that the area measured using EPMA or SEM-EDS covers a similar area to that analysed using LA-ICP-MS. For example, there is commonly scatter from a 1:1 reference line when comparing Ti concentrations determined using LA-ICP-MS against SEM-EDS or EPMA, with a bias to higher concentrations determined by LA-ICP-MS (Pisiak et al., 2017; Fry, 2017, Appendix B – Figure 7). This is probably a result of the small beam size of electron beam instruments which therefore do not incorporate exsolution into the analysis. The beam rastering approach described in section 5.2.1 is suggested as an appropriate way to circumvent this problem.

The choice of external standard can also affect the concentrations determined. For example, when analysing the composition of a natural magnetite standard (BC28), previously well characterised by Dare et al. (2012), results processed using NIST610 generally have elevated Co and Al concentrations, whereas when processed using BCR-2g, Ni is over reported (Figure 5-3). Thus, it is important to be aware of the choice of external reference material used to process LA-ICP-MS data and to ensure that an internally consistent method is used, particularly where multiple laboratories might be involved. Furthermore, incorporation of a natural magnetite standard is also suggested to assess accuracy and long-term reliability of the data, particularly when using external standards which are not matrix-matched with the Fe-Ti oxide of interest.

Mineral inclusions, such as apatite, zircon, titanite and sulphide phases, are common in natural Fe-Ti oxides, particularly igneous magnetite. Therefore, it is important to analyse for some elements which do not have extensive substitution in magnetite so that contaminated analyses can be filtered. This can be done during visual screening of the laser ablation spectra (e.g. Figure

5-5), as well as post-processing (Figure 5-7). Notwithstanding this, literature data are often limited to just summary statistics which makes it difficult to assess for inclusions when studying published datasets. Ideally, full datasets consisting of all individual analyses should be published and these data filtered to remove contaminated analyses, prior to collating and interrogating magnetite compositional data from a variety of sources.

Although employing large laser spot sizes (> 35 micron) can homogenise exsolution on the grain scale, analysing a mixture of exsolved domains and residual magnetite may not represent the original composition prior to oxy-exsolution. Consequently, it is recommended to generally avoid analysing grains with exsolution. Petrographic study of the texture of magnetite in conjunction with its chemistry is important so that analyses with significant exsolution can be filtered prior to interpreting the chemistry.

7.2.3 Vectoring with composition variations

During the formation of porphyry copper deposits, magmatic-hydrothermal fluids are released and extensively alter the surrounding rocks (section 1.2.1.2). It has been shown that some minerals, such as chlorite, characteristic of the more distal alteration assemblages, exhibit systematic compositional spatial variations relative to the porphyry centre (Wilkinson et al., 2015). In a similar manner, the chemistry of hydrothermal magnetite could also be used as a tool to vector towards mineralisation. Furthermore, the particularly high rates of element diffusion in magnetite means that precursor igneous magnetite is prone to having its original chemistry reset during interaction with hydrothermal fluids (section 6.4.6), particularly for faster diffusing elements, such as the monovalent and divalent cations. Thus, it is possible that igneous magnetite present within host rocks as well as porphyry intrusions could also be used as a vectoring tool that might extend beyond the hydrothermal magnetite zone in applicability (Figure 7-7). In fact, in comparison to hydrothermal magnetite, igneous magnetite contains a greater number of trace elements above the limit of detection thereby providing a wider range of elements that could be utilised in this way. Slower diffusing elements are likely to be less prone to having their chemistry reset by such disequilibrium processes, potentially providing a means to 'see through' alteration. Nevertheless, even the slowest diffusing elements, such as Cr, appear to have their chemistry modified by hydrothermal alteration in the propylitic zone, distal from the centre of the porphyry system (section 6.4.6).

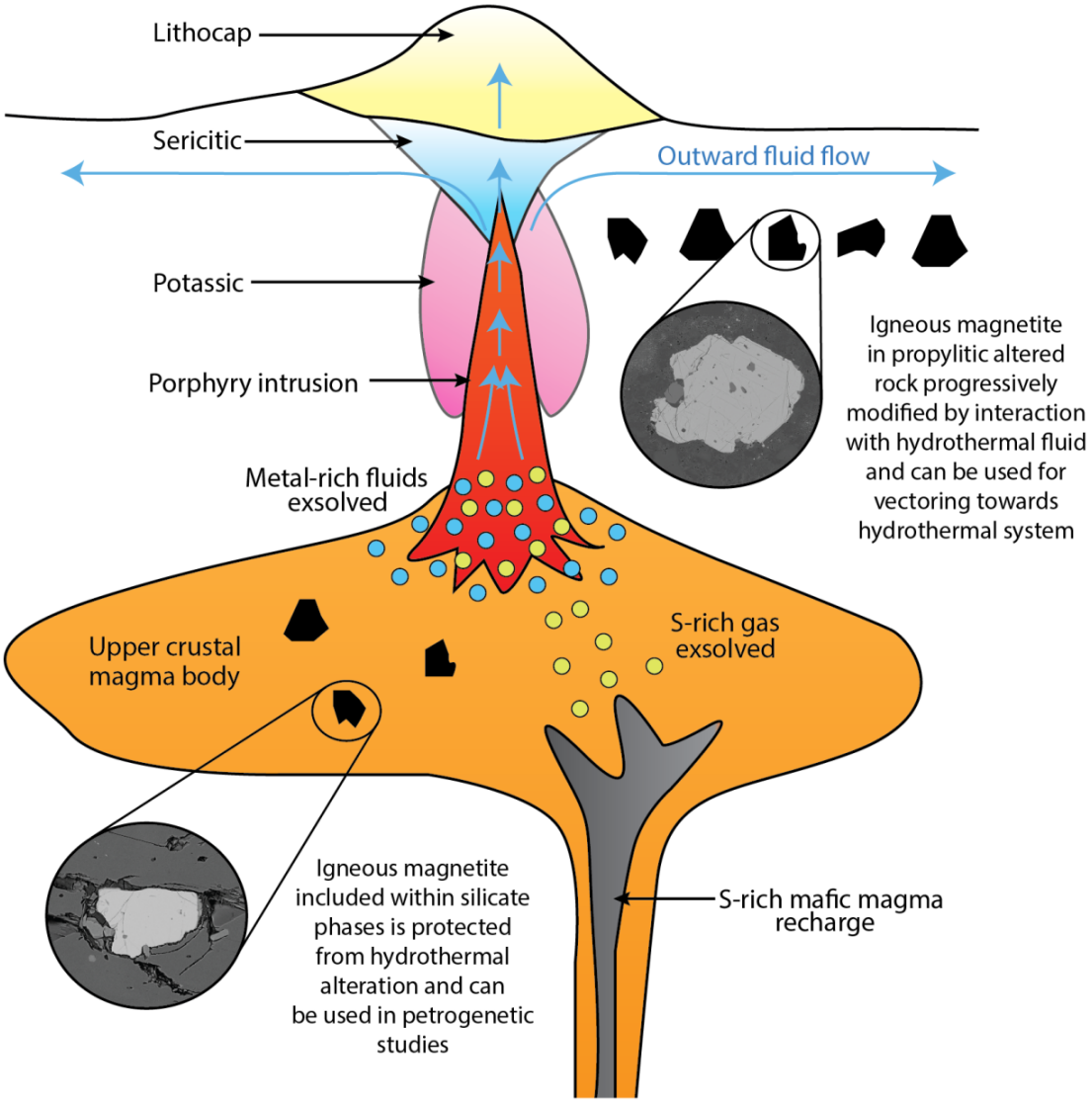


Figure 7-7: Porphyry copper deposits form as a result of magmatic-hydrothermal phenomena associated with the emplacement of hydrous magmas in the upper crust. Hydrothermal fluids released from the magma cool and react with the surrounding rocks, resulting in the deposition of metal sulphides. The original chemistry of magnetite associated with this geological setting can be overprinted by interaction with new batches of magma, e.g. mafic recharge into upper crustal magma reservoir and interaction with hydrothermal fluids e.g. fast-diffusing divalent cations (Ni, Co, Mn, Mg, Zn) could diffuse > 200 microns at 700°C over just 10 years. Igneous magnetite present as inclusions within more resistant phases will be protected from the hydrothermal fluids and will less susceptible to having their chemistry modified post-crystallisation. SEM-BSE image in bottom-right is igneous magnetite included within amphibole in sample OR.1766-LEP; SEM-BSE image in top-right is igneous magnetite from propylitically-altered sample OR.11(2)-RP.

7.2.4 Multielement discrimination diagrams

Discriminant projection analysis was used to separate different populations of hydrothermal magnetite according to multiple minor and trace element variables. First a discriminant diagram was developed to define magnetite associated with four alteration types: potassic, phyllic, propylitic and intermediate-argillic. The discriminant plot was shown to effectively distinguish propylitic magnetite using two supplementary datasets. Although there is a large degree of overlap between hydrothermal magnetite from potassically and phyllically altered rocks, this

might be expected given that phyllic alteration is magnetite destructive. Thus, hydrothermal magnetite present in phyllic alteration is likely to be a relic of potassic alteration, especially given the close spatial relationship of these two alteration types. Magnetite is also not diagnostic of intermediate-argillic alteration, so the distinct composition of the hydrothermal magnetite in this alteration zone probably reflects alteration of original igneous or hydrothermal magnetite by intermediate-argillic hydrothermal fluids. The alteration discriminant diagram (Figure 6-26) could be used to aid mapping the various alteration types using the chemistry of hydrothermal magnetite. Magnetite could be analysed from drill core, samples at surface, or stream or till sediments and hydrothermal magnetite (Ti < 1 wt. %) categorised according to alteration style. An increase in the relative abundance of potassically-associated magnetite could be interpreted as a guide towards ore. Hydrothermal magnetite – discriminated using a 1 wt. % Ti cut-off – from the study by Pisiak et al. (2017) was plotted on DPA-A (Figure 7-8). Most data plots as hydrothermal magnetite from propylitic altered rocks, however, a small proportion of the data plot in the potassic and phyllic alteration fields. It could be that these till samples are more proximal to an ore deposit. Notwithstanding this, there is no clear relationship between the number of potassic or phyllic associated magnetite and percentage of hydrothermal porphyry magnetite, as identified using their LDA models.

Discriminant diagrams were also developed to categorise hydrothermal magnetite according to its association with Cu-Mo, Cu-Au or Cu-Mo-Au porphyry copper systems. Although a plot was designed for use of magnetite from all alteration types, this was not effective. This could be a result of spatial variations in chemistry with distance away from the porphyry copper system. Instead, a plot designed specifically to categorise magnetite from potassically-altered samples is more effective at classifying metal association. Exploration and mining companies are often focused on specific commodities. For example, a company specialising in gold would be more interested in discovering a Cu-Au than a Cu-Mo system. Furthermore, during the development of an arc, there is often a transition in the style of porphyry copper deposit formed, with Cu-Au deposits more prevalent in immature arcs, but predominantly Cu-Mo associated with mature arcs (Richards et al., 2003). It is often the case that one phase of arc development is more fertile that the later one (e.g. Mongolia; Wainwright et al., 2011) with a Cu-Au signal in the former. Conversely in the Bingham district, the supergiant is the Cu-Au-Mo, whereas the smaller systems in the Wasatch are Cu-Au and the least prospective is Cu-Mo (section 6.4.4.1iii; John, 1997). Thus, there could be a certain style of porphyry mineralisation to target in the district. The metal association plot could be of use to discover the expected style of porphyry copper system at an early stage of exploration.

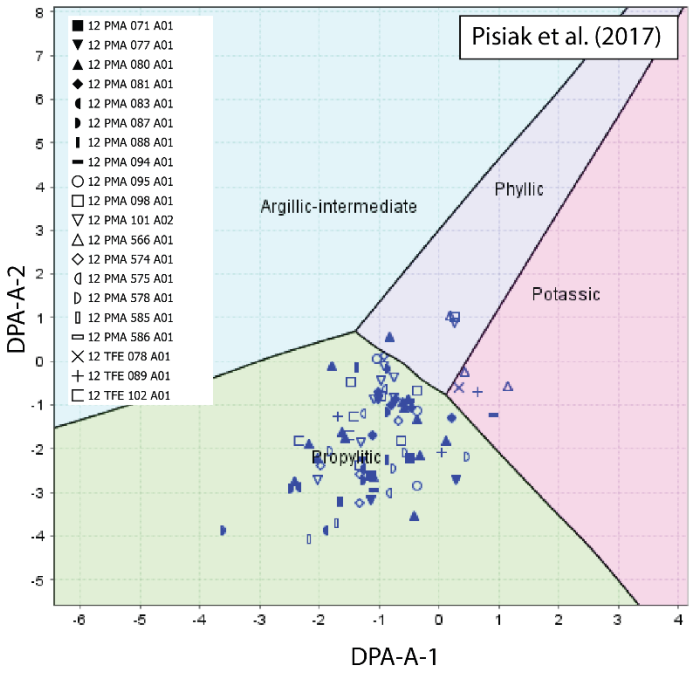


Figure 7-8: Discrimination diagram (DP-A-2 vs. DP-A-1) for hydrothermal magnetite from the study by Pisiak et al. (2017). Samples with magnetite indicated to be associated with potassic and phyllic alteration could be more proximal to the centre of a porphyry copper system.

Finally, discrimination diagrams were developed to assess fertility of Cu-Au and Cu-Mo systems. The alteration discriminant diagram developed earlier was used to first identify hydrothermal magnetite as potassic. Hydrothermal magnetite, classified as potassic, from background and porphyry copper prospects, was then classified as Cu-Au or Cu-Mo using the metal association discriminant plot previously developed for potassic altered rocks only. The fertility plot developed for Cu-Mo systems effectively discriminates potassic magnetite from mineralised Cu-Mo systems from porphyry Cu-Mo prospects. The mineralised porphyry Cu-Mo systems are predominantly from giant deposits, so it was not possible to accurately assess whether size of porphyry Cu-Mo system (based on contained Cu) could be evaluated using magnetite chemistry. The plot developed to assess fertility in Cu-Au systems effectively separates potassic hydrothermal magnetite from mineralised Cu-Au systems from porphyry Cu-Au prospects. The Cu-Au fertility diagram cannot effectively distinguish the size of porphyry Cu-Au deposit, however, some elements, not included in the DPA, exhibit progressive changes with size of porphyry Cu-Au system. Unfortunately, it was not possible to test these metal association and fertility discrimination plots using hydrothermal magnetite from literature, given a lack of datasets containing all elements required to calculate the discriminant components. Notably, Ge is commonly omitted from the list of elements analysed (e.g. Pisiak et al., 2017; Canil et al., 2016), or not reported (e.g. Nadoll et al., 2014), despite that Ge has been shown to be an important element to discriminate various populations of hydrothermal magnetite (e.g. Table 6-7, 6-10, 6-11).

7.2.5 Flow chart on how to use magnetite chemistry as an exploration tool

The following flow chart outlines a series of steps on how best to apply magnetite chemistry as an exploration tool for porphyry copper deposits (Figure 7-9).

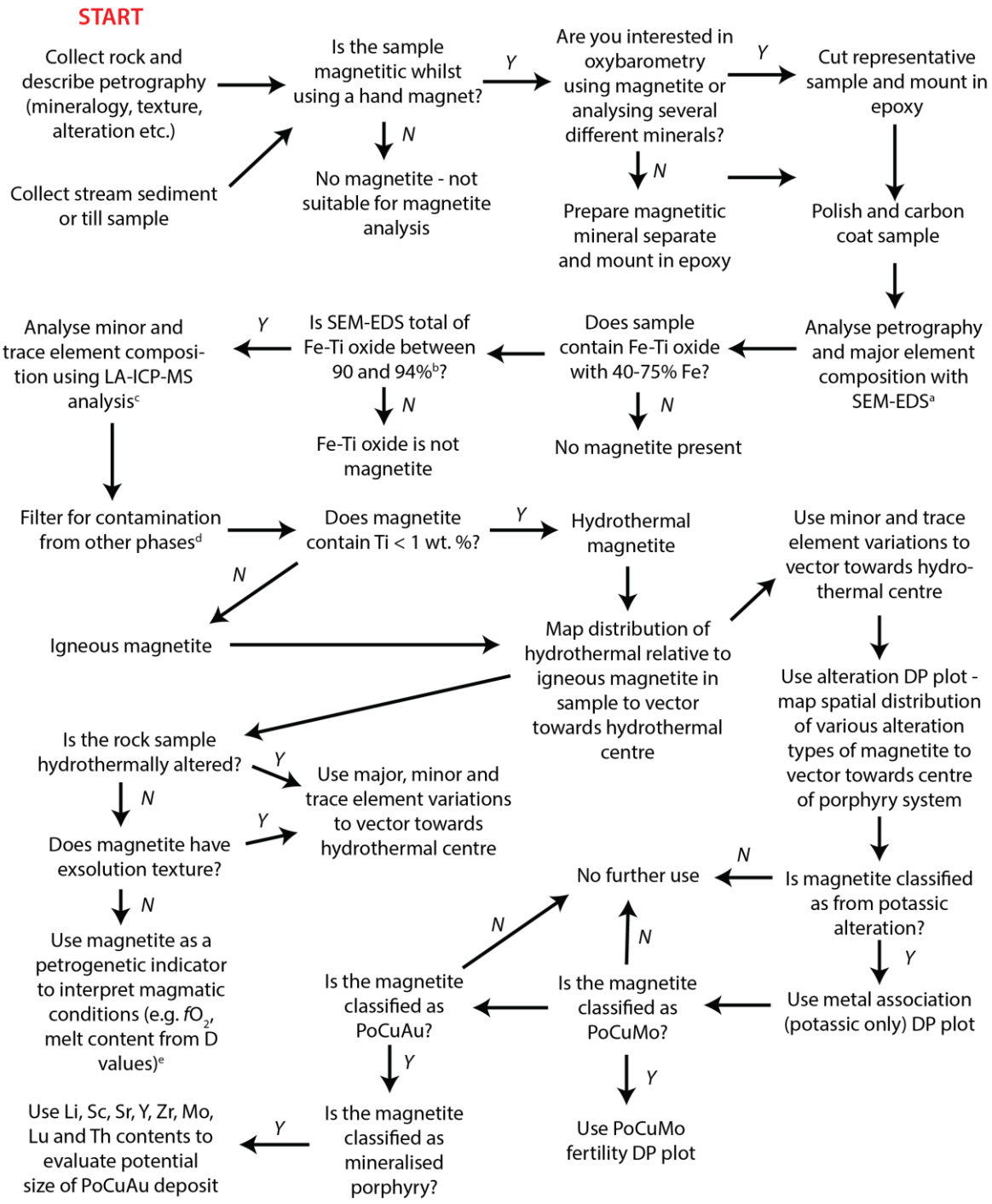


Figure 7-9: Flow chart describing procedure on how to use magnetite chemistry as an exploration tool for porphyry copper deposits. [a]If analysing grains with exsolution, use a rastered beam over a mixture of exsolved magnetite and exsolution (see section 5.2.1). [b]If total is approximately 87-90%, the Fe-Ti oxide is probably hematite or martite (hematite after magnetite). [c]Use reflected light image to assess possible martite (martite is lighter grey in reflected light). [d]Use flow chart in Figure Figure 5-7 (section 5.2.4) to remove contaminated analyses. [e]For use of igneous magnetite as a petrogenetic indicator please refer to section 7.1.2.

The full process is described starting with collection of a rock sample, goes through steps to identify magnetite using SEM-EDS, analyse magnetite using LA-ICP-MS, and distinguish igneous and hydrothermal magnetite. Compositional variations in hydrothermal and igneous magnetite could be used for vectoring towards the centre of a hydrothermal system. Finally, alteration, style of porphyry copper system and fertility can be assessed with hydrothermal magnetite, whereas igneous magnetite may be suitable for petrogenetic studies of the magmatic environment.

7.2.6 Comparing magnetite with other mineral indicators for porphyry copper systems

An ideal indicator mineral for use in exploration should be resistant to physical and chemical weathering and have compositional variation that is sensitive to the environment in which it formed. As well as fitting these criteria, the magnetic properties of magnetite make it easy to identify in a rock and easy to separate, thus offering a good candidate as an indicator mineral. In addition to magnetite, several other accessory and alteration minerals associated with porphyry copper deposits have been utilised as indicator minerals.

Zircon has been applied as an oxybarometer using Ce^{3+}/Ce^{4+} ratios to determine the relative oxidation state of magmas forming porphyry copper deposits (e.g. Ballard, 2002). Experiments by Burnham and Berry (2012) indicated that both Ce^{3+}/Ce^{4+} and Eu^{2+}/Eu^{3+} in zircon varies systematically with fO_2 supporting the belief that these ratios could be used to quantify fO_2 of the melt. These ratios can be approximated in zircon using Ce/Ce^* ($Ce^* = (La \times Pr)^{0.5}$), or Eu/Eu^* ($Eu^* = (Sm \times Gd)^{0.5}$). However, analytical issues pose problems when determining La and Pr in zircon, thereby leading to inaccurate approximation of Ce/Ce*. Furthermore, Ce^{3+}/Ce^{4+} and Eu/Eu^* are both strongly dependent on melt REE concentrations, which are usually poorly constrained and controlled by co-crystallisation of titanite. This thwarts the use of Ce or Eu anomalies in zircon as a redox proxy (Buret et al., 2016; Loader et al., 2017). Notwithstanding this, Ce and Eu anomalies in zircon do exhibit varying trends in fertile and barren suites of rock (Loucks et al., 2017; Ballard, 2002; Loader et al., 2017) indicating they could still be used as signals for porphyry fertility. Zircon is also extremely useful for geochronology; since U and Th are compatible in its structure whereas Pb is largely excluded, and because it is a highly resistant mineral, it is ideal for U-Pb dating. In comparison to magnetite, zircon is less abundant, but considerably more robust to alteration. Diffusion is particularly slow, such that there are often distinct compositional zones each representing different periods in the petrogenetic history. Thus, in the porphyry-forming environment zircon could provide a more reliable tool to interpret the earlier magmatic conditions leading up to mineralisation, whereas magnetite will track later processes, with its chemistry more susceptible to modification by hydrothermal fluids. Magnetite which has

remained unaltered, or preserved as inclusions within another mineral (e.g. Figure 7-10), could be used in conjunction with zircon to approximate fO_2 (e.g. Arato and Audetat, 2017b).

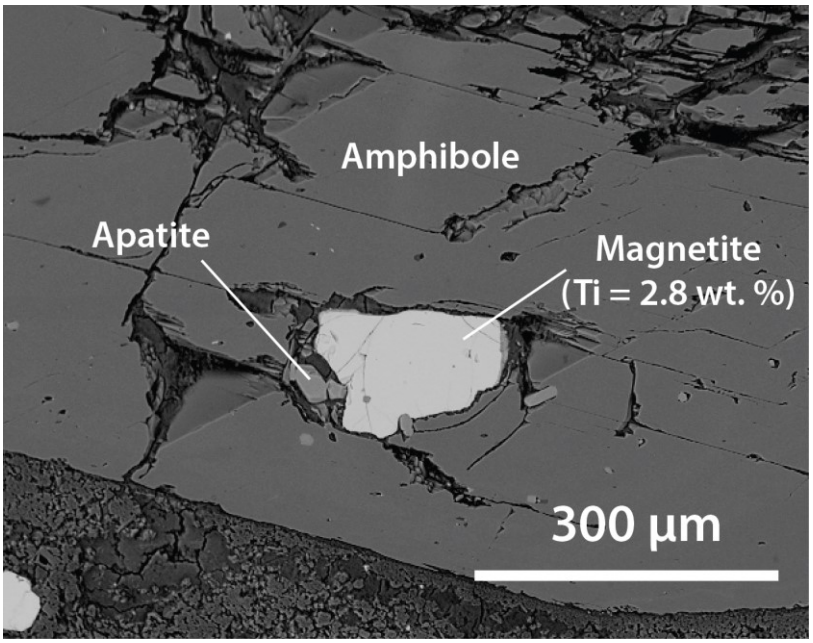


Figure 7-10: Igneous magnetite inclusion in amphibole in sample OR.1766-LEP. Amphibole phenocrysts offers shielding from effects of sub-solidus re-equilibration and hydrothermal alteration.

Compositional variations in the chemistry of chlorite and epidote have been shown to be effective as tools for vectoring towards the deposit centre from within the propylitic zone (Wilkinson et al., 2015; Cooke et al., 2014). Moreover, both minerals have also been suggested to provide insights into the mineral endowment of porphyry systems (Wilkinson et al., 2015; Cooke et al., 2014). The chemistry of hydrothermal magnetite could be used in a similar fashion, both as a vectoring tool and to assess fertility. As well as forming during propylitic alteration, epidote, chlorite and magnetite can form during other types of hydrothermal and metamorphic processes. As a result, there are often multiple generations of these minerals in the vicinity of a porphyry copper system which might be particularly apparent in stream sediment or till samples that have effectively sampled a wide area. Previously, minerals formed prior to mineralisation usually require discrimination from that related to hypogene mineralisation before they can be employed for vectoring. Typically, the most recent phase of intense hydrothermal alteration is hypogene mineralisation, since later non-mineralising alteration events are likely to remobilise mineralisation. The ease at which magnetite chemistry is overprinted in comparison to other silicate phases means magnetite chiefly reflects the most recent phase of alteration. Consequently, magnetite could offer a superior tool for vectoring in comparison to epidote and chlorite, negating the need to discriminate multiple generations of minerals unrelated to mineralisation.

Apatite also shows promise as a mineral indicator for porphyry copper deposits. Its structure is able to accommodate a large range of cations, many of which are strongly incompatible in magnetite, including Sr, Y and REE (Prowatke and Klemme, 2006b). These are highly relevant to potential fertility signatures in porphyry copper systems (Loucks, 2014). Apatite can also incorporate anions, including halogens and SO_4^{2-}, which can be used to trace the evolution of volatiles in magmas (Streck and Dilles, 1998). The trace element chemistry of apatite is sensitive to the environment in which it formed (Mao et al., 2016; Belousova et al., 2002). Distinctions in the trace element chemistry of hydrothermal and magmatic apatite from porphyry copper settings has also been suggested as an exploration tool (Bouzari et al., 2001). However, like magnetite, the chemistry of apatite is readily susceptible to modification by hydrothermal fluids (Harlov et al., 2015), rendering it less useful as a petrogenetic indicator to interpret magmatic conditions unless such overprints can be recognised. Thus, hydrothermal apatite potentially offers more promise as an exploration tool for porphyry copper systems. Nevertheless, its lower abundance in comparison to magnetite, chlorite and epidote may limit its use as a vectoring tool. Apatite, however, could be used in conjunction with magnetite to track a different array of elements, since apatite and magnetite incorporate a different assortment of elements at high concentrations. Moreover, the saturation of apatite is usually concomitant with the saturation of magnetite in arc magmas, which could be related to a decrease in Fe^{3+} in the melt following magnetite fractionation, thereby decreasing the solubility of P (Jenner et al., 2010).

The chemistry of magnetite, alongside other minerals, offers a powerful tool in mineral exploration for porphyry copper deposits. Although drilling will still be required to make a discovery and define a resource, mineral chemistry could be particularly useful in prioritising exploration targets by identifying clues to the extent and location of mineralisation at an early stage of exploration. Importantly, mineral chemistry can be applied at relatively low financial and environment cost in comparison to drilling and could thereby save large sums of money during an exploration campaign. A key capability will be the means to identify system fertility early on in an exploration project; this would have a massive impact on exploration and investor risk and, ultimately, the long term environmental and economic sustainability of exploration and mining projects.

8 Conclusions and future work

8.1 Conclusions

Magnetite-melt partitioning can be described by thermodynamic equilibria between magnetite and melt associated with changing $a Fe_3O_4$(spinel), $XFe^{2+}O$(melt), $XFe^{3+}O_{1.5}$(melt) and fO_2. The divalent cations exhibit linear relationships as a function of $a Fe_3O_4$(spinel)/$XFe^{2+}O$(melt). With increasing fO_2, there is a decrease in $Fe^{2+}O_{melt}$ as a result of the increasing proportion of magnetite and increasing $Fe^{3+}/\Sigma Fe$ of the system. In an andesitic bulk system, there is only a minor variation in the molar proportion of Fe_3O_4 in titanomagnetite with increasing fO_2. Accordingly, in such systems there are large increases in $a Fe_3O_{4mgt}/a Fe^{2+}O_{melt}$ with increasing fO_2. In mafic systems, by contrast, there is less variation in $a Fe_3O_4$(spinel)/$XFe^{2+}O$(melt) with fO_2 because keeping spinel on the liquidus with decreasing fO_2 requires a large decrease in the Fe_3O_4-content of the spinel. Hence, the ratio $a Fe_3O_{4mgt}/a Fe^{2+}O_{melt}$ does not change as much. Similarly, linear trends can be defined for the trivalent cations as a function of $a Fe_3O_4$(spinel)/$XFe^{3+}O_{1.5}$(melt), tetravalent cations as a function of $a Fe_3O_4$(mgt)/($XFe^{3+}O_{1.5}$(melt)*($fO_2^{0.25}$)), and pentavalent cations as a function of ($a Fe3O4_{mgt}$)/($XFe^{3+}O_{1.5}$(melt)$^{2/3}$ *($fO2^{1/3}$)). In andesitic-dacitic bulk systems, with increasing fO_2 there is only a minor variation in $a Fe_3O_4$(spinel) and $XFe^{3+}O_{1.5}$(melt). Consequently, there is not a large variation in partitioning of trivalent cations with increasing fO_2, whereas 4+ and higher valence cations exhibit strong decreases in the magnetite-melt partitioning, predominantly driven by changing fO_2. Notwithstanding this, for many elements, such as Al and Ga, these relationships break down for spinel compositions containing lower fractions of Fe_3O_4 than those studied here and for different bulk compositions. This may plausibly be due to changing activity-composition relations in either the spinel, or in the melt, but separating these variables in mineral/melt partitioning studies is in general difficult, or even impossible, and other experimental or theoretical information is required (O'Neill and Eggins, 2002).

At elevated pressure, the partition coefficients of some elements are depressed in comparison to those at 1-atm. For example, the HFSEs become incompatible relative to Ti and partition coefficients for the divalent cations are lowered. Cations with a larger difference between the ionic radius of the substituting cation (r_i) and the optimal radius of the site (r_0) decrease most at elevated pressure. It is possible that, at higher pressures, the size of the optimal radius of the site (r_0) onto which the cations partition decreases or the Young's modulus of the lattice site changes, which decreases the partition coefficient for some cations, particularly those with a larger difference between r_i and r_0. There is no apparent influence of increasing H_2O content of the melt between 7-12 wt. % on magnetite-melt partitioning.

Diffusion coefficients (D) for a wide range of cations in magnetite vary over 4 orders of magnitude. Diffusion coefficients at a given fO_2 generally increase in the order Cu > Co > Sc > V > Cr. Thus, Cu contents of magnetites are most susceptible to diffusive re-equilibration whereas the original content of slow diffusing elements, such as Cr should be best preserved. Plots of log D as a function of log fO_2 produce V-shaped trends for all the investigated elements, representing two different mechanisms of diffusion that depend on $(fO_2)^{-2/3}$ and $(fO_2)^{2/3}$, probably interstitial and vacancy mechanisms respectively. The preference for interstitial diffusion relative to vacancy diffusion is primarily controlled by the concentration of interstitials relative to vacancies in the lattice which is dictated by fO_2 via $3Fe^{2+} + 2/3\ O_2 \leftrightarrow 2Fe^{3+} + V_{Fe} + 1/3Fe_3O_4$. The minimum of the V-shaped trends in log D-log fO_2 space differs for the various cations. Lower valence cations have greater preference and rate of interstitial diffusion. Cations with higher charge density, lower magnetite-melt partition coefficient, and higher preference for octahedral coordination diffuse at a slower rate by a vacancy mechanism.

Various factors such as exsolution, alteration and impurities create complications and uncertainties when analysing natural Fe-Ti oxides with LA-ICP-MS. When analysing grains with strong exsolution, increasing the spot size above 30 μm adequately homogenises exsolution into the analysis. For the analysis of grains with exsolution, the internal standard for LA-ICP-MS can be determined using SEM-EDS by rastering the beam over an area including both exsolution lamellae and residual magnetite. Caution must be taken when interpreting magnetite chemistry using elements that are major components of possible inclusion phases. Analyses with significant contamination from mineral inclusions can be eliminated by visual screening of the laser ablation spectra and through studying scatter plots of elements that are major constituents of inclusion phases, but not typically present in Fe-Ti oxides at high concentrations. The use of GSD-1g, GSE-1g and NIST 610 as reference materials generates accurate results when using spot sizes greater than 25 μm.

In porphyry copper systems, hydrothermal magnetite typically contains Ti < 0.5 wt. %, whereas igneous magnetite generally contains greater than 1.5 wt. % Ti. For the various deposits studied, there are distinct breaks in the Ti content of magnetite, usually between 0.5 and 1.5 wt. % Ti. Normal distribution probability plots can be used, with the aid of petrographic observations, to discriminate the two types on a case-by-case basis. Nevertheless, in the majority of circumstances, a 1 wt. % threshold can effectively separate these two forms of magnetite. Discriminant projection analyses can be used to categorise various populations of hydrothermal magnetite using elements commonly detected using LA-ICP-MS. The discriminant plots are most effectively used in sequence, first classifying hydrothermal magnetite according to alteration style, then metal association of porphyry copper system, and finally to assess the fertility of Cu-

Au or Cu-Mo systems. The chemistry of igneous magnetite is readily modified during hydrothermal alteration, progressively altering towards that of hydrothermal magnetite. Thus, a large proportion of igneous magnetite in porphyry copper settings may not be diagnostic of the magmatic environment in which it originally crystallised. In order to conduct rigorous petrogenetic evaluations of magmatic conditions using magnetite chemistry, igneous magnetite should be targeted in unaltered volcanic rocks from the same time window as the expected or known porphyry system, or that present as inclusions within phases more resistant to hydrothermal alteration.

8.2 Future work

It was originally intended to primarily study the chemistry of igneous magnetite to interpret magmatic conditions conducive for the formation of porphyry copper deposits. However, it was not anticipated that the samples chosen would contain so little igneous magnetite relative to hydrothermal magnetite, leading to a redirection of the research focus. To better address what the key magmatic controls might be governing the formation of porphyry copper deposits, utilising the partition coefficients defined in this study, igneous magnetite should be targeted from unaltered volcanics from known porphyry belts or from barren terrains. The study by Fry (2017) (Appendix 4) makes a good start on such work, by studying the chemistry of igneous magnetite in volcanics spanning a wide time period prior to and after the formation of three giant porphyry systems in Central Chile (El Teniente, Rio Blanco-Los Bronces and Los Pelambres). However, these data needs further filtering according to the criteria presented in this thesis to eliminate data derived from grains with obvious signs of post-crystallisation alteration and significant exsolution. Ideally, more samples of unaltered volcanic rocks should be sourced from apparently barren (e.g. Japan and Lesser Antilles) and fertile (e.g. Central Chile and Tethyan) arcs to make effective comparisons of the barren and fertile magmatic settings. Moreover, a more powerful petrographic interpretation of the magmatic environment can be made by combining magnetite chemistry with other geochemical information, such as whole-rock chemistry and chemistry of other minerals, as well as geochronology, and also including petrographic constraints on the timing of magnetite crystallisation relative to other phases.

An oxybarometer based on thermodynamic relationships between magnetite-melt partitioning of Mg, Mn, Co, Ni, Zn and Sc and parameters including $a\mathrm{Fe_3O_4}$(spinel), $\mathrm{XFe^{2+}O}$(melt) and $\mathrm{XFe^{3+}O_{1.5}}$(melt) was developed but remains to be tested on natural samples. Similar to the recently developed oxybarometer by Arato and Audetat (2017a), the technique proposed here requires a partition coefficient to be determined and a prior estimate of the crystallisation temperature. A potential advantage of the oxybarometer developed here is that independent $f\mathrm{O_2}$

estimates can be calculated from partition coefficients for up to 6 different elements offering a means to cross-check the reliability of the results. Magnetite and melt inclusions preserved within quartz phenocrysts, so shielded from the effects of sub-solidus re-equilibration, could offer suitable natural samples to test the accuracy of this method. Moreover, samples where the fO_2 could be approximated using other methods of oxybarometry, such as 'two-oxide' barometry (e.g. Ghiorso and Evans, 2008) could be used to validate the accuracy of the oxybarometer based on thermodynamic relationships. If this technique proves to be successful, it could be applied to assess the importance of fO_2 in controlling the formation of porphyry copper deposits and to track the temporal evolution of fO_2 in arc magmas.

Diffusion is sufficiently rapid in magnetite such that diffusion profiles in igneous magnetite are unlikely to be useful in interpreting timescales of magmatic processes. However, at lower temperatures, diffusion gradients are likely to be preserved such that the timescales of hydrothermal activity could be assessed using diffusion coefficients reported here combined with estimates of the fO_2 and T. Importantly, separate estimates of timescales could be calculated for several cations to assess the reliability of the results obtained. The prolonged duration of magmatic-hydrothermal activity has been used to explain the vast Cu contents at El Teniente, the world's largest porphyry Cu deposit (Vry et al., 2010; Maskaev et al., 2004). Thus, the ability to trace the timescales of pulses of hydrothermal fluids using diffusion gradients in hydrothermal magnetite could aid in testing this hypothesis. A suitable example to test this technique would be where the distinct episodes of hydrothermal activity have previously been dated by an alternative high-precision technique, (e.g. Re-Os molybdenite dating – Spencer et al., 2015), so that the timescales calculated could be compared.

The chemistry of hydrothermal magnetite was used to develop discriminant plots that distinguish various populations of hydrothermal magnetite according to alteration association, porphyry system type (metal association), and degree of mineralisation (section 6.4.4.1). These discriminant plots could be further refined by incorporating more data into their development. Importantly, the plots developed to assess fertility require more data from background and altered barren samples for a more robust assessment. Alternative means of categorising level of mineralisation in the systems included in the dataset could also be investigated, for example using Cu grade instead of contained tonnage of Cu. Nevertheless, these discriminant plots show excellent promise as tools in mineral exploration, both to assess metal endowment and vector towards mineralisation. The factors responsible for the chemical distinctions in hydrothermal magnetite are difficult to interpret given the dearth of experiments investigating element partitioning under hydrothermal conditions. Thus, more hydrothermal experiments should be conducted to enable a better understanding of the processes controlling its mineral chemistry.

This would enable much better insights into the key processes necessary for the formation of giant porphyry copper deposits.

Acknowledgements

Firstly, I would like to express my thanks to my supervisor, Jamie Wilkinson, for taking me on as a PhD student, for providing funds for my research and for his continuous support and guidance throughout my work and in the writing of this thesis.

I am also extremely grateful to Andrew Berry and Hugh O'Neill for their considerable help and encouragement. Andrew Berry kindly facilitated and helped fund my visits to the RSES at ANU, provided experimental advice and held weekly progress meetings which were invaluable in ensuring I stayed on track. Hugh O'Neill also provided excellent advice, encouragement and feedback on my experimental work. In particular, the magnetite-bucket experiments were initially Hugh's suggestion, following a similar method, devised by him and Carl Spandler, for studying diffusion in olivine. I also had useful discussions with James Tolley with regard to his work investigating magnetite-melt partitioning in carbonatite systems.

During the experimental studies, I would like to thank Jack Nolan for providing the And-190 starting material, Antony Burnham and Helen Halse for assistance with operating the 1-atm furnace at Imperial College London and Dean Scott and Dave Clarke for providing training and assistance when using piston cylinder apparatus and 1-atm furnaces at ANU. James Tolley also provided assistance whilst conducting the magnetite-bucket experiments. Furthermore, Clara Wilkinson kindly donated the crystals of magnetite (Mt-1) which were used in the magnetite-bucket and piston cylinder experiments.

I am particularly grateful to the Natural History Museum (NHM) for providing free access to their analytical facilities, as well as to Andrew Berry for funding my analytical work at ANU. Without this, the volume of analytical data generated would have been significantly less. With regard to analytical work, I would like to thank Anton Kearsely for providing inductions and assistance in operating the SEM and John Spratt, particularly, who helped me set-up and operate the EPMA. At the NHM, my thanks go to Clara Wilkinson, Will Brownscombe and Elly Harman who assisted with operating the LA-ICP-MS, and Mike Jollands, Pete Tollan and James Tolley who assisted with operating the LA-ICP-MS at ANU. I am particularly thankful to Will for greatly improving the method for collection of LA-ICP-MS data at the NHM, including mapping coordinates between SEM and LA-ICP-MS, installation of automated analysis, and helping me develop customised spreadsheets specifically for processing my data. This greatly expanded the quantity of LA-ICP-MS data that I was able to collect during my PhD.

Rio Tinto Exploration provided a vast number of magnetite separates. In particular, I would like to express my gratitude to Paul Agnew, Alan Kobussen and Debora Araujo for allowing me to visit the Technology and Innovation Centre in Bundoora, Australia, for providing samples and for taking the time to discuss my work with me. The NHM collections also provided numerous samples and I would like to thank Helena Toman for helping me sift through the collections for suitable samples associated with porphyry copper systems.

I am grateful to George Fry for his excellent work on his MSci project which I supervised. His results were particularly interesting and from this work and discussions with George, I myself learnt a lot about the petrography and chemistry of magnetite in natural volcanic samples.

I would also like to thank all my fellow committee members within the SEG chapter at Imperial College London, particularly for their help in organising field trips, and especially that to Eastern Europe where I was able to collect a large number of samples for this work. I am also particularly grateful to all my colleagues at Imperial, in the LODE group, and at RSES for numerous fruitful discussions as well as providing support and enjoyment along the way.

I am grateful to the Imperial President's PhD scholarship scheme for supporting me financially and for providing additional funding each year for research costs. I would also like to thank various bodies, namely, IOM3, Australian Bicentennial Research Grant, European Mineralogical Union and SEG who provided further financial grants to support my research, fund my attendance at conferences and make it possible for me to conduct relevant fieldwork.

In addition to academic support, I would like to thank my family and my friends for keeping me motivated, being there for me when I had problems, and maintaining me in good spirits.

References

Aggarwal, S. and Dieckmann, R. (2002). Point defects and cation tracer diffusion in $(Ti_xFe_{1-x})_{3-\delta}O_4$ 1. Non-stoichiometry and point defects. Physics and Chemistry of Minerals 29: 695-706.

Andersen, D. and Lindsley, D. (1985). New (and final!) models for the Ti-magnetite/ilmenite geothermometer and oxygen barometer (abstract). AGU 1985 Spring Meeting Eos Transactions. San Francisco, USA.

Annen, C., et al. (2006). The genesis of intermediate and silicic magmas in deep crustal hot zones. Journal of Petrology 47: 505-539.

Arancibia, O.N. and Clark, A.H. (1996). Early magnetite–amphibole–plagioclase alteration-mineralization in the Island Copper porphyry copper–gold–molybdenum deposit, British Columbia. Economic Geology 91: 402–438.

Arató, R. and Audétat, A. (2017a). Experimental calibration of a new oxybarometer for silicic magmas based on vanadium partitioning between magnetite and silicate melt. Geochimica et Cosmochimica Acta 209: 284-295.

Arató, R. and Audétat, A. (2017b). Vanadium magnetite–melt oxybarometry of natural, silicic magmas: a comparison of various oxybarometers and thermometers. Contributions to Mineralogy and Petrology 7: 1-22.

Arculus, R. J. (1985). Oxidation status of the mantle - past and present. Annual Review of Earth and Planetary Sciences 13: 75-95.

Audetat, A., et al. (2000). Magmatic-hydrothermal evolution in a fractionating granite: A microchemical study of the Sn-WF-mineralized Mole Granite (Australia). Geochimica et Cosmochimica Acta 64: 3373-3393.

Audétat A. and Simon A. C. (2013). Magmatic controls on porphyry Cu genesis. In Geology and genesis of major copper deposits and districts of the world: a tribute to Richard Sillitoe (J. W. Hedenquist, M. Harris and F. Camus Ed.). Society of Economic Geologists, Special Publication 16: 553-572.

Audetat, A., et al. (2008). The Composition of Magmatic-Hydrothermal Fluids in Barren and Mineralized Intrusions. Economic Geology 103: 877-908.

Ballard, J. R., et al. (2002). Relative oxidation states of magmas inferred from Ce(IV)/Ce(III) in zircon: application to porphyry copper deposits of northern Chile. Contributions to Mineralogy and Petrology 144: 347-364.

Becker, K., et al. (1990). Mössbauer study of high-temperature diffusion in magnetite. Hyperfine Interactions 56: 1431-1435.

Belousova, E., et al. (2002). Apatite as an indicator mineral for mineral exploration: trace-element compositions and their relationship to host rock type. Journal of Geochemical Exploration 76: 45-69.

Bergantz, G.W. and Dowes, R. (1994). Aspects of magma generation and ascent in continental lithosphere. International Geophysics 57: 291-317.

Berry, A. J., et al. (2006). The effect of composition on Cr^{2+}/Cr^{3+} in silicate melts. American Mineralogist 91: 1901-1908.

Berzina, A. (2012). Platinum-group Element Geochemistry of Magnetite from Porphyry-Cu-Mo Deposits and their Host Rocks (Siberia, Russia). Acta Geologica Sinica (English Edition) 86: 106-117.

Bird, M. L. (1971). Distribution of trace elements in olivines and proxenes-an experimental study. PhD Thesis, University of Missouri-Rolla.

Blevin, P. L. (2004). Redox and compositional parameters for interpreting the granitoid metallogeny of eastern Australia: Implications for gold-rich ore systems. Resource Geology 54: 241-252.

Blundy, J., et al. (2006). Magma heating by decompression-driven crystallization beneath andesite volcanoes. Nature 443: 76-80.

Blundy, J., et al. (2015). Generation of porphyry copper deposits by gas-brine reaction in volcanic arcs. Nature Geoscience 8: 235-240.

Blundy, J. and Wood, B. (1994). Prediction of crystal-melt partition-coefficients from elastic-moduli. Nature 372: 452-454.

Bouzari, F., et al. (2016). Hydrothermal alteration revealed by apatite luminescence and chemistry: a potential indicator mineral for exploring covered porphyry copper deposits. Economic Geology 111: 1397-1410.

Brady, J. B. and Cherniak, D. J. (2010). Diffusion in minerals: an overview of published experimental diffusion data. Reviews in Mineralogy and Geochemistry 72: 899-920.

Brandon, A. D. and Draper, D. S. (1996). Constraints on the origin of the oxidation state of mantle overlying subduction zones: An example from Simcoe, Washington, USA. Geochimica et Cosmochimica Acta 60: 1739-1749.

Brown, M. (1994). The generation, segregation, ascent and emplacement of granite magma - the migmatite-to-crustally-derived-granite connection in thickened orogens. Earth-Science Reviews 36: 83-130.

Buddington, A.F. and Lindsley, D.H. (1964). Iron-titanium oxide minerals and synthetic equivalents. Journal of Petrology 5: 310-357.

Buret, Y., et al. (2016). From a long-lived upper-crustal magma chamber to rapid porphyry copper emplacement: Reading the geochemistry of zircon crystals at Bajo de la Alumbrera (NW Argentina). Earth and Planetary Science Letters 450: 120-131.

Burnham, A., et al. (2015). The oxidation state of europium in silicate melts as a function of oxygen fugacity, composition and temperature. Chemical Geology 411: 248-259.

Burnham, A. D. and Berry, A. J. (2012). An experimental study of trace element partitioning between zircon and melt as a function of oxygen fugacity. Geochimica et Cosmochimica Acta 95: 196-212.

Canil, D. (1999). Vanadium partitioning between orthopyroxene, spinel and silicate melt and the redox states of mantle source regions for primary magmas. Geochimica et Cosmochimica Acta 63: 557-572.

Candela, P.A. and Piccoli, P.M. (2005). Magmatic processes in the development of porphyry-type ore systems. Economic Geology 100th Anniversary Volume: 25-37.

Canil, D., et al. (2016). Trace elements in magnetite from porphyry Cu–Mo–Au deposits in British Columbia, Canada. Ore Geology Reviews 72:1116-1128.

Carew, M.J., et al. (2006). Trace element geochemistry of magnetite and pyrite in Fe oxide (±Cu–Au) mineralised systems: insights into the geochemistry of ore-forming fluids. Geochimica Et Cosmochimica Acta 70: A83.

Carroll, M. R. and Rutherford, M. J. (1988). Sulfur speciation in hydrous experimental glasses of varying oxidation-state - results from measured wavelength shifts of sulfur x-rays. American Mineralogist 73: 845-849.

Cherniak, D., et al. (2007). Ti diffusion in quartz. Chemical Geology 236: 65-74.

Cherniak, D. and Watson, E. B. (1994). A study of strontium diffusion in plagioclase using Rutherford backscattering spectroscopy. Geochimica et Cosmochimica Acta 58: 5179-5190

Chou, I. M. (1986). Permeability of precious metals to hydrogen at 2kb total pressure and elevated temperatures. American Journal of Science 286: 638-658.

Cline, J. S. and Bodnar, R. J. (1991). Can economic porphyry copper mineralization be generated by a typical calc-alkaline melt. Journal of Geophysical Research-Solid Earth and Planets 96: 8113-8126.

Cline, Jean S., (1995). Genesis of porphyry copper deposits: The behavior of water, chloride, and copper in crystallizing melts, In Porphyry copper deposits of the American Cordillera (F.W., and Bolm, J.G., Ed. 20). Tucson: Arizona Geological Society.

Cook, N., et al. (2016). Trace element analysis of minerals in magmatic-hydrothermal ores by laser ablation inductively-coupled plasma mass spectrometry: Approaches and opportunities. Minerals 6: 111.

Cooke, D.R., et al. (2013) Geochemistry of porphyry deposits, In Treatise on Geochemistry 2nd Edition. Oxford: Elsevier-Pergamon.

Cooke, D. R., et al. (2014). New advances in detecting the distal geochemical footprints of porphyry systems-epidote mineral chemistry as a tool for vectoring and fertility assessments. In Building Exploration Capability for the 21st century, (HC Golden Ed.), Colorado, USA, Colt Print Services.

Cooke, D.R. et al. (2012). Hydrothermal Features of the Central Wasatch Mountains, Utah. Unpublished report for AMIRA P1060 project, CODES The Australian Research Council Centre for Excellence in Ore Deposits.

Core, D. P., et al. (2006). Unusually Cu-rich magmas associated with giant porphyry copper deposits: Evidence from Bingham, Utah. Geology 34: 41-44.

Cornell, R.M. and Schwertmann, U. (2003). The iron oxides: Structure, properties, reactions, occurrences, and uses, 2 ed. London: Wiley-VCH.

Crank, J. (1975). Diffusion in a plane sheet. The mathematics of diffusion 2: 44-68.

Dare, S. A. S., et al. (2012). Variation in trace element content of magnetite crystallized from a fractionating sulfide liquid, Sudbury, Canada: Implications for provenance discrimination. Geochimica et Cosmochimica Acta 88: 27-50.

Dare, S. A. S., et al. (2014). Trace elements in magnetite as petrogenetic indicators. Mineralium Deposita 49: 785-796.

Davis, J. (2002). Statistics and data analysis in geology. New York: John Wiley & Sons Inc.

Dieckmann, R. (1982). Defects and Cation Diffusion in Magnetite (IV): Nonstoichiometry and Point Defect Structure of Magnetite ($Fe_{3-\delta}O_4$). Berichte der Bunsengesellschaft für physikalische Chemie 86: 112-118.

Dieckmann, R. (1998). Point defects and transport in non-stoichiometric oxides: solved and unsolved problems. Journal of Physics and Chemistry of Solids 59: 507-525.

Dieckmann, R., et al. (1978). Defects and Cation Diffusion in Magnetite (III.) Tracer diffusion of Foreign Tracer Cations as a Function of Temperature and Oxygen Potential. Berichte der Bunsengesellschaft für physikalische Chemie 82: 778-783.

Dieckmann, R. and Schmalzried, H. (1977). Defects and cation diffusion in magnetite (I). Berichte der Bunsengesellschaft für physikalische Chemie 81: 344-347.

Dieckmann, R. and Schmalzried, H. (1986). Defects and cation diffusion in magnetite (VI): point defect relaxation and correlation in cation tracer diffusion. Berichte der Bunsengesellschaft für physikalische Chemie 90: 564-575.

Dohmen, R., et al. (2002). Si and O diffusion in olivine and implications for characterizing plastic flow in the mantle. Geophysical Research Letters 29.

Doyle, C. D. and Naldrett, A. J. (1987). Ideal mixing of divalent cations in mafic magma. II. The solution of NiO and the partitioning of nickel between coexisting olivine and liquid. Geochimica et Cosmochimica Acta 51: 213-219.

Dromgoole, E.L. and Pasteris, J.D. (1987). Interpretation of the sulphide assemblages in a suite of xenoliths from Kilbourne Hole, New Mexico. GSA Special Papers, 215: 25-46.

Droop, G. T. R. (1987). A general equation for estimating Fe-3+ concentrations in ferromagnesian silicates and oxides from microprobe analyses, using stoichiometric criteria. Mineralogical Magazine 51: 431-435.

Duffy, J. A. (1993). A review of optical basicity and its applications to oxidic systems. Geochimica et Cosmochimica Acta 57: 3961-3970.

Dupuis, C. and Beaudoin G. (2011). Discriminant diagrams for iron oxide trace element fingerprinting of mineral deposit types. Mineralium Deposita 46: 319-335.

Ewart, A. and Griffin W. L. (1994). Application of Proton-Microprobe Data to Trace-Element Partitioning in Volcanic-Rocks. Chemical Geology 117: 251-284.

Freer, R. and Hauptman Z. (1978). An experimental study of magnetite-titanomagnetite interdiffusion. Physics of the Earth and Planetary Interiors 16: 223-231.

Frost, B.R. and Lindsley, D.H. (1991) Occurrence of iron-titanium oxides in igneous rocks, In Oxide Minerals: Petrological and Magnetic Significance (D. H. Lindsley Ed.). Washington D. C.: Mineral. Soc. Am.

Frost, B. R. (1991). Introduction to oxygen fugacity and its petrologic importance. In Oxide Minerals: Petrological and Magnetic Significance. Washington D. C., Mineral. Soc. Am.

Frost, B. R., et al. (1988). Fe-Ti oxide-silicate equilibria; assemblages with fayalitic olivine. American Mineralogist 73: 727-740.

Fry, G. (2017). Trace Element Chemistry of Magnetite as an Indicator of the Metallogenic Fertility of Arc Magmas. MSci Thesis, Imperial College London.

Ghiorso, M. S. and Evans, B. W. (2008). Thermodynamics of rhombohedral oxide solid solutions and a revision of the Fe-Ti two-oxide geothermometer and oxygen-barometer. American Journal of Science 308: 957-1039.

Ghiorso, M. S. and Sack, R. O. (1995). Chemical mass transfer in magmatic processes IV. A revised and internally consistent thermodynamic model for the interpolation and extrapolation of liquid-solid equilibria in magmatic systems at elevated temperatures and pressures. Contributions to Mineralogy and Petrology 119: 197-212.
Goldschmidt, V.M. (1954). Geochemistry. Oxford: Oxford University Press.

Greene, A. R., et al. (2006). A detailed geochemical study of island arc crust: the Talkeetna Arc section, south-central Alaska. Journal of Petrology 47: 1051-1093.

Griffin, W.L., et al. (1991). Chromite macrocrysts in kimberlites and lamproites: geochemistry and origin (abstract). 5th Int. Kimberlite Conf., Araxa.

Grigsby, J. D. (1990). Detrital magnetite as a provenance indicator. Journal of Sedimentary Research 60.

Hack, A. C. and Mavrogenes, J. A. (2006). A cold-sealing capsule design for synthesis of fluid inclusions and other hydrothermal experiments in a piston-cylinder apparatus. American Mineralogist 91: 203-210.

Haggerty, S.E. (1976) Oxidation of Opaque Mineral Oxide in Basalts. In Oxide Minerals (Douglas Rumble Ed.). Washington D.C.: Mineral. Soc. Am.

Halse, H. (2014). Using synchrotron radiation to determine the oxidation state of uranium in magmas. PhD Thesis, Imperial College London.

Halter, W., et al. (2005). Magma evolution and the formation of porphyry Cu-Au ore fluids: evidence from silicate and sulfide melt inclusions. Mineralium Deposita 39: 845-863.

Halter, W. E., et al. (2002). The origin of Cu/Au ratios in porphyry-type ore deposits. Science 296: 1844-1846.

Hanchar, J. M. and Watson, E. B. (2003). Zircon saturation thermometry. Reviews in Mineralogy and Geochemistry 53: 89-112.

Harlov, D. E. (2015). Apatite: A fingerprint for metasomatic processes. Elements 11: 171-176.

Hattori, K. (1997). Occurrence and origin of sulfide and sulfate in the 1991 Mount Pinatubo eruption, In Fire and mud: Eruptions and lahars of Mount Pinatubo, Philippines (Newhall, C.G., and Punongbayan, R.S. Ed.). Seattle: USGS.

Hattori, K. H. and Keith, J. D. (2001). Contribution of mafic melt to porphyry copper mineralization: evidence from Mount Pinatubo, Phillipines, and Bingham Canyon, Utah, USA. Minerlalium Deposita 36: 799-806.

Hedenquist, J. W. and Lowenstern, J. B. (1994). The role of magmas in the formation of hydrothermal ore-deposits. Nature 370: 519-527.

Heinrich, C. A., et al. (2004). Magmatic vapor contraction and the transport of gold from the porphyry environment to epithermal ore deposits. Geology 32: 761-764.

Hemingway, B. (1990). Thermodynamic properties for bunsenite, NiO, magnetite, Fe_3O_4, and hematite, Fe_2O_3, with comments on selected oxygen buffer reactions. American Mineralogist 75: 781-790.

Henderson, P., et al. (1985). Structural controls and mechanisms of diffusion in natural silicate melts. Contributions to Mineralogy and Petrology 89: 263-272.

Henley, R.E. and Berger, B.R. (2013). Nature's refineries – Metals and metalloids in arc volcanoes. Earth Science Reviews 125: 146-170.

Hildreth, W. and Moorbath, S. (1988). Crustal contributions to arc magmatism in the Andes of central Chile. Contributions to Mineralogy and Petrology 98: 455-489.

Himmel, L., et al. (1953). Self-diffusion of iron in iron oxides and the Wagner theory of oxidation. Trans. Aime 197: 827-843.

Holzheid, A., et al. (1994). The effect of oxygen fugacity and temperature on solubilities of nickel, cobalt, and molybdenum in silicate melts. Geochimica et Cosmochimica Acta 58: 1975-1981.

Horn, I., et al. (1994). Experimentally determined partitioning of high-field strength-elements and selected transition-elements between spinel and basaltic melt. Chemical Geology 117: 193-218.

Hu, H., et al. (2015). Reequilibration processes in magnetite from iron skarn deposits. Economic Geology 110: 1-8.

Ilton, E. S. and Eugster, H. P. (1989). Base metal exchange between magnetite and a chloride-rich hydrothermal fluid. Geochimica et Cosmochimica Acta 53: 291-301.

Ishihara, S., et al. (1981). Comparative study of Mesozoic granitoids and related W-Mo mineralization in southern Korea and southwestern Japan. Mining Geology 31: 311-320.

Jacob, K., et al. (1977). Activities in the spinel solid solution, phase equilibria and thermodynamic properties of ternary phases in the system Cu-Fe-0. Metallurgical Transactions B8: 451-460.

Jakobsson, S. (2012). Oxygen fugacity control in piston-cylinder experiments. Contributions to Mineralogy and Petrology 164: 397-406.

Jenner, F. E., et al. (2010). The Magnetite Crisis in the Evolution of Arc-related Magmas and the Initial Concentration of Au, Ag and Cu. Journal of Petrology 51: 2445-2464.

John, D. A. (1989). Geologic setting, depths of emplacement, and regional distribution of fluid inclusions in intrusions of the central Wasatch Mountains, Utah. Economic Geology 84: 386-409.

John, D. A. (1997). Geologic setting and characteristic of mineral deposits in the central Wasatch Mountains, Utah. Society of Economic Geologists guidebook series 29: 11-33.

Johnson, M. C. and Rutherford, M. J. (1989). Experimental calibration of the aluminum-in-hornblende geobarometer with application to Long Valley caldera (California) volcanic rocks. Geology 17: 837-841.
Jugo, P. J. (2009). Sulfur content at sulfide saturation in oxidized magmas. Geology 37: 415-418.

Jugo, P. J., et al. (2010). Sulfur K-edge XANES analysis of natural and synthetic basaltic glasses: Implications for S speciation and S content as function of oxygen fugacity. Geochimica et Cosmochimica Acta 74: 5926-5938.

Katayama, I., et al. (1980). Thermodynamic Study on Fe_3O_4--$CuFe_2O_4$ System by E. M. F. Method. Technology Reports of Osaka University 30: 385-390.

Katkov, A. and Lykasov, A. (2003). Spinel phase relations in the Fe_3O_4–$CuFe_2O_4$ system. Inorganic materials 39: 171-174.

Kay, R. W. (1980). Volcanic arc magmas - implications of a melting-mixing model for element recycling in the crust-upper mantle system. Journal of Geology 88: 497-522.

Keith, J. D., et al. (1997). The role of magmatic sulfides and mafic alkaline magmas in the Bingham and Tintic mining districts, Utah. Journal of Petrology 38: 1679-1690.

Kitayama, K. (1987). Phase equilibria in the Fe – Nb - O system at 1200° C. Journal of Solid State Chemistry 69: 101-108.

Klemm, L. M., et al. (2007). Hydrothermal evolution of the El Teniente deposit, Chile: Porphyry Cu-Mo ore deposition from low-salinity magmatic fluids. Economic Geology 102: 1021-1045.

Knipping, J. L., et al. (2015). Trace elements in magnetite from massive iron oxide-apatite deposits indicate a combined formation by igneous and magmatic-hydrothermal processes. Geochimica et Cosmochimica Acta 171: 15-38.

Kohn, S. C. and Schofield, P. F. (1994). The Importance of Melt Composition in Controlling Trace-Element Behavior - an Experimental-Study of Mn and Zn Partitioning between Forsterite and Silicate Melts. Chemical Geology 117: 73-87.

Kress, V. C. and Carmichael, I. S. E. (1991). The compressibility of silicate liquids containing Fe_2O_3 and the effect of composition, temperature, oxygen Fugacity and pressure on their redox states. Contributions to Mineralogy and Petrology 108: 82-92.

Kushiro, I. and Mysen, B. O. (2002). A possible effect of melt structure on the Mg-Fe^{2+} partitioning between olivine and melt. Geochimica et Cosmochimica Acta 66: 2267-2272.

Lee, C. T. A., et al. (2005). Similar V/Sc systematics in MORB and arc basalts: Implications for the oxygen fugacities of their mantle source regions. Journal of Petrology 46: 2313-2336.

Lee, C. T. A., et al. (2012). Copper Systematics in Arc Magmas and Implications for Crust-Mantle Differentiation. Science 336: 64-68.

Lee, C. T. A., et al. (2010). The redox state of arc mantle using Zn/Fe systematics. Nature 468: 681-685.

Leeman, W. P. (1974). Experimental determination of the partitioning of divalent cations between olivine and basaltic liquid. PhD Thesis, University of Oregon.

Lepage, L. D. (2003). ILMAT: an Excel worksheet for ilmenite–magnetite geothermometry and geobarometry. Computers & Geosciences 29: 673-678.

Lindsley, D.H. (1976) The crystal chemistry and structure of oxide minerals as exemplified by the Fe-Ti oxides. In Oxide Minerals (Douglas Rumble Ed.). Washington D.C.: Mineral. Soc. Am.

Lindsley, D. H. and Frost, B. R. (1992). Equilibria among Fe-Ti oxides, pyroxenes, olivine, and quartz; Part I, Theory. American Mineralogist 77: 987-1003.

Lindstrom, D.J. (1976). Experimental study of the partitioning of the transition metals between clinopyroxene and coexisting silicate liquids. PhD Thesis, University of Oregon

Linnen, R. L., et al. (1996). The combined effects of fO_2 and melt composition on SnO_2 solubility and tin diffusivity in haplogranitic melts. Geochimica et Cosmochimica Acta 60: 4965-4976.

Liu X., et al. (2014). Partitioning of copper between olivine, orthopyroxene, clinopyroxene, spinel, garnet and silicate melts at upper mantle conditions. Geochimica Et Cosmochimica Acta 125: 1-22.

Liu, X., et al. (2015). Partitioning of Cu between mafic minerals, Fe–Ti oxides and intermediate to felsic melts." Geochimica et Cosmochimica Acta 151: 86-102.

Liu, Y., et al. (2007). Sulfur concentration at sulfide saturation (SCSS) in magmatic silicate melts. Geochimica et Cosmochimica Acta 71: 1783-1799.

Loader, M. A., et al. (2017). The effect of titanite crystallisation on Eu and Ce anomalies in zircon and its implications for the assessment of porphyry Cu deposit fertility. Earth and Planetary Science Letters 472: 107-119.

Longerich, H. P., et al. (1996). Inter-laboratory note. Laser ablation inductively coupled plasma mass spectrometric transient signal data acquisition and analyte concentration calculation." Journal of Analytical Atomic Spectrometry 11: 899-904.

Loucks, R. (2014). Distinctive composition of copper-ore-forming arcmagmas. Australian Journal of Earth Sciences 61: 5-16.

Lowell, J. D. and Guilbert, J. M. (1970). Lateral and vertical alteration-mineralization zoning in porphyry ore deposits. Economic Geology 65: 373-408.

Lu, F. and Dieckmann, R. (1992). Point defects and cation tracer diffusion in (Co, Fe, Mn)$_{3-\delta}$O$_4$ spinels: I. Mixed spinels (Co$_x$Fe$_{2y}$Mn$_y$)$_{3-\delta}$O$_4$. Solid State Ionics 53: 290-302.

Luhr, J. F. and Carmichael, I. S. (1980). The colima volcanic complex, Mexico. Contributions to Mineralogy and Petrology 71: 343-372.

Makvandi, S., et al. (2015). The surface texture and morphology of magnetite from the Izok Lake volcanogenic massive sulfide deposit and local glacial sediments, Nunavut, Canada: Application to mineral exploration. Journal of Geochemical Exploration 150: 84-103.

Mallmann, G. and O'Neill, H. S. C. (2009). The Crystal/Melt Partitioning of V during Mantle Melting as a Function of Oxygen Fugacity Compared with some other Elements (Al, P, Ca, Sc, Ti, Cr, Fe, Ga, Y, Zr and Nb). Journal of Petrology 50: 1765-1794.

Mao, M., et al. (2016). Apatite trace element compositions: A robust new tool for mineral exploration. Economic Geology 111: 1187-1222.

Maskaev, V., et al. (2004). New chronology for El Teniente, Chilean Andes, from U–Pb, ^{40}Ar/^{39}Ar, Re–Os and fission-track dating: implications for the evolution of a supergiant porphyry Cu-Mo deposit. Andean Metallogeny: New Discoveries, Concepts and Updates. Society of Economic Geologists, SEG Special Publication 11: 15-54.

Mavrogenes J.A. and O'Neill, H.S.C. (1999). The relative effects of pressure, temperature and oxygen fugacity on the solubility of sulfide in mafic magmas. Geochimica Et Cosmochimica Acta 63: 1173-1180.

Meinert, L. D. (1987). Skarn zonation and fluid evolution in the Groundhog Mine, Central mining district, New Mexico. Economic Geology 82: 523-545.

Mercer, C. N., et al. (2015). Time scales of porphyry Cu deposit formation: insights from titanium diffusion in quartz. Economic Geology 110: 587-602.

Metrich, N. and Clocchiatti, R. (1996). Sulfur abundance and its speciation in oxidized alkaline melts. Geochimica et Cosmochimica Acta 60: 4151-4160.

Meyer, C. and Hemley, J. (1967). Geochemistry of hydrothermal ore deposits., New York: Holt, Rinehart and Winston

Morimoto, N., et al. (1988). Nomenclature of pyroxenes. American Mineralogist 73: 1123-1133.

Mungall, J. E. (2002). Roasting the mantle: Slab melting and the genesis of major Au and Au-rich Cu deposits. Geology 30: 915-918.

Muntean, J. L. and Einaudi, M. T. (2000). Porphyry gold deposits of the Refugio district, Maricunga belt, northern Chile. Economic Geology 95: 1445-1472.

Mysen, B. (2007). Partitioning of calcium, magnesium, and transition metals between olivine and melt governed by the structure of the silicate melt at ambient pressure. American Mineralogist 92: 844-862.

Mysen, B. (2012). High-pressure and high-temperature titanium solution mechanisms in silicate-saturated aqueous fluids and hydrous silicate melts. American Mineralogist 97: 1241-1251.
Nadoll, P. (2011). Geochemistry of magnetite from hydrothermal ore deposits and host rocks– Case studies from the Proterozoic Belt Supergroup, Cu-Mo-porphyry+ skarn and Climax-Mo deposits in the western United States. PhD Thesis, University of Otago.

Nadoll, P., et al. (2014). The chemistry of hydrothermal magnetite: a review. Ore Geology Reviews 61: 1-32.

Nadoll, P. and Koenig, A. E. (2011). LA-ICP-MS of magnetite: methods and reference materials. Journal of Analytical Atomic Spectrometry 26: 1872-1877.

Nadoll, P., et al. (2012). Geochemistry of magnetite from hydrothermal ore deposits and host rocks of the Mesoproterozoic Belt Supergroup, United States. Economic Geology 107: 1275-1292.

Nadoll, P., et al. (2015). Geochemistry of magnetite from porphyry Cu and skarn deposits in the southwestern United States. Mineralium Deposita 50: 493.

Nielsen, R. L. and Beard, J. S. (2000). Magnetite-melt HFSE partitioning. Chemical Geology 164: 21-34.

Nielsen, R. L., et al. (1994). Major-element and trace-element magnetite-melt equilibria. Chemical Geology 117(1-4): 167-191.

Ockwig, N. W. and Nenoff, T. M. (2007). Membranes for hydrogen separation. Chemical Reviews 107: 4078-4110.

Ohmoto, H. (2003). Nonredox transformations of magnetite-hematite in hydrothermal systems. Economic Geology 98: 157-161.

O'Neill, H. S. C. and Berry, A. J. (2006). Activity coefficients at low dilution of CrO, NiO and CoO in melts in the system CaO-MgO-Al_2O_3-SiO_2 at 1400 degrees C: Using the thermodynamic behaviour of transition metal oxides in silicate melts to probe their structure. Chemical Geology 231: 77-89.

O'Neill, H. S. C., et al. (2008). The solubility and oxidation state of tungsten in silicate melts: implications for the comparative chemistry of W and Mo in planetary differentiation processes. Chemical Geology 255: 346-359.

O'Neill, H. S. C. and Eggins, S. M. (2002). The effect of melt composition on trace element partitioning: an experimental investigation of the activity coefficients of FeO, NiO, CoO, MoO2 and MoO3 in silicate melts. Chemical Geology 186: 151-181.

O'Neill, H. C., and Mavrogenes, J. A. (2002). The sulfide capacity and the sulphur content at sulfide saturation of silicate melts at 1400°C and 1 bar. Journal of Petrology 43: 1049-1087.

O'Neill HSC and Navrotsky, A. (1983). Simple spinels; crystallographic parameters, cation radii, lattice energies, and cation distribution. American Mineralogist 68: 181-194

O'Neill, H. S. C. and Navrotsky, A. (1984). Cation distributions and thermodynamic properties of binary spinel solid solutions. American Mineralogist 69: 733-753.

O'Neill, H. S. C. and Pownceby, M. I. (1993). Thermodynamic data from redox reactions at high temperatures. II. The MnO-Mn_3O_4 oxygen buffer, and implications for the thermodynamic properties of MnO and Mn_3O_4. Contributions to Mineralogy and Petrology 114: 315-320.

O'Neill, H. S. C. and Wall, V. (1987). The Olivine—Orthopyroxene—Spinel oxygen geobarometer, the nickel precipitation curve, and the oxygen fugacity of the Earth's Upper Mantle. Journal of Petrology 28: 1169-1191.

Onuma, N., et al. (1968). Trace element partition between two pyroxenes and the host lava. Earth and Planetary Science Letters 5: 47-51.

Papike, J. J., et al. (2005). Comparative planetary mineralogy: Valence state partitioning of Cr, Fe, Ti, and V among crystallographic sites in olivine, pyroxene, and spinel from planetary basalts. American Mineralogist 90: 277-290.

Parkinson, I. J. and Arculus, R. J. (1999). The redox state of subduction zones: insights from arc-peridotites. Chemical Geology 160: 409-423.

Pasteris, J. D. (1996). Mount Pinatubo volcano and ''negative'' porphyry copper deposits. Geology 24: 1075-1078.

Pecoits, E., et al. (2009). Petrography and geochemistry of the Dales Gorge banded iron formation: Paragenetic sequence, source and implications for palaeo-ocean chemistry. Precambrian Research 172: 163-187.

Pisiak, L., et al. (2017). Magnetite as an Indicator Mineral in the Exploration of Porphyry Deposits: A Case Study in Till near the Mount Polley Cu-Au Deposit, British Columbia, Canada. Economic Geology 112: 919-940.

Prowatke, D. and Klemme, S. (2006a). Rare earth element partitioning between titanite and silicate melts: Henry's law revisited. Geochimica et Cosmochimica Acta 70: 4997-5012.

Prowatke, D. and Klemme, S. (2006b). Trace element partitioning between apatite and silicate melts. Geochimica et Cosmochimica Acta 70: 4513-4527.

Rapp, J. F. et al. (2010). Extremely high solubility of rutile in chloride and fluoride-bearing metamorphic fluids: An experimental investigation. Geology 38:323-326.

Razjigaeva, N. and Naumova V. (1992). Trace element composition of detrital magnetite from coastal sediments of northwestern Japan Sea for provenance study. Journal of Sedimentary Research 62: 802-809.

Redmond, P., et al. (2004). Copper deposition by fluid cooling in intrusion-centered systems: New insights from the Bingham porphyry ore deposit, Utah. Geology 32: 217-220.

Reubi, O. and Blundy, J. (2009). A dearth of intermediate melts at subduction zone volcanoes and the petrogenesis of arc andesites. Nature 461: 1269-1273.

Richards, J.P. (2003). Tectono-magmatic precursors for porphyry Cu-(Mo-Au) deposit formation. Economic Geology 98: 1515-1533.

Richards, J. P., et al. (1997). Fluid chemistry and processes at the Porgera gold deposit, Papua New Guinea. Mineralium Deposita 32: 119-132.

Richards, J. P., et al. (2013). Geology, geochemistry, geochronology, and economic potential of Neogene volcanic rocks in the Laguna Pedernal and Salar de Aguas Calientes segments of the Archibarca lineament, northwest Argentina. Journal of Volcanology and Geothermal Research 258: 47-73.

Richards, J. P. (2013). Giant ore deposits formed by optimal alignments and combinations of geological processes. Nature Geoscience 6: 911-916.

Richards, J. P. (2015). The oxidation state, and sulfur and Cu contents of arc magmas: implications for metallogeny. Lithos 233: 27-45.

Richards, J. P., et al. (2012). High Sr/Y Magmas Reflect Arc Maturity, High Magmatic Water Content, and Porphyry Cu +/- Mo +/- Au Potential: Examples from the Tethyan Arcs of Central and Eastern Iran and Western Pakistan. Economic Geology 107: 295-332.

Richards, J. P., et al. (2006). The late Miocene–Quaternary Antofalla volcanic complex, southern Puna, NW Argentina: protracted history, diverse petrology, and economic potential. Journal of Volcanology and Geothermal Research 152: 197-239.

Righter, K., et al. (2006). Partitioning of Ni, Co and V between spinel-structured oxides and silicate melts: Importance of spinel composition. Chemical Geology 227: 1-25.

Ringwood, A.E. (1977). Petrogenesis in island arc systems. Maurice Ewing Series 1: 311-324.

Ripley, E. M. and Brophy, J. G. (1995). Solubility of copper in a sulfur-free mafic melt. Geochimica et Cosmochimica Acta 59: 5027-5030.

Rohrlach, B.D. & Loucks, R.R. (2005). Multi-million-year cyclic ramp-up of volatiles in a lower crustal magma reservoir trapped below the Tampakan copper-gold deposit by Mio-Pliocene crustal compression in the Southern Philippines, In T.T. Porter, ed., Super porphyry copper and gold deposits – a global perspective. Adelaide: PGC publishing.

Rousseeuw, P. J. and Leroy, A. M. (1988). A robust scale estimator based on the shortest half. Statistica Neerlandica 42: 103-116.

Rowe, M. C., et al. (2009). Subduction Influence on Oxygen Fugacity and Trace and Volatile Elements in Basalts Across the Cascade Volcanic Arc. Journal of Petrology 50: 61-91.

Rusk, B. G., et al. (2008). Trace elements in hydrothermal quartz: Relationships to cathodoluminescent textures and insights into vein formation. Geology 36: 547-550.
Rusk, B.G., et al. (2009). Barren magnetite breccias in the Cloncurry region, Australia; comparisons to IOCG deposits (abstact). 10th Biennial SGA Meeting of the Society for Geology Applied to Mineral Deposits, Townsville, Australia.

Rusk, B. G., et al. (2004). Compositions of magmatic hydrothermal fluids determined by LA-ICP-MS of fluid inclusions from the porphyry copper–molybdenum deposit at Butte, MT. Chemical Geology 210: 173-199.

Sarbas, B. and Nohl, U. (2008). The GEOROC database as part of a growing geoinformatics network (abstract). Geoinformatics Conference, Potsdam, Germany.

Schilling, F. R. and Partzsch, G. M. (2001). Quantifying partial melt fraction in the crust beneath the Central Andes and the Tibetan plateau. Physics and Chemistry of the Earth Part a-Solid Earth and Geodesy 26: 239-246.

Schmalzried, H. (1962). The self-diffusion of Fe in magnetite in relation to the electron distribution in Fe_3O_4 and Co_3O_4. Z Physik Chem NF 31:184-197.

Schneider, C. A., et al. (2012). NIH Image to ImageJ: 25 years of image analysis. Nature methods 9: 671-675.

Seedorff, E., et al. (2005). Porphyry deposits: Characteristics and origin of hypogene features. Economic Geology 100th Anniversary Volume: 251-298.

Seo, J. H., et al. (2012). Separation of molybdenum and copper in porphyry deposits: The roles of sulfur, redox, and pH in ore mineral deposition at Bingham Canyon. Economic Geology 107: 333-356.

Seo, J. H. and Heinrich, C. A. (2013). Selective copper diffusion into quartz-hosted vapor inclusions: Evidence from other host minerals, driving forces, and consequences for Cu-Au ore formation. Geochimica et Cosmochimica Acta 113: 60-69.

Shannon, R. D. (1976). Revised effective ionic radii and systematic studies of interatomic distances in halides and chalcogenides. Acta crystallographica section A: crystal physics, diffraction, theoretical and general crystallography 32: 751-767.

Shinohara, H. (1994). Exsolution of immiscible vapor and liquid-phases from a crystallizing silicate melt - implications for chlorine and metal transport. Geochimica et Cosmochimica Acta 58: 5215-5221.

Sillitoe, R. H. (2010). Porphyry Copper Systems. Economic Geology 105: 3-41.

Simon, A. C., et al. (2008). The effect of crystal-melt partitioning on the budgets of Cu, An, and Ag. American Mineralogist 93: 1437-1448.

Simon, A. C., et al. (2004). Magnetite solubility and iron transport in magmatic-hydrothermal environments. Geochimica et Cosmochimica Acta 68: 4905-4914.
Singoyi, B., et al. (2006). Determination of trace elements in magnetites from hydrothermal deposits using the LA-ICP-MS technique (abstract). SEG 2006 Conference Society of Economic Geologists, Keystone, USA.

Spandler, C. and O'Neill, H. S. C. (2010). Diffusion and partition coefficients of minor and trace elements in San Carlos olivine at 1,300 C with some geochemical implications. Contributions to Mineralogy and Petrology 159: 791-818.

Spandler, C., et al. (2007). Survival times of anomalous melt inclusions from element diffusion in olivine and chromite. Nature 447: 303-306.

Spencer, E. T., et al. (2015). The distribution and timing of molybdenite mineralization at the El Teniente Cu-Mo porphyry deposit, Chile. Economic Geology 110: 387-421.

Spencer, K. J. and Lindsley, D. H. (1981). A solution model for coexisting iron-titanium oxides. American Mineralogist 66: 1189-1201.

Stanton, R. L. (1994). Ore Elements in Arc Lavas, Oxford: Clarendon Press.

Stormer, J. C. (1983). The effects of recalculation on estimates of temperature and oxygen fugacity from analyses of multicomponent iron-titanium oxides. American Mineralogist 68: 586-594.

Streck, M. J. and Dilles, J. H. (1998). Sulfur evolution of oxidized arc magmas as recorded in apatite from a porphyry copper batholith. Geology 26: 523-526.

Sun, W. D., et al. (2004). Release of gold-bearing fluids in convergent margin magmas prompted by magnetite crystallization. Nature 431: 975-978.

Tahmasebi, P., et al. (2010). Application of discriminant analysis for alteration separation; sungun copper deposit, East Azerbaijan, Iran. Australian Journal of Basic and Applied Sciences 6: 564-576.

Tatsumi, Y. and Eggins, S. (1995). Subduction Zone Magmatism. Oxford: Blackwell.

Toplis, M. (2005). The thermodynamics of iron and magnesium partitioning between olivine and liquid: criteria for assessing and predicting equilibrium in natural and experimental systems. Contributions to Mineralogy and Petrology 149: 22-39.

Toplis, M. and Carroll, M. (1995). An experimental study of the influence of oxygen fugacity on Fe-Ti oxide stability, phase relations, and mineral—melt equilibria in ferro-basaltic systems. Journal of Petrology 36: 1137-1170.

Toplis, M. J. and Corgne, A. (2002). An experimental study of element partitioning between magnetite, clinopyroxene and iron-bearing silicate liquids with particular emphasis on vanadium. Contributions to Mineralogy and Petrology 144: 22-37.

Toplis, M. J., et al. (1994). The Role of Phosphorus in Crystallization Processes of Basalt - an Experimental-Study. Geochimica et Cosmochimica Acta 58: 797-810.

Turnock, A. (1966). Fe-Nb Oxides: Phase Relations at 1180° C. Journal of the American Ceramic Society 49: 177-180.

Uemiya, S. (1999). State-of-the-art of supported metal membranes for gas separation. Separation and purification Methods 28: 51-85.

Ulmer, P. and Luth, R. W. (1991). The graphite-COH fluid equilibrium in P, T, space. Contributions to Mineralogy and Petrology 106: 265-272.

Ulrich, T., et al. (1999). Gold concentrations of magmatic brines and the metal budget of porphyry copper deposits. Nature 399: 676-679.

Ulrich, T., et al. (2001). The evolution of a porphyry Cu-Au deposit, based on LA-ICP-MS analysis of fluid inclusions: Bajo de la Alumbrera, Argentina. Economic Geology and the Bulletin of the Society of Economic Geologists 96: 1743-1774.

Van Baalen, M. (1993). Titanium mobility in metamorphic systems: a review. Chemical Geology 110: 233-249.

Van Orman, J. A. and Crispin, K. L. (2010). Diffusion in oxides. Reviews in Mineralogy and Geochemistry 72: 757-825.

Vogel, T. A., et al. (2001). Origin and emplacement of igneous rocks in the central Wasatch Mountains, Utah. Rocky Mountain Geology 36: 119-162.

Von Quadt, A., et al. (2011). Zircon crystallization and the lifetimes of ore-forming magmatic-hydrothermal systems. Geology 39(8): 731-734.

Vry, V., et al. (2010). Multistage intrusion, brecciation, and veining at El Teniente, Chile: Evolution of a nested porphyry system. Economic Geology 105: 119-153.

Wainwright, A. J., et al. (2011). U–Pb (zircon) and geochemical constraints on the age, origin, and evolution of Paleozoic arc magmas in the Oyu Tolgoi porphyry Cu–Au district, southern Mongolia. Gondwana Research 19: 764-787.

Wallace, P. J. and Carmichael, I. S. E. (1994). S-speciation in submarine basaltic glasses as determined by measurements of sk-alpha x-ray wavelength shifts. American Mineralogist 79: 161-167.

Wijbrans, C., et al. (2015). Experimental determination of trace element partition coefficients between spinel and silicate melt: the influence of chemical composition and oxygen fugacity. Contributions to Mineralogy and Petrology 169: 1-33.

Wilkinson, J. J. (2013). Triggers for the formation of porphyry ore deposits in magmatic arcs. Nature Geoscience 6: 917-925.

Wilkinson, J. J., et al. (2015). The chlorite proximitor: A new tool for detecting porphyry ore deposits. Journal of Geochemical Exploration 152: 10-26.

Williamson, B., et al. (2016). Porphyry copper enrichment linked to excess aluminium in plagioclase. Nature Geoscience 9: 237-241.

Wood, B. J., et al. (1990). Mantle oxidation-state and its relationship to tectonic environment and fluid speciation. Science 248: 337-345.

Wu, C. and Mason, T. O. (1981). Thermopower measurement of cation distribution in magnetite. Journal of the American Ceramic Society 64: 520-522.

Zacharias J. and Wilkinson, J.J. (2007). ExLAM 2000: Excel VBA application for processing of transient signals from laser ablation (LA-ICP-MS) of fluid inclusions and solid phases (abstract). ECROFIXIX Biennial Conference on European Current Research on Fluid Inclusions, Bern, Switzerland.

Zajacz, Z., et al. (2008). Determination of fluid/melt partition coefficients by LA-ICPMS analysis of co-existing fluid and silicate melt inclusions: controls on element partitioning. Geochimica et Cosmochimica Acta 72: 2169-2197.

Appendix 1: Analytical parameters

A1.1 SEM

A Zeiss EVO 15 LS Scanning Electron Microscope (SEM) with Energy Dispersive Spectrometry (EDS) housed at the Imaging and Analysis Centre at the Natural History Museum, London was used to petrologically investigate all experimental run products and natural samples in this PhD. Analytical condititions were 20 kV accelerating voltage and 3 nA beam current. Spot size was typically < 1 micron, although when analysing natural magnetite with strong exsolution, the beam was rastered over an area comparable to that to be analysed with LA-ICP-MS (e.g. 40 x 40 micron).

A1.2 EPMA

A Cameca SX-100 electron microprobe, housed at the Natural History Museum, London was used to measure major and some trace element contents in some experimental run products. Analytical parameters were as follows:

Parameter	**Mineral**	**Glass**
Chapter 2: Titanomagnetite-melt partitioning in an andesitic-dacitic bulk system		
Accelerating voltage (kV)	20	20
Sample current (nA)	10	2
Spot size (µm)	1	10-20
Elements	Si, Al, Mg, Fe, Ca, P, Ti, Mn, Na, Cr, K, V	Si, Al, Mg, Fe, Ca, P, Ti, Mn, Na, Cr, K
Chapter 3: Diffusion and partition coefficients of minor and trace elements in magnetite as a function of oxygen fugacity		
Accelerating voltage (kV)	-	20
Sample current (nA)	-	2
Spot size (µm)	-	10-20
Elements		Ca, Fe, Si
Chapter 4: Titanomagnetite-melt partitioning at high-pressure and temperature in an andesitic hydrous bulk system		
Accelerating voltage (kV)	20	20
Sample current (nA)	10	2
Spot size (µm)	1	10-20
Elements	Si, Al, Mg, Fe, Ca, P, Ti, Mn, Na, Cr, K, V	Si, Al, Mg, Fe, Ca, P, Ti, Mn, Na, Cr, K

The following standards and crystals were used to calibrate EPMA analysis

Element	Standard mineral	Std code	Crystal
Na	Jadite	JAD3 STD048	LTAP
Mg	Forsterite	FOR STD277	LTAP
Al	Corundum	COR4 STD028	LTAP
Si	Fayalite	FAY STD278	LTAP
K	Orthoclase	ORT3 STD067	LPET
Ca	Wollastonite	WOL4 STD097	PET
Ti	Rutile	RUT STD082	LPET
Cr	Chromite	CRO2 STDIC	LPET
Mn	Manganite	MNT STDIC	LLIF
V	Vanadanite	VAN STDIC	LLIF
Fe	Hematite	FeO STDIC	LLIF
P	Scandium Phosphate	SCP STD217	LPET

Peak overlap corrections for Fe, Ti and V were done using Cameca software.

A1.3 LA-ICP-MS

Laser ablation inductively-coupled plasma mass-spectrometry (LA-ICP-MS) was conducted at the LODE Research Facility at the Natural History Museum, London and at the Research School of Earth Sciences (RSES) at the Australian National University (ANU). The LA-ICP-MS at ANU consists of an Agilent 7700x quadrupole ICP-MS coupled to a Resonetics 193nm excimer laser with a custom-built ablation chamber. At the LODE Research Facility, a New Wave Research 193nm excimer laser coupled is coupled to an Agilent 7700x quadrupole ICP-MS. Analytical parameters were as follows:

Parameter	Fe-Ti oxide	Glass
Chapter 2: Titanomagnetite-melt partitioning in an andesitic-dacitic bulk system at 1-atm		
Laser		
Instrument	ESI NWR193	ESI NWR193
Laser type	ArF excimer	ArF excimer
Wavelength	193 nm	193 nm
Laser frequency (Hz)	5	10
Laser analysis type	Spot	Spot
Beam size (μm)	11-35	20-50
Fluence (J cm^{-2})	3.5 J cm^{-2}	3.5 J cm^{-2}
Carrier gas (He)	350-600 ml/min	350 ml/min
Primary standard	GSD-1g	GSD-1g
Secondary standard(s)	GSE-1g, BC28	NIST 612
Internal Standard	Fe (EPMA)	Ca (EPMA)
Mass Spectrometer		
Instrument	Agilent 7700 ICP-Q-MS	Agilent 7700 ICP-Q-MS
Plasma gas flow (Ar)	1.1 l/min	1.1 l/min
Analysis duration	90	90
Blank duration	30	30

Parameter	**Fe-Ti oxide**	**Glass**
Isotopes analysed	^{23}Na, ^{24}Mg, ^{27}Al, ^{29}Si, ^{31}P, ^{39}K, ^{43}Ca, ^{45}Sc, ^{49}Ti, ^{51}V, ^{52}Cr, ^{55}Mn, ^{57}Fe, ^{59}Co, ^{60}Ni, ^{63}Cu, ^{65}Cu, ^{66}Zn, ^{69}Ga, ^{72}Ge, ^{89}Y, ^{90}Zr, ^{93}Nb, ^{95}Mo, ^{115}In, ^{118}Sn, ^{177}Hf, ^{181}Ta, ^{182}W, ^{208}Pb, ^{232}Th and ^{238}U	^{23}Na, ^{24}Mg, ^{27}Al, ^{29}Si, ^{31}P, ^{39}K, ^{43}Ca, ^{45}Sc, ^{49}Ti, ^{51}V, ^{52}Cr, ^{55}Mn, ^{57}Fe, ^{59}Co, ^{60}Ni, ^{63}Cu, ^{65}Cu, ^{66}Zn, ^{69}Ga, ^{72}Ge, ^{89}Y, ^{90}Zr, ^{93}Nb, ^{95}Mo, ^{115}In, ^{118}Sn, ^{177}Hf, ^{181}Ta, ^{182}W, ^{208}Pb, ^{232}Th and ^{238}U
Data reduction	In-house software (ExLAM)	In-house software (ExLAM)
Chapter 3: Diffusion and partition coefficients of minor and trace elements in magnetite as a function of oxygen fugacity		
Laser		
Instrument	ESI NWR193 (LODE)/Res. M-50 (RSES)	ESI NWR193 (LODE)
Laser type	ArF excimer	ArF excimer
Wavelength	193 nm	193 nm
Laser frequency (Hz)	5	10
Laser analysis type	Rectangle (1 µm/s traverse)	Spot
Beam size (µm)	100 x 6	50
Fluence (J cm^{-2})	3.5 J cm^{-2}	3.5 J cm^{-2}
Carrier gas (He)	350-600 ml/min	350 ml/min
Primary standard	BCR-2g	NIST 612
Secondary standard(s)	GSD-1g, GSE-1g	GSD-1g
Internal Standard	Fe (SEM-EDS)	Ca (EPMA)
Mass Spectrometer		
Instrument	Agilent 7700 ICP-Q-MS (LODE and RSES)	Agilent 7700 ICP-Q-MS (LODE)
Plasma gas flow (Ar)	1.1 l/min	1.1 l/min
Analysis duration	90	90
Blank duration	30	30
Isotopes analysed	^{24}Mg, ^{27}Al, ^{29}Si, ^{31}P, ^{43}Ca, ^{45}Sc, ^{49}Ti, ^{51}V, ^{52}Cr, ^{55}Mn, ^{57}Fe, ^{59}Co, ^{60}Ni, ^{63}Cu, ^{65}Cu, ^{66}Zn, ^{69}Ga, ^{72}Ge, ^{75}As, ^{89}Y, ^{90}Zr, ^{93}Nb, ^{95}Mo, ^{115}In, ^{175}Lu, ^{177}Hf, ^{181}Ta, ^{182}W, ^{208}Pb, ^{232}Th and ^{238}U	^{24}Mg, ^{27}Al, ^{29}Si, ^{31}P, ^{43}Ca, ^{45}Sc, ^{49}Ti, ^{51}V, ^{52}Cr, ^{55}Mn, ^{57}Fe, ^{59}Co, ^{60}Ni, ^{63}Cu, ^{65}Cu, ^{66}Zn, ^{69}Ga, ^{72}Ge, ^{75}As, ^{89}Y, ^{90}Zr, ^{93}Nb, ^{95}Mo, ^{115}In, ^{175}Lu, ^{177}Hf, ^{181}Ta, ^{182}W, ^{208}Pb, ^{232}Th and ^{238}U
Data reduction	In-house software (ExLAM) (LODE)/IOLITE software (RSES)	In-house software (ExLAM) (LODE)
Chapter 4: Titanomagnetite-melt partitioning in an andesitic hydrous bulk system at elevated pressure		
Laser		
Instrument	ESI NWR193	ESI NWR193
Laser type	ArF excimer	ArF excimer
Wavelength	193 nm	193 nm
Laser frequency (Hz)	5	10
Laser analysis type	Rectangle (1 µm/s traverse)	Spot
Beam size (µm)	3 x 50	30-50
Fluence (J cm^{-2})	3.5 J cm^{-2}	3.5 J cm^{-2}
Carrier gas (He)	350-600 ml/min	350 ml/min
Primary standard	GSD-1g	GSD-1g

Parameter	**Fe-Ti oxide**	**Glass**
Secondary standard(s)	GSE-1g, BC28	NIST 612
Internal Standard	Fe (EPMA)	Ca (EPMA)
Mass Spectrometer		
Instrument	Agilent 7700 ICP-Q-MS	Agilent 7700 ICP-Q-MS
Plasma gas flow (Ar)	1.1 l/min	1.1 l/min
Analysis duration	90	90
Blank duration	30	30
Isotopes analysed	^{23}Na, ^{24}Mg, ^{27}Al, ^{29}Si, ^{31}P, ^{39}K, ^{43}Ca, ^{45}Sc, ^{49}Ti, ^{51}V, ^{52}Cr, ^{55}Mn, ^{57}Fe, ^{59}Co, ^{60}Ni, ^{63}Cu, ^{65}Cu, ^{66}Zn, ^{69}Ga, ^{72}Ge, ^{75}As, ^{89}Y, ^{90}Zr, ^{93}Nb, ^{95}Mo, ^{115}In, ^{118}Sn, ^{121}Sb, ^{175}Lu, ^{177}Hf,^{181}Ta, ^{182}W, ^{208}Pb, ^{232}Th and ^{238}U	^{23}Na, ^{24}Mg, ^{27}Al, ^{29}Si, ^{31}P, ^{39}K, ^{43}Ca, ^{45}Sc, ^{49}Ti, ^{51}V, ^{52}Cr, ^{55}Mn, ^{57}Fe, ^{59}Co, ^{60}Ni, ^{63}Cu, ^{65}Cu, ^{66}Zn, ^{69}Ga, ^{72}Ge, ^{75}As, ^{89}Y, ^{90}Zr, ^{93}Nb, ^{95}Mo, ^{115}In, ^{118}Sn, ^{121}Sb, ^{175}Lu, ^{177}Hf,^{181}Ta, ^{182}W, ^{208}Pb, ^{232}Th and ^{238}U
Data reduction	In-house software (ExLAM)	In-house software (ExLAM)
Chapter 5: Developing method for LA-ICP-MS of natural magnetite		
Laser		
Instrument	ESI NWR193	
Laser type	ArF excimer	
Wavelength	193 nm	
Laser frequency (Hz)	5	
Laser analysis type	Spot	
Beam size (μm)	10-100	
Fluence (J cm^{-2})	3.5 J cm^{-2}	
Carrier gas (He)	350-600 ml/min	
Primary standard	GSD-1g, GSE-1g, BCR-2g, NIST 610	
Secondary standard(s)	GSD-1g, GSE-1g, BCR-2g, NIST 610, BC28	
Internal Standard	Fe (SEM-EDS – *ImageJ and rastered beam*)	
Mass Spectrometer		
Instrument	Agilent 7700 ICP-Q-MS	
Plasma gas flow (Ar)	1.1 l/min	
Analysis duration	90	
Blank duration	30	
Isotopes analysed	^{7}Li, ^{23}Na, ^{24}Mg, ^{27}Al, ^{29}Si, ^{31}P, ^{39}K, ^{43}Ca, ^{45}Sc, ^{49}Ti, ^{51}V, ^{52}Cr, ^{55}Mn, ^{57}Fe, ^{59}Co, ^{60}Ni, ^{63}Cu, ^{65}Cu, ^{66}Zn, ^{71}Ga, ^{72}Ge, ^{75}As, ^{88}Sr, ^{89}Y, ^{92}Zr, ^{93}Nb, ^{95}Mo, ^{115}In, ^{118}Sn, ^{121}Sb, ^{139}La, ^{140}Ce, ^{175}Lu, ^{177}Hf, ^{181}Ta, ^{182}W, ^{208}Pb, ^{209}Bi, ^{232}Th and ^{238}U	
Data reduction	In-house software (ExLAM)	
Chapter 6: Geochemistry of magnetite from porphyry copper systems		
Laser		
Instrument	ESI NWR193	
Laser type	ArF excimer	

Parameter	Fe-Ti oxide	Glass
Wavelength	193 nm	
Laser frequency (Hz)	5	
Laser analysis type	Spot	
Beam size (μm)	15-50	
Fluence (J cm^{-2})	3.5 J cm^{-2}	
Carrier gas (He)	350-600 ml/min	
Primary standard	GSD-1g	
Secondary standard(s)	GSE-1g, BC28	
Internal Standard	Fe (SEM-EDS)	
Mass Spectrometer		
Instrument	Agilent 7700 ICP-Q-MS	
Plasma gas flow (Ar)	1.1 l/min	
Analysis duration	90	
Blank duration	30	
Isotopes analysed	^{7}Li, ^{23}Na, ^{24}Mg, ^{27}Al, ^{29}Si, ^{31}P, ^{39}K, ^{43}Ca, ^{45}Sc, ^{49}Ti, ^{51}V, ^{52}Cr, ^{55}Mn, ^{57}Fe, ^{59}Co, ^{60}Ni, ^{63}Cu, ^{66}Zn, ^{71}Ga, ^{72}Ge, ^{75}As, ^{88}Sr, ^{89}Y, ^{92}Zr, ^{93}Nb, ^{95}Mo, ^{107}Ag, ^{111}Cd, ^{115}In, ^{118}Sn, ^{121}Sb, ^{139}La, ^{140}Ce, ^{175}Lu, ^{177}Hf, ^{181}Ta, ^{182}W, ^{185}Re, ^{195}Pt, ^{197}Au, ^{205}Tl, ^{208}Pb, ^{209}Bi, ^{232}Th and ^{238}U	
Data reduction	In-house software (ExLAM)	

Detection limits were calculated using the methodology of Longerich et al. (1996) as three times the gas background signal that contains zero analyte for all spot analyses. For traverse analyses where data were processed in natural fashion, if an element concentration fluctuated below 0 along the part of the traverse with a discernible diffusion profile, it was classified as below detection limit.

The accuracy of analyses was interpreted for all LA-ICP-MS analysis by comparing concentrations of secondary standards with reported values. Accuracy was generally better than 10% for all elements apart from P when analyzing GSE-1g using GSD-1g as the external standard. An example of a plot indicating deviation from reported values for GSE-1g and BC-28, analysed whilst collecting natural magnetite data in Chapter 6 are provided in Figure A1-1; all other plots to assess accuracy are provided in Appendix 3.

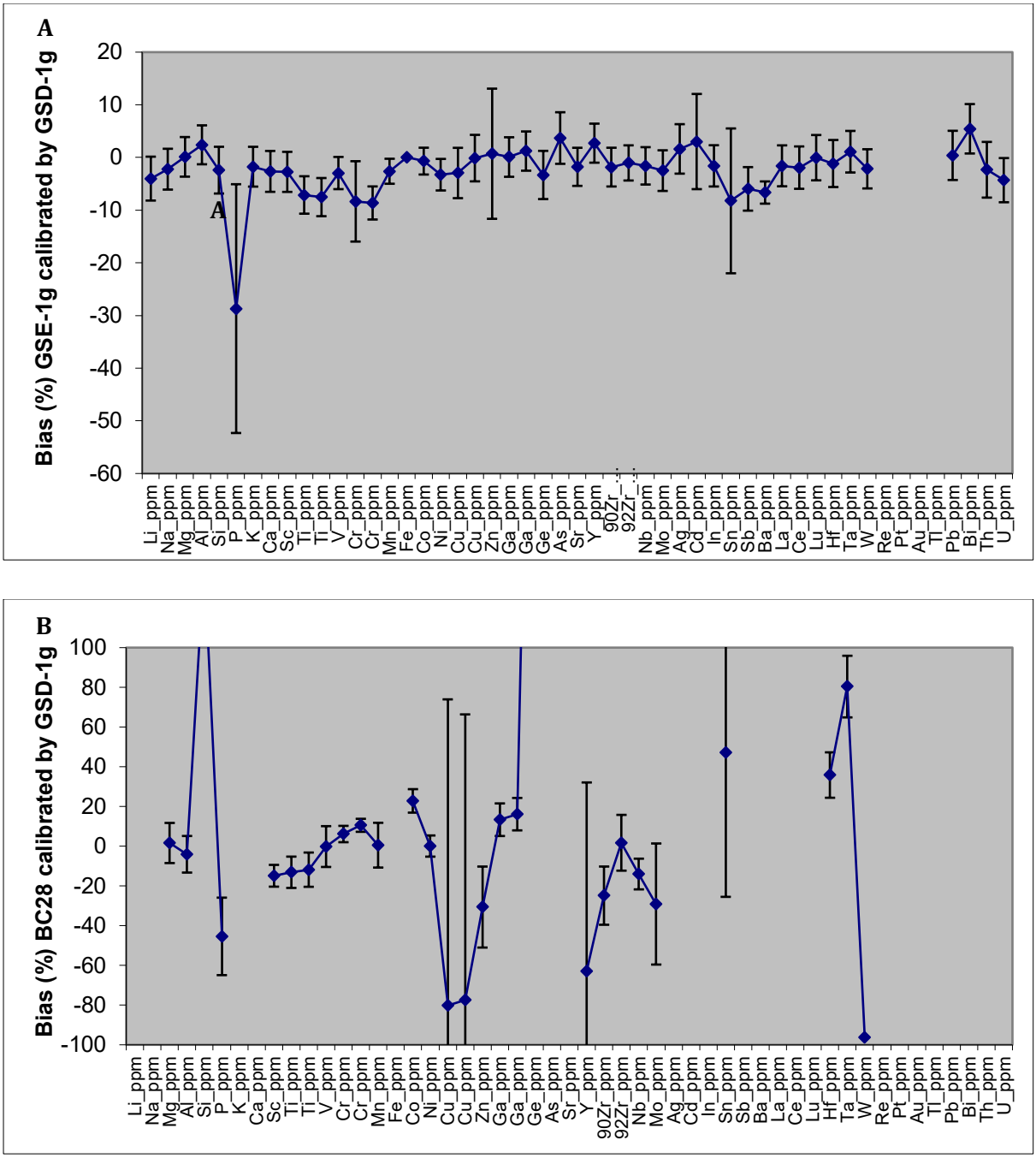


Figure A1-1: Plot showing bias for concentrations in (A) GSE-1g and (B) BC28 determined for data collected for Chapter 6 using GSD-1g as the external standard relative to concentrations reported by Dare et al. (2012). Bias is calculated as (concentration measured-reported concentration)/reported concentration. Error bars are relative standard deviation (%) determined as 100(1σ/mean concentration for multiple analyses).*

A1.1.1 Isotope interferences

A challenge with LA-ICP-MS analysis is the identification of which isotope of a desired element is least likely to suffer from interferences by elemental or molecular species sharing the same mass-to-charge ratio. Such interferences are additive, resulting in an overestimate of the concentration of the species being interfered with. For example, the concentrations of Zr, Cu and Ga determined using certain isotopes have previously been suggested to be susceptible to argide or oxide

formation involving isotopes of lower mass (Dare et al., 2012). Consequently, a series of magnetite analyses from rocks surrounding a porphyry copper deposit (Resolution) were conducted in which several isotopes of Zr, Cu and Ga were measured in order to assess the possible interferences and decide which isotope produces the most reliable results.

A1.1.1.1 Method

All analyses were conducted using a New Wave Research 193nm laser coupled with an Agilent 7700x housed at the Natural History Museum London. Analysis duration was 90s, with the first 30 s monitoring a gas blank prior to ablation. The masses analysed were ^{7}Li, ^{23}Na, ^{24}Mg, ^{27}Al, ^{29}Si, ^{31}P, ^{39}K, ^{43}Ca, ^{45}Sc, ^{49}Ti, ^{51}V, ^{52}Cr, ^{55}Mn, ^{57}Fe, ^{59}Co, ^{60}Ni, **^{63}Cu, ^{65}Cu**, ^{66}Zn, **^{69}Ga, ^{71}Ga**, ^{72}Ge, ^{75}As, ^{88}Sr, ^{89}Y, **^{90}Zr, ^{91}Zr, ^{92}Zr, ^{94}Zr, ^{96}Zr,** ^{93}Nb, ^{95}Mo, ^{115}In, ^{118}Sn, ^{121}Sb, ^{139}La, ^{140}Ce, ^{175}Lu, ^{177}Hf, ^{181}Ta, ^{182}W, ^{208}Pb, ^{209}Bi, ^{232}Th and ^{238}U (Highlighted are those isotopes interrogated). The laser was operated with 3.5 J/cm^{2} fluence and 10 Hz frequency. GSD-1g was used as the calibration standard and GSE-1g was used for monitoring. The Fe content, previously determined using SEM-EDS, was used as the internal standard for processing. Data were reduced using ExLAM 2000.

A1.1.1.2 Results and Discussion

Zirconium

The various isotopes of Zr analysed in magnetite give contrasting values for total concentration of Zr. Despite this, the glasses used as secondary standards do not have this problem. Clearly, there is an interference from another element, present at a high concentration in magnetite, which is responsible.

Zirconium has five isotopes present naturally in the following abundances:

Isotope	^{90}Zr	^{91}Zr	^{92}Zr	^{94}Zr	^{96}Zr
Abundance	51.45%	11.22%	17.15%	17.35%	2.8%

When analysing the glass geochemical reference material GSE-1g using GSD-1g as the calibration standard, there is generally good correlation between the between all isotopes of Zr, apart from ^{96}Zr, which is generally underestimated (due to low abundance/near detection limit values). When analysing a series of natural magnetite grains, however, there are notable differences: ^{90}Zr and ^{91}Zr are strongly correlated; ^{92}Zr is approximately 55.5% of the value of ^{90}Zr (also found by Dare et al., 2012); ^{94}Zr gives slightly lower values than ^{90}Zr; and ^{96}Zr produces significantly lower concentrations, similar to the glass results (Figure A1-2).

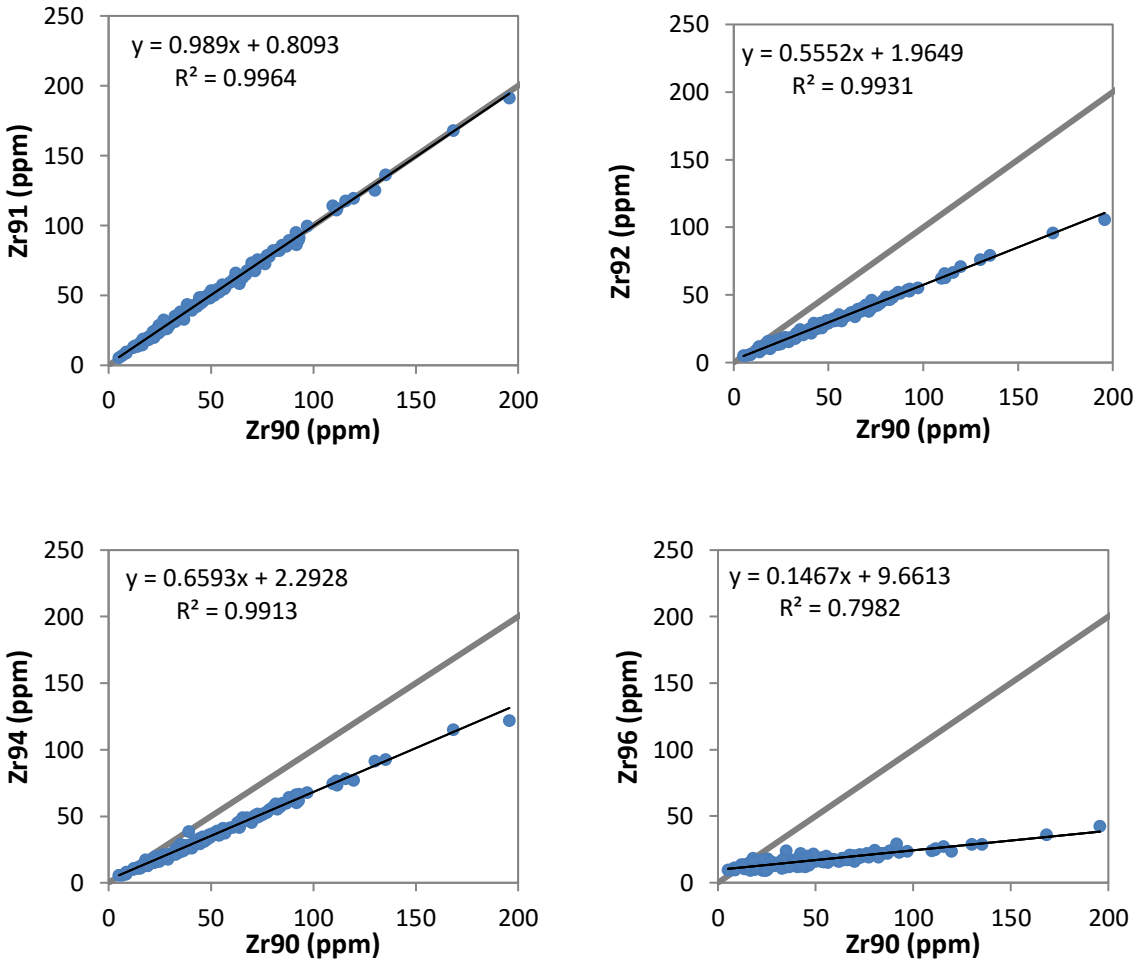


Figure A1-2: Comparison of Zr concentrations derived from the measurement of ^{90}Zr in a series of natural magnetite analyses with concentrations derived from the other isotopes of Zr. Data included are analyses of magnetite associated with propylitic rocks surrounding Resolution porphyry copper deposit. GSD-1g was used as the calibration standard and Fe as the internal standard. Grey line is 1:1 correlation. Black line is a linear regression with the equation for the line and Pearson's linear correlation coefficient provided in the top left of each plot.

It would seem that ^{96}Zr is too low in abundance (2.8%) to produce reliable concentrations in both glass and magnetite. The correlation between ^{91}Zr and ^{90}Zr, which both produce considerably higher concentrations than those generated from ^{92}Zr and ^{94}Zr, is probably due to an interference, likely with another isotope which also has two consecutive isotopes in a similar ratio to ^{90}Zr and ^{91}Zr (~4.6).

When analysing material with a high concentration of Ti (e.g. > 5 wt.%), it is possible that ^{49}Ti and ^{50}Ti could generate interferences on ^{90}Zr and ^{91}Zr respectively, via the production of $^{49}Ti^{40}ArH^+$, $^{50}Ti^{40}Ar$ and $^{50}Ti^{40}ArH^+$. An argide (^{40}Ar) interference on ^{50}Ti was postulated by Dare et al. (2012) to account for elevated ^{90}Zr but this would not account for the equivalent increase in ^{91}Zr observed here.

Other possible argide interferences on Zr isotopes include those involving V and Cr, or doubly-charged species such as $^{180}W^{2+}$ and $^{182}W^{2+}$. The abundances of the Cr isotopes ^{50}Cr and ^{52}Cr are 4.3% and 83.4% respectively; however, because the concentration of Zr determined using ^{90}Zr is greater than when using ^{92}Zr, it is unlikely that argides of Cr are responsible. Furthermore, the concentrations of Cr measured in the magnetite studied here are generally low (< 0.1 wt. %). ^{50}V and ^{51}V could produce ^{40}Ar interferences on ^{90}Zr and ^{91}Zr but the natural abundance of ^{51}V is 99.75% so that there should be almost no effect on ^{90}Zr relative to a large effect on ^{91}Zr if this interference were the sole cause of the problem.

In summary, it is not clear exactly what the nature of the interference is on zirconium isotopes and it would appear likely that more than one interfering element is involved, in the form of argides and argon hydrides. Ti is the most likely major contributor but the isotope ratios do not support this as a sole contributor; other high field strength elements are also enriched in titanomagnetite (e.g. Cr, V) so these could also be involved.

It is concluded that ^{92}Zr is the preferred isotope to measure because it experiences the least contribution from an interference (there could still be minor interference by $^{50}TiArH^{2+}$ or $^{51}VArH^{+}$), but appears to produce reliable concentrations in both glass and magnetite.

Copper

As recommended by Dare et al. (2012), both ^{63}Cu and ^{65}Cu were measured. ^{63}Cu has been suggested as the most accurate isotope to analyse based on the slightly lower concentrations generally observed by Dare et al. (2012). Notwithstanding this, there is a 1:1 correlation between ^{63}Cu and ^{65}Cu in this dataset (Figure A1-3), suggesting there are no significant interferences affecting the Cu concentrations determined. On this basis, ^{63}Cu is recommended as "standard" because of its greater isotopic abundance (69.17% vs. 30.83%) which will yield lower limits of detection and better precision for a given set of operational conditions.

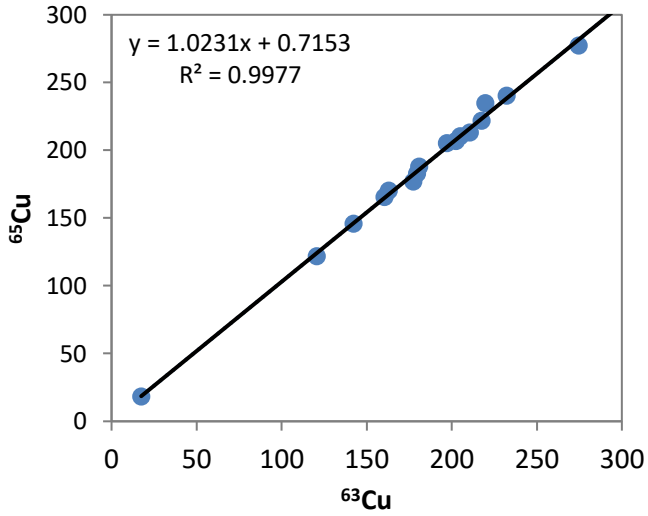


Figure A1-3: Concentration of Cu (ppm) determined using ^{65}Cu vs. that determined using ^{63}Cu. Data included are analyses of magnetite associated with propylitic rocks surrounding Resolution porphyry copper deposit.

Gallium

Similar to Cu, Dare et al. (2012) suggested that two isotopes of Ga, both ^{69}Ga and ^{71}Ga, should be measured. However, both isotopes produce identical results here, with an excellent 1:1 correlation (Figure A1-4). This suggests that there are no significant interferences for Ga during analysis of titanomagnetite. As above, ^{69}Ga is recommended as "standard" because of its greater isotopic abundance (60.108% vs. 39.892%).

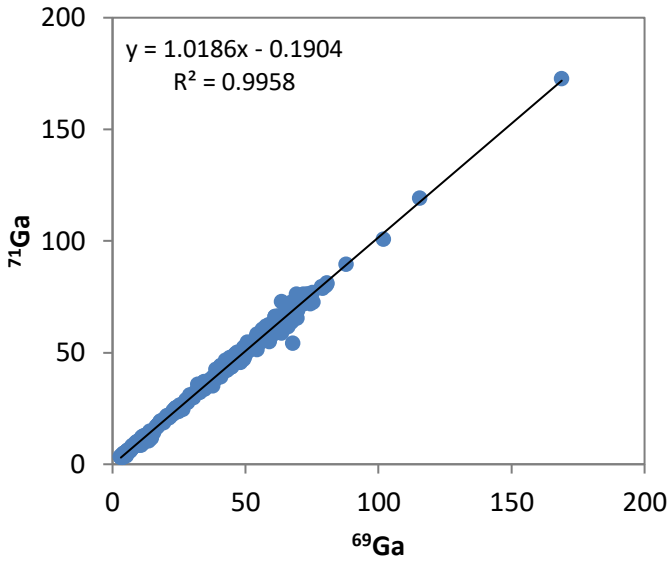


Figure A1-4: Concentrations of Ga (ppm) determined using ^{71}Ga vs. that determined using ^{69}Ga. Data included are analyses of magnetite associated with propylitic rocks surrounding Resolution porphyry copper deposit.

Appendix 2: Experimental set-up

A2.1 1-atm furnace

The one-atmosphere furnace (GERO HTRV 70-250/18) allows for experiments under fixed oxygen fugacity up to temperatures in excess of 1600°C. The furnace is heated using $MoSi_2$ elements, with the power supply controlled by a Eurotherm controller which monitors the temperature with a type-B thermocouple. The samples are separated from the heating elements by an alumina furnace tube that is water cooled at both ends and made gas tight by a cap at the top and a ball valve at the base of the furnace. At the top of the sample rod, a pyrophyllite baffle is glued to insulate the exterior of the furnace. During experiments, samples are held in the hot-spot of the furnace on an alumina rod. To terminate experiments, samples can be mechanically drop quenched into water using a release mechanism at the top of the furnace. Figure A2-1 shows a schematic diagram of the 1-atm gas-mixing furnace used.

In the fO_2 range investigated in this study, the fO_2 can be controlled through mixing different ratios of carbon dioxide (CO) and carbon dioxide (CO_2). Equations from Deines et al. (1974) can be used to calculate the gas flow ratios of CO and CO_2 required to obtain the desired fO_2 at a given temperature.

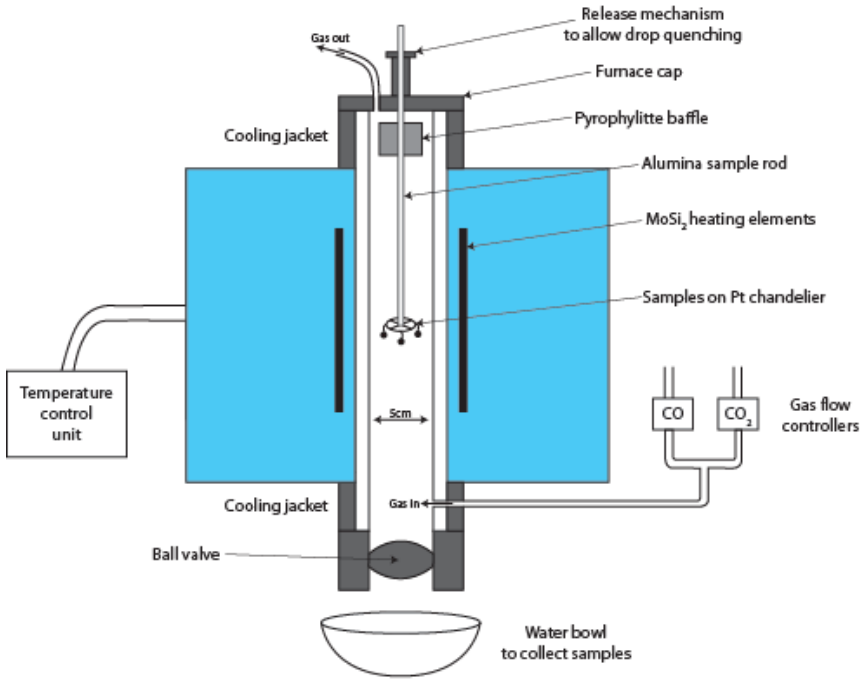


Figure A2-1: Schematic diagram of a 1-atm gas mixing furnace. See text for further explanation.

A2.1.1 Calibrating the 1-atm gas mixing furnace

A calibration is required to locate the hottest part of the furnace. To do so, a thermocouple was passed through an alumina rod to where the sample hangs in the furnace. The vertical temperature distribution can then be determined by lowering the rod through the alumina furnace tube and recording the potential difference between the two thermocouple wires at chosen intervals. Results indicate a 3 cm hot spot in the centre of the furnace across which the temperature varies by < 1°C. Samples were held in this region in all experiments.

The Eurotherm controller employs a thermocouple which is not situated within the hot spot of the furnace and does not record the exact temperature experienced by the sample. An additional calibration is therefore necessary to determine the relationship between the true temperature within the hot spot and the temperature measured by the Eurotherm controller. The furnace used at Imperial College London for experiments in Chapter 2 was calibrated by myself (Figure A2-2). For experiments in Chapter 3 conducted at ANU, the furnace was recently calibrated by lab technicians.

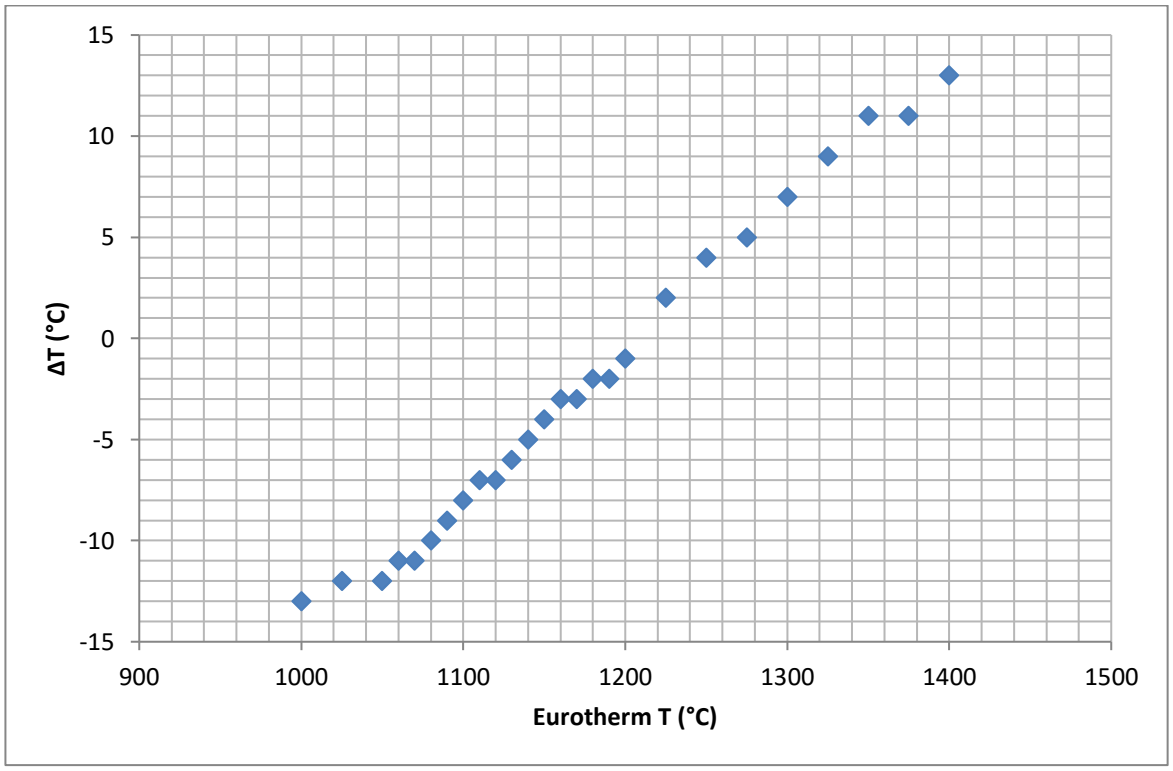


Figure A2-2:. Difference between the temperature of the hotspot within the furnace and the temperature measured by the Eurotherm controller for furnace used in experiments at Imperial College London in Decemeber 2013.

The fO_2 of the furnaces used in all experiments were previously calibrated using an SiO_2 solid state electrode at relevant fO_2 values. Prior to conducting experiments at Imperial College London (Chapter 2), in order to ensure the mass flow controllers were performing correctly, additional calibration experiments were conducted using the solubility of Ni in a silicate melt of anorthite-diopside eutectic composition. Ni metal can coexist with a silicate melt below the nickel-nickel oxide buffer, with Ni dissolving in the melt according to the reaction:

$$Ni_{(metal)} + ½\ O_2 \rightleftharpoons NiO_{(silicate)}$$

The solubility of Ni^{2+} in the silicate melt will be governed by the equilibrium constant:

$$K = \frac{a_{NiO}}{a_{Ni} \times (fO_2)^{0.5}}$$

thus,

$$\log K = -\frac{1}{2} \log fO_2 + logX_{NiO} + log\gamma_{NiO}$$

where X_{NiO} is the mole fraction of NiO dissolved in the silicate melt, and γ_{NiO} is the corresponding activity coefficient of NiO. Using the thermodynamic relation $\Delta G = -RT\ln K$, the fO_2 of the sample can be calculated provided ΔG and the activity of NiO are known. The ΔG expression of Holzheid et al. (1997) and the γ_{NiO} data from O'Neill and Eggins (2002) can be used in conjunction to obtain $\log fO_2$ in terms of temperature (in kelvin) and the NiO content of a melt of anorthite-diopside eutectic composition:

$$\log fO_2 = 2(-\frac{9668}{T} - 0.589 \times \log T + 5.616 + \log X_{NiO})$$

Glasses of the anorthite-diopside eutectic mix (42% anorthite, 58% diopside) were prepared on loops of Ni metal and ran in the furnace at $\log fO_2$ = - 8.0 and – 7.0 at 1400°C for 24 hours. The composition of the glass was analysed using energy dispersive spectrometry (EDS) on a Zeiss Evo 15LS and the corresponding fO_2 calculated (Table A2-1).

Table A2-1. X_{NiO} of anorthite-diopside eutectic glass in equilibrium with Ni, determined by EDS. Errors are 1σ and number of analyses are given in brackets.

Experiment	**log fO_2 (target)**	**T (K)**	**X_{NiO}**	**log fO_2 (calculated)**
AD eutectic on Ni - 1	-8.0	1673	0.0134 ± 0.00046 (12)	-7.87 ± 0.030 (12)
AD eutectic on Ni - 2	-7.0	1673	0.0404 ± 0.00071 (15)	-6.91 ± 0.015 (15)

Temperature in all 1-atm furnace used is accurate to ± 1°C C and $\log fO_2$ is accurate to ± 0.1.

A2.2 Piston-cylinder apparatus

The piston-cylinder experiments allow for experiments at elevated pressure, up to 4 GPa for ½ inch assembly diameter and temperatures in excess of 1800°C. The piston cylinder apparatus used for experiments in Chapter 4 were 150 and 200 ton presses at the RSES, ANU. The presses have 7.5 inch end load ram and a 3 inch Boyd ram making a compact press. Temperature is controlled by passing a current through a graphite cylinder which comprises part of the assembly containing the sample. The design of the assembly allows for inserting a thermocouple for that sample temperature can be monitored and regulated using a Eurotherm controller.

Appendix 3: EPMA and LA-ICP-MS Data

See attached excel files for Chapters 2, 3, 4, 5, and 6.

Appendix 4: Trace Element Chemistry of Magnetite as an Indicator of the Metallogenic Fertility of Arc Magmas (Fry, 2017)

See attached MSci Thesis

Additional References

Deines, P., et al. (1974). Temperature-oxygen fugacity tables for selected gas mixtures in the C-H-O system at one atmosphere total pressure. Bulletin Of the Earth and Mineral Science, the Pennsylvania State University, 88: 32-59.

Holzheid, A., et al. (1997). The activities of NiO, CoO and FeO in silicate melts. Chemical Geology 139: 21-38.